

Acoustic wave propagation in lossy, structured and periodic media

Jean-Philippe Groby

«Habilitation à Diriger des Recherches» in Acoustics
Le Mans University, France, 2017



LE MANS UNIVERSITY

Le Mans - France

HABILITATION À DIRIGER DES RECHERCHES

in Acoustics

Submitted by

Jean-Philippe Groby

Acoustic wave propagation in lossy, structured and periodic media

Presented to the panel composed of

Prof. K. Horoshenkov	University of Sheffield	Reviewer
Prof. A. Norris	Rutgers University	Reviewer
Prof. J. Sánchez-Dehesa	Universitat Politècnica de València	Reviewer
Y. Aurégan, DR CNRS	Laboratoire d'Acoustique de l'Université du Mans, UMR CNRS 6613	Examiner
D. Lesselier, DR CNRS	Laboratoire des Signaux et Systèmes, UMR CNRS 8506	Examiner
Prof. P. Sheng	Hong Kong University of Science and Technology	Examiner
A. Wirgin, DR émérite CNRS	Laboratoire de Mécanique et d'Acoustique, UPR CNRS 7051	Examiner

Acknowledgement

First, I would like to thank the jury members for having accepted to review and evaluate this Habilitation. I am very proud that they accepted despite their busy agenda.

Then, I would like to thank the different directors of the Acoustic Laboratory of Le Mans University (LAUM) since my nomination in 2009 for having encouraged the development of my activities. Generally, I would like to thank every person working in this laboratory for the excellent working atmosphere and the cohesion among the LAUM members.

More specifically, I would like to thank all the colleagues, from France and abroad, with whom I used to work, currently work, and will work. They will recognize part of the joint work we did together in this manuscript. In particular, I would like to thank Armand Wirgin for whom I have great respect. I would also like to express my special attachement to my PhD students and Post-docs, who greatly contributed to this work.

Finally, I would like to thank my friends for discussions, support, and loyalty (they will recognize themselves), Pauline for these last years, Jean-Marc(s) who are from time to time in the corner of my mind, and my parents for their unconditional love. To end, I still miss Walter, who left us too early.

Contents

Foreword	1
I Presentation of the main scientific results	3
1 Gratings and (meta)surfaces	5
1.1 Geophysical application: the site-city effect	5
1.1.1 Site and regional effects: the excitation of Love mode	6
1.1.2 The soil-structure and structure-soil-structure interactions	8
1.1.3 The site-city effect	8
1.2 Acoustic application: metaporous and metaporoelastic materials	9
1.2.1 Usual absorption by rigid frame porous layers	10
1.2.2 Metaporous and metaporoelastic layers	10
2 Periodic and macroscopically inhomogeneous bulk materials and their limitations	15
2.1 Macroscopically inhomogeneous (graded) porous materials	15
2.2 Resonant sonic crystals	16
2.3 Slow sound propagation: design of deep-subwavelength absorbers and other application	18
3 Acoustic characterization of materials and structures	23
3.1 Characterization of porous (rigid frame) materials	23
3.2 Experimental reconstruction of complex wavenumber / frequency dispersion relation	26
Conclusion and perspectives	29
Appendix	31
II Scientific Curriculum Vitæ	43
4 Curriculum vitæ	45
4.1 Short Bio	45

CONTENTS

4.2	Activities	46
5	Scientific output	55
5.1	PhD Dissertation	55
5.2	Peer-reviewed journal articles	55
5.3	Chapters in Book	59
5.4	Technology transfer	60
5.5	Conference proceedings	60
5.6	Workshops	67
5.7	Oral Presentation, Seminars, and other talks	68
III	Selected publications	71
6	Articles related to Chapter 1: Gratings and (meta)surfaces	73
	Geophys. J. Int., 172:725-758, 2008	74
	J. Acoust. Soc. Am., 130:3771-3780, 2011	108
	J. Acoust. Soc. Am., 137: 273-280, 2015	118
	Appl. Acoust., 102: 49-54, 2016	126
7	Articles related to Chapter 2: Periodic and macroscopically inhomogeneous bulk materials and their limitations	132
	Appl. Phys. Lett., 90:181901, 2007	133
	J. Acoust. Soc. Am., 130:1390-1398, 2011	136
	J. Acoust. Soc. Am., 133:247-254, 2013	145
	J. Acoust. Soc. Am., 139:1660-1671, 2016	153
	Appl. Phys. Lett., 109:121902, 2016	165
	arXiv:1708.03343v1	169
	Sci. Rep., 7:5389, 2017	182
8	Articles related to Chapter 3: Acoustic characterization of materials and structures	194
	J. Acoust. Soc. Am., 127:764-772, 2010	195
	J. Appl. Phys., 120:135107, 2016	203
	Appl. Phys. Lett., 110:051902, 2017	211

Foreword

This manuscript attempts to give an overview of my research activities since the beginning of my PhD in 2002.

The first part of the document describes the major scientific achievements. I have tried to present these achievements in three brief chapters, the redaction of which depends on the maturity of the corresponding activities. This brevity is now recommended by most of the French Universities. The first chapter, composed of two sections, gathers activities related to gratings and metasurfaces, including results of my PhD thesis on the modeling and analysis of the elastic wave propagation arising from an earthquake in a city. The design of metaporous and meta-poroelastic materials still represents a large percentage of my current activities. These materials are at the origin of the creation of the Metacoustic company. The second chapter, composed of three sections, gives an overview of activities related to periodic and macroscopically inhomogeneous bulk materials. Works and challenges regarding graded porous and poroelastic materials, resonant sonic crystals and metamaterials (metasurfaces) based on slow sound propagation are presented. This chapter is strongly related to the first one, because every material and structure is bounded in practice and therefore only a small number of configurations can be understood and analyzed as bulk materials. The design of deep-sub-wavelength sound absorbers/insulators represents a large percentage of my activities these last years. The third chapter, composed of two sections, presents activities on the experimental characterization of porous and poroelastic materials and periodic structures as well as the experimental recovery of complex wavenumber/frequency dispersion relations. This last section is in my opinion of particular interest for future characterization of structured materials and metamaterials in various domains of physics, not only for audible acoustics. This part ends with a conclusion and future perspectives. Additional scientific achievements which do not represent a major part of my activities are presented in the appendix. The provided activity list may still not be exhaustive and I might have omitted some important achievements for others.

The second part of the document contains a scientific curriculum vitæ, in the form that is usually used for the evaluation of researchers by the «Comité National de la Recherche Scientifique» (CoNRS section 9). It gathers a regular CV, an overview of my academic and teaching duties, and a list of publications.

The third part of the document contains a selection of publications that I consider representative of my work, organized in accordance with the first part of the present manuscript. Please

note that all my published peer-reviewed articles are available following the links provided in chapter 5 of the *.pdf version of this document or in my personal webpage.

This manuscript, in particularly the first part, has largely benefited from collaborations, the list of which may be long but, without being exhaustive, I would like to mention the colleagues from LAUM, LMA, KULeuven, Univ. of Sheffield, Univ. of Salford, Univ. of Eastern Finland, and Univ. Politècnica de València. I apologize in advance for not having mentioned some colleagues.

Part I

Presentation of the main scientific results

Gratings and (meta)surfaces

This chapter gathers a large percentage of my research activities and focuses on diffraction gratings. These gratings take the form of periodic arrangement of rectangular blocks in contact with a soft layer over a hard half-space, of possibly resonant inclusions embedded in soft layer also in contact with a half-space, or of a combination of these two configurations. Whilst the former may mimic cities excited by an earthquake, the latter were essentially studied for sound absorption purpose. Both applications make use of similar physical features and it is worth noticing here, that the first application was probably the premise of the current seismic metamaterials [1].

1.1 Geophysical application: the site-city effect

The Michoacan earthquake that struck Mexico City in 1985 presented some particular characteristics which have since been encountered at various other locations and again recently in Mexico City, but at a lower level of intensity. Other than the fact that the response in downtown Mexico varied considerably in a spatial sense [2], was quite intense and of very long duration at certain locations (as much as ≈ 3 min [3]), and often took the form of a quasi-monochromatic signal with beatings, a remarkable feature of this earthquake [4, 5] was that such strong motion could be caused by a seismic source located so far from the city. The epicenter was effectively located in the subduction zone off the Pacific coast, approximately 350 km from Mexico City. Despite finer and finer models of the geophysical site, these observations could not find satisfactory explanations [6]. It is now recognized [5] that the characteristics of the abnormal response recorded in downtown Mexico were partially present in the waves entering into the city (notably 60 km from the city [4]) after having accomplished their trip from the source. This is thought to be due to the excitation of Love and generalized-Rayleigh modes by the irregularities of the crust (regional path effect). A still controversial aspect [7, 8, 9, 10] is the influence of the presence of the built features of the urban site as a complementary explanation of the abnormal response: the site-city effect. A building or a group of buildings over a hard half-space, solicited by an SH wave, has been shown to modify the seismic waves on the ground near the building [11] (soil-structure interaction), the modification being larger when more buildings are accounted for because of multiple interaction [12]: that is, the structure-soil-structure interaction.

The response of a soft elastic layer, mimicking the sediment basin over which cities are often

built, over a hard half-space were studied for both SH [13, 14] and PSV polarizations [15]. The presence of a building or a group of buildings was then simulated for both polarizations by modeling them as rectangular blocks in perfect contact with the ground. This model was then extended in the case of periodic arrangement of identical rectangular blocks, mimicking the response of a contemporary city [16]. Similar results were obtained for both polarizations and therefore only results for the SH polarization will be presented for clarity of the explanations. This polarization is also known to be the most destructive one for built structures during an earthquake.

Note that all simulations were performed by considering viscoelastic media with constant quality factors. In particular, semi-analytical calculations were run by employing the Kjartansson formula [17].

1.1.1 Site and regional effects: the excitation of Love mode

As a preamble to this subsection, it is worth noting that site effects, which are the response of the ground in the absence of built structure, are usually studied in geophysics when the site is excited by a normal incident plane wave. The main achievement concerning the study of site and regional effects yields in the study of the excitation of Love mode.

Typical dispersion curve of the lowest frequency Love mode is depicted in Fig. 1.1 (a). The tangential component of the corresponding wavenumber k_1^* yields in the absence of losses in $[k^{[0]}, k^{[1]}]$, where $k^{[0]}$ and $k^{[1]}$ are respectively the wavenumbers of the material occupying the hard half-space and the soft layer. In the presence of losses, the dispersion curve is only slightly modified. This means that such a mode cannot be excited by an incident plane wave at an angle θ^i arising from the hard half-space. Effectively, the wavenumber tangential component reads as $k_1^i = k^{[0]} \cos(\theta^i)$, i.e., $\|k_1^i\| \leq k^{[0]}$ in this case, which does not yield in $[k^{[0]}, k^{[1]}]$. This implies that:

- the so-called quarter-wavelength modes of a soft layer lying on a hard half-space are not modes of the configuration, because they do not satisfy the dispersion relation. It is rather an interference phenomenon of waves in the layer associated with leaky modes.
- the real modes of the configuration, namely the Love modes, cannot be excited by a plane incident wave, but rather by line or point sources. The excitation is performed by coupling the evanescent waves radiated by these types of source with the modes. The Love modes effectively correspond to propagative waves in the layer and evanescent ones in the half-space. Therefore, beyond the excitation problems, the elastic energy is trapped inside the layer. The excitation of the Love mode also leads to longer duration and larger amplitude of the displacement on the ground, see Fig. 1.1 (b-c). The excitation of such modes is characterized by wave packets propagating in the layer as depicted in Fig. 1.1 (d).

As a consequence, the study of site effects (and therefore of regional effects) may not be always conducted by soliciting the sites by plane incident waves, but rather by a point or line sources. This was particularly noticeable during the Michoacan earthquake, where the epicenter was located far from Mexico City (≈ 350 km). This implies that most of the specific features of this earthquake were present at the entrance of the elastic wave in the sedimentary basin of

Mexico City. This also implies that the simulated response of a built structure may not be always accurate, because it is usually solicited by a plane incident wave instead of a mode. The resonance frequency of the subsoil, which occurs at the inflection point of the dispersion curve in Fig. 1.1 (a), is also slightly smaller than the so-called quarter-wavelength resonance of the layer. Both amplitude of the motion and its duration may be much larger than it is commonly simulated.

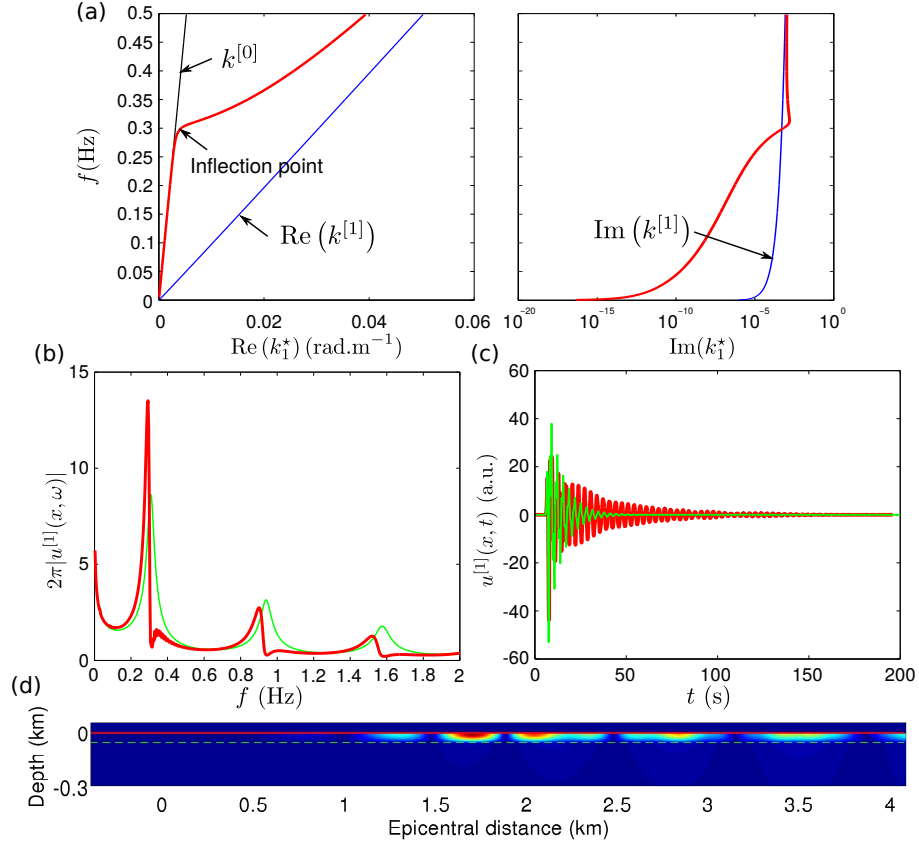


Figure 1.1: (a) Dispersion relation (complex wavenumber/frequency) of the lowest frequency Love mode in a soft layer over a hard half-space mimicking the subsoil of Mexico City (red curve), dispersion relation of the SH wave in the layer (blue curve), and dispersion relation of the SH wave in the hard half-space (black curve). (b) Transfer function of the displacement on the ground when excited by a shallow line source (red curve) and a deep line source close from a normal incidence excitation (green curve). (c) Response to a Ricker like wavelet centered at 0.3 Hz on the ground. (d) Snapshot of the displacement field at 75 s, when the configuration is excited by a shallow line source.

Finally, it is worth noting that the leakage of the Love mode is physically different from the one associated with the so-called quarter-wavelength mode. The present Love mode leakage is due to viscoelastic properties of the layer.

1.1.2 The soil-structure and structure-soil-structure interactions

When a structure is built on the ground, the soil-structure interaction occurs. It is worth noting here, that a built structure is usually designed to possess a first resonant frequency higher than the lowest resonant frequency of the subsoil it is built on. In the presence of a layer, the soil-structure interaction takes the form of both a shift at lower frequency and an increase of the amplitude of the first peak of the layer when excited by a deep line source, as depicted in Fig. 1.2 (a-c). In practice, a built structure, modeled in the present case as a rectangular block, acts as an induced source located at the surface. This induced source radiates evanescent waves in the subsoil which can be coupled with the Love modes, see the typical structure of the wave field in Fig. 1.2 (c). Therefore, the so-called soil-structure interaction is the local excitation of the lowest frequency Love mode by the structure itself. This implies that the presence of built structure induces the excitation of Love modes. Therefore, the excitation of the built structure is not achieved by a plane incident wave anymore, but rather by a Love mode and the mutual interaction between built structures (structure-soil-structure interaction) is performed through Love modes, possibly taking the form of coupled modes.

1.1.3 The site-city effect

While the effect of a finite size assembly of blocks may lead to the excitation of collective modes which strongly resemble Fabry Perot interferences (Fig. 1.2 (f)), the effect of a city was studied by considering a periodic arrangement of identical blocks. In the absence of the soft layer, the problem reads formally as the one of the diffraction of a TE or a TM electromagnetic wave by a perfectly conducting grating. When the wavelength of the impinging plane wave λ^i is a multiple of the grating period d , i.e., $\lambda^i = nd$, $n \in \mathbb{Z}$, the acoustic energy is spread along the grating and no energy is reflected back to the half-space by the grating anymore. The energy is perfectly absorbed by the structure and located along its surface. This phenomenon, known as the Wood anomaly, was first observed by Wood [18] and explained by Cutler [19] in optics/electromagnetism. In the presence of a soft layer below the grating, we showed that the Love modes are excited discretely by the Block waves in a similar way as the Wood anomaly. This excitation leads to sharp peak of the frequency domain response, therefore leading to a larger amplitude and a longer duration of the excitation which may present beatings, see Fig. 1.2 (e) . The presence of built structures was therefore found to be partially responsible of the destructive effects of the Michoacan earthquake in Mexico City as depicted in Fig. 1.2 (d-f).

This first application of diffraction grating shows that the presence of surface irregularities may lead to energy entrapment inside the layer. This energy entrapment may be disastrous in case of an earthquake striking a city or may be desired to design absorbing structures. On one hand, when the resonance frequency of a built structure is lower than the one of the substrate, the built structure resonates and traps the energy. On the other hand, when the resonance frequency of the substrate is lower than the one of the built structures, the soft layer resonates and traps the energy. In particular, it can be shown that the exact physical/mathematical acoustic counterpart of the previous grating configuration is a rigid diffraction grating composed of periodic arrangement of quarter-wavelength resonators covered by a rigid frame porous layer radiating in air [20, 21]. This means that basic rules in structural engineering may directly be translated to the design of sound absorbing structures.

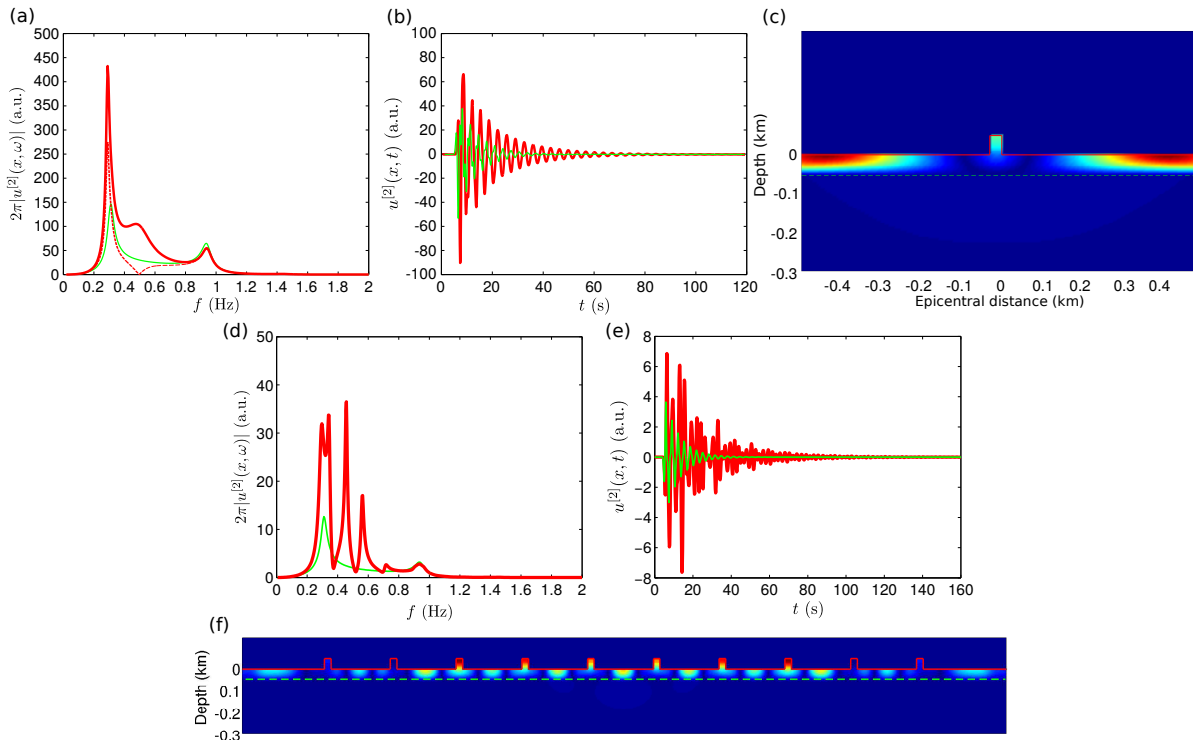


Figure 1.2: (a) Response at the top of a $50 \text{ m} \times 30 \text{ m}$ block in perfect contact with a subsoil mimicking the one of the Mexico-city (red curve), at the bottom of the block (dashed red curve), and in the absence of block (green curve) to a deep source radiating a Ricker wavelet at 0.3 Hz ; (b) corresponding time responses; (c) snapshot of the displacement field at $t = 42 \text{ s}$. (d) Response of a 300 m periodic arrangement of $50 \text{ m} \times 30 \text{ m}$ blocks in perfect contact with a subsoil mimicking the one of the Mexico-city (on the top of the block red curve) and in the absence of block (green curve) to a plane Ricker wavelet at 0.3 Hz (the amplitude of the source is different from the cases (a) and (b)); (e) corresponding time responses; (f) snapshot of the displacement field at $t = 32.5 \text{ s}$ in the presence of 10 blocks.

1.2 Acoustic application: metaporous and metaporoelastic materials

The ability to perfectly absorb an incoming wave field by a sub-wavelength structure is advantageous for several applications in wave physics as energy conversion [22], time reversal technology [23], coherent perfect absorbers [24], or sound-proofing [25] among others. The solution to this challenge requires to solve a complex problem: reducing the geometric dimensions of the structure while increasing the density of states at low frequencies and finding the good conditions to match the impedance with the background medium.

Until now, sound absorption has been mostly achieved by using porous materials or microporated materials [26]. These materials attenuate sound waves through viscothermal losses arising from the interaction of the sound wave with the usually motionless skeleton. Through-

out the manuscript, porous material will refer to motionless skeleton material, while poroelastic material will refer to material with deformable frame. Perfect absorption requires impedance matching with the surrounding medium. This condition may be realized thanks to the critical coupling condition, which relies on the analysis of the scattering matrix eigenvalues, i.e. the reflection coefficient for rigidly backed structures, in the complex frequency plane [27]. This analysis provides the balance between the energy leakage of the system and the dissipated energy. When these two energies exactly counterbalance, the critical coupling condition is fulfilled and perfect absorption is achieved [28, 29].

The present section is organized as follows. First, the limitation of regular acoustic porous materials will be assessed. Then, metaporous and metaporoelastic materials will be presented. These materials represent an efficient alternative to purely porous/poroelastic materials in the inertial regime, in the sense that they provide broadband perfect absorption of incident waves, the wavelengths of which are smaller than 10 times the thickness of the materials.

1.2.1 Usual absorption by rigid frame porous layers

Acoustic wave propagation in rigid frame porous materials is usually modeled through semi-phenomenological fluid models [30, 31]. These equivalent fluid models rely on complex and frequency dependent equivalent density and compressibility, which respectively accounts for the viscous and thermal losses [32]. Different regimes might be considered and of particular interest are the viscous and inertial regimes, which are only related to the viscous losses. These two regimes are separated in frequency from one another by the Biot frequency, $2\pi f_B = \sigma\phi/\rho_0\alpha_\infty$, where σ is the flow resistivity, ϕ is the porosity, α_∞ is the tortuosity, and ρ_0 is the density of the saturating fluid. Below this frequency, the density is mainly imaginary and the pressure field satisfies a diffusion equation, while above this frequency, the density is mainly real and the pressure field satisfies a Helmholtz equation with losses. The lowest frequency absorption peak of a rigidly backed porous layer corresponds to the so-called quarter-wavelength resonance. By first order Taylor expanding the numerator of the reflection coefficient of a rigid frame porous plate rigidly backed around this frequency, we end with an optimal length which reads as $L^{opt} = iZ_0/\omega\rho_{eff} + \pi c_{eff}/2\omega$, where Z_0 is the characteristic impedance of the air medium, and ρ_{eff} and c_{eff} are respectively the effective density and sound speed of the rigid frame porous material. Therefore, it imposes a purely complex value of the effective density and a purely real value of the effective sound speed. In other words, this can only be achieved for a frequency which is slightly above the Biot frequency. Therefore, this results in two limitations: (1) rigidly backed porous materials could only absorb sound for wavelength smaller than 4 times their thickness, and (2) rigidly backed porous materials could only perfectly absorb sound for frequencies larger than the so-called quarter wavelength resonance when the latter corresponds to the Biot frequency. Below this frequency, attenuation is too large, while above this frequency, attenuation is too poor. Therefore, bulky and heavy structures are required to absorb sound at low frequency and very low frequency cannot be absorbed by homogeneous porous materials.

1.2.2 Metaporous and metaporoelastic layers

An efficient way of designing broadband and thin sound absorbing materials is to combine viscothermal losses arising from porous materials with periodic resonant elements. The role of the former is to attenuate sound, while the role of the latter is to trap the sound energy inside the

structures at frequency much lower than the quarter-wavelength resonance one as well as to modify/tune the system attenuation. The periodic embedment of rigid inclusions in a porous plate, the first absorption peak of which is not unity in the inertial regime, leads to an enhancement of the absorption of the structure at low frequency, see Fig. 1.3(a). This enhancement is due to the excitation of a trapped mode, which traps the acoustic energy between the inclusion set and the rigid backing, Fig. 1.3(b). For a given filling fraction and position of the inclusions, the energy leakage of the structure can be exactly compensated by the intrinsic losses and a perfect absorption peak is reached for frequency much lower than the so-called quarter wavelength frequency of the homogeneous porous layer [33, 34]. The Bragg interference arising from the interaction of the inclusions with their image with respect to the rigid backing unfortunately leads to a large reflection of the structure and therefore a lower absorption, as depicted Fig. 1.3 (a). At higher frequencies, the absorption might be enhanced at the resonance frequencies of the porous plate, which are discretely excited thanks to the periodicity. These modified modes of the plate correspond to Wood anomaly in the presence of the porous plate, Fig. 1.3(a). Note that the required filling fraction for perfect absorption is larger for three dimensional inclusions than for two dimensional ones. This implies that perfect absorption might be impossible to achieve for some porous materials by employing some three dimensional inclusion shapes, typically sphere inclusions arranged on a cubic lattice. The absorption can be further enhanced at low frequencies by embedding resonant inclusions, like split ring resonators [35] or Helmholtz resonators [36]. At their resonance frequency, the acoustic energy is trapped in the resonant inclusions and attenuated by viscothermal losses. Split ring resonators (Helmholtz resonators as well but to a lower extent) can be coupled with the rigid backing. Therefore, broadband absorption can be achieved by considering a supercell composed of various split ring resonators with different slit orientations. It is worth noting here, that perfect absorption can only be achieved when the resonance of the inclusion lies in the inertial regime of the porous matrix, Fig. 1.3(c-d). When it lies in the viscous regime, absorption peaks are usually noticed but cannot be unity either because the acoustic energy cannot travel to the resonators, as depicted Fig. 1.3(e-f) in the case of completely embedded Helmholtz resonators, or because the resonator can hardly resonate when filled with a porous materials in the viscous regime.

Whilst the effect of the Bragg frequency may be erased by adjusting the resonance of resonant inclusions at this frequency, it can be more efficient to structure the rigid backing by adding quarter wavelength resonators or Helmholtz resonators [37, 38]. Therefore, the embedded resonant inclusions leads to perfect absorption at low frequencies while the structured rigid backing avoids the Bragg interference associated absorption loss at higher frequencies in optimized structures. Such metaporous materials possess enhanced acoustic properties to drastically reduce treatment thickness.

Accounting for the possible motion of the skeleton paves the way to remove the limitation of the metaporous materials to the inertial regime. Beyond the apparent rigidification of the poroelastic structure by the embedment of purely elastic inclusions, elastic resonators usually resonate at lower frequencies than acoustic ones and can therefore be efficiently designed for low frequency absorption purpose. For example, a preliminary study [39] has shown that the periodic embedment of viscoelastic shells in a poroelastic layer enables the enhancement of the poroelastic plate absorption coefficient thanks to the excitation of the trapped mode, the volume mode of the shell, but also the higher order modes of the shell which occur at much lower frequency than the Biot frequency. If optimally excited, elastic resonances may offer new

possibilities for the design of sub-wavelength metaporoelastic materials, both for the acoustic and elastic energy mitigation.

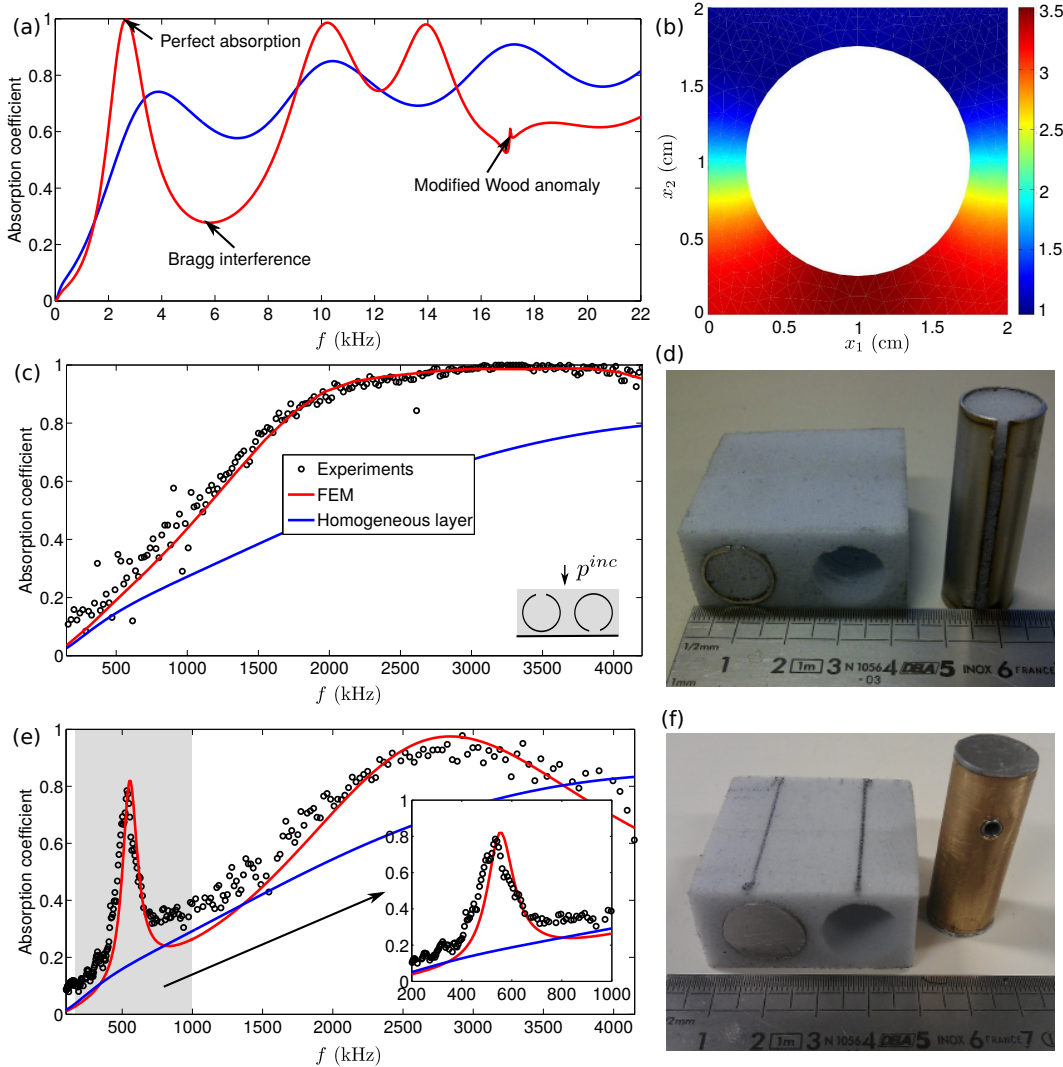


Figure 1.3: (a) Absorption coefficient of a 2 cm-thick porous layer of Fireflex without inclusion (blue curve) and with 2 cm periodic circular inclusions of radius 7.5 mm embedded in (red curve); (b) snapshot of the pressure field at the perfect absorption frequency; (c) Absorption coefficient of a 2 cm-thick melamine layer without inclusion (blue curve), with 4.2 cm periodic supercell composed of two split-ring resonators the opening of which being in opposite directions embedded in (red curve), and experimental validation (o); (d) Sample picture; (e) Absorption coefficient of a 2 cm-thick melamine layer without inclusion (blue curve), with 2.1 cm periodic Helmholtz resonators embedded in (red curve), and experimental validation (o); (f) Sample picture.

This first chapter focuses on gratings and metasurfaces and makes the connections between metasurfaces encountered in different applications. In particular, the design of metaporous and metaporoelastic layers was part of my research project when I was recruited by the CNRS.

Metaporous layers were patented and these solutions are now proposed by Metacoustic, which was created by one of my previous PhD student, C. Lagarrigue. It is worth noting here, that he also received numerous awards for his work on this topic, among which the «Yves Rocard» prize in 2014 from the French Acoustical Society that rewards the best French PhD in acoustics.

Periodic and macroscopically inhomogeneous bulk materials and their limitations

This chapter gathers activities related to the modeling of acoustic wave propagation in bulk materials. Even if bulk materials are necessary of finite depth or lengths in practice, the study of acoustic wave propagation in bulk materials is of particular physical interest, because it enables to exhibit material intrinsic physical features. In the last section of this chapter, we will clearly show the practical limitations of bulk materials. In particular, accounting for the finite size to design deep-subwavelength structures based on slow sound propagation (presented in section 2.3) has represented a large percentage of my activities during these last years.

2.1 Macroscopically inhomogeneous (graded) porous materials

While the acoustic wave propagation in macroscopically homogeneous porous (rigid frame) or poroelastic materials has been extensively studied since the seminal works of Biot [40, 41], the propagation in macroscopically inhomogeneous porous or poroelastic materials has only been studied recently. Contrary to metaporous or metaporoelastic materials, macroscopically inhomogeneous poroelastic materials are materials the macroscopic properties of which depend on the spatial coordinates. These macroscopic properties are porosity, tortuosity, viscous and thermal characteristic lengths, flow and thermal resistivities (or alternatively viscous and thermal permeabilities) for rigid frame porous materials plus Young's modulus, Poisson ratio and loss factor for poroelastic materials. The macroscopic variation of these parameters assumes that the spatial variation occurs at a much larger scale than the representative elementary volume. This mainly offers the possibility to design graded poroelastic materials with enhanced acoustic properties, avoiding reflections from interfaces in layer system and matching the surrounding medium impedance.

Several formulations of the Biot theory are available, the assumptions and validity of which are usually misunderstood. In particular, the initial formulation of the Biot theory [40], which is commonly used by the acoustic community, is only suitable for homogeneous isotropic materials, while the alternative formulation [41], which is commonly used by the geophysics community, is able to cope with inhomogeneous anisotropic materials. Therefore, the wave equation describing the acoustic wave propagation in macroscopically inhomogeneous poroelastic materials was

derived from this alternative formulation. This equation was solved for both graded porous and poroelastic plates along their depths [42, 43]. Unfortunately, despite the availability of numerical solutions and means of optimization for the parameter profiles, this research topic is still limited because, to the author knowledge, none of the current acoustic foam manufacturing procedure is sufficiently robust to manufacture precisely graded porous materials with the desired parameter profiles, even though some attempts were successful [44, 45]. The development and lowering cost of rapid manufacture techniques offers new possibilities. In addition, while the need for parameter profile characterization is of practical interest, every acoustic foams being slightly graded in practice because of the manufacturing process, the required data frequency range to efficiently reconstruct these profiles is very large and makes the inversion procedure developed till now inefficient in practice. Nevertheless, macroscopically inhomogeneous porous material was used to simulate accurately the acoustic response of a blackhole with homogeneous porous core [46]. The radial property gradient material impedance matching the outer and inner impedances was realized by varying radii and distances of equispaced rigid cylinders arranged over each circumference from the outer layer to the inner one.

2.2 Resonant sonic crystals

Acoustic wave propagation in infinite periodic arrangement of scatterers in fluid matrix (sonic crystals) has been extensively studied these last decades because of their peculiar dispersions, notably the presence of band gaps opened either thanks to the periodicity (Bragg interference) [47, 48, 49, 50] or to resonances (usually occurring at low frequency) [51]. This type of structures is particularly innovative to replace current sound barriers [52], because they can be optically transparent, enable or disable the passage of animals, etc.

A design of a natural sonic crystal was proposed by making use of bamboo rods arranged on a triangular lattice, see Fig. 2.1 (b). The triangular lattice was preferred to the square one because it enables broader band gap for almost circular cylindrical scatterers. The discrepancies in shape and radius inherent to natural bamboo rods were not found to highly affect the transmission coefficient trough finite depth structures around the first Bragg band gap. Helmholtz resonators were then added by drilling holes between each node of the bamboo rods. The open band gap was found at very low frequency for wavelength approximately 13 times larger than the lattice period, the discrepancies in the resonator dimensions being small compared to the wavelength at their resonances, see Fig. 2.1 (a-b). Broadening the band gaps was attempted by making use of resonance gradient along the depth of the sonic crystal by lengthening the neck of the Helmholtz resonators or lowering the resonators volume, but failed because of a lack of cumulative effect of resonances in our case. Helmholtz resonators were also found to be very difficult to couple.

Shape and lattice geometries both influence the band gap opening and its frequency width, the optimum being reached when both coincides for simple geometries [53], i.e. triangular scatterers arranged on a triangular lattice, square scatterers on a square lattice, etc. Square scatterers arranged over a square lattice also offers the possibility of tuning the band gap by modifying the orientation of the scatterers inside the lattice, i.e. by rotating the scatterers around their axis [54]. In particular, complete band gaps are opened when the scatterers are rotated of an angle of $\pi/4$ with respect to the lattice directions, while the structure possesses band gap only along the

ΓX direction when the scatterers are aligned with the lattice. Waveguides were designed and experimentally validated by modifying the orientations of some scatterers along a path when the surrounding ones were oriented at $\pi/4$ with respect to the lattice. Moreover, the pass band frequency of the waveguide depending on the orientation of the scatterers, a spatial selective filter was designed in the audible frequency range by measuring the transmission coefficient in a sonic crystals possessing different waveguides each of them being composed of scatterers with slightly different orientations [55]. Therefore, transmission bands are opened inside the band gap at specific location behind the crystal.

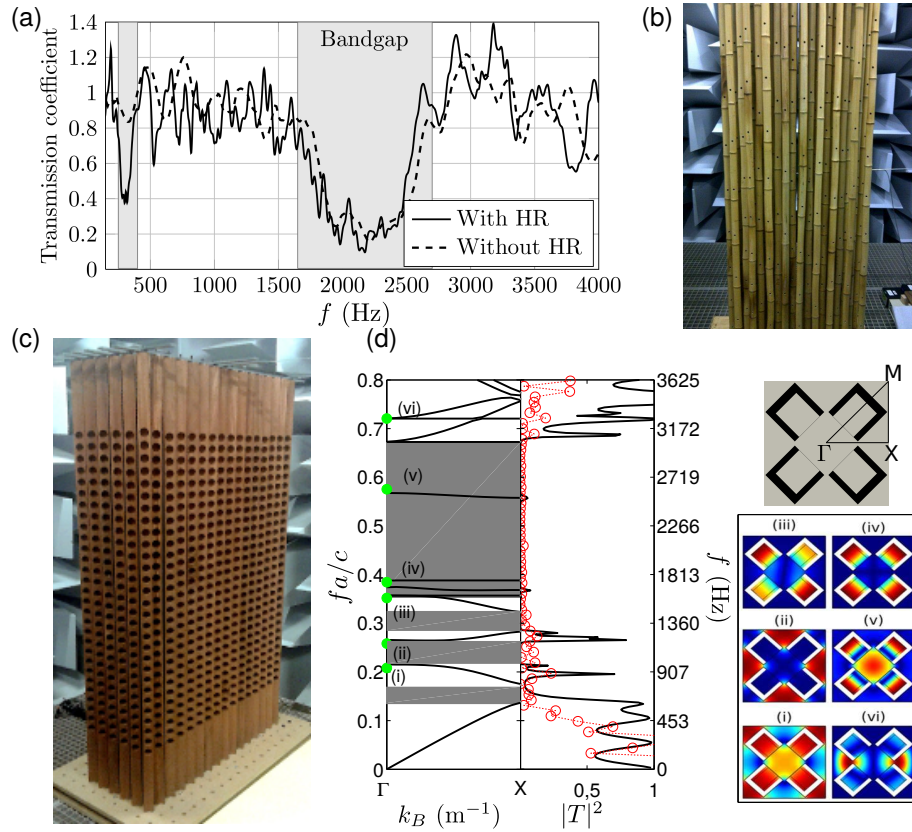


Figure 2.1: (a) Transmission coefficient (amplitude) of a resonant sonic crystal constituted of bamboo rods arranged along a triangular lattice incorporating Helmholtz resonators; (b) Picture of the crystal; (c) Transmission coefficient of a tunable resonant sonic crystal composed of square scatterers incorporating quarter-wavelength resonators. The insets show the pressure field at specific frequencies and the unit cell composed of 4 scatterers is sketched; (d) Picture of the tunable resonant sonic crystal.

The tunability of the latter sonic crystal was further enhanced by adding resonators. Quarter-wavelength resonators were added by periodically drilling identical circular boreholes on one face of the square scatterers. The sonic crystal becomes three-dimensional (Fig. 2.1 (c)), but only the propagation in the plane perpendicular to the scatterers axis was studied. The possible rotation of the scatterers around their axis enables to study the coupling between the resonators and different configurations were studied depending on the number of resonators facing one an-

other: any of them, two of them or four of them. In case of one or two resonators facing one another, the symmetry of the structure is broken and the study of the dispersion relation along the $\Gamma X M \Gamma$ path is not sufficient anymore in the plan. Of particular interest is the configuration with four facing resonators, as depicted in the sketch of Fig. 2.1 (d). Multiple coupled modes are excited, opening propagative and therefore forbidden gaps, see Fig. 2.1 (d). The viscothermal losses cannot be avoided, mainly because of the presence of the quarter-wavelength resonators, and the flattest propagative bands (corresponding to slow sound propagation) are highly attenuated in practice. A resonant sonic crystal possessing a band gap covering two and a half octaves (from 590 Hz to 3220 Hz) with transmission lower than 3% was also designed [56].

The losses in sonic crystals are effectively one of the drawback of their usual description, because they can hardly be accounted for. Viscothermal losses cannot be accounted for in the Plane Wave Expansion [57], because density and bulk modulus are usually frequency dependent. They might be accounted for through the Extended Plane Wave Expansion [58], but still the inherent problem of the necessary identical type of material that compose the matrix and the scatterers is not solved. Probably, the best way to solve this problem relies in the Multiple Scattering Theory [59]. This was particularly pointed out when solving the full viscothermal problem of the scattering of the acoustic wave by periodic circular rods in air [60]. Another disadvantage of the description of sonic crystals as bulk materials, is that in practice they are of finite depth. Therefore, impedance of the structure is required, angle of propagation in the crystal when excited by an oblique incident plane wave is usually unknown, symmetry problems leading to deaf modes arise [61], and Wood anomaly are noticed. Nevertheless, we can make use of Wood anomaly together with viscothermal losses of the matrix material to design perfect absorbers. A finite depth sonic crystal composed of a periodic arrangement of rigid circular scatterers along a square lattice in a porous matrix was studied in [62]. The structure possesses similar behavior as a sonic crystal in the absence of losses, with very low transmission inside frequency ranges which can be associated with band gaps, but also very low transmission inbetween because of the losses in the porous material. Of particular interest is the second band gap when a square lattice is considered, the central frequency of which fits the one of the first Wood anomaly at normal incidence. Therefore, the transmission of this finite depth structure almost vanishes as well as its reflection coefficient leading to perfect absorption. This is particularly important in case of perfect absorption in transmission problems. Note, this is encountered for every finite depth periodic sonic crystal with square lattice, even in the absence of viscothermal losses.

Other properties than band gaps arise from the dispersion relation of acoustic waves in this type of structures, for example negative refraction which was shown in the audible frequency range with the help of another square rod scatterer sonic crystal [63]. Another quite interesting property of dispersion relation in periodic structures in air is slow sound, which occurs in propagative bands when the slope of the bulk wavenumber is lower than the one of the bulk wavenumber in air.

2.3 Slow sound propagation: design of deep-subwavelength absorbers and other application

Slow sound propagation is currently a growing topic in acoustics because of the direct analogy with electromagnetic induced transparency. This phenomenon appears when an opaque medium

exhibits enhanced transmission in a narrow frequency windows along with strong dispersion. This rapid change in transmission leads to strong dispersion giving rise to slow phase velocity or group velocity waves whose frequency is centered on the narrow transmission band [64]. In acoustics, most of theoretical and experimental evidences of slow sound have been achieved by considering sound propagation in pipes with a series of detuned resonators (mostly Helmholtz resonators) separated by a sub-wavelength distance [65], tuned or detuned resonators separated by half of the wavelength giving rise to a coupling between the resonators and the Bragg bandgap [66], in a waveguided sonic crystals [67], in lined ducts [68], etc. Only a few studies have been focusing on the dissipation (dispersion and attenuation) of slow sound propagation [69, 70], even if it has been sometimes noticed or discussed. Dissipation was considered as a side effect of an unexpected adverse reaction. The key point of this section is to make use of slow sound propagation, which appears for a broadband frequency range below the bandgap associated with resonators resonance, or in a narrow frequency band between the bandgaps associated with detuned resonator resonance (induced transparency band), together with the associated dissipation (attenuation + dispersion) to design a sound absorbing metamaterial.

First the dispersion relation in a duct loaded by identical [71] or detuned [72] quarter-wavelength or Helmholtz [73] resonators was studied. The viscothermal losses were accounted for in the resonators and in the duct by making use of the appropriate complex and frequency dependent effective densities and compressibilities [74]. From a description based on locally reacting impedance condition mimicking the loading by the resonators, the effective parameters were derived. The analysis shows that the sound wave propagating in the loaded duct possesses the specific features of slow sound, in the induced transparency band, but also at low frequency. While the sound speed is necessarily dispersive in the induced transparency band, it possesses a plateau at low frequency. As expected from [75], the real part of the effective bulk modulus becomes negative inside the band gap due to the resonance of the loading resonators. Note that the presence of the losses induces a small amount of propagation in the band gap. Therefore, the use of the term «band gap» might be abusive. Note that the decrease of sound speed is as well associated with an increase of the attenuation. Very low sound speed wave also cannot propagate over a large distance in acoustics. This specific type of propagation allows to design sub-wavelength resonators.

In case of rigidly backed structures, these resonators can be quarter-wavelength ones, e.g. Fig. 2.2 (a-b). When periodically arranged, they form a metasurfaces, the resonance of which appears for wavelength much larger than the impinging wave one. Note that the sub-wavelength resonance of these quarter-wavelength resonators is only due to a drastic reduction of the sound speed inside the loaded ducts and not to coiling effect [76]. This metastructure can be critically coupled to the exterior medium by tuning the geometry of the structures. When this condition is fulfilled, the perfect absorption is obtained because the attenuation of the structure exactly compensate its leakage and the zero of the scattering matrix (R in this case) exactly lies on the real frequency axis, see Fig. 2.2 (c). Several structures were designed by using this technique, the absorption band of some being broaden by using detuned sub-wavelength resonators in the unit cell and the absorption of others being deeply sub-wavelength [73], i.e. $\lambda = 88L$, see Fig. 2.2 (a-d). All these structures were validated experimentally. It was found in practice that the limiting parameters in low frequency is the manufacturing of the sample by stereolithography, the structure being not acoustically rigid anymore when very thin.

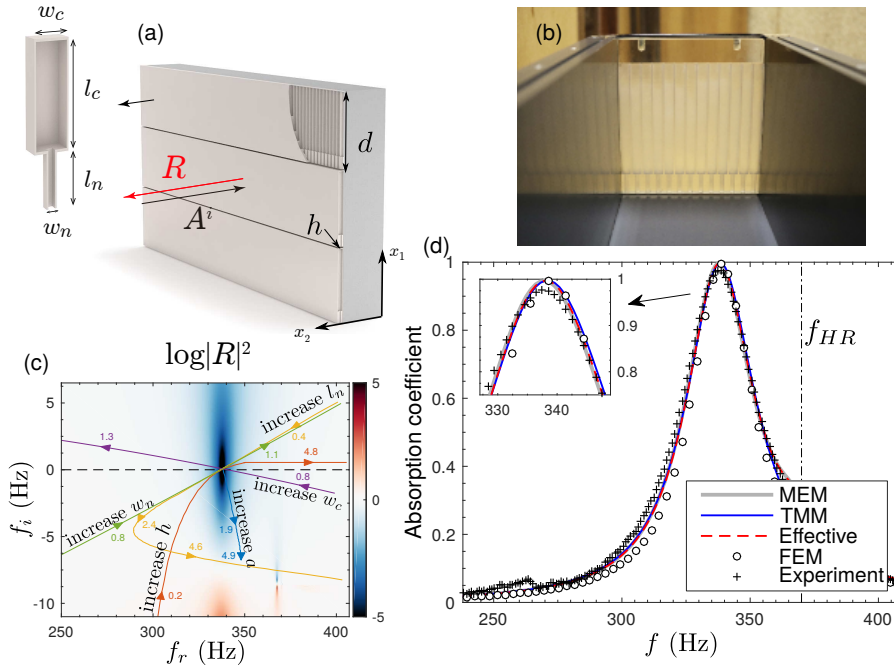


Figure 2.2: (a) Sketch of the perfect absorber for reflection problem; (b) Picture of the perfect absorber sample; (c) Map of $\log|R|^2$ in the complex frequency plane; (d) Absorption coefficient calculated with different methods and measured.

In case of open structures, these resonators are Fabry-Perot ones. When resonators of this type are periodically arranged, the problem of perfect absorption by sub-wavelength structure in transmission problem was tackled. When transmission is allowed, perfect absorption requires both symmetric and antisymmetric problems to be critically coupled; i.e. both zeros of the eigenvalue of the scattering matrix must vanish at the same frequency. In the absence of loading resonators, the zero and pole structure of these two problems are staggered in frequency. Therefore, the perfect absorption cannot be achieved. When identical resonators are plugged on periodically arranged slits and effective parameters are used, the structure possesses an infinite number of zeros and poles for both problems, which are stretch below the band gap due to the loading resonator resonance. An accumulation point can be observed and perfect absorption can theoretically be achieved. However, this perfect absorption cannot be reached in practice because the effective parameter description implies an infinite number of resonators, while this number is necessarily finite in depth. The total number of zeros and poles in the complex frequency domain equals the number of resonators and the accumulation point could not exist anymore. This problem can also be solved by accounting for the finite number of resonators, through the Transfer Matrix Method for example. Nevertheless, nearly perfect absorption structure can be designed [77]. This constitutes one of the main drawback of effective parameter description and therefore of bulk material description in practice. This limitation is particularly true for medium involving resonant elements. Nevertheless, the problem of perfect absorption in transmission problems can be solved by employing similar techniques inspired by slow sound propagation. Instead of designing a structure composed of degenerate resonators [78], rainbow trapping absorbers were designed [79]. The idea consists in breaking the symmetry of the structure by detuning the loading resonators, see Fig. 2.3 (a). The

panels are composed of a periodic array of varying cross-section waveguides, each of them being loaded by Helmholtz resonators with graded dimensions. The low cut-off frequency of the absorption band is fixed by the resonance frequency of the deepest Helmholtz resonator, that reduces drastically the transmission. The preceding Helmholtz resonator is designed with a slightly higher resonance frequency with a geometry that allows the impedance matching to the surrounding medium. Therefore, reflection vanishes and the structure is critically coupled. This results in perfect sound absorption at a single frequency. This process can be repeated by adding additional Helmholtz resonators to the waveguide, each of them with a higher resonance frequency than the preceding one. Zeros of both eigenvalues of the scattering matrix now lies on the real frequency axis, see Fig. 2.3 (d). These structures being asymmetric, the analysis of the scattering matrix eigenvalues is not sufficient to completely describes the acoustic behavior of the designed structure. The associated eigenvectors are additionally analyzed in the complex frequency plane to state which side of the structure is critically coupled. Using this frequency cascade effect, perfect sound absorption over almost two frequency octaves ranging from 300 to 1000 Hz for a transparent panel composed of 9 resonators with a total thickness of 11 cm, i.e., 10 times smaller than the wavelength at 300 Hz was reported, see Fig. 2.3 (a-d). In the case of a sub-wavelength asymmetric panel, we report monochromatic perfect absorption at 300 Hz for a structure whose thickness is 40 times smaller than the working wavelength.

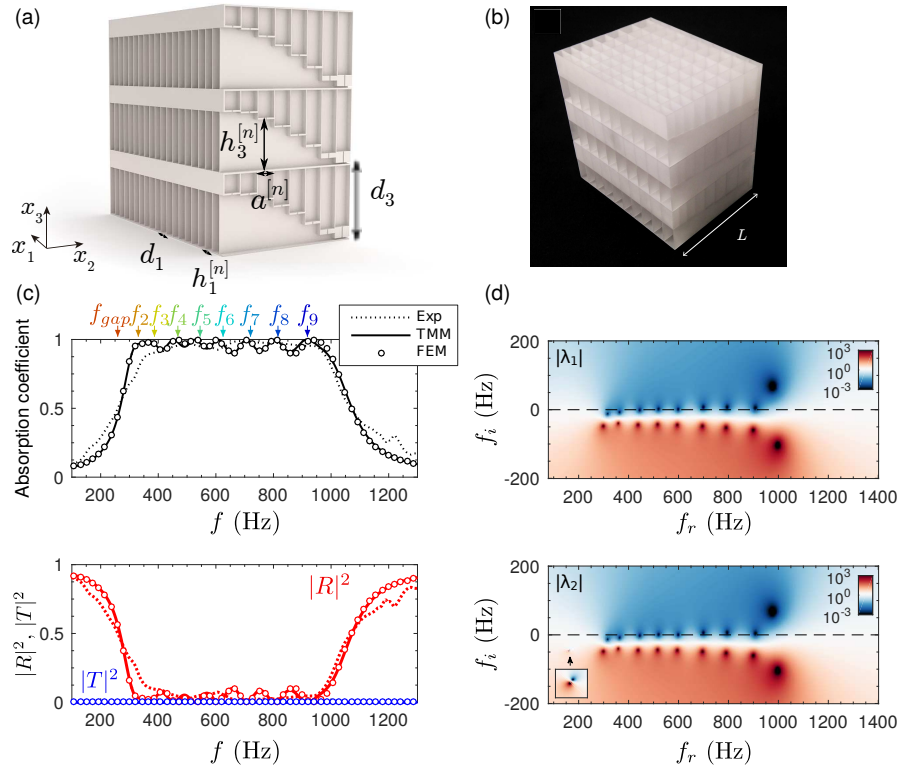


Figure 2.3: (a) Sketch of the rainbow trapping absorber; (b) Picture of the rainbow trapping absorber sample; (c) Absorption, reflection and transmission coefficients calculated with different methods and the experimentally measured ones; (d) Map of both eigenvalues of the scattering matrix in the complex frequency plane.

Another application of this type of structures when rigidly backed is the metadiffuser, which is a diffuser of very small thickness [80, 81]. In critical environments such as auditoria, professional broadcast and recording control rooms, recording studios or conference rooms, reflections can decrease sound quality due to echoes or cause sound coloration. Even when these specular reflections are damped by absorption, the sound field inside a room may be non-diffuse, affecting the quality of the listening. In these situations, diffusers can often help by evenly spreading the acoustic energy in both space and time. The generation of spatially dependent reflective surfaces have been achieved in the past by using phase grating diffusers, also known as Schroeder's diffusers after its first proposal [82] using maximum length sequences. The most used configurations are rigid-backed slotted panels where each slit acts as a quarter-wavelength resonator. Therefore the structure is not sub-wavelength and making use of slow sound propagation enable reducing the thickness of usual diffusers. By tuning the geometry of rigidly backed slotted panels, each slit being loaded by an array of Helmholtz resonators, the reflection coefficient of the panel can be tailored in space to obtain either a custom reflection phase, moderate or even perfect absorption. Using these concepts, ultra-thin diffusers were designed where the geometry of the metadiffuser has been tuned to obtain surfaces with spatially dependent reflection coefficients having uniform magnitude Fourier transforms. Various designs were realized: quadratic residue, primitive root and ternary sequence diffusers were mimicked by metadiffusers whose thickness is $1/46$ to $1/20$ times the design wavelength, i.e. between about a twentieth and a tenth of the thickness of traditional diffusers. A broadband metadiffuser panel of 3 cm thick was designed using optimization methods for frequencies ranging from 250Hz to 2kHz.

This chapters focuses on research activities related to bulk materials in several fields, from graded porous and poroelastic materials to deep-subwavelength sound absorbing structures. While research on graded porous and poroelastic materials was initiated immediately after my PhD defense, researches on deep-subwavelength absorbing and insulating structures were mostly conducted recently. In particular, deep-subwavelength absorbers were designed within the framework of the ANR Metaudible (ANR-13-BS09-003) project co-funded by the Fédération de Recherche pour l'Aéronautique et l'Espace (FNRAE). This project was following the research conducted on metaporous and metaporoelastic layers. Some practical limitations of the bulk descriptions were pointed out mostly due the necessary finite dimensions of real structures. Therefore, the homogenization of metasurfaces and interfaces are currently of growing importance [83].

Acoustic characterization of materials and structures

This chapter gathers activities related to the solution of inverse problems. This activity is not strictly speaking my main subject of research but inverse problems are often solved as subproblems of global ones: material properties of constitutive elements are required to design more complex structures for example. Furthermore, the future commercialization of a growing number of acoustic metamaterials will require specific tools to characterize them. I must also confess a special interest in this field probably inherited from my PhD advisors and Post-doctoral collaborators.

3.1 Characterization of porous (rigid frame) materials

Because of their industrial and economic interests, several methods are available to characterize homogeneous porous (and poroelastic) materials. For porous materials, acoustic and non acoustic techniques must be distinguished. While non acoustic techniques provide direct measurement of specific parameters, like porosity [84] or flow resistivity [85], acoustic techniques require a model of propagation to be inverted, which usually mixes all the parameters. As explained in chapter 1, acoustic wave propagation in porous materials is modeled through complex and frequency dependent effective bulk modulus and density. Several models are available but the most refined ones are semi-phenomenological. These models fit available exact solutions at low and high frequencies (of course lower than the scattering one) but are only approximated in between [30, 31, 86]. Therefore, special attention must be paid to the measurement frequency range and/or we need to be aware that the inverted model is approximated and so that the reconstructed parameters will be necessarily slightly different from their exact values.

Ultrasonic measurements enable to invert high-frequency data where propagation models are accurate. At high frequencies, i.e. for frequencies much higher than the transition (viscous-inertial and isothermal-adiabatic) ones and lower than the scattering limit, effective bulk and density only depend on four parameters whatever the semi-phenomenological model usually employed: the porosity, the tortuosity and the viscous and thermal characteristic lengths. To recover acoustically these four parameters, methods are usually based on cost function minimization [87] and/or modification of the saturating gas [88]. Still both effective bulk modulus

and density can be reconstructed analytically from measured reflected and transmitted fields by an homogeneous porous layer [89]. From these four informations (real and imaginary parts of both effective density and bulk modulus), the four parameters are then reconstructed analytically for each frequency. An analytical method for the reconstruction of porosity, tortuosity and viscous and thermal characteristic lengths was also proposed and tested on usual acoustic foams with accuracy. The problem was regularized thanks to data available at several frequencies [90]. However, one problem of ultrasonic measurements in air lies in the fact that only four over the five [31] or six [91] parameters describing a porous material might be reconstructed. Another one yields in the fact that ultrasonic transducers in air are expensive and usually narrow band. In addition to ultrasonic measurements, impedance tube measurements can be used. This type of measurement (4 microphones in our case) provide reflection and transmission coefficients in the audible frequency range below the cut-off frequency of the tube. Models of propagation are therefore usually approximated in this frequency range, but it corresponds to the range of efficiency and design of the common sound absorbing or insulating structures. Analytical methods are available to reconstruct viscous and thermal characteristic lengths and permeability, porosity and flow resistivity being measured by other non acoustic methods [92, 93]. This requires that porosimeter and flow meter are available in the laboratory, which is not always the case. A method based on the minimization of the difference in the least square sense between the reconstructed and modeled density and bulk modulus was developed and validated on several porous samples. The minimization was constrained to ensure that the thermal characteristic length is larger than the viscous characteristic one and that the thermal permeability is larger than the viscous one. The Johnson-Lafarge model [30, 91] depends on 6 parameters (porosity ϕ , tortuosity α_∞ , viscous and thermal characteristic lengths Λ and Λ' , and viscous and thermal permeabilities k_0 and k'_0) contrary to the Johnson-Champoux one [30, 31], but makes both effective bulk modulus and density depending on only one common parameter, i.e., the porosity. This will also enable the characterization of anisotropic porous materials if the principal directions are known in the near future. This method was completed by a reconstruction procedure making use of Bayesian approach [94, 95]. Bayesian approach allows to account for a priori, to evaluate uncertainties and to detect possible correlations between reconstructed parameters. No correlation were found between the viscous and thermal characteristic lengths, while it is usually assumed the former is half (for fibrous materials) or the third (for foams) of the latter. However, viscous characteristic length was found to be correlated to the tortuosity, thermal characteristic length was found to be correlated to porosity and thermal permeability was found to be correlated to porosity for some materials. Strong correlation may be observed in Fig. 3.1 between thermal characteristic length Λ' and porosity ϕ as testified by the Markov Chain Monte Carlo point alignment. These correlations were found to be mainly due to the frequency range of measurement which is limited at high frequency by the cut-off of the impedance tube. Note also that the correlation between the reconstructed parameters greatly increases when only reflection data are used. The results of both methods were found in excellent agreement with previously proposed methods [96].

One of the drawback of impedance tube measurement is its high frequency limitation by the cut-off frequency of the tube as well as its limitation at low frequency by the spacing between the microphones. The latter problem were fixed by considering several locations of measurement along the tube, the better spacing between two consecutive measurement locations having been found to be equidistant on a logarithmic scale. The former problem were solved, in square impedance tube, by using a single microphone inserted in the corner of the tube and

mounted on a one-dimensional axis robot arm. This set-up allows to record the pressure fields at several locations along the tube length. These pressure fields are then Fourier transformed in space. This problem possessing an analytical solution, the difference between the recorded Fourier transform and the corresponding ansatz is minimized in the least-square sense for each frequency. The recovered parameters are the amplitude and phase of each mode in the forward and backward directions, the corresponding wavenumbers being known thanks to the simple geometry of the problem. Reflection coefficients for each mode are therefore reconstructed [97]. Note that the minimization allows to account for the interaction of several modes of propagation. This technique was in particular used to assess the modeling of sound scattering by living plants [98].

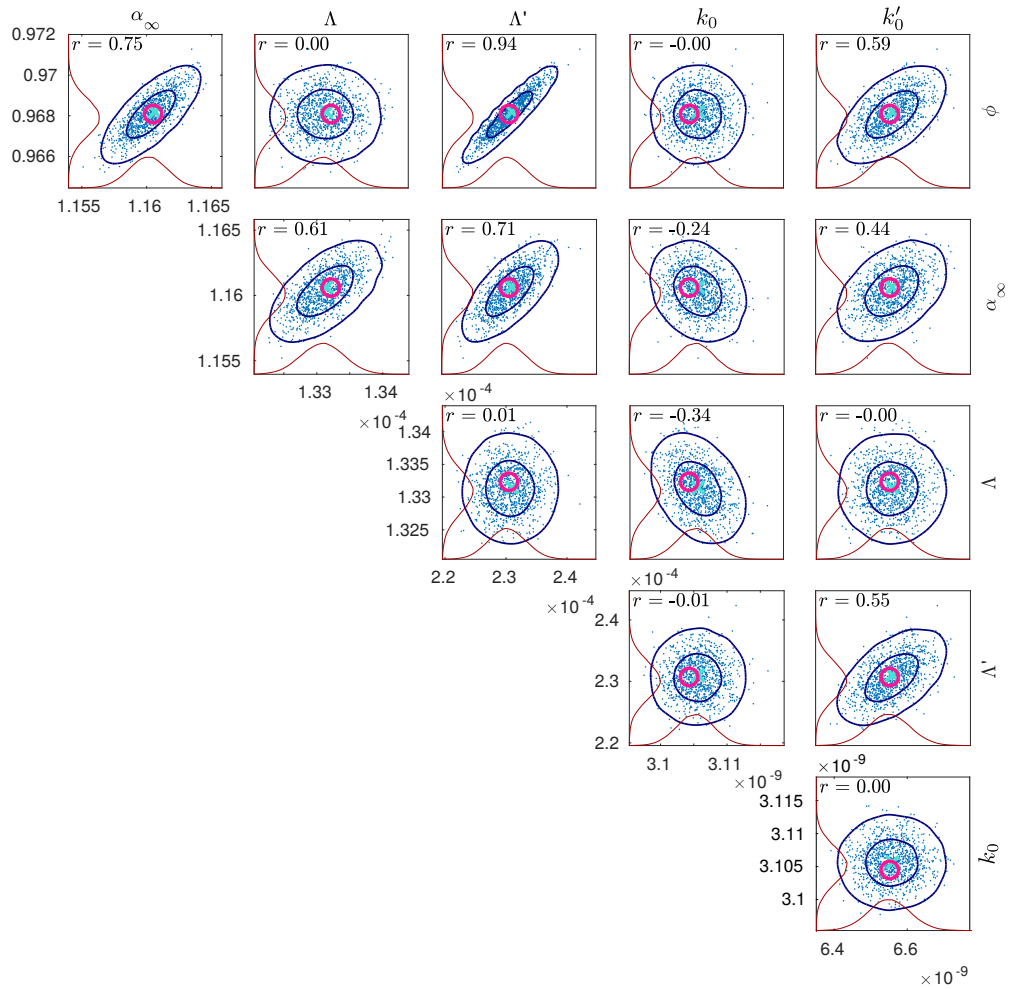


Figure 3.1: Two dimensional marginal posterior distributions of an acoustic foam sample. The dots represent a sample of the Markov Chain Monte Carlo points, and the contours surrounding them show the 50 % and 95 % condense intervals. The blue cross is the Maximum A Posteriori-estimate and the red circle is the Least Square-solution. The red curves on the bottom and left side of each plot are the one dimensional marginal posterior distributions.

To conclude this section, it is worth noting that these techniques are also used to characterize metamaterials and metaporous materials. Effectively, below the cut-off frequency of a square impedance tube, the boundaries of the latter act as perfect mirrors. This creates a perfect periodic pattern of the sample, which is inserted in the tube [20]. While modes of the square impedance tube exactly match the Block ones at normal incidence, when half of the unit cell is inserted in the tube for two-dimensional cases and when a quarter of the unit cell is inserted in the tube for three-dimensional cases, results for a general unit cell inserted in the tube are usually in good agreement with its periodic counterpart, providing awareness of the symmetries.

3.2 Experimental reconstruction of complex wavenumber / frequency dispersion relation

Understanding the dispersive and dissipative properties of materials is critical to the study of wave phenomena. Extracting complex wavenumber information is important, particularly in the context of understanding wave attenuation. In addition to dispersive effects, such as the existence of band gaps, wave attenuation can be caused by factors such as geometric attenuation or intrinsic material loss (e.g. heat dissipation). In any of these cases, the wave attenuation can be interpreted in terms of complex wavenumbers. The recovery of complex wavenumbers is of particular interest for the characterization of the viscoelastic properties of materials, in systems such as thin-film [99], or coated plates [100], the study of mode interactions, i.e. hybridization or repulsion [101, 102, 103], or the recovery of complex band structures arising from structural periodicity or resonant elements [101, 104, 105]. The dispersion of waves propagating through materials is typically interpreted in the context of frequency and wavenumber domain information and obtained from discrete spatiotemporal data via discrete Fourier transforms and related methods [106, 107, 108, 109, 110, 111]. However, such techniques typically only supply real wavenumber information (or their magnitudes) from two-dimensional, discrete, spatiotemporal wave propagation information, such as may be obtained from scanned receiver measurements. Several methods have been proposed to characterize wave attenuation and extract complex wavenumber information [112, 113, 114, 115, 116, 117], but most of them were limited to a single or a small number of modes or were requiring specific set-ups.

The SLaTCoW (Spatial Laplace Transform for COmplex Wavenumber recovery) method requires usual spatio-temporal signal and enables to avoid many of the limitation of the other methods. In the frequency domain, instead of performing a spatial Fourier transform of the field, which is analyzed in the spatial coordinate dual space in terms of real wavenumber/frequency, we perform a spatial Laplace transform, which is analyzed in the spatial coordinate dual space in terms of complex wavenumber/frequency [118]. Depending on the problem, ansatz accounting for the geometrical spreading due to excitation [119] or not are used to minimize a cost function form by their difference with the measured data. Quite similarly to what was performed in the preceding section, the unknowns are the amplitude and phase of each mode, together which the corresponding real and imaginary part of the wavenumbers. This method was successfully used for:

- the study of low frequency (200 Hz-4095 Hz) guided elastic waves in poroelastic materials, which are highly dissipative systems such that the wavenumbers associated with each mode are complex. The method is used to characterize skeleton (matrix) viscoelastic

parameters. This paves the way for the extraction of new experimental information that enables the development of improved models of viscoelastic poroelastic materials.

- the analysis of Zero-Group Velocity (ZGV) Lamb modes at MHz frequencies (1.85 MHz 2MHz) in a Duralumin plate. The ZGV modes are composed of two interfering counter-propagating Lamb modes, and the method reveals mode separation due to leakage and their associated complex wavenumbers, along with motivating the need for more complex multilayer models.
- the characterization of the resonant attenuation of high frequency (10 MHz-400 MHz) surface acoustic waves (SAWs) propagating through a two-dimensional (2D) microscale granular crystal adhered to a substrate with three contact-based resonances. While hybridization due to the out-of-plane mode can be seen using a usual spatial Fourier transform [120], the two combined rotational and in-plane translational resonances are only noticeable by studying the attenuation of the modes, which is further highlighted by this method.

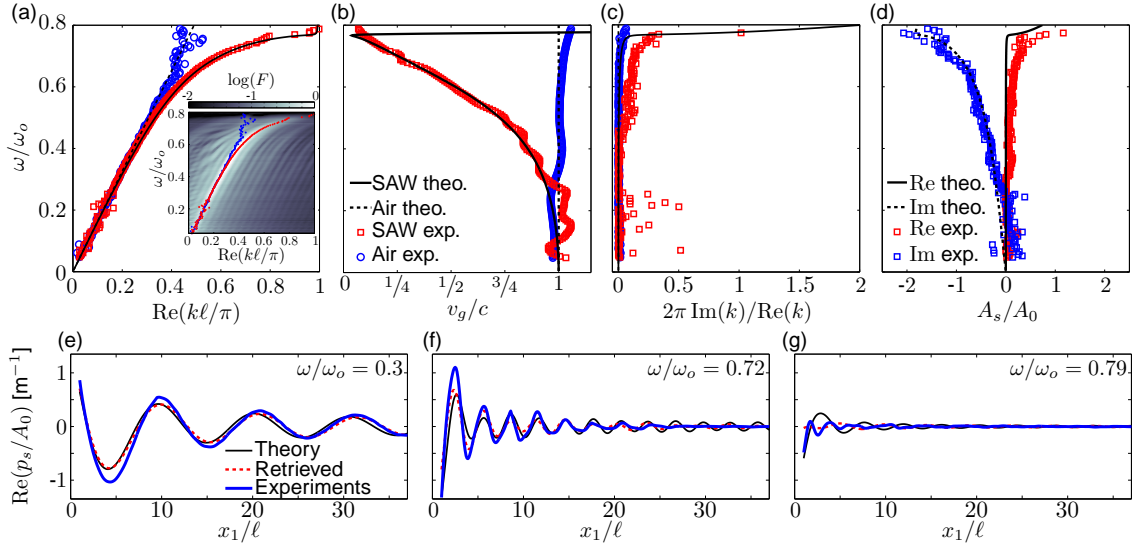


Figure 3.2: Comparison between theoretical (theo.) and experimental (exp.) results. Plotted against the normalized frequency ω/ω_0 are: (a) the real part and (c) the imaginary part of the air and SAW wavenumbers; (b) the normalized group velocity; (d) the amplitude ratio between the SAW and the air modes. Plotted against the normalized distance x_1/l from the speaker are: (e)-(g) the pressure profile along the scan-line at three frequencies; (a) and (c) have the same legend as (b); (f) and (g) have the same legend as (e). The inset in (a) shows the spatial Fourier transform of the experimental pressure against the frequency and the dispersion relations retrieved from the SLaTCoW method.

- the study of the influence of viscothermal losses on the propagation of spoof acoustic waves propagating over a metasurface composed of a periodic arrangement of circular boreholes. This shows the efficiency of the method to discriminate attenuation from geometrical spreading together with the large attenuation of acoustic waves in very dispersive regions, where slow sound occurs, see Fig. 3.2.

Beyond the apparent simplicity of the SLaTCoW method, this method allows to avoid many of the problems inherent to other methods and appears to be a efficient tool to quantify complex wavenumber/ frequency dispersion relation in various systems, involving periodic ones.

This last chapter presents activities related to the characterization of porous and structured materials. With the rapid development of metamaterials, I am convinced that new methods of characterization will be required for their standardization and commercialization. These new tools will also enrich the available procedures and therefore will lead to deep modification in the way inverse problems are tackled. This field is, in my opinion, of major importance for the commercialization of solutions based on metamaterials.

Conclusion and perspectives

This first part attempts to give an overview of my research achievements. Beside the organization in three chapters, each of them attempting to gather results having similar features, all these results recover from the same general idea of the study of mostly acoustic wave propagation in lossy, structured and periodic media. In my opinion, the two main achievements concern the design and the characterization of structures for the insulation and absorption of audible sound. In particular, metaporous and metaporoelastic materials have already proven their efficiency to replace current acoustic foam with a large gain of thickness for enhanced acoustic properties. This type of structures might also offer structural functionalities which have until now not been investigated. Deep-sub-wavelength absorbers, metadiffusers and insulators are also of particular practical interest, but still require some developments. Beside these practical achievements, the physical understanding of the absorption, insulation, elastic wave propagation in cities as well as the coupling between resonators is of large importance for the design of various elements, from the sound absorbing panel to future urban plan of big cities. The rapid development of acoustic metamaterials will undoubtedly require some specific characterization methods and probably some new standards. All along the chapters, I have tried to explain my current understanding of the physical phenomena, potential practical applications, but also limitations of some concepts. I strongly believe that the development of rapid manufacturing techniques will help in solving many of the current difficulties. The first direct application and perspective related to this development is the design, control and manufacturing of graded porous structures which will be investigated in the framework of the ANR MACIA. The second is the design, control and manufacturing of even deeper sub-wavelength resonant elements, which can be used for insulation and absorption purpose for example, as already engaged in the ANR Metaudible (ANR-13-BS09-003). The main challenge is the combination of deep-sub-wavelength and broadband absorbers, as pointed out in [121]. A possible way to avoid the problem of causality arised by the authors is to make use of other dissipation processes as non-linear dissipation or perhaps more simply to make use of efficiently coupled mechanical resonators.

In terms of perspectives, I am currently active in:

- the use of sustainable materials to design sound absorbing structures and more generally the look out for natural acoustic metamaterials, similarly, the Morpho butterflies in optics and electromagnetism for example [122]. Some structures in acoustics and mechanics are bioinspired [123] but to my knowledge no natural acoustic metamaterial has been found

yet. A simple example might be wheat straw, which is currently studied within the framework of the RFI Le Mans Acoustique (Région Pays de la Loire) PavNat project. Wheat straw can be arranged in the form of ball for thermal and acoustic insulation purpose. This material is therefore a periodic arrangement of hollow tubes densely packed, the acoustic behavior of which can be described under the homogenization theory as an anisotropic porous material with inner resonances [124]. Another possible natural metamaterial is based on Posidonia, the study of which is an on-going subject of collaboration with Univ. Politècnica de València (Gandia Campus).

- the design of metaporoelastic materials for acoustic, elastic and vibroacoustic energy mitigation. The skeleton motion being accounted for, the efficient coupling with Helmholtz resonators with elastic boundaries is of particular interest for example [125].
- the design of thin plates incorporating resonant periodic elements for the vibroacoustic energy mitigation, notably in the framework of the RFI Le Mans Acoustique (Région Pays de la Loire) MetaplaQ project.
- the design of thin and light materials for the insulation (and possible absorption) of sound in duct [126], notably within the framework of the ANR MACIA project.
- the physical understanding of the coupling between resonators loading ducts which is challenging in practice because of a lack of precise modeling accounting for the viscothermal losses of higher order Kirchhoff's modes in ducts for shapes different from circular ones and slits.
- the characterization of the complex wavenumber / frequency dispersion relation of various periodic structures.

Of course this list is not exhaustive and the reader will easily understand that this exercise is complicated, this document being intended to be made public.

Beyond pure scientific perspectives, I strongly believe that the COST Action DENORMS (CA1525), which currently gathers more than 90 institutions across Europe and abroad, and which I am chairing, is a huge opportunity for acousticians and physicists working in the field of multifunctional (meta)materials in relation to audible sound to unify their efforts and encourage new collaborations based on emerging ideas.

Appendix

The previous parts report achievements in the topics of my main activity. To give a more complete overview I would also like to mention some activities related to:

- granular phononic crystals:

Discrete lattice models to describe the phononic band structure of granular crystals have only been recently applied. These discrete models do not only apply for the long-wavelength limit, but provide elastic eigenmodes for all possible wavelengths, which can be used to predict, in particular, the frequency forbidden bands for wave propagation [127, 128, 129]. Elastic eigenmodes of a two-dimensional granular crystal made of circular cross-section, infinitely long cylinders distributed periodically on a square lattice, were theoretically evaluated [103]. Each particle possesses two translational and one rotational degrees of freedom. The interactions between the longitudinal, transversal, and rotational motions of the particles can produce a variety of possible phononic band structures. A remarkable coupling between shear and rotational waves in the lowest-frequency incorporating zero-group velocity point was revealed and a possible realization of the Dirac cones was demonstrated.

The existence of surface elastic waves at a mechanically free surface of granular phononic crystals was studied in [130]. The granular phononic crystals were made of spherical particles distributed periodically on a simple cubic lattice. Rayleigh-type surface acoustic waves, where the displacement of the particles takes place in the sagittal plane while the particles possess one rotational and two translational degrees of freedom, were first analyzed. Shear-Horizontal waves, where the displacement of the particles is normal to the sagittal plane while the particles possess one translational and two rotational degrees of freedom were also studied. The existence of zero-group-velocity surface acoustic waves of Rayleigh type was theoretically predicted and interpreted.

Finally, the existence of a localized mode in a semi-infinite monoatomic chain composed of infinitely long cylinders was demonstrated [131] when transversal-rotational waves are considered, while it is well known that these types of modes do not exist when longitudinal waves are considered.

- inverse problem for the characterization of photonic crystals [132]:

Defaults taking the form of a modification of the optical index of some element of a finite-dimension two-dimensional photonic crystal was recovered by means of a MUSIC type algorithm. The resolution was found to be of the order of the periodicity, which can be

quite below the usual resolution limit. During this time, I learned most of what I know now on the Multiple Scattering Theory.

- development of Transfer Matrix Method which does not diverge [133] for large thickness and complex wavenumbers, inspired by work in the field of the characterization of anisotropic materials by Eddy current methods [134].
- development of Finite-Element codes for the wave propagation in viscoacoustic and viscoelastic media [135, 15], incorporating Perfectly Matched Layer [136] and Fictitious Domains [137].

Bibliography

- [1] S. Brûlé, E. H. Javelaud, S. Enoch, and S. Guenneau. Experiments on seismic metamaterials: Molding surface waves. *Phys. Rev. Lett.*, 112:133901, 2014.
- [2] J. Flores, O. Novaro, and T.H. Seligman. Possible resonance effect in the distribution of earthquake damage in Mexico City. *Nature*, 1987.
- [3] L.E. Perez-Rocha, F.J. Sánchez-Sesma, and E. Reinoso. Threedimensional site effects in Mexico-city: evidence from the accelerometric network observation and theoretical results. In *Proceeding of 4th International Conference on Seismics Zonation*, volume 2, pages 327–334, 1991.
- [4] T. Furumura and B.L.N. Kennett. On the nature of regional seismic phase-III. The influence of crustal heterogeneity on the wavefield for subduction earthquakes: the 1989 Michoacan, and 1995 Copala, Guerrero, Mexico earthquake. *Geophys. J. Int.*, 135:1060–1085, 1009.
- [5] M. Cárdenas-Soto and F.J. Chávez-García. Regional path effect on seismic wave propagation in central Mexico. *Bull. Seism. Soc. Am.*, 93:973–985, 2003.
- [6] F. J. Chávez-García and P.Y. Bard. Site effects in Mexico City eight years after the September 1985 Michoacán earthquakes. *Soil Dyn. Earthq. Eng.*, 13:229–247, 1994.
- [7] A. Wirgin and P.-Y. Bard. Effects of buildings on the duration and amplitude of ground motion in Mexico City. *Bull. Seism. Soc. Am.*, 86:914–920, 1996.
- [8] D. Clouteau and D. Aubry. Modifications of the ground motion in dense urban areas. *J. Comput. Acoust.*, 9:1–17, 2001.
- [9] C. Boutin and Roussillon. Wave propagation in presence of oscillators on the free surface. *Int. J. Engrg. Sci.*, 44:80–204, 2006.
- [10] L. Schwan, C. Boutin, L.A. Padrón, M.S. Dietz, P.Y. Bard, and C. Taylor. Site-city interaction : Theoretical, numerical and experimental crossed-analysis. *Geophys. J. Int.*, 205:1006–1031, 2016.
- [11] M.D. Trifunac. Interaction of a shear wall with the soil for incident plane SH wave. *Bull. Seism. Soc. Am.*, 62:63–83, 1972.

- [12] J.E. Luco and L. Contesse. Dynamic structure-soil-structure interaction. *Bull. Seism. Soc. Am.*, 62:449–462, 1993.
- [13] J.-P. Groby and A. Wirgin. Two-dimensional ground motion at a soft viscoelastic layer/hard substratum site in response to SH cylindrical seismic waves radiated by deep and shallow line sources - I. Theory. *Geophys. J. Int.*, 163:165–191, 2005.
- [14] J.-P. Groby and A. Wirgin. Two-dimensional ground motion at a soft viscoelastic layer/hard substratum site in response to SH cylindrical seismic waves radiated by deep and shallow line sources - II. Numerical results. *Geophys. J. Int.*, 163:192–224, 2005.
- [15] J.-P. Groby. *Modélisation de la propagation des ondes élastiques générées par un séisme proche ou éloigné à l'intérieur d'une ville*. PhD thesis, Université de la Méditerranée - Aix-Marseille II, 2005.
- [16] J.-P. Groby and A. Wirgin. Seismic motion in urban sites consisting of blocks in welded contact with a soft layer overlying a hard half space. *Geophys. J. Int.*, 172:725–758, 2008.
- [17] E. Kjartansson. Constant Q wave propagation and attenuation. *J. Geophys. Res.*, 84:4737–4748, 1979.
- [18] R. Wood. A suspected case of the electrical resonance of minute metal particles for light-waves. A new type of absorption. *Proc. Phys. Soc. London*, 18:166–182, 1902.
- [19] C. Cutler. Electromagnetic waves guided by corrugated structures. Technical Report MM 44-160-218, Bell Telephone Lab, 1944.
- [20] J.-P. Groby, W. Lauriks, and T.E. Vigran. Total absorption peak by use of a rigid frame porous layer backed with a rigid multi-irregularities grating. *J. Acoust. Soc. Am.*, 127:2865–2874, 2010.
- [21] J.-P. Groby, B. Brouard, O. Dazel, B. Nennig, and L. Kelders. Enhancing rigid frame porous layer absorption with three-dimensional periodic irregularities. *J. Acoust. Soc. Am.*, 133:821–831, 2013.
- [22] M. Law, L. E. Greene, J. C. Johnson, R. Saykally, and P. Yang. Nanowire dye-sensitized solar cells. *Nat. Mater.*, 4:455–459, 2005.
- [23] P. Derode, A. P. Roux and M. Fink. Robust acoustic time reversal with high-order multiple scattering. *Phys. Rev. Lett.*, 75:4206, 1995.
- [24] L. Chong, Y. Ge, H. Cao, and A. D. Stone. Coherent perfect absorbers: Time-reversed lasers. *Phys. Rev. Lett.*, 105:053901, 2010.
- [25] J. Mei, G. Ma, M. Yang, Z. Yang, W. Wen, and P. Sheng. Dark acoustic metamaterials as super absorbers for low-frequency sound. *Nat. Commun.*, 3:756, 2012.
- [26] T. Cox and P. d'Antonio. *Acoustic Absorbers and Diffusers*. Taylor & Francis, Abingdon, second edition, 2009.
- [27] T. S. Luk, S. Campione, I. Kim, S. Feng, Y. C. Jun, S. Liu, J. B. Wright, I. Brener, P. B. Catrysse, S. Fan, and M. B. Sinclair. Directional perfect absorption using deep subwavelength low-permittivity films. *Phys. Rev. B*, 90:085411, 2014.

-
- [28] G. Ma, M. Yang, S. Xiao, Z. Yang, and P. Sheng. Acoustic metasurface with hybrid resonances. *Nat. Mater.*, 13:873–878, 2014.
- [29] V. Romero García, G. Theocharis, O. Richoux, A. Merkel, V. Tournat, and V. Pagneux. Perfect and broadband acoustic absorption by critically coupled sub-wavelength resonators. *Sci. Rep.*, 6:19519, 2016.
- [30] D. Johnson, J. Koplik, and R. Dashen. Theory of dynamic permeability and tortuosity in fluid-saturated porous media. *J. Fluid Mech.*, 176:379–402, 1987.
- [31] Y. Champoux and J.-F. J. Allard. Dynamic tortuosity and bulk modulus in air-saturated porous media. *J. Appl. Phys.*, 70:1975–1979, 1991.
- [32] C. Zwikker and C. W. Kosten. *Sound Absorbing Materials*. Elsevier Publishing Inc, New-York, 1949.
- [33] J.-P. Groby, A. Duclos, O. Dazel, L. Boeckx, and L. Kelders. Enhancing absorption coefficient of a backed rigid frame porous layer by embedding circular periodic inclusions. *J. Acoust. Soc. Am.*, 130:3771–3780, 2011.
- [34] J.-P. Groby, B. Nennig, C. Lagarrigue, B. Brouard, O. Dazel, and V. Tournat. Using simple shape three-dimensional inclusions to enhance porous layer absorption. *J. Acoust. Soc. Am.*, 136:1139–1148, 2014.
- [35] C. Lagarrigue, J.-P. Groby, V. Tournat, O. Dazel, and O. Umnova. Absorption of sound by porous layers with embedded periodic array of resonant inclusions. *J. Acoust. Soc. Am.*, 134:4670–4680, 2013.
- [36] J.-P. Groby, B. Nennig, C. Lagarrigue, B. Brouard, O. Dazel, and V. Tournat. Enhancing the absorption properties of acoustic porous plates by periodically embedding helmholtz resonators. *J. Acoust. Soc. Am.*, 137:273–280, 2015.
- [37] J.-P. Groby, A. Duclos, O. Dazel, L. Boeckx, and W. Lauriks. Absorption of a rigid frame porous layer with periodic circular inclusions backed by a periodic grating. *J. Acoust. Soc. Am.*, 129:3035–3046, 2011.
- [38] C. Lagarrigue, J.-P. Groby, V. Tournat, and O. Dazel. Design of metaporous supercells by genetic algorithm for absorption optimization on a wide frequency band. *Appl. Acoust.*, 102:49–54, 2016.
- [39] T. Weisser, J.-P. Groby, O. Dazel, F. Gautier, E. Deckers, S. Futatsugi, and L. Monteiro. Acoustic behavior of a rigidly backed poroelastic layer with periodic resonant inclusions by a multiple scattering approach. *J. Acoust. Soc. Am.*, 139:617–630, 2016.
- [40] M. A. Biot. Theory of propagation of elastic waves in a fluid-saturated porous solid. I. Low-frequency range and II. Higher frequency. *J. Acoust. Soc. Am.*, 28:168–178 and 179–191, 1956.
- [41] M. A. Biot. Mechanics of deformation and acoustic propagation in porous media. *J. Appl. Phys.*, 33:1482–1498, 1962.

- [42] L. De Ryck, J.-P. Groby, P. Leclaire, W. Lauriks, A. Wirgin, C. Depollier, and Z.E.A. Fellah. Acoustic wave propagation in a macroscopically inhomogeneous porous medium saturated by a fluid. *Appl. Phys. Lett.*, 90:181901, 2007.
- [43] G. Gautier, J.-P. Groby, O. Dazel, L. Kelders, L. De Ryck, and P. Leclaire. Propagation of acoustic waves in a one-dimensional macroscopically inhomogeneous poroelastic material. *J. Acoust. Soc. Am.*, 130:1390–1398, 2011.
- [44] L. De Ryck, P. Leclaire, J.-P. Groby, W. Lauriks, A. Wirgin, and C. Depollier. Reconstruction of material properties profiles in one-dimensional macroscopically inhomogeneous rigid frame porous media in the frequency domain. *J. Acoust. Soc. Am.*, 124:1591–1606, 2008.
- [45] A. Geslain, J.-P. Groby, O. Dazel, S. Mahasaranon, K. V. Horoshenkov, and A. Khan. An application of the Peano series expansion to predict sound propagation in materials with continuous pore stratification. *J. Acoust. Soc. Am.*, 132:208–215, 2012.
- [46] R. Elliott, A. Venegas, J.-P. Groby, and O. Umnova. Omnidirectional acoustic absorber with a porous core and a metamaterial matching layer. *J. Appl. Phys.*, 115:204902, 2014.
- [47] M. S. Kushwaha, P. Halevi, L. Dobrzynski, and B. Djafari-Rouhani. Acoustic band structure of periodic elastic composites. *Phys. Rev. Lett.*, 71:2022, 1993.
- [48] M.M. Sigalas and E.N. Economou. Elastic and acoustic wave band structure. *J. Sound Vibration*, 158:377–382, 1992.
- [49] R. Martínez-Sala, J. Sancho, J. V. Sánchez, V. Gómez, and J. Llinares. Sound attenuation by sculpture. *Nature*, 378:241, 1995.
- [50] J. D. Joannopoulos, S. G. Johnson, J. N. Winn, and R. D. Meade. *Photonic Crystals: Molding the Flow of Light*. Princeton University Press, Princeton, second edition edition, 2008.
- [51] Z. Liu, X. Zhang, Y. Mao, Y. Y. Zhu, Z. Yang, C.T. Chan, and P. Sheng. Locally resonant sonic materials. *Science*, 289:1734–1736, 2000.
- [52] V. M. García-Chocano, S. Cabrera, and J. Sánchez-Dehesa. Broadband sound absorption by lattices of microperforated cylindrical shells. *Appl. Phys. Lett.*, 101:184101, 2012.
- [53] R. Wang, X.-H. Wang, B.-Y. Gu, and G.-Z. Yang. Effects of shapes and orientations of scatterers and lattice symmetries on the photonic band gap in two-dimensional photonic crystals. *J. Appl. Phys.*, 90:4307–4313, 2001.
- [54] C. Goffaux and J. P. Vigneron. Theoretical study of a tunable phononic band gap system. *Phys. Rev. B*, 64:075118, 2001.
- [55] V. Romero García, C. Lagarrigue, J.-P. Groby, O. Richoux, and V. Tournat. Tunable acoustic waveguides in periodic arrays made of rigid square-rod scatterers: theory and experimental realization. *J. Phys. D: Appl. Phys.*, 46:305108, 2013.
- [56] A. Lardeau, J.-P. Groby, and V. Romero García. Broadband transmission loss using 3D locally resonant sonic crystals. *Crystals*, 6:51, 2016.

-
- [57] J. Vasseur, P. Deymier, B. Chenni, B. Djafari-Rouhani, L. Dobrzynski, and D. Prevost. Experimental and theoretical evidence for the existence of absolute acoustic band gaps in two-dimensional solid phononic crystals. *Phys. Rev. Lett.*, 86:3012, 2001.
- [58] R.P. Moiseyenko and V. Laude. Material loss influence on the complex band structure and group velocity in phononic crystals. *Phys. Rev. B*, 83:064301, 2011.
- [59] C. G. Poulton, A. B. Movchan, R. C. McPhedran, N. A. Nicorovici, and Y. A. Antipov. Eigenvalue problems for doubly periodic elastic structures and phononic band gaps. *Proc. R. Soc. A*, 456:2543–2559, 2000.
- [60] A. Duclos. *Diffusion multiple en fluide visco-thermique, cas du cristal phononique à deux dimensions*. PhD thesis, Université du Maine, 2007.
- [61] V. Romero García, L. M. Garcia-Raffi, and J. V. Sánchez-Pérez. Evanescent waves and deaf bands in sonic crystals. *AIP Adv.*, 1:041601, 2011.
- [62] J.-P. Groby, A. Wirgin, and E. Ogam. Acoustic response of a periodic distribution of macroscopic inclusions within a rigid frame porous plate. *Wave Random Complex*, 18:409–433, 2008.
- [63] H. Pichard, O. Richoux, and J.-P. Groby. Experimental demonstrations in audible frequency range of band gap tunability and negative refraction in two-dimensional sonic crystal. *J. Acoust. Soc. Am.*, 132:2816–2822, 2012.
- [64] L.V. Hau, S.E. Harris, Z. Dutton, and C.H. Behroozi. Light speed reduction to 17 metres per second in an ultracold atomic gas. *Nature*, 397:594–598, 1999.
- [65] A. Santillan and S.I. Bozhevolnyi. Demonstration of slow sound propagation and acoustic transparency with a serie of detuned resonators. *Phys. Rev. B*, 89:184301, 2014.
- [66] G. Yu and X. Wang. Acoustical "transparency" induced by local resonance in bragg bandgaps. *J. Appl. Phys.*, 115:044913, 2014.
- [67] A. Cicek, O.A. Kaya, M. Yilmaz, and B. Ulug. Slow sound propagation in a sonic crystal linear waveguide. *J. Appl. Phys.*, 111:013522, 2012.
- [68] Y. Aurégan and V. Pagneux. Slow sound in lined flow ducts. *J. Acoust. Soc. Am.*, 138:605, 2015.
- [69] W.M. Robertson, C. Baker, and C.B. Brad Bennet. Slow group velocity propagation of sound via defect coupling in a one-dimensional acoustic band gap array. *Am. J. Phys.*, 72:255–257, 2003.
- [70] G. Theocharis, O. Richoux, V. Romero García, A. Merkel, and V. Tournat. Limits of slow sound propagation and transparency in lossy, locally resonant periodic structures. *New J. Phys.*, 16:093017, 2014.
- [71] J.-P. Groby, W. Huang, A. Lardeau, and Y. Aurégan. The use of slow sound to design simple sound absorbing materials. *J. Appl. Phys.*, 117:124903, 2015.
- [72] J.-P. Groby, R. Pommier, and Y. Aurégan. Use of slow sound to design perfect and broadband passive sound absorbing materials. *J. Acoust. Soc. Am.*, 139:1660–1671, 2016.

- [73] N. Jiménez, H. Huang, V. Romero García, V. Pagneux, and J.-P. Groby. Ultra-thin metamaterial for perfect and quasi-omnidirectional sound absorption. *Appl. Phys. Lett.*, 109:121902, 2016.
- [74] M. L. Stinson. The propagation of plane sound waves in narrow and wide circular tubes, and generalization to uniform tubes of arbitrary cross-sectional shape. *J. Acoust. Soc. Am.*, 89:550–558, 1991.
- [75] N. Fang, D. Xi, J. Xu, M. Ambati, W. Srituravanich, C. Sun, and X. Zhang. Ultrasonic metamaterials with negative modulus. *Nat. Mater.*, 5:452 – 456, 2006.
- [76] X. Cai, Q. Guo, G. Hu, and J. Yang. Ultrathin low-frequency sound absorbing panels based on coplanar spiral tubes or coplanar helmholtz resonators. *Appl. Phys. Lett.*, 105:121901, 2014.
- [77] N. Jiménez, V. Romero García, V. Pagneux, and J.-P. Groby. Quasiperfect absorption by subwavelength acoustic panels in transmission using accumulation of resonances due to slow sound. *Phys. Rev. B*, 95:014205, 2017.
- [78] C. Yang, M. Meng, C. Fu, Y. Li, Z. Yang, and P. Sheng. Subwavelength total acoustic absorption with degenerate resonators. *Appl. Phys. Lett.*, 107:104104, 2015.
- [79] N. Jiménez, V. Romero García, V. Pagneux, and J.-P. Groby. Rainbow-trapping absorbers: Broadband, perfect and asymmetric sound absorption by subwavelength panels for transmission problems. *ArXiv*, page 1708.03343, 2017. submitted to Sci. Rep.
- [80] N. Jiménez, T. J. Cox, V. Romero García, and J.-P. Groby. Metadiffusers: Deep-subwavelength sound diffusers. *Sci. Rep.*, 7:5389, 2017.
- [81] Y. Zhu, X. Fan, B. Liang, J. Cheng, and Y. Jing. Ultrathin acoustic metasurface-based schroeder diffuser. *Phys. Rev. X*, 7:021034, 2017.
- [82] M. R. Schroder. Diffuse sound reflection by maximum-length sequences. *J. Acoust. Soc. Am.*, 57:149–150, 1975.
- [83] L. Schwan, O. Umnova, and C. Boutin. Sound absorption and reflection from a resonant metasurface : homogenization model with experimental validation. *Wave Motion*, 72:154–172, 2017.
- [84] L. L. Beranek. Acoustic impedance of porous materials. *J. Acoust. Soc. Am.*, 13:248–260, 1942.
- [85] R. L. Brown and R. H. Bolt. The measurement of flow resistance of porous acoustic materials. *J. Acoust. Soc. Am.*, 13:337–344, 1942.
- [86] J.-F. Allard and N. Atalla. *Propagation of Sound in Porous Media: Modelling Sound Absorbing Materials*. John Wiley & Sons, Ltd, Chichester, 2009.
- [87] Z.E.A. Fellah, C. Depollier, S. Berger, W. Lauriks, P. Trompette, and J.-Y. Chapelon. Determination of transport parameters in air-saturated porous materials via reflected ultrasonic waves. *J. Acoust. Soc. Am.*, 113:2561–2569, 2003.

-
- [88] P. Leclaire, L. Kelders, W. Lauriks, M. Melon, N. Brown, and B. Castagnède. Determination of the viscous and thermal characteristic lengths of plastic foams by ultrasonic measurements in helium and air. *J. Appl. Phys.*, 80:2009–2012, 1996.
- [89] A. M. Nicholson and G. F. Ross. Measurement of the intrinsic properties of materials by time-domain techniques. *IEEE Trans. Instrum. Meas.*, 19:382–492, 1970.
- [90] J.-P. Groby, E. Ogam, L. De Ryck, N. Sebaa, and W. Lauriks. Analytical method for the ultrasonic characterization of homogeneous rigid porous materials from transmitted and reflected coefficients. *J. Acoust. Soc. Am.*, 127, 764–772 2010.
- [91] D. Lafarge, P. Lemarinier, J.-F. Allard, and V. Tarnow. Dynamic compressibility of air in porous structures at audible frequencies. *J. Acoust. Soc. Am.*, 102:1995–2006, 1997.
- [92] R. Panneton and X. Olny. Acoustical determination of the parameters governing viscous dissipation in porous media. *J. Acoust. Soc. Am.*, 119:2027–2040, 2006.
- [93] X. Olny and R. Panneton. Acoustical determination of the parameters governing thermal dissipation in porous media. *J. Acoust. Soc. Am.*, 123:814–824, 2008.
- [94] J. Kaipio and E. Somersalo. *Statistical and Computational Inverse Problems*. Springer-Verlag, New-York, 2005.
- [95] J.-D. Chazot, E. Zhang, and J. Antoni. Acoustical and mechanical characterization of poroelastic materials using a bayesian approach. *J. Acoust. Soc. Am.*, 131:4584–4595, 2012.
- [96] M. Niskanen, J.-P. Groby, A. Duclos, O. Dazel, J.-C. Le Roux, N. Poulain, T. Huttunen, and T. Lähivaara. Deterministic and statistical characterization of rigid frame porous materials from impedance tube measurements. *submitted to J. Acoust. Soc. Am.*, 2017.
- [97] J. Prisutova, K. Horoshenkov, J.-P. Groby, and B. Brouard. A method to determine the acoustic reflection and absorption coefficients of porous media by using modal dispersion in a waveguide. *J. Acoust. Soc. Am.*, 136:2947–2958, 2014.
- [98] J. Prisutova, K. Horoshenkov, B. Brouard, and J.-P. Groby. An application of normal mode decomposition to measure the acoustical properties of low growing plants in a broad frequency range. *Appl. Acoust.*, 117:39–50, 2016.
- [99] R. D. S. Yadava, R. Kshetrimayum, and M. Khaneja. Multifrequency characterization of viscoelastic polymers and vapor sensing based on saw oscillators. *Ultrasonics*, 49:638–645, 2009.
- [100] H.-X. Sun, S.-Y. Zhang, and B.-Q. Xu. Influence of viscoelastic property on laser-generated surface acoustic waves in coating–substrate systems. *J. Appl. Phys.*, 109(7):073107, 2011.
- [101] J. H. Page, P. Sheng, H. P. Schriemer, I. Jones, X. Jing, and D. A. Weitz. Group velocity in strongly scattering media. *Science*, 271:634–637, 1996.
- [102] Z. Liu, C. T. Chan, P. Sheng, A. L. Goertzen, and J. H. Page. Elastic wave scattering by periodic structures of spherical objects: Theory and experiment. *Phys. Rev. B*, 62:2446–2457, 2000.

- [103] H. Pichard, A. Duclos, J-P. Groby, V. Tournat, and V. E. Gusev. Two-dimensional discrete granular phononic crystal for shear wave control. *Phys. Rev. B*, 86:134307, 2012.
- [104] R. J. P. Engelen, D. Mori, T. Baba, and L. Kuipers. Subwavelength structure of the evanescent field of an optical bloch wave. *Phys. Rev. Lett.*, 102:023902, 2009.
- [105] V. Romero García, J. V. Sánchez-Pérez, S. Castiñeira-Ibáñez, and L. M. García-Raffi. Evidences of evanescent bloch waves in phononic crystals. *Appl. Phys. Lett.*, 96:124102, 2010.
- [106] R.O. Schmidt. Multiple emitter location and signal parameter estimation. *IEEE T. Antenn. Propag.*, 34:276–280, 1986.
- [107] E. C. Shang, H. P. Wang, and Z. Y. Huang. Waveguide characterization and source localization in shallow water waveguides using the prony method. *J. Acoust. Soc. Am.*, 83:103–108, 1988.
- [108] R. Roy, A. Paulraj, and T. Kailath. Esprit—a subspace rotation approach to estimation of parameters of cisoids in noise. *IEEE T. Acoust. Speech*, 34:1340–1342, 1986.
- [109] R. Roy and T. Kailath. Esprit-estimation of signal parameters via rotational invariance techniques. *IEEE T. Acoust. Speech*, 37:984–995, 1989.
- [110] F. Schöpfer, F. Binder, A. Wöstehoff, T. Schuster, S. Ende, S. Föll, and R. Lammering. Accurate determination of dispersion curves of guided waves in plates by applying the matrix pencil method to laser vibrometer measurement data. *CEAS Aeronautical Journal*, 4:61–68, 2013.
- [111] F. Philippe, P. Roux, and D. Cassereau. Iterative high-resolution wavenumber inversion applied to broadband acoustic data. *IEEE Trans. Ultrason. Ferroelectr. Freq. Control.*, 55:2306–2311, 2008.
- [112] C. Prada, D. Clorennec, and D. Royer. Power law decay of zero group velocity lamb modes. *Wave Motion*, 45:723–728, 2008.
- [113] G. Rix, C. Lai, and A. Spang Jr. In situ measurement of damping ratio using surface waves. *J. Geotech. Geoenviron. Eng.*, 126:472–480, 2000.
- [114] K. J. Ellefsen, C. H. Cheng, and K. M. Tubman. Estimating phase velocity and attenuation of guided waves in acoustic logging data. *Geophysics*, 54:1054–1059, 1989.
- [115] S. Foti. Small-strain stiffness and damping ratio of pisa clay from surface wave tests. *Géotechnique*, 53:455–461, 2003.
- [116] A. S. Misbah and C. L. Strobbia. Joint estimation of modal attenuation and velocity from multichannel surface wave data. *Geophysics*, 79:EN25–EN38, 2014.
- [117] J.-G. Minonzio, J. Foiret, M. Talmant, and P. Laugier. Impact of attenuation on guided mode wavenumber measurement in axial transmission on bone mimicking plates. *J. Acoust. Soc. Am.*, 130:3574–3582, 2011.

-
- [118] A. Geslain, S. Raetz, M. Hirwia, M. Abi Ghamen, S.P. Wallen, A. Khanolkar, N. Boechler, J. Laurent, C. Prada, A. Duclos, P. Leclaire, and J.-P. Groby. Spatial laplace transform for complex wavenumber recovery and its application to the analysis of attenuation in acoustic systems. *J. Appl. Phys.*, 120:135107, 2016.
- [119] L. Schwan, A. Geslain, V. Romero García, and J.-P. Groby. Complex dispersion relation of surface acoustic waves at a lossy metasurface. *Appl. Phys. Lett.*, 110:051902, 2017.
- [120] M. Hiraiwa, M. Abi Ghanem, S. Wallen, A. Khanolkar, A. A. Maznev, and N. Boechler. Complex contact-based dynamics of microsphere monolayers revealed by resonant attenuation of surface acoustic waves. *Phys. Rev. Lett.*, 116:198001, 2016.
- [121] M. Yang, S. Chen, C. Fu, and P. Sheng. Optimal sound-absorbing structures. *Mater. Horiz.*, 4:673–680, 2017.
- [122] P. Vukusic and J. R. Sambles. Photonic structures in biology. *Nature*, 424:852–855, 2003.
- [123] M. Miniaci, A. A. Krushynska, A. B. Movchan, F. Bosia, and N. Pugno. Spider web-inspired acoustic metamaterial. *Appl. Phys. Lett.*, 109:071905, 2016.
- [124] W. Huang, L. Schwan, V. Romero García, J.-M. Gènevaux, and J.-P. Groby. 3D-printed straw-inspired metamaterial for sound absorption. In *Proceeding of Metamaterials'2017*, Marseille, 2017.
- [125] A. Norris and G. Wickham. Elastic helmholtz resonators. *J. Acoust. Soc. Am.*, 93:617–630, 1993.
- [126] Y. Aurégan, M. Farooqui, and J.-P. Groby. Low frequency sound attenuation in a flow duct using a thin slow sound material. *J. Acoust. Soc. Am. Exp. Lett.*, 139:EL149, 2015.
- [127] V. Gusev and V. Tournat. How acoustic waves are guided in buried subsurface channels in unconsolidated granular media. *Phys. Rev. E*, 78:036602, 2008.
- [128] A. Merkel, V. Tournat, and V. Gusev. Dispersion of elastic waves in three-dimensional noncohesive granular phononic crystals: Properties of rotational modes. *Phys. Rev. E*, 82:031305, 2010.
- [129] A. Merkel, V. Tournat, and V. Gusev. Experimental evidence of rotational elastic waves in granular phononic crystals. *Phys. Rev. Lett.*, 107:225502, 2011.
- [130] H. Pichard, A. Duclos, J.-P. Groby, V. Tournat, L. Zheng, and V. E. Gusev. Surface waves in granular phononic crystals. *Phys. Rev. E*, 93:023008, 2016.
- [131] H. Pichard, A. Duclos, J.-P. Groby, V. Tournat, and V. E. Gusev. Localized transversal-rotational modes in linear chains of equal masses. *Phys. Rev. E*, 89:013201, 2014.
- [132] J.-P. Groby and D. Lesselier. Localization and characterization of simple defects in finite-sized photonic crystals. *J. Opt. Soc. Am. A*, 25:146–152, 2008.
- [133] O. Dazel, J.-P. Groby, B. Brouard, and C. Potel. A stable method to model the acoustic response of multilayered structures. *J. Appl. Phys.*, 113:083506, 2013.

BIBLIOGRAPHY

- [134] H. Yang. A spectral recursive transformation method for electromagnetic waves in generalized anisotropic layered media. *IEEE Trans. Antennas. Propag.*, 45:520–526, 1997.
- [135] J.-P. Groby and C. Tsogka. A time domain method for modeling viscoacoustic wave propagation. *J. Comput. Acoust.*, 14:201–236, 2006.
- [136] J.-P. Bérenger. A perfectly matched layer for the absorption of electromagnetic waves. *J. Comput. Phys.*, 114:185–200, 1994.
- [137] R. Glowinski, T. W. Pan, and J. Periaux. A fictitious domain method for dirichlet problem and applications. *Comput. Methods in Appl. Mech. Eng.*, 111:283–303, 1994.

Part II

Scientific Curriculum Vitæ

Chapter 4

Curriculum vitæ

Jean-Philippe Groby

Laboratoire d'Acoustique de l'Université du Mans (LAUM), UMR CNRS 6613
Avenue Olivier Messiaen
F-72085 LE MANS Cedex 9 France.

Born on 16th August 1979

4.1 Short Bio

Positions and responsibilities

Researcher at CNRS/Chargé de Recherche CNRS, Laboratoire d'Acoustique de l'Université du Mans (LAUM), UMR CNRS 6613, France, since Oct. 2009.

Research interest: Acoustic metamaterials and acoustic structured materials.

Chair of COST Action DENORMS (CA15125).

Elected member of Le Mans University «Commissions Consultatives d'Établissement»(CCE) 60-63 since May 2012.

Nominated INSIS (Institut des Sciences de l'ingénierie et des systèmes - CNRS) innovation representative for LAUM since 2017.

Previous responsibilities

2016 - 2012 Elected member of the LAUM council.

2014 - 2011 Leader of the LAUM Research Group *Acoustics and Mechanics of Porous Materials*.

Past experiences (Post-doctoral fellowships)

Sept. - April 2009 Institut d'Électronique, de Microélectronique et de Nanotechnologie (IEMN)^[1], Univ. Lille 1, UMR CNRS 8520, France.

March - Jan. 2009 Laboratory of Acoustics and Thermal Physics (ATF) now Laboratory for Soft Matter and Biophysics (ZMB), KULeuven, Belgium.

Dec. 2008 - Oct. 2007 Laboratoire des Signaux et Systèmes (L2S)^[2], Centrale-Supélec/Univ. Paris Sud 11, UMR 8506 CNRS, France.

- Sept. 2007 - Oct. 2006 Centre de Mathématiques Appliquées (CMAP)^[3], École Polytechnique, UMR 7641 CNRS, France.
- Sept. 2006 - Oct. 2005 Laboratory of Acoustics and Thermal Physics (ATF), KULeuven, Belgium.

^[1]ANR Project SUPREME.

^[2]*System@tic Paris-Région* Competitiveness Cluster, *Usine Numérique* project, *On-Trac* sub-project (12 months), and direct funding from CEA-LIST (3 months).

^[3]CNRS Post-doctoral fellowship 2006-2007 SPM-24 «Composite imaging».

Education

- 2005 **PhD** in Mechanical Engineering (with honors), Université de la Méditerranée Aix-Marseille II.
Laboratoire de Mécanique et d'Acoustique (LMA), UPR CNRS 7051.
Dissertation: Modeling of elastic waves inside a city generated by distant or nearby seismic sources.
Advisors: A. Wirgin and C. Tsogka.
- 2002 **M.S.** (with honors), major in Acoustics, Université de la Méditerranée Aix-Marseille II.
- 2002 **Degree of Engineer** (with highest honors), major in Marine Engineering, École Supérieure d'Ingénieurs de Marseille (ESIM - now École Centrale Marseille).

4.2 Activities

Expertise

Disciplines	acoustics, elasticity, optics, electromagnetism
Investigation	wave interaction with structured -grating, sonic & photonic crystals, and metamaterials-, continuously inhomogeneous, dissipative, poroelastic, viscoelastic, and anisotropic medium
Fields of application	design of acoustic materials, seismic, characterization of industrial and biological materials, non-destructive testing
Tools	semi-analytical modeling, numerical simulations and experiments both in the ultrasonic and audible frequency ranges
Code development	finite-element codes ^[1] : 2D viscoacoustic, 2D-SH viscoelastic, 2D-PSV viscoelastic, and 2D-TM optic waves equations

^[1]Codes initially developed at LMA, based on ACOUST2D previously developed at LMA and on ELAST2D previously developed at INRIA.

Research supervision

PhD students

M. Malléjac (advisors: J.-P. Groby -40%-, V. Romero García -30%- and V. Tournat -30%-), T. Cavalieri (advisors: J.-P. Groby -40%-, V. Romero García -30%- and G. Gabard -30%-), Safran Aircraft Engines advisors: M. Escoufflaire and J. Mardjono), and J. Boulvert (joint PhD with Univ. Polytechnique de Montréal; French advisors: J.-P. Groby -40%-, V. Romero García -30%- and G. Gabard -30%-, Safran Aircraft Engines advisor: J. Mardjono; Canadian advisor: A. Ross) will start their PhD in October 2017.

- Since 2015 W. Huang, LAUM, funded by the RFI Le Mans Acoustique (Région Pays de la Loire) PavNat project; advisors: J.M. Gèneveau (40%), V. Romero García (30%) and J.-P. Groby (30%).
Acoustic properties of natural materials.
- Since 2015 M. Niskanen, joint PhD between LAUM and Univ. Eastern Finland (Kuopio), funded by the RFI Le Mans Acoustique (Région Pays de la Loire) Decimap project; French advisors: O. Dazel (40%), A. Duclos (30%) and J.-P. Groby (30%); Finnish advisors: T. Huttunen, T. Lähivaara, and J. Kaipio.
Ultrasonic characterization of poroelastic materials saturated by heavy fluids.
- 2014 - 2011 H. Pichard, LAUM, advisors: V. Gusev (40%), A. Duclos (30%) and J.-P. Groby (30%).
Guided waves in granular phononic crystals., defended 28th Nov. 2014.
Currently Post-Doc in Inst. de Mécanique et d'Ingénierie, UMR 5295 CNRS.
- 2013 - 2010 C. Lagarrigue, LAUM, advisors: V. Tournat (40%) and J.-P. Groby (60%).
Efficient Metamaterials in the audible frequency range: Simulation and experiments, defended 27th Sept. 2013.
Awards: Concours National de Création d'Entreprise de Technologie Innovante, coorganized by the French Research ministry and BPI France in 2013; Sarthe Me Up, organized by Conseil Général de la Sarthe in 2013; and Yves Rocard prize from the French Acoustical Society in 2014
Currently founder and CEO of Metacoustic.
- 2011 - 2009 A. Geslain, LAUM, advisors: S. Sahraoui (40%), O. Dazel (30%) and J.-P. Groby (30%).
Natural and induced anisotropy of porous materials: Experiments and modeling, defended 9th Dec. 2011.
Currently Assist. Prof. in Institut Supérieur de l'Automobile et des Transports, Univ Bourgogne.

Strong involvement in the supervision

- Since 2016 J. Leng, joint PhD between LAUM and Univ. Politèc. de Valencia funded by the RFI Le Mans Acoustique (Région Pays de la Loire) MetaplaQ project, advisors: F. Gautier, A. Pelat, V. Romero García and R. Picò.
Design of metaplate for the control of flexural waves
- 2008 - 2005 L. De Ryck, ATF/LMA, advisors: W. Lauriks and A. Wirgin.
Acoustical characterization of macroscopically inhomogeneous porous materials, defended 10th July 2008.
Currently development engineer at Siemens Industry Software NV, Belgium.

Post-Doctoral fellows

- Since 2016 L. Schwan, funded by Le Mans Univ. and RFI Le Mans Acoustique (Région Pays de la Loire) PavNat project.
- 2017 - 2015 N. Jiménez, funded by ANR Metaudible, in collaboration with V. Romero García.
Currently Post-doctoral fellow at the Insitute for Instrumentation and Molecular Imaging (I3M) of the Spanish National Research Council (CSIC), Spain.

- Aug. - May 2016 A. Merkel, funded by RFI Le Mans Acoustique (Région Pays de la Loire) PavNat project.
Currently Post-doctoral fellow at the Instituto Gregorio Millán Barbany, Universidad Carlos III de Madrid, Spain.
- 2014 - 2013 T. Weisser, funded by a Brazilian company, in collaboration with F. Gautier and O. Dazel.
Currently Assist. Prof. in École Nationale Supérieure d'Ingénieurs Sud Alsace, Univ. Haute Alsace.

Other researchers

- 2015 - 2013 C. Lagarrigue, project funded by Ouest Valorisation (SATT), in collaboration with V. Tournat and O. Dazel.
- July - Jan. 2013 J. Prisutova, PhD student from the University of Bradford (advisor K. Horoshenkov) in collaboration with B. Brouard.
Use of impedance tube higher order modes for the characterization of sound absorbing materials: application to the characterization of plant absorption.
- Dec. - Sept. 2010 G. Gautier, KULEuven, in collaboration with O. Dazel and C. Glorieux.
Poroelastic material characterization by use of guided waves.

Academic duties

Projects as Principal Investigator or Task Leader

- 2020 - 2016 Task leader in ANR Chaire industrielle MACIA, Le Mans Univ./SAFRAN Group, Principal Investigator: Y. Aurégan, Chair: G. Gabard.
- 2020 - 2016 Chair and Scientific Representative of the Grant Holder of COST Action DENORMS (CA15125).
Designs for Noise Reducing Materials and Structures.
- 2018 - 2015 RFI Le Mans Acoustique (Région Pays de la Loire) PavNat.
Acoustic and Vibroacoustic properties of natural materials.
- 2017 - 2013 ANR Metaudible (ANR-13-BS09-003) co-funded by Fédération de Recherche pour l'Aéronautique et l'Espace (FNRAE).
Design of metamaterials for the absorption of audible sound.
- 2013 - 2012 High-level foreign researcher fellowship from the Région Pays de la Loire: 6 months grant for Olga Umnova (Univ. de Salford, U.K.).
- 2012 - 2010 PHC TOURNESOL (FL 2011 - 25352YD).
Sustainable design of structured acoustic materials.

Projects as partner or participant (beyond Post-doctoral funding)

- 2019 - 2016 RFI Le Mans Acoustique (Région Pays de la Loire) MetaplaQ project, coordinated by F. Gautier.
Control of flexural waves in beams and plates incorporating local resonators.
- 2017 - 2014 RFI Le Mans Acoustique (Région Pays de la Loire) Decimap project, coordinated by A. Duclos.
Characterization of non-Newtonian fluid saturated porous materials by means of pulse deconvolution.

- 2013 - 2010 ANR Blanc Stabingram (ANR-10-BLAN-0927), coordinated by P. Gondret.
Granular medium destabilization.
- 2007 - 2005 Action CNRS/États-Unis (3321) - Cooperation funding USA/France (NSF 0438765), coordinated by A. Wirgin.
Vibroacoustic characterization of bone - application to the osteoporosis diagnose.

Industrial contracts and technology transfers

- Since 2015 Collaboration contract with Metacoustic.
- Since 2010 Several research contracts with Centre de Transfert de Technologie du Mans (CTTM).
- 2017 Funding for a Master II internship by SNCF
- 2013 Funding for a one year post-doctoral position by a Brazilian compagny.
- 2013 Funding for the project Metacoustic by Ouest Valorisation (SATT).

Editing

I am currently acting as guest editor, together with J. Sánchez-Dehesa and O. Umnova, for the special issue *Modeling of structured materials for sound and vibration* of Acta Acustica united with Acoustic, to be published in Jan. 2018. This special issue follows the DENORMS Action CA15125 Workshop on *Modelling of high performance acoustic structures Porous media, meta-materials and sonic crystals* held in Rome in Jan. 2017.

In 2017-2018, I will act as Editor of the book *Fundamental on Acoustic Periodic structures, Metamaterials, Non-linear propagation, and Porous Materials*, which originates from the DENORMS Action CA15125 Training School, *Sound waves in metamaterials and porous materials* held in Prague in Sept. 2016. Springer accepted to publish this book in the series Materials Sciences.

Since January 2017, I am also member of the Editorial Board of Building Acoustics.

Scientific expert for: Haut Conseil de l'Évaluation de la Recherche et de l'Enseignement Supérieur (HCERES) -PHASE Laboratory, EA CNRS 3028, Toulouse, 2014-; Agence Nationale de la Recherche (ANR); Czech Science Foundation; Campus France (Cofecub); Région Nord Pas de Calais; MITACS; National Research Foundation Singapore; and Polish National Science Centre.

Reviewer for international journals

I am reviewing on average 15 journal articles per year, mainly for the following journals:

Physics: Scientific Reports, Journal of Applied Physics, Proceedings of the Royal Society A, Physics Letters A.

Acoustics: Journal of the Acoustical Society of America, Waves in Random and Complex Media, Wave Motion, Ultrasonics, Journal of Sound and Vibration, Acta Acustica united with Acustica.

Applied Mathematics: Journal of Computational Physics, Mathematical and Computer Modelling, Journal of Mathematical Imaging and Vision, Applied Mathematical Modelling.

Others: Soil Dynamics and Earthquake Engineering, Radio Science, Cold Regions Science and Technology, International Journal of Thermophysics, Journal of Applied Geophysics, Geophysical prospecting, Aerospace, International Journal of Mechanical Sciences, Frontiers in Mechanical Engineering.

Membership

Member of the French Acoustical Society (SFA).

Chairman and organizer of structured sessions in national and international congresses

- Sept. 2017 *Special Session on Acoustic Metamaterials for Noise Reduction*, Metamaterials'2017, Marseilles, together with V. Romero García.
- July 2017 Chair of one of the seven sessions on *Acoustic and elastic metamaterials*, 13th International Conference on Theoretical and Computational Acoustics, Vienna, organized by A. Norris.
- June 2017 Chair of the session *DENORMS - Noise control using acoustic metamaterials, metasurfaces and sonic crystals as well as porous materials*, 61st Meeting of the Society for Electronics, Telecommunications, Computers, Automatic Control and Nuclear Engineering, Kladovo, together with D. Ćirić, organized by D. Ćirić.
- June 2017 Chair of the session *Acoustic properties of materials, Noise*, 4th International Conference on Electrical, Electronic and Computing Engineering, Kladovo, together with D. Ćirić, organized by D. Ćirić.
- April 2016 *Structured materials in vibroacoustics and acoustics*, 13ème Congrès Français d'Acoustique, Le Mans, together with M. Collet and M. Ouisse.
Porous materials, 13ème Congrès Français d'Acoustique, Le Mans, together with B. Nennig.
- June 2015 *Structured materials and metamaterials for the control of audible sound*, Euronoise 2015, Maastricht, together with O. Umnova.
- April 2014 *Acoustic materials*, 12ème Congrès Français d'Acoustique, Poitiers, together with B. Nennig.
- April 2012 *Sound absorbing materials and porous media (In Memory of Walter Lauriks)*, Acoustics 2012, Nantes, together with O. Umnova and C. Glorieux.

Organizer of national and international congresses, Training Schools, and Workshops

In 2017-2018, I will mainly co-organize a Workshop (Leuven, 7th-9th Feb 2018) and a Training School (Le Mans, 4th-6th Dec. 2017) both in the framework of DENORMS Action, and the 5th Symposium on the Acoustics of Poro-Elastic Media (Le Mans, 6th-8th Dec. 2017).

- Sept. 2017 DENORMS Action Brainstorming Workshop *Sandpit: New approaches to design of noise reducing materials and structures*, Novi-Sad, together with A. Krynkin, T. Zielinski, M. Rychtarikova, N. Dauchez, A. Duval, L. Cveticanin, O. Umnova, and P. Rasera.
- Sept. 2017 DENORMS - GDR Meta thematic day *Industrial applications of acoustic metamaterials*, Marseilles, together with A.-C. Hladky, S. Benchabane, S. Guenneau, and B. Gralak.
- Jan. 2017 DENORMS Action Workshop *Modelling of high performance acoustic structures, porous media, metamaterials and sonic crystals*, Rome, together with F. Asdrubali, P. Rasera, O. Umnova, A. Krynkin, T. Zielinski, and A. Duval.

- Sept. 2016 DENORMS Action Training Schools *Sound waves in metamaterials and porous materials*, Prague, together with M. Cervenka, P. Rasera, O. Umnova, A. Krynkin, T. Zielinski, and A. Duval.

Short-term visits

- 2017 One month invited researcher at the Department of Applied Physics, Polytechnical University of Valencia, Gandia, Spain. Short Term Scientific Mission funded by DENORMS Action.
- 2012 One month invited researcher at the Centre for Sustainable Environments, Univ. of Bradford, U.-K.
- 2010 Two months invited researcher at the Acoustics and Thermal Physics, KULeuven, Belgium.
- 2007 Two weeks visitor at the Department of Mathematical Sciences, Univ. of Delaware, USA.
- 2006 Two weeks visitor at the Department of Mathematics, Univ. of Louisville, USA.
- 2005 Two weeks visitor at the Department of Mathematics, Univ. of Chicago, USA.

Member of recruitment panel

- 2016 Assistant Professor position 60 MCF 4151, LAUM.

PhD jury member

- 2017 Z. Liu, *Modélisation électromagnétique et imagerie d'endommagements de laminés composites à renforcement de fibres*, Univ. Paris-Saclay.
- 2015 G. Rodeghiero, *Panneaux complexes anisotropes et imagerie électromagnétique rapide*, Univ. Paris-Sud.
- W. Trabelsi, *Propriétés acoustiques de milieux poreux saturés présentant des hétérogénéités aléatoirement ou périodiquement distribuées*, Univ. du Havre.
- C. Sacristan, *Étude des propriétés acoustiques et comportement à l'impact de matériaux poreux de type mousses métalliques homogènes et inhomogènes*, Univ. de Bourgogne.
- 2014 H. Pichard as co-advisor, *Guided waves in granular phononic crystals*, Univ. du Maine.
- 2013 C. Lagarrigue as co-advisor, *Metamatériaux performants dans la gammes des fréquences audibles : Simulations et validations expérimentales*, Univ. du Maine.
- 2011 J. Descheemaeker, *Elastic characterization of porous materials by surface and guided wave propagation analysis*, KULeuven.
- 2011 A. Geslain as co-advisor, *Anisotropie naturelle et induite des matériaux poreux : Étude expérimentale et modélisation*, Univ. du Maine.
- 2010 M. Naas, *Propagation des ondes ultrasonores dans des milieux poreux inhomogènes : application à l'os trabéculaire*, Univ. du Maine.

Teaching duties

Lectures in Summer Schools

- 2017 *Multiple Scattering Theory: Introduction and Practical tools*, in METAgineering 2017: Principles and engineering applications of the acoustic metamaterials, organized by GDR-Meta, Oléron, July 2017.

I was involved in the application of «Cursus Master Ingénierie (CMI)» Acoustics in Le Mans Univ. and in the new training program of both Acoustics Licence and Master degrees. Consequently, two new lectures will be delivered next year: *Maxwell's equations* at Master 1 degree and *Periodic structures and metamaterials* at Master 2 degree. Currently, I am teaching both lectures and practicals approximatively 50 hours/year.

Teaching

- Since 2014 Teaching in the session *Acoustic Materials*; Univ. du Maine, Third year course ENSIM.
- Since 2013 Coordinator of the module *Physical optics*; Univ. du Maine, License 3 SPI.
- Since 2012 Coordinator of the module *Langage Compilé*; Univ. du Maine, Master 1 major «Acoustics and Mechanics».
- Since 2010 Teaching in the session *Porous materials*; Univ. du Maine, Master 2 major Acoustic.
- 2012 - 2010 Coordinator of the module *Maxima* (formal calculation); Univ. du Maine, Master 1 major «Acoustics and Mechanics».
- Nov. 2008 Advising of Master students (Civil-Engineering & Architecture) during the design and building of 5 architectural structures (Folies Liègeoises) sponsored by the city of Liège.
- 2005 - 2002 Weekly problem sessions *Acoustics*; Second year course ESIM.
- 2002 Weekly problem sessions *Solid Mechanics*; First year course ESIM.
- 2002 Laboratory experiments *Vibrations*; Third year course ESIM.

Supervising of Master 2 student projects

- 2017 L. Fei, together with V. Romero García and V. Tournat.
One dimensional acoustic wave propagation in duct with periodic membranes.
- T. Cavaliere, together with V. Romero García and C. Chaufour.
Modeling of sound barriers: Application of sonic crystals to railway noise reduction.
- 2015 W. Huang, together with V. Romero García.
Sound absorbing materials combining Helmholtz resonators and membranes.
- A. Lardeau, together with V. Romero García.
Acoustic wave propagation in three-dimensional resonant sonic crystals.
- 2012 C. Olivier, together with J.-C. Le Roux (CTTM) and O. Dazel.
Low frequency characterization of porous materials by use of an impedance sensor.
- L. Foze-Ndjomo, together with V. Tournat and O. Dazel.
Numerical modeling of graded granular material.
- 2011 H. Pichard, together with O. Richoux.
Study of sonic crystals constituted of square inclusions in the audible frequency range.

A. Drira, together with V. Tournat and O. Dazel.

Biot waves in disordered granular layer submitted to gravity.

2010 B. Bergeot, together with O. Dazel.

Contribution to the ultrasonic characterization of macroscopically inhomogeneous porous materials.

Supervising of Master 1 student project

2014 W. Huang and A. Lardeau.

Acoustic absorption by structures mimicking wheat straw like arrangement.

Scientific output

5.1 PhD Dissertation

Modélisation de la propagation des ondes élastiques générées par un séisme proche ou éloigné à l'intérieur d'une ville, Université de la Méditerranée - Aix-Marseille II, 2005.

5.2 Peer-reviewed journal articles

- [A1] J.-P. Groby, C. Tsogka, and A. Wirgin, *Simulation of seismic response in a city-like environment*, *Soil Dyn. Earthq. Eng.*, **25**: 487-504, 2005.
- [A2] J.-P. Groby and A. Wirgin, *Two-dimensional ground motion at a soft viscoelastic layer/hard substratum site in response to SH cylindrical seismic waves radiated by deep and shallow line sources - I. Theory*, *Geophys. J. Int.*, **163**: 165-191, 2005.
- [A3] J.-P. Groby and A. Wirgin, *Two-dimensional ground motion at a soft viscoelastic layer/hard substratum site in response to SH cylindrical seismic waves radiated by deep and shallow line sources - II. Numerical results*, *Geophys. J. Int.*, **163**: 192-224, 2005.
- [A4] E. Franceschini, M.-C. Pautin, S. Mensah, and J.-P. Groby, *Soft tissue absorption tomography with correction for scattering aberrations*, *Ultrason. Imaging*, **27**: 221-236, 2005.
- [A5] J.-P. Groby and C. Tsogka, *A time domain method for modeling viscoacoustic wave propagation*, *J. Comput. Acoust.*, **14**: 201-236, 2006.
- [A6] J.-P. Groby, L. De Ryck, P. Leclaire, A. Wirgin, W. Lauriks, R.P. Gilbert, and Y.S. Xu, *Use of specific Green's functions for solving direct problems involving a heterogeneous rigid frame porous medium slab solicited by acoustic waves*, *Math. Methods Appl. Sci.*, **30**: 91-122, 2007.
- [A7] L. De Ryck, J.-P. Groby, P. Leclaire, W. Lauriks, A. Wirgin, C. Depollier, and Z.E.A. Fellah, *Acoustic wave propagation in a macroscopically inhomogeneous porous medium saturated by a fluid*, *Appl. Phys. Lett.*, **90**: 181901, 2007.

- [A8] L. De Ryck, Z.E.A. Fellah, J.-P. Groby, P. Leclaire, W. Lauriks, A. Wirgin, and C. Depollier, *Acoustic wave propagation and internal fields in macroscopically-inhomogeneous rigid frame porous materials*, J. Appl. Phys., **102**: 024910, 2007.
- [A9] J.-P. Groby and D. Lesselier, *Localization and characterization of simple defects in finite-sized photonic crystals*, J. Opt. Soc. Am. A, **25**: 146-152, 2008.
- [A10] J.-P. Groby and A. Wirgin, *Seismic motion in urban sites consisting of blocks in welded contact with a soft layer overlying a hard half space*, Geophys. J. Int., **172**: 725-758, 2008.
- [A11] J.-P. Groby, A. Wirgin, and E. Ogam, *Acoustic response of a periodic distribution of macroscopic inclusions within a rigid frame porous plate*, Wave Random Complex, **18**: 409-433, 2008.
- [A12] L. De Ryck, P. Leclaire, J.-P. Groby, W. Lauriks, A. Wirgin, and C. Depollier, *Reconstruction of material properties profiles in one-dimensional macroscopically inhomogeneous rigid frame porous media in the frequency domain*, J. Acoust. Soc. Am., **124**: 1591-1606, 2008.
- [A13] R.P. Gilbert, Y. Lui, J.-P. Groby, E. Ogam, A. Wirgin, and Y. Xu, *Computing porosity of cancellous bone using ultrasonic waves II: The muscle, cortical, cancellous bone system*, Math. Comput. Model., **50**: 421-429, 2009.
- [A14] J.-P. Groby, A. Wirgin, L. De Ryck, W. Lauriks, Y.S. XU, and R.P. Gilbert, *Acoustic response of a rigid-frame porous medium plate with a periodic set of inclusions*, J. Acoust. Soc. Am., **126**: 685-693, 2009.
- [A15] J.-P. Groby, E. Ogam, L. De Ryck, N. Sebaa, and W. Lauriks, *Analytical method for the ultrasonic characterization of homogeneous rigid porous materials from transmitted and reflected coefficients*, J. Acoust. Soc. Am., **127**: 764-772, 2010.
- [A16] J.-P. Groby, W. Lauriks, and T.E. Vigran, *Total absorption peak by use of a rigid frame porous layer backed with a rigid multi-irregularities grating*, J. Acoust. Soc. Am., **127**: 2865-2874, 2010.
- [A17] E. Ogam, Z.E.A. Fellah, N. Sebaa, and J.-P. Groby, *Non-ambiguous recovery of Biot poroelastic parameters of cellular panels using transmitted ultrasonic waves*, J. Sound Vibration, **330**: 1074-1090, 2011.
- [A18] J.-F. Allard, O. Dazel, G. Gautier, J.-P. Groby, and W. Lauriks, *Prediction of sound reflexion by corrugated porous surfaces*, J. Acoust. Soc. Am., **129**: 1696-1706, 2011.
- [A19] J.-P. Groby, A. Duclos, O. Dazel, L. Boeckx, and W. Lauriks, *Absorption of a rigid frame porous layer with periodic circular inclusions backed by a periodic grating*, J. Acoust. Soc. Am., **129**: 3035-3046, 2011.
- [A20] J. Descheemaeker, C. Glorieux, W. Lauriks, J.-P. Groby, L. Boeckx, and P. Leclaire, *Study of circumferential waves on a poroelastic cylinder*, Acta Acust. united Ac., **97**: 734-743, 2011.
- [A21] A. Geslain, O. Dazel, S. Sahraoui, J.-P. Groby, and W. Lauriks, *Influence of static compression on mechanical parameters of acoustic foams*, J. Acoust. Soc. Am., **130**: 818-825, 2011.
- [A22] G. Gautier, J.-P. Groby, O. Dazel, L. Kelders, L. De Ryck, and P. Leclaire, *Propagation of acoustic waves in a one-dimensional macroscopically inhomogeneous poroelastic material*, J. Acoust. Soc. Am., **130**: 1390-1398, 2011.

- [A23] J.-P. Groby, A. Duclos, O. Dazel, L. Boeckx, and L. Kelders, *Enhancing absorption coefficient of a backed rigid frame porous layer by embedding circular periodic inclusions*, J. Acoust. Soc. Am., **130**: 3771-3780, 2011.
- [A24] J.-P. Groby, E. Ogam, A. Wirgin, and S. Xu, *Recovery of material parameters of a soft elastic layer*, Complex Var. Elliptic, **57**: 317-336, 2012.
- [A25] B. Nennig, Y. Renou, J.-P. Groby, and Y. Aurégan, *A mode matching approach for modeling two dimensional porous grating with infinitely rigid or soft inclusions*, J. Acoust. Soc. Am., **131**: 3841-3852, 2012.
- [A26] A. Geslain, J.-P. Groby, O. Dazel, S. Mahasaranon, K. V. Horoshenkov, and A. Khan, *An application of the Peano series expansion to predict sound propagation in materials with continuous pore stratification*, J. Acoust. Soc. Am., **132**: 208-215, 2012.
- [A27] J.-P. Groby, O. Dazel, C. Depollier, E. Ogam, and L. Kelders, *Scattering of acoustic waves by macroscopically inhomogeneous poroelastic tubes*, J. Acoust. Soc. Am., **132**: 477-486, 2012.
- [A28] H. Pichard O. Richoux, and J.-P. Groby, *Experimental demonstrations in audible frequency range of band gap tunability and negative refraction in two-dimensional sonic crystal*, J. Acoust. Soc. Am., **132**: 2816-2822, 2012.
- [A29] H. Pichard, A. Duclos, J.-P. Groby, V. Tournat, and V.E. Gusev, *Two-dimensional discrete granular phononic crystal for shear wave control*, Phys. Rev. B, **86**: 134307, 2012.
- [A30] C. Lagarrigue, J.-P. Groby, and V. Tournat, *Sustainable sonic crystal made of resonating bamboo rods*, J. Acoust. Soc. Am., **133**: 247-254, 2013.
- [A31] J.-P. Groby, B. Brouard, O. Dazel, B. Nennig, and L. Kelders, *Enhancing rigid frame porous layer absorption with three-dimensional periodic irregularities*, J. Acoust. Soc. Am., **133**: 821-831, 2013.
- [A32] O. Dazel, J.-P. Groby, B. Brouard, and C. Potel, *A stable method to model the acoustic response of multilayered structures*, J. Appl. Phys., **113**: 083506, 2013.
- [A33] C. Lagarrigue, J.-P. Groby, V. Tournat, O. Dazel, and O. Umnova, *Absorption of sound by porous layers with embedded periodic array of resonant inclusions*, J. Acoust. Soc. Am., special issue Porous Materials, **134**: 4670-4680, 2013.
- [A34] O. Dazel, B. Brouard, J.-P. Groby, et Peter Goransson *A normal modes technique to reduce the order of poroelastic models - Application to 2D and coupled 3D models*, Int. J. Numer. Meth. Eng. **96**: 110-128, 2013.
- [A35] V. Romero García, C. Lagarrigue, J.-P. Groby, O. Richoux, and V. Tournat *Tunable acoustic waveguides in periodic arrays made of rigid square-rod scatterers: theory and experimental realization*, J. Phys. D: Appl. Phys., **46**: 305108, 2013.
- [A36] G. Ogam, J.-P. Groby, and E. Ogam, *A non-linear vibration spectroscopy model for structures with closed cracks*, Int. J. NonLin. Mech., **59**: 60-68, 2014.
- [A37] H. Pichard, A. Duclos, J.-P. Groby, V. Tournat, and V.E. Gusev, *Localized transversal-rotational modes in linear chains of equal masses*, Phys. Rev. E, **89**: 013201, 2014.

- [A38] C. Glorieux, J. Descheemaeker, J. Vandenbroeck, J.-P. Groby, L. Boeckx, P. Khurana, and N.B. Roozen, *Temperature and frequency dependence of the visco-elasticity of a poro-elastic layer*, Appl. Acoust., **83**: 123-126, 2014.
- [A39] A. Elliott, R. Venegas, J.-P. Groby, and O. Umnova, *Omnidirectional acoustic absorber with a porous core and a metamaterial matching layer*, J. Appl. Phys., **115**: 204902, 2014.
- [A40] J.-P. Groby, B. Nennig, C. Lagarrigue, B. Brouard, O. Dazel, and V. Tournat, *Using simple shape three-dimensional inclusions to enhance porous layer absorption*, J. Acoust. Soc. Am., **136**: 1139-1148, 2014.
- [A41] J. Prisutova, K. Horoshenkov, J.-P. Groby, and B. Brouard, *A method to determine the acoustic reflection and absorption coefficients of porous media by using modal dispersion in a waveguide*, J. Acoust. Soc. Am., **136**: 2947-2958, 2014.
- [A42] J.-P. Groby, B. Nennig, C. Lagarrigue, B. Brouard, O. Dazel, and V. Tournat, *Enhancing the absorption properties of acoustic porous plates by periodically embedding Helmholtz resonators*, J. Acoust. Soc. Am., **137**: 273-280, 2015.
- [A43] J.-P. Groby, W. Huang, A. Lardeau, and Y. Aurégan, *The use of slow sound to design simple sound absorbing materials*, J. Appl. Phys., **117**: 124903, 2015.
- [A44] C. Lagarrigue, J.-P. Groby, V. Tournat, and O. Dazel, *Design of metaporous supercells by genetic algorithm for absorption optimization on a wide frequency band*, Appl. Acoust., **102**: 49-54, 2016.
- [A45] T. Weisser, J.-P. Groby, O. Dazel, F. Gautier, E. Deckers, S. Futatsugi and L. Monteiro, *Acoustic behavior of a rigidly backed poroelastic layer with periodic resonant inclusions by a multiple scattering approach*, J. Acoust. Soc. Am., **139**: 617-630, 2016.
- [A46] H. Pichard, A. Duclos, J.-P. Groby, V. Tournat, L. Zheng, and V.E. Gusev, *Surface waves in granular phononic crystals*, Phys. Rev. E, **93**: 023008, 2016.
- [A47] E. Deckers, C. Claeys, O. Atak, J.-P. Groby, O. Dazel, and W. Desmet, *A Wave Based Method to predict the absorption, reflection and transmission coefficient of two-dimensional rigid frame porous structures with periodic inclusions*, J. Comput. Phys., **312**: 115-138, 2016.
- [A48] J.-P. Groby, R. Pommier, and Y. Aurégan, *Use of slow sound to design perfect and broadband passive sound absorbing materials*, J. Acoust. Soc. Am., **139**: 1660-1671, 2016.
- [A49] K. Horoshenkov, J.-P. Groby, and O. Dazel, *Asymptotic limits of some models for sound propagation in porous media and the assignment of the pore characteristic lengths*, J. Acoust. Soc. Am., **139**: 2463-2474, 2016.
- [A50] Y. Aurégan, M. Farooqui, and J.-P. Groby, *Low frequency sound attenuation in a flow duct using a thin slow sound material*, J. Acoust. Soc. Am., **139**: EL149, 2016.
- [A51] A. Lardeau, J.-P. Groby, and V. Romero García, *Broadband transmission loss using 3D locally resonant sonic crystals*, Crystals, **6**: 51-62, 2016.
- [A52] N. Jiménez, W. Huang, V. Romero García, V. Pagneux, and J.-P. Groby, *Ultra-thin metamaterial for perfect and quasi-omnidirectional sound absorption*, Appl. Phys. Lett., **109**: 121902, 2016.

- [A53] A. Geslain, S. Raetz, M. Hirwia, M. Abi Ghamen, S.P. Wallen, A. Khanolkar, N. Boechler, J. Laurent, C. Prada, A. Duclos, P. Leclaire, and J.-P. Groby, *Spatial Laplace transform for complex wavenumber recovery and its application to the analysis of attenuation in acoustic systems*, J. Appl. Phys., **120**: 135107, 2016.
- [A54] J. Prisutova, K. Horoshenkov, B. Brouard, and J.-P. Groby, *An application of normal mode decomposition to measure the acoustical properties of low growing plants in a broad frequency range*, Appl. Acoust., **117**: 39-50, 2016.
- [A55] N. Jiménez, V. Romero García, V. Pagneux, and J.-P. Groby, *Quasiperfect absorption by subwavelength acoustic panels in transmission using accumulation of resonances due to slow sound*, Phys. Rev. B, **95**: 014205, 2017.
- [A56] L. Schwan, A. Geslain, V. Romero García, and J.-P. Groby, *Complex dispersion relation of surface acoustic waves at a lossy metasurface*, Appl. Phys. Lett., **110**: 051902, 2017.
- [A57] N. Jiménez, J.-P. Groby, V. Pagneux, and V. Romero García, *Iridescent Perfect Absorption using Critically-Coupled Acoustic Metamaterials*, Applied Sciences, **7**:618-628, 2017.
- [A58] N. Jiménez, T. J. Cox, V. Romero García, and J.-P. Groby, *Metadiffusers: Deep-subwavelength sound diffusers*, Sci. Rep., **7**:, 5389, 2017.

Submitted Publications

- [AS59] N. Jiménez, V. Romero García, V. Pagneux, and J.-P. Groby, *Rainbow-trapping absorbers: Broadband, perfect and asymmetric sound absorption by subwavelength panels with transmission*, submitted to Scientific Reports in June 2017, ArXiv, 1708.03343.
- [AS60] M. Niskanen, J.-P. Groby, A. Duclos, O. Dazel, J. C. Le Roux, N. Poulain, T. Huttunen, and T. Lähivaara, *Deterministic and statistical characterization of rigid frame porous materials from impedance tube measurements*, submitted to Journal of the Acoustical Society of America in June 2017.
- [AS61] M. Gaborit, L. Schwan, O. Dazel, J.-P. Groby, T. Weisser, and P. Goransson, *Coupling FEM, Bloch Waves and TMM in meta-poroelastic laminates*, submitted to Acta Acustica united with Acustica, special issue *Modeling of structured materials for sound and vibration*, in June 2017.
- [AS62] N. Jiménez, V. Romero García, and J.-P. Groby, *Perfect absorption of sound by rigidly-backed porous materials*, submitted to Acta Acustica united with Acustica, special issue *Modeling of structured materials for sound and vibration*, in Sept. 2017.

5.3 Chapters in Book

In 2017-2018, I will write a chapter on «Metamaterials for sound absorption» together with N. Jiménez which will be included in *Fundamental on Acoustic Periodic structures, Metamaterials, Non-linear propagation, and Porous Materials*. This book arises from the COST Action DENORMS CA15125 Training School, *Sound waves in metamaterials and porous materials*, which was held in Prague in Sept. 2016. Springer has accepted to publish this book in the series Materials Sciences. I will also write a chapter on «Multiple Scattering Theory» which will be included in *Fundamentals and applications of acoustic metamaterials: from infrasound to heat*

control. This book arises from the GRD META Training School, *METAgenierie 2017*, which was held in Oléron in July 2017. ISTE publishing has accepted to publish this book.

5.4 Technology transfer

Enveloppe Soleau

- [ENV1] Enveloppe Soleau 469554 280113, «Métaporeux performants pour l'absorption acoustique à basse fréquence», 2013.

Patent

- [P1] WO2015028760 - ACOUSTIC PANEL, published on 5th March 2015, C. Lagarrigue, J.-P. Groby, V. Tournat, O. Dazel, and B. Nennig
G10K 11/172 (20060101) - ACOUSTIC PANEL, published on 21th July 2016, C. Lagarrigue, J.-P. Groby, V. Tournat, O. Dazel, and B. Nennig

5.5 Conference proceedings

Invited talks

- [INV1] J.-P. Groby, O. Dazel, T.E. Vigran, and W. Lauriks, *Total absorption peak by use of a rigid frame porous layer backed by a rigid grating*, 2nd Pan-American/Iberian Meeting on Acoustics, 161th ASA Meeting, J. Acoust. Soc. Am., **128**: 2392, Cancun, Nov. 2010.
- [INV2] J.-P. Groby, O. Dazel, C. Lagarrigue, K. Horoshenkov, S. Mahasaranon, and A. Khan, *Propagation of acoustic waves in a one dimensional macroscopically inhomogeneous porous material under the rigid frame approximation*, Internoise 2012, New-York City, Aug. 2012.
- [INV3] J.-P. Groby, B. Nennig, C. Lagarrigue, B. Brouard, O. Dazel, O. Umnova, and V. Tournat, *Design of sound absorbing metamaterials by periodically embedding 3D inclusions in rigidly backed porous plate*, Eurodyn 2014, Porto, June 2014.
- [INV4] J.-P. Groby, B. Nennig, C. Lagarrigue, B. Brouard, O. Dazel, O. Umnova, and V. Tournat, *Design of sound absorbing metamaterials by periodically embedding three-dimensional resonant or non-resonant inclusions in rigidly backed porous plate*, 168th ASA Meeting, J. Acoust. Soc. Am., **136**: 2077, Indianapolis, Oct. 2014.
- [INV5] J.-P. Groby, R. Pommier, and Y. Aurégan, *Sound Absorption by a Structure with Straight Rectangular Pores Loaded by Periodically Distributed Detuned Resonators*, Progress In Electromagnetics Research Symposium, PIERS 2015, Prague, Juillet 2015.
- [INV6] J.-P. Groby, N. Jiménez, L. Schwan, C. Lagarrigue, W. Huang, V. Romero García, V. Tournat, V. Pagneux, O. Dazel, T. Weisser, Y. Aurégan, and B. Nennig, *From meta-porous materials to subwavelength absorbers: some recipes to design perfect sound absorbers*, 4th International Conference on Electrical, Electronic and Computing Engineering, Kladovo, June 2017.

- [INV7] V. Romero García, N. Jiménez, V. Pagneux, and J.-P. Groby, *Perfect and broadband acoustic absorption in deep sub-wavelength structures for the reflection and transmission problems*, Acoustics '17, J. Acoust. Soc. Am., **141**:3640, Boston, May 2017.
- [INV8] J.-P. Groby, A. Lardeau, and V. Romero García, *Broadband transmission loss in the audible regime with a 3D sonic crystals by use of resonance overlap*, Acoustics '17, J. Acoust. Soc. Am., **141**:3885, Boston, May 2017.
- [INV9] N. Jiménez, V. Romero García, V. Pagneux, and J.-P. Groby *Rainbow-trapping absorbers for transmission problems: broadband and perfect sound absorbing panels*, 24th International Congress on Sound and Vibration, London, July 2017.
- [INV10] N. Jiménez, V. Romero García, V. Pagneux, and J.-P. Groby *Rainbow-trapping absorbers for transmission problems: broadband and perfect sound absorbing panels*, 13th International Conference on Theoretical and Computational Acoustics, Vienna, July 2017.

Full papers

- [CA1] P. Dufourcq, J.-P. Groby, M. Lagier, P. Témin, and G. Vanderborck, *Détection vibroacoustique non-linéaire d'endommagements dans une structure poutre*, 16ème Congrès Français de Mécanique, Nice, Sept. 2003.
- [CA2] J.-P. Groby and C. Tsogka, *A time domain method for modeling wave propagation phenomena in viscoacoustic media*, 6th Int. Conf. on Mathematical and Numerical Aspects of Wave Propagation, Cohen G. et al. (eds.), Springer, pp. 911-915, Jyväskylä, July 2003.
- [CA3] J.-P. Groby, C. Tsogka, and A. Wirgin, *A time domain method for modeling SH viscoelastic wave propagation in a city-like environment*, 11th Int. Conf. on Soil Dynamics & Earthquake Engineering, Doolin D. et al. (eds.), University and Stallion Press, Berkeley, pp. 887-894, Berkeley, Jan. 2004.
- [CA4] E. Ogam, Z.E.A. Fellah, J.-P. Groby, and A. Wirgin, *Eigenmode analysis of the cortical osseous tissue-marrow coupled system*, 5th Congress of the International Society for Analysis, its Applications and Computation, pp. 1407-1418, Catania, July 2005.
- [CA5] J.-P. Groby, C. Tsogka, E. Ogam, A. Wirgin, and Z.E.A. Fellah, *A time domain method to model viscoelastic wave propagation in long cortical bones*, 5th Congress of the International Society for Analysis, its Applications and Computation, pp. 1419-1428, Catania, July 2005.
- [CA6] E. Ogam, A. Wirgin, Z. Fellah, J.-P. Groby, W. Lauriks, J.-Y. Chapelon, C. Depollier, L. De Ryck, R. Gilbert, N. Sebaa, T. Scotti, and Y. Xu, *Recovery of the mechanical parameters of long bones from their vibroacoustic impulse response*, 1st Symposium on the Acoustics of Poro-Elastic Materials, pp. 181-188, Lyon, Dec. 2005.
- [CA7] L. De Ryck, Z.E.A. Fellah, J.-P. Groby, E. Ogam, N. Sebaa, J.-Y. Chapelon, C. Depollier, R. Gilbert, T. Scotti, A. Wirgin, and Y. Xu, *Acoustic identification of a porous cylinder*, 1st Symposium on the Acoustics of Poro-Elastic Materials, pp. 211-220, Lyon, Dec. 2005.
- [CA8] J.-P. Groby, E. Ogam, A. Wirgin, Z.E.A. Fellah, W. Lauriks, J.-Y. Chapelon, C. Depollier, L. De Ryck, R. Gilbert, N. Sebaa, and Y. Xu, *2D mode excitation in a porous slab saturated with air in the high frequency approximation*, 1st Symposium on the Acoustics of Poro-Elastic Materials, pp. 53-60, Lyon, Dec. 2005.

- [CA9] A. Wirgin and J.-P. Groby, *Amplification and increased duration of earthquake motion on uneven stress-free-ground*, 3rd International Symposium on the Effects of Surface Geology on Seismic Motion, Bard P.-Y. et al. (eds.), LCPC, Paris, pp. 559-568, Grenoble, Sept. 2006.
- [CA10] B. Morvan, A.-C. Hladky-Hennion, J. Vasseur, J.-P. Groby, B. Dubus, A. Tinel, and B. Djafari-Rouhani, *Negatively refracted transverse wave: study of the ultrasonic field at the exit of an elastic phononic crystal*, IEEE International Ultrasonics Symposium, Rome, Sept. 2009.
- [CA11] J.-P. Groby, E. Ogam, O. Dazel, T.E. Vigran, and W. Lauriks, *Pic d'absorption totale d'une lame poreuse sous l'approximation du squelette rigide collée contre un réseau surfacique multi-composant*, 10ème Congrès Français d'Acoustique, Lyon, April 2010.
- [CA12] E. Ogam, Z.E.A. Fellah, J.-P. Groby, and A. Wirgin, *Résolution de problèmes inverses d'estimation de paramètres poroélastiques des matériaux poreux par inversion de données ultrasonores transmises*, 10ème Congrès Français d'Acoustique, Lyon, April 2010.
- [CA13] A-C. Hladky-Hennion, J. Vasseur, C. Croënne, J.-P. Groby, B. Dubus, B. Djafari-Rouhani, B. Morvan, and A. Tinel, *Réfraction négative d ondes transverses dans les cristaux phononiques*, 10ème Congrès Français d'Acoustique, Lyon, April 2010.
- [CA14] J. Descheemaeker, J.-P. Groby, P. Leclaire, W. Lauriks, and L. Boeckx, *Surface and guided waves in porous materials*, 10ème Congrès Français d'Acoustique, Lyon, April 2010.
- [CA15] C. Lagarrigue, O. Dazel, J.-P. Groby, and V. Tournat, *Parametric study of a meta-porous made of solid inclusions embedded in a rigid frame porous material*, Acoustics 2012, 11ème Congrès Français d'Acoustique and 2012 Annual IOA Meeting, Nantes, April 2012.
- [CA16] B. Brouard, J.-P. Groby, O. Dazel, B. Nennig, and L. Kelders, *Enhancement of the absorption of a backed rigid frame porous layer using a 2-dimensional periodic multi-irregularities rigid backing*, Acoustics 2012, 11ème Congrès Français d'Acoustique and 2012 Annual IOA Meeting, Nantes, April 2012.
- [CA17] K. V. Horoshenkov, S. Masaharanon, K. Khan, A. Geslain, J.-P. Groby, and O. Dazel, *Acoustical properties of macroscopically inhomogeneous porous medium*, Acoustics 2012, 11ème Congrès Français d'Acoustique and 2012 Annual IOA Meeting, Nantes, April 2012.
- [CA18] K. V. Horoshenkov, O. Dazel, and J.-P. Groby, *The asymptotic behaviour of some models for the acoustical properties of rigid frame porous media*, Internoise 2012, New-York City, Aug. 2012.
- [CA19] C. Lagarrigue, O. Dazel, J.-P. Groby, and V. Tournat, *Parametric study of a meta-porous made of solid inclusions embedded in a rigid frame porous material*, Internoise 2012, New-York City, Aug. 2012.
- [CA20] J.-P. Groby, O. Dazel, L. De Ryck, A. Khan, and K. Horoshenkov, *Acoustic characterization of graded porous materials under the rigid frame approximation*, International Congress on Acoustics 2013, Montréal, June 2013.
- [CA21] J. Prisutova, K. Horoshenkov, J.-P. Groby, and B. Brouard, *Laboratory measurement of the acoustic absorption coefficient of living plants via modal dispersions*, 21st International Congress on Sound and Vibration, Beijing, July 2014.

- [CA22] W. Huang, J.-P. Groby, V. Romero García, and N. Jiménez, *Fentes minces chargées par des résonateurs de Helmholtz pour l'absorption du son dans l'audible*, 13ème Congrès Français d'Acoustique, Le Mans, April 2016.
- [CA23] A. Lardeau, J.-P. Groby, and V. Romero García, *Propagation d'ondes acoustiques dans un milieu périodique avec résonateurs*, 13ème Congrès Français d'Acoustique, Le Mans, April 2016.
- [CA24] A. Geslain, J.-P. Groby, A. Duclos, and P. Leclaire, *Caractérisation de nombres d'ondes complexes par transformée de Laplace : application aux ondes guidées dans les matériaux poreux*, 13ème Congrès Français d'Acoustique, Le Mans, April 2016.
- [CA25] V. Romero García, N. Jiménez, W. Huang, J.-P. Groby, and V. Pagneux, *Ultra-thin acoustic metamaterial panels based on resonant bricks for perfect absorption*, Metamaterials' 2016, Chania, Sept. 2016.
- [CA26] N. Jiménez, J.-P. Groby, V. Romero García, and V. Pagneux, *Design of sub-wavelength acoustic absorbing panels using accumulation of resonances due to slow sound*, Metamaterials' 2016, Chania, Sept. 2016.
- [CA28] T. Weisser, L. Schwan, O. Dazel, and J.-P. Groby, *High broadband absorption of acoustic waves by elastic-framed metaporous layer*, Metamaterials' 2016, Chania, Sept. 2016.
- [CA27] L. Schwan, A. Geslain, J.-P. Groby, and V. Romero García, *Surface acoustic waves propagation at lossy metasurfaces: experimental and theoretical characterization of complex dispersion relations*, Metamaterials' 2016, Chania, Sept. 2016.
- [CA28] J. Leng, A. Pelat, V. Romero García, R. Picó, J.-P. Groby, and F. Gautier, *Tunability of the resonant modes of an Acoustic Black Hole embedded in an infinite thin plate*, Internoise 2017, Hong-Kong, Aug. 2017.
- [CA29] W. Huang, L. Schwan, V. Romero García, J.-M. Gèneveau, and J.-P. Groby, *3D-Printed straw-inspired metamaterial for sound absorption*, Metamaterials' 2017, Marseille, Sept. 2017.
- [CA30] N. Jiménez, T. Cox, V. Romero García, and J.-P. Groby, *Metadiffusers: sound diffusers with deep-subwavelength dimensions*, Metamaterials' 2017, Marseille, Sept. 2017.

Abstracts

- [CR1] J.-P. Groby and A. Wirgin, *On the causes of anomalous seismic response in an urban site with a two-component soft layer overlying a hard substratum*, European Geosciences Union Meeting, Nice, May 2004.
- [CR2] J.-P. Groby, C. Tsogka, and A. Wirgin, *2D ground motion in a city modeled as an assembly of blocks anchored in an inhomogeneous half space: The influence of the geometry of the half space*, European Geosciences Union Meeting, Nice, May 2004.
- [CR3] L. Le Marrec, J.-P. Groby, C. Tsogka, W. Lauriks, E. Ogam, S. Erard, and Z.E.A. Fellah, *Acoustical identification of a cortical bone-like cylindrical tube*, 1st European Symposium on Ultrasonic Characterization of Bone, Paris, March 2006.
- [CR4] E. Ogam, C. Masson, S. Erard, A. Wirgin, Z.E.A. Fellah, J.-P. Groby, and Y. Xu, *On the vibratory response of a human tibia: comparison of 1D Timoshenko model, 3D FEM and experiment*, 1st European Symposium on Ultrasonic Characterization of Bone, Paris, March 2006.

- [CR5] A. Wirgin and J.-P. Groby, *Theoretical evidence for increases of duration and amplification of peak earthquake ground motion at sites with non-planar stress-free surfaces*, 1st European Conference on Earthquake Engineering and Seismology, Genève, Sept. 2006.
- [CR6] L. Le Marrec, J.-P. Groby, A. Wirgin, and L.R. Rakotomanana, *Low-frequency approximation for recovering relaxed viscoelastic parameters of bones*, Int. Conf. on Modeling of Heterogeneous Materials with Application in Construction and Biomedical Engineering, Jirásek M. et al. (eds.), pp 284-285, Prague, June 2007.
- [CR7] J.-P. Groby, A. Wirgin, E. Ogam, L. De Ryck, W. Lauriks, and C. Depollier, *Acoustic response of a sonic-like crystal within a rigid frame porous plate*, Acoustics'08, J. Acoust. Soc. Am., **123**: 3039, Paris, July 2008.
- [CR8] E. Ogam, A. Wirgin, Z.E.A. Fellah, C. Masson, P. Guillemain, F. Gabrielli, J.-P. Groby, and R.P. Gilbert, *Vibration spectroscopy and guided wave propagation data as indicators of structural and mechanical degradation of human bones*, Acoustics'08, J. Acoust. Soc. Am., **123**: 3786, Paris, July 2008.
- [CR9] A. Geslain, O. Dazel, J.-P. Groby, and S. Sahraoui, *Influence de la compression sur les propriétés élastiques des matériaux poreux*, 10ème Congrès Français d'Acoustique, Lyon, April 2010.
- [CR10] E. Ogam, Z.E.A. Fellah, J.-P. Groby, R.P. Gilbert, and A. Wirgin, *Recovery of structural degradation indicators of human bones using elastic waves*, 159th ASA Meeting and Noise-Con 2010, J. Acoust. Soc. Am., 127: 2032, Baltimore, April 2010.
- [CR11] A. Geslain, O. Dazel, J.-P. Groby, S. Sahraoui, and W. Lauriks, *Influence of static compression on the mechanical property of acoustic foams*, 1st mediterranean congress on Acoustics, Salé, Oct. 2010.
- [CR12] J.-F. Allard, O. Dazel, G. Gautier, J.-P. Groby, and W. Lauriks, *Coupled mode method to predict the reflexion coefficient of periodically corrugated porous layers*, 1st mediterranean congress on Acoustics, Salé, Oct. 2010.
- [CR13] O. Dazel, J.-P. Groby, B. Brouard, G. Gautier, and L. Kelders, *A general method for modeling highly dissipative multilayered sound packages*, Forum Acusticum 2011, Aalborg, Juin 2011.
- [CR14] J.-P. Groby, O. Dazel, A. Duclos, B. Brouard, L. Kelders, and L. Boeckx, *Absorption of a rigid frame porous layer with periodic circular inclusions and backed by a periodic grating*, 3rd Symposium on the Acoustics of Poro-Elastic Materials, Ferrara, Dec. 2011.
- [CR15] B. Nennig, Y. Renou, J.-P. Groby, and Y. Aurégan, *Absorption of rigid frame porous grating with various shape rigid of soft inclusions*, 3rd Symposium on the Acoustics of Poro-Elastic Materials, Ferrara, Dec. 2011.
- [CR16] O. Dazel, A. Geslain, F. Ablitzer, and J.-P. Groby, *A microstructural approach for modeling compression effects of porous foams*, 3rd Symposium on the Acoustics of Poro-Elastic Materials, Ferrara, Dec. 2011.
- [CR17] C. Lagarrigue, J.-P. Groby, and V. Tournat, *Sustainable sonic crystal made of Helmholtz resonators in the audible frequency range*, 3rd Symposium on the Acoustics of Poro-Elastic Materials, Ferrara, Dec. 2011.

- [CR18] J.-P. Groby, O. Dazel, A. Duclos, G. Gautier, L. Kelders, L. De Ryck, and P. Leclaire, *Propagation of acoustic waves in a one-dimensional macroscopically inhomogeneous poroelastic material*, 3rd Symposium on the Acoustics of Poro-Elastic Materials, Ferrara, Dec. 2011.
- [CR19] C. Glorieux, J. Descheemaeker, J.-P. Groby, L. Boeckx, and P. Khurana, *Temperature dependence of elasticity of poro-elastic layer*, Acoustics 2012, 11ème Congrès Français d'Acoustique et 2012 Annual IOA Meeting, Nantes, April 2012.
- [CR20] B. Brouard, J.-P. Groby, D. Parmentier, O. Dazel, L. Kelders, and M. Henry, *Semi-analytical characterisation of a homogeneous rigid frame porous material without using P-P probes*, Acoustics 2012, 11ème Congrès Français d'Acoustique et 2012 Annual IOA Meeting, Nantes, April 2012.
- [CR21] H. Pichard, A. Duclos, J.-P. Groby, V. Tournat, and V. Gusev, *Elastic waves in phononic granular membranes*, Acoustics 2012, 11ème Congrès Français d'Acoustique et 2012 Annual IOA Meeting, Nantes, April 2012.
- [CR22] V. Gusev, H. Pichard, A. Duclos, J.-P. Groby, and V. Tournat, *Granular crystals as phononic metamaterials for shear waves*, Meta 2012, Paris, April 2012.
- [CR23] J.-P. Groby, V. Tournat, V. Romero García, and O. Umnova, *Heuristic homogenization to overcome the homogenization limit of the effective parameters of two dimensional Sonic Crystal slabs*, Meta'13, Sharjah, March 2013.
- [CR24] H. Pichard, A. Duclos, J.-P. Groby, V. Tournat, and V. Gusev, *Localized transversal-rotational modes in linear chain of equal masses*, 2013 International Congress on Ultrasonics, Singapour, May 2013.
- [CR25] H. Pichard, A. Duclos, J.-P. Groby, V. Tournat, and V. Gusev, *Two-dimensional granular phononic crystal for shear wave control*, 2013 International Congress on Ultrasonics, Singapour, May 2013.
- [CR26] V. Romero García, C. Lagarrigue, J.-P. Groby, O. Richoux, and V. Tournat, *Tunable Acoustic Waveguides in Sonic Crystals Made of Square-Rod Scatterers. Experiments and Theory.*, Phononics 2013, Sharm El-Sheikh, June 2013.
- [CR27] J. Pristova, K. Horoshenkov, J.-P. Groby, and B. Brouard, *Laboratory measurement of the acoustic absorption coefficient based on the modal dispersion*, 166th ASA Meeting, J. Acoust. Soc. Am., **134**: 4004, San-Francisco, Dec. 2013.
- [CR28] C. Lagarrigue, J.-P. Groby, B. Nennig, V. Tournat, O. Dazel, B. Brouard, and O. Umnova, *Absorption acoustique dans la gamme des fréquences audibles par un métaporeux : influence de la géométries des inclusions*, 12ème Congrès Français d'Acoustique, Poitiers, April 2014.
- [CR29] T. Weisser, J.-P. Groby, O. Dazel, F. Gautier, S. Futatsugi, and L. Monteiro, *Comportement acoustique de matériaux poroélastiques avec inclusions périodiques*, 12ème Congrès Français d'Acoustique, Poitiers, April 2014.
- [CR30] E. Ogam, Z.E.A. Fellah, J.-P. Groby, and C. Depollier, *Le problème inverse de diffraction des ondes acoustiques audibles par un cylindre poroélastiques saturé d'air*, 12ème Congrès Français d'Acoustique, Poitiers, April 2014.
- [CR31] B. Brouard, J. Pristova, J.-P. Groby, and K. Horoshenkov, *Détermination de coefficients d'absorption et de réflexion de matériaux au delà de la fréquence de coupure du tube à impédance*, 12ème Congrès Français d'Acoustique, Poitiers, April 2014.

- [CR32] H. Pichard, A. Duclos, J.-P. Groby, V. Tournat and V. Gusev *Ondes de surface dans le cristaux phononiques granulaires*, 12ème Congrès Français d'Acoustique, Poitiers, April 2014.
- [CR33] J.-P. Groby, W. Huang, A. Lardeau, Y. Aurégan, et O. Umnova, *Low frequency sound absorbing metamaterial combining slits and quarter wavelength resonators*, 4th Symposium on the Acoustics of Poro-Elastic Materials, Stockholm, Dec. 2014.
- [CR34] T. Weisser, J.-P. Groby, O. Dazel, F. Gautier, S. Futatsugi, and L. Monteiro, *Acoustic metaporous with periodic inclusions: extension to poroelastic material*, 4th Symposium on the Acoustics of Poro-Elastic Materials, Stockholm, Dec. 2014.
- [CR35] E. Carcreff, A. Duclos, J.-P. Groby, and S. Bourguignon, *A dispersive attenuation model for ultrasonic wave propagation in porous materials*, 4th Symposium on the Acoustics of Poro-Elastic Materials, Stockholm, Dec. 2014.
- [CR36] J.-P. Groby, and D. Parmentier, *Acoustic foam characterization using a four microphone measurement technique combined with a minimization procedure*, Poster session of the 4th Symposium on the Acoustics of Poro-Elastic Materials, Stockholm, Dec. 2014.
- [CR37] C. Lagarrigue, J.-P. Groby, and V. Tournat, *Optimised thin Metaporous materials for absorption applications in the audible frequency range*, Euronoise 2015, Maastricht, May 2015.
- [CR38] J.-P. Groby, Y. Aurégan, and O. Umnova, *Sound absorption by a structure with straight rectangular tubes loaded by periodically distributed resonators*, Euronoise 2015, Maastricht, May 2015.
- [CR39] T. Weisser, J.-P. Groby, O. Dazel, F. Gautier, E. Deckers, S. Futatsugi, and L. Monteiro, *Influence du comportement poroélastique sur la réponse acoustique de matériaux métaporeux avec inclusions périodiques résonantes*, 22ème Congrès Français de Mécanique, Lyon, Aug. 2015.
- [CR40] M. Niskanen, A. Duclos, T. Lähivaara, O. Dazel, J.-P. Groby, and T. Huttunen, *Characterization of a porous plate saturated by water*, 13ème Congrès Français d'Acoustique, Le Mans, April 2016.
- [CR41] D. Lafarge, N. Nemati, W. Huang, J.-P. Groby, V. Romero García, and J.-M. Génevaux, *Ondes de Bloch-Kirchhoff en géométrie 2D périodique*, 13ème Congrès Français d'Acoustique, Le Mans, April 2016.
- [CR42] C. Lagarrigue, J.-P. Groby, V. Tournat, O. Dazel, B. Nennig, and O. Umnova, *Metaporeux, une solution innovante pour le traitement acoustique basse fréquence*, 13ème Congrès Français d'Acoustique, Le Mans, April 2016.
- [CR43] R. Longo, A. Duclos, and J.-P. Groby, *Mesures ultrasonores en transmission et réflexion en utilisant des signaux continus : application aux matériaux poreux*, 13ème Congrès Français d'Acoustique, Le Mans, April 2016.
- [CR44] N. Jiménez, W. Huang, J.-P. Groby, V. Romero García, and V. Pagneux, *Absorption quasi-parfaite du son par un métamatériau acoustique suite à l'accumulation de résonances due à une propagation lente*, 13ème Congrès Français d'Acoustique, Le Mans, April 2016.

- [CR45] G. Yan, S. Raetz, J.-P. Groby, A. Duclos, A. Geslain, N. Chigarev, and V. Tournat, *Etude expérimentale des modes de lamb à Vitesse de Groupe Nulle (ZGV) dans le plan complexe des nombres d'ondes*, 13ème Congrès Français d'Acoustique, Le Mans, April 2016.
- [CR46] T. Weisser, J.-P. Groby, and O. Dazel, *Propriétés d'isolation acoustique de parois métaporeuses avec inclusions périodiques*, 13ème Congrès Français d'Acoustique, Le Mans, April 2016.
- [CR47] G. Yan, S. Raetz, J.-P. Groby, A. Duclos, A. Geslain, N. Chigarev, and V. Tournat, *Experimental complex dispersion curve by use of spatial Laplace transform: application to ZGV Lamb modes*, Laser-Ultrasonics 2016, Linz, July 2016.
- [CR48] K.V. Horoshenkov, M. Niskanen, J.-P. Groby, O. Dazel, and A. Duclos, *Acoustic media with pore size distribution and assignment of the pore characteristic lengths and permeabilities*, 174th Acoustical Society of America Meeting, J. Acoust. Soc. Am., **140**: 3430, New Orleans, Dec. 2017.
- [CR49] R. Longo, A. Duclos, and J.-P. Groby, *Ultrasonic measurements by means of continuous waves in a foam saturated with air*, Acoustics '17, J. Acoust. Soc. Am., **141**:3905, Boston, May 2017.

5.6 Workshops

Invited talks

- [INVW1] J.-P. Groby, C. Lagarrigue, O. Dazel, B. Brouard, V. Tournat, B. Nennig, L. Kelders, and L. Boeckx, *Absorption of a rigid frame porous layer with periodic resonant inclusions and periodic irregularities of the rigid backing*, Wave propagation in complex media and applications, Heraklion, May 2012.
- [INVW2] J.-P. Groby, C. Lagarrigue, B. Brouard, O. Dazel, V. Tournat, B. Nennig, O. Umnova, and K. Horoshenkov, *From heterogeneous porous materials to sound absorbing metaporous materials*, Light-weighting and acoustical materials in vehicles, Compiègne, Oct. 2013.
- [INVW3] J.-P. Groby, N. Jemenez, W. Huang, V. Romero García, V. Pagneux and Y. Aurégan, *Perfect sub-wavelength absorption in reflection and transmission problems*, Metamaterials beyond photonics, ICMS, Edinburgh, 2016.

Abstracts

- [W1] M. Gaborit, O. Dazel, J.-P. Groby, L. Schwan, T. Weisser, and P. Göransson, *Coupling of Bloch waves and Finite-Element models: case of metaporous sandwich structures*, Modelling of high performance acoustic structures Porous media, metamaterials and sonic crystals, Rome, 2017.
- [W2] L. Schwan, A. Geslain, V. Romero-García, and J.-P. Groby, *Theory and experiments on surface acoustic waves at a lossy metasurface: complex dispersion relation and surface slow sound*, Modelling of high performance acoustic structures Porous media, metamaterials and sonic crystals, Rome, 2017.
- [W3] N. Jiménez, J.-P. Groby, V. Romero-García, V. Pagneux, W. Huang, and T. Cox, *Subwavelength absorbers and metasurfaces*, Modelling of high performance acoustic structures Porous media, metamaterials and sonic crystals, Rome, 2017.

5.7 Oral Presentation, Seminars, and other talks

- [O1] J.-P. Groby, C. Tsogka, and A. Wirgin, *Propagation d'ondes dans les milieux viscoacoustiques et application en sismique*, GDR ONDES GT1-3, Paris, May 2002.
- [O2] J.-P. Groby, C. Tsogka, and A. Wirgin, *Ville sous séisme : réponse semi-analytique*, Réunion Générale «Interférence d'ondes» du GDR ONDES, Marseille, Dec. 2003.
- [O3] J.-P. Groby, C. Tsogka, and A. Wirgin, *Effet site-ville : Influence de la géométrie du demi-espace inhomogène*, GDR ONDES GT1-3, Paris, May 2004.
- [O4] J.-P. Groby, C. Tsogka, and A. Wirgin, *Earthquakes in big cities*, Katholiek Universiteit Leuven, Leuven, Dec. 2004.
- [O5] J.-P. Groby, C. Tsogka, and A. Wirgin, *Modeling of elastic waves inside a city generated by distant or nearby seismic sources*, Katholiek Universiteit Leuven, Leuven, Oct. 2005.
- [O6] Z.E.A. Fellah, J.-P. Groby, E. Ogam, T. Scotti, and A. Wirgin, *Identification acoustique d'un cylindre poroélastique*, Réunion Générale «Interférences d'Ondes» du GDR ONDES, Besançon, Nov. 2005.
- [O7] J.-P. Groby, C. Tsogka and A. Wirgin, *Investigations des phénomènes liés à la propagation des ondes élastiques générées par un séisme proche ou éloigné à l'intérieur d'une ville*, CEREGE, Aix-en-Provence, Jan. 2005.
- [O8] J.-P. Groby, C. Tsogka, and A. Wirgin, *Modeling of elastic waves inside a city generated by distant or nearby seismic sources*, Univ. of Louisville, Louisville, Jan. 2006.
- [O9] L. De Ryck, J.-P. Groby, P. Leclaire, W. Lauriks, A. Wirgin, C. Depollier, and Z.E.A. Fellah, *Acoustic wave propagation in rigid frame macroscopically-inhomogeneous porous medium*, 25ème anniversaire du Laboratoire d'Acoustique de l'Université du Maine, Le Mans, May 2006.
- [O10] J.-P. Groby, *A time domain method for modeling of wave propagation in viscoelastic medium and equations/method for modeling wave propagation in inhomogeneous porous medium*, Freie Universität Berlin, Berlin, June 2006.
- [O11] L. De Ryck, Z.E.A. Fellah, J.-P. Groby, P. Leclaire, W. Lauriks, and A. Wirgin, *Characterization of 1D macroscopically-heterogeneous porous materials*, GDR ONDES GT1-3, Paris, Oct. 2006.
- [O12] J.-P. Groby, *Modélisation de la propagation d'une onde élastique générée par un séisme proche ou éloigné à l'intérieur d'une ville*, Journée des Post-Doctorants du CMAP, Palaiseau, Feb. 2007.
- [O13] J.-P. Groby, *Modélisation de la propagation des ondes élastiques générées par un séisme proche ou éloigné à l'intérieur d'une ville*, Géosciences Azur, Sophia Antipolis, June 2007.
- [O14] J.-P. Groby, L. de Ryck, W. Lauriks, P. Leclaire, C. Depollier, and A. Wirgin, *Propagation d'ondes acoustiques dans les milieux poreux macroscopiquement inhomogènes et saturés d'air*, Exposé sollicité du groupe thématique GT1, Réunion Générale «Interférence d'ondes» du GDR ONDES, Pessac, Nov. 2007.
- [O15] J.-P. Groby, D. Lesselier, and H. Ammari, *Localisation et caractérisation de défauts simples dans les cristaux photoniques de dimensions finies*, Réunion Générale «Interférence d'ondes» du GDR ONDES, Pessac, Nov. 2007.

- [O16] J.-P. Groby, *Réponse acoustique d'une lame poreuse (squelette rigide) comportant des inclusions périodiques*, Laboratoire d'Acoustique de l'Université du Maine, Le Mans, Nov. 2007.
- [O17] J.-P. Groby, *Réponse acoustique d'une lame poreuse (squelette rigide) comportant des inclusions périodiques*, Laboratoire d'Ondes et Milieux Complexes, Le Havre, Feb. 2008.
- [O18] J.-P. Groby and D. Lesselier, *Localisation et caractérisation de défauts simples dans un cristal photonique 2D de dimensions finies*, Journées «Imagerie optique non conventionnelle» du GDR ONDES & ISIS, Paris, March 2008.
- [O19] J.-P. Groby, *Réponse acoustique d'une lame poreuse (squelette rigide) comportant des inclusions périodiques*, Institut de Recherche Mathématique de Rennes, Rennes, April 2008.
- [O20] J.-P. Groby, *Réponse acoustique d'une lame poreuse (squelette rigide) comportant des inclusions périodiques*, Laboratoire de Mécanique Physique, Talence, April 2008.
- [O21] J.-P. Groby, *Réponse acoustique d'une lame poreuse saturée d'air (squelette rigide) comportant des inclusions périodiques*, Institute of Electronics, Microelectronics and Nanotechnology, Lille, Dec. 2008.
- [O22] J.-P. Groby, W. Lauriks, and T.E. Vigran, *Total absorption peak by use of a rigid frame porous layer backed with a rigid multi-irregularities grating*, Réunion Générale «Interférence d'ondes» du GDR ONDES, Paris, Nov. 2009.
- [O23] J.-P. Groby, *Réponse acoustique d'une lame poreuse (squelette rigide) comportant des inclusions périodiques ou à laquelle est adossé un réseau surfacique multi-composant*, Laboratoire de Mécanique et d'Acoustique, Marseille, Feb. 2010.
- [O24] O. Dazel, J.-P. Groby, B. Brouard, G. Gautier, and L. Kelders, *Algorithme récursif pour éliminer les problèmes liés aux exponentielles croissantes dans les méthodes type matrice de transfert*, Journées Acoustique des milieux poreux, Valenciennes, June 2011.
- [O25] B. Nennig, Y. Renoux, J.-P. Groby, and Y. Aurégan, *Effet d'inclusions périodiques de fort contraste dans un matériau poreux et amélioration de l'absorption*, Journées Acoustique des milieux poreux, Valenciennes, June 2011.
- [O26] J.-P. Groby, C. Lagarrigue, O. Dazel, B. Brouard, V. Tournat, B. Nennig, L. Kelders, L. Boeckx, and O. Umnova *Absorption of a rigid frame porous layer with periodic resonant inclusions and periodic irregularities of the rigid backing*, Univ. of Bradford, Oct. 2012.
- [O27] J.-P. Groby, V. Tournat, V. Romero García and O. Umnova *A heuristic procedure to determine the effective properties of finite-depth sonic crystals*, GDRE 2501, Paris, Dec. 2012.
- [O28] J.-P. Groby, *Noise reduction: some recipes to design subwavelength sound absorbing structures*, Acoustic Workshop Harbin Engineering University and Institute of Le Mans Acoustique, Harbin, Oct. 2016.
- [O29] J.-P. Groby, *Noise reduction: some recipes to design subwavelength sound absorbing structures*, Univ. Politècnica de València, Gandia, March 2017.

Part III

Selected publications

Chapter 6

Articles related to Chapter 1: Gratings and (meta)surfaces

Contents

Geophys. J. Int., 172:725-758, 2008	74
J. Acoust. Soc. Am., 130:3771-3780, 2011	108
J. Acoust. Soc. Am., 137: 273-280, 2015	118
Appl. Acoust., 102: 49-54, 2016	126

Seismic motion in urban sites consisting of blocks in welded contact with a soft layer overlying a hard half-space

Jean-Philippe Groby¹ and Armand Wirgin²

¹CMAP, UMR 7641 CNRS/École Polytechnique, 91128 Palaiseau cedex, France

²LMA, UPR 7051 CNRS, 31 chemin Joseph Aiguier, 13402 Marseille cedex 20, France. E-mail: wirgin@lma.cnrs-mrs.fr

Accepted 2007 November 1. Received 2007 November 1; in original form 2006 October 30

SUMMARY

We address the problem of the response to a seismic wave of an urban site consisting of N_b blocks overlying a soft layer underlain by a hard substratum. The results of a theoretical analysis, appealing to a space–frequency mode-matching (MM) technique, are compared to those obtained by a space–time finite-element (FE) technique. The two methods are shown to give rise to the same prediction of the seismic response for $N_b = 1, 2$ and 40 blocks. The mechanism of the interaction between blocks and the ground, as well as that of the mutual interaction between blocks, are studied. It is shown, in the first part of this paper, that the presence of a small number of blocks modifies the seismic disturbance in a manner which evokes qualitatively, but not quantitatively, what was observed during the 1985 Michoacan earthquake in Mexico City. Anomalous earthquake response at a much greater level, in terms of duration, peak and cumulative amplitude of motion, is shown, by a theoretical and numerical analysis in the second part of this paper, to be induced by the presence of a large (≥ 10) number of identical equi-spaced blocks that are present in certain districts of many cities.

Key words: Earthquake ground motions; Surface waves and free oscillations; Site effects.

1 INTRODUCTION

The Michoacan earthquake that struck Mexico City in 1985 presented some particular characteristics which have since been encountered at various other locations (Semblat *et al.* 2000; Savage 2004; Haghshenas *et al.* 2006; Iwata *et al.* 2006; Maeda *et al.* 2006), but at a lower level of intensity. Other than the fact that the response in downtown Mexico varied considerably in a spatial sense (Flores *et al.* 1987), was quite intense and of very long duration at certain locations (as much as ≈ 3 min Perez-Rocha *et al.* 1991), and often took the form of a quasi-monochromatic signal with beatings (Mateos *et al.* 1993), a remarkable feature of this earthquake (studied in Furumura & Kennett 1998; Cardenas-Soto & Chavez-Garcia 2003; Groby & Wirgin 2005a,b) was that such strong motion could be caused by a seismic source so far from the city (the epicentre was located in the subduction zone off the Pacific coast, approximately 350 km from Mexico City). It is now recognized (Cardenas-Soto & Chavez-Garcia 2003, 2006) that the characteristics of the abnormal response recorded in downtown Mexico were partially present in the waves entering into the city (notably 60 km from the city as recorded by Furumura & Kennett 1998) after having accomplished their trip from the source, this being thought to be due to the excitation of Love and generalized-Rayleigh modes by the irregularities of the crust (Furumura & Kennett 1998; Chavez-Garcia & Salazar 2002; Cardenas-Soto & Chavez-Garcia 2003).

In this investigation, we focus on the influence of the presence of the built features of the urban site as a complementary explanation

of the abnormal response: the so-called *city-site effect*. A building or a group of buildings over a hard half-space, solicited by a plane incident *SH* wave, has been shown to modify the seismic waves on the ground near the building (Trifunac 1972; Luco & Cotesse 1993), the modification being larger when more buildings are taken into account because of multiple interaction: that is, the so-called *structure–soil–structure interaction*. For models of the geophysical structure involving only a hard half-space, the stress-free base block (of the shear wall) mode appears to be the main cause of the modification (Luco & Cotesse 1993).

The studies that deal with a geophysical structure involving, in addition, a soft-layer overlying the hard half-space, have been mainly concerned either with an infinite set of periodically arranged (Wirgin & Bard 1996; Boutin & Roussillon 2004, 2006) or randomly arranged (Clouteau & Aubry 2001; Lombaert *et al.* 2004) buildings on, or partially imbedded in, the ground. In Wirgin & Bard (1996), the authors suggest that the large duration and amplitude are strongly linked to resonant phenomena of the soft-layer associated with waves whose structure is close to that of Love waves. The solicitation being of the form of a plane incident wave, such modes cannot be excited in the absence of buildings (Groby & Wirgin 2005a).

In Hill & Levander (1984) and Levander & Hill (1984), it was shown that the modes of a soft layer/hard half-space can be excited when the interface between the substratum and the layer present some irregularities. These effects were qualified as ‘vertical and lateral interferences’ in a previous numerical study (Aki & Larner 1970). The question of the excitation of modes, via surface irregularities

constituted by the set of buildings on the ground, was subsequently addressed in Groby *et al.* (2005). In Wirgin & Groby (2006a,b) it was found that the excitation of vibration modes associated with a periodically modulated surface impedance, modelling a periodic distribution of blocks emerging from a flat ground, can lead to enhanced durations and amplifications of the cumulative displacement and velocity as compared to what is found for a flat stress-free or constant surface impedance surface. Wirgin & Groby (2006a) show that these modes manifest themselves by amplified evanescent waves in the substratum.

The contributions Boutin & Roussillon (2004, 2006) employ homogenized models of a periodic city, but the fact that these models are restricted to low frequencies may explain why they do not account for the amplifications obtained in Groby *et al.* (2005) and Wirgin & Groby (2006a). In a host of other numerical studies (Fernandez-Ares & Bielak 1973; Chavez-Garcia & Bard 1994; Faeh *et al.* 1994; Clouteau & Aubry 2001; Guéguen *et al.* 2002; Boutin & Roussillon 2004; Lombaert *et al.* 2004; Boutin & Roussillon 2006), the presence of buildings is found either to hardly modify, or to de-amplify, the seismic disturbance, in contradiction with what is shown in Semblat *et al.* (2003), Tsogka & Wirgin (2003) and Groby (2005).

In Rial (1989), the spatial variability of damage to structures on the ground was attributed to the variability of the resonance frequencies of the buildings and of the soil structure beneath each building, with the implication that the most dangerous situation is when the natural frequency of the building (often treated as a one degree, or several degrees, of freedom oscillator Jennings & Bielak 1973; Guéguen 2000; Clouteau & Aubry 2001; Boutin & Roussillon 2006; Roussillon 2006) is coincident with that (obtained by a 1-D analysis) of the substructure below the base of the building (a well-known paradigm in the civil engineering community known as the ‘double resonance’).

Another point of view is to consider the building as a seismic source, either when it is solicited artificially by a vibrator located on its roof (Jennings 1970; Wong & Trifunac 1974), or when it re-emits vibrations received from the incident seismic disturbance [or other form of sollicitation such as that coming from an underground nuclear explosion (Doby *et al.* 1979; Shaw 1979)]. It is not unreasonable to think that the presence of one or more buildings on the ground enables the excitation of the (Love, Rayleigh) modes of the underground system. This is known to be possible when a flat stress-free surface overlying a soft layer in welded contact with a hard substratum is solicited by a source located in the layer or substratum (Groby & Wirgin 2005a) and should therefore also occur when the source (i.e. the building) is on the free surface.

This work originated in the observation that no satisfactory ‘theoretical’ explanation has been given until now of the influence of buildings on anomalous seismic response in urban environments with soft layers, or large basins, overlying a hard substratum. The principal reason for this knowledge gap probably lies in the complexity of the sites examined in previous studies and in the complexity of the phenomena. Thus, it appears to be opportune to develop a theoretical model which is as complete and as simple as possible.

This paper is divided into two parts (other than the introductory sections, conclusion and appendices). The first part is concerned with city configurations having a small number (one or two) blocks, and the second part with a cities having a large number (≥ 10) of blocks.

2 DESCRIPTION OF THE CONFIGURATION AND OF THE THEORETICAL ASPECTS OF ITS SEISMIC RESPONSE

We focus on a portion of a modern city consisting of a set of blocks (i.e. groups of close or touching buildings separated by streets or avenues or, less often, well-separated buildings) (see Fig. 1). The blocks are assumed to be in welded contact, across the flat ground surface, with the substructure. The latter is composed of a horizontal soft layer of thickness h underlain by a hard half space. Each block (or building in the case of well-separated buildings) is homogenized (see Fig. 1; this *does not mean* that the set of blocks is reduced to a single horizontal, homogeneous layer, as in Boutin & Roussillon 2004, 2006) and thereafter characterized by three constants: its height b_j , width w_j and length L . All the blocks have the same rectangular geometry (but not necessarily the same sizes) and composition. Let d_j be the x_1 coordinate of the centre of the base segment of the j th block. The distance between the blocks j and i is denoted by $d_{ji} = |d_j - d_i|$ and is not necessarily constant between successive pairs of blocks.

It has been shown (Adam *et al.* 2000), in the context of a similar problem, that if $L > d_{ji}$ and $L > w_j$ for all the pertinent indices i, j , then there is no substantial difference in the shear ground motion between a 2-D (L infinite) and the corresponding 3-D (L finite) configuration, so that from now on we shall limit our analysis to the 2-D ‘city’, with x_3 the ignorable coordinate of the $Ox_1 x_2 x_3$ cartesian coordinate system in Fig. 1.

Let $\mathbb{B} \in \mathbb{Z}$ denote the set of indices by which the blocks are identified (e.g. for three blocks: $\{1, 2, 3\}$ or $\{-1, 0, 1\}$). The cardinal of \mathbb{B} is designated by N_b (i.e. N_b denotes the number of blocks in the configuration, and this number will either be finite or infinite).

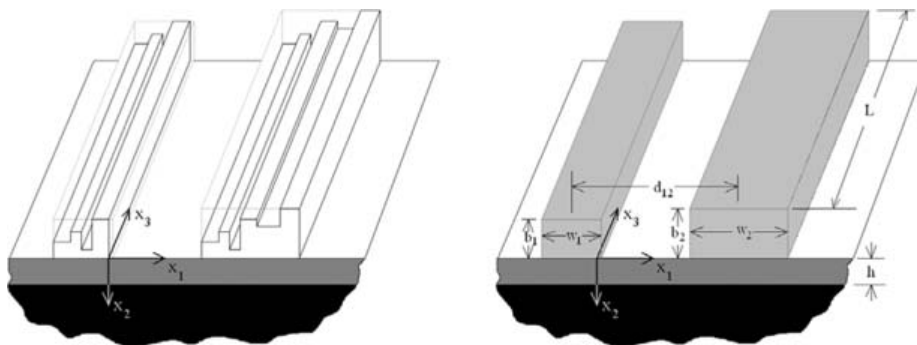


Figure 1. Left-hand panel: view of the 2-D city (only two of the blocks are represented). Right-hand panel: the blocks are homogenized.

Γ_f is the stress-free surface composed of a ground portion Γ_g , assumed to be flat and horizontal, and a portion Γ_{ag} , constituting the reunion of the above-ground-level boundaries $\Gamma_{ag}^{(j)}$; $j \in \mathbb{B}$ of the blocks. The ground Γ_g is flat and horizontal, and is the reunion of Γ_g and the base segments $\Gamma_{bs}^{(j)}$; $j \in \mathbb{B}$ joining the blocks to the underground.

The medium in contact with, and above, Γ_f is air. The medium in contact with, and below Γ_G is the mechanically soft layer occupying the domain Ω_1 , which is laterally infinite, and whose lower boundary is Γ_h , also assumed to be flat and horizontal. The soft material in the layer is in welded contact across Γ_h with the mechanically hard material in the semi-infinite domain (substratum) Ω_0 .

The domain of the j th block is denoted by $\Omega_2^{(j)}$ and the reunion of all the $\Omega_2^{(j)}$; $j \in \mathbb{B}$ is denoted by Ω_2 . The material in each block is in welded contact with the material in the soft layer across the base segments $\Gamma_{bs}^{(j)}$; $j \in \mathbb{B}$.

The media filling Ω_0 , Ω_1 and $\bigcup_{j \in \mathbb{B}} \Omega_2^{(j)}$ are $M^{[0]}$, $M^{[1]}$ and $M^{[2]}$, respectively and the latter are assumed to be initially stress-free, linear, isotropic and homogeneous. $M^{[0]}$ is non-dissipative whereas $M^{[1]}$ and $M^{[2]}$ are dissipative, described by a constant quality factor $Q^{[j]}$ in the frequency range of excitation. As is common in seismological applications involving viscoelastic media (Faeh *et al.* 1994), we shall assume that $Q^{[j]}(\omega) = Q^{[j]}$, with $Q^{[j]}$ constants, $j = 1, 2$. This implies (Kjartansson 1979) that

$$\mu^{[j]}(\omega) = \mu_{\text{ref}}^{[j]} \left(\frac{-i\omega}{\omega_{\text{ref}}} \right)^{\frac{2}{\pi} \arctan\left(\frac{1}{Q^{[j]}}\right)}; \quad j = 1, 2, \quad (1)$$

wherein ω_{ref} is a reference angular frequency, chosen herein to be equal to 9×10^{-2} Hz. Hence

$$c^{[j]}(\omega) = c_{\text{ref}}^{[j]} \left(\frac{-i\omega}{\omega_{\text{ref}}} \right)^{\frac{1}{\pi} \arctan\left(\frac{1}{Q^{[j]}}\right)}; \quad j = 1, 2, \quad (2)$$

with $c_{\text{ref}}^{[j]} := \sqrt{\frac{\mu_{\text{ref}}^{[j]}}{\rho^{[j]}}}$ the phase velocity in $M^{[j]}$, wherein the density and rigidity are $\rho^{[j]}$ and $\mu^{[j]}$, respectively.

The seismic disturbance is delivered to the site in the form of a shear-horizontal (*SH*) cylindrical wave (radiated by a line source parallel to the x_3 axis and located in Ω_0 or a *SH* plane wave propagating initially in Ω_0).

Our analysis deals with the propagation of 2-D *SH* waves (i.e. waves that depend exclusively on the two cartesian coordinates $\mathbf{x} := (x_1, x_2)$ and that are associated with motion in the x_3 direction only).

We shall be interested in the spectra and time histories of seismic response at various points of the urban structures: at the midpoint of the top segments of a block, at the midpoint of the bottom segment of a block (which constitutes the interface between the block and the soft layer) and at the midpoint of the segment on the ground joining two successive blocks. Hereafter, we shall employ the term ‘duration’ to signify the temporal interval between the onset of the seismic response pulse and the moment this pulse attains 1/100th of its peak value.

The governing equations of the wave–structure interaction in both the space–time and space–frequency frameworks are given in Appendix A. A brief description is given of the finite-element (FE) formulation (in the space–time framework), applicable only to the case $N_b < \infty$.

The mode-matching (MM) formulation appeals to the space–frequency formulation and is described in Appendices B–F. The field representations are described in Appendix B. The interrelations between the unknown field coefficients are given in Appendix C. The

determination of the various unknowns is treated in Appendix D. The existence and nature of structural modes is examined in detail in Appendix E. The way these structural modes are excited by a seismic source and make themselves felt in the various subdomains of the structure is treated in Appendix F.

3 NUMERICAL RESULTS FOR ONE BLOCK IN A MEXICO CITY-LIKE SITE

The results in this section apply to a single block whose base segment centre is located at (0 m, 0 m). The latter is supposed to be situated in a Mexico City-like site wherein $\rho^{[0]} = 2000 \text{ kg m}^{-3}$, $c^{[0]} = 600 \text{ m s}^{-1}$, $Q^{[0]} = \infty$, $\rho^{[1]} = 1300 \text{ kg m}^{-3}$, $c^{[1]} = 60 \text{ m s}^{-1}$ and $Q^{[1]} = 30$, with the soft layer thickness being $h = 50 \text{ m}$. In addition, the material constants of the block are: $\rho^{[2]} = 325 \text{ kg m}^{-3}$, $c^{[2]} = 100 \text{ m s}^{-1}$ and $Q^{[2]} = 100$.

The source is placed consecutively at (0 m, 3000 m) or (−65 m, 3000 m), which are deep locations for which Love modes can hardly be excited in the absence of the block, and at (−3000 m, 100 m), a shallow location at the which Loves modes can easily be excited in the absence of the block (Grobey & Wirgin 2005a,b).

The eigenfrequencies of the block displacement-free base block are $\nu_{0m}^{FB} = \frac{c^{[2]}(2m+1)}{4b}$, and the Haskell frequencies are $\nu_m^{HASK} = \frac{2m+1}{2} \frac{c^{[1]}}{2b}$, wherein $m = 0, 1, 2, \dots$. Thus, the Haskell frequencies are 0.3, 0.9, 1.5... Hz. The fundamental displacement-free base block eigenfrequency (whose value is supposed to be close to the one of the corresponding quasi-mode), depends on the choice of the mechanical parameters of the medium filling Ω_2 , and occurs at $\nu_{00}^{DFB} = \frac{c^{[2]}}{4b} \approx \frac{25}{b}$. This expression agrees with the empirical one: $\nu_{00}^{FB} \approx \frac{30}{b}$ employed in Boutin & Roussillon (2004).

If the zeroth-order quasi-mode is dominant, the dispersion relation (73) takes the form:

$$0 = \cot(k^{[2]}b) - \frac{ik^{[2]}w}{2\pi} \frac{\mu^{[2]}}{\mu^{[0]}} \int_{-\infty}^{\infty} \left[\frac{\cos(k_2^{[1]}h) - i \frac{\mu^{[0]}k_2^{[0]}}{\mu^{[1]}k_2^{[1]}} \sin(k_2^{[1]}h)}{\cos(k_2^{[1]}h) - i \frac{\mu^{[1]}k_2^{[1]}}{\mu^{[0]}k_2^{[0]}} \sin(k_2^{[1]}h)} \right] \times \text{sinc}^2\left(k_1 \frac{w}{2}\right) \frac{dk_1}{k_2^{[0]}} = \mathcal{F}_1 - \mathcal{F}_2 \quad (3)$$

The block is 50 m high and 30 m wide. The displacement-free base block eigenfrequencies are then 0.5 Hz, 1.5 Hz, ... Fig. 2 gives an indication of the modes of the configuration. One notes that the eigenfrequencies (frequencies at which $\text{Re}(\mathcal{F}_1) = \text{Re}(\mathcal{F}_2)$, at the least) are $\nu \approx 0.3, 0.5, 1.0, 1.53, 1.75$ and 1.93 Hz. The attenuations of the quasi-Love mode at $\nu \approx 0.3$ and 0.9 Hz, and of the quasi displacement-free base block model at $\nu \approx 0.5$ and 1.5 Hz are relatively small. The attenuation of the quasi stress-free base block mode (close to the zeros of $\tan(k^{[2]}b)$) at $\nu_{0,1}^{QSFb} \approx 1 \text{ Hz}$ is relatively large.

We now examine the displacement field on the horizontal boundaries of the block.

We first consider that the seismic disturbance is delivered to the site by a ‘deep line source’ located at $\mathbf{x}^s = (0, 3000 \text{ m})$. This means that in the absence of the block, the displacement field is composed mainly of propagative waves in the substratum and interfering propagative waves in the layer.

Fig. 3 depicts the spectra and time histories of the ‘total displacement at the centre of the top and bottom segments of the block’,

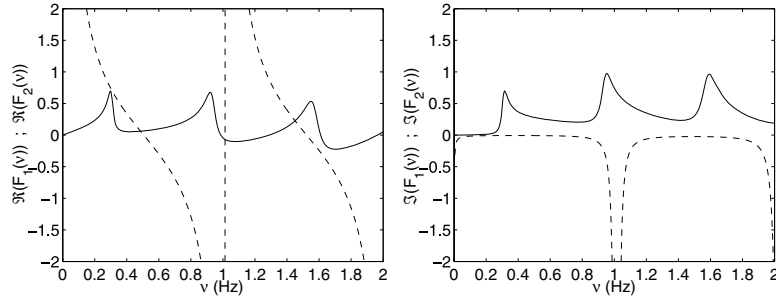


Figure 2. Indications concerning the solution of the dispersion relation $\mathcal{F} = \mathcal{F}_1 - \mathcal{F}_2 = 0$ for a single 50×30 m block in a Mexico City-like site. In the left panel, the solid curve describes $\text{Re}(\mathcal{F}_1)$ versus frequency (ν in Hz) and the dashed curve describes $\text{Re}(\mathcal{F}_2)$ versus frequency. The right panel again contains two curves: the solid one describes $\text{Im}(\mathcal{F}_1)$ versus frequency and the dashed curve describes $\text{Im}(\mathcal{F}_2)$ versus frequency.

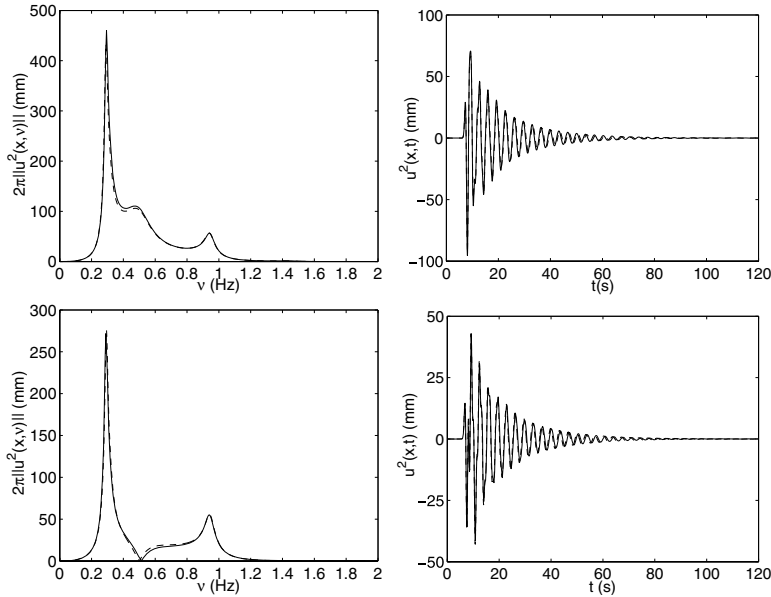


Figure 3. 2π times the spectra (left panels) and time histories (right panels) of the total displacement response to a cylindrical wave (radiated by a deep source located at $\mathbf{x}^s = (0 \text{ m}, 3000 \text{ m})$ at the centre of the summit segment (top panels) and at the centre of the base segment (bottom panels) of a single 50×30 m block. The dashed curves correspond to the semi-analytical (mode-matching, one mode) result, and the solid curves to the numerical (finite-element) result.

as computed by the MM method (with account taken of one quasi-mode) and the FE method, for a deep source. No notable differences are found between the results of the two methods of computation. The agreement between the FE and MM solutions is found to be as favourable for shallow sources as for deep sources. The neglect of the quasi-modes of order larger than 0 is valid for this block width. The block acts as a ribbon source of width w located at the base segment.

Fig. 4 depicts the spectra and the time histories of ‘the total displacement on the ground in the absence of the block’ as well as ‘the total displacement at the centres of the top and base segments of the block’ for a deep source. In the time domain, a small increase of the duration, and a fairly large increase of the peak amplitude, can be noted, particularly on the top segment of the block, where the quasi displacement-free block mode makes itself felt.

In the frequency domain, there is an increase of the maximum amplitude and of the sharpness of the first resonance peak of the substructure, which is a characteristic feature of the *soil–structure interaction*. The displacement field vanishes at the base segment for a frequency close to ν_{00}^{DF} .

We now consider what happens when the seismic disturbance is delivered to the site by a ‘shallow line source’ located at $\mathbf{x}^s = (-3000 \text{ m}, 100 \text{ m})$. This means that, in the absence of the block, the displacement field in the substructure is that of Love modes at the resonance frequencies of these modes.

Fig. 5 compares the displacement on the ground in the absence of the block to that in the block (on the top and bottom segments thereof) for a shallow source. In the time domain, the durations are substantially the same when the block is present or absent, but the peak and cumulative amplitudes are larger in the presence of the block. In the frequency domain, both the sharpness and amplitude of the first peak, corresponding to the first Love mode in absence of the blocks, increase. This means that the ‘soil–structure interaction’ obtained for a deep source is also found for a shallow source. The fact that the position of this peak is hardly shifted means that the structure of the quasi-Love mode is very nearly that of the Love mode existing in the absence of the block. However, the presence of the block enables this mode to be excited more efficiently than in its absence, that is, when the site is solicited solely by the shallow source and not by waves re-emitted by the block.

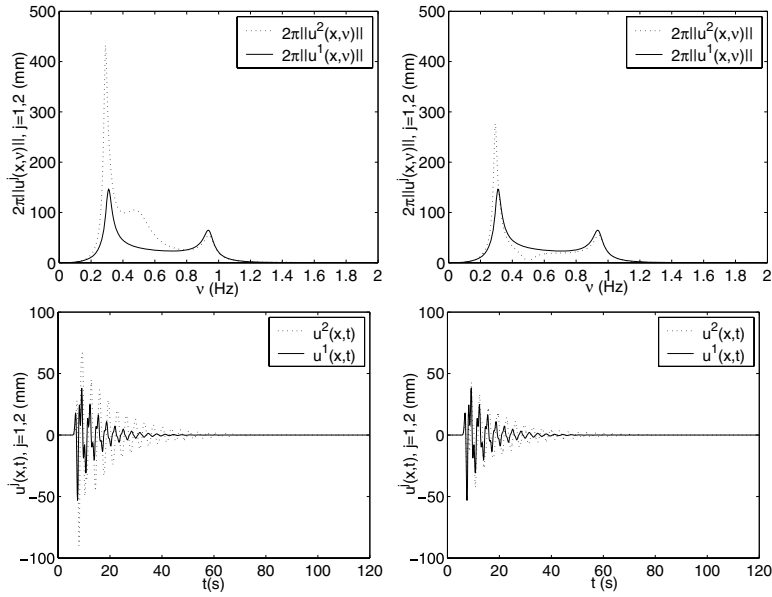


Figure 4. Comparison of 2π times the spectrum (on the top) and time history (on the bottom) of the total displacement on the ground in absence of the block (solid curves) with the total displacement (dotted curves) at the centre of the top segment (left panel) and at the centre of the base segment (right panel) of a single 50×30 m block, for a deep source located at $\mathbf{x}^s = (0 \text{ m}, 3000 \text{ m})$.

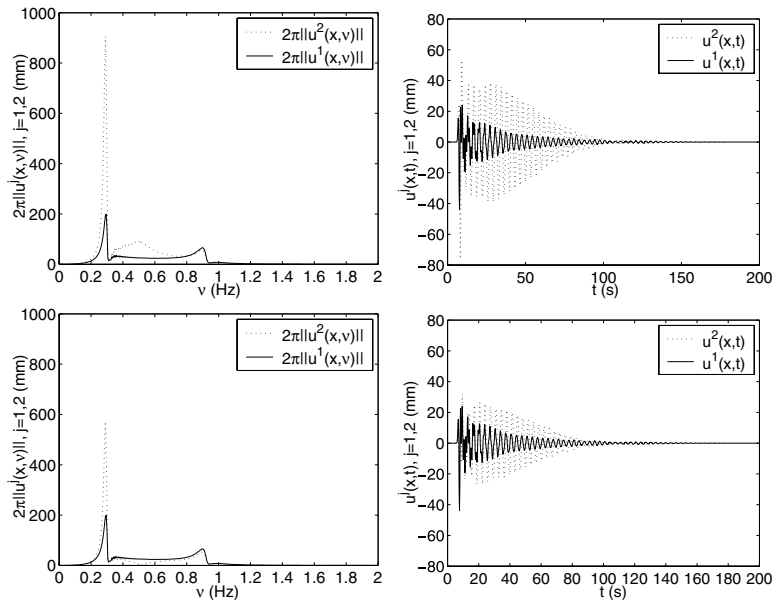


Figure 5. Comparison of 2π times the spectrum (left panels), and time history (right panels) of the total displacement on the ground in the absence of the block (solid curves) with the total displacement, (dotted curves) at the centre of the top segment (top panels) and of the bottom segment (bottom panels) of a single 50×30 m block, for a shallow line source located at $\mathbf{x}^s = (-3000 \text{ m}, 100 \text{ m})$.

In order to better visualize the excitation of the quasi-Love mode due to the presence of the block, we show, in Fig. 6, the snapshots at various instants, of the displacement field in response to the cylindrical wave radiated by a deep line source located at $\mathbf{x}^s = (0 \text{ m}, 3000 \text{ m})$. We note, in the layer regions of these figures, waves that are re-radiated from the base segments of the block and that are trapped in the layer.

4 NUMERICAL RESULTS FOR TWO-BLOCK CONFIGURATIONS IN A MEXICO CITY-LIKE SITE

Let us now consider the configuration involving ‘two blocks’, which is the simplest configuration for studying interblock coupling effects. The latter go by the name of *structure–soil–structure interaction*.

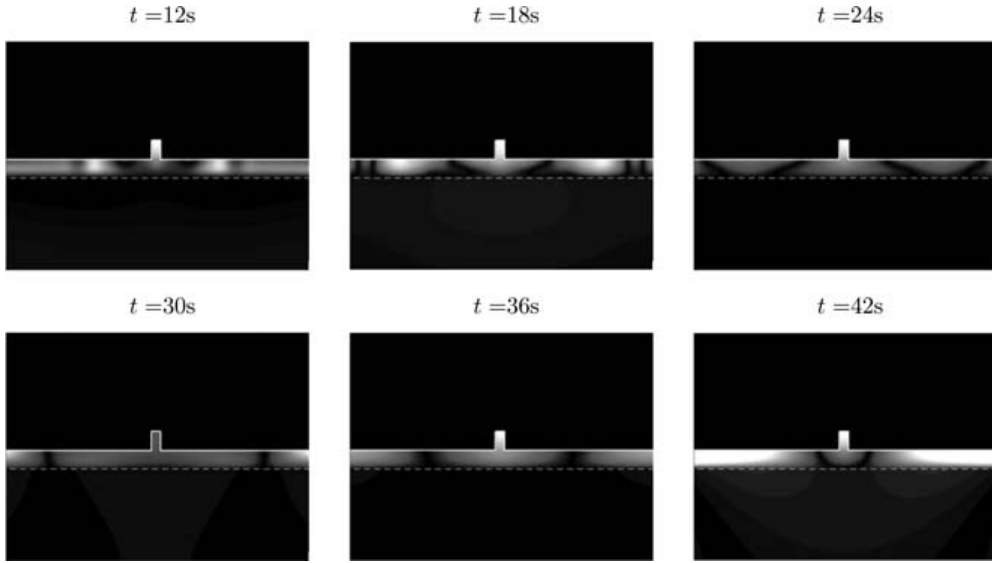


Figure 6. Snapshots at various instants, $t = 12$ s, $t = 18$ s, $t = 24$ s, $t = 30$ s, $t = 36$ s, $t = 42$ s, of the total displacement field for a one 50×30 m-block configuration, solicited by the cylindrical wave radiated by a deep line source located at $\mathbf{x}^s = (0 \text{ m}, 3000 \text{ m})$.

The two blocks, situated in a Mexico City-like environment, are located such that the centre of the base segment of block 1 is $(0 \text{ m}, 0 \text{ m})$ and that of block 2 is $(-65 \text{ m}, 0 \text{ m})$.

The parameters of the site are the same as in the one-block configuration.

Only one kind of solicitation is considered, that is, the incident cylindrical wave is radiated by a deep line source located at $(0 \text{ m}, 3000 \text{ m})$.

If the zeroth-order quasi-mode coefficient is relevant, the dispersion relation of the configuration takes the form (see Appendix E4):

$$(\mathcal{F}_1^{(1)} - \mathcal{F}_2^{(1)})(\mathcal{F}_1^{(2)} - \mathcal{F}_2^{(2)}) - \mathcal{F}_2^{(12)}\mathcal{F}_2^{(21)} = \mathcal{F} = 0, \quad (4)$$

wherein $\mathcal{F}_j^{(j)} - \mathcal{F}_2^{(j)} = 0$, $j = 1, 2$ is the dispersion relation of the configuration with one block of characteristics of the block j (see eq. 3) and the term $\mathcal{F}_2^{(12)}\mathcal{F}_2^{(21)} = (\cos(k^{[2]}b_1)Q_{00}^{(12)})(\cos(k^{[2]}b_2)Q_{00}^{(21)})$ accounts for the coupling between the two blocks.

The latter are both 50 m high and 30 m wide and their centre-to-centre separation is 65 m.

The displacement-free base block eigenfrequencies are 0.5 Hz, 1.5 Hz, . . . Fig. 7 gives an indication of the solution of the dispersion relation. Eigenfrequencies (i.e. solutions of $\text{Re } \mathcal{F} = 0$) are found at 0.3, 0.55, 1.0, 1.4 Hz, . . . The attenuations associated with the quasi-Love mode at 0.3 Hz and the multidisplacement-free base block mode at 0.55 Hz are rather small. The eigenfrequencies are not close to each other.

The response at the centre of the summit segment of one of the blocks computed by the FE method is compared in Fig. 8 to the corresponding response computed by the MM method (with account taken only of the zeroth-order quasi-mode. The response on the other block is found to be almost identical to this response.

In Fig. 9 we depict the displacements in one of the two blocks (i.e. at the centres of the summit and base segments) with the displacement on the ground (at the same point as occupied by the centre of the base segment of the block) in the absence of the blocks. The response on the other block is found to be almost identical to this response. We observe an increase of the duration and of the

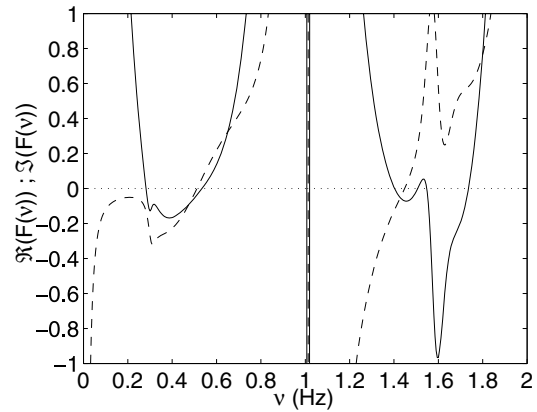


Figure 7. Indications concerning the dispersion relation $\mathcal{F} = 0$ for two blocks. The solid curves represent $\text{Re}(\mathcal{F})$ and the dashed curves $\text{Im}(\mathcal{F})$.

peak and cumulative amplitudes (particularly on the top segments) which seems to be due to the strong response at the frequency corresponding to the excitation of the multidisplacement-free base block mode. Once again, the displacement at the centre of the base segments vanishes at a frequency corresponding to the occurrence of the displacement-free base mode of the block.

In order to better visualize the excitation of the quasi-Love mode due to the presence of the two blocks, we show, in Fig. 10, the snapshots at various instants, of the displacement field, for two identical 50×30 m blocks in response to the cylindrical wave radiated by a deep line source located at $\mathbf{x}^s = (0 \text{ m}, 3000 \text{ m})$. We note, in the layer region of these figures, waves that are re-radiated from the base segments of the blocks and which evolve into a field with a series of nodes and anti-nodes characteristic of a sum of modes dominated by the quasi-Love modes. Coupling between the two blocks (structure-soil-structure interaction) is also notable in Fig. 10 at $t = 21$ s.

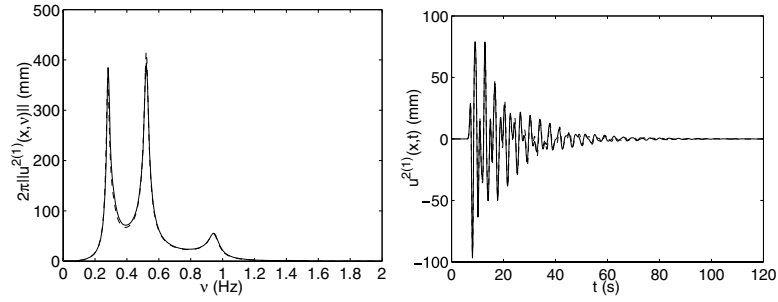


Figure 8. 2π times the spectra (left panel) and time histories (right panel) of the total displacement at the centre of the summit segment of block 1 as computed by the mode-matching method (with account taken only of the zeroth-order quasi-mode (dashed curves) and the finite element method (solid curves). Two blocks, deep line source.

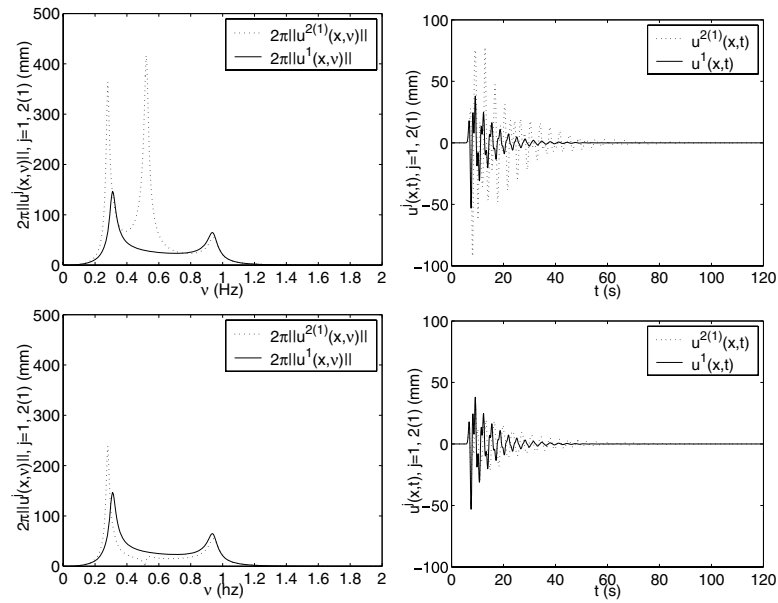


Figure 9. Comparison of 2π times the spectrum (left panels) and of the time history (right panels) of the total displacement on the ground in the absence of blocks (solid curves) and in the presence of blocks (dashed curves). From the top to the bottom: at the centre of the summit segment of block 1, and at the centre of the base segment of block 1. Two 50×30 m blocks solicited by the cylindrical wave radiated by a deep line source located at $\mathbf{x}^s = (0, 3000)$ m.

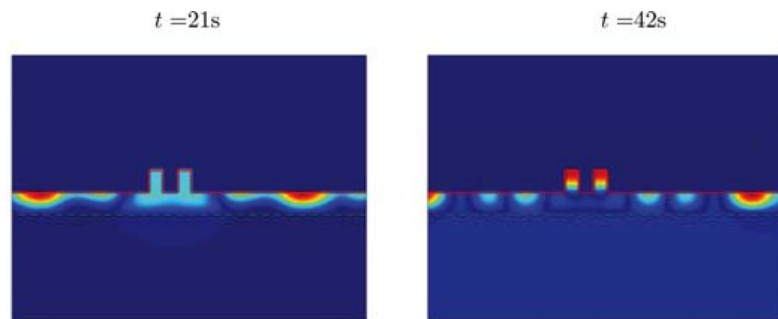


Figure 10. Snapshots at $t = 21$ s and $t = 42$ s of the total displacement field for a two identical 50×30 m-block configuration, solicited by the cylindrical wave radiated by a deep line source located at $\mathbf{x}^s = (0 \text{ m}, 3000 \text{ m})$.

5 DISCUSSION CONCERNING THE CONFIGURATIONS WITH A SMALL NUMBER OF BLOCKS

The response, to the cylindrical wave radiated by a line source located in the substratum, of a finite set of blocks, each block modelling one, or a group of buildings, in welded contact with a soft layer overlying a hard half-space, was investigated in a theoretical manner via the MM technique.

The capacity of this technique to account for the complex phenomena provoked by the presence of blocks on the ground was demonstrated by comparison of the numerical results to which it leads to those obtained by a FE method.

It was shown that the presence of blocks induces a modification of the phenomena that are produced by the configuration without blocks, or of a configuration of closed blocks disconnected from the geophysical half-space. In particular, the blocks modify the dispersion relation of what, in the absence of the blocks, constitutes the Love modes.

Three different and complementary points of view were developed (in the framework of the MM theory) concerning the dispersion relation relative to the configuration with blocks. The first emphasizes the role of the substructure [i.e. the geophysical (flat ground/layer/substratum) structure]. The second emphasizes the role of each particular block of the superstructure. The third point of view emphasizes the couplings of the fields in the superstructure with those in the substructure.

The first two points of views enable the definition of two new types of modes relative to the configuration with blocks: the *quasi-Love modes*, which are small perturbations of the Love mode (which can exist when no blocks are present), and the *quasi displacement-free base block modes*, which are small perturbations of the displacement-free base block mode (which can exist when no geophysical structure is present).

These two types of quasi-modes account for coupling between a particular block of the superstructure with the substructure, but not for the couplings between blocks (when more than one block is present). Thus, the so-called *soil-structure interaction* is shown to be due to the excitation of quasi Love modes.

The third point of view emphasizes the coupling between blocks (when more than one block is present). It was shown that this coupling, manifested by the existence of coupling matrices in the expressions for the quasi mode amplitudes, is of the same form as the coupling between one particular block and the substructure, which underlines the fact that the coupling between blocks is carried out via the substructure.

The study of the dispersion relation for the multiblock configurations is very complex, but can be carried numerically. This was done for a two-block configuration and showed that a *multidisplacement-free base block mode* can be produced. The latter was shown to correspond to a coupled mode, constituted by a combination of quasi displacement-free base block modes of each block, which are no longer excited as such in a configuration with more than one block. The multidisplacement-free base block mode was shown to account for the so-called *structure-soil-structure interaction*.

It was underlined that the modes of a complete one- or multiblock configuration do not constitute the reunion of the modes of the individual component structures. Thus, the phenomena for a complete N_b block configuration are not the sum of the phenomena for $N_b - 1$, $N_b - 2$, ..., 0 block configurations.

The excitation of these modes was then studied in the particular case of one and two blocks. A common feature of the influence of

one/or more blocks is the excitation of the quasi-Love mode, which occurs even for solicitation by the waves radiated by a deep source (recall that, for this type of solicitation, it is not possible to excite ordinary Love modes in a flat ground (i.e. no blocks)/soft horizontal layer/hard substratum configuration Groby & Wirgin 2005a). The trace of quasi-Love mode excitation in the frequency domain was shown to be: (i) for a deep source, a shift to lower frequency and an increase of the amplitude of the first (lowest-frequency) peak of the response, and (ii) for a shallow source [the case in which waves whose structure is close to that of Love waves already exist in the layer and substratum in the absence of the block(s)], an increase of the amplitude, and little or no shift, of the first resonance peak.

Generally speaking, the peak and cumulative amplitudes and duration of the time histories are larger for a one- and two-block configuration than for flat ground, at locations within the block, but no spectacular effects, such as those noted during the Michoacan earthquake were found in the numerical simulations, either for the one- or two-block 'cities'. This indicates that it is probably not sufficient to carry out experiments and numerical simulations on an isolated block or building (Manos *et al.* 1995; Guéguen 2000; Todorovska 2002) (or even on a couple of blocks or buildings) in order to predict correctly the seismic response of the block when it is surrounded by other blocks (the situation of most blocks in a typical city).

A configuration involving a larger number of blocks is difficult to study theoretically in the framework of the MM formulation, which is why configurations with an infinite number of blocks, each one of which is close to the average shape and composition of the blocks of typical cities, are investigated hereafter.

6 PRELIMINARY REMARKS CONCERNING THE CASE OF CITIES WITH A LARGE NUMBER OF BLOCKS

We again focus on the presence of the built features of the urban site as a complementary explanation of abnormal response. Previously, we treated the cases of one or two identical built features in the form of cylindrical blocks. Now, we study the case of many (10, 20, 40, ... ∞) identical blocks. Such a configuration is a more realistic representation of a real city due to the large number of blocks it incorporates, but the assumptions that the blocks are: (i) cylindrical, (ii) identical and (iii) periodically arranged, are rather far removed from reality, except in restricted portions of modern cities and megacities. Nevertheless, these assumptions are not more unrealistic than random dispositions of blocks with random sizes (Clouteau & Aubry 2001; Tsogka & Wirgin 2003; Groby *et al.* 2005) and compositions, and have the advantage of enabling a theoretical analysis which can shed some light on the physical origins of the above-mentioned exotic phenomena.

The periodic model of cities built on sites with a soft layer overlying a hard substratum solicited by seismic waves originated in the work of Wirgin & Bard (1996). Unfortunately, the theoretical apparatus underlying the numerical results was not given in this paper, and the distance between blocks in the computational results was taken to be 2000 m, which, in our present opinion, is unrealistically large (unless the blocks represent skyscrapers, of which there are usually few, and largely distant one from the other).

Thus the purpose of what follows is twofold: (i) give the missing theoretical foundations of the results of Wirgin & Bard (1996) and

(ii) treat cities that are more realistic than those in Wirgin & Bard (1996) and in the first part of this paper.

7 CANDIDATE SITES AND THEORY OF THEIR SEISMIC RESPONSE

Many earthquake-prone cities and megacities (New Delhi, Tokyo, Mexico City, Istanbul, San Francisco, Basel, etc.) are built on soft soil underlain by a hard substratum and contain districts with periodic, or nearly periodic arrangements of blocks. An attempt will be made hereafter to analyse the seismic response of districts of this type in Mexico City.

This city is idealized in exactly the same manner as previously, the only changes being that: (i) the number of blocks N_b is now large (≥ 10), and (ii) the solicitation takes the form of a plane wave (corresponding to very deep sources). The angle of incidence of this wave is taken to be $\theta^i = 0$ (i.e. normal incidence).

The MM formulation appeals to the space–frequency formulation and is described in Appendices G–K. The field representations are described in Appendix G. The interrelations between the unknown field coefficients are given in Appendix H. The determination of the various unknowns is treated in Appendix I. The existence and nature of structural modes is examined in detail in Appendix J. The way

these structural modes are excited by a seismic source and make themselves felt in the various subdomains of the structure is treated in Appendix K.

8 NUMERICAL RESULTS FOR THE SEISMIC RESPONSE IN MEXICO CITY

8.1 Preliminaries

The numerical results are obtained in two manners: (i) by the MM method (described in the previous section) as it applies to configurations consisting of an infinite number of equally spaced, equally sized rectangular blocks and (ii) by the FE method [briefly described in Appendix A, and in more detail in Groby & Tsogka (2006) and Groby *et al.* (2005)] as it applies to configurations with a large (but finite) number of equally spaced, equally sized rectangular blocks.

The discussions concerning the numerical aspects of the dispersion relations will be based on material stemming from the MM method. For the purpose of the analysis, and to allow for an easier comparison with the results exposed in the first part of this paper, we rewrite (the lowest-order approximation of the dispersion relation)

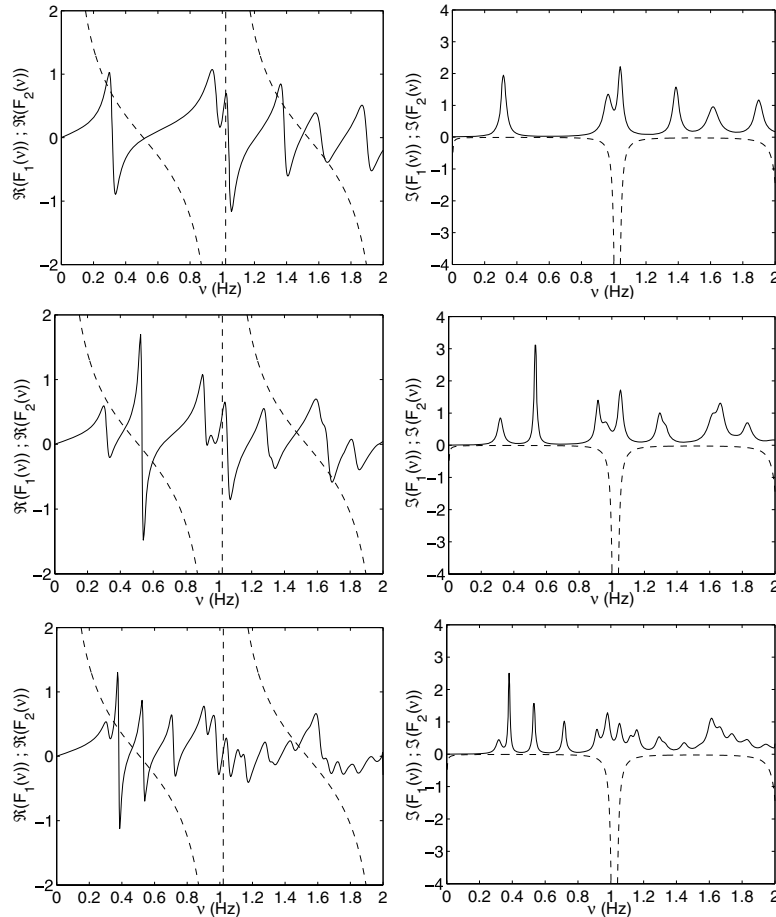


Figure 11. Indications concerning the solution of the dispersion relation $\mathcal{F}_1 - \mathcal{F}_2 = 0$ for the Mexico City-like urban site. In the left panels: the solid and dashed curves depict $\text{Re}(\mathcal{F}_1)$ and $\text{Re}(\mathcal{F}_2)$, respectively versus frequency (ν in Hz). In the right panels: the solid and dashed curves depict $\text{Im}(\mathcal{F}_1)$ and $\text{Im}(\mathcal{F}_2)$, respectively versus frequency. The top, middle and bottom panels are related to $d = 65, 150$ and 300 m, respectively.

(J13) in the form

$$\cos(k^{[2]}b) - \sum_{n=-\infty}^{\infty} \frac{iwk^{[2]}\mu^{[2]}}{\mu^{[0]}k_n^{[0]}d} I_{0n}^- I_{0n}^+ \frac{C_n^{[01]}}{C_n^{[10]}} \sin(k^{[2]}b) = \mathcal{F}_1 - \mathcal{F}_2 = 0, \quad (5)$$

wherein $\mathcal{F}_1 = \cos(k^{[2]}b)$.

The sources of the major earthquakes in Mexico City have usually been shallow and located in the subduction zone off the Pacific coast, approximately 350 km from Mexico City), so that modelling the solicitation of this city by a plane incident bulk wave is not realistic (Groby & Wirgin 2005a,b). Nevertheless, we assume such a (normally incident) plane bulk wave solicitation, notably to enable an easy quantitative comparison between the finite and infinite city responses and qualitative comparison with previous studies (Wirgin & Bard 1996; Clouteau & Aubry 2001; Semblat *et al.* 2003; Boutin & Roussillon 2004, 2006).

The central frequency of the Ricker pulse associated with the solicitation is chosen to be $\nu_0 = 0.5$ Hz. The material parameters are as in the first part of this paper.

The blocks are again 50 m high, 30 m in width, and their centre-to-centre spacing are successively chosen to be 65 m, 150 m and 300 m. The natural frequencies of the displacement-free base block modes are $\nu_m^{SFB} = 0.5$ Hz, 1.5 Hz, . . . , and the quasi-Cutler mode

natural frequencies (which are specific to the periodic nature of the site, with characteristic dimension d), are obtained from $\mathcal{F} = 0$.

8.2 Dispersion characteristics of the modes for an infinite number of blocks

Fig. 11 gives indications concerning the solutions of the dispersion relation of the global configuration (i.e. blocks plus underground) for centre-to-centre spacings $d = 65, 50$ and 300 m. For a centre-to-centre spacing $d = 65$ m, the influence of the periodic nature of the city (embodied in the parameter d) appears essentially at a high frequency outside the spectral bandwidth of the solicitation, while for $d = 150$ and 300 m this influence can make itself felt in the spectral range of the solicitation through the quasi-Cutler modes. Quasi-Love and quasi-displacement free base block modes should be excited at ≈ 0.3 and ≈ 0.5 Hz, respectively, both associated with a low attenuation. The stress-free base block mode is excited at ≈ 1 Hz, but is highly attenuated for all three d .

Quasi-Cutler modes are clearly excited with a low attenuation. In particular, for a relatively large centre-to-centre spacing (i.e. $d = 300$), the spectral density of this type of mode is large. The fundamental quasi-Love natural frequency is probably very close to the fundamental quasi-Cutler natural frequency.

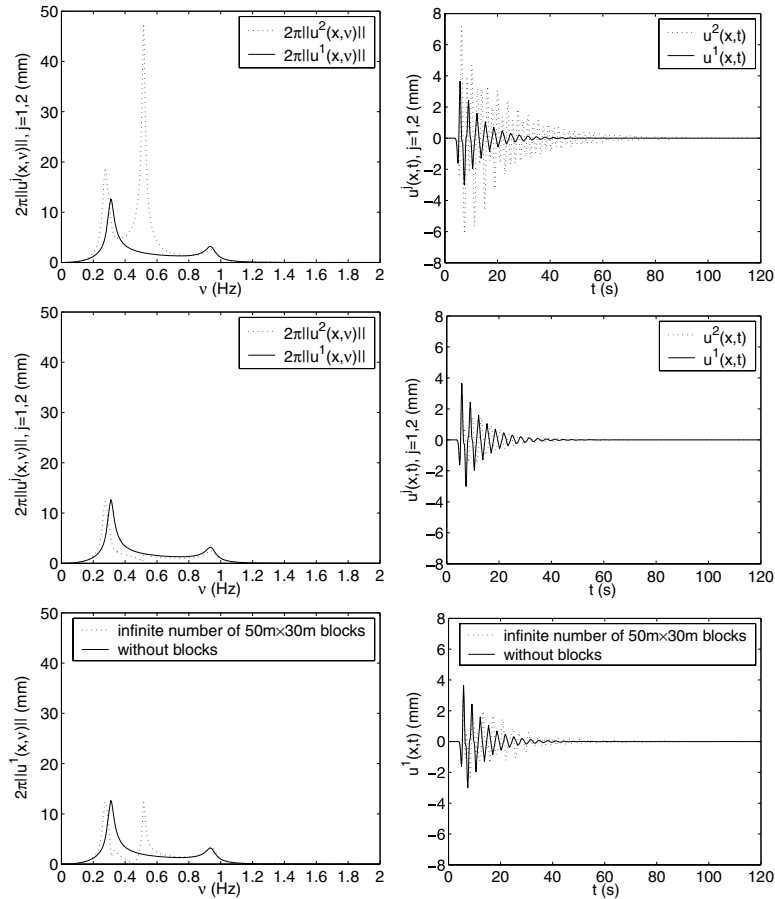


Figure 12. Comparison of 2π times the spectrum (left panels) and time history (right panels) of the total displacement on the ground in the absence of blocks (solid curves) with the displacement at three locations in the presence of blocks (dashed curves): (i) at the centre of the summit segment of a block (top panels), (ii) on the ground, at a location halfway between two adjacent blocks (bottom panels), (iii) at the centre of the base segment of a block (middle panels), $N_b = \infty$ and $d = 65$ m.

8.3 Seismic response for an infinite number of blocks with period $d = 65$ m compared to that of no blocks

In Fig. 12 we compare the spectra and time histories in the presence and absence of the $d = 65$ set of blocks.

The first resonance peak in the spectra is shifted to a lower frequency and is of higher amplitude when the blocks are present. This is the indication of the excitation of the fundamental quasi-Love mode responsible for what was previously termed the *soil–structure interaction*. The peak relative to the excitation of the perturbed displacement-free base block mode has a relatively high amplitude, due to both the spectrum of the incident wave and to the presence of the other blocks. Effectively, the resonance frequency does not correspond to that of the displacement-free base block mode (at which frequency the response is nil at the centre of the base segment of the block), and the particular shape of the spectrum at the centre of the base segment of the block is characteristic of the excitation of a multidisplacement-free base block mode and not to the excitation of a quasi displacement-free base block mode (as shown previously). This coupled mode also takes into account the so-called structure–soil–structure interaction as was suggested in Section J.3 of Appendix J.

A splitting of the first peak appears in the ground (between the blocks) response. The second of the split peaks has a low quality factor, which fact means the quasi-absence of beatings in the time history of response.

The temporal displacements are of higher amplitude and duration in the presence of blocks than in the absence of blocks, particularly at the centre of the top segment of the block. These results are evocative of those obtained previously for two blocks.

8.4 Comparison of the seismic responses for one, two and an infinite number of blocks with centre-to-centre separations $d = 65$ m

In Fig. 13, we compare the spectra and time histories of response for one-block, two-block, and infinite-block configurations at the centre of the ‘top segment’ of one of the blocks. This figure shows that the effect of increasing the number of blocks is essentially to increase the height of the second (i.e. higher-frequency) resonance peak at the expense of the first resonance peak, and thus to introduce stronger high-frequency oscillations in the temporal response. As the quality factor of the second resonance peak increases with N_b , the durations

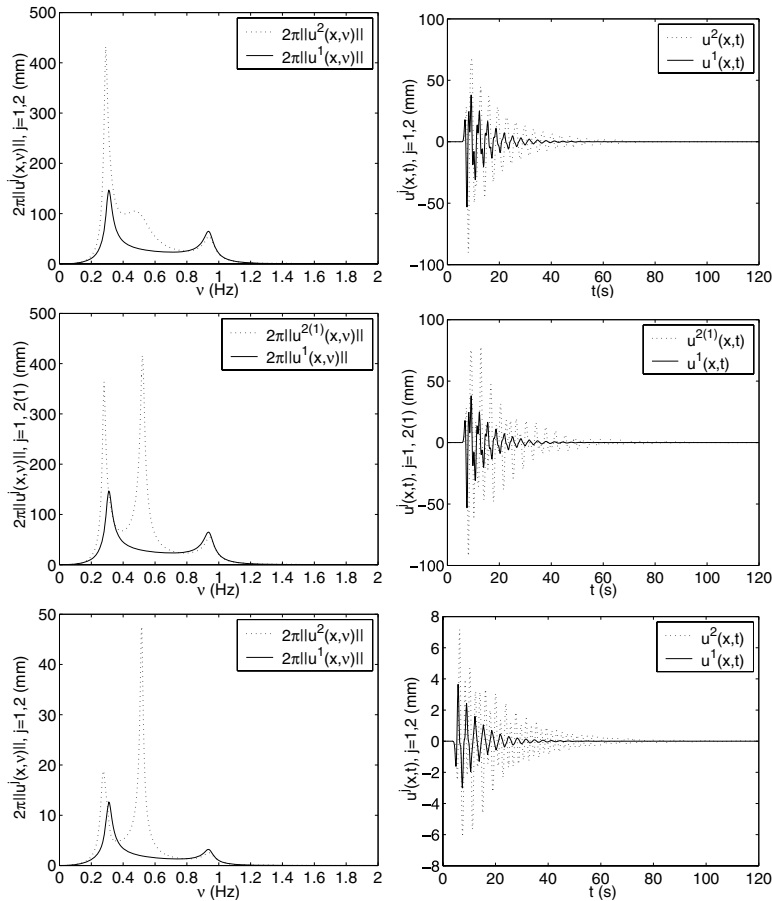


Figure 13. Comparison of 2π times the spectrum (left panels) and time history (right panels) of the total displacement on the ground in the absence of blocks (solid curves) with the displacement at the centre of the *top segment* of a 50×30 m block (dashed curves) for: (i) one such blocks (top panels), (ii) two such blocks with centre-to-centre spacing $d = 65$ m (middle panels), and (iii) an infinite number of such blocks with centre-to-centre spacing $d = 65$ m (bottom panels). Note that the one- and two-block results apply to the response to the (approximately a normally incident plane) wave emitted by a deep line source situated at (0 m, 3000 m) whose amplitude, at ground level is different from that of the plane wave solliciting the infinite block structure, which is why the maximal amplitudes of response are different.

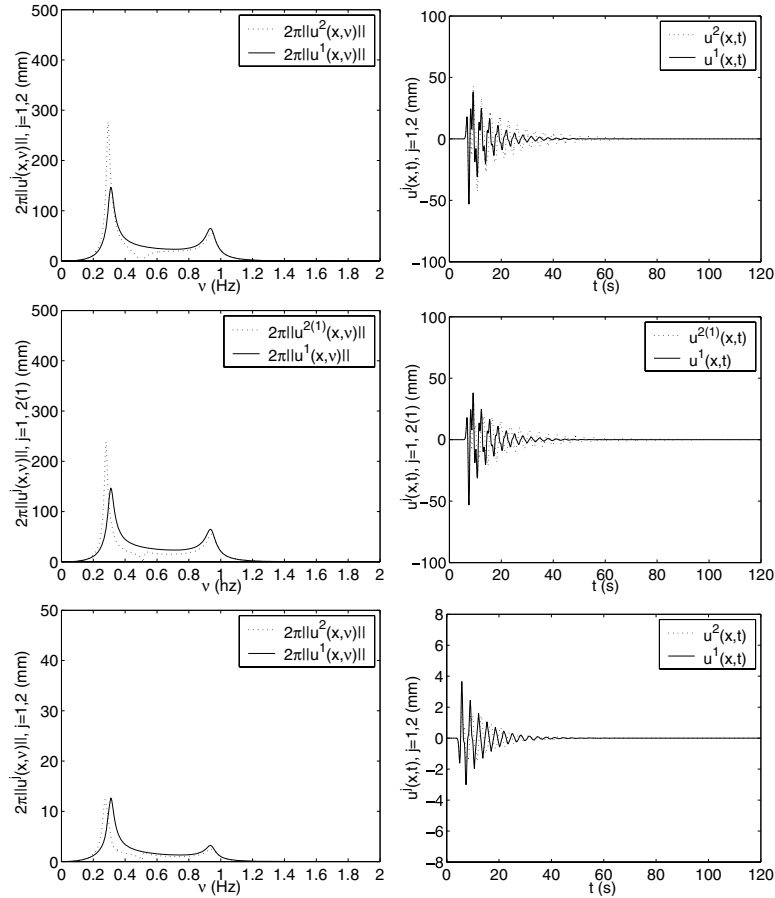


Figure 14. Comparison of 2π times the spectrum (left panels) and time history (right panels) of the total displacement on the ground in the absence of blocks (solid curves) with the displacement at the centre of the *bottom segment* of a 50×30 m block (dashed curves) for: (i) one such blocks (top panels), (ii) two such blocks with centre-to-centre spacing $d = 65$ m (middle panels), and (iii) an infinite number of such blocks with centre-to-centre spacing $d = 65$ m (bottom panels). Note that the one- and two-block results apply to the response to the wave emitted by a deep line source situated at (0 m, 3000 m) whose amplitude, at ground level is different from that of the plane wave solliciting the infinite block structure, which is why the maximal amplitudes of response are different.

also increase with N_b . ‘The combined effect of the increased quality factors and higher frequency oscillations is increased cumulative motion of the block’.

In Fig. 14, we compare the spectra and time histories of seismic response for one-block, two-block and infinite-block configurations at the centre of the ‘bottom segment’ of one of the blocks. Since the second resonance now is synonymous with a minimum of response, the aforementioned effects are not produced at the base of the block. In fact, with increasing N_b , we actually observe a decrease of the height of the first resonance peak, whose effect is to decrease the amplitude and duration of motion in the time histories. This might furnish an explanation of why some researchers have found that the presence of buildings results in de-amplification.

8.5 Comparison of the seismic responses for 10, 20, 40 block configurations with that of a configuration having an infinite number of blocks for centre-to-centre separations $d = 65$ m

In Fig. 15, we compare the spectra and time histories of seismic response at the centre of the ‘top segment’ of a centrally located block in configurations with 10, 20, 40 and an infinite number of

50×30 m blocks separated by $d = 65$ m. On the whole, these displacement responses are very similar, in both the frequency and time domains, marked by relatively long duration (≈ 2 min), and large maximum and cumulative amplitudes. However, for the finite values of N_b , there appears some splitting of the $N_b = \infty$ low frequency resonance peak which gives rise to beatings in addition to those due to the presence of the two main resonance peaks.

The presence of the additional low-frequency peaks in this figure is linked either to the (finite) number of blocks considered and/or to the total width W of the finite configuration (for $N_b = 10, 20, 40$; W is equal to 650, 1300 and 2600 m, respectively). These peaks cannot be accounted-for in the dispersion relations written above, since they result from an analysis of configurations for an infinite number of blocks (and for which $W = \infty$).

8.6 Illustration of the spatial variability of response in a configuration of ten blocks for centre-to-centre separations $d = 65$ m

Fig. 16 depicts snapshots of the displacement field in the entire configuration containing ten blocks whose centre-to-centre distance is $d = 65$ m. It can be noted that: (i) the motions are still quite

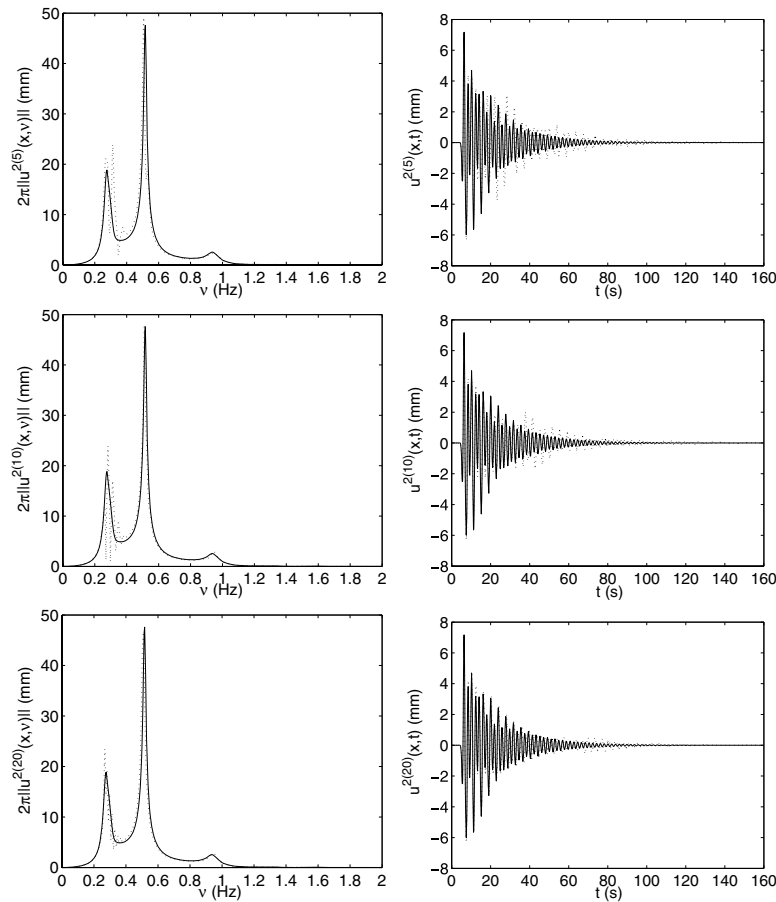


Figure 15. Comparison of 2π times the spectra (left panels) and time histories (right panels) of the total displacement at the centre of the top segment of a 50×30 m block of a configuration with an infinite number of blocks (solid curves) with the displacement at the same location of a central block (dashed curves) of configurations having: (i) ten such blocks (top panels), (ii) twenty such blocks (middle panels), and (iii) forty such blocks. In all cases, the centre-to-centre spacing is $d = 65$ m.

strong in portions of the configuration some 50 s after the arrival of the initial pulse, (ii) that the motion is quite variable spatially and temporally speaking, (iii) the spatial variability extends even to within a given block.

The spatial variability of response is one of the characteristics of the motion that has often been recorded within Mexico City (Flores *et al.* 1987; Chavez-Garcia & Bard 1994).

8.7 Comparison of responses of the configuration without blocks to the one with $N_b = \infty$ blocks for $d = 300$ m

In Fig. 17, we compare the spectra and time histories in the presence and in the absence of the blocks. When the blocks are present, their number is infinite and their centre-to-centre distance is 300 m.

The excitation of the multidisplacement-free base block mode cannot be clearly distinguished because of the excitation of quasi-Cutler modes whose existence is related to the periodic nature of the block distribution. Note should be taken of the fact that now (i.e. for $d = 300$ m) these modes are visible (with a large quality factor) within the bandwidth of the solicitation, whereas they were invisible for the $d = 65$ m periodic structure. As previously, the soil–

structure interaction appears as a resonance peak associated with the excitation of the fundamental quasi-Love mode.

These features show up at all three locations of the configuration with blocks. They manifest themselves in the time domain by: (i) a larger duration (multiplied by ≈ 4 on the top segment of the blocks with respect to its value in the absence of the blocks), (ii) a larger peak amplitude (at the top of the blocks) and larger cumulative motion and (iii) pronounced beatings at all locations due to the periodic nature of the configuration.

These features are once again evocative of those which have been observed during earthquakes in certain districts Mexico City. However, the excitation of the quasi-Cutler mode, which is strongly linked to the quasi-periodic or periodic nature of a district of the city (these districts actually exist, as seen in aerial or satellite photographs of many cities and mega cities), can, at best, explain only part of the features of response in this city, since the latter is not usually solicited by a (normally incident) plane wave.

It was shown in Groby & Wirgin (2005a) and Groby & Wirgin (2005b) that the correct solicitation of a configuration for the study of the Michoacan earthquake (and many other earthquakes affecting Mexico City) is a cylindrical wave radiated by a shallow, laterally distant source that gives rise to Love waves after travelling within the crust from the hypocentre to the city. In the same studies, it was

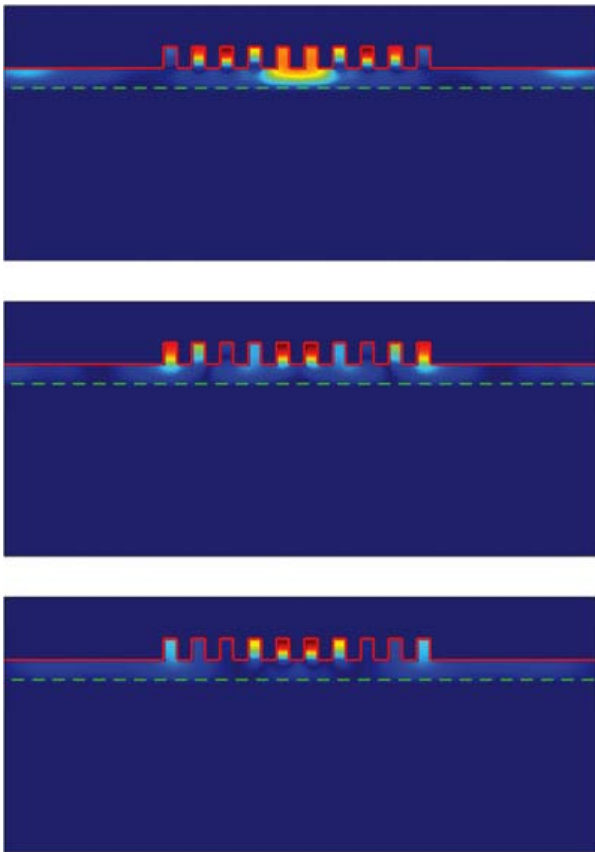


Figure 16. Snapshots at instants $t = 25$ s (top panel), $t = 32.5$ s (middle panel), $t = 50$ s (bottom panel), of the total displacement field for 10 identical 50×30 m blocks whose centre-to-centre spacing is $d = 65$ m.

shown that this type of solicitation is another cause for the large duration, large amplitude, and beatings of Mexico City response. Unfortunately, source wave solicitation cannot be treated by the quasi-modal analysis of periodic structures.

9 DISCUSSION RELATIVE TO STRUCTURES WITH A LARGE NUMBER OF BLOCKS

In this part of the paper, the response, to a plane wave initially propagating in the substratum, of a large or infinite set of identical, equi-spaced blocks, each block modelling a group of buildings, in welded contact with a soft layer overlying a hard half space, was investigated in a theoretical manner via the MM technique.

The capacity of the MM technique to account for the complex phenomena provoked by the presence of blocks on the ground was demonstrated by comparison of the numerical results to which it leads to those obtained by a FE method.

It was shown that the presence of the blocks induces a modification of the phenomena that are produced by the configuration without blocks, or of a configuration of closed blocks disconnected from the geophysical half-space. In particular, the blocks modify the dispersion relation of what, in the absence of the blocks, constitutes the Love modes. Moreover, the periodic nature of the urban site is responsible for the existence of another (collective) vibra-

tional mode which is a variant of the Cutler mode encountered in electromagnetic wave guide structures.

The dispersion relation for the periodic configurations with an infinite number of blocks (see Appendix J.3) is very complex, but an approximation of this relation lends itself to a fairly explicit theoretical analysis, inspired notably by the method first adopted in the electromagnetic wave community. The general features of this dispersion relation, revealed by the theoretical analysis (and manifested by the existence of several types of vibrational modes), were shown to actually exist by means of the numerical study.

The excitation of the vibrational modes was then studied in the particular case of city districts with 10 and an infinite number of identical, periodically disposed blocks. A common feature of the influence of the blocks is the excitation of the quasi-Love mode, which occurs even for solicitation by a plane wave (recall that, for this type of solicitation, it is not possible to excite ordinary Love modes in a flat ground (i.e. no blocks)/soft horizontal layer/hard substratum configuration Groby & Wirgin 2005a). The trace of quasi-Love mode excitation in the frequency domain was shown to be a shift to lower frequency and an increase of the amplitude of the first (lowest-frequency) peak of the response.

The change of the phenomena provoked by plane wave solicitation, from a configuration without blocks (for which there exist only bulk waves in the geophysical structure), to one with blocks (for which there exist quasi-Love modes characterized by a field in the substratum that is predominantly a surface wave in the substratum) is a manifestation of the so-called *soil-structure interaction*.

Multidisplacement-free base block modes were shown to be excited in all the configurations and to correspond to a coupled mode.

The modifications of the frequency-domain response (and less so of the time-domain response) were found to be fairly substantial for structures involving blocks separated by 65 m in the Mexico City-like site. In particular, 10 or 20 blocks separated by 65 m, were shown to give rise to anomalous features (amplifications of peak and cumulative motion, large durations and beatings) that are even closer to those observed in Mexico City than configurations with a larger number ($40, \infty$) of blocks.

All the anomalous features found for the Mexico City-like site with 10 or an infinite number of blocks were found to be closer to the actually observed anomalous features observed during earthquakes in Mexico City when the separation between blocks is 300 m rather than 65 m. This was found to be due to the fact that the structure with the larger period enables the quasi-Cutler mode to make itself felt within the range of frequencies of the source.

10 CONCLUSION

The theoretical findings and numerical results of the present study cannot account for all the anomalous phenomena observed in many of the earthquakes in Mexico City (notably the exceptionally long durations) for the obvious reasons that the model adopted herein, that is, *SH* plane wave solicitation, 2-D, periodic geometries, simple underground (horizontal homogeneous soft layer of infinite lateral extent overlying a homogeneous lossless hard substratum), simple homogenized building blocks, linear soil behaviour, etc., is incomplete, and in some respects, rather far removed from reality. Nevertheless, the results of our study indicate that it is possible that the excitation of vibrational modes, whose structure is closely related to those described herein, was responsible for at least part of the large-scale, anomalous mechanical effects that have caused so much damage in past earthquakes in urban areas such as Mexico City.

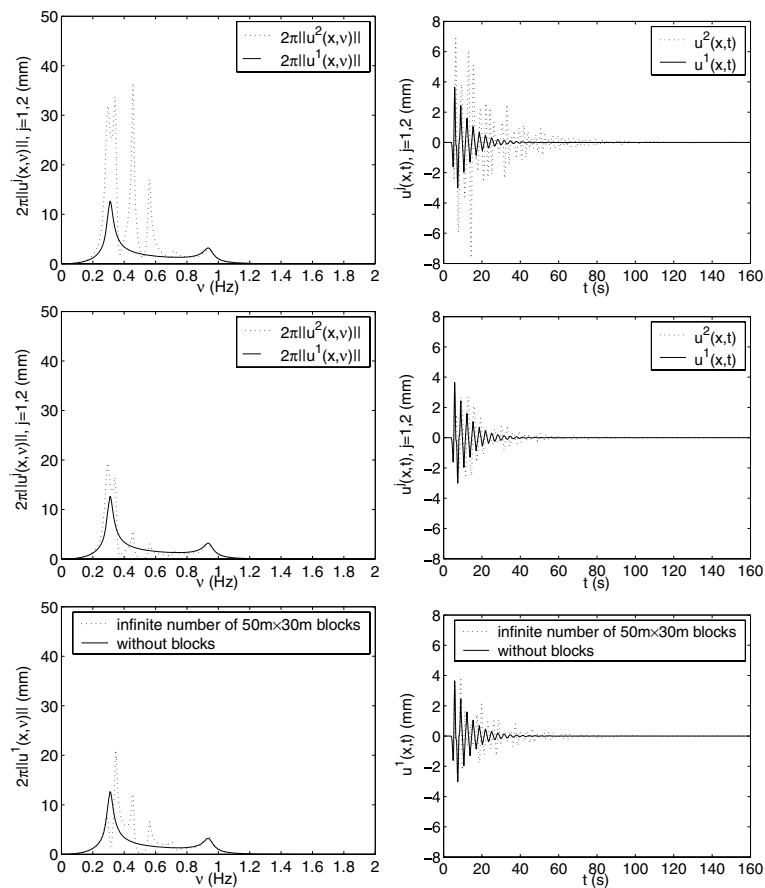


Figure 17. Comparison of 2π times the spectrum (left panels) and time history (right panels) of the total displacement on the ground in the absence of blocks (solid curves) with the displacements (dashed curves) at the centre of the top segment (top panels), centre of the bottom segment (middle panels) and midpoint on the ground between adjacent 50×30 m blocks, of a $N_b = \infty$ configuration in which $d = 300$ m.

The most important finding of this work, which substantiates those obtained in Wirgin & Bard (1996), Tsogka & Wirgin (2003) and Groby *et al.* (2005), is that city blocks can modify substantially the seismic motion in an urban area. Moreover, provided the blocks are arranged quasi-periodically with a sufficiently large period d , the seismic motion is of longer duration, and of higher cumulative (sometimes peak) amplitude on the ground (and, of course, in the buildings) than when the built structures are not present.

Although the quasi-periodic or periodic nature of our ‘cities’ would seem to favour the existence of a particular type of collective mode, many of the deleterious effects associated with what may be close to this mode have also been predicted to occur in non-periodic cities as well (Tsogka & Wirgin 2003; Groby *et al.* 2005).

Another objection to what may appear as our alarming prediction of the extent of motion in a city is that it applies to a 2-D configuration whereas real cities are 3-D in nature and therefore should scatter more of the incident energy and give rise to smaller surface motion than 2-D structures. However, this objection should be relativized, as is illustrated by a comparison of the surface motion of 2-D and 3-D valleys, embankments, and basins (Singh & Sabina 1977; Lee & Langston 1983; Lee 1984; Sanchez-Sesma 1983; Sanchez-Sesma *et al.* 1984; Sanchez-Sesma 1987; Sanchez-Sesma *et al.* 1989; Adam *et al.* 2000). For instance, in Lee & Langston (1983), it is found that the motion in the central region of a 3-D basin is larger

than that, at the corresponding location, of a 2-D basin of similar cross-section.

It thus appears to be advisable to integrate (as is starting to be done (Fernandez-Ares & Bielak 1973)) the presence, composition and layout, of city blocks, together with, and to the same extent as, the features of the underground structure and composition, into the large-scale 3-D computer codes that are increasingly being employed (Wald & Graves 1998) to predict the level and durations of shaking in highly populated, economically important, earthquake-prone urban sites.

ACKNOWLEDGMENTS

This research was carried out partially within the framework of the ACI CATNAT of the French Ministry of Research.

REFERENCES

- Adam, M., Pflanz, G. & Schmid, G., 2000. Two- and three-dimensional modelling of half-space and train-track embankment under dynamic loading, *Soil Dyn. Earthqu. Eng.*, **19**, 559–573.
- Aki, K. & Larner, K.L., 1970. Surface motion of a layered medium having an irregular interface due to incident plane SH waves, *J. geophys. Res.*, **75**, 933–954.

- Auld, B.A., Gagnepain, J.J. & Tan, 1976. Horizontal shear surface waves on corrugated surfaces, *Electron. Lett.*, **12**, 650–651.
- Bécache, E., Joly, P. & Tsogka, C., 2001. Fictitious domains, mixed finite elements and perfectly matched layers for 2D elastic wave propagation, *J. Comput. Acoust.*, **9**, 1175–1203.
- Borgnis, C.H. & Papas, C.H., 1958. Electromagnetic waveguides and resonators, in *Handbuch der Physik*, Vol. **16**, pp. 378–384, ed. Flügge, S., Springer, Berlin.
- Bravo, M.A., Sanchez-Sesma, F.J. & Chavez-Perez, S., 1990. A hybrid approach to study the seismic response of soft-soil sedimentary basins, in *Engineering Seismology and Site Response*, pp. 183–193, eds Cakmak, A.S. & Herrera, I., Computational Mechanics Publ., Southampton.
- Boutin, C. & Roussillon, P., 2004. Assesment of the urbanisation effect on seismic response, *Bull. seism. Soc. Am.*, **94**, 252–268.
- Boutin, C. & Roussillon, P., 2006. Wave propagation in presence of oscillators on the free surface, *Int. J. Engrg. Sci.*, **44**, 180–204.
- Cardenas-Soto, M. & Chavez-Garcia, F.J., 2003. Regional path effect on seismic wave propagation in central Mexico, *Bull. seism. Soc. Am.*, **93**, 973–985.
- Cardenas-Soto, M. & Chavez-Garcia, F.J., 2006. Seismic wavefield analysis in Mexico City using accelerometric arrays, *Abstracts of the First European Conference on Earthquake Engineering and Seismology*, SSS, Geneva, 166.
- Chavez-Garcia, F.J. & Bard, P.Y., 1994. Site effects in Mexico-city eight years after the september 1985 Michoacan earthquakes, *Soil Dyn. Earthq. Eng.*, **13**, 229–247.
- Chavez-Garcia, F.J. & Salazar, L., 2002. Strong motion in central Mexico: a model on data analysis and simpler modeling, *Bull. seism. Soc. Am.*, **92**, 3087–3101.
- Clouteau, D. & Aubry, D., 2001. Modifications of the ground motion in dense urban areas, *J. Comput. Acoust.*, **9**, 1–17.
- Collino, F. & Tsogka, C., 2001. Application of the PML absorbing layer model to the linear elastodynamic problem in anisotropic heterogeneous media, *Geophysics*, **66**, 294–305.
- Cutler, C.C., 1944. Electromagnetic waves guided by corrugated structures, *Bell Telephone Lab. Technical Report* MM44–160–218.
- Doby, R., Idriss, I.M. & Ng, E., 1979. A reply, *Bull. seism. Soc. Am.*, **69**, 2127–2128.
- Faeh, D., Suhadolc, P., Mueller St. & Panza, G.F., 1994. A Hybrid method for the estimation of ground motion in sedimentary bays: quantitative modeling for Mexico City, *Bull. seism. Soc. Am.*, **84**, 1711–1797.
- Fernandez-Ares, A. & Bielak, J., 1973. Urban seismology: interaction between earthquake ground motion and multiple buildings in urban regions, in *ESG 2006*, pp. 87–96 eds Bard, P.-Y., Chaljub, E., Cornu, C., Cotton, F. & Guéguen, P., LCPC, Paris.
- Flores, J., Novaro, O. & Seligman, T.H., 1987. Possible resonance effect in the distribution of earthquake damage in Mexico City, *Nature*, 326.
- Furumura, T. & Kennett, B.L.N., 1998. On the nature of regional seismic phase-III. The influence of crustal heterogeneity on the wavefield for subduction earthquakes: the 1989 Michoacan, and 1995 Copala, Guerro, Mexico earthquake, *Geophys. J. Int.*, **135**, 1060–1085.
- Groby, J.P., 2005. Modélisation de la propagation des ondes élastiques générées par un séisme proche ou éloigné à l'intérieur d'une ville, *PhD thesis*, Université de la Méditerranée-Aix-Marseille II.
- Groby, J.P. & Tsogka, C., 2006. A time domain method for modeling viscoacoustic wave propagation, *J. Comput. Acoust.*, **14**, 201–236.
- Groby, J.-P. & Wirgin, A., 2004. On the causes of anomalous seismic response in an urban site with a two-component soft layer overlying a hard substratum, *EGU 1st General Assembly*, Nice.
- Groby, J.P. & Wirgin, A., 2005a. 2D ground motion at a soft viscoelastic layer/hard substratum site in response to SH cylindrical seismic waves radiated by deep and shallow line sources I. Theory, *Geophys. J. Int.*, **163**, 165–191.
- Groby, J.P. & Wirgin, A., 2005b. 2D ground motion at a soft viscoelastic layer/hard substratum site in response to SH cylindrical seismic waves radiated by deep and shallow line sources II. Numerical results, *Geophys. J. Int.*, **163**, 192–224.
- Groby, J.P., Tsogka, C. & Wirgin, A., 2005. Simulation of seismic response in a city-like environment, *Soil Dyn. Earthq. Eng.*, **25**, 487–504.
- Guéguen, P., 2000. Interaction sismique entre le sol et le bâti: de l'interaction sol-structure à l'interaction site-ville, *Phd thesis*, Université Grenoble I, Grenoble.
- Guéguen, P., Bard, P.Y. & Chávez-Garcia, F.J., 2002. Site-City seismic interaction in Mexico city-like environments: an analytical study, *Bull. seism. Soc. Am.*, **92**, 794–811.
- Gulyaev, Y.V. & Plesskii, V.P., 1978. Slow, shear surface acoustic waves in a slow-wave structure on a solid surface, *Sov. Phys. Tech. Phys.*, **23**, 266–269.
- Haghshenas, E., Jafari, M., Bard, P.-Y., Moradi, A.S. & Hatzfeld, D., 2006. Preliminary results of site effects assessment in the city of Tabriz (Iran) using earthquakes recording, in *ESG 2006*, pp. 993–1001, eds Bard, P.-Y., Chaljub, E., Cornu, C., Cotton, F. & Guéguen, P., LCPC, Paris.
- Hill, N.R. & Levander, A.R., 1984. Resonances of low-velocity layers with lateral variations, *Bull. seism. Soc. Am.*, **74**, 521–537.
- Hougardy, R.W. & Hansen, R.C., 1958. Oblique surface waves over a corrugated conductor, *IRE Trans. Anten. Prop.*, **AP-6**, 370–376.
- Hurd, R.A., 1954. The propagation of an electromagnetic wave along an infinite corrugated surface, *Canad. J. Phys.*, **32**, 727–734.
- Iwata, T., Kagawa, T., Petukhin, A. & Onishi, Y., 2006. Basin and crustal structure model for strong ground motion simulation in Kinki, Japan, in *ESG 2006*, eds Bard, P.-Y., Chaljub, E., Cornu, C., Cotton, F. & Guéguen, P., LCPC, Paris, 435–442.
- Jennings, P.C., 1970. Distant motions from a building vibration test, *Bull. seism. Soc. Am.*, **60**, 2037–2043.
- Jennings, P.C. & Bielak, J., 1973. Dynamics of building-soil interaction, *Bull. seism. Soc. Am.*, **63**, 9–48.
- Kjartansson, E., 1979. Constant Q wave propagation and attenuation, *J. geophys. Res.*, **84**, 4737–4748.
- Lee, V.W., 1984. Three-dimensional diffraction of plane P, SV & SH waves by a hemispherical alluvial basin, *Soil Dynam. Earthq. Engrg.*, **3**, 133–144.
- Lee, J.-J. & Langston, C.A., 1983. Wave propagation in a three-dimensional circular basin, *Bull. seism. Soc. Am.*, **73**, 1637–1653.
- Levander, A.R. & Hill, N.R., 1984. P-SV resonances in irregular low-velocity surface layer, *Bull. seism. Soc. Am.*, **75**, 847–864.
- Lombaert, G., Clouteau, D., Ishizawa, O. & Mezher, N., 2004. The city-site effect : a fuzzy substructure approach and numerical simulations, In Doolin et al. ed., *Proc. 11th Intl. Conf. on Soil Dyn. & Earthq. Engrg.*, vol **2**, 68–74.
- Luco, J.E. & Contesse, L., 1993. Dynamic structure-soil-structure interaction, *Bull. seism. Soc. Am.*, **62**, 449–462.
- Maeda, N., Nakajima, Y., Matsuda, I. & Abeki, N., 2006. Evaluation of seismic amplification characteristics at a university campus with complicated relief of basement, in *ESG 2006*, pp. 443–451, eds Bard P.-Y., Chaljub, E., Cornu, C., Cotton, F. & Guéguen, P., LCPC, Paris.
- Manos, G.C., Demosthenous, M., Triamataki, M., Yasin, B. & Skalkos, P., 1995. Construction and instrumentation of a 5 storey masonry infilled RC building at the Volvi-Thessaloniki Euro-Seistest site: correlation of measured and numerically predicted dynamic properties, in *Proceedings of the Third International Conference on Earthquake Engineering*, Amman, Jordan, **2**, 449–462.
- Mateos, J.L., Flores, J., Novaro, O., Seilgman, T.H. & Alvarez-Costado, J.M., 1993. Resonant response models for the valleys of Mexico-II. The trapping of horizontal P waves, *Geophys. J. Int.*, **113**, 449–462.
- Morse, P.M. & Feshbach, H., 1953. *Methods of Theoretical Physics*, Mc Graw-Hill, New York.
- Perez-Rocha, L.E., Sanchez-Sesma, F.J. & Reinoso, E., 1991. Three-dimensional site effects in mexico-city: evidence from the accelerometric network observation and theoretical results, in *Proceeding of the 4th International Conference on Seismics Zonation*, Vol. **II**, pp. 327–334.
- Rial, J.A., 1989. Seismic wave resonances in 3-D sedimentary basins, *Geophys. J. Int.*, **99**, 81–90.
- Rotman, W., 1951. A study of single surface corrugated guides, *Proc. IRE*, **39**, 952–959.
- Roussillon, P., 2006. Interaction sol-structure et interaction site-ville: aspects fondamentaux et modélisation, *Phd thesis*, INSA, Lyon.

- Sanchez-Sesma, F.J., 1983. Diffraction of elastic waves by three-dimensional surface irregularities, *Bull. seism. Soc. Am.*, **73**, 1621–1636.
- Sanchez-Sesma, F.J., 1987. Site effects on strong ground motion, *Soil Dyn. Earthq. Eng.*, **6**, 124–132.
- Sanchez-Sesma, F.J., Chavez-Perez, S. & Avilez, J., 1984. Scattering of elastic waves by three-dimensional topographies, *Proc. 8th World Conf. Earthquake Engrg.*, **2**, 639–646.
- Sanchez-Sesma, F.J. & Luzon, F., 1995. Seismic response of three-dimensional alluvial valleys for incident P, S, and Rayleigh waves, *Bull. seism. Soc. Am.*, **85**, 269–284.
- Sanchez-Sesma, F.J., Perez-Rocha, L.E. & Chavez-Perez S., 1989. Diffraction of elastic waves by three-dimensional surface irregularities. Part II, *Bull. seism. Soc. Am.*, **79**, 101–112.
- Savage, B.K., 2004. Regional Seismic wavefield propagation, *PhD thesis*, California Institute of Technology.
- Semblat, J.-F., Duval, A.-M. & Dangla, P., 2000. Numerical analysis of seismic wave amplification in Nice (France) comparison with experiments, *Soil Dyn. Earthq. Eng.*, **19**, 347–362.
- Semblat, J.F., Guégen, P., Kham, M., Bard, P.Y. & Duval, A.M., 2003. Site-city interaction at local and global scales, in *Proceedings of the 12th European Conference on Earthquake Engineering*, paper no. 807.
- Shaw, D.E., 1979. Comment on 'Duration characteristics of horizontal components of strong-motion earthquake records', *Bull. seism. Soc. Am.*, **69**, 2125–2126.
- Singh, S.K. & Ordaz, M., 1993. On the origin of long coda observed in the lake-bed strong-motion records of Mexico City, *Bull. seism. Soc. Am.*, **83**, 1298–1306.
- Singh, S.K. & Sabina, F.J., 1977. Ground motion amplification by topographic depressions for incident P waves under acoustic approximation, *Bull. seism. Soc. Am.*, **67**, 345–352.
- Todorovska, M.I., 2002. Full-scale experimental studies of soil-structure interaction, *ISET, J. Earthqu. Tech.*, **39**, 139–165.
- Trifunac, M.D., 1972. Interaction of a shear wall with the soil for incident plane SH wave, *Bull. seism. Soc. Am.*, **62**, 63–83.
- Tsogka, C. & Wirgin, A., 2003. Simulation of seismic response in an idealized city, *Soil Dyn. Earthq. Eng.*, **23**, 391–402.
- Wald, D.J. & Graves, R.W., 1998. The seismic response of the Los Angeles Basin, California, *Bull. seism. Soc. Am.*, **88**, 337–356.
- Wirgin, A., 1988. Love waves in a slab with rough boundaries, in *Recent Developments in Surface Acoustic Waves*, pp. 145–155, eds Parker D.F. & Maugin, G.A., Springer series on wave phenomena, Berlin.
- Wirgin, A., 1995. Resonant response of a soft semi-circular cylindrical basin to an SH seismic wave, *Bull. seism. Soc. Am.*, **85**, 285–299.
- Wirgin, A. & Bard, P.-Y., 1996. Effects of buildings on the duration and amplitude of ground motion in Mexico City, *Bull. seism. Soc. Am.*, **86**, 914–920.
- Wirgin, A. & Groby, J.P., 2006a. Amplification and increased duration of earthquake motion on uneven stress-free ground, <https://hal.ccsd.cnrs.fr/ccsd-00076746>, <http://fr.arxiv.org/abs/physics/0605239>.
- Wirgin, A. & Groby, J.-P., 2006b. Amplification and increased duration of earthquake motion on uneven stress-free ground, in *ESG 2006*, pp. 559–568, eds Bard, P.-Y., Chaljub, E., Cornu, C., Cotton, F. & Guéguen, P., LCPC, Paris.
- Wong, H.L. & Trifunac, M.D., 1974. Surface motion of sediment-elliptical alluvial valley for incident plane SH waves, *Bull. seism. Soc. Am.*, **64**, 1389–1408.

APPENDIX A: GOVERNING EQUATIONS

A1 Space–time and space–frequency wave equations

The space–time framework wave equation for SH waves in a linear, isotropic medium M is:

$$\nabla \cdot (\mu(\mathbf{x}, \omega) \nabla u(\mathbf{x}, t)) - \rho(\mathbf{x}) \partial_t^2 u(\mathbf{x}, t) = -\rho(\mathbf{x}) f(\mathbf{x}, t), \quad (\text{A1})$$

wherein u and f are the components of displacement and force density, respectively, in the \mathbf{i}_3 direction (\mathbf{i}_j the unit vector along the x_j axis), the sources of plane waves corresponding to $f = 0$ and those of cylindrical waves to $f \neq 0$.

Since our configuration involves three homogeneous media $M^{[j]}$; $j = 0, 1, 2$, and the applied force is assumed to be non vanishing only in Ω_0 :

$$(c^{[j]}(\omega))^2 \nabla \cdot \nabla u^{[j]}(\mathbf{x}, t) - \partial_t^2 u^{[j]}(\mathbf{x}, t) = -f(\mathbf{x}, t) \delta_{j0}; \mathbf{x} \in \Omega_j; j = 0, 1, 2, \quad (\text{A2})$$

in which $\delta_{j0} = 1$ for $j = 0$, $\delta_{j0} = 0$ for $j \neq 0$, and $c^{[j]}(\omega) = \sqrt{\mu^{[j]}(\omega)/\rho^{[j]}}$ is the phase velocity in $M^{[j]}$.

The space–frequency framework versions of the wave equations are obtained by expanding the force density and displacement in Fourier integrals: $f(\mathbf{x}, t) = \int_{-\infty}^{\infty} f(\mathbf{x}, \omega) e^{-i\omega t} d\omega$, $u^{[j]}(\mathbf{x}, t) = \int_{-\infty}^{\infty} u^{[j]}(\mathbf{x}, \omega) e^{-i\omega t} d\omega$, wherein ω is the angular frequency, so as to give rise to the Helmholtz equations

$$\nabla \cdot \nabla u^{[j]}(\mathbf{x}, \omega) + (k^{[j]}(\omega))^2 u^{[j]}(\mathbf{x}, \omega) = -f(\mathbf{x}, \omega) \delta_{j0}; \forall \mathbf{x} \in \Omega_j; j = 0, 1, 2, \quad (\text{A3})$$

wherein $k^{[j]}(\omega) := \frac{\omega}{c^{[j]}}$. These three (Helmholtz) equations are solved further on by a mode-matching method.

A2 Sources and incident fields

The driving force density for a cylindrical wave radiated from a line source located at $\mathbf{x}^s : (x^s_1, x^s_2) \in \Omega_0$ is

$$f(\mathbf{x}, \omega) = S(\omega) \delta(\mathbf{x} - \mathbf{x}^s), \quad (\text{A4})$$

with $\delta(\cdot)$ the Dirac delta distribution and

$$S(\omega) = \frac{12\pi\alpha^2\omega^2}{\sqrt{\pi}} \frac{\omega^2}{4\alpha^3} \exp\left(it_s\omega - \frac{\omega^2}{4\alpha^2}\right), \quad (\text{A5})$$

to which corresponds

$$S(t) = -24\pi\alpha^4 [-3(t_s - t) + 2\alpha^2(t_s - t)^3] \exp[-\alpha^2(t_s - t)^2]. \quad (\text{A6})$$

The incident signal is thus of the form of a pseudo Ricker-type pulse in the time domain, whose characteristic period is $\alpha = \pi/t_p$, $t_p = t_s = 2$ sec being the time at which the pulse attains its maximal value.

The (incident) wave associated with the line source is

$$u^i(\mathbf{x}, \omega) = S(\omega) \frac{i}{4} H_0^{(1)}(k^{[0]} \|\mathbf{x} - \mathbf{x}^s\|), \quad (\text{A7})$$

with $H_0^{(1)}(\cdot)$ the Hankel function of the first kind and order 0.

In the case of plane-wave incidence:

$$u^i(\mathbf{x}, \omega) = S(\omega) \exp\{i[k_1^i x_1 - k_2^i x_2]\}; \quad \mathbf{x} \in \mathbb{R}^2, \quad (\text{A8})$$

wherein θ^i is the angle of incidence, and $k_1^i = k^{[0]} \sin \theta^i$, $k_2^i = k^{[0]} \cos \theta^i$.

A3 Boundary and radiation conditions in the space–frequency framework

The stress-free nature of $\Gamma_f = \Gamma_g \cup \Gamma_{ag}$, with $\Gamma_{ag} := \bigcup_{j \in \mathbb{B}} \Gamma_{ag}^{(j)}$, translates to:

$$\mu^{[1]}(\omega) \partial_n u^{[1]}(\mathbf{x}, \omega) = 0; \quad \mathbf{x} \in \Gamma_g, \quad (\text{A9})$$

$$\mu^{[2]}(\omega) \partial_n u^{[2(j)]}(\mathbf{x}, \omega) = 0; \quad \mathbf{x} \in \Gamma_{ag}^{(j)}, \quad j \in \mathbb{B} \quad (\text{A10})$$

wherein \mathbf{n} denotes the generic unit vector normal to a boundary and ∂_n designates the operator $\partial_n = \mathbf{n} \cdot \nabla$.

The fact that $M^{[1]}$ and $M^{[2]}$ are in welded contact across $\Gamma_{bs} := \bigcup_{j \in \mathbb{B}} \Gamma_{bs}^{(j)}$ means that:

$$u^{[1]}(\mathbf{x}, \omega) - u^{[2(j)]}(\mathbf{x}, \omega) = 0; \quad \mathbf{x} \in \Gamma_{bs}^{(j)}, \quad j \in \mathbb{B} \quad (\text{A11})$$

$$\mu^{[1]}(\omega) \partial_n u^{[1]}(\mathbf{x}, \omega) - \mu^{[2]}(\omega) \partial_n u^{[2(j)]}(\mathbf{x}, \omega) = 0; \quad \mathbf{x} \in \Gamma_{bs}^{(j)}, \quad j \in \mathbb{B}. \quad (\text{A12})$$

Similarly, across Γ_h :

$$u^{[1]}(\mathbf{x}, \omega) - u^{[0]}(\mathbf{x}, \omega); \quad \mathbf{x} \in \Gamma_h, \quad (\text{A13})$$

$$\mu^{[1]}(\omega) \partial_n u^{[1]}(\mathbf{x}, \omega) - \mu^{[0]}(\omega) \partial_n u^{[0]}(\mathbf{x}, \omega); \quad \mathbf{x} \in \Gamma_h. \quad (\text{A14})$$

The radiation condition in the substratum is:

$$u^{[0]}(\mathbf{x}, \omega) - u^i(\mathbf{x}, \omega) \sim \text{outgoing waves}; \quad \|\mathbf{x}\| \rightarrow \infty, \quad x_2 > h. \quad (\text{A15})$$

A4 Boundary and radiation conditions in the space–time framework

Since our finite element (FE) method, described amply in Groby & Tsogka (2006), Groby (2005) and Groby *et al.* (2005), for solving the space–time domain wave equation (A1) in a heterogeneous medium M (in our case, involving three homogeneous components, $M^{[0]}$, $M^{[1]}$ and $M^{[2]}$) relies on the assumption that M be a continuum, it does not appeal to any boundary conditions except on Γ_f where the vanishing traction condition is invoked (fictitious domain method). Furthermore, since the essentially unbounded nature of the geometry of the city cannot be implemented numerically, we take this geometry to be finite and surround it (except on the Γ_f portion) by a perfectly matched layer (PML) (Collino & Tsogka 2001) which enables closure of the computational domain without generating unphysical reflected waves (from the PML layer). In a sense, this replaces the radiation condition of the unbounded domain. The stress-free boundary condition on Γ_f is modelled with the help of the fictitious domain method (Bécache *et al.* 2001), which allows us to account for the diffraction of waves by a boundary of complicated geometry, not necessarily matching the volumic mesh.

The FE solutions are compared in the main body of this paper with their counterparts obtained by a mode matching (MM) method, which is based on separation of variables. Since the details of the FE method are given in Groby & Tsogka (2006), Groby (2005) and Groby *et al.* (2005), from now on, we shall be only concerned with the MM method (implemented in the space–frequency domain).

Whatever be the method, the problem is to determine the time record of the displacement fields $u^{[1]}(\mathbf{x}, t)$ on Γ_g and $u^{[2(j)]}(\mathbf{x}, t)$ on $\Gamma_{ag}^{(j)}$, $j \in \mathbb{B}$.

APPENDIX B: FIELD REPRESENTATIONS IN THE SPACE–FREQUENCY FRAMEWORK FOR $N_B < \infty$

The MM method appeals to separation of variables and gives rise to the following field representations in cartesian coordinates.

$$u^{[0]}(\mathbf{x}, \omega) = u^i(\mathbf{x}, \omega) + \int_{-\infty}^{\infty} B^{[0]}(k_1, \omega) \exp\left\{i\left[k_1 x_1 + k_2^{[0]}(x_2 - h)\right]\right\} \frac{dk_1}{k_2^{[0]}}; \quad \mathbf{x} \in \Omega_0, \quad (\text{B1})$$

with

$$k_2^{[j]} = \sqrt{(k^{[j]})^2 - (k_1)^2}, \quad \text{Re } k_2^{[j]} \geq 0, \quad \text{Im } k_2^{[j]} \geq 0, \quad \omega \geq 0. \quad (\text{B2})$$

In the case of *plane-wave excitation* we can write

$$u^i(\mathbf{x}, \omega) = \int_{-\infty}^{\infty} A^{[0]-}(k_1, \omega) \exp \left\{ i \left[k_1 x_1 - k_2^{[0]} x_2 \right] \right\} \frac{dk_1}{k_2^{[0]}}; \quad \mathbf{x} \in \mathbb{R}^2, \quad (\text{B3})$$

wherein

$$A^{[0]-}(k_1, \omega) = S(\omega) k_2^{[0]} \delta(k_1 - k_1^i), \quad (\text{B4})$$

whereas in the case of *cylindrical wave excitation*, the plane wave representation of the Hankel function (Morse & Feshbach 1953) tells us that

$$u^i(\mathbf{x}, \omega) = \begin{cases} \int_{-\infty}^{\infty} A^{[0]+}(k_1, \omega) \exp \left\{ i \left[k_1 x_1 + k_2^{[0]} x_2 \right] \right\} \frac{dk_1}{k_2^{[0]}}; & \mathbf{x} \in \Omega_0^+ \\ \int_{-\infty}^{\infty} A^{[0]-}(k_1, \omega) \exp \left\{ i \left[k_1 x_1 - k_2^{[0]} x_2 \right] \right\} \frac{dk_1}{k_2^{[0]}}; & \mathbf{x} \in \Omega_0^- \end{cases}, \quad (\text{B5})$$

wherein

$$\Omega_0^+ = \{\forall x_1 \in \mathbb{R}; x_2 > x_2^s\} \quad \Omega_0^- = \{\forall x_1 \in \mathbb{R}; h < x_2 < x_2^s\}, \quad (\text{B6})$$

$$A^{[0]\pm}(k_1, \omega) = S(\omega) \frac{i}{4\pi} \exp \left\{ -i \left[k_1 x_1^s \pm k_2^{[0]} x_2^s \right] \right\}. \quad (\text{B7})$$

Since we shall be interested only in the field in Ω_0^- , we can write

$$u^{[0]}(\mathbf{x}, \omega) = \int_{-\infty}^{\infty} A^{[0]-}(k_1, \omega) \exp \left\{ i \left[k_1 x_1 - k_2^{[0]} x_2 \right] \right\} \frac{dk_1}{k_2^{[0]}} \\ + \int_{-\infty}^{\infty} B^{[0]}(k_1, \omega) \exp \left\{ i \left[k_1 x_1 + k_2^{[0]} (x_2 - h) \right] \right\} \frac{dk_1}{k_2^{[0]}}; \quad \mathbf{x} \in \Omega_0^-. \quad (\text{B8})$$

By proceeding in the same manner as previously we find

$$u^{[1]}(\mathbf{x}, \omega) = \int_{-\infty}^{\infty} A^{[1]}(k_1, \omega) \exp \left\{ i \left[k_1 x_1 - k_2^{[1]} x_2 \right] \right\} \frac{dk_1}{k_2^{[1]}} \\ + \int_{-\infty}^{\infty} B^{[1]}(k_1, \omega) \exp \left\{ i \left[k_1 x_1 + k_2^{[1]} x_2 \right] \right\} \frac{dk_1}{k_2^{[1]}}; \quad \mathbf{x} \in \Omega_1. \quad (\text{B9})$$

$$u^{[2(j)]}(\mathbf{x}, \omega) = \sum_{m=0}^{\infty} B_m^{[2(j)]}(\omega) \cos \left[k_{1m}^{[2(j)]} \left(x_1 - d_j + \frac{w_j}{2} \right) \right] \cos \left[k_{2m}^{[2(j)]} (x_2 + b_j) \right] \\ ; \quad \mathbf{x} \in \Omega_2^j, \quad \forall j \in \mathbb{B}, \quad (\text{B10})$$

with

$$k_{1m}^{[2(j)]} = \frac{m\pi}{w_j}; \quad k_{2m}^{[2(j)]} = \sqrt{(k^{[2(j)]})^2 - (k_{1m}^{[2(j)]})^2}; \quad \text{Re } (k_{2m}^{[2(j)]}) \geq 0 \quad \text{Im } (k_{2m}^{[2(j)]}) \geq 0 \quad \text{for } \omega \geq 0. \quad (\text{B11})$$

Note that (B10) satisfies the stress-free boundary condition on the vertical and upper segments of each block.

APPENDIX C: INTERRELATIONS BETWEEN THE UNKNOWN COEFFICIENTS FOR THE CASE $N_B < \infty$

From (A10) and (A11) we obtain

$$A^{[1]}(k_1, \omega) - B^{[1]}(k_1, \omega) \\ = \frac{1}{2\pi i} \sum_{j \in \mathbb{B}} e^{-ik_1(d_j - w_j/2)} \sum_{m=0}^{\infty} B_m^{[2(j)]}(\omega) \frac{\mu^{[2]} k_{2m}^{[2(j)]} w_j}{\mu^{[1]}} J_m^{(j)-}(k_1, \omega) \sin(k_{2m}^{[2(j)]} b_j); \quad \forall k_1 \in \mathbb{R}, \quad (\text{C1})$$

wherein

$$I_m^{(j)\pm}(k_1, \omega) := \int_0^1 \exp(\pm i k_1 w_j \eta) \cos(k_{1m}^{[2(j)]} w_j \eta) d\eta. \quad (C2)$$

Eq. (A12) leads to

$$B_m^{[2(l)]}(\omega) = \frac{\epsilon_m}{\cos(k_{2m}^{[2(l)]} b_l)} \int_{-\infty}^{\infty} [A^{[1]}(k_1, \omega) + B^{[1]}(k_1, \omega)] I_n^{(l)+}(k_1, \omega) e^{i k_1 (d_l - w_l/2)} \frac{dk_1}{k_2^{[1]}} \quad (C3)$$

$$; \forall m = 0, 1, 2, \dots, \quad l \in \mathbb{B},$$

wherein $\epsilon_m = 1$ for $m = 0$, and $\epsilon_m = 2$ for $m > 0$.

From (A13) we obtain

$$-\mu^{[0]} A^{[0]-}(k_1, \omega) e^{-i k_2^{[0]} h} + \mu^{[0]} B^{[0]}(k_1, \omega) + \mu^{[1]} A^{[1]}(k_1, \omega) e^{-i k_2^{[1]} h} - \mu^{[1]} B^{[1]}(k_1, \omega) e^{i k_2^{[1]} h} = 0; \forall k_1 \in \mathbb{R}. \quad (C4)$$

Eq. (A14) gives rise to

$$\frac{A^{[0]-}(k_1, \omega) e^{-i k_2^{[0]} h}}{k_2^{[0]}} + \frac{B^{[0]}(k_1, \omega)}{k_2^{[0]}} - \frac{A^{[1]}(k_1, \omega) e^{-i k_2^{[1]} h}}{k_2^{[1]}} - \frac{B^{[1]}(k_1, \omega) e^{i k_2^{[1]} h}}{k_2^{[1]}} = 0; \forall k_1 \in \mathbb{R}. \quad (C5)$$

APPENDIX D: DETERMINATION OF THE VARIOUS UNKNOWNNS

D0.1 Elimination of $B_m^{[2(j)]}(\omega)$ to obtain an integral equation for $B^{[0]}(k_1, \omega)$

After a series of substitutions in the formulae given in Appendix C, the following integral equation for $B^{[0]}(k_1, \omega)$ is obtained (wherein K_1 and $K_2^{[j]}$ play the same roles, and are related to each other in the same manner, as k_1 and $K_2^{[j]}$, respectively):

$$C(k_1, \omega) B^{[0]}(k_1, \omega) - \int_{-\infty}^{\infty} D(k_1, K_1, \omega) B^{[0]}(K_1, \omega) dK_1 = F(k_1, \omega); \forall k_1 \in \mathbb{R}, \quad (D1)$$

with:

$$C(k_1, \omega) = \cos(k_2^{[1]} h) - i \frac{\mu^1 k_2^1}{\mu^0 k_2^0} \sin(k_2^{[1]} h), \quad (D2)$$

$$D(k_1, K_1, \omega) = \left[\cos(K_2^{[1]} h) - i \frac{\mu^1 K_2^1}{\mu^0 K_2^0} \sin(K_2^{[1]} h) \right] \times \frac{i}{2\pi} \sum_{j \in \mathbb{B}} e^{i(k_1 - K_1)(d_j - w_j/2)} \sum_{m=0}^{\infty} \epsilon_m \frac{\mu^{[2]} k_{2m}^{[2(j)]} w_j}{\mu^{[0]} K_2^{[0]}} \tan(k_{2m}^{[2(j)]} b_j) I_m^{(j)-}(k_1) I_m^{(j)+}(K_1) \quad (D3)$$

$$; \forall k_1, K_1 \in \mathbb{R},$$

and

$$F(k_1, \omega) = A^{[0]-}(k_1, \omega) e^{-i k_2^{[0]} h} \left[\cos(k_2^{[1]} h) + i \frac{\mu^1 k_2^1}{\mu^0 k_2^0} \sin(k_2^{[1]} h) \right] + \int_{-\infty}^{\infty} \frac{A^{[0]-}(K_1, \omega)}{i} e^{-i K_2^{[0]} h} \left[\cos(K_2^{[1]} h) + i \frac{\mu^0 K_2^0}{\mu^1 K_2^1} \sin(K_2^{[1]} h) \right] \times \frac{1}{2\pi} \sum_{j \in \mathbb{B}} e^{i(k_1 - K_1)(d_j - w_j/2)} \sum_{m=0}^{\infty} \epsilon_m \frac{\mu^{[2]} k_{2m}^{[2(j)]} w_j}{\mu^{[0]} K_2^{[0]}} \tan(k_{2m}^{[2(j)]} b_j) I_m^{(j)-}(k_1) I_m^{(j)+}(K_1) dK_1 \quad (D4)$$

$$; \forall k_1 \in \mathbb{R},$$

Eq. (D1) is a Fredholm integral equation of the second kind for the unknown function $\{B^{[0]}(k_1, \omega); k_1 \in \mathbb{R}\}$.

By means of the changes of variables $k_1 = k^{[0]} \sigma_1$, $K_1 = k^{[0]} S^{[1]}$ (note that σ_1 and $S^{[1]}$ are dimensionless), we can cast (D1) into the form

$$B^{[0]}(\sigma_1, \omega) = \frac{F(\sigma_1, \omega) + \int_{-\infty}^{\infty} E(\sigma_1, S_1, \omega) [1 - \delta(S_1 - \sigma_1)] B^{[0]}(S_1, \omega) dS_1}{C(\sigma_1, \omega) - E(\sigma_1, \sigma_1, \omega)}; \forall \sigma_1 \in \mathbb{R}. \quad (D5)$$

An iterative approach for solving this integral equation consists in computing successively:

$$B^{[0(0)]}(\sigma_1, \omega) = \frac{F(\sigma_1, \omega)}{C(\sigma_1, \omega) - E(\sigma_1, \sigma_1, \omega)}; \forall \sigma_1 \in \mathbb{R}, \quad (D6)$$

$$B^{[0](1)}(\sigma_1, \omega) = B^{[0]}(\sigma_1, \omega) + \frac{\int_{-\infty}^{\infty} E(k_1, S_1, \omega) [1 - \delta(S_1 - \sigma_1)] B^{0}(S_1, \omega) dS_1}{C(\sigma_1, \omega) - E(\sigma_1, \sigma_1, \omega)}; \forall \sigma_1 \in \mathbb{R}, \quad (D7)$$

and so on.

D0.2 Elimination of $B^{[0]}(k_1, \omega)$ to obtain a linear system of equations for $B_m^{[2]j}(\omega)$

The procedure is again to make a series of substitutions which now lead to the linear system of equations for $B_n^{[2]l}(\omega)$, $\forall l \in \mathbb{B}$, $\forall n \in \mathbb{N}$:

$$C_n(\omega) B_n^{[2]l}(\omega) = F_n^{(l)}(\omega) + \sum_{j \in \mathbb{B}} \sum_{m \in \mathbb{N}} D_{nm}^{(lj)}(\omega) B_m^{[2]j}(\omega); \forall l \in \mathbb{B}; \forall n \in \mathbb{N}, \quad (D8)$$

wherein

$$C_n(\omega) = \cot(k_{2n}^{[2]l} b); \forall n \in \mathbb{N}, \quad (D9)$$

$$F_n^{(l)}(\omega) = \frac{2\epsilon_n}{\sin(k_{2n}^{[2]l} b_l)} \int_{-\infty}^{\infty} A^{[0]l-}(k_1, \omega) e^{-ik_1^{[0]l} h} \left[\frac{I_n^{(l)+}(k_1) e^{ik_1(d_l - w_l/2)}}{\cos(k_2^{[1]l} h) - i \frac{\mu^{[1]l} k_2^{[1]l}}{\mu^{[0]l} k_2^{[0]l}} \sin(k_2^{[1]l} h)} \right] \frac{dk_1}{k_2^{[0]l}}; \forall l \in \mathbb{B}; \forall n \in \mathbb{N}, \quad (D10)$$

and

$$D_{nm}^{(lj)}(\omega) = \frac{ik_{2m}^{[2]j} \mu^{[2]l} w_j \epsilon_n \sin(k_{2m}^{[2]j} b_j)}{2\pi \sin(k_{2n}^{[2]l} b_l) \mu^{[0]l}} \times \int_{-\infty}^{\infty} I_n^{(l)+}(k_1) I_m^{(j)-}(k_1) \left[\frac{\cos(k_2^{[1]l} h) - i \frac{\mu^{[0]l} k_2^{[0]l}}{\mu^{[1]l} k_2^{[1]l}} \sin(k_2^{[1]l} h)}{\cos(k_2^{[1]j} h) - i \frac{\mu^{[1]j} k_2^{[1]j}}{\mu^{[0]j} k_2^{[0]j}} \sin(k_2^{[1]j} h)} \right] e^{ik_1((d_l - d_j) - \frac{w_l - w_j}{2})} \frac{dk_1}{k_2^{[0]l}}; \forall l, j \in \mathbb{B}; \forall n, m \in \mathbb{N}. \quad (D11)$$

Eq. (44) can be written as:

$$B_n^{[2]l}(\omega) = \frac{F_n^{(l)}(\omega) + \sum_{j \in \mathbb{B}} \sum_{m=0}^{\infty} D_{nm}^{(lj)}(\omega) (1 - \delta_{nm} \delta_{lj}) B_m^{[2]j}(\omega)}{C_n(\omega) - D_{nn}^{(ll)}(\omega)}; \forall l \in \mathbb{B}; \forall n \in \mathbb{N}, \quad (D12)$$

An iterative procedure for solving this linear set of equations is as follows:

$$(B_n^{[2]l}(\omega))^{(0)} = \frac{F_n^{(l)}(\omega)}{C_n(\omega) - D_{nn}^{(ll)}(\omega)}; \forall l \in \mathbb{B}; \forall n \in \mathbb{N}, \quad (D13)$$

$$(B_n^{[2]l}(\omega))^{(p)} = \frac{F_n^{(l)}(\omega) + \sum_{j \in \mathbb{B}} \sum_{m=0}^{\infty} D_{nm}^{(lj)}(\omega) (1 - \delta_{nm} \delta_{lj}) (B_m^{[2]j}(\omega))^{(p-1)}}{C_n(\omega) - D_{nn}^{(ll)}(\omega)}; p = 1, 2, \dots; \forall l \in \mathbb{B}; \forall n \in \mathbb{N}. \quad (D14)$$

APPENDIX E: MODAL ANALYSIS FOR $N_B < \infty$

E1 The emergence of the natural modes of the configuration from the iterative solution of the integral equation for $B^{[0]}(k_1, \omega)$

Eqs (D6), (D7), etc. show that the n th order iterative approximation of the solution to the integral equation (D1) is of the form

$$B^{[0](n)}(\sigma_1, \omega) = \frac{\mathcal{N}^{(n)}(\sigma_1, \omega)}{C(\sigma_1, \omega) - E(\sigma_1, \sigma_1, \omega)} := \frac{\mathcal{N}^{(n)}(\sigma_1, \omega)}{\mathcal{D}(\sigma_1, \omega)}; n = 1, 2, \dots, \quad (E1)$$

wherein

$$\mathcal{N}^{(0)}(\sigma_1, \omega) = F(\sigma_1, \omega), \quad (E2)$$

$$\mathcal{N}^{(n>0)}(\sigma_1, \omega) = F(\sigma_1, \omega) + \int_{-\infty}^{\infty} E(\sigma_1, S_1, \omega) [1 - \delta(S_1 - \sigma_1)] B^{[0](n-1)}(S_1, \omega) dS_1, \quad (\text{E3})$$

from which it becomes apparent that the solution $B^{[0](n)}(\sigma_1, \omega)$, to any order of approximation, is expressed as a fraction, the denominator $\mathcal{D}(\sigma_1, \omega)$ of which (not depending on the order of approximation), can become small for certain values of σ_1 and ω so as to make $B^{[0](n)}(\sigma_1, \omega)$, and (possibly) the field in the substratum, large for these values. When this happens, a *natural mode of the configuration*, comprising the blocks, the soft layer and the hard substratum, is excited, this taking the form of a *resonance* with respect to $B^{[0](n)}(\sigma_1, \omega)$, that is, with respect to a plane wave component of the field in the substratum. As $B^{[0]}(k_1, \omega)$ is related to $A^{[1]}(\sigma_1, \omega)$ and $B^{[1]}(\sigma_1)$ via (C4)–(C5), the structural resonance manifests itself for the same σ_1 and ω as concerns the field in the layer.

We say that $B^{[0](n)}(\sigma_1, \omega)$, and the fields in the layer and substratum, can become *possibly* large at resonance because until now we have not taken into account the numerator $\mathcal{N}^{(n)}(\sigma_1, \omega)$, which might be small when the denominator is small, or such as to prevent, by other means, the fields in the layer and substratum from becoming large. Moreover, since the field is expressed as a sum of plane waves, the fact that $B^{[0]}(k_1, \omega)$ may become large for some k_1^* , does not necessarily mean that the sum of plane waves (including waves whose horizontal wavenumber $k_1 \neq k_1^*$), and therefore the field, will be large at a resonance frequency.

E2 Quasi Love modes

Let us return to the denominator of the expression of $B^{[0](n)}$, which, for convenience, we rewrite in terms of k_1 :

$$\begin{aligned} \mathcal{D}(k_1, \omega) &= C(k_1, \omega) - k^{[0]} D(k_1, k_1, \omega) \\ &= \left[\cos(k_2^{[1]} h) - i \frac{\mu^{[1]} k_2^{[1]}}{\mu^{[0]} k_2^{[0]}} \sin(k_2^{[1]} h) \right] - \left[\cos(k_2^{[1]} h) - i \frac{\mu^{[0]} k_2^{[0]}}{\mu^{[1]} k_2^{[1]}} \sin(k_2^{[1]} h) \right] \\ &\quad \times \frac{i}{2\pi} \sum_{j \in \mathbb{B}} \sum_{m=0}^{\infty} \epsilon_m \frac{\mu^{[2]} k_{2m}^{[2(j)]} w_j}{\mu^{[0]} k_2^{[0]}} \tan(k_{2m}^{[2(j)]} b_j) I_m^{(j)-}(k_1) I_m^{(j)+}(k_1); \forall k_1 \in \mathbb{R}, \end{aligned} \quad (\text{E4})$$

wherein it is easy to show that

$$I_m^{(j)\pm}(k_1) = \frac{i^m}{2} e^{\pm i k_1 \frac{w_j}{2}} \left[\text{sinc}\left(\frac{\pm k_1 w_j}{2} + \frac{m\pi}{2}\right) + (-1)^m \text{sinc}\left(\frac{\pm k_1 w_j}{2} - \frac{m\pi}{2}\right) \right], \quad (\text{E5})$$

with $\text{sinc}(\zeta) := \frac{\sin(\zeta)}{\zeta}$. Since $\mathcal{C}(k_1, \omega) := C(k_1, \omega) = 0$ is the dispersion relation for (i.e. providing the means of determining the (k_1, ω) couples leading to a possible resonance associated with the excitation of) Love modes, we can say that (E4) is the dispersion relation for *quasi Love modes*. We note that: (i) quasi Love modes are different from Love modes which, at present, means that the (k_1, ω) couples for which $\mathcal{D}(k_1, \omega) = 0$ are not identical to the (k_1, ω) couples for which $\mathcal{C}(k_1, \omega) = 0$, (ii) when $b_j \rightarrow 0$; $\forall j \in \mathbb{B}$, the dispersion relation for quasi Love modes becomes the dispersion relation for Love modes, (iii) for small $k_{20}^{[2(j)]} b$ and/or small $\mu^{[2]}/\mu^{[1]}$ and/or $k^{[2]} w$, the quasi Love modes are a small perturbation of Love modes, which means here that the (k_1, ω) couples for which $\mathcal{D}(k_1, \omega) = 0$ are close to the (k_1, ω) couples for which $\mathcal{C}(k_1, \omega) = 0$, (iv) the dispersion relation for quasi Love modes is independent of the number of blocks (provided this number is greater than 0).

To substantiate these remarks (when necessary) and obtain a more detailed picture of the features of the quasi Love modes as compared to those of the Love modes, we must analyse more closely (E4). For $m = 0$ we have

$$I_0^{(j)\pm}(k_1) = e^{\pm i k_1 \frac{w_j}{2}} \text{sinc}\left(\frac{k_1 w_j}{2}\right), \quad (\text{E6})$$

and for $k_1 w \neq \pm m\pi$, we have

$$I_m^{(j)\pm}(k_1) = \frac{\pm 2k_1 w_j i^m}{(k_1 w_j)^2 - (m\pi)^2} e^{\pm i k_1 \frac{w_j}{2}} \sin\left(\frac{\pm k_1 w_j}{2} + \frac{m\pi}{2}\right). \quad (\text{E7})$$

To make a complex issue relatively simple, we assume that $k_1 w$ is effectively such as to be different from $m\pi$ for $m = 0, 1, 2, \dots$. Then

$$\begin{aligned} \mathcal{D}(k_1, \omega) &= \cos(k_2^{[1]} h) - i \frac{\mu^{[1]} k_2^{[1]}}{\mu^{[0]} k_2^{[0]}} \sin(k_2^{[1]} h) - \left[\frac{\mu^{[1]} k_2^{[1]}}{\mu^{[0]} k_2^{[0]}} \cos(k_2^{[1]} h) - i \sin(k_2^{[1]} h) \right] \\ &\quad \times \frac{i}{2\pi} \frac{\mu^{[2]}}{\mu^{[1]}} \sum_{j \in \mathbb{B}} \left\{ \frac{k^{[2]}}{k_2^{[1]}} \tan(k^{[2]} b_j) \text{sinc}^2\left(\frac{k_1 w_j}{2}\right) + 2 \sum_{m=1}^{\infty} \frac{k_{2m}^{[2]}}{k_2^{[1]}} \frac{4(k_1 w_j)^2}{[(k_1 w)^2 - (m\pi)^2]^2} \right. \\ &\quad \left. \times \sin\left(\frac{k_1 w_j}{2} + \frac{m\pi}{2}\right) \sin\left(-\frac{k_1 w_j}{2} + \frac{m\pi}{2}\right) \tan(k_{2m}^{[2(j)]} b_j) \right\}, \end{aligned} \quad (\text{E8})$$

which rather clearly substantiates the aforementioned remarks.

Consider the first term in $\{\dots\}$. This term is significant only for small $k_1 w_j/2$ due to the sinc function whose modulus decays rapidly as its argument increases. Another feature of this term is that it vanishes when $k^{[2]} b_j = l\pi$; $l = 0, 1, 2, \dots$, which occurs when the zeroth-order

quasi-mode in a block encounters a stress-free boundary condition at the base of the block (i.e., $u_2^{[2(j)]}|_{x_2=0} = 0$), in which case the latter is disconnected from the underground (since no wave can penetrate into the layer) from the point of view of the fundamental block quasi mode. This corresponds to the *stress-free base block mode*. It is then logical that this quasi mode of the block should not perturb the dispersion characteristics of the mode of the whole configuration.

The analysis of the series term in $\{..\}$ is more difficult. It is clear that a few terms of this series should be retained, unless $k^{[2]} b$ and/or $k_1 w$ are very small. The subsequent terms of the series become rapidly small (with m) due to the fact that $\tan(k_{2m}^{[2(j)]} b_j) \sim i \tanh(m\pi b_j/w_j) \rightarrow i$; $m \rightarrow \infty$ and $k_{2m}^{[2(j)]} \frac{4(k_1 w_j)^2 i}{[(k_1 w_j)^2 - (m\pi)^2]^2} = O(m^{-3})$; $m \rightarrow \infty$.

In any case, it seems legitimate to adopt the following picture of what is going on: the base of a given block is a location where diffraction is produced resulting in incident (from either the block into the underground or from the underground into the block) bulk waves being transformed into diffracted bulk and surface waves, as is testified by the presence of the terms $I_m^{(j)+}$ and $I_m^{(j)-}$ in the series, and by the fact that these diffraction effects disappear as the width of the base segment goes to zero. Naturally, the presence of these locally produced diffracted waves perturbs the overall wave structure (with respect to what it was in the absence of the blocks) and therefore results in a modification of the characteristics of the modes in the layer and substratum (which were Love modes when the blocks were absent). This picture is consistent with the observation that the diffracted waves are more difficult to produce when the base segment of a block appears as a stress-free surface due to the fact that either $k^{[2]} b_j = l\pi$; $l = 0, 1, 2, \dots$ or $\mu^{[2]}/\mu^{[1]} < 1$.

Beyond this, it is necessary to carry out a numerical study in order to see how the different parameters involved in the problem, notably those of the block, modify the dispersion characteristics of the modes of the configuration with respect to what these modes were (i.e. Love modes) in the absence of the blocks. The numerical study should also seek to evaluate the modification of the response (notably on the ground) of the configuration due to the presence of blocks.

E3 The emergence of the natural modes of the configuration from the linear system of equations for $B_m^{[2(l)]}$: quasi displacement-free base block modes

Eqs (D13)–(D14) signify that $(B_n^{[2(l)]})^{(p)}$ becomes large when $C_n - D_m^{(l)}$ becomes small, and that this occurs at all orders p of approximation. The fact that $(B_n^{[2(l)]})^{(p)}$ becomes inordinately large is associated with the excitation of a natural mode of the configuration. The equation $C_n(\omega) - D_m^{(l)}(\omega) = 0$ is the approximate dispersion relation of the n th natural mode of the configuration.

Let us examine this relation in more detail.

$$\cot(k_{2n}^{[2(l)]} b_l) - \frac{i\mu^{[2]} k_{2n}^{[2(l)]} w_l}{2\pi\mu^{[0]}} \int_{-\infty}^{\infty} I_n^{(l)+}(k_1) I_n^{(l)-}(k_1) \left[\frac{\cos(k_2^{[1]} h) - i \frac{\mu^{[0]} k_2^{[0]}}{\mu^{[1]} k_2^{[1]}} \sin(k_2^{[1]} h)}{\cos(k_2^{[1]} h) - i \frac{\mu^{[1]} k_2^{[1]}}{\mu^{[0]} k_2^{[0]}} \sin(k_2^{[1]} h)} \right] \frac{dk_1}{k_2^{[0]}} \\ := \mathcal{F}_{1n}^{(l)}(\omega) - \mathcal{F}_{2n}^{(l)}(\omega) = 0, \quad (\text{E9})$$

which shows that the natural modes of the configuration result from the *interaction* of the fields in two substructures: the superstructure (i.e. block(s) above the ground), associated with the term $\mathcal{F}_{1n}^{(l)}(\omega)$, and the substructure (i.e. soft layer plus hard half-space below the ground), associated with the term $\mathcal{F}_{2n}^{(l)}(\omega)$. Each of these two substructures possesses its own natural modes, that is, arising from $\mathcal{F}_{1n}^{(l)} = 0$ for the superstructure, and $\mathcal{F}_{2n}^{(l)} = 0$ for the substructure, but the *natural modes of the complete structure (superstructure plus substructure) are neither the modes of the superstructure nor those of the substructure* since they are defined by $\mathcal{F}_{1n}^{(l)} - \mathcal{F}_{2n}^{(l)} = 0$.

In order to find the natural frequencies of the complete structure, we first analyse the natural frequencies of each substructure and assume that all media in the structure are non-dissipative (i.e. elastic).

The solutions of the dispersion relation for the superstructure are:

$$\mathcal{F}_{1n}^{(l)}(\omega) := \cot(k_{2n}^{[2(l)]} b_l) = 0 \Leftrightarrow \omega = \omega_{nm}^{(l)} = c^{[2]} \sqrt{\left(\frac{(2m+1)\pi}{2b_l}\right)^2 + \left(\frac{n\pi}{w_l}\right)^2}; \quad m, n = 0, 1, 2, \dots, \quad (\text{E10})$$

which are the natural frequencies of vibration of a block with a *displacement-free base* (i.e. at these natural frequencies, $u^{[2(l)]}|_{x_2=0}$ vanishes on the base segment of the block).

Now consider the dispersion relation for the substructure of the entire structure. Due to the fact that the integrand is an even function of k_1 , it becomes

$$\mathcal{F}_{2n}^{(l)}(\omega) := \frac{i\mu^{[2]} k_{2n}^{[2(l)]} w_l}{\pi\mu^{[0]}} \int_0^{\infty} I_n^{(l)+}(k_1) I_n^{(l)-}(k_1) \left[\frac{\cos(k_2^{[1]} h) - i \frac{\mu^{[0]} k_2^{[0]}}{\mu^{[1]} k_2^{[1]}} \sin(k_2^{[1]} h)}{\cos(k_2^{[1]} h) - i \frac{\mu^{[1]} k_2^{[1]}}{\mu^{[0]} k_2^{[0]}} \sin(k_2^{[1]} h)} \right] \frac{dk_1}{k_2^{[0]}} = 0. \quad (\text{E11})$$

A few preliminary remarks are in order: i) since the term $\mathcal{F}_{2n}^{(l)}$ in the dispersion relation is absent in the absence of the infrastructure, we can say that the natural modes of the complete configuration are *quasi displacement-free base block modes*; quasi displacement-free base block modes are different from displacement-free base block modes which, at present, means that the (n, ω) couples for which $\mathcal{F}_{1n}^{(l)} = 0$ are not identical to the (n, ω) couples for which $\mathcal{F}_{2n}^{(l)} = 0$, ii) for small $\mu^{[2]}/\mu^{[1]}$, the quasi displacement-free base block modes are a small perturbation of displacement-free base block modes, which means here that the (n, ω) couples for which $\mathcal{F}_{1n}^{(l)} = 0$ are close to the (n, ω) couples for which $\mathcal{F}_{2n}^{(l)} = 0$; this is a relatively logical result in that when $\mu^{[2]}/\mu^{[1]}$ is small, the waves coming from the infrastructure have

more trouble penetrating into the blocks and modifying therein the modal structure, iii) the dispersion relation for quasi displacement-free base block modes is independent of the number of blocks (provided this number is greater than 0); this is a somewhat surprising result related to the choice of the iteration method for solving the linear system of equations for $B_n^{[2](l)}$, since a more accurate choice of method (one of which is described in Section E4) can be shown to lead to a somewhat different (although much more complicated) dispersion relation which depends on the number of blocks in the configuration.

We now analyse in more detail $\mathcal{F}_{2n}^{(l)}$, and, in particular, $\mathcal{F}_{20}^{(l)}$. Recalling (E6), we get:

$$\mathcal{F}_{20}^{(l)} = \frac{ik^{[2]}w_l \mu^{[2]}}{\pi \mu^{[0]}} \int_0^\infty \text{sinc}^2\left(\frac{k_1 w_l}{2}\right) \left[\frac{\cos(k_2^{[1]}h) - i \frac{\mu^{[0]}k_2^{[0]}}{\mu^{[1]}k_2^{[1]}} \sin(k_2^{[1]}h)}{\cos(k_2^{[1]}h) - i \frac{\mu^{[1]}k_2^{[1]}}{\mu^{[0]}k_2^{[0]}} \sin(k_2^{[1]}h)} \right] \frac{dk_1}{k_2^{[0]}} := \int_0^\infty \mathcal{G}(k_1, \omega) dk_1. \quad (\text{E12})$$

Proceeding as Groby & Wirgin (2005a) and Groby & Wirgin (2005b), we decompose the integral into three parts (under the assumption $k^{[1]} > k^{[0]} > 0$) so as to obtain:

$$\mathcal{F}_{20}^{(l)} = \mathcal{F}_{20}^{1(l)} + \mathcal{F}_{20}^{2(l)} + \mathcal{F}_{20}^{3(l)} \quad (\text{E13})$$

wherein

$$\mathcal{F}_{20}^{1(l)} = \int_0^{k^{[0]}} \mathcal{G}(k_1, \omega) dk_1 \quad \mathcal{F}_{20}^{2(l)} = \int_{k^{[0]}}^{k^{[1]}} \mathcal{G}(k_1, \omega) dk_1 \quad \int_{k^{[1]}}^\infty \mathcal{G}(k_1, \omega) dk_1. \quad (\text{E14})$$

As shown in Groby & Wirgin (2005a) and Groby & Wirgin (2005b), \mathcal{F}_{20}^2 usually dominates the other two terms, and this is due to the fact that the denominator in the integrand of \mathcal{F}_{20}^2 can vanish for k_1 over a large portion of the interval of integration for frequencies at which Love modes are excited in the infrastructure, this occurring near the Haskell frequencies

$$v_l^{LOVE} \approx v_m^{HASK} = \frac{2m+1}{2} \frac{c^{[1]}}{2h}; m \in \mathbb{N}, \quad (\text{E15})$$

which corresponds to

$$k_m^{[0] LOVE} \approx k_m^{[0] HASK} = \frac{2\pi v_m^{HASK}}{c^{[0]}} = \frac{2m+1}{2} \frac{\pi c^{[1]}}{hc^{[0]}}; m \in \mathbb{N}. \quad (\text{E16})$$

$$k_m^{[1] LOVE} \approx k_m^{[1] HASK} = \frac{2\pi v_m^{HASK}}{c^{[1]}} = \frac{2m+1}{2} \frac{\pi}{h}; m \in \mathbb{N}. \quad (\text{E17})$$

The sinc^2 function in the integrand of \mathcal{F}_{20}^2 is significantly large only in the interval $[0, 2\pi/w]$, so that a minimal requirement for capturing most of the contribution of the Love modes in \mathcal{F}_{20}^2 at their frequencies of resonance is that $k_1^{LOVE} < \frac{2\pi}{w}$.

Of course, there exist other terms in the dispersion relation of the $n=0$ mode, that is, \mathcal{F}_{20}^1 , \mathcal{F}_{20}^3 , and the contributions of the higher-than-fundamental Love modes to \mathcal{F}_{20}^2 . As concerns \mathcal{F}_{20}^1 and \mathcal{F}_{20}^3 , we note that the former is complex and the latter is pure imaginary, whereas \mathcal{F}_{10}^1 is real, so that we would expect to have \mathcal{F}_{20}^1 and \mathcal{F}_{20}^3 to contribute less to the dispersion relation than \mathcal{F}_{20}^2 . The contribution to the n th order natural mode of higher-than-fundamental Love modes to \mathcal{F}_{20}^2 is empirically found to be always less than that of the zeroth order Love mode.

The analysis of the $n > 0$ natural modes of the complete structure proceeds in the same manner as previously, and will not be given here.

E4 Another look at quasi displacement-free base block modes

The system of linear equations (D8) can be written as

$$B_n^{[2](l)}(\omega) = P_n^{(l)}(\omega) + \sum_{j \in \mathbb{B}} \sum_{m=0}^\infty Q_{nm}^{(lj)}(\omega) B_m^{2(j)}(\omega); \forall l \in \mathbb{B}; \forall n \in \mathbb{Z}, \quad (\text{E18})$$

wherein

$$P_n^{(l)}(\omega) = \frac{2\epsilon_n}{\cos(k_{2n}^{[2](l)} b_l)} \int_{-\infty}^\infty A^{[0]l-}(k_1, \omega) e^{-ik_2^{[0]l} h} \left[\frac{I_n^{(l)+}(k_1) e^{ik_1(d_l - w_l/2)}}{\cos(k_2^{[1]l} h) - i \frac{\mu^{[1]}k_2^{[1]l}}{\mu^{[0]}k_2^{[0]l}} i \sin(k_2^{[1]l} h)} \right] \frac{dk_1}{k_2^0} \\ ; \forall l \in \mathbb{B}; \forall n \in \mathbb{Z}, \quad (\text{E19})$$

and

$$Q_{nm}^{(lj)}(\omega) = \frac{i w_j}{2\pi} \frac{\epsilon_n}{\cos(k_{2n}^{[2](j)} b_j)} \frac{\mu^{[2]l} k_{2m}^{[2]l}}{\mu^{[0]l}} \sin(k_{2m}^{[2](l)} b_l) \\ \times \int_{-\infty}^\infty I_n^{(l)+}(k_1) I_m^{(j)-}(k_1) \left[\frac{\cos(k_2^{[1]l} h) - i \frac{\mu^{[0]l} k_2^{[0]l}}{\mu^{[1]l} k_2^{[1]l}} \sin(k_2^{[1]l} h)}{\cos(k_2^{[1]l} h)} - i \frac{\mu^{[1]l} k_2^{[1]l}}{\mu^{[0]l} k_2^{[0]l}} \sin(k_2^{[1]l} h) \right] e^{ik_1((d_l - d_j) - \frac{w_l - w_j}{2})} \frac{dk_1}{k_2^{[0]l}} \\ ; \forall l, j \in \mathbb{B}; \forall n, m \in \mathbb{Z}. \quad (\text{E20})$$

The factor $P_n^{(l)}(\omega)$ is clearly related to the driving function and must be set to zero in a modal analysis. The resulting set of equations, has a non trivial solution only if its determinant vanishes. The dispersion relation $\det \{\delta_{nm} \delta_{lj} - Q_{nm}^{(lj)}\} = 0$ can then be solved by a procedure, called the *partition method*, particularly appropriate if the off-diagonal elements of the matrix $\{\delta_{nm} \delta_{lj} - Q_{nm}^{(lj)}\}$ are small compared to the diagonal elements: first one considers the matrix to have one row and one column,

$$1 - Q_{00}^{(11)} = 0, \quad (E21)$$

then to have two rows and two columns,

$$\det \begin{pmatrix} 1 - Q_{00}^{(11)} & -Q_{01}^{(11)} \\ -Q_{10}^{(11)} & 1 - Q_{11}^{(11)} \end{pmatrix} = 0 \Rightarrow (1 - Q_{00}^{(11)}) (1 - Q_{11}^{(11)}) - Q_{01}^{(11)} Q_{10}^{(11)} = 0, \quad (E22)$$

etc.

If the off-diagonal elements of the matrix are considered to be negligible compared to the diagonal elements, the dispersion relation (E22) is simply that the product of the diagonal elements of the matrix should be nil, which means that any diagonal element of the matrix should be nil.

Consider the case in which it is $1 - Q_{00}^{(11)}$ that vanishes. This is equivalent to

$$0 = \cot(k^{[2]}b) - \frac{ik^{[2]}w_1}{2\pi} \frac{\mu^{[2]}}{\mu^{[0]}} \int_{-\infty}^{\infty} I_0^{(1)+}(k_1) I_0^{(1)-}(k_1) \left[\frac{\cos(k_2^{[1]}h) - i \frac{\mu^{[0]}k_2^{[0]}}{\mu^{[1]}k_2^{[1]}} \sin(k_2^{[1]}h)}{\cos(k_2^{[1]}h) - i \frac{\mu^{[1]}k_2^{[1]}}{\mu^{[0]}k_2^{[0]}} \sin(k_2^{[1]}h)} \right] \frac{dk_1}{k_2^{[0]}}, \quad (E23)$$

which is the same as the dispersion relation of the zeroth-order quasi displacement-free base block mode obtained in the previous section. Thus, there is no apparent gain in adopting the analysis of the present section over that of the previous section in an attempt to resolve the difficulty mentioned previously connected with the fact that the dispersion relations do not depend on the number N_b of blocks in the city.

To resolve this problem, we must take into account the off-diagonal elements of the matrix because these elements contain the information on the number of blocks. Unfortunately, the inclusion of these off-diagonal elements makes the dispersion relation increasingly complicated and difficult to analyse as the order of approximation of the partition method (which consists in solving increases (it is already quite complicated at first order). The only way to solve these dispersion relations (which consist in equating determinants of increasing rank to zero) is by numerical computation.

When more than one block (e.g. 2 blocks) are present, the dispersion relations becomes (if the off-diagonal elements of the matrix for each block considered independently can be neglected):

$$\det \begin{pmatrix} 1 - Q_{00}^{(11)} & -Q_{00}^{(12)} \\ -Q_{00}^{(21)} & 1 - Q_{00}^{(22)} \end{pmatrix} = (1 - Q_{00}^{(11)}) (1 - Q_{00}^{(22)}) - Q_{00}^{(12)} Q_{00}^{(21)} = 0 \quad (E24)$$

which is quite different from the zeroth-order quasi displacement-free base block dispersion relation because the *coupling term* $Q_{00}^{(12)} Q_{00}^{(21)}$ does not vanish and cannot be neglected. This term corresponds to the so-called *structure–soil–structure interaction* and accounts for the distance separating the two buildings. Its form is close to that of the term representative of the action of the geophysical structure. Nevertheless, due to its complexity, it is difficult to carry out an analytical study of this relation.

The *partition method* emphasizes the role of the global superstructure, while the *iteration method*, described in Section E3, emphasizes the role of only one component (i.e. one block) of the superstructure. The partition method also accounts for all the possible interactions between blocks (the term $\cot(k_{20}b_l)$) and the geophysical structure through the terms $Q_{nm}^{(lj)}$, and the interaction between blocks through the terms $Q_{nm}^{(lj)}$ and $Q_{nm}^{(lj)}$.

Ultimately, the choice of method reduces to determining which one gives the best results, that is, results that are closest to reality. This can be determined only by full-blown numerical studies, the results of which will have to be compared to those of the FE method (employed as a reference). In fact, we find that the partition method gives the best results, and is therefore employed in all the subsequent numerical computations.

APPENDIX F: EXPRESSION OF THE FIELDS $u^{[2](j)}(\mathbf{x}, \omega)$, $u^{[1]}(\mathbf{x}, \omega)$ AND $u^{[0]}(\mathbf{x}, \omega)$ FOR LINE SOURCE EXCITATION

Once the quasi-modal coefficients $B_m^{[2](l)}$, $\forall m \in \mathbb{N}$, $\forall l \in \mathbb{B}$ are obtained from the system of equations (E18), the field in the block domain $\Omega^{[2](l)}$ is computed via (B10). This field vanishes on the ground at the frequency of occurrence of the *displacement-free base mode* of the block.

If $m > 0$, quasi modal coefficients can be neglected, so that the field in the block $l \in \mathbb{B}$ takes the form

$$u^{[2](l)} \approx B_0^{[2](l)}(\omega) \cos(k^{[2]}(x_2 + b_l)) \quad (F1)$$

which indicates that the displacement field is independent of x_1 and takes the form of a standing wave in the block.

Let us next consider the field in the layer. Combining (C1), (C3), (C4) and (C5), leads, via (B9), to:

$$u^{[1]}(\mathbf{x}, \omega) = u_c^{[1]}(\mathbf{x}, \omega) + \sum_{l \in \mathbb{B}} u_{\mathbb{B}}^{[1](l)}(\mathbf{x}, \omega), \quad (F2)$$

with

$$u_c^{[1]}(\mathbf{x}, \omega) = \frac{iS(\omega)}{2\pi} \int_{-\infty}^{\infty} \frac{\cos(k_2^{[1]}x_2) e^{i(k_1(x_1-x_1^s)+k_2^{[0]}(x_2^s-h))}}{\cos(k_2^{[1]}h) - i\frac{\mu^{[1]}k_2^{[1]}}{\mu^{[0]}k_2^{[0]}} \sin(k_2^{[1]}h)} \frac{dk_1}{k_2^{[0]}}, \quad (\text{F3})$$

and

$$u_{\mathbb{B}}^{[1]l}(\mathbf{x}, \omega) = \frac{i}{2\pi} \sum_{n=0}^{\infty} \frac{\mu^{[2]}}{\mu^{[0]}} B_n^{[2]l} k_{2n}^{[2]l} w_l \sin(k_{2n}^{[2]l} b_l) \times \int_{-\infty}^{\infty} \frac{\cos(k_2^{[1]}(x_2-h)) + i\frac{\mu^{[0]}k_2^{[0]}}{\mu^{[1]}k_2^{[1]}} \sin(k_2^{[1]}(x_2-h))}{\cos(k_2^{[1]}h) - i\frac{\mu^{[1]}k_2^{[1]}}{\mu^{[0]}k_2^{[0]}} \sin(k_2^{[1]}h)} I_n^{(l)-}(k_1) e^{i(k_1(x_1-(d_l-\frac{w_l}{2}))+k_2^{[0]}(x_2-h))} \frac{dk_1}{k_2^{[0]}}. \quad (\text{F4})$$

This expression indicates that the field in the layer is composed of: i) the field obtained in the absence of blocks and induced by the incident cylindrical wave, ii) the fields induced by the presence of each block. The displacement field $u^{[1]}(\mathbf{x}, \omega) - u_c^{[1]}(\mathbf{x}, \omega)$ appears as a sum of block fields which are strongly linked together, since each coefficient $B_n^{[2]l}$ is calculated by taking into account the presence of the other blocks via (E18).

Let us finally consider the field in the substratum. Combining (C1), (C3), (C4) and (C5), leads, via (B8), to:

$$u^{[0]}(\mathbf{x}, \omega) = \{u^i(\mathbf{x}, \omega) + u_c^{d[0]}(\mathbf{x}, \omega)\} + \sum_{j \in \mathbb{B}} u_{\mathbb{B}}^{[0]j}(\mathbf{x}, \omega) \quad (\text{F5})$$

with

$$u_c^{d[0]}(\mathbf{x}, \omega) = \frac{iS(\omega)}{4\pi} \int_{-\infty}^{\infty} \frac{\cos(k_2^{[1]}h) + i\frac{\mu^{[1]}k_2^{[1]}}{\mu^{[0]}k_2^{[0]}} \sin(k_2^{[1]}h)}{\cos(k_2^{[1]}h) - i\frac{\mu^{[1]}k_2^{[1]}}{\mu^{[0]}k_2^{[0]}} \sin(k_2^{[1]}h)} e^{i(k_1(x_1-x_1^s)+k_2^{[0]}(x_2+x_2^s-2h))} \frac{dk_1}{k_2^{[0]}}, \quad (\text{F6})$$

and

$$u_{\mathbb{B}}^{[0]l}(\mathbf{x}, \omega) = \frac{i}{2\pi} \sum_{n=0}^{\infty} \frac{\mu^{[2]}}{\mu^{[0]}} B_n^{[2]l} k_{2n}^{[2]l} w_l \sin(k_{2n}^{[2]l} b_l) \times \int_{-\infty}^{\infty} \frac{I_n^{(l)-}(k_1) e^{i(k_1(x_1-(d_l-\frac{w_l}{2}))+k_2^{[0]}(x_2-h))}}{\cos(k_2^{[1]}h) - i\frac{\mu^{[1]}k_2^{[1]}}{\mu^{[0]}k_2^{[0]}} \sin(k_2^{[1]}h)} \frac{dk_1}{k_2^{[0]}}. \quad (\text{F7})$$

This expression indicates that the field in the substratum is composed of: (i) the field obtained in the absence of blocks, including the incident plus diffracted fields, the latter being induced by the incident cylindrical wave, (ii) the fields induced by the presence of each block; the latter takes the form of a sum of block fields which are strongly linked together, since each coefficient $B_n^{[2]j}$ is calculated by taking into account the presence of the other blocks via (E18).

F1 Computational details for $N_b < \infty$

All intervals over the which integration is performed in the calculation of the quasi-modal coefficients, through the linear system (E18), that is, in the calculation of $P_n^{(l)}$ and of $Q_{nm}^{(j)}$, $(n, m) \in \mathbb{N}^2$, $(j, l) \in \mathbb{B}^2$, and in the calculation of the displacement fields $u^{[1]} = u_c^{[1]} + \sum_{l \in \mathbb{B}} u_{\mathbb{B}}^{[1]l}$ and

$u^{[0]} = u^i + u_c^{[0]d} + \sum_{l \in \mathbb{B}} u_{\mathbb{B}}^{[0]l}$, are first reduced to $\int_0^{+\infty}$. These intervals are then separated into $\mathcal{I}_1 = [0, \text{Re}(k^0)]$ (interference of propagative waves), $\mathcal{I}_2 = [\text{Re}(k^0), \text{Re}(k^1)]$ (excitation of quasi-Love waves) and $\mathcal{I}_3 = [\text{Re}(k^1), +\infty[$ (evanescent waves in the layer) in order to point out the different type of waves associated with the different possible phenomena in the geophysical structure. The numerical evaluation of these integrals is carried out by the procedure described in Groby & Wirgin (2005b).

F2 Interpretation of the fields $u_{\mathbb{B}}^{0(j)}$ and $u_{\mathbb{B}}^{1(j)}$

If the leading term of the quasi modal representation in each block $l \in \mathbb{B}$ is dominant (i.e. the higher-order terms can be neglected), the fields $u_{\mathbb{B}}^{[0]j}(\mathbf{x}, \omega)$ in (F4) and $u_{\mathbb{B}}^{[1]j}(\mathbf{x}, \omega)$ in (F7) reduce to:

$$u_{\mathbb{B}}^{[1]j}(\mathbf{x}, \omega) = \frac{i}{2\pi} \frac{\mu^{[2]}}{\mu^{[0]}} B_0^{[2]j} k^{[2]j} w_j \sin(k^{[2]j} b_j) \int_{-\infty}^{\infty} \frac{\left[\cos(k_2^{[1]}(x_2-h)) + i\frac{\mu^{[0]}k_2^{[0]}}{\mu^{[1]}k_2^{[1]}} \sin(k_2^{[1]}(x_2-h)) \right] \text{sinc}(k_1 \frac{w_j}{2}) e^{i(k_1(x_1-d_j)+k_2^{[0]}(x_2-h))}}{\cos(k_2^{[1]}h) - i\frac{\mu^{[1]}k_2^{[1]}}{\mu^{[0]}k_2^{[0]}} \sin(k_2^{[1]}h)} \frac{dk_1}{k_2^{[0]}}, \quad (\text{F8})$$

$$u_{\mathbb{B}}^{[0](j)}(\mathbf{x}, \omega) = \frac{i}{2\pi} \frac{\mu^{[2]}}{\mu^{[0]}} B_0^{[2](j)} k^{[2]} w_j \sin(k^{[2]} b_j) \int_{-\infty}^{\infty} \frac{\text{sinc}\left(k_1 \frac{w_j}{2}\right) e^{i(k_1(x_1-d_j)+k_2^{[0]}(x_2-h))}}{\cos\left(k_2^{[1]} h\right) - i \frac{\mu^{[1]} k_1^{[1]}}{\mu^{[0]} k_2^{[0]}} \sin\left(k_2^{[1]} h\right)} dk_1. \quad (\text{F9})$$

It can be shown that each $u_{\mathbb{B}}^{[0](j)}(\mathbf{x}, \omega)$ may be interpreted as the field radiated by a ribbon source of width w_j , located at the base of each block $j \in \mathbb{B}$, and whose amplitude is of the form $\frac{\mu^{[1]}}{\mu^{[2]}} B_0^{[2](j)} k^{[2]} w_j \sin(k^{[2]} b_j)$. These sources are induced sources, that is, they do not introduce energy into the system, but each of them induces a modification of the repartition of the energy over the excitation frequency bandwidth. These sources are located at the top of the layer and should excite quasi-Love waves, as shown in Groby & Wirgin (2005a,b) and Groby & Wirgin (2004) (for applied sources).

If $m > 0$ quasi modes are relevant, the even-order modes correspond to ribbon sources of width w_l , located at d_l , $l \in \mathbb{B}$, while the odd-order modes correspond to line sources located at the edges of the blocks. The amplitudes of both of these types of induced sources depend on the order of the quasi modes and on the characteristics of the corresponding block.

APPENDIX G: FIELD REPRESENTATIONS IN THE SPACE-FREQUENCY FRAMEWORK FOR $N_B = \infty$

The formulation for the case of $N_b < \infty$ identical (or non-identical) blocks was given in Appendix B.

The new feature here is the existence of an infinite number (i.e. $N_b = \infty$) of identical (in shape, dimensions and composition) blocks, separated (horizontally) one from the other by the constant distance d (called the period).

At present, the blocks are identified by indices in the set $\mathbb{B} = \{\dots, -1, 0, 1, \dots\} = \mathbb{Z}$, with the understanding that the centre of the segment $\Gamma_{b_s}^0$ is at the origin.

Owing to the assumed plane wave nature of the incident wave, the periodic nature of Γ_G , and the fact that the blocks are assumed to be identical in height (b), width (w), and composition, the field is quasi-periodic spatially speaking (this constituting the so-called *Floquet relation*, that is,

$$u^{[l]}(x_1 + nd, x_2) = u^{[l]}(x_1, x_2) e^{i k_1^{[l]} nd}, \quad \forall \mathbf{x} \in \Omega_j; \quad \forall n \in \mathbb{Z}; \quad j = 0, 1. \quad (\text{G1})$$

wherein $k_1^{[l]} := k^{[l]} s^i$, $s^i = \sin \theta^i$, and θ^i is the incident angle.

By virtue of separation of variables and the Floquet relation it is found that

$$u^{[0]}(\mathbf{x}, \omega) = u^i(\mathbf{x}, \omega) + \sum_{n=-\infty}^{\infty} B_n^{[0]} \exp\left\{i\left[k_{1n} x_1 + k_{2n}^{[0]}(x_2 - h)\right]\right\}; \quad \mathbf{x} \in \Omega_0. \quad (\text{G2})$$

However, we can write

$$u^i(\mathbf{x}, \omega) = \sum_{n=-\infty}^{\infty} A_n^i \exp\left\{i\left[k_{1n} x_1 - k_{2n}^{[0]} x_2\right]\right\}; \quad \mathbf{x} \in \mathbb{R}^2, \quad (\text{G3})$$

wherein

$$A_n^i = S(\omega) \delta_{n0}. \quad (\text{G4})$$

$k_{10} = k_1^i$, and $k_{20}^{[l]} = \sqrt{(k^{[l]})^2 - (k_1^{[l]})^2} := k_2^{[l]i}$, so that

$$u^{[0]}(\mathbf{x}, \omega) = \sum_{n=-\infty}^{\infty} A_n^i \exp\left\{i\left[k_{1n} x_1 - k_{2n}^{[0]} x_2\right]\right\} + \sum_{n=-\infty}^{\infty} B_n^{[0]} \exp\left\{i\left[k_{1n} x_1 + k_{2n}^{[0]}(x_2 - h)\right]\right\}; \quad \mathbf{x} \in \Omega_0. \quad (\text{G5})$$

In the same manner we find:

$$u^{[1]}(\mathbf{x}, \omega) = \sum_{n=-\infty}^{\infty} A_n^{[1]} \exp\left\{i\left[k_{1n} x_1 - k_{2n}^{[1]} x_2\right]\right\} + \sum_{n=-\infty}^{\infty} B_n^{[1]} \exp\left\{i\left[k_{1n} x_1 + k_{2n}^{[1]}(x_2 - h)\right]\right\}; \quad \mathbf{x} \in \Omega_1. \quad (\text{G6})$$

The Floquet relation actually extends to Ω_2 wherein it takes the form

$$u^{[2]j}(x_1, x_2, \omega) = u^{[2]0}(x_1, x_2, \omega) e^{i k_1^{[2]j} d}, \quad j \in \mathbb{Z}, \quad (\text{G7})$$

wherein (as for the case $N_b < \infty$)

$$u^{[2]0}(\mathbf{x}, \omega) := u^{[2]}(\mathbf{x}, \omega) = \sum_{m=0}^{\infty} B_m^{[2]} \cos \left[k_{1m}^{[2]} \left(x_1 + \frac{w}{2} \right) \right] \cos \left[k_{2m}^{[2]} (x_2 + b) \right] \quad (G8)$$

$$; \mathbf{x} \in \Omega_2^{(0)},$$

with:

$$k_{1m}^{[2]} = \frac{m\pi}{w} \quad k_{2m}^{[2]} = \sqrt{(k^{[2]})^2 - (k_{1m}^{[2]})^2} \quad \text{Re } k_{2m}^{[2]} \geq 0 \quad \text{Im } k_{2m}^{[2]} \geq 0 \quad \omega \geq 0. \quad (G9)$$

APPENDIX H: INTERRELATIONS BETWEEN THE VARIOUS UNKNOWN COEFFICIENTS FOR THE CASE $N_B = \infty$

By applying the various boundary conditions, we find:

$$A_n^{[1]} - B_n^{[1]} = \frac{w}{id} e^{ik_{1n}w/2} \sum_{m=0}^{\infty} B_m^{[2]} \frac{\mu^{[2]} k_{2m}^{[2]}}{\mu^{[1]} k_{2n}^{[1]}} I_{mn}^- \sin(k_{2m}^{[2]} b); \forall n \in \mathbb{Z}, \quad (H1)$$

$$B_m^{[2]} = \frac{\epsilon_m}{\cos(k_{2m}^{[2]} b)} \sum_{n \in \mathbb{Z}} [A_n^{[1]} + B_n^{[1]}] I_{mn} e^{-ik_{1n}w/2}; \forall m = 0, 1, 2, \dots, \quad (H2)$$

$$-\mu^{[0]} k_{2n}^{[0]} A_n^{[0]} e^{-ik_{2n}^{[0]} h} + \mu^{[0]} k_{2n}^{[0]} B_n^{[0]} + \mu^{[1]} k_{2n}^{[1]} A_n^{[1]} e^{-ik_{2n}^{[1]} h} - \mu^{[1]} k_{2n}^{[1]} B_n^{[1]} e^{ik_{2n}^{[1]} h} = 0; \quad (H3)$$

$$\forall n \in \mathbb{Z},$$

$$A_n^{[0]} e^{-ik_{2n}^{[0]} h} + B_n^{[0]} - A_n^{[1]} e^{-ik_{2n}^{[1]} h} - B_n^{[1]} e^{ik_{2n}^{[1]} h} = 0; \forall n \in \mathbb{Z}, \quad (H4)$$

wherein

$$I_{mn}^{\pm} = \int_0^1 \exp(\pm i k_{1n} w \eta) \cos(k_{1m}^{[2]} w \eta) d\eta$$

$$= \frac{i^m}{2} e^{\pm ik_{1n} \frac{w}{2}} \left\{ \text{sinc} \left[(k_{1m}^{[2]} \pm k_{1n}) \frac{w}{2} \right] + (-1)^m \text{sinc} \left[(-k_{1m}^{[2]} \pm k_{1n}) \frac{w}{2} \right] \right\}. \quad (H5)$$

APPENDIX I: DETERMINATION OF THE VARIOUS UNKNOWNNS

I1 Elimination of $B_m^{[2]}$ to obtain a linear system of equations for $B_n^{[0]}$.

After a series of substitutions (see Appendix H), the following matrix equation is obtained for $B_n^{[0]}$:

$$C_n^{[1]0} B_n^{[0]} - \sum_{m=-\infty}^{\infty} D_{nm} B_m^{[0]} = F_n; \forall n \in \mathbb{Z}, \quad (I1)$$

wherein:

$$C_n^{[j]l} := \cos(k_{2n}^{[l]} h) - i \frac{\mu^{[j]} k_{2n}^{[j]}}{\mu^{[l]} k_{2n}^{[l]}} \sin(k_{2n}^{[l]} h); \quad \forall n \in \mathbb{Z}, \quad j, l = 0, 1, \quad (I2)$$

$$D_{nm} := \sum_{l=0}^{\infty} \frac{i \epsilon_l \mu_2 k_{2l}^{[2]} w}{\mu^{[0]} k_{2n}^{[0]} d} I_{ln}^- I_{lm}^+ \tan(k_{2l}^{[2]} b) C_m^{[0]1} e^{i(k_{1n} - k_{1m})w/2}, \quad (I3)$$

and

$$F_n = S(\omega) e^{-ik_{2n}^{[0]} h} C_n^{[1]0} \delta_{n0} + \sum_{l=0}^{\infty} \frac{i S(\omega) e^{-ik_{2l}^{[0]} h} w \epsilon_l \mu^{[2]} k_{2l}^{[2]} \sin(k_{2l}^{[2]} b) I_{ln}^- I_{l0}^+}{\mu^{[0]} k_{2n}^{[0]} d} C_0^{[0]1} e^{i(k_{1n} - k_{1l})w/2}. \quad (I4)$$

Eq. (I1) is a matrix equation, which, in principle, enables the determination of the vector $\mathbf{b}^{[0]} : \{B_n^{[0]}; n = 0, \pm 1, \pm 2, \dots\}$.

I2 Elimination of $B_n^{[0]}$ to obtain a linear system of equations for $B_m^{[2]}$

The procedure is again to make a series of substitutions (see Appendix H) which now leads to the linear system for $B_l^{[2]}$; $\forall l \in \mathbb{N}$:

$$B_l^{[2]} = P_l + \sum_{m=0}^{\infty} Q_{ml} B_m^{[2]}, \forall l \in \mathbb{N}, \quad (15)$$

wherein

$$Q_{ml} = \sum_{n=-\infty}^{\infty} \frac{i\epsilon_l w k_{2m}^{[2]} \mu^{[2]} \sin(k_{2m}^{[2]} b) I_{mn}^- I_n^+ C_n^{[01]}}{\mu^{[0]} k_{n2}^{[0]} d \cos(k_{2l}^{[2]} b) C_n^{[10]}}, \quad (16)$$

and

$$P_l = \sum_{n=-\infty}^{\infty} A_n^l \frac{2\epsilon_l \exp(-ik_{n2}^{[0]} h) \exp(-ik_{n1} \frac{w}{2}) I_n^+}{\cos(k_{2l}^{[2]} b) C_n^{[10]}} = S(\omega) \frac{2\epsilon_l \exp(-ik_2^l h) \exp(-ik_1^l \frac{w}{2}) I_{l0}^+}{\cos(k_{2l}^{[2]} b) C_0^{[10]}}. \quad (17)$$

Eq. (15) is a matrix equation, which, in principle, enables the determination of the vector $\mathbf{b}^{[2]} : \{B_m^{[2]}; m = 0, 1, 2, \dots\}$.

APPENDIX J: MODAL ANALYSIS FOR $N_B = \infty$

J1 General considerations

At this point, it is important to recall that the ultimate goal of this investigation is to predict the response of an urban site to a seismic wave. This response takes the form of the displacement field at various locations on the ground as a function of time. Thus, the field quantities of interest are the *space-time* expressions of $u^{[j]}$; $j = 0, 1, 2$.

On account of what was written above, the space-time framework diffracted field in Ω_0 can be written as

$$u^{[0]d}(\mathbf{x}, \omega) = \int_{-\infty}^{\infty} dk_1 \int_{-\infty}^{\infty} d\omega B^{[0]}(k_1, \omega) \exp\left\{i\left[k_1 x_1 + k_2^{[0]}(x_2 - h) - \omega t\right]\right\}, \quad (J1)$$

with similar types of expressions for the fields in Ω_1 and Ω_2 , as well as for the (incident) excitation field (note that $B^{[0]}(k_1) = \sum_{n=-\infty}^{\infty} B_n^{[01]} \delta(k_{1n} - k_1)$ in the case of a periodic city). These expressions possess at least four important features.

The first feature, underlined in Groby & Wirgin (2005a) and Groby & Wirgin (2005b), is that the time framework fields are expressed as integrals over the horizontal wavenumber k_1 and angular frequency ω of functions that represent, for each k_1 and ω (and assuming there is no material attenuation in the media), either a propagating or evanescent plane wave, the amplitude of which is a function such as $B^{[0]}(k_1, \omega)$.

A second important feature, underlined in Groby & Wirgin (2005a,b) and in the first part of this paper, is that the amplitude functions, such as $B^{[0]}(k_1, \omega)$, exhibit resonant behaviour (i.e. can become large in the presence of material losses, or even larger (and sometimes, infinite) in the absence of material losses), in the neighborhood of certain values, k_1^* of k_1 and ω^* of ω , which are characteristic of the *modes* of the structure giving rise to these fields.

The third feature, brought out in Groby & Wirgin (2005a) and Groby & Wirgin (2005b), is that resonances can be provoked by the solicitation when: a) the frequency ω of one of the spectral components of the latter is equal to one of the natural frequencies ω^* and b) the horizontal wavenumber of one of the component plane waves of the excitation field is equal to k_1^* .

The fourth feature is that a mode (such as the well-known Love mode) corresponds to $\|k_1^*\|$ larger than $\|k^{[0]}\|$, which means that the plane wave associated with an excited mode is necessarily evanescent in Ω_0 . Consequently, to bring $\|k_1\|$ (which is a sort of momentum) up to the required level, requires a momentum boost which is provided either by the incident field (i.e. the latter should contain evanescent wave components with horizontal wavenumbers $\|k_1\| > \|k^{[0]}\|$) and/or by the scattering structure (site) itself.

In Groby & Wirgin (2005a) and Groby & Wirgin (2005b), the site had horizontal, flat boundaries and interfaces and all the media were homogeneous, so that it could not provide the required momentum boost. Moreover, it was shown in Groby & Wirgin (2005a) and Groby & Wirgin (2005b) (and again, earlier herein) that if the incident field takes the form of a propagating (bulk) plane wave, the (Love) modes of the site cannot be excited, this being possible only if the incident field contains the required evanescent wave component, as is the situation in which the wave is radiated by a line source.

At present, the incident field takes the form of a propagating plane wave and the momentum boost is provided by the periodic unevenness of the surface (in quanta of $\frac{2\pi}{d}$), as manifested by the presence of evanescent waves in the field representations, so that we can expect the configuration to exhibit resonant behaviour corresponding to the excitation of some sort of modes.

The remainder of this section is devoted to the characterization of these modes and to the methods for finding the (k_1^*, ω^*) with which they are associated.

J2 The emergence of the quasi-Love modes of the configuration from the iterative solution of the matrix equation for $B_n^{[0]}$

Eq. (11) can be rewritten as

$$B_n^{[0]} = \frac{\sum_{m=-\infty}^{\infty} D_{nm} B_m^{[01]} (1 - \delta_{mn}) + F_n}{C_n^{[10]} - D_{nn}}; \forall n \in \mathbb{Z}. \quad (J2)$$

which can be solved in iterative manner as follows:

$$B_n^{[0]^{(l)}} = \frac{\mathcal{N}_n^{(l)}}{C_n^{[10]} - D_{nn}} := \frac{\mathcal{N}_n^{(l)}}{\mathcal{D}_n}, \quad (J3)$$

wherein

$$\mathcal{N}_n^{(0)} = F_n, \quad (J4)$$

$$\mathcal{N}_n^{(l>0)} = F_n + \sum_{m=-\infty}^{\infty} D_{nm} B_m^{[0]^{(l-1)}} (1 - \delta_{mn}), \quad (J5)$$

from which it becomes apparent that the solution $B_n^{[0]^{(l)}}$, to any order l of approximation, is expressed as a fraction, the denominator of which (not depending on the order of approximation), can become small for certain values of k_{1n} and ω so as to make $B_n^{[0]^{(l)}}(\omega)$, and (possibly) the field in the substratum, large at these values.

When this happens, a *natural mode of the configuration*, comprising the blocks, the soft layer and the hard half substratum, is excited, this taking the form of a *resonance* with respect to $B_n^{[0]^{(l)}}$, that is, with respect to the field in the substratum. As $B_n^{[0]}$ is related to $A_n^{[1]}$ and $B_n^{[1]}$ via (H3)–(H4), the structural resonance also manifests itself in the layer for the same k_{1n} and ω .

The matrix equation (98) can be written as

$$(\mathbf{C} - \mathbf{D}) \mathbf{b}^0 = \mathbf{f} \quad (J6)$$

wherein: the matrix $\mathbf{C}^{[10]}$ has components $C_{nm}^{[10]} = C_n^{[10]} \delta_{nm}$, \mathbf{D} has components D_{nm} , and the vectors \mathbf{b}^0 and \mathbf{f} have components B_n^0 and F_n , respectively. The *modes* of the configuration are obtained by turning off the excitation (Wirgin & Bard 1996), embodied in the vector \mathbf{f} . Thus, the non-trivial solution of the homogeneous matrix equation (J6) is the solution of (the *dispersion relation*)

$$\det(\mathbf{C}^{[10]} - \mathbf{D}) = 0. \quad (J7)$$

The equations

$$D_n = C_n^{[10]} - D_{nn} = C_n^{[10]} - \sum_{l=0}^{\infty} \frac{i\epsilon_l \mu_2 k_{2l}^{[2]} w}{\mu^{[0]} k_{2n}^{[0]} d} I_n^- I_n^+ \tan(k_{2l}^{[2]} b) C_n^{[01]}; n = 0, \pm 1, \dots, \quad (J8)$$

associated with a singularity in the iterative procedure (J3), also correspond to an approximation of the dispersion equation of the modes (J7) when the off-diagonal elements of the matrix $\mathbf{C}^{[10]} - \mathbf{D}$ are small compared to the diagonal elements. Such a situation does not necessarily prevail, but it is nevertheless useful to obtain a first idea of the natural frequencies of the modes from the simple relations (J8) rather than from the much more complicated relation (J7).

We note that:

$$C_n^{[10]} = 0, \quad (J9)$$

is the dispersion relation for ordinary *Love modes*. Consequently,

$$D_n = 0, \quad (J10)$$

is the dispersion relation of what we term *quasi-Love modes* which are generally different from ordinary Love modes.

When $b \rightarrow 0$, the dispersion relation for quasi-Love modes becomes the dispersion relation $D_n = C_n^{[10]} = 0$ for ordinary Love modes, and for small $\frac{\mu^2 k_{2m}^{[2]} w}{\mu^1 k_{2n}^{[1]} d}$, the quasi-Love modes are a small perturbation of ordinary Love modes.

J3 The emergence of the quasi displacement-free base block modes and quasi-Cutler modes of the configuration from iterative solutions of the linear system of equations for $B_m^{[2]^{(l)}}$

J3.1 Approximate dispersion relations arising from the first type of iterative scheme

An iterative procedure for solving the linear set of equations (I5) is expressed by:

$$B_l^{[2]^{(0)}} = \frac{P_l}{1 - Q_{ll}}; \forall l \in \mathbb{N}, \quad (J11)$$

$$B_l^{[2]^{(p)}}(\omega) = B_l^{[2]^{(0)}}(\omega) + \frac{\sum_{m=0}^{\infty} Q_{ml} (1 - \delta_{ml}) B_m^{[2]^{(p-1)}}}{1 - Q_{ll}}; l = 1, 2, \dots; p = 1, 2, \dots \quad (J12)$$

The fact that $B_l^{[2]^{(p)}}$ becomes large when $1 - Q_{ll}$ is small (which occurs at all orders p of approximation) is associated with the excitation of a natural mode of the configuration. The equations $1 - Q_{ll} = 0$; $l \in \mathbb{N}$ are the approximate dispersion relations of the l th natural modes ($l \in \mathbb{N}$) of the configuration. They are approximate in nature because they are obtained by neglecting the off-diagonal terms in the matrix equation (I5).

Nevertheless, let us examine this dispersion relation in more detail:

$$\mathcal{F}_m := \cot(k_{2m}^{[2]}b) - \sum_{n=-\infty}^{\infty} i\epsilon_m \frac{w}{d} \frac{k_{2m}^{[2]}\mu^{[2]}}{k_{2n}^{[0]}\mu^{[0]}} \frac{C_n^{[01]}}{C_n^{[10]}} J_{mn}^- J_{ln}^+ := \mathcal{F}_{1m} - \mathcal{F}_{2m} = 0; m \in \mathbb{N}, \quad (\text{J13})$$

which shows that the modes of the configuration result from the *interaction* of the fields in two substructures: the *superstructure* (i.e. the blocks above the ground), associated with the term \mathcal{F}_{1m} and the *substructure* (i.e. the soft layer plus the hard half space below the ground) associated with the term \mathcal{F}_{2m} . Each of these two substructures possesses its own modes, that is, arising from $\mathcal{F}_{1m} = 0$, for the superstructure, and $\mathcal{F}_{2m} = 0$, for the substructure, but the modes of the complete structure are neither the modes of the superstructure nor those of the substructure, since they are defined by $\mathcal{F}_{1m} - \mathcal{F}_{2m} = 0$; $m \in \mathbb{N}$.

In order to obtain the natural frequencies of the complete structure, we first analyse the natural frequencies of each substructure, and assume that all the media are non-dissipative (i.e. elastic).

The solutions of the (approximate) dispersion relations for the superstructure are:

$$\mathcal{F}_{1m} := \cot(k_{2m}^{[2]}b) = 0 \Leftrightarrow \omega = \omega_{mn} = c^{[2]} \sqrt{\left(\frac{(2n+1)\pi}{2b}\right)^2 + \left(\frac{m\pi}{w}\right)^2}; n, m = 0, 1, 2, \dots, \quad (\text{J14})$$

which are the natural frequencies of vibration of a block with *displacement-free base* (i.e. at these natural frequencies, $u^{[2]}|_{x_2=0}$ vanishes on the base segment of the block).

Next consider the dispersion relations for the geophysical (sub)structure $\mathcal{F}_{2m} = 0$; $m \in \mathbb{N}$. As pointed out earlier in this paper, the sum in this relation can be split into three parts corresponding to: (i) propagative waves in both the substratum and the layer, (ii) evanescent waves in the substratum and propagative waves the layer, (iii) evanescent waves in both the substratum and layer. Only the second part can lead to a vanishing denominator, and also to the satisfaction of the dispersion relation of Love modes.

We note that for small $\frac{\mu^{[2]}}{\mu^{[0]}}$, and/or small $\frac{w}{d}$, the quasi displacement-free base block modes are a small perturbation of the displacement-free base block modes. We also note that the approximate dispersion relations for the configuration involving an infinite set of equi-spaced identical blocks are similar to the dispersion relations obtained above for a small number of blocks, in that they betray the existence of a combination of quasi-Love and quasi displacement-free base block modes.

J3.2 Approximate dispersion relations resulting from a second type of iterative scheme

Let \mathbf{Q} denote the matrix of components Q_{ml} , \mathbf{I} the identity matrix, and \mathbf{b} and \mathbf{p} the vectors of components $B_l^{[2]}$ and P_l , respectively.

The system of linear equations (I5) can be written as the matrix equation (for the determination of the unknown vector \mathbf{b})

$$(\mathbf{I} - \mathbf{Q})\mathbf{b} = \mathbf{p}. \quad (\text{J15})$$

The *modes* of the configuration are obtained by turning off the excitation (Wirgin 1995), embodied in \mathbf{p} . The non-trivial solutions of (J15) are then obtained from

$$\det(\mathbf{I} - \mathbf{Q}) = 0. \quad (\text{J16})$$

An iterative (partition) procedure for solving this equation, which is different from the preceding one, and is particularly appropriate if the off-diagonal elements of the matrix are small (but non neglected) compared to the diagonal elements, is first to consider the matrix to have one row and one column, that is,

$$1 - Q_{00} = 0, \quad (\text{J17})$$

then to consider it to have two rows and two columns,

$$\det \begin{pmatrix} 1 - Q_{00} & -Q_{01} \\ Q_{10} & 1 - Q_{11} \end{pmatrix} = (1 - Q_{00})(1 - Q_{11}) - Q_{01}Q_{10} = 0, \quad (\text{J18})$$

and so forth.

We shall not go into the details of these various approximate expressions of the dispersion relation because they become extremely involved beyond (J17). However, it is of historical and didactic interest to examine (J17) in detail. This is done in the next section.

J3.3 Solution of the zeroth-order dispersion relation arising in the two types of iterative schemes: the Cutler mode

We rewrite the lowest-order approximation of the dispersion relation (J15) (equivalent to (J8) for $n = 0$) in the form first given in Wirgin (1988):

$$\mathcal{D}_0 = 1 - i \frac{w}{d} \frac{k_{2m}^{[2]}\mu^{[2]}}{k_{2n}^{[0]}\mu^{[0]}} \tan(k_{2m}^{[2]}b) \sum_{n \in \mathbb{Z}} \frac{k_{2n}^{[0]}}{k_{2n}^{[0]}} \text{sinc}^2\left(k_{1n} \frac{w}{2}\right) \frac{C_n^{[01]}}{C_n^{[10]}} = 0. \quad (\text{J19})$$

We now consider the cases (first studied in Cutler 1944; Rotman 1951; Hurd 1954; Borgnis & Papas 1958; Hougardy & Hansen 1958; Auld *et al.* 1976; Gulyaev & Plesskii 1978; Wirgin 1988) in which the layer is filled with the same material $M^{[0]}$ as that of the substratum (actually, in most of the cited publications, $M^{[2]}$ was also taken equal to $M^{[0]}$, but this is not done here, for the moment at least). Thus, $\mu^{[1]} = \mu^{[0]}$ and

$k^{[1]} = k^{[0]}$. In addition, we recall that $M^{[0]}$ is non-dissipative, so that $\mu^{[0]}$ and $k^{[0]}$ are real. We shall also suppose, to simplify matters, that $\mu^{[2]}$ and $k^{[2]}$ are real (i.e. $M^{[2]}$ is lossless).

Then

$$\mathcal{D}_0 = 1 - i\delta\kappa \tan(k^{[2]}b) \sum_{n \in \mathbb{Z}} \frac{k^{[0]}}{k_{2n}^{[0]}} \operatorname{sinc}^2\left(k_{1n} \frac{w}{2}\right) = 0, \quad (\text{J20})$$

in which $\delta := \frac{w}{d}$, $\alpha := \frac{k^{[2]}}{k^{[0]}}$, $\kappa := \frac{k_2^{[2]}\mu^{[2]}}{k_2^{[0]}\mu^{[0]}} = \alpha \frac{\mu^{[2]}}{\mu^{[0]}}$, $\beta = \frac{b}{d}$. Suppose that there exists an integer N for which one of the terms in the series is very large compared to the rest of the series. We thus can write

$$\mathcal{D}_0 = 1 - i\delta\kappa \tan(k^{[2]}b) \left[\frac{k^{[0]}}{k_{2N}^{[0]}} \operatorname{sinc}^2\left(k_{1N} \frac{w}{2}\right) + R_0 \right] = 0, \quad (\text{J21})$$

with

$$R_0 := \sum_{n \in (\mathbb{Z} - \{N\})} \frac{k^{[0]}}{k_{2n}^{[0]}} \operatorname{sinc}^2\left(k_{1n} \frac{w}{2}\right). \quad (\text{J22})$$

Let $k_1 := k_{1N}$ and $k_2 := k_{2N}^{[0]}$. It follows that

$$k_{1n} = k_1 + 2(n - N)\frac{\pi}{d} \Rightarrow k_{1n} \frac{w}{2} = k_1 \frac{w}{2} + (n - N)\pi \frac{w}{d} = k_1 \frac{w}{2} + (n - N)\pi\delta. \quad (\text{J23})$$

Now, for the $n = N$ term to be large, at the very least $\|k_1 \frac{w}{2}\| \ll 1$ and $k_{2N}^{[0]} \approx 0$. The first of these two conditions is synonymous with

$$\operatorname{sinc}\left(k_1 \frac{w}{2}\right) \approx 1. \quad (\text{J24})$$

A corollary is that

$$\sin\left(k_{1n} \frac{w}{2}\right) = \sin\left(k_1 \frac{w}{2}\right) \cos((n - N)\pi\delta) + \cos\left(k_1 \frac{w}{2}\right) \sin((n - N)\pi\delta) \approx \sin((n - N)\pi\delta). \quad (\text{J25})$$

We shall also assume that $\delta \approx 1$ so that $\sin(k_{1n} \frac{w}{2}) \approx \sin((n - N)\pi) \approx 0 \Rightarrow R_0 \approx 0$, whence

$$1 - i\delta\kappa \tan(k^{[2]}b) \frac{k^{[0]}}{k_2} \operatorname{sinc}^2\left(k_1 \frac{w}{2}\right) = 0, \quad (\text{J26})$$

which is the dispersion relation obtained by Rotman (1951).

If account is taken of (J24), then

$$1 - i\delta\kappa \tan(k^{[2]}b) \frac{k^{[0]}}{k_2} = 0, \quad (\text{J27})$$

which, when $\kappa = 1$ (i.e. the case $M^{[2]} = M^{[0]}$), constitutes the dispersion relation first obtained by Cutler (1944).

Let us examine this relation in detail. Since all the parameters in the Cutler dispersion relation are real, the latter has no solution unless $k_2 = \sqrt{(k^{[0]})^2 - (k_1)^2}$ is imaginary, that is, $k_2 = i\|\sqrt{(k^{[1]})^2 - (k_0)^2}\|$, which occurs if $|k_1| > k^{[0]}$. If we recall that imaginary k_2 corresponds to an evanescent (i.e. surface) wave, then we can say that the *Cutler mode* is associated with the excitation of a surface wave.

We now inquire as to the conditions in which the Cutler mode can be excited. The first step is to find the values of (k_1, ω) which are solutions of

$$1 - \delta\kappa \tan(k^{[2]}b) \frac{k^{[0]}}{\|k_2\|} = 0; |k_1| > k^{[0]}. \quad (\text{J28})$$

Another point of view is to consider k_1 to be the wavenumber (of a surface wave) to which is associated the phase velocity c_1 such that $k_1 = \frac{\omega}{c_1}$. Then it is easy to obtain (from J28)

$$c_1 = c^{[0]} \sqrt{\frac{1}{1 + \left[\delta\kappa \tan\left(\frac{\omega b}{c^{[2]}}\right)\right]^2}}. \quad (\text{J29})$$

This relation, first published in Gulyaev & Plesskii (1978), shows that even if $M^{[2]}$ is non-dispersive (recall that it was assumed, from the start, that $M^{[0]}$ is non-dispersive), then the phase velocity of the Cutler mode is dispersive, that is, $c_1 = c_1(\omega)$ [which, of course, is the reason why one speaks of a dispersion relation in connection with a (e.g. Cutler) mode].

Several remarks are in order: (i) the Cutler mode corresponds to a *slow (surface) wave* with respect to the bulk plane waves in Ω_0 , since $c_1 \leq c^{[0]}$, (ii) $c_1(\omega)$ is a periodic function of ω , since $c_1(\omega + \frac{l\pi c^{[2]}}{b}) = c_1(\omega)$; $\forall l \in \mathbb{N}$, (iii) $c_1(\omega) = c^{[0]}$ for $\frac{\omega b}{c^{[2]}} = l\pi$; $\forall l \in \mathbb{N}$, (iv) $c_1(\omega) = 0$ for $\frac{\omega b}{c^{[2]}} = (2l + 1)\frac{\pi}{2}$; $\forall l \in \mathbb{N}$, (v) the phase velocity of the Cutler mode is all the closer to the phase velocity of bulk waves in $M^{[0]}$ for all ω , the smaller is κ , (vi) on the contrary, for a Cutler mode with phase velocity very different from that of bulk waves in $M^{[0]}$, we must have a large contrast between the material properties of $M^{[0]}$ and $M^{[2]}$.

Let us now inquire as to the means of actually exciting a Cutler mode with an incident plane bulk wave. At first, this seems impossible (for the same reason it is not possible to excite a Love mode with an incident plane bulk wave). But we must not forget that the field in Ω_0 is

composed not only of diffracted plane bulk waves, but also of diffracted evanescent waves, the possibility of these waves to exist being due to the uneven (at present, periodically uneven) geometry of the stress-free surface at the site.

The discussion concerning the Cutler mode began with the assumptions: (i) the term in the expression of the diffracted field in Ω_0 corresponding to the N th order diffracted plane wave dominates all the other terms, and (ii) this diffracted wave is an evanescent wave, that is, $k_{2N}^{[0]}$ is imaginary. In the dispersion equation context, k_1 is a variable that has no particular connection with the solicitation. When the site is solicited by a plane bulk wave, then $k_{1N} = k_1^i + \frac{2\pi}{d}N$, with $k_1^i = k^{[0]} \sin \theta^i$ the factor directly related to the solicitation (θ^i the angle of incidence). Thus, for the N th order evanescent diffracted wave to be excited, we must have

$$k_1 = k_{1N} \Rightarrow k_1 = k_1^i + \frac{2\pi}{d}N, \quad (\text{J30})$$

with N such that $k_{2N}^{[0]} = i \|\sqrt{(k_{1N})^2 - (k^{[0]})^2}\|$. This so-called *coupling relation*, that is (J30), translates the fact that the periodic topography adds the momentum $\frac{2\pi}{d}N$ necessary to convert the incident bulk wave into an evanescent wave (whose phase velocity is smaller than that of the bulk wave, and whose horizontal wavenumber is therefore larger than the wavenumber $k^{[0]}$ of the incident bulk wave).

In order for a *resonance* to occur in the N th order mode, the frequency of one of the components of the spectrum of the excitation must be equal to a natural frequency of the mode. Although this is a necessary condition, it is not a sufficient condition, because we must also have $\|k_1\| = \|k_{1N}\| > \|k^{[0]}\|$.

A remark is in order concerning what happens when R_0 is not neglected in the expression of \mathcal{D}_0 . The subset, in this remainder term, involving the n for which k_{2n} is imaginary (i.e. corresponding to evanescent waves), will modify somewhat the (real) solutions of what formerly constituted the Cutler dispersion relation, whereas the subset involving the n for which k_{2n} is real (i.e. corresponding to propagative waves) adds an imaginary part to the (real) solutions of what formerly constituted the Cutler dispersion relation. Thus, the evanescent Cutler wave becomes a leaky wave, that is, a wave with complex k_1 .

J3.4 Solution of the zeroth-order dispersion relation when $M^{[1]} \neq M^{[0]}$: the quasi-Cutler mode

The dispersion relation (J19) has been studied in Wirgin (1988) and is a subset of the dispersion relations analysed in Section J2 of Appendix J. Not much more, other than what is revealed by a numerical analysis, can be added to the text in Sections J2 and J3.3, due to the complexity of (J19).

To make a long story short, one finds that the presence of the layer transforms the Cutler mode into a *quasi Cutler mode* which is all the closer to a Cutler mode the smaller is the layer thickness h and/or the closer the material parameters of the layer are to those of the substratum. If, on the other hand, h is not very small, and/or the material parameters of the layer are very different from those of the substratum, then the quasi-Cutler mode becomes an entity entirely different from that of the Cutler mode; in fact, it resembles a Love mode, so that it is better to represent the phenomena in terms of quasi-Love modes (as in Section J2) than in terms of quasi-Cutler modes.

APPENDIX K: COMPUTATION OF THE FIELDS $U^{[0]}$, $U^{[1]}$ AND $U^{[2]}$ FOR $N_B = \infty$

The quasi-modal coefficients $B_m^{[2]}(\omega)$, $\forall m \in \mathbb{N}$ are obtained by employing the partition procedure (i.e. reducing the infinite-order matrix in (J15) to a $M \times M$ matrix and the vectors to M -tuple vectors, solving the finite-order matrix equation so obtained, and increasing M until convergence is obtained of the successive M th order approximate solutions). Once the $B_m^{[2]}(\omega)$, $\forall m \in \mathbb{N}$ are computed in this manner, the field in the block domain Ω_2 is obtained via (G8). This field vanishes on the ground at the frequencies of occurrence of the *displacement-free base* modes of the block.

Let us next consider the field in the layer. Combining (H1)–(H4) leads, via (G5), to:

$$\begin{aligned} u^{[1]}(\mathbf{x}, \omega) &= \frac{2S(\omega) \exp \left[i \left(k_1^i x_1 - k_{02}^{[2]} h \right) \right] \cos \left(k_{02}^{[1]} x_2 \right)}{C_0^{[10]}} \\ &+ \sum_{n=-\infty}^{\infty} \sum_{m=0}^{\infty} B_m^{[2]} i \frac{\mu^{[2]} k_{2m}^{[2]} w}{\mu^{[0]} k_{n2}^{[0]} d} \frac{J_{mn}^-}{C_n^{[10]}} \sin \left(k_{2m}^{[2]} b \right) \exp \left[i k_{n1} \left(\frac{w}{2} + x_1 \right) \right] \\ &\times \left\{ \cos \left[k_{n2}^{[1]} (x_2 - h) \right] + i \frac{\mu^{[0]} k_{n2}^{[0]}}{\mu^{[1]} k_{n2}^{[1]}} \sin \left[k_{n2}^{[1]} (x_2 - h) \right] \right\}. \end{aligned} \quad (\text{K1})$$

Let us finally consider the field in the substratum. Combining (H1)–(H4) leads, via (G6), to:

$$\begin{aligned} u^{[0]}(\mathbf{x}, \omega) &= u^i(\mathbf{x}, \omega) \\ &+ S(\omega) \exp \left\{ i \left[k_1^i x_1 + k_{02}^{[0]} (x_2 - 2h) \right] \right\} \frac{\cos \left(k_{02}^{[1]} h \right) + i \frac{\mu^{[1]} k_{02}^{[1]}}{\mu^{[0]} k_{02}^{[0]}} \sin \left(k_{02}^{[1]} h \right)}{C_0^{[10]}} \\ &+ \sum_{n=-\infty}^{\infty} i \exp \left\{ i \left[k_{n1} x_1 + k_{n2}^{[0]} (x_2 - h) \right] \right\} \sum_{m=0}^{\infty} B_m^{[2]} \frac{\mu_2 k_{2m}^{[2]} w}{\mu^{[0]} k_{n2}^{[0]} d} \frac{J_{mn}^-}{C_0^{[10]}} \sin \left(k_{2m}^{[2]} b \right) \exp \left(i k_{n1} \frac{w}{2} \right). \end{aligned} \quad (\text{K2})$$

Expressions (K1) and (K2) indicate that both displacement fields $u^{[1]}(\mathbf{x}, \omega)$ and $u^{[2]}(\mathbf{x}, \omega)$ are composed of: (i) the field obtained in the absence of the blocks and induced in the layer or substratum by the incident plane wave, (ii) the field induced by the presence of the blocks, which appears as a field radiated by an infinite number of identical source distributions (each one related to a given block). In particular, each of these induced sources takes the form of a ribbon source of width w located at the base segment of a block when it is related to the zeroth-order quasi-mode (see the companion paper).

When a mode is excited (i.e. at a resonance frequency), one or several of the $B_m^{[2]}$ can become large, in which case it is possible for the fields to become large at resonance. This will be demonstrated in the numerical examples which follow.

Enhancing the absorption coefficient of a backed rigid frame porous layer by embedding circular periodic inclusions

J.-P. Groby,^{a)} O. Dazel, and A. Duclos

Laboratoire d'Acoustique de l'Université du Maine, UMR6613 CNRS/Université du Maine, Avenue Olivier Messiaen, F-72085 Le Mans Cedex 9, France

L. Boeckx

Huntsman Europe, Everlaan 45, B-3078 Everberg, Belgium

L. Kelders

Laboratory of Acoustic and Thermal Physics, KULeuven, Celestijnenlaan 200-D, B-3001 Heverlee, Belgium

(Received 30 November 2010; revised 31 August 2011; accepted 18 September 2011)

The acoustic properties of a porous sheet of medium static air flow resistivity (around $10\,000\text{ N m s}^{-4}$), in which a periodic set of circular inclusions is embedded and which is backed by a rigid plate, are investigated. The inclusions and porous skeleton are assumed motionless. Such a structure behaves like a multi-component diffraction grating. Numerical results show that this structure presents a quasi-total (close to unity) absorption peak below the quarter-wavelength resonance of the porous sheet in absence of inclusions. This result is explained by the excitation of a complex trapped mode. When more than one inclusion per spatial period is considered, additional quasi-total absorption peaks are observed. The numerical results, as calculated with the help of the mode-matching method described in this paper, agree with those calculated using a finite element method. © 2011 Acoustical Society of America. [DOI: 10.1121/1.3652865]

PACS number(s): 43.55.Ev, 43.20.Fn, 43.20.Ks, 43.20.Gp [KVH]

Pages: 3771–3780

I. INTRODUCTION

Porous materials suffer from a lack of absorption at low frequencies, when compared to their efficiency at higher frequencies. The purpose of the present article is to investigate an alternative to multi-layering by considering periodic inclusions embedded in a porous sheet attached to a rigid plate. This configuration results in a diffraction grating and a sonic-crystal,¹ constituted by the grating and its image or by the combination of grating, used in reflection. The inclusions and porous skeleton are assumed motionless.

The influence of a volume heterogeneity on absorption and transmission of a porous layer without rigid backing was previously investigated by use of the multipole method in Refs. 1 and 2. This was done by embedding a periodic set of high-contrast inclusions in a macroscopically homogeneous porous layer. The sizes of the inclusions are comparable to the wavelength in the porous medium, and the thickness and weight of the porous layer are relatively small for better efficiency when compared to those of usual multilayered packages. This leads either to an increase of the absorption coefficient, in the case of one layer of inclusions, or to band-gaps and a total absorption peak, in case of multi-layered set of inclusions (sonic crystal). The influence on the absorption was explained by mode excitation of the configuration, enabled by the periodic inclusions, whose structure leads to energy entrapment. Other works related to volume heterogeneities in macroscopically homogeneous porous material were carried out essentially by means of the homogenization proce-

dure,^{3,4} possibly leading to double porosity materials,⁵ when the wavelength is larger than the size of heterogeneities.

The influence of the irregularities of the rigid plate, on which porous sheets are often attached, on the absorption coefficient was previously investigated by use of the multimodal method in Ref. 6, by considering periodic rectangular irregularities filled with air. In the particular case of one irregularity per spatial period, this leads to a total absorption peak associated with excitation of the fundamental modified mode of the backed plate. This is excited thanks to the surface grating. Other works related to surface irregularities were carried out, notably related to local resonances associated with fractal irregularities.^{7,8}

Local resonance and trapped modes are another possibility to localize the field. Trapped modes were largely studied in waveguides⁹ or in periodic structures.¹⁰ Here, both theoretically and numerically, we investigate the changes in the absorption coefficient due to the embedding of a multiple inclusions grating in a rigid frame porous layer glued against a rigid wall. The effects of the modified mode of the plate and Bragg interference are clearly visible on the absorption curve, while a quasi-total (close to unity) absorption is obtained for a frequency below the fundamental quarter-wavelength resonance of the backed porous sheet. This peak exhibits some of the specific features of a trapped mode excitation.

II. FORMULATION OF THE PROBLEM

A. Description of the configuration

Both the incident plane acoustic wave and the porous layer are assumed to be invariant with respect to the

^{a)} Author to whom correspondence should be addressed. Electronic mail: Jean-Philippe.Groby@univ-lemans.fr

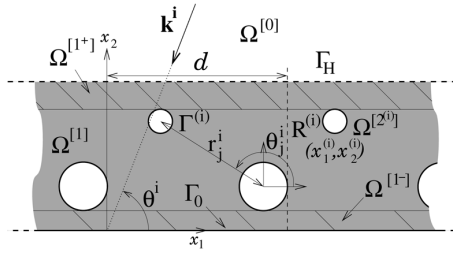


FIG. 1. Cross-sectional plane view of the configuration.

Cartesian coordinate x_3 . A cross-sectional $x_1 - x_2$ plane view of the 2D scattering problem is shown Fig. 1.

Before the addition of the cylindrical inclusions, the layer is made of a porous material saturated by air (e.g., a foam), which is modeled (by homogenization) as a macroscopically homogeneous equivalent fluid $M^{[1]}$. The porous sheet is backed by a rigid surface. The upper and lower flat, mutually-parallel boundaries of the layer, whose x_2 coordinates are H and 0 , are designated by Γ_H and Γ_0 , respectively. $M^{[0]}$, the ambient fluid that occupies $\Omega^{[0]}$, and $M^{[1]}$ are in firm contact through Γ_H , making the pressure and normal velocity continuous across Γ_H ($[p(\mathbf{x})] = 0$ and $[\rho^{-1}\partial_n p(\mathbf{x})] = 0$, wherein \mathbf{n} denotes the generic unit vector normal to a boundary and ∂_n designates the operator $\partial_n = \mathbf{n} \cdot \nabla$). Γ_0 is rigid [Neumann type boundary conditions, $\partial_n p(\mathbf{x}) = 0$].

N^c inclusions, with a common spatial periodicity d , are embedded in the porous layer and create a diffraction grating in the x_1 direction. Depending on the arrangement of the N^c inclusions in the unit cell, a diffraction grating or a sonic-crystal of period d^c can be formed ($d^c \leq d$). The set of indices by which the cylinders within the unit cell are identified is denoted by $\mathcal{N}^c \in \mathbb{N}$. The j th inclusion occupies the disk $\Omega^{[2^{(j)}]}$ of radius $R^{(j)}$ and is centered at $\mathbf{x}^{(j)} = (x_1^{(j)}, x_2^{(j)})$, $j \in \mathcal{N}^c$. The inclusions are infinitely rigid (Neumann type boundary conditions on $\Gamma^{(j)}$), i.e., the contrast between the material that occupies $\Omega^{[2^{(j)}]}$ and $M^{[1]}$ is very large. This also means that the inclusions can consist in rigid tubes or holes posteriorly processed to create a rigid bound, because the only important thing is the Neumann type boundary conditions at the exterior boundary of the inclusion. This process can be used to reduce the weight of the final structure. Two subspaces $\Omega^{[1^{\pm}]} \in \Omega^{[1]}$ are also defined, corresponding to the upper and lower part, respectively, of the porous layer without inclusions. The inclusions and porous skeleton are assumed motionless.

The total pressure, wavenumber, and wave speed are denoted by the generic symbols p , k , and c , respectively, with $p = p^{[0]}$, $k = k^{[0]} = \omega/c^{[0]}$ in $\Omega^{[0]}$, and $p = p^{[1]}$, $k = k^{[1]} = \omega/c^{[1]}$ in $\Omega^{[1]}$, wherein $\omega = 2\pi\nu$ is the angular frequency, with ν the frequency.

Rather than to solve directly for the pressure $\bar{p}(\mathbf{x}, t)$ [with $\mathbf{x} = (x_1, x_2)$], we prefer to deal with $p(\mathbf{x}, \omega)$, related to $\bar{p}(\mathbf{x}, t)$ by the Fourier transform $p(\mathbf{x}, \omega) = \int_{-\infty}^{\infty} \bar{p}(\mathbf{x}, t) e^{i\omega t} dt$. Henceforth, we drop the ω in $p(\mathbf{x}, \omega)$ so as to denote the latter by $p(\mathbf{x})$.

The wavevector \mathbf{k}^i of the incident plane wave lies in the sagittal plane and the angle of incidence is θ^i measured

counterclockwise from the positive x_1 axis. The incident wave propagates initially in $\Omega^{[0]}$ and is expressed by $p^i(\mathbf{x}) = A^i e^{i(k_1^i x_1 - k_2^{[0]i}(x_2 - H))}$, wherein $k_1^i = -k^{[0]i} \cos \theta^i$, $k_2^{[0]i} = k^{[0]i} \sin \theta^i$, and $A^i = A^i(\omega)$ is the signal spectrum.

The plane wave nature of the incident wave and the periodic nature of $\bigcup_{j \in \mathcal{N}^c} \Omega^{[2^{(j)}]}$ imply the Floquet relation

$$p(x_1 + qd, x_2) = p(x_1, x_2) e^{ik_1^i qd}; \forall \mathbf{x} \in \mathbb{R}^2; \forall q \in \mathbb{Z}. \quad (1)$$

Consequently, it suffices to examine the field in the central cell of the plate.

The uniqueness of the solution to the forward-scattering problem is ensured by the radiation condition:

$$p^{[0]}(\mathbf{x}) - p^i(\mathbf{x}) \sim e^{ik^{[0]i} \cdot \mathbf{x}} / \sqrt{|\mathbf{x}|}, \quad |\mathbf{x}| \rightarrow \infty, \quad x_2 > H. \quad (2)$$

B. Material modeling

Rigid frame porous material M is modeled using the Johnson-Champoux-Allard model. The dynamic compressibility K and dynamic density ρ , linked to the sound speed through $c = \sqrt{1/(K\rho)}$ are^{11,12}

$$\frac{1}{K} = \frac{\gamma P_0}{\phi \left(\gamma - (\gamma - 1) \left(1 + i \frac{\omega'_c}{\text{Pr}\omega} G(\text{Pr}\omega) \right)^{-1} \right)}, \quad (3)$$

$$\rho = \frac{\rho_f \alpha_\infty}{\phi} \left(1 + i \frac{\omega_c}{\omega} F(\omega) \right),$$

wherein $\omega_c = \sigma\phi/\rho_f \alpha_\infty$ is the Biot frequency, $\omega'_c = \sigma'\phi/\rho_f \alpha_\infty$, γ the specific heat ratio, P_0 the atmospheric pressure, Pr the Prandtl number, ρ_f the density of the fluid in the (inter-connected) pores, ϕ the open porosity, α_∞ the high frequency limit of the tortuosity, σ the static air flow resistivity, and σ' the static thermal resistivity. The scaling functions $G(\text{Pr}\omega)$ ¹³ and $F(\omega)$ ¹⁴ are given by

$$G(\text{Pr}\omega) = \sqrt{1 - i\eta\rho_f \text{Pr}\omega \left(\frac{2\alpha_\infty}{\sigma'\phi\Lambda'} \right)^2}, \quad (4)$$

$$F(\omega) = \sqrt{1 - i\eta\rho_f \omega \left(\frac{2\alpha_\infty}{\sigma\phi\Lambda} \right)^2},$$

where η is the dynamic viscosity of the fluid, Λ' the thermal characteristic length, and Λ the viscous characteristic length. The “static thermal resistivity” is related to the thermal characteristic length through $\sigma' = 8\alpha_\infty \eta / \phi \Lambda'^2$ (Ref. 13).

While the configuration is similar to those already studied in Refs. 1 and 2, it is different in that the porous sheet is backed by a rigid plate, but also more complex in that the unit cell can be composed of more than one non overlapping inclusion, when the x_2 -coordinates of the center of two inclusions are separated by a distance lower than the sum of their radii. In this latter case, the interaction between these inclusions cannot be modeled as exposed in Ref. 1, and a more complex interaction model should be employed.¹⁵ The method of solution is also briefly summarized hereafter.

C. Field representations in $\Omega^{[0]}$ and $\Omega^{[1\pm]}$

The continuity relations across the interfaces Γ_H and Γ_0 are first considered in Sec. III A. The field representations in $\Omega^{[0]}$ and $\Omega^{[1\pm]}$ are needed as the first step. The continuity conditions across $\Gamma^{(j)}$, $\forall j \in \mathcal{N}^c$ will be treated in Sec. III B.

Separation of variables, the radiation condition, and the Floquet theorem lead to the representation

$$p^{[0]}(x) = \sum_{q \in \mathbb{Z}} \left[e^{-ik_{2q}^{[0]}(x_2-H)} \delta_q + R_q e^{ik_{2q}^{[0]}(x_2-H)} \right] e^{ik_{1q} x_1}, \quad \forall \mathbf{x} \in \Omega^{[0]}, \quad (5)$$

wherein δ_q is the Kronecker symbol, $k_{1q} = k_1^i + 2q\pi/d$, $k_{2q}^{[0]} = \sqrt{(k^{[0]})^2 - (k_{1q})^2}$ with $\text{Re}(k_{2q}^{[0]}) \geq 0$ and $\text{Im}(k_{2q}^{[0]}) \geq 0$. R_q is the reflection coefficient of the plane wave denoted by the subscript q .

It is first convenient to use Cartesian coordinates (x_1, x_2) to represent the field in $\Omega^{[1\pm]}$. This field is composed of the diffracted field in the plate and the fields scattered by the inclusions, whose form depends on the position of \mathbf{x} , either below or above the inclusions.¹⁶ Referring to Ref. 1, whatever the arrangement of the inclusions, x_2 is always larger than $\max_{j \in \mathcal{N}^c} (x_2^{(j)} + R^{(j)})$ in $\Omega^{[1+]}$, while x_2 is always smaller than $\min_{j \in \mathcal{N}^c} (x_2^{(j)} - R^{(j)})$ in $\Omega^{[1-]}$. The total field in $\Omega^{[1\pm]}$ can be written in Cartesian coordinates as

$$p^{[1\pm]}(\mathbf{x}) = \sum_{q \in \mathbb{Z}} \left(f_q e^{-ik_{2q}^{[1\pm]} x_2} + g_q e^{ik_{2q}^{[1\pm]} x_2} \right) e^{ik_{1q} x_1} + \sum_{q \in \mathbb{Z}} \sum_{j \in \mathcal{N}^c} \sum_{l \in \mathbb{Z}} K_{ql}^{\pm} B_l^{(j)} e^{i(k_{1q}(x_1-x_1^{(j)})) \pm k_{2q}^{[1\pm]}(x_2-x_2^{(j)})}, \quad (6)$$

wherein $B_l^{(j)}$ are the coefficients of the field scattered by the j th cylinder of the unit cell, f_q and g_q are the coefficients of the diffracted waves inside the layer associated with the plane wave denoted by q , and $K_{ql}^{\pm} = 2(-i)^l e^{\pm i l \theta_q} / dk_{2q}^{[1\pm]}$ with θ_q such that $k^{[1\pm]} e^{i \theta_q} = k_{1q} + ik_{2q}^{[1\pm]}$ (Ref. 15).

III. DETERMINATION OF THE ACOUSTIC PROPERTIES OF THE CONFIGURATION

A. Application of the continuity conditions across Γ_H and Γ_0

The continuity of the pressure field and of the normal component of the velocity is applied across Γ_H and the Neumann condition is applied on Γ_0 . After introducing the proper field representations therein, i.e., Eqs. (5) and (6), and making use of the orthogonality relation $\int_{-d/2}^{d/2} e^{i(k_{1n}-k_{1l})x_1} dx_1 = d\delta_{nl}$, $\forall (l, n) \in \mathbb{Z}^2$, a linear set of equations results. After some algebra and rearrangements, this linear set reduces to a coupled system of equations for solution of R_q , f_q and g_q in terms of $B_l^{(j)}$.

B. Application of the multipole method

The expressions of f_q and g_q in terms of $B_l^{(j)}$ are introduced in the so-called diffracted field inside the layer. The latter field accounts for the direct, diffracted waves inside the layer and for the reflected waves at the boundaries Γ_0 and Γ_H , previously scattered by each inclusions. This expression, when compared with the expression of the direct scattered field by the inclusions, is valid in the whole domain $\Omega^{[1]}$. To proceed further, the Cartesian form of this field is converted to the cylindrical harmonic form in the polar coordinate system attached to each inclusion, as stated for example in Ref. 1. Effectively, central to the multipole method are the local field expansions or multipole expansions around each inclusion.

Introducing $A_L^{(j)}$, the coefficient of the locally-incident field, the pressure field in the vicinity of the J th inclusion, in terms of its attached coordinate system, reads as

$$p^{[1]}(r_J) = \sum_{L \in \mathbb{Z}} B_L^{(J)} H_L^{(1)}(k^{[1]} r_J) e^{iL\theta_J} + \sum_{L \in \mathbb{Z}} \left[\sum_{l \in \mathbb{Z}} S_{L-l} B_l^{(J)} + \sum_{j \neq J} \sum_{l \in \mathbb{Z}} S_{L-l}^{(j)} B_l^{(j)} \right] + \sum_{j \in \mathcal{N}^c} \sum_{l \in \mathbb{Z}} \sum_{q \in \mathbb{Z}} Q_{Llq}^{(j)} B_l^{(j)} + \sum_{q \in \mathbb{Z}} F_{qL}^{(J)} \left] J_L(k^{[1]} r_J) e^{iL\theta_J} = \sum_{L \in \mathbb{Z}} \left[B_L^{(J)} H_L^{(1)}(k^{[1]} r_J) + A_L^{(J)} J_L(k^{[1]} r_J) \right] e^{iL\theta_J}, \quad (7)$$

with

$$F_{qL}^{(J)} = \frac{2\delta_q \alpha_q^{[0]}}{D_q} \cos(k_{2q}^{[1]} x_2^{(J)} - L\theta_q) e^{ik_{1q}^{[1]} x_1^{(J)}}, S_{L-l} = \sum_{i=1}^{\infty} H_{L-l}^{(1)}(k^{[1]} id) \left[e^{ik_i id} + (-1)^{L-l} e^{-ik_i id} \right], Q_{Llq}^{(j)} = \frac{2(-i)^{L-l} e^{ik_{1q}(x_1^{(j)}-x_1^{(j)})}}{dk_{2q}^{[1]} D_q} \left[(\alpha_q^{[1]} - \alpha_q^{[0]}) e^{ik_{2q}^{[1]} H} \times \cos(k_{2q}^{[1]}(x_2^{(j)} - x_2^{(j)}) - (l-L)\theta_q) + \alpha_q^{[1]} \cos(k_{2q}^{[1]}(x_2^{(j)} + x_2^{(j)} - H) - (l+L)\theta_q) + i\alpha_q^{[0]} \sin(k_{2q}^{[1]}(x_2^{(j)} + x_2^{(j)} - H) - (l+L)\theta_q) \right], D_q = \alpha_q^{[0]} \cos(k_{2q}^{[1]} H) - i\alpha_q^{[1]} \sin(k_{2q}^{[1]} H), \quad (8)$$

wherein S_{L-l} is the lattice sum often referred to as the Schlömilch series for non-dissipative material, $H_L^{(1)}$ is the L th order Hankel function of the first kind, J_L is the L th order Bessel function, and $\alpha_q^{[j]} = k_{2q}^{[j]} / \rho^{[j]}$, $j = 0, 1$. The terms $S_{L-l}^{(j)}$ account for the coupling between the multiple inclusions inside the unit cell and take the form

$$S_{Ll}^{(j,j)} = \sum_{q \in \mathbb{Z}} \frac{(-i)^{L-l} 2e^{\pm i(L-l)\theta_q}}{dk_{2q}^{[1]}} \times e^{i(k_{1q}(x_1^{(j)}-x_1^{(j)}) \pm k_{2q}^{[1]}(x_2^{(j)}-x_2^{(j)}))} (1 - \delta_{lj}), \quad (9)$$

wherein the signs + and - correspond to $x_2^j \geq x_2^i$ and $x_2^j \leq x_2^i$, respectively, which can be found in Ref. 1 when $|x_2^{(j)} - x_2^{(i)}| > R^{(i)} + R^{(j)}$ or

$$S_{Ll}^{(j)} = \left[\mathbf{H}_{L-l}^{(1)}(r_J^j) e^{i(l-L)\theta_j^j} + \sum_{o \in \mathbb{Z}} S_{o-l} B_l^{(j)} J_{L-o}(k^{[1]} r_J^j) e^{i(o-L)\theta_j^j} \right] (1 - \delta_{lj}), \quad (10)$$

when $|x_2^{(j)} - x_2^{(i)}| \leq R^{(i)} + R^{(j)}$. This latter form agrees with the one found in Ref. 15 when the inclusions are aligned inside the unit cell, i.e., $x_2^{(j)} = x_2^{(i)}$, $\forall j \in \mathcal{N}^c$, which imposes $\theta_j^j = 0$ or $\theta_j^j = \pi$. In Eq. (10), (r_J^j, θ_j^j) is the coordinate of $\mathbf{x}^{(j)}$ in the polar coordinate system attached to the J th inclusions, i.e., centered at $\mathbf{x}^{(j)}$.

Finally, it is well known that the coefficients of the scattered field and those of the locally-incident field are linked by a matrix relation derived from the boundary condition on $\Gamma^{(j)}$ only, i.e., $B_L^{(j)} = V_L^{(j)} A_L^{(j)}$, wherein $V_L^{(j)}$ are the cylindrical harmonic reflection coefficients. These coefficients take the form $V_L^{(j)} = -\dot{\mathbf{H}}_L^{(1)}(k^{[1]} R^{(j)}) / \dot{\mathbf{J}}_L(k^{[1]} R^{(j)})$ in the case of Neumann type boundary conditions, with $\dot{\chi}(x) = d\chi/dx$, χ being either Hankel or Bessel functions. Introducing the expression of $A_L^{(j)}$ derived from Eq. (7) in the previous relation gives rise to the linear system of equations for the solution of $B_L^{(j)}$. This linear system may be written in the matrix form, where \mathbf{B} denotes the infinite column matrix of components $B_L^{(j)}$,

$$(\mathbf{I} - \mathbf{V}(\mathbf{S} + \mathbf{Q}))\mathbf{B} = \mathbf{V}\mathbf{F}, \quad (11)$$

wherein \mathbf{I} is the identity matrix and \mathbf{F} is a vector of components $\sum_{q \in \mathbb{Z}} F_{qL}^{(j)}$. This accounts for the solicitation of the J th inclusion by a wave that is previously diffracted inside the layer. \mathbf{V} is a diagonal square matrix of components $V_L^{(j)}$. \mathbf{S} and \mathbf{Q} are two matrices of components $S_{L-l} + S_{L-l}^{(j)}$, which account for the coupling between the J -th and the j -th inclusion inside the layer, and $\sum_{q \in \mathbb{Z}} Q_{Llq}^{(j)}$ accounts for the coupling between the J th and the j th inclusion through waves diffracted by the layer.

The expressions of the components involved in $(\mathbf{I} - \mathbf{V}(\mathbf{S} + \mathbf{Q}))\mathbf{B} = \mathbf{V}\mathbf{F}$ are identical to those found in Ref. 1, when the half-space behind the layer vanishes and when the center of the cylinders are defined as they are in the present article.

C. Evaluation of the fields, reflection and absorption coefficients

Once the linear system (11) is solved, the expression of R_q in terms of $B_l^{(j)}$ reads as

$$R_q = \frac{\alpha^{[0]i} \cos(k_2^{[1]j} L) + i\alpha^{[1]i} \sin(k_2^{[1]j} L)}{D_i} + \sum_{q \in \mathbb{Z}} \sum_{j \in \mathcal{N}^c} \sum_{l \in \mathbb{Z}} \frac{4(-i)^l \alpha_q^{[1]}}{dk_{2q}^{[1]} D_q} B_l^{(j)} \cos(k_2^{[1]} x_2^{(j)} - l\theta_q) e^{-ik_{1q} x_1^{(j)}}. \quad (12)$$

The first term corresponds to the reflection coefficient in terms of waves in absence of inclusion, i.e., for $q=0$ or for the incident plane component indexed by i , and the second term accounts for the inclusions.

Introduced in Eq. (5), the reflected field is expressed as a sum of the field with inclusions and without. In case of an incident plane wave with spectrum $A^i(\omega)$, the conservation of energy relation takes the form

$$1 = \mathcal{R} + \mathcal{A}, \quad (13)$$

with \mathcal{R} and \mathcal{A} the hemispherical reflection and absorption coefficients, respectively. \mathcal{R} is defined by

$$\mathcal{R} = \sum_{q \in \mathbb{Z}} \frac{\text{Re}(k_{2q}^{[0]}) \|R_q\|^2}{k_2^{[0]i} \|A^i\|^2} = \sum_{q=-\tilde{q}_-}^{\tilde{q}_+} \frac{k_{2q}^{[0]} \|R_q\|^2}{k_2^{[0]i} \|A^i\|^2}, \quad (14)$$

wherein \tilde{q}_\mp are such that $\tilde{q}_\mp < d/2\pi(k^{[0]} \pm k_1^i) < \tilde{q}_\mp + 1$ and the expression of R_q are given by Eq. (12). \mathcal{A} takes the form⁶

$$\mathcal{A} = \frac{1}{dk_2^{[0]i} \|A^i\|^2} (\mathcal{A}_D + \mathcal{A}_S), \quad (15)$$

wherein

$$\mathcal{A}_D = \frac{\rho^{[0]}}{\text{Re}(\rho^{[1]})} \int_{\Omega_{[1]}} \text{Im} \left((k^{[1]})^2 \right) \|p^{[1]}(\mathbf{x})\|^2 d\bar{\omega} \quad (16)$$

is the inner absorption of domain $\Omega^{[1]}$. $d\bar{\omega}$ is the differential element of surface in the sagittal plane and

$$\mathcal{A}_S = \text{Re} \int_{\Gamma_H} \frac{\rho^{[0]} \text{Im}(\rho^{[1]})}{\rho^{[1]} \text{Re}(\rho^{[1]})} p^{[1]*}(\mathbf{x}) \nu_{01} \cdot \nabla p^{[1]}(\mathbf{x}) d\gamma \quad (17)$$

is the surface absorption related to interfaces Γ_H . $d\gamma$ is the differential arc length in the cross-sectional plane, ν_{01} is the outward-pointing unit vector to the boundary Γ_H , and p^* is the complex conjugate of p .

\mathcal{A}_S accounts for the absorption induced by the viscous dissipation at the interfaces. Indeed, it is obvious from Eq. (17) that \mathcal{A}_S does not vanish because of the presence of $\text{Im}(\rho^{[1]})$, which is a consequence of the modeling of viscous dissipation phenomenon.¹⁷

Because of the complicated shape of $\Omega^{[1]}$ and the non-vanishing term \mathcal{A}_S \mathcal{A} will not be calculated by the expression given in Ref. 15, but rather by $\mathcal{A} = 1 - \mathcal{R}$.

IV. NUMERICAL RESULTS, VALIDATION AND DISCUSSION

The infinite sum $\sum_{q \in \mathbb{Z}}$ over the indices of k_{1q} depends on the frequency and on the period of the grating. An empirical truncation rule is employed, as in Refs. 1, 2, and 6, and determined by performing a large number of numerical experiments $\sum_{q=-Q_-}^{Q_+}$ such that $Q_\mp = \text{int}(d/2\pi(3\text{Re}(k^{[1]} \pm k_1^i)) + 10)$. In these equations, $\text{int}(a)$ represents the integer part of a .

The infinite sum $\sum_{m \in \mathbb{Z}}$ over the indices of the modal representation of the diffracted field by a cylinder is

truncated¹⁸ as $\sum_{m=-M}^M$, such that $M = \text{int}(\text{Re}(4.05 \times (k^{[1]}R)^{1/3} + k^{[1]}R)) + 10$.

Finally, the infinite sum (lattice sum) embedded in S_{L-l} in Eqs. (8) and (10) $\sum_{i=1}^{\infty}$ is found to be slowly convergent, particularly in the absence of dissipation, and is found to be strongly dependent on the index $L-l$. A large literature exists on this problem.^{19,20} Here, the fact that the medium $M^{[1]}$ is dissipative greatly simplifies the evaluation of the Schlömilch series. The superscript l in $S_{L-l}^{(l)}$ identifies the integer over which the sum is performed, i.e., $\sum_{i=1}^l$. This sum is carried out until the conditions $|\text{Re}((S_{L-l}^{(l+1)} - S_{L-l}^{(l)})/S_{L-l}^{(l)})| \leq 10^{-5}$ and $|\text{Im}((S_{L-l}^{(l+1)} - S_{L-l}^{(l)})/S_{L-l}^{(l)})| \leq 10^{-5}$ are reached.²

Numerical calculations have been performed for various geometrical parameters whose values are reported in Table I, and within the frequency range of audible sound, particularly at low frequencies. For all calculations, the ambient and saturating fluid is air ($\rho^{[0]} = \rho_f = 1.213 \text{ kg m}^{-3}$, $c^{[0]} = \sqrt{\gamma P_0 / \rho_f}$, with $P_0 = 1.01325 \times 10^5 \text{ Pa}$, $\gamma = 1.4$, and $\eta = 1.839 \times 10^{-5} \text{ kg m}^{-3} \text{ s}^{-1}$). Two of the main constraints in designing acoustically absorbing materials are the size and weight of the configuration. Particular attention is placed on the thickness and the frequencies of the absorption gain, which have to be as small as possible. The absorption gain is defined in reference to the absorption of the same configuration without inclusion embedded. The initial configuration consists in a 2 cm thick porous sheet of Fireflex (Recticel, Belgium) backed by a rigid plate. The material characteristics are reported in Table II and were determined by use of methods described in Refs. 11, 21–23. Circular cylinders of 7.5 mm radius are embedded with a spatial periodicity of 2 cm. As mentioned in Sec. II A, the inclusions can be constituted of various material (or geometries like tubes), while the outside boundary is circular and can be modeled with a Neumann type boundary condition.

A. One inclusion per spatial period

We first consider only one inclusion centered in the unit cell, i.e., $(x_1^{(1)}, x_2^{(1)}) = (d/2, H/2) = (1 \text{ cm}, 1 \text{ cm})$. The first two modified modes of the plate, which are excited because of the periodic arrangement of the inclusions, Appendix A, have frequencies $\nu_{(1,1)} \approx 14 \text{ kHz}$ and $\nu_{(2,1)} \approx 16 \text{ kHz}$. The attenuation associated with both modes is relatively large (see Fig. 3).

Different types of waves correspond to each kind of mode related to the grating, i.e., mode of the grating (MG) and modified mode of the backed layer (MMBL): evanescent waves in $\Omega^{[1]}$ (and also in $\Omega^{[0]}$) for the MG, and evanescent

TABLE I. Geometry of the considered configurations.

N	d (cm)	H (cm)	$(x_1^{(j)}, x_2^{(j)})$ (cm)	$R^{(j)}$ (cm)
C1	1	2	(1,1)	0.75
C2	2	3.5	$(x_1^{(1)}, x_2^{(1)}) = (1, 1)$ $(x_1^{(2)}, x_2^{(2)}) = (0.5, 1 + \sqrt{3}d/2)$	$R^{(1)} = 0.75$ $R^{(2)} = 0.5$

TABLE II. Parameters of the porous foam used in the article.

ϕ	α_{∞}	Λ (μm)	Λ' (μm)	σ (N s m^{-4})	ν_c (Hz)
0.95	1.42	180	360	8900	781

waves in $\Omega^{[0]}$ and propagative waves in $\Omega^{[1]}$ for the MMBL. In order to determine which type of mode is excited by the plane incident wave, we have plotted in Fig. 2 the transfer function as calculated by $\text{TF}(\nu) = p(\mathbf{x}, \nu) / p^{[0]i}(\mathbf{x}, \nu)$ on Γ_0 ($x_2 = 0$) at 1 cm from the center of the inclusion (between two inclusions), when excited at normal incidence. The transfer function is separated on the different intervals corresponding to the different type of waves that are involved in the total pressure calculation: $\text{TF}(\nu)$ is the total transfer function, $\text{TF}_1(\nu)$ is the contribution of the propagative waves in both $\Omega^{[0]}$ and $\Omega^{[1]}$, $\text{TF}_2(\nu)$ is the contribution of the evanescent waves in $\Omega^{[0]}$ and propagative ones in $\Omega^{[1]}$, and $\text{TF}_3(\nu)$ is the contribution of the evanescent waves in both $\Omega^{[0]}$ and $\Omega^{[1]}$. The transfer function possesses a large peak at $\approx 15 \text{ kHz}$, around $\nu_{(1,1)}$ and $\nu_{(2,1)}$. This also proves that the MMBL are the most excited modes, related to the grating, around these frequencies. The peak results from a continuous transition between evanescent waves in both materials to evanescent waves in the air medium (around 13 kHz, Fig. 2). This also means that this peak is neither a MMBL nor a MG, but results from a complex combination of these two types of modes, with a structure closer to that of the MMBL. Because of this structure, the energy is trapped in the layer, leading to an increase in the absorption coefficient. The translation of the excitation of these modes in terms of absorption, i.e., the peak around 17 kHz in Fig. 3, is smaller than the one depicted in Ref. 6, because (i) the attenuation associated with the modes in the present configuration is larger, and (ii) the static flow resistivity of the foam considered here is larger. The design of a structure composed of a layer with inclusions embedded is more based on compromises than with irregularities of the rigid backing.⁶ These compromises relate the spatial periodicity, the radius of the

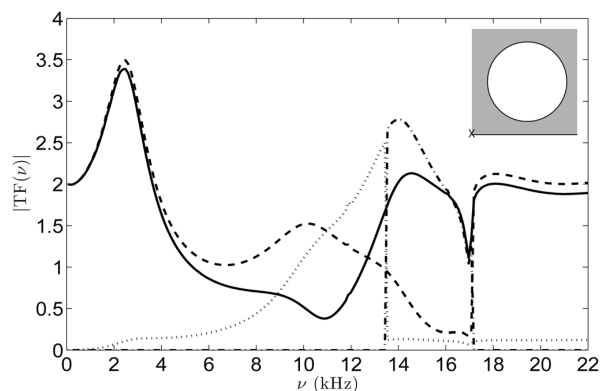


FIG. 2. Configuration C1 – Transfer function, $\text{TF}(-)$, on Γ_0 at 1 cm from the center of the inclusion (between two inclusions), and its different contributions when the configuration is excited at normal incidence: $(- -)$ TF_1 , (\dots) TF_2 , and $(-\cdot)$ TF_3 .

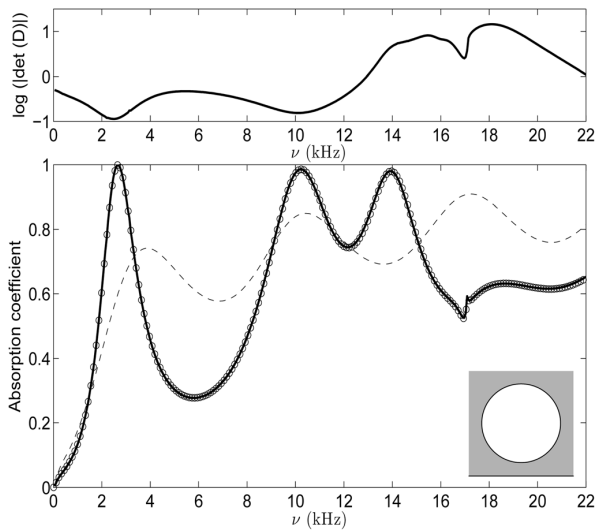


FIG. 3. Configuration C1 – Absorption coefficient of a $H=2$ cm thick porous sheet of Fireflex backed by a rigid plate (---) without inclusion embedded and (—) with a $R=7.5$ mm radius circular cylinder embedded per spatial period $d=2$ cm, when the configuration is excited at normal incidence. The Finite Element result is plotted with (o). The absolute value of the determinant of the propagation matrix $\mathbf{D} = \mathbf{I} - \mathbf{V}(\mathbf{S} + \mathbf{Q})$ is plotted on top of the figure.

inclusion, or better, the ratio R/d , which cannot be too small and which constrains the layer thickness and the properties of the latter.

Figure 3 depicts the absorption coefficient calculated for this geometry. This result was validated numerically by matching the absorption coefficient calculated with the present method with the one calculated with a finite element method. Quadratic finite elements were used to approximate the pressure inside the unit cell, thereby leading to a discretized problem of 2196 elements and 1238 nodes. The periodicity relation, i.e., the Floquet condition, was applied on both sides of the discretized domain, i.e., at each nodes of x_1 -coordinate 0 and d . For this periodicity relation to be correctly implemented, these two sides were discretized with similar

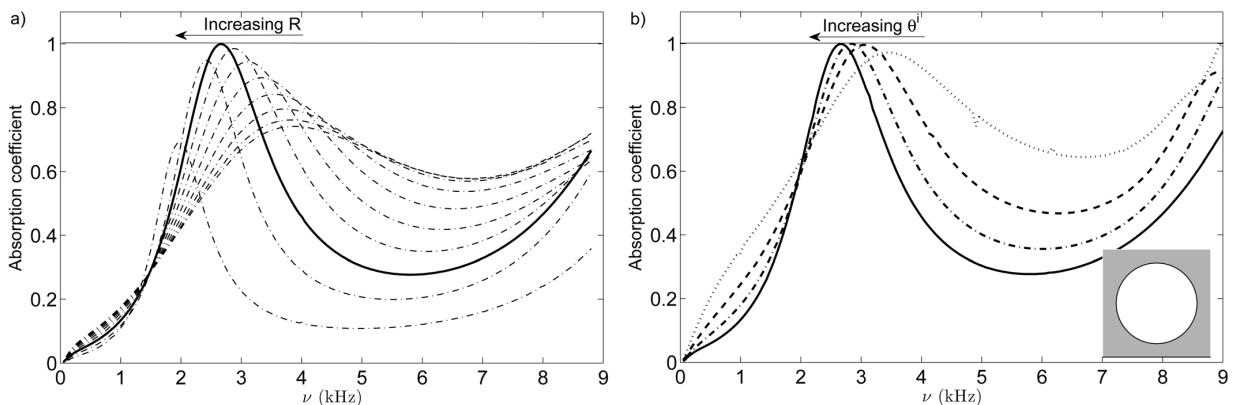


FIG. 4. Configuration C1 – Absorption coefficient of a $H=2$ cm thick porous sheet of Fireflex backed by a rigid plate (a) for a radius R increasing from 1.5 mm to 9.5 mm (with a step of 1 mm) circular cylinder embedded per spatial period $d=2$ cm, when the configuration is excited at normal incidence, and (b) for $R=7.5$ mm radius circular cylinder embedded per spatial period $d=2$ cm, when the configuration is excited at $\theta^i = \pi/2$ (—), $\theta^i = \pi/3$ (- - -), $\theta^i = \pi/4$ (- · - ·), and $\theta^i = \pi/6$ (· · ·).

nodes, i.e., identical x_2 -coordinates. The results match well, thus validating the described method (see Fig. 3). When compared to the finite element method, the mode-matching technique enables analytic calculations and is less time consuming (approximately a quarter of the time) for the configurations and frequency range considered in this article. This is due to the fact that the dimensions and frequency range considered therein enable to account only for a small number of terms in the infinite sums over m, q , and for the correct evaluation of the lattice sum.

Because of the rigid backing, which acts as a perfect mirror, the response of the configuration possesses some particular features related to multi-layered grating. We also introduce $d_2 = 2x_2^{(1)}$, the distance between the center of the circular cylinder and the center of its image. Each grating interferes with one another at the Bragg frequencies $\nu_{(n)}^b = n\text{Re}(c^{(1)})/2d_2$. In particular, the first Bragg frequency, $\nu_{(1)}^b \approx 6$ kHz, is largely employed to determine the central frequency of the band gaps for phononic crystals corresponding to a maximum of reflected energy and to a minimum of transmitted energy—band gaps—in case of phononic crystal. The absorption coefficient also presents a minimum at $\nu_{(1)}^b$.

A particular feature of the response of this configuration is that the absorption coefficient presents a peak close to unity at a low frequency ν_l below the so-called fundamental quarter-wave resonance frequency, i.e., below what can be associated with an essential spectrum.

A sensitivity analysis, performed by varying one parameter while the others are kept constant at value, shows that the radius of the inclusion has a large influence on ν_l and on the amplitude of the corresponding absorption peak. The radius R was varied from 1.5 mm to 9.5 mm, Fig. 4(a). In terms of amplitude of the absorption peak, $R=7.5$ mm is the optimal value, while ν_l decreases when R increases. In contrast, $d=2$ mm is the optimal value in terms of the peak amplitude, but ν_l increases when d increases from 1.75 cm to 3.75 cm. The spatial periodicity of the arrangement acts inversely on ν_l than it does on the frequencies of the modes closely related to d like the MMBL and the MG, Appendix.

In fact, the amplitude of the absorption peak increases with the filling ratio R/d until being close to unity and drastically decreases after this value. This is either because the wave can no longer propagate in the layer towards the rigid backing and is mainly reflected on the circular grating, or because the density of inclusion becomes insignificant. In the same way, when the angle of incidence decreases $[\pi/2; \pi/6]$, the ν_i increases in opposition to the frequencies of the MMBL and of the MG. The amplitude of the peak is quite close to unity until $\pi/6$. For smaller values of incidence angle, the amplitude of this low frequency peak begins to decrease, Fig. 4(b).

When $R = 7.5$ mm and $d = 20$ mm, ν_i is all the smaller that the inclusion is distant from the rigid backing, i.e., that $x_2^{(1)}$, the center of the inclusion, is large. The amplitude of the peak is close to unity whatever $x_2^{(1)}$, in [0.8 cm; 1.2 cm] the range conditioned by the layer thickness and the inclusion radius.

The features of this low frequency absorption peak resembles phenomena that are related to trapped modes in waveguides⁹ or embedded Rayleigh-Bloch waves.^{10,24} These modes have finite energy and correspond to a solution which decays down away from the perturbation. Figure 5 shows a snapshot of the module of the pressure field at ν_i . This clearly exhibits a maximum on the side of the rigid plate and a minimum on the side of Γ_0 , which is typical of a trapped mode. Everything seems to happen as if a Dirichlet waveguide of thickness $2H$ presents symmetric obstacles formed by the inclusion and its image. In our case, these trapped modes are complex, because the boundaries of the waveguide are not Dirichlet conditions but Neumann and continuity conditions, and because $M^{[1]}$ is a dissipative medium. The determinant as calculated for the configuration C1, Fig. 3, presents a minimum at ν_i , which suggests that a complex (trapped) mode CTM stands at this frequency. In contrast, it is clear from Fig. 2, that the peak around ν_i is mainly associated with propagative waves in both domains, a small part of it being associated with evanescent waves in the layer which entraps the energy. This phenomena was already encountered in Ref. 25 and attributed to the periodicity of the configuration. Another explanation of the quasi-absorption peak is related to the modification of wave path and structure global properties inside the

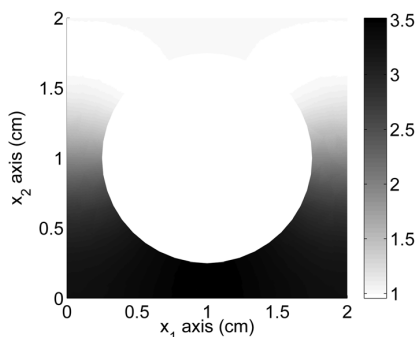


FIG. 5. Configuration C1 – Snapshot of the module of the pressure field inside the porous sheet at $\nu_i = 2674$ Hz, when the configuration is excited at normal incidence.

porous sheet. For a particular ratio R/d , the pressure gradient and thereby the velocity, which is a cause of viscous loss, is large between the inclusions and between the inclusions and the rigid backing. This loss phenomenon results from a continuous modification of the quarter-wavelength resonance when the inclusion radius increases.

Other layer thicknesses were tested. It was found that for most of the layer thickness, in the suitable range for the application, and a centered $(x_1^{(1)}, x_2^{(1)}) = (d/2, H/2)$ inclusion, a couple (R, d) exists for which a quasi-total absorption peak exists below the quarter-wavelength resonance frequency.

Finally, because the parameters of a foam are often difficult to predict before its polymerization, a sensitivity analysis has been performed with regards to the acoustic and structural parameters of the porous sheet. Each parameter of the porous foam is varied one after the other, while keeping the other constant at their value as shown in Table II. Each parameter is assumed to be independent from the other, but their variations correspond to those encountered in practice. The amplitude and frequency of the absorption peaks are weakly dependent on a variation of ϕ ([0.85; 0.95]), Λ ([160 μm ; 200 μm]) and Λ' ([300 μm ; 420 μm]). In particular, the amplitude (more than 0.98) and frequency (a shift of a few decade of Hz) of the CTM is quasi independent of a variation of these parameters. When α_∞ increases from 1.02 to 1.42, the sound speed in the material decreases and ν_i decreases, while the amplitude of the associated peak stands close to one. The static flow resistivity σ strongly influences the amplitude of the peak. When it increases, the amplitude admits a maximum and the peak is wider, while ν_i increases. The resistivity σ ([3900 N s m^{-4} ; 12900 N s m^{-4}]) is the parameter that mostly influences the results, and its value has to be close to the one used in the simulations, i.e., in our case, a value between 7000 N s m^{-4} and 11000 N s m^{-4} is acceptable.

B. Two or more inclusions per spatial period

Various configurations were tested, involving two or more inclusions per spatial period. The frequency band investigated stands below the quarter-wavelength resonance frequency of the associated porous sheet or at least below the first Bragg frequency, i.e., below the frequency of the first modified mode of the porous sheet. The lowest frequency bound is naturally the solid-fluid decoupling frequency or at least the Biot frequency.

Two absorption peaks close to unity were found for a $H = 3.5$ cm thick porous sheet, when a second circular cylinder of radius $R^{(2)} = 5$ mm is added to the configuration C1, Fig. 6. The center of this cylinder is such that $r_1^2 = d = 2$ cm and $\theta_1^2 = \pi/3$. The configuration C2 was derived from a triangular lattice by reducing the radius of the upper cylinder to decrease the structure thickness. The first absorption peak stands around $\nu_i^{(1)} \approx 1850$ Hz, just below the first quarter-wavelength resonance frequency of the $H = 3.5$ cm thick porous sheet, and the second stands around $\nu_i^{(2)} \approx 4120$ Hz. These two peaks correspond to a minimum of $|\det(\mathbf{D})|$ and can therefore be explained by excitation of trapped modes, shifted in the complex plane.

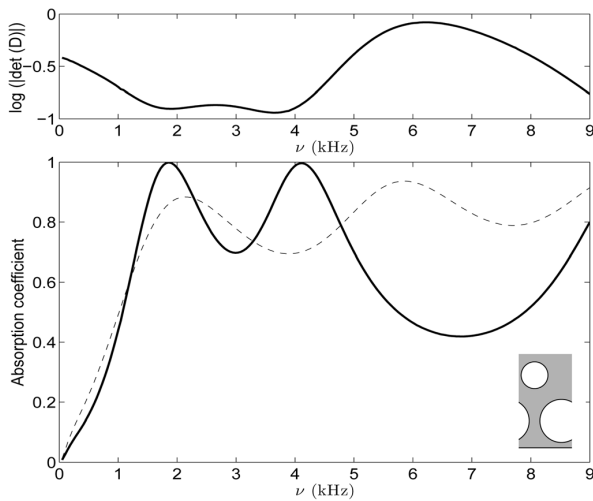


FIG. 6. Configuration C2 – Absorption coefficient of a $H = 3.5$ cm thick porous sheet of Fireflex backed by a rigid plate (---) without inclusion embedded and (-) with a $R^{(1)} = 75$ mm radius circular cylinder and a $R^{(2)} = 5$ mm radius circular cylinder embedded with $d = 2$ cm, when the configuration is excited at normal incidence.

When the inclusions are inversely placed, i.e., the center of the first inclusion is (1 cm, 2.5 cm) and $r_1^2 = d = 2$ cm and $\theta_1^2 = -\pi/3$, results are not identical and no quasi-total absorption peak is encountered. This means that the configuration is not reversible.

The procedure was run a second time with the addition of a third inclusion of radius $R^{(3)} = 2.5$ mm to the configuration C2, $r_2^3 = d = 2$ cm and $\theta_2^3 = 2\pi/3$. Three quasi-total absorption peaks were encountered around $\nu_i^{(1)} \approx 1500$ Hz, $\nu_i^{(2)} \approx 3300$ Hz, and $\nu_i^{(3)} \approx 5000$ Hz.

This phenomenon was already encountered in Ref. 26, where N trapped modes were found when N cylinders were placed across a wave tank. Nevertheless, this configuration imposes use of $H = 5$ cm thick plate, and the absorption gain was considered insignificant over the whole frequency range considered. The addition of inclusions that imposes a thickening of the structure is rapidly becoming of no practical use because of the large absorption of the porous layer itself.

Based on the fact that the frequency $\nu_i^{(1)}$ decreases when $x_2^{(1)}$ increases, several attempts were followed to construct a porous sheet with a unit cell composed of varying $x_2^{(j)}$ central coordinate circular cylinder arranged in a kind of garland. For example, the absorption coefficient of eight circular cylinders per unit cell, embedded in a 2 cm thick porous sheet, was studied. The radius of the eight cylinders was $R^{(j)} = 75$ mm and the projection of the center-to-center distance between two adjacent cylinders $x_1^{(j,j+1)}$ was 2 cm. The $x_2^{(j)}$ were chosen such that $x_2^{(1)} = 1.1$ cm, $x_2^{(2)} = 1.05$ cm, $x_2^{(3)} = 1$ cm, $x_2^{(4)} = 0.95$ cm, $x_2^{(5)} = 0.9$ cm, $x_2^{(6)} = 0.95$ cm, $x_2^{(7)} = 1$ cm, and $x_2^{(8)} = 1.05$ cm. The absorption peak at ν_i was no more total, and no particular increase of its width was noticed. This means that the periodicity has a large influence on the results and that the phenomenon cannot be simply explained by trapped modes but rather by complex embedded Rayleigh-Bloch waves. A similar procedure was followed by decreasing

the radius and the center-to-center distance, the cylinders being aligned, without particular effects on the absorption.

V. CONCLUSION

The influence of embedding periodic circular inclusions on the absorption of a porous sheet attached to a rigid plate was studied theoretically and numerically. In addition to the absorption features related to the excitation of modified modes of the plate and to Bragg interference, it is shown that the structure can possess a quasi-total (close to unity) absorption peak below the quarter-wavelength resonance frequency. This occurs in case of one array of cylinders embedded in a porous sheet, whose thickness and parameters, mainly the static flow resistivity, are correctly chosen. This particular feature enables the design of small dimension absorption packages and was explained by complex trapped mode excitation, which leads to an increase of the pressure gradient inside the layer. This quasi-total absorption peak was validated by use of the finite element method, thus validating the described method and results.

In case of more than one circular cylinder per spatial period, it was found that the N^c quasi-total absorption peak can be obtained for a particular arrangement along the porous thickness, i.e., close to triangular lattice. Nevertheless, this rapidly leads to a large thickness of the structure, and the embedding of the additional inclusions become useless. Garland arrangements were also tested without particular effect, or at least without as spectacular effect as the one already observed for one inclusion per spatial period.

The method offers an alternative to multi-layering and double porosity materials for the design of sound absorption packages. Nevertheless, accounting for the full Biot theory to model the behavior of the porous sheet and the possible coupling between the frame and the inclusions, would be of large interests for lower frequency applications.

ACKNOWLEDGMENT

The authors would like to thank Matthew Boucher for his useful help during the writing of the paper. We are saddened by the sudden death (September 19, 2010) of our highly respected colleague Walter Lauriks, to whom we are very grateful for the important inspiration he shared with us in relation to this work.

APPENDIX: MODAL ANALYSIS OF THE CONFIGURATION

The modes of the configuration without inclusions embedded (i.e., a rigid porous layer backed with a planar rigid wall), whose dispersion relation is

$$D^i = \alpha^{[0]i} \cos(k_2^{[1]i} H) - i\alpha^{[1]i} \sin(k_2^{[1]i} H) = 0, \quad (A1)$$

wherein $\alpha_0^{[j]} = \alpha^{[j]i}$, $j = 0, 1$, and $k_{20}^{[1]} = k_2^{[1]i}$, $j = 0, 1$, cannot be excited by a plane incident wave initially traveling in the air medium.⁶ Effectively, Fig. 7 depicts the real and the

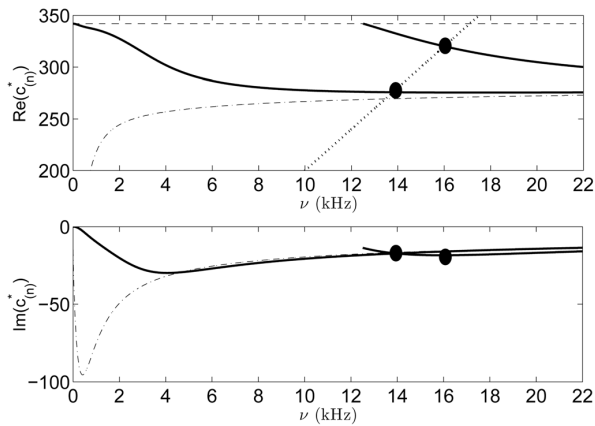


FIG. 7. Real and imaginary part of the root of the dispersion relation in absence of inclusions $c_{(n)}^*$, $n = 1, 2$ (—), of the sound speed in air (---), and of the sound speed in the homogeneous porous material (-·-). Real part of the modified mode of the backed layer $c_{(n,q)}^*$, $n = 1, 2$, $q = 1, 2$, for $d = 2$ cm are pointed out by dot.

imaginary parts of the roots $c_{(n)}^*(\omega) = \omega/k_{1,(n)}^*(\omega)$ of Eq. (A1), as calculated for a $H = 2$ cm thick porous layer, whose acoustical characteristics are those used in Sec. IV. Under the rigid frame assumption and for frequencies higher than the Biot frequency (and lower than the diffusion limit), a porous material can be considered as a modified fluid, its associated dissipation being considered as a perturbation of a fluid. For Eq. (A1) to be true without dissipation, $k_2^{[0]i}$ should be purely imaginary while $k_2^{[1]i}$ should be purely real. Under the previous assumptions, this implies that $\text{Re}(c_{(n)}^*)$ should stand in $[\text{Re}(c^{[1]}), c^{[0]}]$, i.e., $|k_1^i|$ should stand in $[k^{[0]}; \text{Re}(k^{[1]})]$. Or for a plane incident wave initially propagating in the air medium $|k_1^i|$ is always smaller than $k^{[0]}$. It is also necessary to note that in the diffusion regime, i.e., for frequencies largely below the Biot Frequency, any mode exists. This fact constitutes the major difference when compared with a traditional fluid. Effectively, largely below the Biot frequency, $k^{[1]}$ is purely imaginary. This implies that $k_2^{[1]i}$ is also purely imaginary for all values of k_1^i and that D^i never vanishes.

When inclusions are periodically embedded in the porous sheet, the dispersion relation of the modes of the configuration is $\det(\mathbf{I} - \mathbf{V}(\mathbf{S} + \mathbf{Q})) = 0$. The roots of this dispersion relation are difficult to determine because of the complex nature of the matrix $\mathbf{I} - \mathbf{V}(\mathbf{S} + \mathbf{Q})$. Here, we focus on the case of only one grating, i.e., $N^c = 1$, in order to emphasize the excitation of the modified mode of the backed layer (MMBL) (Ref. 6). Proceeding as in Ref. 2, an iterative scheme can be employed to solve.¹¹ The equation is re-written in the form $(1 - V_L \mathcal{M}_{LL})B_L = V_L \mathcal{F}_L + V_L \sum_{l \in \mathbb{Z}} \mathcal{M}_{Ll} B_l (1 - \delta_{Ll})$. The iterative scheme reads as

$$\begin{cases} B_L^{[0]} &= V_L \mathcal{F}_L / (1 - \mathcal{M}_{LL}) \\ B_L^{[n+1]} &= \left(V_L \sum_{l \in \mathbb{Z}} \mathcal{M}_{Ll} B_l^{[n]} (1 - \delta_{Ll}) + V_L \mathcal{F}_L \right) / \\ &\quad (1 - V_L \mathcal{M}_{LL}), \end{cases} \quad (\text{A2})$$

from which it becomes apparent that the solution $B_L^{[n]}$, to any order of approximation, is expressed as a fraction, the denominator of which not depending on the order of approximation can become small for certain couples (k_{1q}, ω) , so as to make $B_L^{[n]}$, and possibly the field large.

When this happens, a natural mode of the configuration, comprising the inclusions and the plate, is excited, thus taking the form of a resonance with respect to $B_L^{[n]}$, i.e., with respect to a plane wave component of the field in the plate relative to the inclusions. As $B_L^{[n]}$ is related to f_q , g_q , and R_q , the structural resonance manifests itself for the same (k_{1q}, ω) , in the fields of the plate and in the air.

The approximate dispersion relation

$$\mathcal{D}_L = 1 - V_L \left(S_0 + \sum_{q \in \mathbb{Z}} Q_{LLq} \right) = 0, \quad (\text{A3})$$

is the sum of a term linked to the grating embodied in $V_L S_0$ with a term linked to the plate embodied in $V_L \sum_{q \in \mathbb{Z}} Q_{LLq}$, whose expressions are given in Eq. (8).

This can be interpreted as a perturbation of the dispersion relation of the gratings by the presence of the plate. The zeroth order lattice sum can be rewritten²⁰ in the form $\sum_{q \in \mathbb{Z}} 2/dk_{2q}^{[1]}$ (additional constants are neglected). Introducing this expression into (A3) gives

$$\mathcal{D}_L = 1 - V_L \sum_{q \in \mathbb{Z}} \frac{2\mathcal{N}_{Lq}}{dk_{2q}^{[1]} D_q} = 0, \quad (\text{A4})$$

with

$$\begin{aligned} \mathcal{N}_{Lq} &= \alpha_q^{[1]} \cos(k_{2q}^{[1]} H) - i\alpha_q^{[1]} \sin(k_{2q}^{[1]} H) \\ &\quad + \alpha_q^{[1]} \cos(k_{2q}^{[1]} (2x_2^{(1)} - H) - 2L\theta_q) \\ &\quad + i\alpha_q^{[0]} \sin(k_{2q}^{[1]} (2x_2^{(1)} - H) - 2L\theta_q). \end{aligned} \quad (\text{A5})$$

It is then convenient, for the clarity of the explanations, to consider (i) $M^{[1]}$ to be a non-dissipative medium (a perfect fluid) and (ii) the low frequency approximation of V_L , valid when $k^{[1]} R^{(1)} \ll 1$. The latter hypothesis ensures that the V_L reduces to $V_l \approx (-1)^l \pi (k^{[1]} R^{(1)})^2 / i4 + O((k^{[1]} R^{(1)})^2)$, $l = -1, 0, 1$. Equation (A4) then reduces to

$$\mathcal{D}_l \approx 1 - \sum_{q \in \mathbb{Z}} \frac{(-1)^l (k^{[1]} R^{(1)})^2}{2idk_{2q}^{[1]} D_q / \mathcal{N}_{lq}} = 0, \quad l = -1, 0, 1. \quad (\text{A6})$$

By referring to the Cutler mode,²⁷ but also to the modal analysis carried out in Ref. 2, the latter dispersion relation is satisfied (in the non-dissipative case) when the denominator of Eq. (A6) is purely imaginary and vanishes. These conditions are achieved when $|k_{1q}| \in [k^{[0]}, \text{Re}(k^{[1]})]$ and when either $D_q = 0$ or $\alpha_q^{[1]} = 0$ (i.e., $k_{2q}^{[1]} = 0$), which respectively corresponds to modified modes of the backed-layer (MMBL) and to modes of the grating (MG). Both of them are determined by the intersection of $c_{1q} = \omega/k_{1q}$ respectively with $c_{(n)}^*(\omega)$

as calculated for the backed-layer and with $\text{Re}(c^{[1]})$. The MMBL are pointed out by the dots in Fig. 7. The associated attenuation of each mode can then be determined by the values of $\text{Im}(c_{l(n)}^*)$ and $\text{Im}(c^{[1]})$ at the frequencies at which the modes are excited. The attenuation associated with MG is also higher than the one associated with MMBL for all frequencies. Moreover, MG corresponds to the highest boundary of $|k_{1q}|$ for Eq. (A6) to be true. This implies that MG should be difficult to excite. The latter type of mode can only be poorly excited by a plane incident wave, particularly at low frequencies.

- ¹J.-P. Groby, E. Ogam, and A. Wirgin, "Acoustic response of a periodic distribution of macroscopic inclusions within a rigid frame porous plate," *Waves Random Complex Media* **18**, 409–433 (2008).
- ²J.-P. Groby, A. Wirgin, L. De Ryck, W. Lauriks, Y. X. U., and R. Gilbert, "Acoustic response of a rigid frame porous medium plate with a periodic set of inclusions," *J. Acoust. Soc. Am.* **126**, 685–693 (2009).
- ³V. Tournat, V. Pagneux, D. Lafarge, and L. Jaouen, "Multiple scattering of acoustic waves and porous absorbing media," *Phys. Rev. E* **70**, 026609 (2004).
- ⁴E. Gourdon and M. Seppi, "On the use of porous inclusions to improve the acoustical response of porous materials: Analytical model and experimental verification," *Appl. Acoust.* **71**, 283–298 (2010).
- ⁵X. Olny and C. Boutin, "Acoustic wave propagation in double porosity media," *J. Acoust. Soc. Am.* **113**, 73–89 (2003).
- ⁶J.-P. Groby, W. Lauriks, and T. Vigran, "Total absorption peak by use of a rigid frame porous layer backed by a rigid multi-irregularities grating," *J. Acoust. Soc. Am.* **127**, 2865–2874 (2010).
- ⁷B. Sapoval, B. Hebert, and S. Russ, "Experimental study of a fractal acoustical cavity," *J. Acoust. Soc. Am.* **105**, 2014–2019 (1999).
- ⁸B. Sapoval, S. Felix, and M. Filoche, "Localisation and damping in resonators with complex geometry," *Eur. Phys. J.* **161**, 225–232 (2008).
- ⁹C. Linton and P. McIver, "Embedded trapped modes in water waves and acoustics," *Wave Motion* **45**, 16–29 (2007).
- ¹⁰R. Porter and D. Evans, "Embedded rayleigh-bloch surface waves along periodic rectangular arrays," *Wave Motion* **43**, 29–50 (2005).
- ¹¹J.-F. Allard and N. Atalla, *Propagation of Sound in Porous Media: Modeling Sound Absorbing Materials* (Wiley, Chichester, 2009), Chap. 5, pp. 73–107.
- ¹²L. De Ryck, J.-P. Groby, P. Leclaire, W. Lauriks, A. Wirgin, C. Depollier, and Z. Fellah, "Acoustic wave propagation in a macroscopically inhomogeneous porous medium saturated by a fluid," *Appl. Phys. Lett.* **90**, 181901 (2007).
- ¹³Y. Champoux and J.-F. Allard, "Dynamic tortuosity and bulk modulus in air-saturated porous media," *J. Appl. Phys.* **70**, 1975–1979.
- ¹⁴D. Johnson, J. Koplik, and R. Dashen, "Theory of dynamic permeability and tortuosity in fluid-saturated porous media," *J. Fluid Mech.* **176**, 379–402 (1987).
- ¹⁵L. Botten, N. Nicorovici, A. Asatryan, R. McPhedran, C. Poulton, C. de Sterke, and P. Robinson, "Formulation for electromagnetic scattering and propagation through grating stacks of metallic and dielectric cylinders for photonic crystal calculations. Part I Method," *J. Opt. Soc. Am. A* **17**, 2165–2176 (2000).
- ¹⁶S. Wilcox, L. Botten, R. McPhedran, C. Poulton, and C. de Sterke, "Modeling of defect modes in photonic crystals using the fictitious source superposition method," *Phys. Rev. E* **71**, 056606 (2005).
- ¹⁷C. Zwicker and C. Kosten, *Sound Absorbing Materials* (Elsevier, Amsterdam, 1949), p. 1.
- ¹⁸P. Barber and S. Hill, "Light Scattering by Particles: Computation Methods," in *Advanced Series in Applied Physics 2* (World Scientific, London, 1990), Chap. 2, p. 30.
- ¹⁹V. Twersky, "On scattering of waves by the infinite grating of circular cylinders," *IRE Trans. Antennas Propag.* **10**, 737–765 (1962).
- ²⁰C. Linton, "Schlommel series that arise in diffraction theory and their efficient computation," *J. Phys. A* **39**, 3325–3339 (2006).
- ²¹R. Brown and R. Bolt, "The measurement of flow resistance of porous acoustic materials," *J. Acoust. Soc. Am.* **13**, 337–344 (1942).
- ²²P. Leclaire, L. Kelders, W. Lauriks, N. Brown, M. Melon, and B. Castagnède, "Determination of the viscous and thermal characteristic lengths of plastic foams by ultrasonic measurements in helium and air," *J. Appl. Phys.* **80**, 2009–2012 (1996).
- ²³Z. Fellah, F. Mitri, M. Fellah, E. Ogam, and C. Depollier, "Ultrasonic characterization of porous materials: Inverse problem," *J. Sound Vib.* **302**, 746–759 (2007).
- ²⁴R. Porter and D. Evans, "Rayleigh-bloch surface waves along periodic gratings and their connection with trapped modes in waveguides," *J. Fluid Mech.* **386**, 233–258 (1999).
- ²⁵R. Craster, S. Guenneau, and S. Adams, "Mechanism for slow waves near cutoff frequencies in periodic waveguides," *Phys. Rev. B* **79**, 045129 (2009).
- ²⁶T. Utsunomiya and R. Eatck Taylor, "Trapped modes around a row of circular cylinders in a channel," *J. Fluid Mech.* **386**, 259–279 (1999).
- ²⁷C. Cutler, "Electromagnetic waves guided by corrugated structures," Technical Report MM No. 44-160-218, Bell Telephone Lab (1944).

Enhancing the absorption properties of acoustic porous plates by periodically embedding Helmholtz resonators

J.-P. Groby,^{a)} C. Lagarrigue, B. Brouard, O. Dazel, and V. Tournat
*Laboratoire d'Acoustique de l'Université du Maine, L'Université Nantes Angers Le Mans,
 Université du Maine, CNRS, UMR-6613 CNRS, Avenue Olivier Messiaen, 72085 Le Mans, France*

B. Nennig
*Laboratoire d'Ingénierie des Systèmes Mécaniques et des Matériaux, EA 2336, Supméca, 3 Rue Fernand
 Hainaut, 93407 Saint-Ouen Cedex, France*

(Received 14 February 2014; revised 3 October 2014; accepted 19 November 2014)

This paper studies the acoustical properties of hard-backed porous layers with periodically embedded air filled Helmholtz resonators. It is demonstrated that some enhancements in the acoustic absorption coefficient can be achieved in the viscous and inertial regimes at wavelengths much larger than the layer thickness. This enhancement is attributed to the excitation of two specific modes: Helmholtz resonance in the viscous regime and a trapped mode in the inertial regime. The enhancement in the absorption that is attributed to the Helmholtz resonance can be further improved when a small amount of porous material is removed from the resonator necks. In this way the frequency range in which these porous materials exhibit high values of the absorption coefficient can be extended by using Helmholtz resonators with a range of carefully tuned neck lengths.

© 2015 Acoustical Society of America. [<http://dx.doi.org/10.1121/1.4904534>]

[KVVH]

Pages: 273–280

I. INTRODUCTION

Air saturated porous materials, namely, foams and wools, are often used as sound absorbing materials. Nevertheless, they suffer from a lack of absorption efficiency at low frequencies which is inherent to their absorption mechanisms, even when used as optimized multilayer or graded porous materials. Actually, these mechanisms only rely on viscous and thermal losses. In the inertial and adiabatic regimes,¹ when the frequencies are higher than the Biot frequency f_b , relatively thin porous plates provide excellent tools to absorb sound, but they fail in the viscous and isothermal regimes, i.e., at lower frequencies. In the inertial and adiabatic regimes, the acoustic pressure satisfies an Helmholtz equation, with losses, while in the viscous and isothermal regimes, it satisfies a diffusion equation.

These last decades, several solutions have been proposed to overcome this lack of efficiency. They usually consist in coupling the viscous and thermal losses of porous materials with additional absorption mechanisms, mainly associated with resonance phenomenon arising from the addition of heterogeneities.

(1) The absorption enhancement of double porosity materials^{2–4} arises from resonances of the microporous material (pressure diffusion mechanisms) excited by the macropores in case of a initial porous material layer. The theory describing the behavior of these materials is well established by homogenization. For high contrast flow resistivity between the micro and the macro porous materials, the absorption enhancement is obtained at the

diffusion frequency f_d , which only depends on the geometry and organization of the holes in infinite double porosity medium. For an optimal absorption efficiency of a double porosity plate, f_d should be in practice around the frequency for which the penetration depth is of the same order of the homogeneous microporous plate thickness. This theory can also be used to model poroelastic materials,⁵ but the low frequency properties of activated carbon (large resistivity contrast) cannot be completely explained by their double porosity structure, but also by sorption mechanisms.

- (2) Another possibility consists in plugging dead-end pores, i.e., quarter-wavelength resonators, on open pores to create dead-end porosity materials.⁶ This results in anomalies in the absorption coefficient when the wavelength is on the order of the dead-end pore length. Nevertheless, the absorption enhancement is still not completely understood and is subjected to the inertial regime with regards to the dead-end pores. Moreover, the current manufacturing process involving salt grains and liquid metal does not yet offer the possibility of the full control over the densities and the lengths of the dead-end pores.
- (3) Metaporous materials, in which modes are excited, trapping the energy between periodic rigid inclusions embedded in the porous plate and the rigid backing or in the inclusions themselves (split-ring resonators), have been proposed. The absorption properties of the porous plate are enhanced at lower frequencies than the quarter wavelength frequency,^{7,8} when the absorption of the initial plate is not unity at this frequency. When split-ring resonators are correctly arranged and coupled with the rigid backing, the absorption coefficient can be higher than 0.9 for wavelengths smaller than 10 times the material thickness and over a large frequency band, which largely

^{a)} Author to whom correspondence should be addressed. Electronic mail: jean-philippe.groby@univ-lemans.fr

overcome the usual limit of the quarter wavelength.⁹ Moreover, this last technique is only efficient in the inertial regime, because the split-ring resonators are filled by porous materials enabling to lower their resonance frequency. This means that it is possible to absorb the energy at frequencies higher than the Biot frequency f_v with very thin structures, but that an increase of the metaporous plate thickness does not necessarily lead to enhanced absorption for lower frequencies. Indeed, the resonators cannot resonate when filled by a porous material in the viscous and isothermal regime, because the pressure field satisfies a diffusion equation. Adding periodic air cavities to the rigid backing enable to partially solve this problem, but it requires either deep cavity or large lateral periodicity.^{10,11}

Recently, membrane-type metamaterials that exhibit nearly total reflection at an anti-resonance frequency¹² or nearly total absorption due to the flapping motion of asymmetric rigid platelets added to the membrane¹³ have been proposed, but their absorption properties are limited in the metamaterial resonance frequency range. The use of Helmholtz resonators as sound attenuators in ducts has already been proposed,^{14–16} but not their use together with acoustic porous materials as common sound absorbing materials. Metamaterials have induced a revival of interest in Helmholtz resonators (HRs) to manufacture negative bulk modulus and mass density materials.^{17,18} In Ref. 17, split hollow sphere were embedded in a sponge matrix. This material exhibit negative bulk modulus at the HR resonance. The effective properties, mainly wave velocity and effective stiffness, of an infinite porous material with embedded resonators were recently investigated in Ref. 19 by homogenization. The scale separation assumption implies long wavelength condition. Different behavior depending on the ratio between the HR resonant frequency f_r and f_v were exhibited, while negative stiffness was demonstrated around the resonance frequency, but the absorption properties of the structure were not analyzed.

The aim of this paper is to improve the absorbing properties of a porous material by periodically embedding HRs. The analysis is performed in the viscous and inertial regimes of the porous material thanks to a finite element method.²⁰ HR has two main effects: (1) an additional internal resonance, that dominates the absorbing material response at f_r ; (2) another additional resonance, that dominates the absorbing properties at higher frequencies.²⁰ Both effects will be investigated in order to enhanced absorption on a wide frequency range without long-wavelength limitation. The paper is organized as follows: The configurations and the main assumptions are described and a parametric study is then presented; Finally, experimental validations are proposed. These last results illustrate the main trends of the parametric study on practical cases.

II. PRELIMINARY REMARKS

The absorption enhancement of metaporous materials both in viscous and inertial regimes is a multi and interconnected parameter optimization process, which depends on

the porous material parameters, material thickness, dimensions of the inclusions, dimensions of the resonators, and periodicities. Here, we will focus on the influence of the periodic embedment of HRs around their resonance, keeping in mind previous conclusions on metaporous materials (Refs. 7–9 and 20):

- (1) If the absorption is not total at the quarter-wavelength resonance, the embedment of periodic inclusions in a porous slab attached to a rigid backing leads to an increase of this absorption peak and shifts this peak to lower frequency. This mainly depends on the volume of the inclusion at low frequency. A total absorption peak can be obtained if the required filling fraction can be reached. This filling fraction depend on the parameters of the porous materials. Still increasing the filling fraction after total absorption has been reached, deteriorates the absorption coefficient, while still shifting the maximum absorption peak to lower frequencies.
- (2) If the absorption coefficient is already total at the quarter-wavelength resonance, embedding periodic inclusions shift this peak to low frequency, but the absorption is deteriorated.
- (3) The shift to low frequency depends on the filling fraction and on the position of the inclusion barycenter. The larger is the distance between the inclusion and the rigid backing, the lower is the absorption peak frequency. This absorption enhancement is subjected to the periodic set of inclusions and its interaction with its image, to material parameters, but not directly to the plate thickness.^{7,20}
- (4) When the total absorption peak is obtained, the acoustic energy is trapped between the inclusion and the rigid backing.
- (5) When a total absorption peak can be obtained, the required filling fraction is larger in 3D than in 2D.²⁰ Moreover, the frequency at which this total absorption peaks is reached is higher in 3D than in 2D for a given material properties and thickness.

The studied configurations also derived from two-dimensional ones, because it enables lower filling fraction and larger resonator volume. The neck of the embedded HRs will not be outer but rather inner also enabling larger resonator volume and larger filling fraction, both being constrain by the structure thickness. Inner neck enable to save volume when compared to outer neck. The studied HRs derive from the configuration studied in Ref. 21, without outer neck. Moreover, the HRs being embedded in a porous material the viscous dissipation in the neck is neglected when compared to the dissipation in the porous material.

III. FORMULATION OF THE PROBLEM

A. Description of the configuration

A parallelepiped unit cell of the 3D scattering problem together with a sketch of one HR are shown in Fig. 1. Before the addition of the HR, the layer is a rigid frame porous material saturated by air (e.g., a foam or a wool) which is modeled as a macroscopically homogeneous equivalent fluid M^p using the Johnson-Champoux-Allard model.^{1,22} The upper

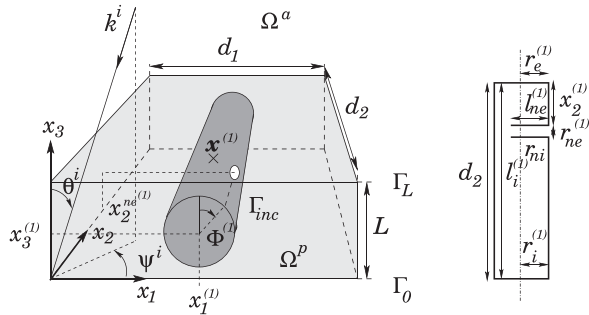


FIG. 1. Example of a \mathbf{d} -periodic fluid-like porous sheet backed by a rigid wall with a periodic inclusion embedded in.

and lower flat and mutually parallel boundaries of the layer, whose x_3 coordinates are L and 0 , are designated by Γ_L and Γ_0 , respectively. The upper semi-infinite material M^a , i.e., the ambient fluid that occupies Ω^a , and M^p are in a firm contact at the boundary Γ_L , i.e., the pressure and normal velocity are continuous across Γ_L . A Neumann type boundary condition is applied on Γ_0 , i.e., the normal velocity vanishes on Γ_0 .

HRs deriving from 2D configuration are embedded in the porous layer with a spatial periodicity $\mathbf{d} = \langle d_1, d_2, 0 \rangle$ and create a two-dimensional diffraction grating in the plane x_1 – x_2 . The lengths of the HRs are d_2 , while the lengths of the HR cavities are $l_i^{(j)}$, outer and inner radii are $r_e^{(j)}$ and $r_i^{(j)}$. HRs positions are referred to as the barycenter of the outer volume $(x_1^{(j)}, d_2/2, x_3^{(j)})$. HR necks are cylinders of circular cross-sections of lengths $l_n^{(j)}$. The outer and inner radii of the neck are $r_{ne}^{(j)}$ and $r_{ni}^{(j)}$, respectively. The neck x_2 -coordinates are $x_{2n}^{(j)}$, while their angular positions are $\Phi^{(j)}$. The inner volume and the neck of the HRs are filled with air medium.

The incident wave propagates in Ω^a and is expressed by $p^i(\mathbf{x}) = A^i e^{i(k_1^i x_1 + k_2^i x_2 - k_3^i (x_3 - L))}$, wherein $k_1^i = -k^a \sin \theta^i \cos \psi^i$, $k_2^i = -k^a \sin \theta^i \sin \psi^i$, $k_3^i = k^a \cos \theta^i$, and $A^i = A^i(\omega)$ is the signal spectrum. The azimuth of the incident wave vector is ψ^i and its elevation θ^i .

In each domain Ω^α ($\alpha = a, p$), the pressure field fulfills the Helmholtz equation

$$\nabla \cdot \left(\frac{1}{\rho^\alpha} \nabla p^\alpha \right) + \frac{(k^\alpha)^2}{\rho^\alpha} p^\alpha = 0, \quad (1)$$

with the density ρ^α and the wave number $k^\alpha = \omega/c^\alpha$, defined as the ratio between the angular frequency ω and the sound speed c^α .

As the problem is periodic and the excitation is due to a plane wave, each field (X) satisfies the Floquet-Bloch relation

$$X(\mathbf{x} + \mathbf{d}) = X(\mathbf{x}) e^{i\mathbf{k}_\perp \cdot \mathbf{d}}, \quad (2)$$

where $\mathbf{k}_\perp^i = \langle k_1^i, k_2^i, 0 \rangle$ is the in-plane component of the incident wave number. Consequently, it suffices to examine the field in the elementary cell of the material to get the fields, via the Floquet relation, in the other cells. The periodic wave equation is solved with a FE method. This FE

method as well as the absorption coefficient calculation method are described and validated in Ref. 20.

B. Material modeling

The rigid frame porous material is modeled using the Johnson-Champoux-Allard model. The compressibility and density, linked to the sound speed through $c^p = \sqrt{1/(K^p \rho^p)}$ are^{1,22}

$$\frac{1}{K^p} = \frac{\gamma P_0}{\phi \left(\gamma - (\gamma - 1) \left[1 + i \left(\frac{\omega'_c}{\text{Pr} \omega} \right) G(\text{Pr} \omega) \right]^{-1} \right)}, \quad (3)$$

$$\rho^p = \frac{\rho^a \alpha_\infty}{\phi} \left(1 + i \frac{\omega_\nu}{\omega} F(\omega) \right),$$

wherein $\omega_\nu = 2\pi f_\nu = \sigma \phi / \rho^a \alpha_\infty$ is the angular Biot frequency, $\omega'_c = \sigma' \phi / \rho^a \alpha_\infty$ is the adiabatic/isothermal crossover angular frequency, γ the specific heat ratio, P_0 the atmospheric pressure, Pr the Prandtl number, ρ^a the density of the fluid in the (interconnected) pores, ϕ the porosity, α_∞ the tortuosity, σ the flow resistivity, and σ' the thermal resistivity. The correction functions $G(\text{Pr} \omega)$ (Ref. 1) and $F(\omega)$ (Ref. 22) are given by

$$G(\text{Pr} \omega) = \sqrt{1 - i\eta \rho^a \text{Pr} \omega \left(\frac{2\alpha_\infty}{\sigma' \phi \Lambda'} \right)^2},$$

$$F(\omega) = \sqrt{1 - i\eta \rho^a \omega \left(\frac{2\alpha_\infty}{\sigma \phi \Lambda} \right)^2}, \quad (4)$$

where η is the viscosity of the fluid, Λ' the thermal characteristic length, and Λ the viscous characteristic length. The thermal resistivity is related to the thermal characteristic length¹ through $\sigma' = 8\alpha_\infty \eta / \phi \Lambda'^2$.

IV. PARAMETRIC STUDY, RESULTS, AND DISCUSSION

In this section, the influence of the main parameters will be investigated for one HR per period and two HRs per period. First, the influence of the ratio f_r/f_ν , which summarizes the porous material main characteristics, is studied. Then, trends for the main geometric quantities, i.e., the neck orientation and the filling fraction, are drawn. Finally, the influence of the angle of the incident plane wave is examined to evaluate the absorption of this material for practical applications submitted to incident diffuse field.

In all simulations and experimental validations, the thickness of the porous slab, periodicity along the x_2 direction, x_3 position of the HRs, and inner length of the HRs as well as the outer and inner radius of the neck are fixed at $L = 22.5$ mm, $d_2 = 42$ mm, $l_i^{(j)} = 40$ mm, $x_3^{(j)} = 11.5$ mm, $r_{ne}^{(j)} = 2$ mm, and $r_{ni}^{(j)} = 1.5$ mm. The inclusion are not placed at $x_3^{(j)} = L/2$, but at a larger x_3 -coordinates, enabling a lower frequency of the trap mode. The volume of the HRs can be modified by changing the outer and inner radius (and the neck length), while the neck characteristics can be modified through their lengths and orientations. The dimensions of the different studied configuration are reported in Table I.

TABLE I. Dimensions of the main studied configurations.

Configuration	d_1 (mm)	$x_1^{(j)}$ (mm)	$x_{2n}^{(j)}$ (mm)	$(r_e^{(j)}, r_i^{(j)})$	$\Phi^{(j)}$	$l_{ne}^{(j)}$ (mm)
C1	21	10.5	12	(8,6.8)	0	10
C2	21	10.5	12	(8,6.8)	$0, \pi/2, \pi$	10
C3	21, 26, 31, 36	10.5, 13, 15.5, 18	12	(8,6.8)	0	10
C4	42	10.5	12	(8,6.8)	0	11
		31.5	12	(8,6.8)	0	10, 8, 6, 4
C5	42	10.5	12	(8,6.8)	0	11
		31.5	12	(8,6.8), (7,6.8), (6,6.8)	0	10, 9, 8
C6	42	11.5	12	(8,6.8)	0	10
		30.5	12	(8,6.8)	0	10
C7	42	11.5	12	(8,6.8)	0	11
		30.5	12	(8,6.8)	0	7

Three different materials are considered: A small flow resistivity foam *S1* (referred to as blue foam in Ref. 23), a medium flow resistivity Melamine foam *S2*, and a wool *S3* (GR 32 nu, ISOVER). These materials have been chosen in such a way that the ratio of resonant frequency of the HR over their Biot frequencies are $f_r/f_v \ll 1$ for *S3*, $f_r/f_v \leq 1$ for *S2*, and $f_r/f_v \geq 1$ for *S1*, respectively. The parameters of these three porous materials are reported in Table II and have been evaluated using the traditional methods (Flowmeter for the resistivity and ultrasonic methods for the 4 other parameters, together with a cross-validation by impedance tube measurement) described in Ref. 24.

A. Results for one HR per period

HRs are designed with $l_n = 10$ mm leading to configuration C1. The HRs resonate, in first approximation, at $f_r = (c^a/2\pi)\sqrt{A/Vl_{eff}} = 540$ Hz, where $A = \pi r_{ni}^2$ is the cross-section area of the neck, $V = l_i \pi r_i^2 - (l_n - r_{ne} + r_{ni}) \pi r_{ne}^2$ the volume of the resonators, and $l_{eff} = l_n + 8r_{ne}/3\pi$ is the effective length of the neck.²⁵ This frequency is approximated because no exact formula exists for inner neck resonators. The main advantage of using HRs is that they can resonate at a very low frequency for small dimensions¹⁹ compared to other 2D shape resonators (double or simple split-ring resonators).

1. Influence of the ratio f_r/f_v and absorption at f_r

The effect of the ratio f_r/f_v is first investigated. Figures 2(a), 2(b), and 2(c) depict the absorption coefficients of configuration C1, when the porous material is *S1*, *S2*, and *S3*, respectively. The resonance of the HR leads to absorption enhancement at f_r whatever the porous material properties in particular, the flow resistivity, i.e., whatever the Biot frequency. Nevertheless, this enhancement is large when f_r/f_v is

TABLE II. Acoustical parameters of the porous material constituting the sheet of thickness L .

	ϕ	α_∞	Λ (μm)	Λ' (μm)	σ (N s m^{-4})
<i>S1</i>	0.96	1.07	273	672	2843
<i>S2</i>	0.98	1.02	180	240	12000
<i>S3</i>	0.97	1.03	56	85	28500

larger than or close to unity and decreases when f_r becomes smaller than f_v [see Fig. 2(d)]. This conclusion can be expected from those driven from the analysis of the effective parameters of infinite porous materials with weak concentration of HRs.¹⁶ However, in the present article, the HR density is large so that the considered configurations do not fit homogenization requirements. When f_r/f_v is larger than unity, the HRs resonance already leads to a quasi-total absorption peak. The associated wavelength in the air is 27 times larger than the sample thickness at f_r . This means that the absorption properties of porous materials in the inertial regime can be enhanced by embedding air filled HRs, but also that this type of structure can accurately absorb sound for wavelengths much larger than the sample thickness. For lower ratio f_r/f_v , modifying the input impedance of the HRs by removing small amount of porous material just in front of the neck leads to a larger absorption peak of the configuration at f_r [see Fig. 2(d)]. This is due to a lowering of the input impedance, which enables a larger energy advection. Therefore, a larger velocity gradient in the neck and in its vicinity is induced leading to a larger viscous dissipation. Nevertheless, this is associated with a narrowing of the absorption peak.

At higher frequency, the excitation of the trapped mode leads to a wide enhanced absorption peak at lower frequency than the quarter wavelength resonance one when *S1* and *S2* material are used, while the absorption is lower in case of *S3* material. Indeed, the absorption of *S3* material is nearly optimal and the addition of a periodic set of rigid inclusions degrades its performances [see point (1) of Sec. II]. An absorption enhancement would have been possible in this last case if the layer thickness would have been smaller. An important remark is that the outer radius has not been optimized neither for *S1* nor *S2*, therefore the absorption is not unity at the trapped mode frequency. In particular, the required filling fraction is around $ff = V_{HR}/V_{cell} = 0.4255$ for *S2* for a total absorption peak and is larger in the present case. The first resonance of the HR is excited in each cases around 4100 Hz, while the absorption is lower at the Bragg interference around 6500 Hz. Note that the mode of the backed layer possibly excited by the periodicity d_2 is not excited. This means that the configuration behavior is close to the one of a two-dimensional configuration, i.e., the neck has a weak influence on the results at high frequency.

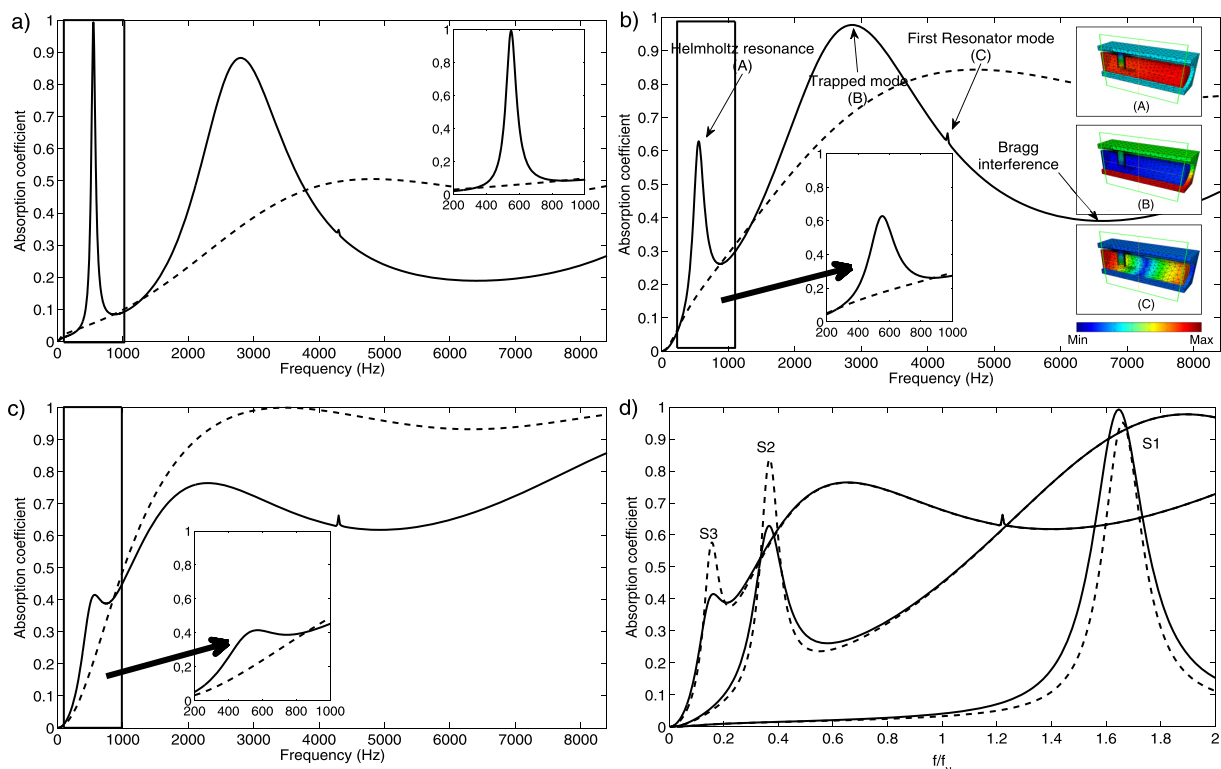


FIG. 2. (Color online) Absorption coefficient of configuration C1 (black curves) and associated homogeneous sheet (dashed curves) occupied by the foam (a) S1, $f_r/f_v \geq 1$, (b) S2, $f_r/f_v \leq 1$, and (c) S3, $f_r/f_v \ll 1$, when excited at normal incidence. The insets show zooms of the absorption coefficient around the HRs frequencies, and the snapshot of the sound pressure field at the frequency of the HR resonance, of the trapped mode, and of the first HR resonance. (d) absorption coefficient of configuration C1 occupied by the foam S1, S2 and S3 in function of f/f_v (solid line) and with a small amount of porous material removed in front the neck (dashed line).

2. Influence of the neck orientation and filling fraction

Both the influence of neck orientation and of the filling fraction are then investigated for configuration C1 and S2 porous material in Figs. 3(a) and 3(b), respectively. The largest absorption enhancement is obtained when the neck is facing the air interface, i.e., $\Phi = 0$. In this configuration, the energy advection by the HR is large. When the neck is facing

the rigid backing, i.e., $\Phi = \pi$, the HR and the rigid backing are coupled, which lowers f_r , but the value of the absorption peak is then lower because of a poor energy advection. The presence of both the surrounding inclusion and the rigid backing can be interpreted as a neck extension that lowers f_r when the neck face the rigid backing. The lowering of the absorption amplitude can be interpreted in terms of penetration depth: the energy trapped in the HR is larger when the

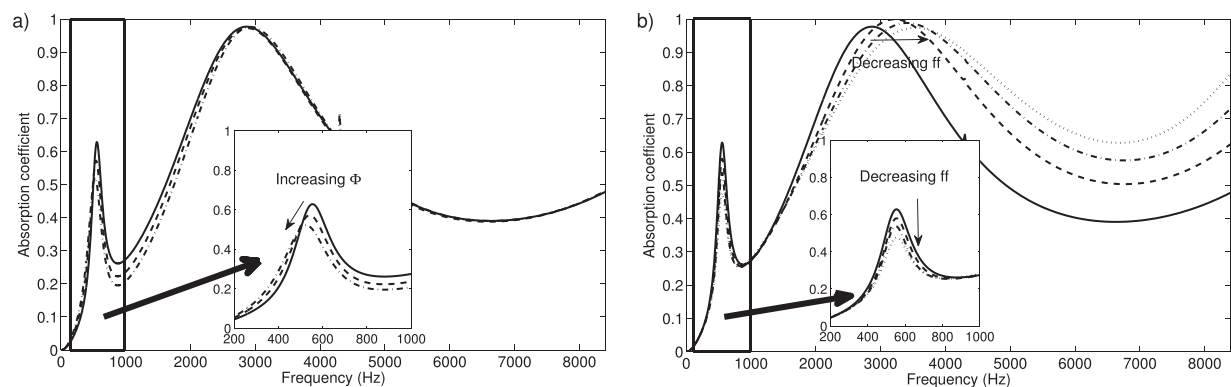


FIG. 3. Absorption coefficient of (a) configurations C2: $\Phi = 0$ solid curve, $\Phi = \pi/2$ dashed curve and $\Phi = \pi$ dashed-dotted curve; and (b) configuration C3: $d_1 = 21$ mm solid curve, $d_1 = 26$ mm dashed curve, $d_1 = 31$ mm dashed-dotted curve and $d_1 = 36$ mm dotted curve. The material layer is the foam S2 and the configuration is excited at normal incidence. The insets show zooms of the absorption coefficient around the HRs frequencies.

neck is close to the interface than when the neck is deep because it penetrates more easily. Increasing Φ , lower the absorption peak associated with the resonance frequency, similarly to what was found in case of split-ring resonators,⁹ but lower the amplitude of the absorption peak. The absorption peak associated with the excitation of the trapped mode is weakly affected by a modification of Φ . Decreasing ff by increasing the periodicity d_1 lowers the amplitude of the absorption peak associated with the HRs resonance, while largely affects both position and amplitude of trapped mode associated peak. In particular, the optimal filling fraction being around $ff = 0.4255$, the absorption peak is close to unity when $d_1 = 26$ mm.

The absorption efficiency related to the HR resonance is largely affected by their concentration.

3. Influence of the angle of incidence

The influence of the angle of incidence is finally investigated for configuration C1 and S2 porous material in Fig. 4 for various elevation at fixed azimuth $\psi^i = 0$. While a modification of θ^i largely modifies the absorption curve, a variation of ψ^i at fixed θ^i does not strongly affect the absorption curves below 6000 Hz. Nevertheless, the absorption curves have been found symmetric for ψ^i varying from $[0; \pi/2]$ and $[\pi/2; \pi]$, whose fact again is an argument for a two-dimensional like configuration. The frequency of the absorption peaks associated the HRs excitation is by definition not affected by the variation of θ^i , while the one associated with the trapped mode is. This is due to the real and localized resonant features of the HR which is not affected by the excitation. Increasing θ^i increases the amplitude of absorption peak at f_i because the initial absorption of the porous layer is larger. Similarly, the larger θ^i is the larger is the amplitude of the absorption peak associated with the trapped mode.

To conclude, the HR resonance induce an increase of the absorption coefficient in the viscous regime which is larger when the input impedance is smaller, when the HR spatial density is larger and when the neck is closer to the porous/air interface. At higher frequencies than the viscous regime, this configuration behaves as a 2D one, and can enable to reach a total absorption peak at the trapped mode

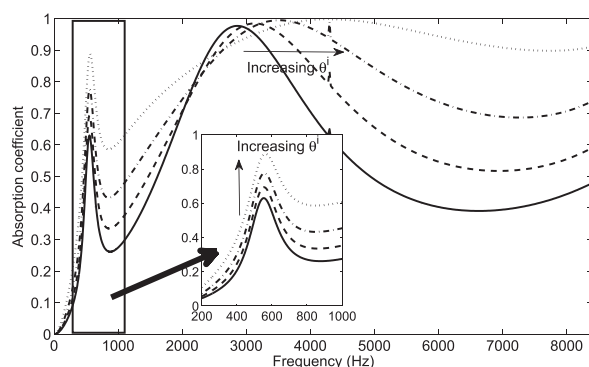


FIG. 4. Absorption coefficient of the configurations C1 occupied by the foam S2 when excited at $\theta^i = 0$, $\theta^i = \pi/6$, $\theta^i = \pi/4$, and $\theta^i = \pi/3$ for $\psi^i = 0$. The insets show zooms of the absorption coefficient around the HRs frequencies.

resonance frequency for a lower filling fraction than if 3D inclusions would have been embedded in.

B. Results for two HRs per period

It is found to be quite difficult to accurately couple the HRs as it is the case with split-ring resonators,^{9,26} particularly when modifying the neck orientation. This can be explained because the opening of a 3D-extruded split ring tends to a slit, which yields a larger coupling surface. A near field coupling of resonators²⁷ has not been exhibited in our configuration when the HR necks are facing one with each other, even for tiny distance between the necks. The actual coupling between the HRs is also qualified as “far field” coupling. The largest absorption enhancement is obtained when the neck is facing the air interface. The neck x_2 -coordinate was also investigated without particular modification of the associated absorption peak.

In what follows, two HRs per period are considered and the coupling between these two HRs is investigated. Either the outer radius or the neck length of one HR is modified in order to widen the large absorption peak associated with the HR resonances. Obviously, the modification of one induce a modification of the other. Figure 5 depicts the absorption coefficient of configuration C4 when $l_n^{(2)}$ varies from 4 to 11 mm, and of configuration C5 when $r_e^{(2)}$ varies from 8 to 6 mm. Decreasing $l_n^{(2)}$ widens the absorption peak till the HRs are decoupled. The modification of the neck length of one of the HRs does not modify the absorption curve at higher frequencies. Decreasing $r_e^{(2)}$ also widens the large absorption peak till the HRs are decoupled. The absorption follows similar trend when $r_e^{(2)}$ decreases as when $l_n^{(2)}$ decreases. However, the absorption is modified at higher frequencies when $r_e^{(2)}$ is modified. The peak associated with the trapped mode excitation possesses an optimum (in amplitude) for $ff = 0.4255$, which means that this filling fraction can be obtained with two different scatterers in case of two scatterers per spatial period. The fundamental modified mode of the backed layer, associated with the periodicity $d_2 = 42$ mm, is excited around 8000 Hz because the unit cell is now quite different from the one containing only one scatterer. This offers the possibility of an absorption enhancement at the location of the Bragg interference by optimizing the excitation of this mode around 6000 Hz.

To conclude, the detuning of HRs in a unit cell enables to widen the enhanced absorption frequency band due the HRs resonance. The modification of neck length is easier and seems to be more efficient than a modification of the volume cavity to achieve this widening.

V. EXPERIMENTAL VALIDATION

The sample is composed of a Melamine foam S2 as the porous matrix and two HRs of cylindrical shapes as shown in Fig. 6(a). The brass hollow cylindrical shells are 8 mm outer radius, 6.8 mm inner radius, and 40 mm long. They are closed by two 1 mm thick circular aluminum plates glued on both ends of each shell. Therefore, the total length of the resonator is 42 mm. The x_3 coordinate of both cylinder axis is 11.5 mm, while $x_1^{(1)} = 11.5$ mm and $x_1^{(2)} = 30.5$ mm defining

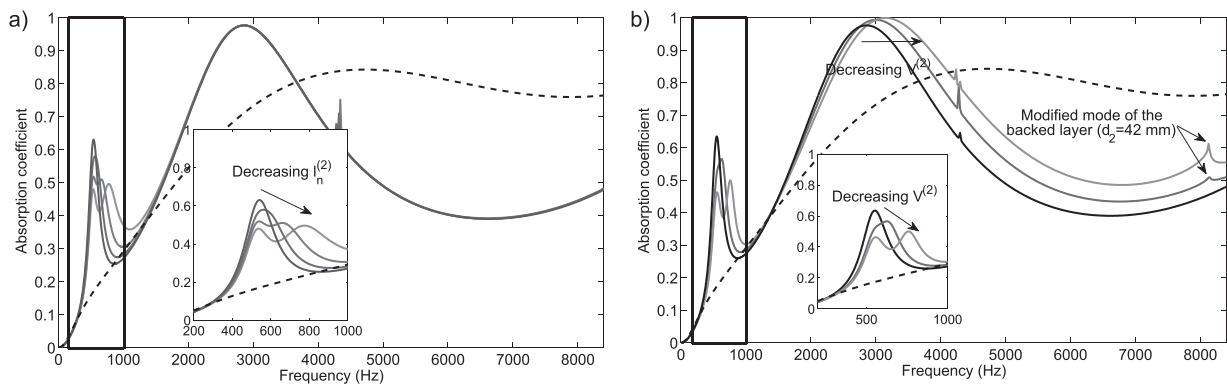


FIG. 5. Absorption coefficient of configurations C4 (a) when $l_n^{(2)}$ vary from 4 to 11 mm, and of configurations C5 (b) when $r_e^{(2)}$ vary from 8 to 6 mm and of the associated homogeneous sheet (dashed curves) occupied by the foam S2 when excited at normal incidence. The insets show zooms of the absorption coefficients around the HRs frequencies.

configuration C6. The HRs are drilled at 12 mm from one end with a 4 mm diameter hole. Aluminum necks of inner radius 1.5 mm and length l_n are inserted in. The initial 22.5 mm-thick Melamine foam is drilled and the resonators are embedded in. The sample is placed at the end of an impedance tube having a square cross-section with a side length 42 mm, against a copper plug that closes the tube and acts as a rigid boundary. By assuming that plane waves

propagate below the cut-off frequency of the tube 4150 Hz, the infinitely rigid boundary conditions of the tube act like perfect mirrors and create a periodicity pattern in the x_1 and x_2 directions with a periodicity of 42 mm. This technique was previously used in Refs. 9–11 and 20 and allows to determine experimentally the absorption coefficient of a quasi-infinite 3D periodic structure just with one or a correctly arranged small number of unit cells.

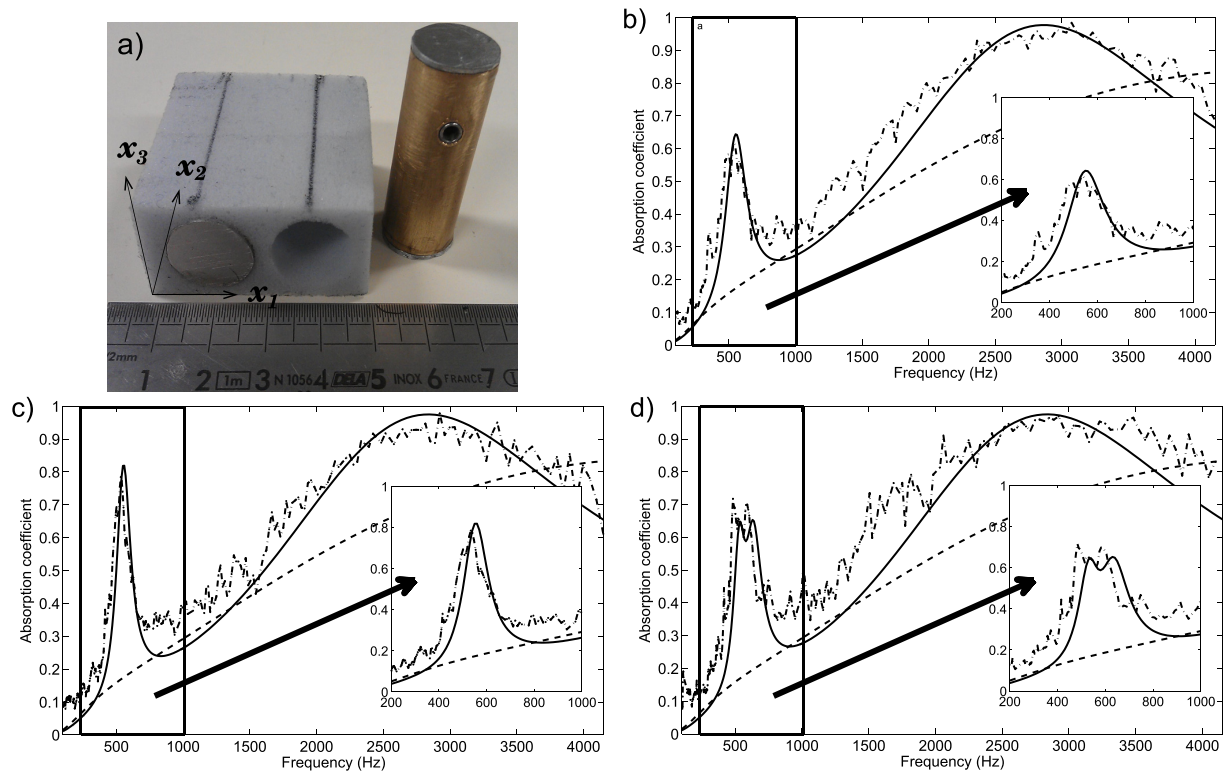


FIG. 6. (Color online) (a) Pictures of the sample. (b) Absorption coefficient of the Melamine foam with two embedded HRs, configuration C6. (c) Absorption coefficient of the Melamine foam with two HRs embedded in, configuration C6, with a small amount of porous material removed in front of the neck. (d) Absorption coefficient of the Melamine foam with $l_n^{(1)} = 11$ mm and $l_n^{(2)} = 7$ mm HRs embedded in, configuration C7, with the porous material removed in front of the neck. FE calculations (solid curves) and corresponding experimental results (dashed-dotted curves) are shown. The insets show zooms of the absorption coefficient around the HRs frequencies. The absorption coefficient of the initial Melamine foam is also shown (dashed line).

The absorption coefficient of this sample is depicted in Fig. 6(b), showing a good agreement between the FE modeling and the measurements. The differences are attributed to imperfections in the sample manufacturing and material parameters. When compared to the initial Melamine plate, the absorption is largely increased around 3000 Hz, because of the excitation of a trapped mode that traps the energy between the cylindrical inclusions and the rigid backing, and around 560 Hz because of the HR resonance. In particular, the absorption coefficient is 0.65 at f_r , which corresponds to an increase of nearly 250% of the initial Melamine plate absorption.

When a small amount of porous material is removed just in front of the neck, the input impedance of HRs is smaller allowing the advection to be larger. The amplitude of the absorption coefficient at the resonance frequency of the HRs is 26% larger and reaches 0.82, as shown in Fig. 6(c). The narrowing of the absorption peak is also observed.

The lengths of the HRs necks are modified to be $l_n^{(1)} = 11 \text{ mm}$ ($f_r^{(1)} = 521 \text{ Hz}$) and $l_n^{(2)} = 7 \text{ mm}$ ($f_r^{(2)} = 618 \text{ Hz}$), configuration C7, in order to validate the widening of the high absorption frequency band. These two lengths have been determined in order to shift the two modes in frequency to enlarge the enhanced absorption bandwidth but not sufficiently to lead to two separated peaks. While the absorption coefficient is modified around the resonance frequency of the HRs, the absorption coefficient is unchanged at higher frequency [see Fig. 6(d)]. The absorption coefficient is larger than 0.5 over a 120 Hz range (between 500 Hz and 620 Hz) in the case of two identical resonators, while it is over a 190 Hz range (between 500 Hz and 690 Hz) in case of these two different resonators, which represents a widening of 60% of the enhanced absorption bandwidth.

VI. CONCLUSION

The absorption of a small thickness porous foam is enhanced both in the viscous and inertial regimes by periodically embedding HRs. This embedment leads to trapped mode excitation that enhance the absorption coefficient for frequencies lower than the quarter-wavelength frequency and to HR excitation. In particular, a large absorption is reached for wavelength in the air 27 times larger than the sample thickness. The absorption amplitude and bandwidth is then enlarged by removing porous material in front of the HR neck, enabling a lower input impedance of the global effective material, and by adjusting the resonance frequencies of detuned HRs. The numerical parametric analysis and the experimentally tested configurations, pave the way of future development of very thin broadband large absorption metamaterials based on optimized HRs coupled with porous materials. In particular, compound cells with slightly detuned HRs seems to be a promising direction.

ACKNOWLEDGMENTS

This work was partly supported by the ANR Project METAUDIBLE No. ANR-13-BS09-0003 co-founded by ANR and FRAE.

- ¹Y. Champoux and J.-F. Allard, "Dynamic tortuosity and bulk modulus in air-saturated porous media," *J. Appl. Phys.* **70**, 1975–1979 (1991).
- ²X. Olny and C. Boutin, "Acoustic wave propagation in double porosity media," *J. Acoust. Soc. Am.* **114**, 73–84 (2003).
- ³J.-L. Auriault and C. Boutin, "Deformable porous media with double porosity. III Acoustics," *Transp. Porous Media* **14**, 143–162 (1994).
- ⁴O. Dazel, F.-X. Bécot, and L. Jaouen, "Biot effects for sound absorbing double porosity materials," *Acta Acust. Acust.* **98**, 567–576 (2012).
- ⁵R. Venegas and O. Umnova, "Acoustical properties of double porosity granular materials," *J. Acoust. Soc. Am.* **130**, 2765–2776 (2011).
- ⁶T. Dupont, P. Leclaire, O. Sicot, X. Gong, and R. Panneton, "Acoustic properties of air-saturated porous materials containing dead-end porosity," *J. Appl. Phys.* **110**, 094903 (2011).
- ⁷J.-P. Groby, A. Duclos, O. Dazel, L. Boeckx, and L. Kelders, "Enhancing the absorption coefficient of a backed rigid frame porous layer by embedding circular periodic inclusions," *J. Acoust. Soc. Am.* **130**, 3771–3780 (2011).
- ⁸B. Nennig, Y. Renoux, J.-P. Groby, and Y. Aurégan, "A mode matching approach for modeling two dimensional porous grating with infinitely rigid or soft inclusions," *J. Acoust. Soc. Am.* **131**, 3841–3852 (2012).
- ⁹C. Lagarrigue, J.-P. Groby, V. Tournat, O. Dazel, and O. Umnova, "Absorption of sound by porous layers with embedded periodic array of resonant inclusions," *J. Acoust. Soc. Am.* **134**, 4670–4680 (2013).
- ¹⁰J.-P. Groby, W. Lauriks, and T. Vigran, "Total absorption peak by use of a rigid frame porous layer backed with a rigid multi-irregularities grating," *J. Acoust. Soc. Am.* **127**, 2865–2874 (2010).
- ¹¹J.-P. Groby, B. Brouard, O. Dazel, B. Nennig, and L. Kelders, "Enhancing the absorption of a rigid frame porous layer by use of a rigid backing with three-dimensional periodic multi-irregularities," *J. Acoust. Soc. Am.* **133**, 821–831 (2013).
- ¹²Z. Yang, J. Mei, M. Yang, N. Chan, and P. Sheng, "Membrane-type acoustic metamaterial with negative dynamic mass," *Phys. Rev. Lett.* **101**, 204301 (2008).
- ¹³J. Mei, G. Ma, M. Yang, Z. Yang, W. Wen, and P. Sheng, "Dark acoustic metamaterials as super absorbers for low-frequency sound," *Nature Commun.* **3**, 756 (2012).
- ¹⁴S. Kim, Y.-H. Kim, and J.-H. Jang, "A theoretical model to predict the low-frequency sound absorption of a Helmholtz resonator array," *J. Acoust. Soc. Am.* **119**, 1933–1936 (2006).
- ¹⁵S.-H. Seo, "Silencer design by using array resonators for low-frequency band noise reduction," *J. Acoust. Soc. Am.* **118**, 2332–2338 (2005).
- ¹⁶W. Yunker, C. Stevens, G. Flowers, and R. Dean, "Sound attenuation using microelectromechanical systems fabricated acoustic metamaterials," *J. Appl. Phys.* **113**, 024906 (2013).
- ¹⁷C.-L. Ding and X.-P. Zhao, "Multi-band and broadband acoustic metamaterial with resonant structures," *J. Phys. D: Appl. Phys.* **44**, 215402 (2011).
- ¹⁸H. Zeng, C. Luo, H. Chen, S. Zhia, and X. Zhao, "Flute-model acoustic metamaterials with simultaneously negative bulk modulus and mass density," arXiv:1210.2527 (2012).
- ¹⁹C. Boutin, "Acoustics of porous media with inner resonators," *J. Acoust. Soc. Am.* **134**, 4717–4729 (2013).
- ²⁰J.-P. Groby, B. Nennig, C. Lagarrigue, B. Brouard, O. Dazel, and V. Tournat, "Using simple shape three-dimensional rigid inclusions to enhance porous layer absorption," *J. Acoust. Soc. Am.* **136**, 1139–1148 (2014).
- ²¹A. Selamet and I. Lee, "Helmholtz resonators with extended neck," *J. Acoust. Soc. Am.* **113**, 1975–1985 (2003).
- ²²D. Johnson, J. Koplik, and R. Dashen, "Theory of dynamic permeability and tortuosity in fluid-saturated porous media," *J. Fluid Mech.* **176**, 379–402 (1987).
- ²³J.-P. Groby, E. Ogam, L. De Ryck, N. Sebaa, and W. Lauriks, "Analytical method for ultrasonic characterization of homogeneous rigid porous materials from transmitted and reflected coefficients," *J. Acoust. Soc. Am.* **127**, 764–772 (2010).
- ²⁴J.-F. Allard and N. Atalla, *Propagation of Sound in Porous Media: Modelling Sound Absorbing Materials* (John Wiley & Sons, Chichester, UK, 2009), Chap. 5, pp. 73–107.
- ²⁵U. Ingard, "On the theory and design of acoustic resonators," *J. Acoust. Soc. Am.* **25**, 1037–1061 (1953).
- ²⁶Y. Cheng and X. Liu, "Coupled resonant modes in twisted acoustic metamaterials," *Appl. Phys. A* **109**, 805–811 (2012).
- ²⁷T. Johansson and M. Kleiner, "Theory and experiments on the coupling of two Helmholtz resonators," *J. Acoust. Soc. Am.* **110**, 1315–1328 (2001).



Design of metaporous supercells by genetic algorithm for absorption optimization on a wide frequency band



C. Lagarrigue*, J.-P. Groby, O. Dazel, V. Tournat

LUNAM Université, Université du Maine, CNRS, LAUM UMR 6613, Av. O. Messiaen, 72085 Le Mans, France

ARTICLE INFO

Article history:

Received 16 January 2015

Received in revised form 25 August 2015

Accepted 10 September 2015

Keywords:

Metamaterials

Porous materials

Metaporous

Finite element method

Genetic algorithm optimization

ABSTRACT

The optimization of acoustic absorption by metaporous materials made of complex unit cells with 2D resonant inclusions is realized using genetic algorithm. A nearly total absorption over a wide frequency band can be obtained for thin structures, even for frequencies below the quarter wavelength resonances i.e., in a sub-wavelength regime. The high absorption performances of this material are due to the interplay of usual visco-thermal losses, local resonances and trapped modes. The density of resonant and trapped modes in this dissipative porous layer, is a key parameter for broadband absorption. The best configurations and critical coupling conditions are found by genetic algorithm optimization. Several types of resonators are included gradually in the studied configurations (split-rings, Helmholtz resonators, back cavities) with increasing complexity. The optimization leads to a metaporous structure with a 2-cm sub-wavelength layer thickness, exhibiting a nearly total absorption between 1800 Hz and 7000 Hz. The influence of the incidence angle on the absorption properties is also shown.

© 2015 Published by Elsevier Ltd.

1. Introduction

Acoustic porous materials are widely used in noise control applications for their interesting sound absorbing properties in the middle and high frequency ranges (>1000 Hz) but they suffer from a lack of efficiency at lower frequencies [1]. These last decades, several ways to avoid the problem of absorption in the low part of the audible frequency range (<1000 Hz) have been proposed. The generally implemented solutions make use of multi-layer packages. This solution has limits at low frequencies while trying to keep the thickness of the treatment relatively small compared to the incident wavelength that has to be absorbed. Recently, new directions have been explored, based on combining resonant and scattering phenomena with the traditional viscous and thermal losses. Whatever the frequency is, the key is to excite modes of the structure that will trap the energy inside it for a long time and therefore enhance the absorption of the whole structure. Among different studied configurations, i.e., double porosity [2,3], dead-end porosity [4], multiple scattering [5], we focus here on configurations composed of periodic rigid inclusions and resonant inclusions embedded in a porous layer (often referred as metaporous materials) [6–8].

The effect on the absorption properties of a periodic embedment of both non-resonant and resonant inclusions in a porous layer has been studied in two (or three) dimensions, when the porous layer is either backed by a rigid backing [6–9], possibly incorporating cavities [10], or radiating in a semi-infinite half-space [11] in the case of transmission problems. Different inclusion shapes have been studied [6,7,12,13] showing similar results at low frequencies. The enhanced absorption compared to simple porous media has been explained by the coupling of several phenomena: scattering by periodic inclusions and/or back cavities local resonances that trap the energy inside the inclusions or cavities, excitation of a localized mode that traps energy between the rigid backing and the inclusions, and excitation of the modified mode of the backed layer similar to Wood's anomaly. The rigid backing acts as a perfect mirror and allows interaction between the inclusion and its image to excite the trapped mode [6]. In these previous studies, the relatively simple configurations allowed for some analytical and semi-analytical modeling, together with numerical simulations and experiments. Consequently, the observed effects of perfect absorption (i.e. the absorption coefficient is 1), or nearly perfect absorption (the absorption coefficient is close to 1) for narrow frequency bands could be interpreted and associated to specific processes. The dependencies of the absorption properties on the metaporous cell parameters (such as the inclusion shape, size, position, and resonance frequency) could be interpreted and in some cases predicted and tailored.

* Corresponding author.

E-mail address: clement.lagarrigue@univ-lemans.fr (C. Lagarrigue).

Table 1
Supercells geometric parameters range values.

x_i (mm)	y_i (mm)	ϕ_i (rad)	r_i (mm)	e_i (%)
[4; 16]	[4; 16]	[0; 2π]	[2; 10]	[10; 90]

Table 2
Parameters used for the routines.

Routine	Selection	Mutation	Crossover	Sharing	Scaling
Type	Roulette	Multipoint	Non-uniform	Large exploration	Exponential
Parameter		3	$b = 1$	$\alpha = 0.8$ $\sigma = 0.95$	$q = 1$

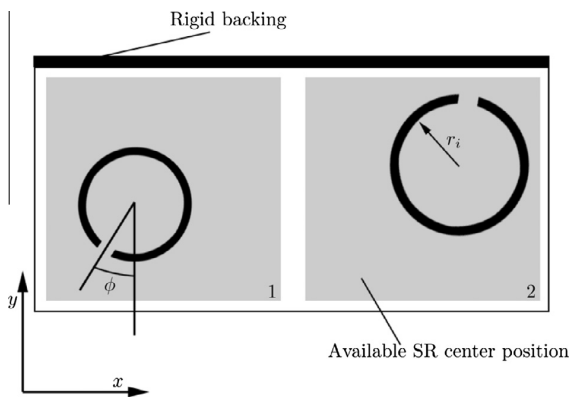


Fig. 1. Outline of a random unit cell.

Table 3
Parameters of the porous foam used in the article.

ϕ	α_∞	A (μm)	A' (μm)	σ (N s m^{-4})	f_v (Hz)
0.95	1.42	180	360	8900	781

In the present article, we propose a way to design metaporous materials able to strongly absorb the incident acoustic energy over a wide frequency band, for wavelengths in air larger than the material thickness. As mentioned previously, the density of modes trapping the energy inside the layer should be large enough in the frequency range of interest, which requires complex metaporous unit cells (or super-cells). The number of parameters defining the metaporous super-cell can consequently become large (all geometrical parameters of the inclusions and back cavities, parameters of the porous medium) and the effect of varying one of them on the absorption properties is unpredictable due to the influence on several coupled or competing absorption processes. In particular, the perfect absorption condition which can be analytically found in some configurations defined by only few parameters (see e.g. the one-dimensional case of a weakly lossy resonator, critically coupled to a waveguide cavity in [14], or the two-dimensional case of membrane resonator panel in [15]) is impossible to predict in the case of metaporous two-dimensional and three-dimensional super-cells composed of several resonators, back cavities and a porous material with frequency dependent acoustic properties. Therefore, in order to find metaporous super-cell configurations having high and broadband absorption, we make use of Genetic Algorithm (GA) optimization. In other words, we find empirically the metaporous super-cell parameters such that the different wave

processes (scattering, trapped modes, local resonances and critical coupling, frequency dependent wave dissipation...) play together for high and broadband absorption.

The configuration analyzed in the following is composed of an infinite periodic set of two-dimensional (2D) metaporous super-cells. Each super-cell can contain 2D resonant inclusions embedded in a porous layer which is backed by a hard wall with or without resonant cavities. For the sake of clarity and to analyze the influence of each elements, we decided to make an incremental study where the complexity of the super-cells increases by the successive addition of ingredients. The optimization by the in-home genetic algorithm code begins with a previous configuration analyzed in [8] and evolves to account for more resonators per super-cells and a larger number of degrees of freedom.

2. Optimization by genetic algorithm

The genetic algorithm is set to find the configuration having the highest acoustic absorption in average over 80 points on the frequency range from 100 Hz to 7 kHz.

The geometry of the problem is two-dimensional and periodic, the inclusions being split-rings and 2D Helmholtz resonators and the cavities being 2D. The problem therefore reduces to the solution of the pressure field in the unit cell because of the periodicity and excitation by a plane incident wave. Bloch-Floquet conditions are applied to the left and right boundaries to consider the infinite periodicity as explained in [16]. For this to be correctly implemented, the two sides were discretized with similar nodes, i.e. identical vertical coordinates. All simulations are performed by considering a normal incident wave arising from a semi infinite space to the bottom of the cell. The top of the cell is considered perfectly rigid (Neumann type boundary condition). All the geometrical parameters are chosen by the algorithm except two: the thickness (20 mm) of the plate and the spatial periodicity (40 mm). The other parameters (summarized in Table 1) are set in a range of values that allow almost all configurations: where $i = 1$ or 2 , x_i and y_i are respectively the longitudinal and the vertical position of the inclusion i , ϕ_i is the angular position of the slit, the origin is chosen centered on each inclusion and the direction is $-y$, r_i is the internal radius of the inclusion and e_i is the thickness.

The program is coded in Fortran and uses classical minimum search (selection, mutation and crossover [17,18]) and fast convergence (sharing, scaling and elitism [17,19]) routines. Because of the possible high number of parameters, these routines are configured

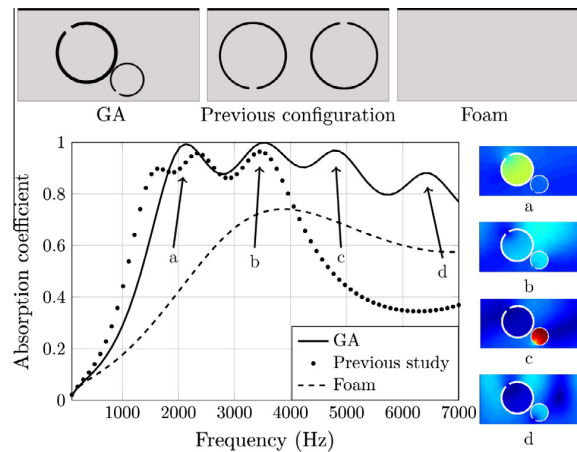


Fig. 2. Absorption coefficient for a super-cell composed of two split-rings.

Table 4
Geometric parameter values for the first optimization results called GA.

x_1 (mm)	x_2 (mm)	y_1 (mm)	y_2 (mm)	ϕ_1 (rad)	ϕ_2 (rad)	r_1 (mm)	r_2 (mm)	e_1 (mm)	e_2 (mm)
15	24	10	5	1.25π	22	7	4	0.85	0.75

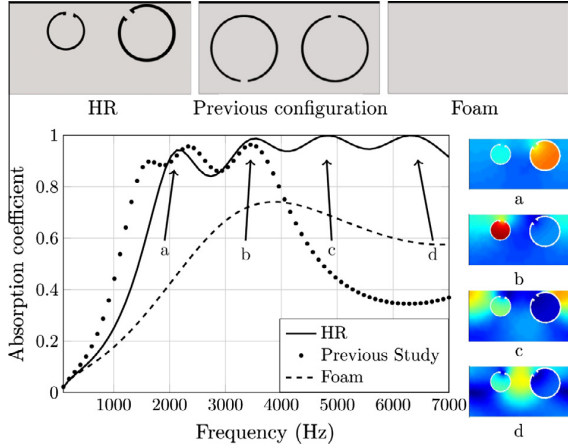


Fig. 3. Absorption coefficient for a supercell composed of two 2D Helmholtz resonators.

to ensure a large exploration of the possibilities. All the types of routines and factors used are summarized in Table 2.

During an iteration of the optimization process, a population is set with different geometry parameters, then each individual acoustic response is simulated with a Finite Element Method (FEM) program. This program has been developed and validated in [16,6,8] and uses the open source software FreeFem++ to mesh each configurations. Linear finite elements are used to approximate the pressure inside the unit cell, thereby leading to a discretized problem of 1500 elements and 800 nodes. The porous mesh is configured to be adaptive and to always have elements 10 times smaller than the smallest wavelength in air ($\lambda = 5$ cm for 7 kHz in this case). The mesh is refined in the inclusion opening to ensure a good discretization of the pressure field. For each individual, the size and the number of mesh elements are recalculated according to the size of the inclusions. The optimization is done by comparing each absorption coefficient and by choosing the best geometries for the next iteration. The implemented porous model is an equivalent fluid where the effective density is modeled by the Johnson et al. model [20] and the bulk modulus by the Champoux–Allard model [21]. The inclusions are considered rigid. The FEM program gives the absorption coefficient as:

$$A(j) = 1 - \sum_q \frac{\text{Re}(k_{2q})}{k_{20}^i} |R_q(j)|^2 \quad (1)$$

with $R_q(j)$ the reflexion coefficients of the q th Bloch-wave for the frequency j , k_{2q} the Bloch-wavenumber along the normal incidence and k_{20}^i the incident plane wave.

Table 5
Geometric parameters values for the second optimization results called HR.

x_1 (mm)	x_2 (mm)	y_1 (mm)	y_2 (mm)	ϕ_1 (rad)	ϕ_2 (rad)	r_1 (mm)	r_2 (mm)	l_1 (mm)	l_2 (mm)
12.5	30	14	13.5	0.91π	1.25π	4	6	0.1	0.14

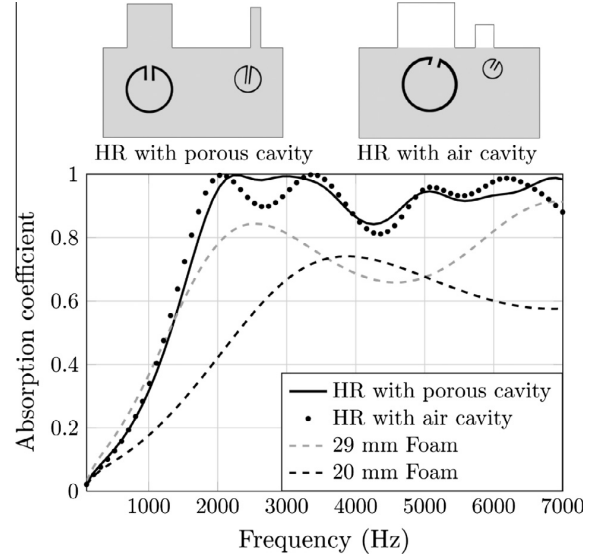


Fig. 4. Absorption coefficient for a supercell composed of two 2D Helmholtz resonators and two cavities.

Here, the fitness [17,18] is linked to the absorption coefficient averaged over the considered frequency range and defined such as $f_i = 1 - \alpha_i$, where

$$\alpha_i = \frac{1}{n_{freq}} \sum_{j=1}^{n_{freq}} A(j), \quad (2)$$

with n_{freq} the number of frequencies of the absorption coefficient calculated by the FEM code. To avoid optimization results providing non-realistic geometries, the GA needs to be constrained. The solution chosen here is to make the list of all non-realistic solutions (overlapping inclusions for example) and to penalize the fitness if the GA chooses one of them (if non-realistic solution: $f_i = 1, f_i = 1 - \alpha_i$ else). All simulations are done with populations of 30 individuals and 1000 generations to ensure a good convergence of the results.

The genetic algorithm is first used to optimize a metaporous, whose unit cell is composed of a porous plate (fireflex®, Recticel®, a porous material widely used for its good acoustic and fire resistant properties) backed with a rigid wall and two resonant inclusions. Fig. 1 depicts one of the unit cell analyzed during the optimization process and Table 3 gives porous matrix parameters.

With σ the static flow resistivity, α_∞ the tortuosity, ϕ the porosity, Λ the viscous characteristic length, Λ' the thermal characteristic length and f_v the Biot frequency.

Table 6
Geometric parameters values for the optimizations with HR and back cavity.

Inclusions	x_1 (mm)	x_2 (mm)	y_1 (mm)	y_2 (mm)	ϕ_1 (rad)	ϕ_2 (rad)	r_1 (mm)	r_2 (mm)	l_1 (mm)	l_2 (mm)
HRC1	10	32	10.5	13	π	0.91π	5	3	1.2	1
HRC2	10.5	24.5	12	15.5	1.08π	1.16π	6	2	1.2	1.6
Cavity	h_1 (mm)	h_2 (mm)	w_1 (mm)	w_2 (mm)	x_1 (mm)	x_2 (mm)				
HRC1	9.8	9	10	2	15	35				
HRC2	10	5	12.5	4	14	31				

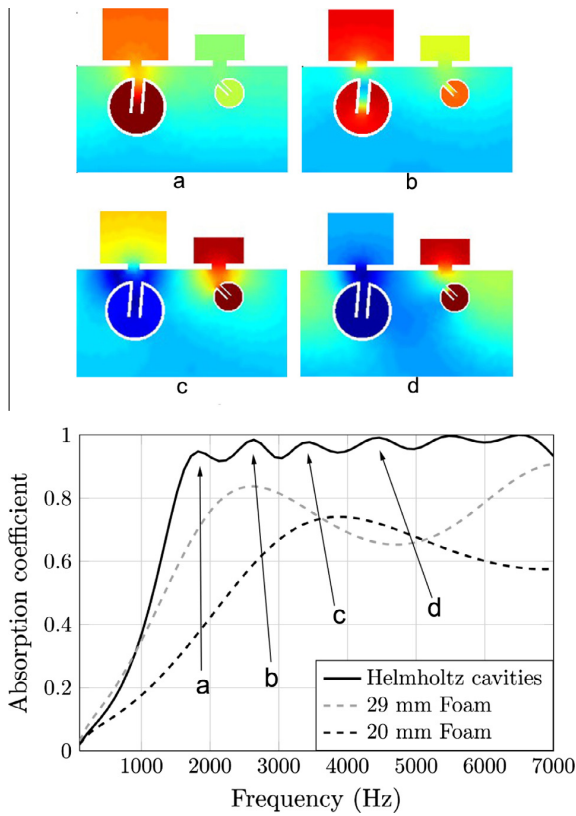


Fig. 5. Absorption coefficient for a supercell composed of two 2D HR and two Helmholtz air cavity.

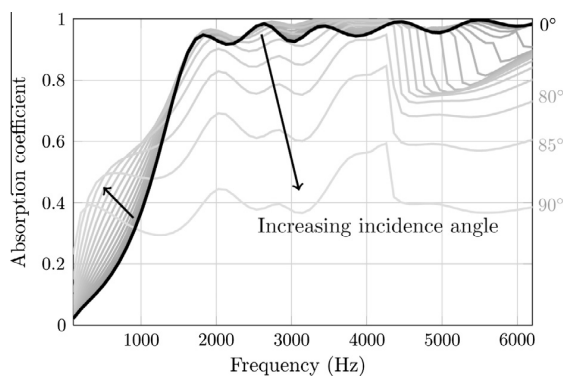


Fig. 6. Comparison of the absorption coefficient in function of the incidence angle.

3. Optimization results

Compared to the previously studied configurations [8], the split-ring positions, radii and split-ring thicknesses are here optimized by the GA. Fig. 2 shows a comparison of the results of a first optimization, the previously proposed unit cell and the foam without any inclusion. GA results (dimensions summarized in Table 4) exhibit a very good enhancement of the absorption properties with a fitness of 0.25 while the unit cell of the previous configuration has a fitness of 0.42 and the foam alone 0.41. In the GA optimized cell, the two inclusions are almost in contact. It is still manufacturable by inserting these two inclusions in contact, or by considering only one inclusion with this special shape manufactured with a 3D printer.

In Fig. 2 two different localized modes are observed: at 3500 Hz, snapshot (b) and at 6500 Hz snapshot (d), that trap the energy between the rigid backing and the inclusions. The two other peaks are clearly due to the resonance of the inclusions (snapshot (a) and (c)). The addition of this four phenomena leads to the absorption enhancement over the frequency band considered. Even if the absorption coefficient of the GA results is lower than the previous study in the lowest frequency range, it does not exhibit the Bragg effect around 6 kHz. This effect appears in periodic media when the periodicity is half wavelength of the incident wave [22]. In here, it is related to the distance between the inclusion and its image with respect to the rigid backing. Here it is minimized by tuning the resonance effects near this frequency (the resonance of an inclusion snapshot (c) and a localized mode snapshot (d)).

Unfortunately, these resonance frequencies are all related to the size and position of the inclusions and it is not possible to reach a larger absorption coefficient at low frequency without considering split-rings larger than the thickness of the plate. This possibility is not compatible with our constrain of fixed thickness. To try to solve this problem, a neck is added to the split-rings to lower the resonance frequency and to add another degree of freedom in the GA. This type of inclusion is called in this paper 2D Helmholtz Resonator or 2DHR (see Fig. 3).

The results are close to the first simulation with a fitness of 0.24. The absorption coefficient is now lower below 2600 Hz but larger elsewhere, in particular near the Bragg frequency where it has completely vanished. These results are different from what we were expecting by using inclusions that can have lower resonance frequencies but changing resonances for the low frequency range, would have destroyed the absorption coefficient elsewhere resulting in a much higher fitness (see Table 5).

Another way to overcome this limit is to add air filled back cavity. They can act as quarter wavelength resonators but must be very long in comparison to the dimension of the plate to have a sufficiently low resonance frequency and this is also out of the scope of this article. However, these cavities can be curved allowing to make a ultra thin low frequency sound absorbing panels based on coplanar spiral tubes or coplanar Helmholtz resonators [23].

The initial goal of enhancing the absorption coefficient below the Biot frequency with the inclusions or with the back cavities

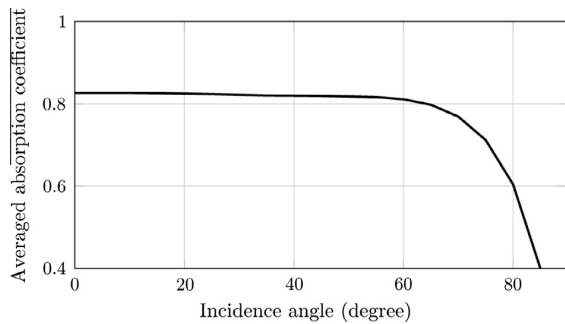


Fig. 7. Averaged absorption coefficient in function of the incidence angle.

is aborted because of this dimensions constraint. Now cavities are still added, but with reasonable dimensions (less than the thickness of the plate) to add more resonances and to keep the absorption coefficient near 1 over a larger frequency range. The rigid backing is now modified and present two rectangular cavities per spatial period. Two other runs are performed, one with the cavity filled with the same porous media and a second one with a cavity filled with air (see Fig. 4).

These two results (dimensions are summarized in Table 6) present respectively a fitness of 0.22 and 0.21 that are better than the previous one(s). The absorption coefficient is compared with the one of the two corresponding homogeneous layer thicknesses: 20 mm and 29 mm. This last value corresponds to the total thickness of the porous plate + cavity. The absorption coefficient now reaches 1 near 2000 Hz and stays close to unity for higher frequencies, except near 4200 Hz. In this simulations, the GA tends to place again the inclusions in front of the cavity, with the slit facing the back cavity. This results in the excitation of coupled modes between one inclusion and one cavity and gives rise to the absorption coefficient for frequencies lower than the resonance frequency of both elements. For example, in case of a unit cell with air cavity, a coupled mode is excited at 1800 Hz whereas the split-ring resonance is near 2400 Hz. This phenomenon is developed in the next simulation. As expected, even with these optimizations the metaporous cannot reach high absorption at very low frequency. There is clearly a limit at 1500 Hz due to the Biot frequency ($f_v = 781$ Hz for Fireflex material). Below this value, the acoustic propagation is described by a diffusion equation, that cannot allow the HR (filled with porous material) to resonate. Thus, below this frequency, this kind of resonators are of poor interest, unless the porous inside is removed. In this case, the resonance frequency will increase and this will not be interesting anymore for our application.

The next simulations consider a similar configuration as before with air filled back cavities and partially closed openings. This allows to lower the resonance frequency of the cavities because it is now considered as an Helmholtz resonator.

This optimized geometry reaches a fitness of 0.17, which is the best metaporous that can be obtained here. The frequency band of high absorption is now close to unity from 1600 Hz to 7000 Hz with the same thickness than previously (2 cm layer thickness and 9 mm of depth back cavity). The phenomenon of interaction between two elements is clearly visible. At 1600 (snapshot a of Fig. 5) the left HR and the left cavity resonate together and a high pressure zone is clearly visible between them. This exhibits a coupled mode and lower the resonance frequency of the ensemble (same phenomenon at 3400 Hz, snapshot c for the right inclusion and cavity). At 2800 Hz (snapshot b) of Fig. 5) the two elements resonate again but this time, the pressure is localized inside each resonator (same phenomenon at 4500 Hz, snapshot d). This mean that they resonate at their own resonance frequency.

Geometries depicted here are also efficient for other incidence angle. In Fig. 6 only the results of simulation for the last geometry are plotted but the other exhibit the identical behavior. The figure shows the absorption coefficient for incidence angles from 0° (normal incidence, the black curve) to 90° (grazing incidence, gray curves). This is summarized in Fig. 7 where the averaged absorption coefficient over the frequency is plotted in function of the incidence angle. These figures show that the absorption coefficient remains large for a wide range of angle incidence (from 0° to 75°) and only decreases near the grazing incidence. This means that only optimizing for the incidence angle is acceptable to design geometries efficient for diffuse field.

The absorption increases at low frequency when the incidence angle increases because the incident wave propagate over a longer distance to reach the rigid backing and being reflected. Other phenomena are not angle dependent like the inclusions or back cavities resonances and can be always excited.

4. Conclusion

Absorption by metaporous materials is driven by several processes, local resonances, localized mode excitation and mode couplings. It is difficult to tune all of these processes to tailor a high absorption over a wide frequency band because it requires complex geometry super-cells with numerous and interconnected geometrical degrees of freedom. We have successfully used a genetic algorithm to find nearly perfect absorption conditions over a frequency band of 100–7000 Hz: it appears that for a 2-cm thick layer, it is possible to have an almost unity absorption band from 1800 Hz to 7000 Hz by using split-rings (with necks) and back cavities. It is also shown that this optimized unit cell is efficient for non normal incidence angles and provides a good absorption even for incidence angles close from the grazing one. This study only focuses on super-cells with a couple of resonators but there are numerous configurations that could be advantageous. In particular, Helmholtz resonators filled with air (instead of porous medium) could lead to resonances with moderate quality factors below the porous medium Biot frequency, which is not possible with porous filled resonators. If the neck is sufficiently long, it is possible to obtain an arbitrary low resonance frequency and improve even more the absorption properties at long wavelengths.

References

- [1] Allard J-F, Atalla N. Propagation of sound in porous media: modelling sound absorbing materials. Chichester: John Wiley & Sons; 2009 [chapter 5].
- [2] Olny X, Boutin C. Acoustic wave propagation in double porosity media. *J Acoust Soc Am* 2003;114:73–89.
- [3] Auriault J, Boutin C. Deformable porous media with double porosity iii: acoustics. *Trans Porous Media* 1994;14(2):143–62.
- [4] Dupont T, Leclaire P, Sicot O, Gong X, Panneton R. Acoustic properties of air-saturated porous materials containing dead-end porosity. *J Appl Phys* 2011;110:094903.
- [5] Tournat V, Pagneux V, Lafarge D, Jaouen L. Multiple scattering of acoustic waves and porous absorbing media. *Phys Rev E* 2004;70:026609.
- [6] Groby J-P, Ducloux A, Dazel O, Boeckx L, Kelders L. Enhancing absorption coefficient of a backed rigid frame porous layer by embedding circular periodic inclusions. *J Acoust Soc Am* 2011;130:3771–80.
- [7] Nennig B, Renoux Y, Groby J-P, Aurégan Y. A mode matching approach for modeling two dimensional porous grating with infinitely rigid or soft inclusions. *J Acoust Soc Am* 2012;131:3841–52.
- [8] Lagarrigue C, Groby J, Tournat V, Dazel O, Umnova O. Absorption of sound by porous layers with embedded periodic arrays of resonant inclusions. *J Acoust Soc Am* 2013;134(6):4670–80.
- [9] Groby J-P, Lagarrigue C, Brouard B, Dazel O, Tournat V, Nennig B. Using simple shape three-dimensional rigid inclusions to enhance porous layer absorption. *J Acoust Soc Am* 2014;136(3):1139–48.
- [10] Groby J-P, Ducloux A, Dazel O, Boeckx L, Lauriks W. Absorption of a rigid frame porous layer with periodic circular inclusions backed by a periodic grating. *J Acoust Soc Am* 2011;129:3035–46.
- [11] Groby J-P, Wirgin A, Ogam E. Acoustic response of a periodic distribution of macroscopic inclusions within a rigid frame porous plate. *Waves Random Complex Media* 2008;18:409–33.

- [12] Lagarrigue C, Groby J-P, Tournat V, Dazel O. Parametric study of a metaporous made of inclusions embedded in a rigid frame porous material glued on a rigid backing. In: Proc of acoustics 2012; 2012 [hal-00810737].
- [13] Hyun H, Siu-Kit L. Effects of inclusion shapes within rigid porous materials on acoustic performance. In: 164th meeting of the acoust soc Am, Kansas City, vol. 132; 2012. p. 1905.
- [14] Romero-García V, Theocharis G, Richoux O, Merkel A, Tournat V, Pagneux V. Perfect and broadband acoustic absorption by critical coupling. Available from: 1501.00191.
- [15] Ma G, Yang M, Xiao S, Yang Z, Sheng P. Acoustic metasurface with hybrid resonances. *Nat Mater* 2014;13(9):873–8. <<http://dx.doi.org/10.1038/nmat3994>>.
- [16] Allard J, Dazel O, Gautier G, Groby J, Lauriks W. Prediction of sound reflection by corrugated porous surfaces. *J Acoust Soc Am* 2011;129:1696.
- [17] Goldberg D. *Genetic algorithms in search, optimization, and machine learning*. 1st ed. Addison-Wesley Professional; 1989.
- [18] Spears WM, De Jong KA. An analysis of multi-point crossover; 1991. p. 301–15.
- [19] Michalewicz Z. *Genetic algorithms + data structures = evolution programs*. Springer; 1998.
- [20] Johnson D, Koplik J, Dashen R. Theory of dynamic permeability and tortuosity in fluid-saturated porous media. *J Fluid Mech* 1987;176(1):379–402.
- [21] Champoux Y, Allard J. Dynamic tortuosity and bulk modulus in air-saturated porous media. *J Appl Phys* 1991;70(4):1975–9.
- [22] Joannopoulos J. *Photonic crystals: molding the flow of light*. Princeton Univ Pr; 2008 [chapters 5 and 10].
- [23] Cai X, Guo Q, Hu G, Yang J. Ultrathin low-frequency sound absorbing panels based on coplanar spiral tubes or coplanar Helmholtz resonators. *Appl Phys Lett* 2014;105(12):121901.

Chapter **7**

Articles related to Chapter 2: Periodic and macroscopically inhomogeneous bulk materials and their limitations

Contents

Appl. Phys. Lett., 90:181901, 2007	133
J. Acoust. Soc. Am., 130:1390-1398, 2011	136
J. Acoust. Soc. Am., 133:247-254, 2013	145
J. Acoust. Soc. Am., 139:1660-1671, 2016	153
Appl. Phys. Lett., 109:121902, 2016	165
arXiv:1708.03343v1	169
Sci. Rep., 7:5389, 2017	182

Acoustic wave propagation in a macroscopically inhomogeneous porous medium saturated by a fluid

L. De Ryck, J.-P. Groby, P. Leclaire,^{a)} and W. Lauriks^{b)}

Laboratorium voor Akoestiek en Thermische Fysica, K. U. Leuven, Celestijnenlaan 200D, 3001 Heverlee, Belgium

A. Wirgin and Z. E. A. Fellah

Laboratoire de Mécanique et d'Acoustique, UPR 7051 CNRS, 31 chemin Joseph Aiguier, 13009 Marseille, France

C. Depollier

Laboratoire d'Acoustique de l'Université du Maine, Avenue Olivier Messiaen, 72000 Le Mans, France

(Received 10 August 2006; accepted 9 December 2006; published online 30 April 2007)

The equations of motion in a macroscopically inhomogeneous porous medium saturated by a fluid are derived. As a verification of their validity, these equations are reduced and solved for rigid frame porous systems. The reflection and transmission coefficients and their corresponding time signals are calculated numerically using wave splitting Green's function approach for a two-layer porous system considered as one single porous layer with a sudden change in physical properties. The results are compared to experimental results and to those of the classical transfer matrix method for materials saturated by air in the ultrasonic frequency range. © 2007 American Institute of Physics. [DOI: 10.1063/1.2431570]

An inhomogeneous medium is one with properties that vary with position. Inhomogeneous and layered materials can be found in many fields of physics, for instance, in optics and electromagnetism^{1,2} or in acoustics.^{3,4} Other examples are geophysical⁵ or granular⁶ media. The study of the acoustic wave propagation in inhomogeneous porous media is of great interest in building and civil engineering and in petroleum prospecting.

In this letter, acoustic propagation in fluid-saturated macroscopically inhomogeneous porous materials is studied. These media have received far less attention than homogeneous porous media.⁷⁻¹⁰ It is assumed that the wavelengths are greater than the average heterogeneity size at the pore scale so that the physical properties are homogenized. However, these properties can vary with the observation point within the material at the macroscopic scale of the specimen. The equations of motion are derived from Biot's alternative formulation of 1962 (Ref. 11) in which the total stress tensor, the fluid pressure, the solid displacement, and the fluid/solid relative displacement are used. It was briefly stated by Biot¹¹ and confirmed¹² that these variables should be employed for porous media with inhomogeneous porosity. The equations of motion for an inhomogeneous porous medium with elastic skeleton are derived. A verification of their validity is the study of a porous material saturated by air in the rigid frame approximation, i.e., when the fluid is light and the solid skeleton immobile.¹⁰ In this case, a wave equation is derived and solved numerically for a two-layer porous system treated as one single porous medium with a sudden but continuous change in physical properties. This provides an excellent means of comparing the proposed method: wave splitting Green's function approach (WS-GF),² which is applicable to any depth-dependent inhomogeneous system, to the results of the well established transfer matrix method (TMM) devel-

oped to calculate the acoustical properties of multilayer porous systems.¹⁰ Experimental results obtained at ultrasonic frequencies in a two-layer material saturated by air are compared to the simulations.

The constitutive linear stress-strain relations in an initially stress-free, isotropic porous medium are¹¹

$$\sigma_{ij} = 2\mu\epsilon_{ij} + \delta_{ij}(\lambda_c\theta - \alpha M\zeta), \quad (1)$$

$$p = M(-\alpha\theta + \zeta), \quad (2)$$

where σ_{ij} is the total stress tensor and p the fluid pressure in the pores; δ_{ij} denotes the Kronecker symbol (the summation on repeated indices is implied); $\theta = \nabla \cdot \mathbf{u}$ and $\zeta = -\nabla \cdot \mathbf{w}$ are, respectively, the dilatation of the solid and the variation of fluid content where \mathbf{u} is the solid displacement and $\mathbf{w} = \phi(\mathbf{U} - \mathbf{u})$ the fluid/solid relative displacement (\mathbf{U} is the fluid displacement); ϕ is the porosity; $\epsilon_{ij} = \frac{1}{2}(u_{i,j} + u_{j,i})$ the strain tensor of the solid (the comma denotes spatial partial derivatives); $\lambda_c = \lambda + \alpha^2 M$, where λ , μ , M are elastic constants and α a coefficient of elastic coupling. These parameters were defined by Biot and Willis.¹³ Applying the momentum conservation law in the absence of body forces, the equations of motion are written

$$\nabla \cdot \boldsymbol{\sigma} = \rho_f \ddot{\mathbf{w}}, \quad (3)$$

$$-\nabla p = \rho_f \ddot{\mathbf{u}} + m \ddot{\mathbf{w}} + \frac{\eta}{\kappa} F \dot{\mathbf{w}}, \quad (4)$$

where the dot and double dot notations refer to the first and second order time derivatives, respectively; ρ_f is the density of the fluid in the (interconnected) pores, ρ the bulk density of the porous medium, such that $\rho = (1 - \phi)\rho_s + \phi\rho_f$, where ρ_s is the density of the solid; $m = \rho_f \tau_\infty / \phi$ is a mass parameter defined by Biot,¹¹ τ_∞ is the tortuosity, η the viscosity of the fluid, κ the permeability, and F the viscosity correction function. For an inhomogeneous porous layer or a half space

^{a)}Electronic mail: philippe.leclaire@fys.kuleuven.be

^{b)}Electronic mail: walter.lauriks@fys.kuleuven.be

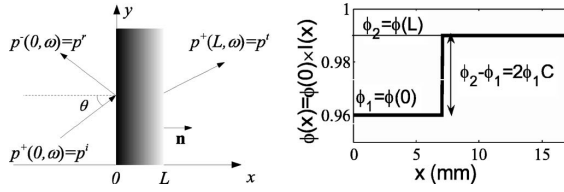


FIG. 1. Slab of inhomogeneous porous material and example of a simulated inhomogeneity profile for $\phi(x)$.

whose properties vary along the depth x , the following parameters in the above equations are now dependent on x : λ , μ , λ_c , α , M , ϕ , ρ , m , τ_∞ , κ , and F . Inserting Eqs. (1) and (2) into Eqs. (3) and (4) yields the equations of motion in terms of the displacements

$$\begin{aligned} \nabla[(\lambda_c + 2\mu) \nabla \cdot \mathbf{u} + \alpha M \nabla \cdot \mathbf{w}] - \nabla \wedge [\mu \nabla \wedge \mathbf{u}] \\ - 2 \nabla \mu \nabla \cdot \mathbf{u} + 2 \nabla \mu \wedge (\nabla \wedge \mathbf{u}) + 2[\nabla \mu \cdot \nabla] \mathbf{u} = \rho \ddot{\mathbf{u}} \\ + \rho_f \ddot{\mathbf{w}}, \end{aligned}$$

$$\nabla[M \nabla \cdot \mathbf{w} + \alpha M \nabla \cdot \mathbf{u}] = \rho_f \ddot{\mathbf{u}} + m \ddot{\mathbf{w}} + \frac{\eta}{\kappa} F \ddot{\mathbf{w}}, \quad (5)$$

where the x dependence of the constitutive parameters has been removed to simplify the notations.

Under the assumption of a rigid frame, $\mathbf{u}=0$, Eqs. (1) and (3) vanish. The system of equations reduces to Eqs. (2) and (4) and can be written in the frequency domain in a more suitable form for acoustical applications as

$$-j\omega p = K_e(x, \omega) \nabla \cdot [\phi(x) \dot{\mathbf{U}}], \quad (6)$$

$$-\nabla p = j\omega \rho_e(x, \omega) \phi(x) \dot{\mathbf{U}}, \quad (7)$$

where $\rho_e(x, \omega)$ and $K_e(x, \omega)$ are, respectively, the effective density and bulk modulus of the inhomogeneous equivalent fluid. Their expressions are

$$\rho_e(x, \omega) = \rho_f \frac{\tau_\infty(x)}{\phi(x)} \left[1 - j \frac{R_f(x) \phi(x)}{\omega \rho_f \tau_\infty} F(x, \omega) \right], \quad (8)$$

$$\begin{aligned} K_e(x, \omega) \\ = \frac{\gamma P_0 / \phi(x)}{\gamma - (\gamma - 1) [1 - j R_f(x) \phi(x) G(x, B^2 \omega) / B^2 \omega \rho_f \tau_\infty]^{-1}}, \end{aligned} \quad (9)$$

where γ is the specific heat ratio, P_0 the atmospheric pressure, and B^2 the Prandtl number. The correction functions $F(x, \omega)$ and $G(x, B^2 \omega)$ depend on x for inhomogeneous media. They are well-defined functions incorporating, respectively, the viscous characteristic length Λ of Johnson *et al.*⁹ and the thermal characteristic length Λ' of Champoux and Allard.¹⁴ The effective density and bulk modulus of the inhomogeneous equivalent fluid are functions of the frequency-independent parameters $\phi(x)$, $\tau_\infty(x)$, $\Lambda(x)$, $\Lambda'(x)$, and of the flow resistivity $R_f(x) = \eta / \kappa(x)$. The wave equation in p can be obtained by combining Eqs. (6) and (7).

The second order differential operator of the wave equation in a homogeneous fluid can be factorized and this yields a system of two coupled first order differential equations. This is the wave splitting description, which was

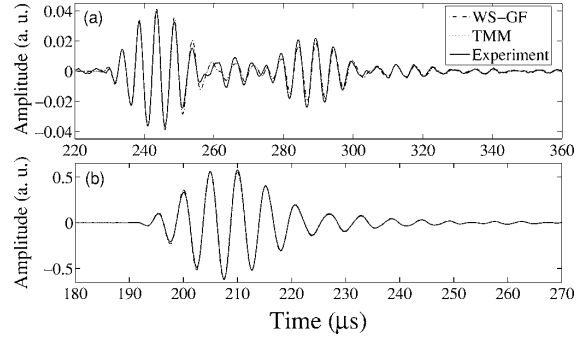


FIG. 2. Signal (a) reflected and (b) transmitted by a two-layer porous system. The incidence is normal.

mainly used in scattering problems in the time domain in electromagnetism¹⁵ and then adapted to the frequency domain.² An inhomogeneous porous slab on which impinges an incident wave is shown in Fig. 1. Applied to the wave equation in the ambient fluid, the so-called “vacuum wave splitting transformation”² is $p^\pm = [p \pm Z_0 \phi(x) \dot{\mathbf{U}} \cdot \mathbf{n}] / 2$, where $Z_0 = \rho_f c_0$ is the characteristic impedance of the fluid surrounding the slab [used instead of $Z_e(x, \omega) = \sqrt{\rho_e(x, \omega) K_e(x, \omega)}$ of the fluid in the slab] and \mathbf{n} the unit normal vector (Fig. 1). A system of linear first order coupled differential equations is obtained from Eqs. (6) and (7):

$$\partial_x p^+ = A^+(x, \omega) p^+ + A^-(x, \omega) p^-,$$

$$\partial_x p^- = -A^-(x, \omega) p^+ - A^+(x, \omega) p^-, \quad (10)$$

with $A^\pm(x, \omega) = j\omega / 2 [(Z_0 / K_e(x, \omega)) \pm (\rho_e(x, \omega) / Z_0)]$.

The computation principle is the following: p^\pm are first calculated in the surrounding homogeneous fluid at $x=L$. An infinitely thin homogeneous layer of thickness dx is inserted at $x=L-dx$ with the corresponding values of ρ_e and K_e . At $x=L$ a new set of p^\pm is determined with the help of Eq. (10). A new layer is added at $x=L-2dx$. Using the updated values of p^\pm at $x=L$, the pressure subfields $p^\pm(L-dx, \omega)$ are calculated. The operation is repeated until the last layer is added at $x=0$. For each new layer, the continuity conditions on p and $\phi(x) \dot{\mathbf{U}} \cdot \mathbf{n}$ are implicitly accounted for on both sides of the cumulated slab. The initialization of the procedure requires that p^\pm must be determined at $x=L$. To avoid this calculation, Green’s function approach^{2,15} is used. Two Green’s functions G^\pm are defined by $\forall x \in [0, L]$, $p^\pm(x, \omega) = G^\pm(x, \omega) p^\pm(L, \omega)$. Green’s functions are characteristic of the sole material properties and describe the internal field. The boundary conditions at $x=L$ are known and are $G^+(L, \omega) = 1$ and $G^-(L, \omega) = 0$. The system of coupled first order linear differential equations in G^\pm obtained by inserting Green’s functions in Eq.

TABLE I. Properties of the two-layer medium studied.

	ϕ	τ_∞	Λ (μm)	Λ' (μm)	R_f (Ns m ⁻⁴)	Thickness (mm)
Layer 1	0.96	1.07	273	672	2843	7.1
Layer 2	0.99	1.001	230	250	12 000	10.0

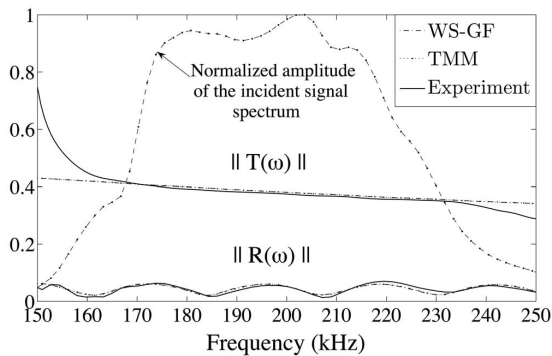


FIG. 3. Normal incidence reflection and transmission coefficients $R(\omega)$ and $T(\omega)$.

(10) can be solved numerically using a Runge-Kutta routine. The reflection and transmission coefficients $R(\omega)$ and $T(\omega)$ are deduced from p^\pm ,

$$p^-(0, \omega) = R(\omega)p^+(0, \omega), \quad (11)$$

$$p^+(L, \omega) = T(\omega)p^+(0, \omega). \quad (12)$$

In the numerical simulations of the reflected and transmitted waves, the physical properties are multiplied by a function $I(x)$ to create the change of their values with depth. This function can be called “inhomogeneity function” and is given by $I(x) = 1 + C(1 - \text{erf}(-(x - x_0)/r))$, where C is a constant (different for each property modeled), erf the error function, x_0 the position of the jump, and r a steepness factor. The steeper is the jump the finer the stepping dx must be for better accuracy. 400 points were chosen to discretize the total slab and $dx = 17.1/400 = 0.0428$ mm. The value chosen for r was $r = 0.1dx$. Smaller values of r had little effect on the computed results. Smoothing the jump by taking $r = 10dx$ resulted in an important reduction of the signal reflected at the interface between the two layers.

The experimental principle and the inhomogeneity function are shown in Fig. 1, where an airborne ultrasonic wave is generated and detected by specially designed (ULTRAN) transducers in a frequency range between 150 and 250 kHz. The incident wave is partly reflected, partly transmitted, and partly absorbed by layers of highly porous polyurethane foams put in contact, not glued. The physical parameters (Table I) of each layer were measured¹⁶ and, within the bounds of the experimental error, those of layer 2 were adjusted to best fit the results for the layered system. The ther-

mal length can be interpreted as a measure of the average pore size (although the “pore” is not straightforwardly defined) while the viscous characteristic length would correspond to an average size of the “constrictions” in the porous medium. The two materials considered are structurally different as one has a fairly high thermal length, resulting in a fairly low flow resistivity. The reflection experiment was carried out with a single transducer used in the pulse-echo mode.¹⁷ Another transducer was required on the other side of the specimen to measure the transmission. A particularly good agreement between the experimental and the simulated results is found for the reflected and transmitted signals [Figs. 2(a) and 2(b)]. The waveforms were calculated from the experimental incident wave form, which was recorded and introduced into the simulation routines. The agreement is also very good for the reflection and transmission coefficients (Fig. 3) in the frequency range of 170–230 kHz. In all figures, the WS-GF curves cannot be distinguished from the TMM curves. The discrepancies below 170 and above 230 kHz in Fig. 3 are attributed to the limited bandwidth of the incident signal, making the experimental results more sensitive to noise outside the useful bandwidth.

The authors are grateful to O. Matsuda for his useful comments on earlier versions of this letter.

¹O. Matsuda and O. B. Wright, *J. Opt. Soc. Am. B* **19**, 3028 (2002).

²O. Forslund and S. He, *Prog. Electromagn. Res.* **19**, 147 (1998).

³J. L. Buchanan, R. P. Gilbert, A. Wirgin, and Y. S. Xu, *Marine Acoustics: Direct and Inverse Problems* (SIAM, Philadelphia, 2004), Vol. 3, Section 1.5.

⁴D. J. Van Manen, J. O. A. Robertsson, and A. Curtis, *Phys. Rev. Lett.* **94**, 164301 (2005).

⁵J. G. Berryman and R. R. Greene, *Geophysics* **45**, 213 (1980).

⁶V. Tourmat, V. Zaitsev, V. Gusev, V. Nazarov, P. Béquin, and B. Castagnède, *Phys. Rev. Lett.* **92**, 085502 (2004).

⁷M. A. Biot, *J. Acoust. Soc. Am.* **28**, 168 (1956).

⁸K. Attenborough, *Phys. Rep.* **82**, 181 (1982).

⁹D. L. Johnson, J. Koplik, and R. Dashen, *J. Fluid Mech.* **176**, 379 (1987).

¹⁰J. F. Allard, *Propagation of Sound in Porous Media: Modeling Sound Absorbing Materials* (Chapman and Hall, London, 1993), pp. 79 and 145.

¹¹M. A. Biot, *J. Appl. Phys.* **33**, 1482 (1962).

¹²J. M. Carcione, *Wavefield in Real Media: Wave Propagation in Anisotropic, Anelastic and Porous Media* (Pergamon, Amsterdam, 2001), Vol. 31, p. 261.

¹³M. A. Biot and D. G. Willis, *J. Appl. Mech.* **24**, 594 (1957).

¹⁴Y. Champoux and J. F. Allard, *J. Appl. Phys.* **70**, 1975 (1991).

¹⁵S. He, *J. Math. Phys.* **34**, 4628 (1993).

¹⁶P. Leclaire, L. Kelders, W. Lauriks, N. R. Brown, M. Melon, and B. Castagnède, *J. Appl. Phys.* **80**, 2009 (1996).

¹⁷Z. E. A. Fellah, S. Berger, W. Lauriks, C. Depollier, P. Trompette, and J. Y. Chapelon, *J. Appl. Phys.* **93**, 9352 (2003).

Propagation of acoustic waves in a one-dimensional macroscopically inhomogeneous poroelastic material

G. Gautier and L. Kelders

Laboratorium voor Akoestiek en Thermische Fysica, KULeuven, Celestijnenlaan 200D, B-3001 Leuven, Belgium

J. P. Groby^{a)} and O. Dazel

Laboratoire d'Acoustique de l'Université du Maine, UMR6613 CNRS/Université du Maine, F-72085 Le Mans Cedex 9, France

L. De Ryck

LMS international NV, 3001 Leuven, Belgium

P. Leclaire

Laboratoire de Recherche en Mécanique et Acoustique, ISAT/Université de Bourgogne, 49 rue Mademoiselle Bourgeois, B.P. 31-58027 Nevers cedex, France

(Received 14 January 2011; revised 12 May 2011; accepted 22 May 2011)

Wave propagation in macroscopically inhomogeneous porous materials has received much attention in recent years. The wave equation, derived from the alternative formulation of Biot's theory of 1962, was reduced and solved recently in the case of rigid frame inhomogeneous porous materials. This paper focuses on the solution of the full wave equation in which the acoustic and the elastic properties of the poroelastic material vary in one-dimension. The reflection coefficient of a one-dimensional macroscopically inhomogeneous porous material on a rigid backing is obtained numerically using the state vector (or the so-called Stroh) formalism and Peano series. This coefficient can then be used to straightforwardly calculate the scattered field. To validate the method of resolution, results obtained by the present method are compared to those calculated by the classical transfer matrix method at both normal and oblique incidence and to experimental measurements at normal incidence for a known two-layers porous material, considered as a single inhomogeneous layer. Finally, discussion about the absorption coefficient for various inhomogeneity profiles gives further perspectives. © 2011 Acoustical Society of America. [DOI: 10.1121/1.3605530]

PACS number(s): 43.55.Ev, 43.20.Gp, 43.20.Fn, 43.20.Bi [KVK]

Pages: 1390–1398

I. INTRODUCTION

The study of wave propagation in macroscopically inhomogeneous porous media was initially motivated by (1) the design of sound absorbing porous materials with optimal material and geometrical property profiles¹ and (2) the retrieval of the spatially varying material parameters of industrial foams.² These, and other inverse problems, are of great importance in connection with the characterization of the mechanical properties of naturally occurring macroscopically inhomogeneous porous materials, such as bones. The literature on inhomogeneous media is extensive in several fields of physics, from optics and electromagnetism,^{3,4} to acoustics,^{5,6} and geophysics⁷ and granular media.⁸ Many natural and man-made materials are porous, and therefore heterogeneous at a microscopic scale. The wave equation in macroscopically inhomogeneous porous media was derived from the alternative formulation of Biot's theory⁹ in Ref. 10 and solved in the case of rigid frame inhomogeneous porous materials via the Wave Splitting method and "transmission" Green's functions approach or via an iterative Born approximation procedure based on the specific Green's function of

the configuration.¹¹ The recovery of several profiles of spatially varying material parameters by means of an optimization approach, was then achieved in Ref. 2 still in the rigid frame approximation.

When saturated by a light fluid such as air, the frame is moving below the solid/fluid decoupling frequency. Moreover, in many applications porous materials are saturated by a heavy fluid such as water or bone marrow. They can also be excited mechanically. In these cases, the rigid frame approximation is not valid and the full macroscopically inhomogeneous poroelastic model should be used and solved.

It is assumed that the wavelengths are larger than the average heterogeneity size at the pore scale so that the physical properties are homogenized. However, these properties can vary with the observation point within the material at the macroscopic scale of the specimen. Macroscopically inhomogeneous poroelastic materials imply that both acoustic and elastic properties are space-dependent at the macroscopic scale.

First, the constitutive linear stress-strain relations and the momentum conservation law in the absence of body forces are recalled for an inhomogeneous poroelastic material. These equations are then solved for a one-dimensional macroscopically inhomogeneous poroelastic material via the

^{a)} Author to whom correspondence should be addressed. Electronic mail: jean-philippe.groby@univ-lemans.fr

state vector formalism or the so-called Stroh formalism¹² together with Peano series.^{13,14} The Stroh formalism is largely used to model acoustic wave propagation in stratified anisotropic elastic materials.^{15,16} Similar methods (transmission matrix method) are used in electromagnetism to model the propagation of electromagnetic waves in anisotropic or gyrotropic stratified materials.^{17,18} In the frequency domain, it consists in the rewriting of the constitutive linear stress-strain relations and the momentum conservation law in terms of the state vector, whose components can be chosen arbitrarily as long as they are continuous along the inhomogeneity of the material. This leads after spatial Fourier transform to a first-order ordinary differential system of equations whose unknown is the state vector. The spatial dependence of the materials properties are accounted for through the spatially dependent matrix components. The solution of the system appears in terms of Peano series, which are well fitted for wave propagation problems in functionally graded materials.¹⁹ These series apply to continuously varying poroelastic properties and avoids problems related to a lack of discretization when the materials are approximated by stratified ones. Numerical results obtained with this method are compared to calculations of the classical transfer matrix method performed with the validated MAINE3A code²⁰ for a known two-layers porous material, considered as a single inhomogeneous layer. The transfer matrix method is particularly suitable to solve problems involving a layered configuration.

Numerical results are also compared to experimental measurements at normal incidence. The experiment consists in recording waves reflected by the chosen two-layered porous medium laid on the floor of a semi-anechoic room when excited at normal incidence by a dipolar source.

Finally, applications in material design for engineering applications are treated, by comparing the absorption coefficient of a macroscopically inhomogeneous porous plate with various inhomogeneity profiles that are either continuous or discontinuous.

II. EQUATIONS OF MACROSCOPICALLY INHOMOGENEOUS POROUS MATERIALS

As pointed out by several authors,^{9,21,22} the generalized formulation of the Biot theory⁹ is suitable to macroscopically inhomogeneous porous media and also to take into account anisotropy and viscoelastic frames. Recently, another formulation was proposed in Ref. 23 that is also suitable to macroscopically inhomogeneous porous media. The article focuses on the alternative Biot's formulation, which is largely employed in acoustics and geophysics.

Rather than dealing directly with the arbitrary field $\bar{s}(\mathbf{x}, t)$ [with $\mathbf{x} = (x_1, x_2)$], we prefer to deal with the $s(\mathbf{x}, \omega)$, related to $\bar{s}(\mathbf{x}, t)$ by the Fourier transform $\bar{s}(\mathbf{x}, t) = \int_{-\infty}^{\infty} s(\mathbf{x}, \omega) e^{i\omega t} d\omega$, wherein $\omega = 2\pi\nu$ is the angular frequency, with ν the frequency. Henceforth, we drop the ω in $s(\mathbf{x}, \omega)$ so that it is written $s(\mathbf{x})$.

From the alternative formulation of Biot,⁹ the stress strain relations in an initially stress free, statistically isotropic poroelastic material take the form

$$\begin{cases} \sigma_{ij} = 2N\varepsilon_{ij} + (\lambda_c\theta - \alpha M\zeta)\delta_{ij}, \\ p = M(\zeta - \alpha\theta), \end{cases} \quad (1)$$

where in δ_{ij} denotes the Kronecker symbol. The components of the total stress tensor are σ_{ij} , the fluid pressure in the pores is p , and the components of the strain tensor are $\varepsilon_{ij} = 1/2(u_{i,j} + u_{j,i})$, with the solid displacement \mathbf{u} , $\theta = u_{i,i}$, and $\zeta = -w_{i,i}$ with the fluid/solid relative displacement $\mathbf{w} = \phi(\mathbf{U} - \mathbf{u})$ (\mathbf{U} being the fluid displacement and ϕ the porosity). The Einstein summation notation is implicit in the expressions of θ and ζ . The material properties²⁴ are the bulk modulus of the closed porosity system, i.e., in which the pore volume is sealed, $\lambda_c = \lambda + \alpha^2 M$, the Lamé coefficients of the elastic frame λ and N , an additional elastic parameter M , and an elastic coupling coefficient α .

These mechanical coefficients are related to the more commonly used in acoustics P , Q , and R coefficients from the original formulation²⁵ through

$$\begin{aligned} \alpha &= \phi(Q + R)/R, & M &= R/\phi^2, \\ \lambda_c &= P - Q^2/R - 2N + \alpha^2 M. \end{aligned} \quad (2)$$

The expressions of P , Q , and R , in case of air saturated materials, reduce to²⁶

$$\begin{aligned} R &= \phi\tilde{K}_f, & Q &= \tilde{K}_f(1 - \phi), \\ P &= K_b + 4N/3 + (1 - \phi)^2\tilde{K}_f/\phi, \end{aligned} \quad (3)$$

wherein the bulk modulus of the skeleton is $K_b = 2N(1 + \nu)/3(1 - 2\nu)$, the Poisson coefficient (of the skeleton) is ν , and

$$\tilde{K}_f = \frac{\gamma P_0}{\gamma - (\gamma - 1) \left[1 + i \frac{\omega'_c}{\omega \text{Pr}} G(\omega \text{Pr}) \right]^{-1}}. \quad (4)$$

The correction function $G(\omega \text{Pr})$, introduced in Ref. 27 to account for the thermal losses, is

$$G(\omega \text{Pr}) = \sqrt{1 - i\eta\rho_f\omega \text{Pr} \left(\frac{2\tau_\infty}{R'_t\phi\Lambda'} \right)^2}, \quad (5)$$

whith $\omega'_c = R'_t\phi/\rho_f\tau_\infty$, γ the specific heat ratio, Pr the Prandtl number, τ_∞ the tortuosity, R'_t the "thermal resistivity," and Λ' the thermal characteristic length. The thermal resistivity is related to the thermal characteristic length²⁷ through $R'_t = 8\tau_\infty\eta/\phi\Lambda'^2$.

In the absence of body forces, the conservation of momentum and the generalized Darcy's law lead to the following equations in the frequency domain:

$$\begin{cases} \omega^2\rho_f w_i + \omega^2\rho u_i = -\sigma_{ij}, \\ \omega^2\rho_f u_i + \omega^2\tilde{\rho}_{\text{eq}} w_i = p_{,i}, \end{cases} \quad (6)$$

wherein the bulk density of the porous medium is ρ , such that $\rho = (1 - \phi)\rho_s + \phi\rho_f$ with ρ_s the density of the solid

and ρ_f the density of the saturating fluid, and the mass parameter $\tilde{\rho}_{\text{eq}}$ (Refs. 9 and 28) is

$$\tilde{\rho}_{\text{eq}} = \frac{\rho_f \tau_\infty}{\phi} \left[1 + i \frac{\omega_c}{\omega} F(\omega) \right]. \quad (7)$$

The correction function $F(\omega)$, introduced in Ref. 28 and which accounts for the viscous losses, is given by

$$F(\omega) = \sqrt{1 - i\eta\rho_f\omega \left(\frac{2\tau_\infty}{R_f\phi\Lambda} \right)^2}, \quad (8)$$

with the Biot frequency $\omega_c = R_f\phi/\rho_f\tau_\infty$, the flow resistivity R_f and the viscous characteristic length Λ . The mass parameter $\tilde{\rho}_{\text{eq}}$ is the complex frequency dependent equivalent density used in the rigid frame approximation, while the complex frequency dependent equivalent bulk modulus \tilde{K}_{eq} used in this approximation is related to \tilde{K}_f through $\tilde{K}_f = \phi\tilde{K}_{\text{eq}}$. For most foams, the elastic coupling coefficient α reduces to 1, $M = \tilde{K}_{\text{eq}}$ and λ_c reduces to $\lambda_c = K_b - 2/3N + \alpha^2M$.

In the previous equations, N , λ (and ν), λ_c , α , M , ϕ , τ_∞ , Λ , Λ' , R'_t , R'_f are \mathbf{x} dependent.

III. NUMERICAL EVALUATION OF THE PRESSURE FIELD

A. Description of the configuration

Both the incident plane acoustic wave and the plate are assumed to be invariant with respect to the Cartesian coordinate x_3 . A cross-sectional x_1 - x_2 plane view of the 2D scattering problem is shown in Fig. 1.

The upper and lower boundaries of the layer are flat and parallel. They are designated by Γ_L and Γ_0 and their x_2 coordinates are L and 0 . The porous material $M^{[1]}$ occupies the domain $\Omega^{[1]}$. The inhomogeneity of the plate occurs along the x_2 direction, i.e., N , λ (and ν), λ_c , α , M , ϕ , τ_∞ , Λ , Λ' , R'_t , R'_f are x_2 -dependent. An isotropic macroscopically inhomogeneous porous material is considered. The material can be viewed as a functionally graded material. The surrounding and saturating fluid is the air medium (density $\rho_f = 1.213 \text{ kg m}^{-3}$, atmospheric pressure $P_0 = 1.01325 \times 10^5 \text{ Pa}$, and viscosity $\eta = 1.839 \times 10^{-5} \text{ kg m}^{-1} \text{ s}^{-1}$). The inhomogeneous porous layer is backed by a rigid plate at Γ_0 .

We denote the total pressure, wavevector and density, respectively, with $p^{[0]}$, $k^{[0]}$ and $\rho^{[0]}$ in $\Omega^{[0]}$ and the total stress tensor, the fluid pressure in the pores, the solid displacement, and solid/fluid relative displacement respectively with $\boldsymbol{\sigma}^{[1]}$, $p^{[1]}$, $\mathbf{u}^{[1]}$ and $\mathbf{w}^{[1]}$ in $\Omega^{[1]}$.

The wavevector \mathbf{k}^i of the incident plane wave lies in the sagittal plane and the angle of incidence is θ^i measured counterclockwise from the positive x_1 axis. The incident wave, initially propagating in $\Omega^{[0]}$, is expressed by $p^i(\mathbf{x}) = A^i e^{i(k_1 x_1 - k_2^i(x_2 - L))}$, wherein $k_1 = -k^{[0]} \cos \theta^i$, $k_2^i = k^{[0]} \sin \theta^i$ and $A^i = A^i(\omega)$ is the signal spectrum.

The uniqueness of the solution to the forward-scattering problem is ensured by the radiation condition:

$$p^{[0]}(x) - p^i(x) \sim \text{outgoing waves}; |\mathbf{x}| \rightarrow \infty, x_2 > L. \quad (9)$$

B. The state vector formalism and Peano series

The spatial Fourier transform of the Eqs. (1) and (6) is first performed. The transform $\hat{s}(x_2, k_1)$ of $s(\mathbf{x})$ is also introduced and can be written in the form $s(\mathbf{x}) = \hat{s}(x_2, k_1) e^{ik_1 x_1}$ because of the plane wave nature of the excitation. Henceforth, we drop the k_1 in $\hat{s}(x_2, k_1)$ so that it is written $\hat{s}(x_2)$. The geometry of the configuration being planar and infinite along the x_2 -axis, the fields components that are continuous along the inhomogeneity and the boundary conditions apply either to $s(\mathbf{x})$ or to $\hat{s}(x_2)$.

Inside the domain $\Omega^{[1]}$ the normal components of the total stress tensor, $\sigma_{12}^{[1]}$ and $\sigma_{22}^{[1]}$, the pressure $p^{[1]}$, the solid displacements, $u_1^{[1]}$ and $u_2^{[1]}$, and the normal component of the solid/fluid relative displacement $w_2^{[1]}$ are continuous along the x_2 -axis. It seems natural to choose these 6 parameters as components of the state vector. Nevertheless, it seems better to adapt these components to the considered boundary problem. On one hand, at the interface Γ_L , the normal components of the stress tensor ($\sigma_{12}^{[1]} = 0$, $\sigma_{22}^{[1]} = -p^{[0]}$), the pressure ($p^{[1]} = p^{[0]}$), and normal component of the velocity $-i\omega(w_2^{[1]} + u_2^{[1]}) = V_2^{[0]}$ with $V_2^{[0]}$ the normal component of the velocity in $\Omega^{[0]}$ are continuous. On the other hand, the solid displacement and the normal component of the solid/fluid relative velocity vanish at the interface Γ_0 , i.e., $u_1^{[1]} = 0$, $u_2^{[1]} = 0$ and $-i\omega(w_2^{[1]} + u_2^{[1]}) = 0$. Because $u_2^{[1]}$ and $w_2^{[1]}$ are continuous at any x_2 in $\Omega^{[1]}$, the normal component of the velocity $-i\omega(w_2^{[1]} + u_2^{[1]})$ is also continuous. The normal component of the solid/fluid relative displacement w_2 is also replaced by $V_2^{[1]} = -i\omega(w_2^{[1]} + u_2^{[1]})$ in Eqs. (1) and (6). This parameter is preferred to $w_2^{[1]}$ to define the wave vector.

After spatial transform, the Eqs. (1) and (6) split into two systems of equations (see the Appendix): one set of six first order differential equations only depending on the components of the column state vector $\hat{W} = \langle \hat{\sigma}_{12}^{[1]}, \hat{\sigma}_{22}^{[1]}, \hat{p}^{[1]}, \hat{u}_1^{[1]}, \hat{u}_2^{[1]}, \hat{V}_2^{[1]} \rangle$, and one set of two equations that linked the two last unknowns, $\hat{\sigma}_{11}^{[1]}$ and $\hat{w}_{11}^{[1]}$, to the components of the state vector. The problem also reduces to the solution of the first order differential matrix system composed of the first six first order differential equations:

$$\frac{\partial}{\partial x_2} \hat{W} - \mathbf{A} \hat{W} = 0, \quad (10)$$

with $\mathbf{A} = -\mathbf{B}^{-1}\mathbf{D}$, wherein

$$\mathbf{B} = \begin{bmatrix} 1 & 0 & 0 & 0 & ik_1(\lambda_c - \alpha M) & -\frac{k_1 \alpha M}{\omega} \\ 0 & 1 & 0 & 0 & 0 & 0 \\ 0 & 0 & -1 & 0 & 0 & 0 \\ 0 & 0 & 0 & N & 0 & 0 \\ 0 & 0 & 0 & 0 & \lambda_c + 2N - \alpha M & i\frac{\alpha M}{\omega} \\ 0 & 0 & 0 & 0 & (\alpha - 1)M & i\frac{M}{\omega} \end{bmatrix}, \quad (11)$$

and

$$D = \begin{bmatrix} 0 & 0 & ik_1 \left(\frac{\rho_f}{\tilde{\rho}_{eq}} - \frac{k_1^2 \alpha M}{\tilde{\rho}_{eq} \omega^2} \right) & \rho \omega^2 - \frac{\rho_f^2}{\tilde{\rho}_{eq}} \omega^2 - k_1^2 \left(\lambda_c + 2N - \frac{\rho_f}{\tilde{\rho}_{eq}} \alpha M \right) & 0 & 0 \\ ik_1 & 0 & 0 & 0 & (\rho - \rho_f) \omega^2 & i \rho_f \omega \\ 0 & 0 & 0 & 0 & (\rho_f - \tilde{\rho}_{eq}) \omega^2 & i \tilde{\rho}_{eq} \omega \\ -1 & 0 & 0 & 0 & ik_1 N & 0 \\ 0 & -1 & -\frac{k_1^2 \alpha M}{\tilde{\rho}_{eq} \omega^2} & ik_1 \left(\lambda_c - \frac{\rho_f}{\tilde{\rho}_{eq}} \alpha M \right) & 0 & 0 \\ 0 & 0 & 1 - \frac{k_1^2 M}{\tilde{\rho}_{eq} \omega^2} & ik_1 M \left(\alpha - \frac{\rho_f}{\tilde{\rho}_{eq}} \right) & 0 & 0 \end{bmatrix}. \quad (12)$$

The matrices \mathbf{B} and \mathbf{D} are x_2 -dependent, because $\lambda_c(x_2)$, $\alpha(x_2)$, $M(x_2)$, $N(x_2)$, $\tilde{\rho}_{eq}(x_2)$, and $\rho(x_2)$ are x_2 -dependent. This dependence has not been detailed in (11) and (12) for conciseness.

The solution of system (10) takes the form

$$\hat{W}(L) = M \hat{W}(0), \quad (13)$$

wherein \mathbf{M} is the so-called matricant,¹⁴ which relates the value of the state vector $\hat{W}(0)$, at $x_2=0$, to the value of the state vector $\hat{W}(L)$, at $x_2=L$. Since A is x_2 dependent (i.e., the plate is not homogeneous or piecewise constant) and A does not commute for different values of x_2 , i.e., $[A(x_2), A(x'_2)] = A(x_2)A(x'_2) - A(x'_2)A(x_2) \neq 0$, $\forall (x_2, x'_2) \in [0, L]^2$, $x_2 \neq x'_2$, the matricant \mathbf{M} does not contain matrix exponentials or multiplications of matrix exponentials. The matricant is rather defined by the so-called multiplicative integral satisfying the Peano expansion.^{13,14,19,29} This avoids any problem related to lack of discretization when the continuously varying material is approximated by a piecewise constant material. The Peano series reads as

$$M = I + \int_0^L A(x_2) dx_2 + \int_0^L A(x_2) \left[\int_0^{x_2} A(\zeta) d\zeta \right] dx_2 + \dots \quad (14)$$

and the evaluation of \mathbf{M} is performed via the iterative scheme

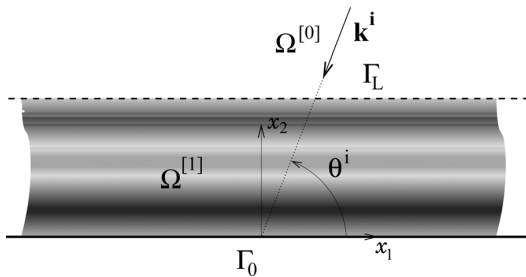


FIG. 1. Cross-sectional plane view of the configuration.

$$\begin{cases} \mathbf{M}^{\{0\}} = \mathbf{I}, \\ \mathbf{M}^{\{n\}} = \mathbf{I} + \int_0^L A(x_2) \mathbf{M}^{\{n-1\}}(x_2) dx_2, \end{cases} \quad (15)$$

such that $\lim_{n \rightarrow \infty} \mathbf{M}^n = \mathbf{M}$.

C. The boundary problem

The application of the boundary conditions at both interfaces Γ_L [$\hat{\sigma}_{12}^{[1]} = 0$, $\hat{\sigma}_{22}^{[1]} = -\hat{p}^{[0]}$, $\hat{p}^{[1]} = \hat{p}^{[0]}$, $\hat{V}_2^{[1]} = \hat{V}_2^{[0]} = -i/\omega \rho \frac{\partial \hat{p}^{[0]}}{\partial x_2}$] and Γ_0 ($\hat{u}_1 = 0$, $\hat{u}_2 = 0$, $\hat{V}_2^{[1]} = 0$) yields the state vectors $\hat{W}(L)$ and $\hat{W}(0)$, which are required to solve the problem. From the separation of variables, the radiation conditions, and the spatial Fourier transform, the pressure field in $\Omega^{[0]}$ can be written as

$$\hat{p}^{[0]} = A^i e^{-ik_2^{[0]}(x_2-L)} + A^i R e^{ik_2^{[0]}(x_2-L)}, \quad (16)$$

where R is the reflection coefficient. The state vectors become

$$\hat{W}(L) = \begin{bmatrix} \hat{\sigma}_{12}^{[1]}(L) \\ \hat{\sigma}_{22}^{[1]}(L) \\ \hat{p}^{[1]}(L) \\ \hat{u}_1^{[1]}(L) \\ \hat{u}_2^{[1]}(L) \\ \hat{u}_2^{[1]}(L) \\ -\frac{i}{\omega \rho} \frac{\partial \hat{p}^{[0]}}{\partial x_2} \Big|_{x_2=L} \end{bmatrix} = \begin{bmatrix} 0 \\ -\hat{p}^{[0]}(L) \\ \hat{p}^{[0]}(L) \\ \hat{u}_1^{[1]}(L) \\ \hat{u}_2^{[1]}(L) \\ \hat{u}_2^{[1]}(L) \\ -\frac{i}{\omega \rho} \frac{\partial \hat{p}^{[0]}}{\partial x_2} \Big|_{x_2=L} \end{bmatrix} = \mathbf{S} + \mathbf{L} \cdot \begin{bmatrix} A^i R \\ \hat{u}_1^{[1]}(L) \\ \hat{u}_2^{[1]}(L) \end{bmatrix}, \quad (17)$$

and

$$\hat{W}(0) = \begin{bmatrix} \hat{\sigma}_{12}^{[1]}(0) \\ \hat{\sigma}_{22}^{[1]}(0) \\ \hat{p}^{[1]}(0) \\ \hat{u}_1^{[1]}(0) \\ \hat{u}_2^{[1]}(0) \\ \hat{u}_2^{[1]}(0) \\ \hat{V}_2^{[1]}(0) \end{bmatrix} = \begin{bmatrix} \hat{\sigma}_{12}^{[1]}(0) \\ \hat{\sigma}_{22}^{[1]}(0) \\ \hat{p}^{[1]}(0) \\ 0 \\ 0 \\ 0 \\ 0 \end{bmatrix} = \mathbf{L}^0 \cdot \begin{bmatrix} \hat{\sigma}_{12}^{[1]}(0) \\ \hat{\sigma}_{22}^{[1]}(0) \\ \hat{p}^{[1]}(0) \end{bmatrix}, \quad (18)$$

wherein \mathbf{S} accounts for the excitation of the system by the plane incident wave, \mathbf{L}^L relates the unknowns $R, \hat{u}_1^{[1]}(L)$ and $\hat{u}_2^{[1]}(L)$ to the state vector $\widehat{\mathbf{W}}(L)$, and \mathbf{L}^0 relates the unknowns $\hat{\sigma}_{12}^{[1]}(0), \hat{\sigma}_{22}^{[1]}(0)$ and $\hat{p}^{[1]}(0)$ to the state vector $\widehat{\mathbf{W}}(0)$. Their expressions are

$$\mathbf{S} = \begin{bmatrix} 0 \\ -A^i \\ A^i \\ 0 \\ 0 \\ -A^i k_2^{[0]}/\omega\rho^{[0]} \end{bmatrix}, \quad \mathbf{L}^0 = \begin{bmatrix} 1 & 0 & 0 \\ 0 & 1 & 0 \\ 0 & 0 & 1 \\ 0 & 0 & 0 \\ 0 & 0 & 0 \\ 0 & 0 & 0 \end{bmatrix}, \quad \text{and} \quad (19)$$

$$\mathbf{L}^L = \begin{bmatrix} 0 & 0 & 0 \\ -1 & 0 & 0 \\ 1 & 0 & 0 \\ 0 & 1 & 0 \\ 0 & 0 & 1 \\ k_2^{[0]}/\omega\rho^{[0]} & 0 & 0 \end{bmatrix}.$$

Finally, the introduction of (17) and (18) in (13) gives rise to the final system of equations, whose solution contain the reflection coefficient R

$$[[\mathbf{L}^L][-\mathbf{M} \cdot \mathbf{L}^0]] \cdot \begin{bmatrix} A^i R \\ \hat{u}_1^{[1]}(L) \\ \hat{u}_2^{[1]}(L) \\ \hat{\sigma}_{12}^{[1]}(0) \\ \hat{\sigma}_{22}^{[1]}(0) \\ \hat{p}^{[1]}(0) \end{bmatrix} = -\mathbf{S}. \quad (20)$$

This system is solved for each frequency and directly provide the reflection coefficient associated with the plane incident wave. The pressure field in $\Omega^{[0]}$ can then be calculated through $p^{[0]} = \hat{p}^{[0]} e^{ik_1 x_1}$. A similar system can be cast when the inhomogeneous porous plate is not backed and radiate in the air medium. In this case, a transmitted field is required and the transmission coefficient is also calculated.

IV. VALIDATION ON A MULTILAYERED POROUS MEDIUM

In order to validate the present method, calculations are performed for a known two-layers poroelastic medium configuration considered as a single poroelastic plate. Each layer of the plate is a porous foam saturated by air. The characteristic properties of each layer have been determined by classical methods²⁶ and are given in Table I. The layer 1 is a Eurocell foam while layer 2 is a Fireflex (Recticel, Wetteren/East-Flanders, Belgium) foam.

The choice of this configuration is motivated by the fact that the results of the present method can be compared with

TABLE I. Properties of the two-layer medium studied.

	ϕ	τ_∞	Λ (μm)	Λ' (μm)	R_f (N s m^{-4})	ρ (kg m^{-3})	N (Pa)	ν	Thickness (mm)
Layer 1	0.95	1.1	15	45	42000	126	280000 (1-0.05i)	0.24	50
Layer 2	0.96	2.2	110	352	9000	37	60000 (1-0.05i)	0.21	19.8

known results from the classical Transfer Matrix Method (TMM) provided by MAINE3A²⁰ and with experimental measurements.

To consider the slab as a single inhomogeneous material, the jump discontinuities in the two-layered system are smoothed by using the following analytical continuous and continuously differentiable function:

$$I(x_2) = 1 + \frac{C}{2} \left[1 + \text{erf} \left(\frac{x_2 - x_2^0}{r} \right) \right], \quad (21)$$

wherein C is the step value, which is different for each parameter in Table I, erf is the error function, x_2^0 is the position of the jump, and r corresponds to the steepness of the continuous jump such that the smaller r is, the steeper is the jump.

The number of iterations required for the correct evaluation of the matricant increases with frequency. A change of variable like that proposed in Refs. 30 and 31 seems inaccurate, because the characteristic parameters are frequency dependent for porous materials. Moreover, a large number of iterations is required for the correct evaluation, because poroelastic materials are highly dissipative.

The configuration is discretized in with 1000 points and the number of iterations for the evaluation of the Peano series is 250. The jump position and its slope are fixed to $x_2^0 = 50$ mm and $r = 10^{-6}$, while the total thickness is $L = 69.8$ mm.

A. Numerical validation

The results calculated with the present method are first compared with those from the classical TMM provided by MAINE3A at normal and oblique incidences. Figure 2 depicts the real and imaginary parts of the reflection coefficient at normal and oblique incidences by the two-layers medium studied. The curves cannot be distinguished one from another.

This provides a validation of the model and of the solving method.

The real and imaginary part of the reflection coefficient calculated with MAINE3A under the rigid frame approximation (\circ) and with the Limp model³² (\square) are also plotted Fig. 2. Below 4000 Hz the rigid frame approximation is not valid at the Biot resonances. This test emphasizes the added value of the new method modeling the wave propagation in macroscopically inhomogeneous poroelastic foams at low frequencies, and validates the method in the high frequency range. The peaks at low frequencies are also attributed to Biot and not to Limp effects. The method is also stable and robust.

B. Experimental validation

The principle of the experiment is shown in Fig. 3. A $1.58 \text{ m} \times 1.06 \text{ m}$ plate of Eurocell of 5 cm thick is laid on the floor of the semi-anechoic room available in ATF,

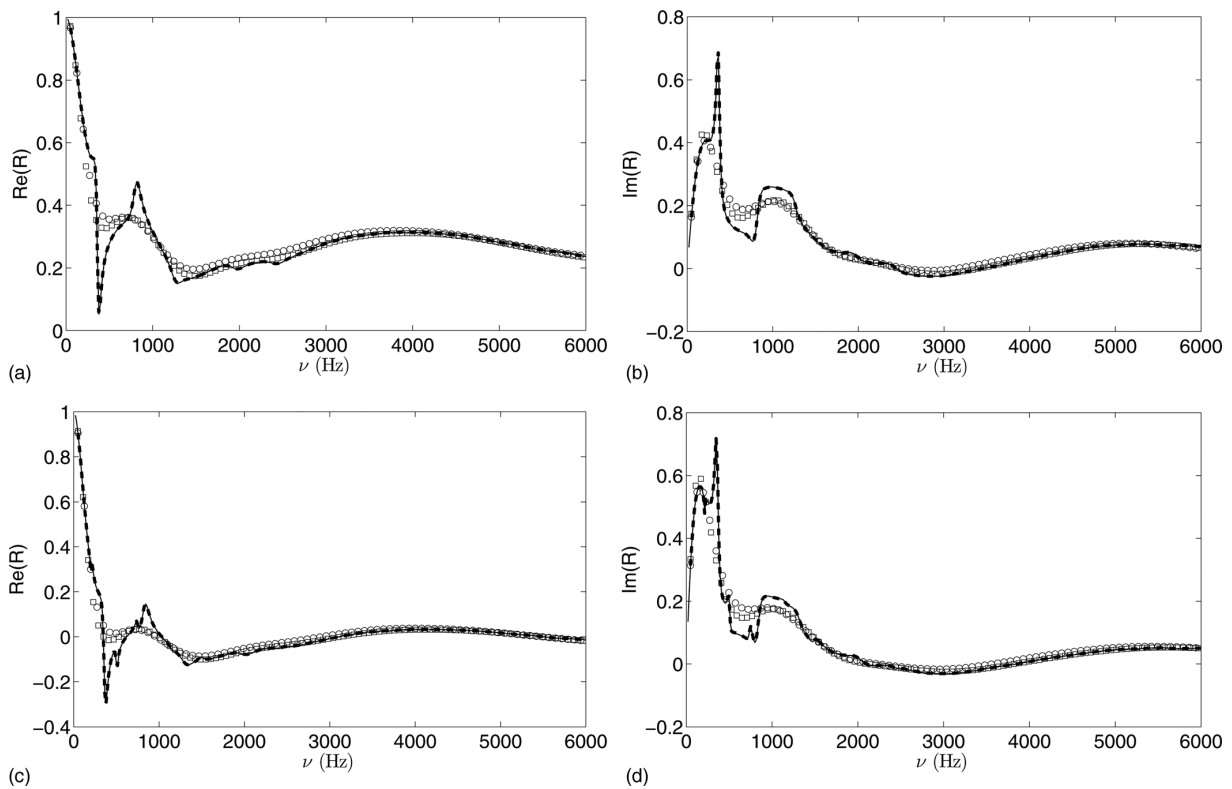


FIG. 2. Real and imaginary part of the reflection coefficient at normal incidence (a) and (b) and at $\theta^i = \pi/6$ (c) and (d) calculated with the present method (—), with MAINE3A (---), with MAINE3A under the approximation of the equivalent fluid model (○), and with MAINE3A with the Limp model (□).

KULeuven. A $1.5 \text{ m} \times 2 \text{ m}$ plate of Fireflex of 1.98 cm thick was then laid above of the Eurocell foam. The two foams are in contact and not glued. The floor is supposed to be rigid.

A dipolar source, radiating a sweep from 100 Hz to 5000 Hz, is placed at the center of the Eurocell foam at $x_2^s = 83 \text{ cm}$ above the ground. A microphone is placed successively at $x_2^{(1)} = 8.5 \text{ cm}$ and $x_2^{(2)} = 9.5 \text{ cm}$ above the ground at the center of the source. The source center was determined by recording the sweep signal with the microphone at various positions along the x_1 and x_3 axis. The source center corresponds to the maximum of amplitude recorded by the microphone. This guaranties that the recordings are performed at normal incidence. The x_2 position of both the source and of the microphone ensure that, locally, the field can be approximated by a plane wave. The recorded signals are averaged over 30 waveforms. The pressures recorded at both positions take the form $p^{(j)} = A^j e^{-ik^{(0)}x_2^{(j)}} + A^j \text{Re} e^{ik^{(0)}x_2^{(j)}}$, $j = 1, 2$ at normal incidence. It directly equals

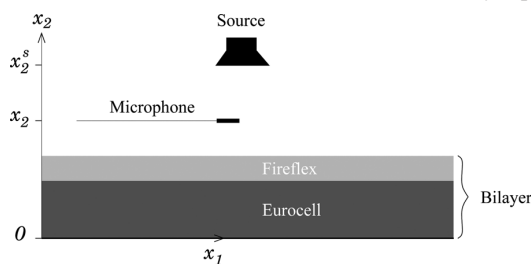


FIG. 3. Experimental setup.

the spatial Fourier transform $\hat{p}^{(j)} = p^{(j)}$, because the pressure is recorded at normal incidence. From these two measurements, the reflection coefficient at normal incidence can be determined through

$$R = \frac{p^{(1)} e^{-ik^{(0)}x_2^{(2)}} - p^{(2)} e^{-ik^{(0)}x_2^{(1)}}}{p^{(2)} e^{ik^{(0)}x_2^{(1)}} - p^{(1)} e^{ik^{(0)}x_2^{(2)}}}. \quad (22)$$

This formula is commonly used when the measuring technique, sometimes referred to as the Tamura method³³ or sometimes referred to as PP-method,³⁴ is used. Figure 4 depicts the absolute value of the experimental reflection coefficient calculated with the present method and measured between 500 Hz to 5000 Hz. This frequency bandwidth is usually considered as being the one over which the reflection methods give accurate results. A fairly good match is found between the curves. In particular, the peak around 800 Hz, which corresponds to a modified Biot resonance of the Eurocell, is well recovered. The discrepancies between the two curves can be explained by the fact that (1) a plane incident wave is assumed, (2) the foams are of finite size, (3) the boundary conditions between the rigid backing and the Eurocell foam does not correspond to perfectly rigid, (4) the two foams are not perfectly in contact, and by (5) the spacing between the two positions of the microphone. In order to emphasize the pertinence of a macroscopically inhomogeneous porous material approach, the absolute value of the reflection coefficient calculated for an homogeneous plate of thickness $L = 6.98 \text{ cm}$ of Eurocell and of Fireflex is also

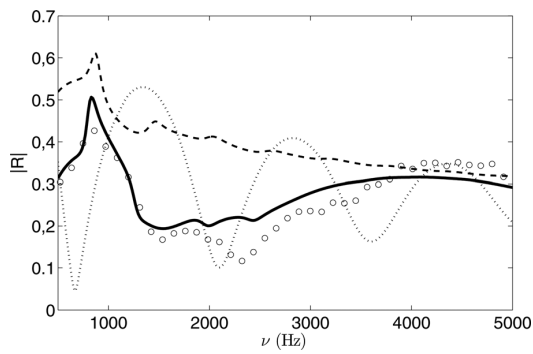


FIG. 4. Comparison between $|R|$ calculated with the present method (—) and recovered with the measurement (○) and $|R|$ for a L -thick homogeneous plate of Fireflex (●●●) and of Eurocell (---).

plotted Fig. 4. Both results are quite far from the experimental curve and from the numerical calculation when the two-layers configuration is modeled as a macroscopically inhomogeneous material.

V. ASSUMPTION ON OTHER PROPERTY PROFILES

Macroscopically inhomogeneous porous materials offer the possibility of wider applications in sound absorbing material design than their macroscopically homogeneous counterparts. In the following, examples of absorbing material design are presented.

First, the acoustical properties of the previously studied two-layered plate see (Table I) are considered but the jump occurs at $x_2^0 = L/2$, i.e., the thickness of both foams is equal to 3.49 cm. The slope is then varied from $r = 10^{-6}$ to $r = 10^{-2}$. Then, a Hanning profile is considered by using the following analytical continuous and continuously differentiable function:

$$H(x) = 1 + \frac{C}{2} \left[1 - \cos\left(\frac{x}{L}\right) \right], \quad (23)$$

wherein C is the relative difference in amplitude between the value at both sides and the value in the middle of the slab.

Figure 5 depicts the profile generated for R_f as an example (the other parameters also vary with an identical profile)

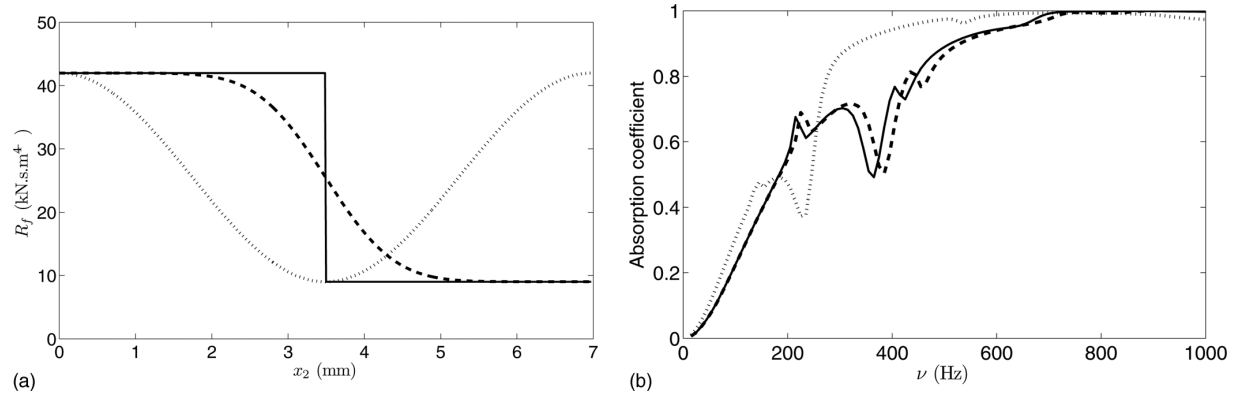


FIG. 5. Example of the a profile considered (a) and the corresponding absorption coefficient (b): slope profiles with $r = 10^{-6}$ (—) and $r = 10^{-2}$ (---) and Hanning profile (●●●).

for $r = 10^{-6}$, $r = 10^{-2}$ and a Hanning profile, together with the corresponding absorption coefficient $A = 1 - |R|^2$. The absorption coefficient is one of the most important parameters when designing a foam. These last years, this coefficient has received a large attention, particularly the attempt of increasing its value at low frequencies. Porous foams suffer from a weak absorption at low frequency when compared to their efficiency at higher frequencies. While a modification of the slope only induces a frequency shift at higher frequencies, the use of the Hanning profile enables to increase the absorption coefficient at low frequency. When the foam stack is reversed, the absorption coefficient differs in case of single slope profiles, while it remains the same with symmetrical profiles as Hanning profile.

VI. CONCLUSION

A model of the acoustic response of macroscopically inhomogeneous elastic frame porous materials derived from the alternative Biot's theory of 1962 was solved. A fast and stable numerical method, derived from the state vector formalism together with Peano series was developed to solve the macroscopically inhomogeneous poroelastic wave equations. To our knowledge, these equations are solved and these methods are derived for the first time for poroelastic materials. A validation of this method was made on the example of a two-layers medium, by comparison to the exact solution obtained by the transfer matrix method (MAINE3A) at both normal and oblique incidence and by comparison to experimental results at normal incidence. In the numerical procedure, the jump of properties between the layers was accounted for in the form of a single continuous function. This result validates the present procedure. Finally, examples of the absorption coefficient are given for various property profiles. These examples illustrate the possibility of designing acoustically absorbing materials by controlling the gradient of parameters. This last point requires further investigation, in particular, how the properties vary when the foam is compressed. Another possible application of the equations and method of solution derived here is the development of an optimized inversion procedure to characterize macroscopically inhomogeneous porous materials.

APPENDIX: DERIVATION OF THE FIRST-ORDER LINEAR ORDINARY DIFFERENTIAL SYSTEM

The expanded form of the spatial Fourier transform of (1) and (6) is

$$\begin{aligned}
 \hat{\sigma}_{11}^{[1]} &= ik_1(\lambda_c + 2N)\hat{u}_1^{[1]} + \lambda_c \frac{\partial \hat{u}_2^{[1]}}{\partial x_2} + ik_1 \alpha M \hat{w}_1 + \alpha M \frac{\partial \hat{w}_2^{[1]}}{\partial x_2}, \\
 \hat{\sigma}_{12}^{[1]} &= ik_1 N \hat{u}_2^{[1]} + N \frac{\partial \hat{u}_1^{[1]}}{\partial x_2}, \\
 \hat{\sigma}_{22}^{[1]} &= (\lambda_c + 2N) \frac{\partial \hat{u}_2^{[1]}}{\partial x_2} + ik_1 \lambda_c \hat{u}_1^{[1]} + ik_1 \alpha M \hat{w}_1 + \alpha M \frac{\partial \hat{w}_2^{[1]}}{\partial x_2}, \\
 \hat{p}_{[1]} &= -\alpha M ik_1 \hat{u}_1^{[1]} - \alpha M \frac{\partial \hat{u}_2^{[1]}}{\partial x_2} - ik_1 M \hat{w}_1 - M \frac{\partial \hat{w}_2^{[1]}}{\partial x_2}, \\
 \rho \omega^2 \hat{u}_1^{[1]} + \rho_f \omega^2 \hat{w}_1 &= -ik_1 \hat{\sigma}_{11}^{[1]} - \frac{\partial \hat{\sigma}_{12}^{[1]}}{\partial x_2}, \\
 \rho \omega^2 \hat{u}_2^{[1]} + \rho_f \omega^2 \hat{w}_2^{[1]} &= -ik_1 \hat{\sigma}_{12}^{[1]} - \frac{\partial \hat{\sigma}_{22}^{[1]}}{\partial x_2}, \\
 \rho_f \omega^2 \hat{u}_1^{[1]} + \tilde{\rho}_{eq} \omega^2 \hat{w}_1 &= ik_1 \tilde{p}_{[1]}, \\
 \rho_f \omega^2 \hat{u}_2^{[1]} + \tilde{\rho}_{eq} \omega^2 \hat{w}_2^{[1]} &= \frac{\partial \tilde{p}_{[1]}}{\partial x_2}. \tag{A1}
 \end{aligned}$$

The solid/fluid relative displacement $\hat{w}_2^{[1]}$ is then replaced by $\hat{V}_2^{[1]} = -i\omega(\hat{w}_2^{[1]} + \hat{u}_2^{[1]})$. From the first and seventh equations of (A1), $\hat{w}_1^{[1]}$ and $\hat{\sigma}_{11}^{[1]}$ can be expressed in terms of $\hat{p}^{[1]}$, $\hat{u}_1^{[1]}$, $\hat{u}_2^{[1]}$, $\hat{V}_2^{[1]}$

$$\begin{aligned}
 \hat{w}_1^{[1]} &= \frac{1}{\tilde{\rho}_{eq} \omega^2} \left(ik_1 \hat{p}^{[1]} - \rho_f \omega^2 \hat{u}_1^{[1]} \right), \hat{\sigma}_{11}^{[1]} = ik_1 (\lambda_c + 2N) \hat{u}_1^{[1]} \\
 &+ (\lambda_c - \alpha M) \frac{\partial \hat{u}_2^{[1]}}{\partial x_2} + i \frac{\alpha M \partial \hat{V}_2^{[1]}}{\omega \partial x_2} \\
 &+ ik_1 \alpha M \hat{w}_1 = ik_1 (\lambda_c + 2N - \alpha M \frac{\rho_f}{\tilde{\rho}_{eq}}) \hat{u}_1^{[1]} \\
 &+ (\lambda_c - \alpha M) \frac{\partial \hat{u}_2^{[1]}}{\partial x_2} + \frac{\alpha M \partial \hat{V}_2^{[1]}}{\omega \partial x_2} - \frac{k_1^2}{\tilde{\rho}_{eq} \omega^2} \alpha M \hat{p}^{[1]}. \tag{A2}
 \end{aligned}$$

The introduction of (A2) in the six other equations of the system (A1) leads to six first-order linear differential equations in terms of $\hat{\sigma}_{12}^{[1]}$, $\hat{\sigma}_{22}^{[1]}$, $\hat{p}^{[1]}$, $\hat{u}_1^{[1]}$, $\hat{u}_2^{[1]}$, and $\hat{V}_2^{[1]}$:

$$\begin{aligned}
 \frac{\partial \hat{\sigma}_{12}^{[1]}}{\partial x_2} + ik_1 (\lambda_c - \alpha M) \frac{\partial \hat{u}_2^{[1]}}{\partial x_2} - \frac{k_1 \alpha M \partial \hat{V}_2^{[1]}}{\omega \partial x_2} + ik_1 \left(\frac{\rho_f}{\tilde{\rho}_{eq}} - \frac{k_1^2}{\tilde{\rho}_{eq} \omega^2} \alpha M \right) \hat{p}^{[1]} + \left(\rho \omega^2 - \frac{\rho_f^2}{\tilde{\rho}_{eq}} \omega - k_1^2 \left(\lambda_c + 2N - \alpha M \frac{\rho_f}{\tilde{\rho}_{eq}} \right) \right) \hat{u}_1^{[1]} &= 0, \\
 \frac{\partial \hat{\sigma}_{22}^{[1]}}{\partial x_2} + ik_1 \hat{\sigma}_{12}^{[1]} + \omega^2 (\rho - \rho_f) \hat{u}_2^{[1]} + i \rho_f \omega \hat{V}_2^{[1]} &= 0, \quad -\frac{\partial \hat{p}^{[1]}}{\partial x_2} + \omega^2 (\rho_f - \tilde{\rho}_{eq}) \hat{u}_2^{[1]} + i \tilde{\rho}_{eq} \omega \hat{V}_2^{[1]} = 0, \\
 N \frac{\partial \hat{u}_1^{[1]}}{\partial x_2} - \hat{\sigma}_{12}^{[1]} + ik_1 N \hat{u}_2^{[1]} &= 0, \\
 (\lambda_c + 2N - \alpha M) \frac{\partial \hat{u}_2^{[1]}}{\partial x_2} + i \frac{\alpha M}{\omega} \frac{\partial \hat{V}_2^{[1]}}{\partial x_2} - \hat{\sigma}_{22}^{[1]} + ik_1 \left(\lambda_c - \frac{\rho_f}{\tilde{\rho}_{eq}} \alpha M \right) \hat{u}_1^{[1]} - \frac{k_1^2 \alpha M}{\tilde{\rho}_{eq} \omega^2} \hat{p}^{[1]} &= 0, \\
 M(\alpha - 1) \frac{\partial \hat{u}_2^{[1]}}{\partial x_2} + i \frac{M \partial \hat{V}_2^{[1]}}{\omega \partial x_2} + \left(1 - \frac{k_1^2}{\tilde{\rho}_{eq} \omega^2} M \right) \hat{p}^{[1]} + ik_1 M \left(\alpha - \frac{\rho_f}{\tilde{\rho}_{eq}} \right) \hat{u}_1^{[1]} &= 0. \tag{A3}
 \end{aligned}$$

Introducing the state vector $\hat{\mathbf{W}} = (\hat{\sigma}_{12}^{[1]}, \hat{\sigma}_{22}^{[1]}, \hat{p}^{[1]}, \hat{u}_1^{[1]}, \hat{u}_2^{[1]}, \hat{V}_2^{[1]})$, the first-order linear ordinary differential system can be written in the form

$$\mathbf{B} \frac{\partial}{\partial x_2} \hat{\mathbf{W}} + \mathbf{D} \hat{\mathbf{W}} = \mathbf{0}, \tag{A4}$$

wherein \mathbf{B} and \mathbf{D} are defined in Eqs. (11) and (12).

¹L. De Ryck, W. Lauriks, Z. E. A. Fellah, A. Wirgin, J. P. Groby, P. Leclaire, and C. Depollier, "Acoustic wave propagation and internal fields in rigid frame macroscopically inhomogeneous porous media," *J. Appl. Phys.* **102**, 024910 (2007).

²L. De Ryck, W. Lauriks, P. Leclaire, J. P. Groby, A. Wirgin, and C. Depollier, "Reconstruction of material properties profiles in one-

dimensional macroscopically inhomogeneous rigid frame porous media in the frequency domain," *J. Acoust. Soc. Am.* **124**, 1591–1606 (2008).

³O. Matsuda and O. B. Wright, "Reflection and transmission of light in multilayers perturbed by picosecond strain pulse propagation," *J. Opt. Soc. Am. B*, **19**, 3028–3041 (2002).

⁴O. Forslund and S. He, "Electromagnetic scattering from an inhomogeneous grating using a wave-splitting approach," *Prog. Electromagn. Res.* **19**, 147–171 (1998).

⁵J. L. Buchanan, R. P. Gilbert, A. Wirgin, and Y. Xu, *Marine Acoustics: Direct and Inverse Problems* (SIAM, Philadelphia, 2004).

⁶J. van Manen, J. O. A. Robertsson, and A. Curtis, "Modeling of wave propagation in inhomogeneous media," *Phys. Rev. Lett.*, **94**, 164301 (2005).

⁷J. G. Berryman and R. R. Greene, "Discrete inverse methods for elastic waves in layered media," *Geophysics*, **45**, 213–233 (1980).

⁸V. Tournat, V. Zaitsev, V. Gusev, V. Nazarov, P. Bequin, and B. Castagnede, "Probing weak forces in granular media through nonlinear dynamic

- dilatancy: Clapping contacts and polarization anisotropy," *Phys. Rev. Lett.* **92**, 085502 (2004).
- ⁹M. A. Biot, "Mechanics of deformation and acoustic propagation in porous media," *J. Appl. Phys.* **33**, 1482–1498 (1962).
- ¹⁰L. De Ryck, J.-P. Groby, P. Leclaire, W. Lauriks, A. Wirgin, C. Depollier, and Z. E. A. Fellah, "Acoustic wave propagation in a macroscopically inhomogeneous porous medium saturated by a fluid," *Appl. Phys. Lett.* **90**, 181901 (2007).
- ¹¹J.-P. Groby, L. De Ryck, P. Leclaire, A. Wirgin, W. Lauriks, R. P. Gilbert, and Y. S. Xu, "Use of specific Green's functions for solving direct problems involving a heterogeneous rigid frame porous medium slab solicited by acoustic waves," *Math. Meth. Appl. Sci.* **30**, 91–122 (2007).
- ¹²A. N. Stroh, "Steady state problems in anisotropic elasticity," *J. Math. Phys.* **41**, 77–103 (1962).
- ¹³G. Peano, "Integration par serie des equations differentielles lineaires (Integration of linear differential equations by series expansion)," *Math. Annal.* **32**, 450–456 (1888).
- ¹⁴M. C. Pease, *Methods of Matrix Algebra* (Academic Press, New York, 1965), Chaps. 6 and 7.
- ¹⁵A. Shuvalov, O. Poncelet, and M. Deschamps, "General formalism for plane guided waves in transversely inhomogeneous anisotropic plates," *Wave Motion* **40**, 413–426 (2004).
- ¹⁶A. Shuvalov, O. Poncelet, M. Deschamps, and C. Baron, "Long-wavelength dispersion of acoustic waves in transversely inhomogeneous anisotropic plates," *Wave Motion* **42**, 367382 (2005).
- ¹⁷J. L. Tsalamangas and N. K. Uzunoglu, "Radiation from a dipole in the proximity of a general anisotropic grounded layer," *IEEE Trans. Antennas Propagat.* **33**, 165–172 (1985).
- ¹⁸J. R. Bowler, L. D. Sabbagh, and H. A. Sabbagh, "A theoretical and computational model of eddy-current probes incorporating volume integral and conjugate gradient methods," *IEEE Trans. Magn.* **25**, 2650–2664 (1989).
- ¹⁹A. L. Shuvalov, E. Le Clezio, and G. Feuillard, "The state-vector formalism and the Peano series solution for modelling guided waves in functionally graded anisotropic piezoelectric plates," *Int. J. Eng. Sci.* **46**, 929–947 (2008).
- ²⁰B. Brouard, D. Lafarge, and J. F. Allard, "A general method of modelling sound propagation in layered media," *J. Sound Vib.* **83**, 129–142 (1995).
- ²¹M. Carcione, *Wavefield in Real Media: Wave Propagation in Anisotropic, Anelastic and Porous Media* (Pergamon, New York, 2001), Chap. 7.
- ²²S. R. Pride and J. G. Berryman, "Connecting theory to experiment in poroelasticity," *J. Mech. Phys. Solids* **46**, 719–747 (1998).
- ²³O. Dazel, B. Brouard, C. Depollier, and S. Griffiths, "An alternative Biot's displacement formulation for porous materials," *J. Acoust. Soc. Am.* **121**, 3509–3516 (2007).
- ²⁴M. A. Biot and D. G. Willis, "The elastic coefficients of the theory of consolidation," *J. Appl. Mech.* **24**, 594–601 (1957).
- ²⁵M. A. Biot, "Theory of propagation of elastic waves in fluid-saturated porous solid," *J. Acoust. Soc. Am.* **28**, 168–178 (1956).
- ²⁶J.-F. Allard and N. Atalla, *Propagation of Sound in Porous Media: Modelling Sound Absorbing Materials* (John Wiley and Sons, Chichester, UK, 2006), Chaps. 5 and 6.
- ²⁷J.-F. Allard and Y. Champoux, "New empirical equations for sound propagation in rigid frame porous materials," *J. Acoust. Soc. Am.* **91**, 3346–3353 (1992).
- ²⁸D. J. Johnson, J. Koplik, and R. Dashen, "Theory of dynamic permeability and tortuosity in fluid-saturated porous media," *J. Fluid Mech.* **176**, 379–402 (1987).
- ²⁹C. Baron, "Le developpement en serie de Peano du matricant pour l'etude de la propagation des ondes elastiques en milieux a proprietes continueement variables (Matricant Peano series development to study elastic waves propagation in continuously varying properties materials)," Ph.D. thesis, Universite de Bordeaux I (2005).
- ³⁰N. A. Haskell, "The dispersion of surface waves on multilayered media," *Bull. Seismol. Soc. Am.* **43**, 377–393 (1953).
- ³¹W. T. Thomson, "Transmission of elastic wave through a stratified solid medium," *J. Appl. Phys.* **21**, 89–93 (1950).
- ³²O. Doutres, N. Dauchez, J. M. Genevaux, and O. Dazel, "Validity of the limp model for porous materials: A criterion based on the Biot theory," *J. Acoust. Soc. Am.* **122**, 2038–2048 (2007).
- ³³M. Tamura, *Spatial Fourier transform method of measuring reflection coefficients at oblique incide I: Theory and numerical examples, Technical report* (National Institute for Environmental Studies, Tsukuba, Japan, 1990).
- ³⁴J.-F. Allard and Y. Champoux, "In-situ two-microphone technique for the measurement of the acoustic surface impedance at oblique incidence and low frequencies," *Noise Control Eng. J.* **32**, 15–23 (1989).

Sustainable sonic crystal made of resonating bamboo rods

C. Lagarrigue,^{a)} J. P. Groby, and V. Tournat

LUNAM Université, Université du Maine, CNRS Unité Mixte de Recherche 6613, LAUM, Av. O. Messiaen, 72085 Le Mans Cedex 9, France

(Received 21 November 2011; revised 4 September 2012; accepted 14 September 2012)

The acoustic transmission coefficient of a resonant sonic crystal made of hollow bamboo rods is studied experimentally and theoretically. The plane wave expansion and multiple scattering theory (MST) are used to predict the bandgap in transmission coefficient of a non-resonant sonic crystal composed of rods without holes. The predicted results are validated against experimental data for the acoustic transmission coefficient. It is shown that a sonic crystal made from a natural material with some irregularities can exhibit a clear transmission bandgap. Then, the hollow bamboo rods are drilled between each node to create an array of Helmholtz resonators. It is shown that the presence of Helmholtz resonators leads to an additional bandgap in the low-frequency part of the transmission coefficient. The MST is modified in order to account for the resonance effect of the holes in the drilled bamboo rods. This resonant multiple scattering theory is validated experimentally and could be further used for the description and optimization of more complex resonant sonic crystals.

© 2013 Acoustical Society of America. [<http://dx.doi.org/10.1121/1.4769783>]

PACS number(s): 43.55.Ev, 43.55.Rg, 43.55.Ti, 43.20.Fn [KVH]

Pages: 247–254

I. INTRODUCTION

With the growing interest for sustainable development, new acoustic materials more respectful to the environment should be designed.¹ In acoustics, the usual absorbing and insulating materials, that can be found in buildings, for example, come from the petrochemical industry and can be hazardous to one's health. However, some more ecological and natural solutions exist involving natural porous materials or sonic crystals made of recycled materials.²

Phononic crystals have received much more attention from the acoustical community in the last decade because of their particular acoustic properties, including bandgaps.³ Numerous studies have been reported in the ultrasonic frequency range for steel rods embedded in water,⁴ epoxy,⁵ or air.⁶ Indeed, the acoustic waves cannot propagate through this periodic arrangement over some frequency bands depending on the characteristics of a unit cell.⁷ This is due to multiple scattering leading to destructive interferences between the rods.

In order to improve the width and central frequencies of the bandgaps for acoustic insulation, structure characteristics should be adapted. We denote by "suitable lattice" the lattice with the best desired characteristics in the audible frequency range designed in accordance with the bamboo mean radius. By acting on the characteristics of the individual cells, transmission loss related to the periodicity can be combined with additional resonant effects at low frequencies, improving the acoustic properties of the structure. Until now, research has mostly focused on split ring like resonators.^{8,9} This type of resonator is easy to build, can be very well calibrated, and can resonate for frequencies below the first bandgap frequency. Such structures are useful for acoustic insulation¹⁰

because of the transmission losses increasing due to these resonances at low frequencies. The bandgap can be enhanced, by tuning the resonators, to create "metamaterials" with more efficient or different properties, like those of an acoustic lens.¹¹

In this paper, the sonic crystal is made with resonant bamboos. By drilling a hole in each initially closed cavity, a bamboo rod becomes a stack of Helmholtz resonators (HRs). The dimensions of bamboo rods used in this paper enable resonance of the HR at very low frequencies. The use of natural material induces dispersion on the dimensions of the scatterers hence on their resonance frequencies. This dispersion can be useful to design a wide frequency range acoustic insulator. The so-designed structure possesses a low transmission coefficient around 300 Hz. These frequencies have never been reached before with natural materials, to our knowledge.

The first part of the paper is devoted to the determination of suitable parameters for a bamboo rod sonic crystal efficient in the audible frequency range by use of the plane wave expansion (PWE) method. Previous investigations on airborne sonic crystals with resonant inclusions have been achieved by using a semi analytical method.^{12,13} Here, the experimental response of the sample is then compared with multiple scattering theory (MST) calculations.¹⁴ Finally, a careful study of the Helmholtz resonator associated bandgap (orientation of the neck, effect of the number of the lines) allows one to account for the resonant character of the scatterers in the MST calculations and to correctly predict the acoustic behavior of the sample.

II. DESIGN OF THE SONIC CRYSTAL

The phononic crystal under study is a periodic arrangement of rods in air, i.e., a sonic crystal (SC). Typically, rods are arranged in a square or triangular lattice.¹⁵ To determine whether or not a bandgap could exist, an important parameter

^{a)} Author to whom correspondence should be addressed. Electronic mail: clement.lagarrigue.etu@univ-lemans.fr

is the filling ratio (Fr), between the area of the scatterer and the area of the unit cell, given by

$$Fr = \frac{\pi d^2}{2a^2\sqrt{3}} \quad (1)$$

for a triangular arrangement where the unit cell is a regular hexagon. The diameter of a rod is $d = 2R$ and the distance between two adjacent rod centers, i.e., the lattice periodicity, is a , see Fig. 1. In order to create sufficiently strong destructive interactions between diffracted waves by each rods and to observe a forbidden band, it is usually observed that Fr yields between 0.4 and 0.6 (Ref. 16) for a square arrangement. In this range, the destructive interferences create an absolute bandgap where no wave can propagate in any direction inside the crystal. When the Fr is out of this range only a pseudo bandgap (bandgap in only one direction) is observed. A specific feature of the triangular arrangement is the possibility of creating absolute bandgap for Fr below 0.4 and have a full bandgap in a lower frequency range.¹⁷

No wave can propagate through a SC in the frequency range of the bandgap, and consequently, such an arrangement is a good candidate to achieve acoustic shielding. The bandgap width depends on Fr and a bandgap appears when the half of the wavelength is equal to the separation distance between the successive rows. The central frequency of the first bandgap can then be easily calculated through $f = c/\sqrt{3}a$ (where c is the speed of sound in the medium) as a first approximation. The determination of the bandgap can be achieved by using the PWE. A large contrast between the impedance of the fluid and the impedance of the rods is required for the energy to be strongly scattered in any directions and so for the SC to be efficient.

A. Determination of the lattice periodicity

The goal is to design a natural sonic crystal efficient in the audible frequency range. Because of their peculiar shape, bamboo rods are used. They are made of a wood tough enough for them to be approximated as infinitely rigid scatterers. Each rods is 2.60 m high with an external diameter d^n between 3.7 and 4.3 cm. As a first approximation, the mean

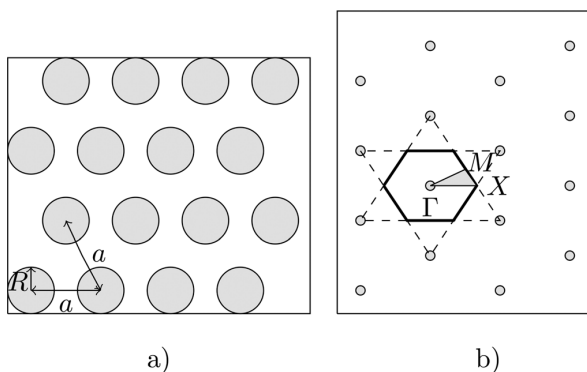


FIG. 1. Diagram of a triangular lattice for an ideal sonic crystal. (a) Direct space, where rods have a radius r and a lattice constant a . (b) Reciprocal space with the irreducible Brillouin zone.

diameter of all the bamboo rods can be used as the diameter of each scatterers for a PWE calculation. This mean diameter is $d = 2R = 4$ cm, wherein R is the mean radius of all the bamboo rods. The PWE is used to determine the more suitable bandgap for a low frequency application (the widest with the lowest central frequency as possible with regards to the radius constraint) and so, the most suitable lattice shape and periodicity. The acoustic wave equation is rewritten in the reciprocal space (2D spatial Fourier transform) where the problem becomes a standard eigenvalue problem. This eigenvalue problem is solved numerically over the first Brillouin zone. A triangular lattice is chosen because such lattices enable absolute bandgap with a larger periodicity than a square lattice. The acoustic field is calculated for a unit cell along the First Brillouin zone with coordinates $\Gamma = (0, 0)$, $X = (4\pi/a, 0)$, and $M = (\pi/a, \pi/\sqrt{3}a)$.

To ensure a good convergence of the results, the PWE is computed with 169 waves. When the periodicity increases, the bandgap central frequency decreases, but its width drastically shrinks and then the absolute character of the bandgap disappears. A lattice constant of 9 cm is chosen. The corresponding filling ratio is $Fr = 0.18$. This value seems to be the best compromise between the bandgap width and a low bandgap central frequency. With these parameters the first absolute bandgap lies between 2000 Hz and 2550 Hz and particularly, the bandgap lies between 1600 and 2550 Hz in the ΓX direction (see Fig. 2). This configuration is used in the following.

The PWE is useful to determine bandgaps for a sonic crystal made of perfectly rigid cylinders but is limited to the study of infinite structures. PWE cannot take into account the diffraction effects on the boundaries of a finite SC. For finite structures of sufficiently large extend, the global behavior remains almost the same as the one of the corresponding and PWE results constitute a first good approximation. As ultrasound in water can easily be highly directive, diffraction issues due to the finite size of the experimental device can be easily avoided. However, measurements are quite sensitive to these diffraction issues in the audible frequency range. To account for the finite size of the sonic crystal and for the position of the microphone, another method should be used. The finite difference time domain method³ or multiple scattering theory¹⁸ (MST) are good candidates. The MST is used here to calculate the acoustic field transmitted through the SC, which

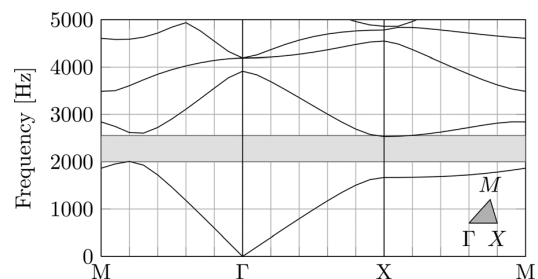


FIG. 2. Band diagram for a sonic crystal in a triangular lattice with a radius of 2 cm and a lattice constant of 9 cm. Dispersion curves are plotted along the direction of the irreducible Brillouin zone ΓXM where ΓX is the normal incidence. The grey area shows the absolute bandgap.

is compared with experimental results. The MST also account for the dispersion of rod radii. However, the rod position is fixed by the lattice periodicity, because accounting for it would requires a large amount of (and complicated) distance measurements. Moreover, the PWE does not allow for internal resonance. Moreover, the MST is modified (see Sec. III C) to account for possible resonant effects of the scatterers.

B. Determination of the transmission loss with multiple scattering theory

MST, usually known as the Korringa–Kohn–Rostoker approach, was mainly developed for the calculation of electronic band structures. This method was widely used in elasticity and electromagnetism.¹⁹ The main idea is to separate the fields distributed in the 2D space into non-overlapped regions, each of them containing a rod. The total acoustic field is calculated for each region as being the sum of the diffracted field by the scatterer and the incident field on this scatterer, the latter being composed of the scattered field by the other scatterers (Graf's addition theorem) and by the direct incident field. Let us consider a structure made of N parallel circular cylinders, identified by superscript $n \in \mathcal{N}$, of radius r^n , located at $\mathbf{r}^n = (r^n, \theta^n)$ in the global polar coordinate system in the cross-sectional plane. As indicated above, the key to the multiple scattering method are the local field expansions or multiple expansions in the vicinity of each cylinder in the polar coordinate system linked to that cylinder

$$p(\mathbf{r}_n) = \sum_{m \in \mathbb{Z}} \left(A_m^n H_m^{(1)}(kr^n) + B_m^n J_m(kr^n) \right) e^{im\theta^n}, \quad (2)$$

where $H_m^{(1)}$ is the first-kind Hankel function of order m , J_m is the Bessel function of order m , A_m^n are the coefficients of the scattered field by the n -th cylinder, B_m^n are those of the incident field impinging upon the n -th cylinder. The local incident field on the n -th cylinder is generated by the actual incident field p^{inc} as well as by the fields that are scattered by all other cylinders $j, j \neq n$. Their coefficients also take the form

$$B_m^n = K_m^n + \sum_{j \in \mathcal{N}, j \neq n} \sum_{q \in \mathbb{Z}} S_{mq}^{nj} B_q^j, \quad (3)$$

where K_m^n are the coefficients of the actual incident field, i.e., a planar incident wave in the cross-sectional plane, $K_m^n = (-i)^m \exp(ikr^n \cos(\theta^i - \theta^n) - im\theta^i)$, and $S_{mp}^{nj} = H_{m-p}^{(1)}(kr_n^j) e^{i(q-m)\theta_n^j}$ are translation terms, (r_n^j, θ_n^j) being the coordinates of the j -th cylinder in the polar coordinate system associated with the n -th cylinder. Coefficients A_m^n and B_m^n are related together via the boundary condition on the n -th cylinder, i.e., $A_m^n = D_m^n B_m^n$, wherein D_m^n is the scattering coefficient. This leads to the final linear system, which may be written in the matrix form, where \mathbf{B} denotes the infinite column matrix of components B_m^n

$$(\mathbf{I} - \mathbf{DS})\mathbf{B} = \mathbf{K}, \quad (4)$$

wherein \mathbf{I} is the identity matrix, \mathbf{S} is the matrix of components S_{mp}^{nj} , $\mathbf{D} = \text{diag} D_m^n$, and \mathbf{K} is the infinite column matrix of components K_m^n .

Once Eq. (4) is solved for B_m^n , the field in the entire space can then be calculated.²⁰ The infinite sum $\sum_{m \in \mathbb{Z}}$ over the indices of the modal representation of the diffracted field by a cylinder is truncated²¹ as $\sum_{m=-M}^M$ such that $M = \text{int}(\text{Re}(4.05 \times (kr^n)^{1/3} + kr^n)) + 10$. In the former equation, $\text{int}(a)$ represents the integer part of a and 10 is a security factor.

MST accounts for the properties (radius, position, and filling property) of each scatterer,¹⁸ for visco-thermal dissipation, and allows one to calculate the acoustic field at any location of the system. Nevertheless, only one incidence angle of a plane wave can be considered at each calculation. Each rod radius is measured and used in the model to be the closest to the real SC described in Sec. II C. The acoustic field behind the SC is averaged along the lateral direction on 17 points.²² The air medium can be considered as a perfect fluid (without dissipation) and Neumann type boundary condition can be used at the air-bamboo interface. The scattering coefficient D_m^n of the n -th bamboo rod accounted for in the calculation through $A_m^n = D_m^n B_m^n$ takes the form (in the $e^{-i\omega t}$ temporal convention)

$$D_m^n = -\frac{J'_m(kR^n)}{H_m^{(1)'}(kR^n)}, \quad (5)$$

where J'_m and $H_m^{(1)'}$ are the derivatives of, respectively, the Bessel and Hankel functions of the first kind with respect to the radial coordinate.

To validate the hypothesis of perfect fluid and Neumann type boundary condition, results calculated under this hypothesis and those calculated with an impedance condition^{23,24} are compared in Fig. 3. In this latter case, the scattering coefficient D_m^n takes the form

$$D_m^n = -\frac{J'_m(kR^n) + i\beta_m^n J_m(kR^n)}{H_m^{(1)'}(kR^n) + i\beta_m^n H_m^{(1)}(kR^n)}, \quad (6)$$

where the characteristic surface admittance β_m^n expresses the thermo-viscous effects in the boundary layers. The expression of the characteristic surface admittance in this case is

$$\beta_m^n = \frac{1 - i}{2} k \left[\frac{m^2}{k^2 (R^n)^2} \delta_v + (\gamma - 1) \delta_h \right], \quad (7)$$

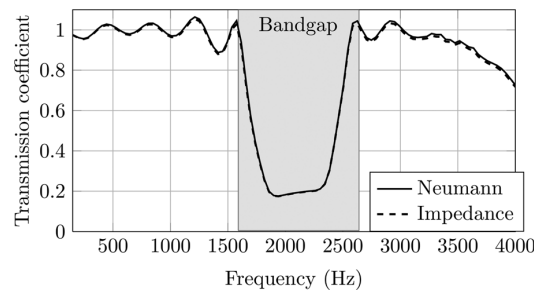


FIG. 3. Transmission coefficient of the SC calculated with MST and a lattice constant of 9 cm in normal wave incidence (ΓX). Neumann type boundary condition (—) and impedance conditions are used (---) at the air-rod interface. The grey rectangle depicts the bandgap location calculated with PWE.

where $\delta_v = \sqrt{2\nu_v/\omega}$ is the viscous skin depth (the air kinematic viscosity is $\nu_v = 1.5 \times 10^{-5} \text{ m}^2 \text{ s}^{-1}$), $\delta_h = \sqrt{2\nu_h/\omega}$ is the heat skin depth (the air thermal diffusivity is $\nu_h = 2.5 \times 10^{-5} \text{ m}^2 \text{ s}^{-1}$) and $\gamma = 1.4$ the capacity ratio. In the frequency range of interest, dimensions of the skin depths are negligible in comparison with the dimensions of the crystal and of the rods. The visco-thermal effects have a small influence on the acoustic field below 6 kHz for our SC, see Fig. 3. The fluid can be considered as a perfect fluid and Neumann type boundary conditions are used in the following.

Results exhibit a bandgap in the transmission coefficient curve between 1600 and 2550 Hz in the ΓX direction that confirm the PWE estimation (see Fig. 2).

C. Experimental results

The sample is a SC made of $N = 45$ bamboos of radius ranging between 3.7 and 4.3 cm, i.e., $R^n \in [3.7 \text{ cm}; 4.3 \text{ cm}]$, and 2.60 m high. The crystal consists of 9 rows of 5 columns (see Fig. 4).

This SC can be considered has a 2D SC because its height is larger than the dimensions in the other directions. All experiments are performed in an anechoic room. Figure 5 depicts the experimental set-up. A loudspeaker connected to the low frequency generator output of the spectrum analyzer (Stanford Research SR785) produces a chirp signal between 100 and 4000 Hz. The loudspeaker is placed far enough (2.80 m) from the SC for the incident wave to be considered as a plane incident wave in the ΓX direction. A Microphone B&K 1/4-inch records the transmitted field at 9 cm behind the SC (i.e., a lattice period) to minimize diffraction due to the finite nature of our sample. The transmitted signal is recorded on 17 points along the x_2 coordinate over two lattice periods around the central rod (one on each side), and is sent to the spectrum analyzer. Two measurements are conducted, with and without the sample. The ratio between the two recorded spectra averaged over the 17 points of measurement gives the transmission coefficient. Experimental results are compared to MST calculations in



FIG. 4. (Color online) Picture of the tested structure.

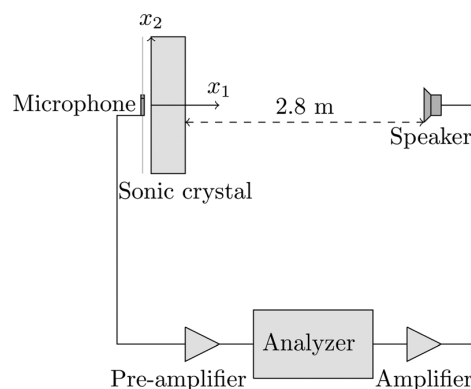


FIG. 5. Experimental setup.

Fig. 6. A bandgap is observed between 1600 and 2550 Hz, with a transmission coefficient below 0.2, which corresponds to an attenuation of about 14 dB. MST captures well the specific features of the wave interaction by the SC: diffraction due to the finite size, small dispersion of the rod radii, etc. The transmission coefficient calculated when the rod radii dispersion is accounted for and when the radii of all the rods are equal to the mean radius value, i.e., $R^n = R = 2 \text{ cm}$, are almost the same. This means that the radii dispersion weakly affects the first bandgap for this SC. Discrepancies between experimental and MST calculated transmission coefficient appear for frequencies higher than 4000 Hz. They can be attributed to the surface irregularities and to the position dispersion of bamboos that introduce disorder not accounted for in the MST calculation.

In Fig. 6 the calculated and experimental transmission coefficients are sometimes higher than 1. Passive structures cannot create energy and the transmission coefficient cannot be higher than 1. In our case the microphone is close enough to the device to record constructive interferences created by the multiple scattering inside the SC leading to transmission coefficient higher than 1. These constructive interferences are normally trapped inside the SC but can be recorded near the crystal boundaries. This effect disappears when the microphone is placed far enough from the SC but then diffraction phenomena related to the finite size of the sample

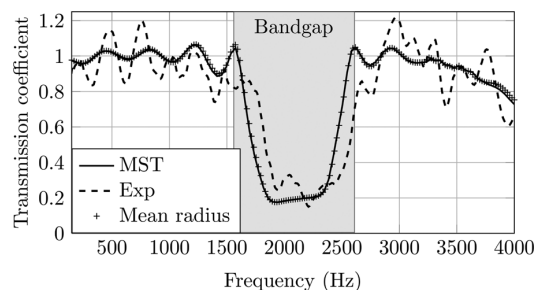


FIG. 6. Comparison between the transmission coefficient calculated by MST with all the radii accounted for (—), by MST with the mean radius (···), and measured experimentally (---) for a triangular lattice sonic crystal of 9×5 rods of 4 cm of diameter.

appear and quickly degrade the experimental and numerical results. Another possibility would be to use an intensity probe to record the energy flow.

Experimental results are validated by PWE and MST calculations and prove the efficiency of a natural sonic crystal in the audible frequency range. Moreover, natural disorder does not influence the efficiency of the scattering effect in the considered frequency range.

III. SONIC CRYSTAL WITH LOCALLY RESONANT SCATTERERS

The idea to improve the transmission losses of the so-designed sonic crystal is to combine bandgap with resonance phenomena.²⁵ Current research use resonant scatterers like split ring^{26,27} or Helmholtz resonators.²⁸ This kind of scatterer can resonate for frequencies below the first bandgap and the corresponding wavelength is larger than the scatterer radius or the lattice periodicity. Helmholtz resonators (HRs) are already used in architectural acoustics to reduce undesirable low frequency noise through perforated plates,²⁹ for example.

In bamboos, the internodal regions of the stem are hollow and closed which creates a stack of closed cavities. By drilling a hole of 9 mm diameter in each cavity, bamboo becomes a stack of HRs. The holes were drilled at approximately a third of the internodal length of each cavity. This was empirically determined in order to mostly excite the HR fundamental resonance. For a specific rod, the holes are drilled in such a way that they are all aligned along the axis of the rod. The angle that measures the orientation of the holes (the neck) with respect to the incident plane wave is also identical for all the HRs of a specific rod. In the same way, all the HRs of a specific rod are considered identical, because the incident wave strikes a rod in the middle region, where the dimension of the internodal length and external radius are almost the same. Under the long wavelength approximation, i.e., in low frequencies, the behavior of each rod constituted by a stack of HRs can be accounted for as an unique equivalent HR. The n -th rod HR fundamental resonance frequency can be estimated, under the long wavelength approximation, as

$$f_H^n = \frac{c}{2\pi R_i^n} \frac{R_h}{\sqrt{L\delta l}}, \quad (8)$$

with R_h the radius of the hole, R_i^n the internal radius of the n -th bamboo cavity, L the internodal length, whose value is the mean of the internodal lengths measured on all bamboos, $\delta l = l + 0.48\sqrt{\pi R_h^2}$ the corrected thickness of the rod wall,³⁰ i.e., the corrected neck length, describing an additional volume of fluid constrained to flow into or out of the openings, wherein l is the neck length, and c the sound velocity of the fluid (here, $c = 340 \text{ m s}^{-1}$). The angle of the neck α^n of the n -th rod is measured counter-clockwise from the incident wave orientation.

A. Influence of the Helmholtz resonator

The distance between two nodes yields between 20 and 28 cm, because of the natural heterogeneity in the rod shape.

For $R_h = 0.45 \text{ cm}$, R_i^n from 1.55–1.85 cm, and $l = 0.3 \text{ cm}$, the resonance frequency is estimated between 230 and 380 Hz by Eq. (8). The thickness of the wall of each cavity, which is the neck length, is considered constant, so that the variation in the internal radius is accounted for through $R_i^n = R^n - l$. Several experiments are performed to determine the influence of the Helmholtz resonators on the acoustic properties of the structure. A comparison between the transmission coefficient of the sonic crystal with and without HR is shown in Fig. 7. The neck of each rod is oriented along the same axis, i.e., $\alpha^n = \alpha$, $\forall n \in [0, 45]$, in front of the incident wave, i.e., $\alpha = 0^\circ$.

The HR resonance influence is clearly visible in the transmission coefficient, around 300 Hz, which corresponds to the fundamental frequency estimated above. Higher order resonances are also excited and enhance the transmission losses around 500 and 800 Hz. The bandgap, between 1600 and 2550 Hz, due to the periodicity of the arrangement is not modified. Replacing rigid scatterers by resonant ones does not influence the bandgap associated to periodicity when keeping identical dimensions and when f_H^n is far enough from the bandgap location. Another peak in the transmission coefficient is added. The width of the HR “bandgap” is around 150 Hz, which is wider than the one of the peak induced by the resonance of a single HR, because of radius and cavity length spread in the natural Helmholtz resonator sonic crystal (HRSC).

B. Influence of the neck orientation of the Helmholtz resonator

In order to analyze the influence of the neck orientation on the structure behavior, the same experiment is repeated with $\alpha = 45^\circ$ and 90° . The experimental transmission coefficients for $\alpha = 0^\circ, 45^\circ$, and 90° are compared in Fig. 8.

The orientation of the HR neck does not seem to influence the transmission coefficient. Another measurement, which is not shown here, was performed with randomly chosen α^n , i.e., the neck are randomly oriented. No strong influence was again observed. Small discrepancies are visible for frequencies higher than 2600 Hz. These are due to surface irregularities and to the fact that bamboos are not straight. Indeed, by turning each bamboo around its axis, the distance between some of them might be changed of a few millimeters. In the HR frequency range (between 230 and 380 Hz),

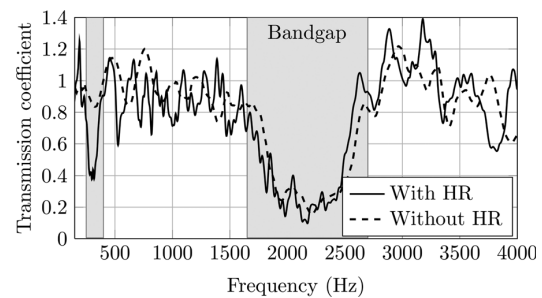


FIG. 7. Experimental transmission coefficient of a triangular lattice sonic crystal of 45 bamboos with (—) and without (---) Helmholtz resonators.

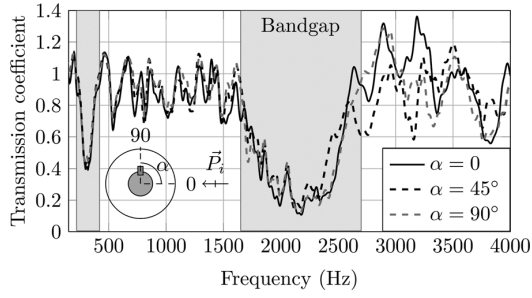


FIG. 8. Experimental transmission coefficient showing the influence of HR orientation for triangular lattice SC of constant lattice of 9 cm and 9×5 bamboos. \vec{P}_i corresponds to the direction of propagation of the incident wave.

the wavelength is much larger than the external radius of a rod, i.e., $kr^n \ll 1$, $\forall n \in [1, 45]$. The low frequency approximation of the scattering by the cylinders is also valid. Consequently, the scattering by the resonant rod can be considered as originated from a line scatterer and is then independent of the scatterer orientation.

These experiments confirm that creating a sonic crystal with this kind of resonator improves the acoustic insulation by adding more transmission losses in the low frequency range. Helmholtz resonators absorb sound at their resonance frequency, independently of the position of their neck.

The expected effect of the Helmholtz resonance on the solid rod crystal band structure is the opening of an hybridization gap around the resonator natural frequency, covering the whole Brillouin zone, i.e., independent of the wave vector. A PWE simulated band structure taking account for the Helmholtz resonator effects is in principle possible, but would not account for the three-dimensional character of this problem of finite size resonator stacks, and for the distribution of resonances.

C. Implementation of the resonant behavior in the MST

The resonance of the HR can be implemented in a straightforward manner in the MST, because the scattered field is independent from the angle α^n , by multiplying the scattering coefficient by a Lorentzian band-cut filter function [see Eq.(5)] in order to account for the resonance effect of the holes in the drilled bamboo rods. The central frequency of this function is equal to the resonance frequency of the resonator. The scattering coefficients \tilde{D}_m^n become

$$\tilde{D}_m^n = D_m^n R b^n, \quad (9)$$

with

$$R b^n = 1 - \Pi^n \left(\frac{Q}{1 - iQ \left(\frac{\omega}{\omega_H^n} - \frac{\omega_H^n}{\omega} \right)} \right), \quad (10)$$

wherein Π^n is a rectangular function centered at ω_H^n and of width 40 Hz, $\omega_H^n = 2\pi f_H^n$ is the resonance frequency of n -th

bamboo rod estimated by considering a constant internodal length $L = 24$ cm, and Q is the quality factor. The resonance frequency f_H^n depends on the internal radius [Eq. (8)] and is also dependent on the considered bamboo rod. The quality factor Q was hypothesized independent from the rod. It was determined by adjusting, in the MST (now called RMST), the frequency width of the transmission coefficient deep due to the HR and amplitude around ω_H^n with experimental results measured in the one line configuration. The so-determined value is $Q = 20$. Experimental and simulated results for the whole configuration, i.e., with five lines, are presented in Fig. 9 and exhibit good agreement. This validates the way the HR resonances are implemented in the RMST.

The RMST predicts the bandgap associated with the HR well. In this HR bandgap, a transmission coefficient of 0.4 is reached which corresponds to a 8 dB attenuation. Nevertheless, the experimental HR bandgap is wider and of lower amplitude than the one predicted. This small discrepancy is due to the dispersion of the bamboo internal radius and internodal length, i.e., dispersion of the HR dimensions. While the variation of the internal radius is accounted for, the one of the cavity length is fixed at $L = 24$ cm. In practice, L varies from 20 to 28 cm. This variation could modify substantially the resonance frequencies and enlarge the HR bandgap. Because of this enlargement, the amount of energy that is trapped is also lower, explaining the differences in the HR bandgap depth.

To improve the HRSC performances, the HR bandgap effect can be increased by adding resonators, i.e., by adding bamboos. The number of bamboos is raised from $N = 45$ to 84 by designing an HRSC of 7 lines of 12 bamboos each.

D. Influence of the crystal size

Experimental measurements are done with a crystal of 12 bamboos per line with increasing number of lines from 1 to 7. The SC bandgap is practically unchanged, so that special attention is paid to the HR deep in the transmission. Figure 10 depicts the transmission coefficient for frequencies around the HR frequency resonance for these configurations. The 7 lines crystal exhibits a transmission coefficient of 0.2, which corresponds to a 14 dB attenuation. The HR deep is also deeper than in the 45 bamboos configuration. Two minima, respectively at 290 and 340 Hz, are noticed. These are due to the

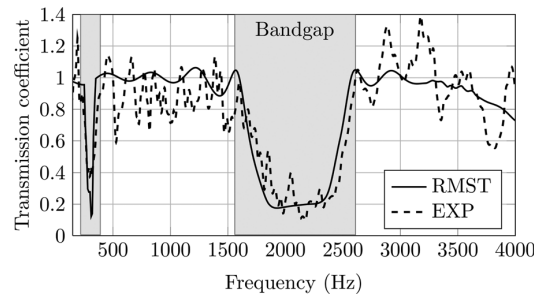


FIG. 9. Comparison between the RMST calculation and experimental results obtained for a triangular lattice sonic crystal of 45 resonant bamboos with a lattice period of 9 cm.

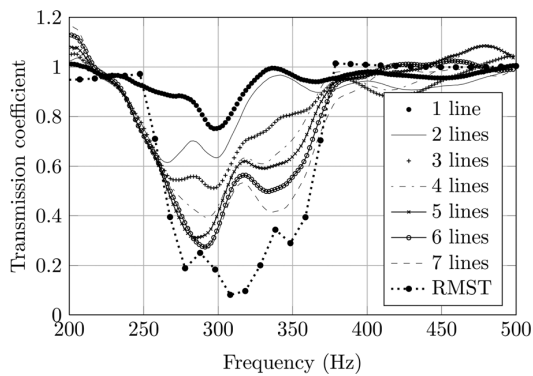


FIG. 10. Zoom of the HR resonance band in the transmission coefficient that shows influence of the number of lines for a triangular lattice sonic crystal of 84 bamboos (7×12) with a lattice constant of 9 cm.

smaller radius additional bamboos. Indeed, the external radius of the added bamboos are smaller than those used in the 45 bamboo configuration. Their radius lies between 3.3 and 3.8 cm. The resonance contribution of the added bamboos is slightly different than the one of the bamboos used in the initial HRSC. The difference makes these resonances distinct, therefore leading to two peaks. If they were closer, a coupled mode would have been excited, with only one thinner peak of deeper amplitude. Nevertheless, the advantage is an enlargement of the HR deep. The figure shows that the difference between the resonance frequencies of two consecutive lines must be less than 20 Hz to couple these resonances.

The RMST shows good agreement with experimental results, Fig. 10. RMST predicts that a wider HR bandgap could have been obtained with a smoother radius variation along coordinate x_1 .

IV. CONCLUSION AND DISCUSSION

The behavior of a triangular sonic crystal predicted with the PWE method and made with natural scatterers is studied for the audible frequency range. The scatterers are bamboo rods and are arranged periodically with a lattice constant of 9 cm. The multiple scattering by this sonic crystal induces a bandgap between 1600 and 2500 Hz. Because of the considered frequency range, the inherent disorder and surface irregularities of natural materials as well as visco-thermal effects, do not influence the results and a quite efficient bandgap for a small sample (45 scatterers, 9 lines, and 5 rows) is observed. All experiments are validated with a multiple scattering theory algorithm. To improve properties of the SC, bamboos are drilled to transform the cylindrical rigid scatterers into stacks of Helmholtz resonators and create a locally resonant sonic crystal. These resonances add anomalies in the transmission coefficient at very low frequency (300 Hz) and do not affect the SC bandgap. A careful study of the behavior of the HR resonance has enabled us to modify the MST to account for the resonant features of the HR. The transmission coefficient amplitude inside the HR bandgap is 0.4, which corresponds to a loss of 8 dB, for a 45 bamboos configuration and 0.2, which corresponds to a loss of 14 dB, for an 84 bamboos configuration.

This lack of efficiency is due to the too few number of resonators excited in the recorded zone.

However, the transmission losses due to the resonance effect seems to be widened and deepened by the careful choice of the distribution of HRs. The next step could be to design a sonic crystal with a gradient of properties, in particular, a gradient of HR resonances.

¹M. Saadatnia, G. Ebrahimi, and M. Tajvidi, "Comparing sound absorption characteristic of acoustic boards made of Aspen particles and different percentage of Wheat and Barely straws," in *Abstracts of 17th World Conference on Non-Destructive Testing* (2008).

²J. Sanchez-Dehesa, V. Garcia-Chocano, D. Torrent, F. Cervera, S. Cabrera, and F. Simon, "Noise control by sonic crystal barriers made of recycled materials," *J. Acoust. Soc. Am.* **129**, 1173–1183 (2011).

³J. Vasseur, P. Deymier, A. Khelif, P. Lambin, B. Djafari-Rouhani, A. Akjouj, L. Dobrzynski, N. Fettouhi, and J. Zemmouri, "Phononic crystal with low filling fraction and absolute acoustic band gap in the audible frequency range: A theoretical and experimental study," *Phys. Rev. E* **65**, 056608 (2002).

⁴Z. Liu, X. Zhang, Y. Mao, Y. Zhu, Z. Yang, C. Chan, and P. Sheng, "Locally resonant sonic materials," *Science* **289**, 1734–1736 (2000).

⁵J. Vasseur, P. Deymier, B. Chenni, B. Djafari-Rouhani, L. Dobrzynski, and D. Prevost, "Experimental and theoretical evidence for the existence of absolute acoustic band gaps in two-dimensional solid phononic crystals," *Phys. Rev. Lett.* **86**, 3012–3015 (2001).

⁶X. Hu, K. Ho, C. Chan, and J. Zi, "Homogenization of acoustic metamaterials of Helmholtz resonators in fluid," *Phys. Rev. B* **77**, 172301 (2008).

⁷J. Joannopoulos, *Photonic Crystals: Molding the Flow of Light* (Princeton University Press, Princeton, 2008), Chaps. 5, 10.

⁸S. Guenneau, A. Movchan, G. Pétursson, and S. Ramakrishna, "Acoustic metamaterials for sound focusing and confinement," *New J. Phys.* **9**, 399–418 (2007).

⁹E. Fuster-Garcia, V. Romero-Garcia, J. Sanchez-Perez, and L. Garcia-Raffi, "Targeted band gap creation using mixed sonic crystal arrays including resonators and rigid scatterers," *Appl. Phys. Lett.* **90**, 244104 (2007).

¹⁰D. P. Elford, L. Chalmers, F. V. Kusmartsev, and G. M. Swallowe, "Matryoshka locally resonant sonic crystal," arXiv:1102.0399v1 (2011).

¹¹X. Hu, C. T. Chan, and J. Zi, "Two-dimensional sonic crystals with Helmholtz resonators," *Phys. Rev. E* **71**, 055601 (2005).

¹²C. Linton and D. Evans, "The interaction of waves with arrays of vertical circular cylinders," *J. Fluid Mech.* **215**, 549–569 (1990).

¹³O. Umnova, K. Attenborough, and C. Linton, "Effects of porous covering on sound attenuation by periodic arrays of cylinders," *J. Acoust. Soc. Am.* **119**, 278–284 (2006).

¹⁴F. Zaviska, "Über die beugung elektromagnetischer wellen an parallelen, unendlich langen kreiszyhndern," *Ann. Phys.* **345**, 1023–1056 (1913).

¹⁵A. Phani, J. Woodhouse, and N. Fleck, "Wave propagation in two-dimensional periodic lattices," *J. Acoust. Soc. Am.* **119**, 1995–2005 (2006).

¹⁶T. Miyashita, "Sonic crystals and sonic wave-guides," *Meas. Sci. Technol.* **16**, R47–R63 (2005).

¹⁷M. Plihal and A. A. Maradudin, "Photonic band structure of two-dimensional systems: The triangular lattice," *Phys. Rev. B* **44**, 8565–8571 (1991).

¹⁸J. Page, A. Sukhovich, S. Yang, M. Cowan, F. Van Der Biest, A. Tourin, M. Fink, Z. Liu, C. Chan, and P. Sheng, "Phononic crystals," *Phys. Status Solidi B* **241**, 3454–3462 (2004).

¹⁹X. Wang, X.-G. Zhang, Q. Yu, and B. N. Harmon, "Multiple-scattering theory for electromagnetic waves," *Phys. Rev. B* **47**, 4161–4167 (1993).

²⁰Z. Liu, C. Chan, P. Sheng, A. Goertzen, and J. Page, "Elastic wave scattering by periodic structures of spherical objects: Theory and experiment," *Phys. Rev. B* **62**, 2446–2457 (2000).

²¹P. Barber and S. Hill, *Light Scattering by Particles: Computational Methods* (World Scientific, Singapore, 1990), Vol. 2, Chap. 2, p. 30.

²²D. Felbacq, G. Tayeb, and D. Maystre, "Scattering by a random set of parallel cylinders," *J. Opt. Soc. A* **11**, 2526–2538 (1994).

²³S. Guenneau, A. Movchan, F. Zolla, N. Movchan, and A. Nicolet, "Acoustic band gaps in arrays of neutral inclusions," *J. Comput. Appl. Math.* **234**, 1962–1969 (2010).

²⁴V. Tournat, V. Pagneux, D. Lafarge, and L. Jaouen, "Multiple scattering of acoustic waves and porous absorbing media," *Phys. Rev. E* **70**, 026609 (2004).

- ²⁵H. Larabi, Y. Pennec, B. Djafari-Rouhani, and J. O. Vasseur, "Multicoaxial cylindrical inclusions in locally resonant phononic crystals," *Phys. Rev. E* **75**, 066601 (2007).
- ²⁶Z. Hou, J. Liu, W. Kuang, Y. Liu, and S. Wu, "Sonic crystal with open resonant cavities," *Phys. Rev. E* **75**, 026608 (2007).
- ²⁷V. Romero-García, J. Sánchez-Pérez, and L. García-Raffi, "Tunable wideband bandstop acoustic filter based on two-dimensional multiphysical phenomena periodic systems," *J. Appl. Phys.* **110**, 014904 (2011).
- ²⁸Z. Wang, S. Lee, C. Kim, C. Park, K. Nahm, and S. Nikitov, "Effective medium theory of the one-dimensional resonance phononic crystal," *J. Phys.: Condens. Matter* **20**, 055209 (2008).
- ²⁹R. Zulkifli, M. Nor, A. Ismail, M. Nuawi, and M. Tahir, "Effect of perforated size and air gap thickness on acoustic properties of coir fibre sound absorption panels," *Eur. J. Sci. Res.* **28**, 242–252 (2009).
- ³⁰L. Kinsler, A. Frey, A. Coppens, and J. Sanders, *Fundamentals of Acoustics* (Wiley-VCH, Verlag, Germany, 1999), Vol. 1, p. 284.

Use of slow sound to design perfect and broadband passive sound absorbing materials

J.-P. Groby,^{a)} R. Pommier, and Y. Aurégan

Laboratoire d'Acoustique de l'Université du Maine (LAUM), Unité Mixte de Recherche 6613 Centre National de la Recherche Scientifique, Avenue O. Messiaen, 72085 Le Mans, France

(Received 17 July 2015; revised 21 March 2016; accepted 21 March 2016; published online 6 April 2016)

Perfect (100%) absorption by thin structures consisting of a periodic arrangement of rectangular quarter-wavelength channels with side detuned quarter-wavelength resonators is demonstrated. The thickness of these structures is 13–17 times thinner than the acoustic wavelength. This low frequency absorption is due to a slow sound wave propagating in the main rectangular channel. A theoretical model is proposed to predict the complex wavenumber in this channel. It is shown that the speed of sound in the channel is much lower than in the air, almost independent of the frequency in the low frequency range, and it is dispersive inside the induced transparency band which is observed. The perfect absorption condition is found to be caused by a critical coupling between the rectangular channel (sub-wavelength resonators) and the incoming wave. It is shown that the width of a large absorption peak in the frequency spectrum can be broadened if several rectangular channels in the unit cell are detuned. The detuning is achieved by varying the length of the side resonators for each channel. The predicted absorption coefficients are validated experimentally. Two resonant cells were produced with stereolithography which enabled the authors to incorporate curved side resonators. © 2016 Acoustical Society of America.

[<http://dx.doi.org/10.1121/1.4945101>]

[KVH]

Pages: 1660–1671

I. INTRODUCTION

A perfect absorber, i.e., a structure which absorbs 100% of the incident acoustic energy, of very small thickness is of great scientific and engineering interest. Until now, porous or fibrous materials¹ have been the common choice for noise passive control due to their ability to dissipate sound through thermal and viscous losses. This results in limitations: to absorb low frequency sound, bulky and heavy treatments are required even when optimized multilayer or graded materials² are used. Acoustic absorption can also be performed by means of micro-perforated panels^{3,4} with tuned cavity depth behind the panels. A large review of the existing acoustic absorbing structures can be found in Ref. 5. To overcome imperfect impedance matching to the incoming wave on structures with dimensions comparable to the wavelength, several strategies have been followed these last decades usually consisting in coupling porous materials with resonant features, double porosity materials,⁶ metaporous materials,^{7–10} dead-end porosity materials,^{11,12} or in coupling purely resonant components, membranes,^{13–15} Helmholtz resonators,^{15,16} or quarter-wavelength resonators (QWRs) making use of slow sound.^{12,17}

In these last types of passive absorption systems the balance between the rate of energy leakage and the inherent losses of the resonators is of fundamental relevance for their reflection properties.^{15,18} When these are well balanced, the critical coupling condition is fulfilled, leading to an impedance matching and maximum absorption at the resonance frequency. In the present article, we critically couple periodic

QWRs loaded by detuned QWRs to lower their resonance frequencies making use of the slow sound propagation together with the inherent attenuation. In acoustics, most of the theoretical and experimental evidences of slow sound have been achieved by considering sound propagation (i) in pipes with a series of detuned resonators (mostly Helmholtz resonators) separated by a subwavelength distance creating an induced transparency band (ITB),¹⁹ or with a series of tuned or detuned resonators separated by half of the wavelength giving rise to a coupling between the resonators and the Bragg bandgap;²⁰ (ii) in waveguided sonic crystals;²¹ or (iii) in lined ducts.²² So far, only a few studies have been focusing on the dissipation (dispersion and attenuation) of slow sound propagation,²³ even if dissipation has been sometimes noticed or discussed^{19,20,24} and only a few studies make use of the slow sound together with its attenuation to design a sub-wavelength acoustic absorber in two dimensions.¹⁷

A periodic structure whose unit cell consists of unique QWR of rectangular cross-section, named pore in the following, loaded by detuned QWRs is first critically coupled. The main advantage of this subwavelength resonator when compared to a usual Helmholtz one is a relatively large aperture enabling easy tuning of the resistivity of the structure. To some extent, it acts similarly as tapered labyrinthine acoustic metamaterials.²⁵ In a second step, a periodic structure whose unit cell consists in several pores of rectangular cross-section also loaded by different detuned QWRs are critically coupled. This pore differs from the length of the side resonators. Perfect absorption can be achieved over a large frequency band for wavelength again much larger than the usual 4 times the depth of the structure limit. Absorption in

^{a)}Electronic mail: Jean-Philippe.Groby@univ-lemans.fr

diffuse field is also investigated. Absorption at higher frequencies is also large in this configuration thanks to the coupling between the higher order resonances of the pores and ITBs of each pore avoiding the bandgap. The effective parameters enabling the description of the structure behavior are derived. It is shown that detuning enables to open the ITB. Slow sound propagation is demonstrated and equations of the speed of sound are derived. The speed of sound possesses a plateau at low frequency and is necessarily dispersive inside the ITB.¹⁹ Finally, experimental validations are performed at normal incidence on samples with curved loading QWRs produced by stereolithography showing good agreement with the calculations.

II. DESCRIPTION OF THE CONFIGURATION

A unit cell of the three-dimensional (3D) scattering problem together with a sketch of a loaded rectangular pore are shown in Figs. 1(a) and 1(b). Before the addition of the loading QWRs, the unit cell is composed of N rectangular cross-section straight pores. The n th pore of section $w_1^{(n)} \times w_2^{(n)}$ and height $L^{(n)}$ is occupied by a material $M^{p(n)}$, whose parameters account for both the viscous and thermal losses at each lateral boundary and are recalled in Appendix A. The total thickness of the structure is $L = \max_{n \in N}(L^{(n)})$. The upper and lower flat and mutually parallel boundaries of the structure, whose x_3 coordinates are L and $L - L^{(n)}$, are designated by Γ_L and $\Gamma_0^{(n)}$, respectively. The thermal (and viscous) losses are neglected on these two boundaries and a Neumann type boundary condition is applied on them, i.e., the normal velocity vanishes on Γ_L and $\Gamma_0^{(n)}$. The corner of the n th tube is located at $x_1 = d_1^{(n)}$ and $x_2 = d_2^{(n)}$, which both refer to the boundary on which a Neumann type boundary condition is applied, i.e., the interface $\Gamma_N^{(n)}$, or to the lower left corner in case of loading on two opposite sides of the pore. The upper semi-infinite material M^a , i.e., the ambient fluid that occupies Ω^a , and $M^{p(n)}$ are in firm contact at the boundaries $\Gamma_{ap}^{(n)}$, $\forall n \in N$, i.e., the pressure and normal velocity are continuous across $\Gamma_{ap}^{(n)}$.

A periodic set of QWRs ($r_n^{(n)}$ in radii and $l_n^{(n)}$ in length tubes) are plugged on the pore lateral sides of inner normal \mathbf{n} , i.e., $\mathbf{n} = \pm 1$ if the tubes are plugged along the positive or

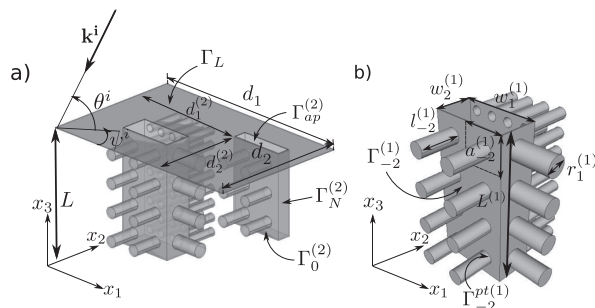


FIG. 1. (a) Example of a $d_1 \times d_2$ -periodic structure, whose unit cell is composed of two rectangular pores and (b) sketch of a loaded rectangular pore by a periodic set of QWRs of circular cross-section.

negative x_1 axis or $\mathbf{n} = \pm 2$ if the tubes are plugged along the positive or negative x_2 axis. These QWRs are arranged with a square lattice of size $a_n^{(n)}$. The material $M_n^{p(n)}$ that occupies each tube $\Omega_n^{p(n)}$ is modeled as a circular tube where both the viscous and thermal losses are accounted for, see Appendix A. This material is in firm contact with $M^{p(n)}$ through $\Gamma_n^{p(n)}$, i.e., the pressure and normal velocity are continuous across $\Gamma_n^{p(n)}$. The thermal losses are neglected at the surfaces ending each tube and a Neumann type boundary condition is applied on these boundaries. The conditions on $\Gamma_n^{p(n)}$ also reduce to an impedance one applied on the whole interface $\Gamma_n^{(n)}$ in the following, because the considered wavelengths are much larger than the dimensions of $\Gamma_n^{p(n)}$ and the periodicity of this arrangement $a_n^{(n)}$. This impedance classically reads as $Z_n^{(n)} = \pm i Z_n^{t(n)} \cotan(k_n^{t(n)} l_n^{t(n)}) / \phi_n^{t(n)}$, wherein $Z_n^{(n)} = \sqrt{\rho_n^{t(n)} K_n^{t(n)}}$ is the impedance of $M_n^{t(n)}$, $k_n^{t(n)}$ is the wavenumber inside the tube, $\phi_n^{t(n)}$ is the ratio between the area of $\Gamma_n^{p(n)}$ over one of the unit cells, i.e., a surface porosity $\phi_n^{t(n)} = \pi (r_n^{t(n)})^2 / (a_n^{(n)})^2$. The sign \pm depends on whether the resonators are plugged on the right/top (+ sign) or left/bottom (- sign) side of the pore. In what follows, only the positive sign will be used and

$$Z_n^{(n)} = i Z_n^{t(n)} \cotan(k_n^{t(n)} l_n^{t(n)}) / \phi_n^{t(n)}. \quad (1)$$

Note that the use of an impedance condition is suitable in the presence of a series of side resonators along the main pore. Therefore, a single pair of side detuned resonators can hardly be modeled through an impedance condition.²⁶

The incident wave propagates in Ω^a and is expressed by $p^i(\mathbf{x}) = A^i e^{i(k_1^i x_1 + i(k_2^i x_2 - k_3^i (x_3 - L)))}$, wherein $k_1^i = -k^a \cos \theta^i \sin \Phi^i$, $k_2^i = k^a \cos \theta^i \cos \Phi^i$, with θ^i the elevation and Φ^i the azimuth, and $A^i = A^i(\omega)$ is the signal spectrum.

In each domain Ω^α ($\alpha = a, p^{(n)}, t^{(n)}$), the pressure field fulfills the Helmholtz equation

$$\nabla \cdot \left(\frac{1}{\rho^\alpha} \nabla p^\alpha \right) + \frac{(k^\alpha)^2}{\rho^\alpha} p^\alpha = 0, \quad (2)$$

with the density ρ^α and the wavenumber $k^\alpha = \omega/c^\alpha$, defined as the ratio between the angular frequency ω and the sound speed $c^\alpha = \sqrt{K^\alpha/\rho^\alpha}$.

As the problem is periodic and the excitation is due to a plane wave, each field (X) satisfies the Floquet-Bloch relation

$$X(\mathbf{x} + \mathbf{d}) = X(\mathbf{x}) e^{i k_i^i d}. \quad (3)$$

Consequently, it suffices to examine the field in the elementary cell of the material to get the fields, via the Floquet relation, in the other cells.

III. SOLUTION OF THE PROBLEM

A. Field representations

Separation of variables, radiation conditions, and Floquet theorem lead to the representations

$$p^a(\mathbf{x}) = \sum_{(q,g) \in \mathbb{Z}^2} [A^i e^{-ik_{3qg}^a(x_3-L)} \delta_{qg} + R_{qg} e^{ik_{3qg}^a(x_3-L)}] e^{ik_{1q}^a x_1 + ik_{2g}^a x_2}, \quad \forall \mathbf{x} \in \Omega^a, \quad (4)$$

wherein δ_{qg} is the Kronecker symbol, $k_{1q}^a = k_1^i + (2q\pi/d_1)$, $k_{2g}^a = k_2^i + (2g\pi/d_2)$, and $k_{3qg}^a = \sqrt{(k^a)^2 - (k_{1q}^a)^2 - (k_{2g}^a)^2}$, with $\text{Re}(k_{3qg}^a) \geq 0$ and $\text{Im}(k_{3qg}^a) \geq 0$. The reflection coefficient of the plane wave denoted by the subscripts q and g is R_{qg} .

According to Refs. 27 and 28, the pressure field $p^{(n)}$ admits the pseudo-modal representation, that already accounts for the boundary conditions on $\Gamma_0^{(n)}$, Γ_N , and $\Gamma_n^{(n)}$,

$$p^{(n)} = \sum_{(m,o) \in \mathbb{N}^2} A_{mo}^{(n)} \Phi_{1m}^{(n)}(x_1 - d_1^{(n)}) \Phi_{2o}^{(n)}(x_2 - d_2^{(n)}) \times \cos(k_{3mo}^{(n)}(x_3 + L^{(n)} - L)), \quad \forall \mathbf{x} \in \Omega^{(n)}, \quad (5)$$

wherein $A_{mo}^{(n)}$ are the coefficients of the pseudo-modal representation, $k_{3mo}^{(n)} = \sqrt{(k^{(n)})^2 - (k_{1m}^{(n)})^2 - (k_{2o}^{(n)})^2}$, with $\text{Re}(k_{3mo}^{(n)}) \geq 0$ and $\text{Im}(k_{3mo}^{(n)}) \geq 0$, and $\Phi_{1m}^{(n)}(x_1)$ and $\Phi_{2o}^{(n)}(x_2)$ are the mode in the x_1 and x_2 directions, respectively. The different modal expansion and mode dispersion relations are presented in Appendix B, depending on either the impedance condition is applied on any, one, or two opposite sides of the pore. For simplicity, we will consider the modal decomposition only in the x_1 direction. The modes $\Phi_{1m}^{(n)}(x_1)$ are either orthogonal or bi-orthogonal and the orthogonality relation reads as $\int_0^{w_1} \Phi_{1m}^{(n)}(x_1) \Phi_{1M}^{(n)}(x_1) dx_1 = \delta_{Mm} w_1^{(n)} N_{1m}^{(n)}$. In particular, the zero-order low frequency approximation $\tilde{k}_{10}^{(n)}$, arising from the condition $k_{10}^{(n)} w_1 \ll 1$, is

$$\tilde{k}_{10}^{(n)} = \frac{1}{w_1^{(n)}} \sqrt{\frac{-i\omega \rho^{p(n)} w_1^{(n)}}{Z_1^{(n)}}}, \quad (6)$$

when an impedance condition is applied on a single side and is

$$\tilde{k}_{10}^{(n)} = \frac{1}{w_1^{(n)}} \sqrt{\frac{-i\omega \rho^{p(n)} w_1^{(n)} (Z_1^{(n)} + Z_{-1}^{(n)} - i\omega \rho^{p(n)} w_1^{(n)})}{Z_1^{(n)} Z_{-1}^{(n)}}}, \quad (7)$$

when impedance conditions are applied on both sides of the pores.

B. The linear system for the solution of R_{qg}

The application of the boundary conditions on each interface $\Gamma_{ap}^{(n)}$ leads to two sets of coupled equations in terms of $A_{mo}^{(n)}$ and R_{qg} .

The combination of these two sets of equations leads to the solution either in terms of R_{qg} or in terms of $A_{mo}^{(n)}$, these two solutions being linked one with each other. In particular, the linear system of equations for the solution for R_{qg} , $\forall (q, g) \in \mathbb{Z}^2$, is

$$R_{qg} - \frac{i\rho^a}{k_{3qg}} \sum_{(Q,G) \in \mathbb{Z}^2} R_{QG} \sum_{n \in \mathbb{N}} \sum_{(m,o) \in \mathbb{Z}^2} \frac{k_{3mo}^{(n)} \phi^{p(n)}}{\rho^{p(n)} N_{1m}^{(n)} N_{2o}^{(n)}} \times \tan(k_{3mo}^{(n)} L^{(n)}) I_{1mq}^{(n)-} I_{2og}^{(n)-} I_{1mq}^{(n)+} I_{2og}^{(n)+} = A^i \delta_{qg} + A^i \sum_{n \in \mathbb{N}} \sum_{(m,o) \in \mathbb{Z}^2} \frac{i\rho^a k_{3mo}^{(n)} \phi^{p(n)}}{k_{3qg}^{(n)} \rho^{p(n)} N_{1m}^{(n)} N_{2o}^{(n)}} \times \tan(k_{3mo}^{(n)} L^{(n)}) I_{1mq}^{(n)-} I_{2og}^{(n)-} I_{1mq}^{(n)+} I_{2og}^{(n)+}, \quad (8)$$

where $\phi^{p(n)} = w_1^{(n)} w_2^{(n)} / d_1 d_2$ is the surface porosity of the n th pore, such that $\cup_{n \in \mathbb{N}} \phi^{p(n)} = \phi^p$ is the global surface porosity of the structure, and $I_{mq}^{(n)\pm}$ depicts the aperture of the pore on the semi-infinite half space through $\Gamma_{ap}^{(n)}$. The expressions of $I_{mq}^{(n)\pm}$ are given in Appendix C.

The system [Eq. (8)] is solved for each (q, g) pair. The absorption coefficient A is then calculated through

$$A = 1 - \sum_{(q,g) \in \mathbb{Z}^2} \frac{\text{Re}(k_{3qg}^a)}{k_{300}^a} \|R_{qg}\|^2. \quad (9)$$

The dimensions of the studied configurations are given in Table I.

IV. ANALYSIS OF THE DISPERSION RELATION IN A PORE

For simplicity, the superscript p refers to the pore, while the exponent t refers to the QWR. In Ref. 17, the dispersion relation [Eq. (B1)] was analyzed showing that the low frequency solution [Eq. (6)] could be used as a first approximation and exhibits a combined effect of a large decrease of the sound speed together with an increase of the attenuation in a slit of width w_1 with the ratio $\phi^t l / w_1$. Following this idea and considering one straight pore of cross section $w_1 \times w_2$ loaded by two sets of identical QWRs, two cases should be analyzed: when the impedances are applied on two adjacent sides of the pore (case 1) and when they are applied on two opposite sides of the pore, for example, along the x_1 axis (case 2). At low frequency ($k^l \ll 1$), the speed of sound in the pore, $c = \omega / \tilde{k}_3^p$, reads as $c = c^p / \sqrt{1 + (Z^p c^p \phi^t l / Z^t c^t) (1/w_1 + 1/w_2)}$ for case 1 and as $c = c^p / \sqrt{1 + (2Z^p c^p \phi^t l / Z^t c^t w_1)}$ for case 2. In this last case, the last term of the numerator of Eq. (7), which traduces the coupling between the two sets of QWRs, vanishes because it is of second order in terms of k^l and therefore does not influence the speed of sound at low frequency. No coupling can be noticed at low frequency. The formulas only differ from the dependence in terms of w_2 . In case 1, both w_1 and w_2 are constrained by the presence of the QWRs, i.e., $w_1 \geq a$ and $w_2 \geq a$, while in case 2 w_1 can be very small, allowing the speed of sound to be very small and increasing the attenuation, $\text{Im}(\tilde{k}_3^p) = \text{Im}(k^p \sqrt{1 + (2Z^p c^p \phi^t l / Z^t c^t w_1)})$. This last case also appears more efficient, and we will also focus on cases where the impedances are applied on opposite sides.

Let us now consider the detuned case when both sets of QWRs only differ from their length, i.e., l_1 and l_{-1} , and in particular, the dimension of configuration C1. Figures 2(a) and 2(b) depict, respectively, the real and imaginary part of k_3^p and the real part of c_3^p . Again, the low frequency solution

TABLE I. Dimension of the considered configurations (mm).

Conf.	L	$d_1 \times d_2$	$w_1^{(n)} \times w_2^{(n)}$	$d_1^{(n)} \times d_2^{(n)}$	l_1, l_{-1}	a	r
C1	30	84×42	1.5×20	$(24.5 \times 11); (58 \times 11)$	$(35, 24); (24, 35)$	5	1.75
C1, Eq. (12)	#	42×42	#	/	35, 24	#	#
C2	28	84×84	3.25×7	$(2.5 \times 7.65); (9.5 \times 13.4)$	$(50, 30); (43, 23)$	7	2.5
			#	(16.5×19.4)	$(35, 19)$	#	#
			#	$(74.5 \times 7.65); (67.5 \times 13.4)$	$(50, 30); (43, 23)$	#	#
			#	(60.5×19.4)	$(35, 19)$	#	#
			#	$(2.5 \times 73.1); (9.5 \times 67.35)$	$(30, 50); (23, 43)$	#	#
			#	(16.5×61.35)	$(19, 35)$	#	#
			#	$(74.5 \times 73.1); (67.5 \times 67.35)$	$(30, 50); (23, 43)$	#	#
			#	(60.5×61.35)	$(19, 35)$	#	#
C2, Eq. (12)	#	(42×42)	#	/	$(50, 30); (43, 23)$	#	#
			#	/	$(35, 19)$	#	#

[Eq. (7)] can be used as a good approximation of $k_{10}^{(n)}$. The slope of $\text{Re}(k_3^p)$ is smaller than the one of $\text{Re}(k^p)$ inside the passband, which again shows a decrease of the sound speed in the pore. At low frequency, the speed of sound reads as $c = c^p / \sqrt{1 + [Z^p c^p \phi^t (l_1 + l_{-1}) / Z^t c^t w_1]}$. This behavior is identical to the one of a configuration comprising a single set of QWR of length $l_{\text{tot}} = l_1 + l_{-1}$. The first advantage of using two sets of resonators instead of a single one is to shift the first bandgap, due to the quarter-wavelength resonance of the tubes, at a higher frequency, because obviously $c / 4l_{\text{tot}} < c / 4l_1$ and $c / 4l_{\text{tot}} < c / 4l_{-1}$. This allows propagation of waves at a small speed over a larger frequency band leading to possible large absorption. The second advantage lies in the detuning allowed by the balance of this total length on both sides of the pore leading to an ITB, Fig. 2(a). The bandgap arises when $\text{Re}(\tilde{k}_{10}) > \text{Re}(k^p)$ at first approximation. Around the resonances of the two sets of resonators $\tan(k^t l_j) \approx -1 / (k^t l_j - \pi/2)$, $j = \pm 1$. The frequencies for which $\text{Re}(\tilde{k}_3^p) = 0$ satisfies the equation $\text{Re}\{k^t + (Z^p c^p \phi^t / Z^t c^t w_1) ([\pi - k^t (l_1 + l_{-1}) - k^t w_1 \phi^t \rho^p / \rho^t] / (k^t l_1 - \pi/2)(k^t l_{-1} - \pi/2))\} = 0$. This equation clearly exhibits the two resonances of the QWRs and a third frequency coupling the resonators. The low frequency bounds of both bandgaps are $f_l^{(1)} \approx 2400$ Hz and $f_l^{(2)} \approx 3500$ Hz and correspond to the QWRs resonance, while the higher frequency bound of the first bandgap is $f_h^{(1)} \approx 2800$ Hz. The higher bound of the second bandgap can be found through the approximation $\tan(k^t l_j) \approx k^t l_j - \pi$, $j = \pm 1$. This clearly shows that the ITB is due to the interaction of the first resonances of both

resonators. In absence of losses, it can be shown that k_{10} goes to infinity at the first resonance, while the higher order modes k_{1n} , $n > 1$ shift down of a value of π/w_1 . Similarly, at the second resonance, k_{11} goes to infinity, while the higher order modes k_{1n} , $n > 2$ again shift down of a value of π/w_1 . When losses are accounted for, and for a small value of $k_{1n} w_1$, these modes do not intersect anymore and a single continuous function \tilde{k}_{10} is found. The speed of sound reads as

$$c = c^p / \sqrt{1 + \frac{Z^p c^p \phi^t}{Z^t c^t w_1} \left(\frac{\pi/k^t - (l_1 + l_{-1}) - w_1 \phi^t \rho^p / \rho^t}{(k^t l_1 - \pi/2)(k^t l_{-1} - \pi/2)} \right)}$$

inside the ITB, where the last term of the numerator traduces the coupling between the two resonators. An important remark is that while the speed of sound possesses a plateau at low frequency, where the velocity is not dispersive, the speed of sound inside the ITB is necessarily dispersive and accounts for the coupling between the detuned resonators.

V. DERIVATION OF THE EFFECTIVE PARAMETERS

Adopting the same type of analysis as in Ref. 17, i.e., assuming the unique propagation of the modes $m=0$ and $o=0$ in the pores, $k_1^{(n)} w_1^{(n)} \ll 1$ and $k_2^{(n)} w_2^{(n)} \ll 1$, and the dominance of the zeroth order terms in I_{0q}^{\pm} ensuring $I_{00}^+ I_{00}^- / N_0 \approx 1$, the system Eq. (8) reduces to the unique calculation of R_{00} , which takes the following form:

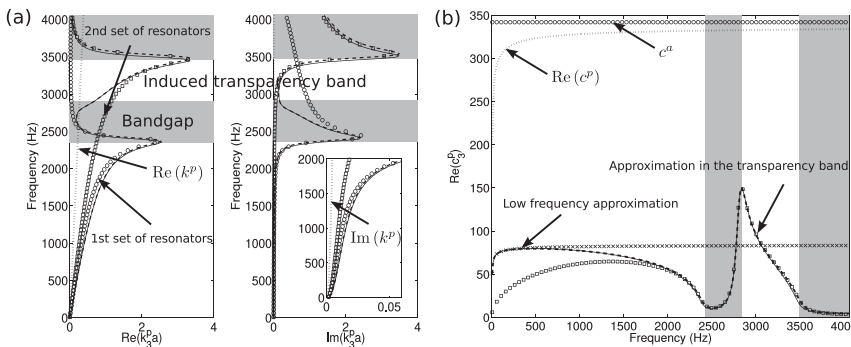


FIG. 2. Configuration 1. (a) Real and imaginary parts of k_3^p (solid line) and \tilde{k}_3^p (dashed line), both real and imaginary parts of k^p (dotted line) and of \tilde{k}_3^p (dashed line) when only the first (o) and the second (□) set of QWRs are present are also plotted. The inset shows a zoom at low frequency of the imaginary part. (b) Real part of c_3^p (solid line) and \tilde{c}_3^p (dashed line) together with its low frequency approximation (x) and its approximation inside the ITB (□). Real part of c^p (dotted line) and c^a (o) are also plotted.

$$R_{00} = A^i \frac{\frac{\sin \theta^i}{Z_0} + \sum_n \frac{i\phi^{p(n)}k_3^{(n)} \tan(k_3^{(n)}L^{(n)})}{\omega\rho^{(n)}}}{\frac{\sin \theta^i}{Z_0} - \sum_n \frac{i\phi^{p(n)}k_3^{(n)} \tan(k_3^{(n)}L^{(n)})}{\omega\rho^{(n)}}}. \quad (10)$$

It is very important to specify that the condition leading to the dominance of the zeroth order terms in I_{0q}^\pm is only attached to the arrangement of the pores in the unit cell. A simple identification with the classical formula of the reflection coefficient of a rigidly backed homogeneous slab leads to a surface admittance of each pore

$$Y_{\text{eff}}^{(n)} = \frac{-i\phi^{p(n)}k_3^{(n)} \tan(k_3^{(n)}L^{(n)})}{\omega\rho^{(n)}}, \quad (11)$$

which does not depend on the angle of incidence. Another identification leads to $Z_{\text{eff}}^{(n)} = \omega\rho^{(n)}/k_3^{(n)}\phi^{p(n)}$ and $k_{\text{eff}}^{(n)} = k_3^{(n)}$ for this locally reacting material,¹ considering each pore independently. Let us also consider only one straight pore per spatial period for simplicity.

Similar to what was done in Ref. 17, the total porosity of the pore $\phi_{\text{tot}} = \phi^p(1 + \phi'(l_1 + l_{-1})/w_1)$ should be introduced for these quantities to be consistent and in

$$\rho_{\text{eff}} = \left(1 + \frac{\phi'(l_1 + l_{-1})}{w_1}\right) \frac{\rho^{(1)}}{\phi_{\text{tot}}}, \quad K_{\text{eff}} = \frac{K^p \left(1 + \frac{\phi'(l_1 + l_{-1})}{w_1}\right)}{\phi_{\text{tot}} \left(1 + \frac{Z^p \phi'}{w_1 Z^p k^p} \left(\tan(k'l_1) + \tan(k'l_{-1}) - \frac{\rho^p w_1 k^t \phi'}{\rho^t} \tan(k'l_1) \tan(k'l_{-1})\right)\right)}. \quad (12)$$

At low frequency, when $k'l_1 \ll 1$ and $k'l_{-1} \ll 1$, the effective bulk modulus reduces to $K_{\text{eff}} = K^p[1 + (\phi'(l_1 + l_{-1})/w_1)]/\phi_{\text{tot}}[1 + (K^p \phi'(l_1 + l_{-1})/w_1 K^t)]$. Particularly noticeable is the comparison with the first order homogenization theory.²⁹⁻³¹ Classically, the homogenized bulk modulus K_{hom} and density ρ_{hom} are

$$\begin{aligned} \frac{1}{\rho_{\text{hom}}} &= \frac{\phi_{\text{tot}}}{\rho} = \frac{\phi^p}{\rho^{(1)}}, \\ \frac{1}{K_{\text{hom}}} &= \frac{\phi_{\text{tot}}}{K} = \frac{\phi^p}{K^p} + \frac{\phi^p(l_1 + l_{-1})w_2}{K^t d_1 d_2} \\ &= \frac{\phi^p}{K^p} \left(1 + \frac{\phi^t K^p(l_1 + l_{-1})}{K^t w_1}\right), \end{aligned} \quad (13)$$

which fit the low frequency approximation of Eq. (12).

Figure 3 depicts the real [Fig 3(a)] and imaginary [Fig. 3(b)] part of both effective parameters normalized by ϕ_{tot}/P_0 for the bulk modulus and by ϕ_{tot}/ρ^a for the density. The bulk modulus is lower than in absence of the resonators while a large tortuosity-like effect is exhibited for the effective density. This tortuosity-like effect is responsible for the

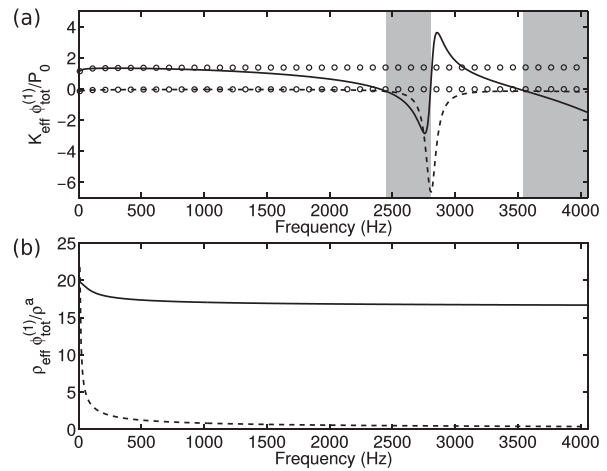


FIG. 3. Configuration 1. (a) Real (solid line) and imaginary (dashed line) of $K_{\text{eff}}\phi_{\text{tot}}/P_0$ and (b) real (solid line) and imaginary (dashed line) of $\rho_{\text{eff}}\phi_{\text{tot}}/\rho^a$. The low frequency approximation, which fit the classical homogenization theory, of $K_{\text{eff}}\phi_{\text{tot}}/P_0$ also plotted (o).

particular, for $\lim_{\omega \rightarrow 0} \phi_{\text{tot}} K_{\text{eff}} = P_0$. The effective density and bulk modulus, where the approximation [Eq. (7)] is made, reads as

low speed of sound encountered at the low frequency. It is closer to the concept of static tortuosity introduced in the Pride-Lafarge model¹ than the usual tortuosity which refers to high frequency behavior of regular porous materials. The expressions of the effective bulk modulus and density are valid below the first bandgap for the whole material, because of the arrangement of the pores and dispersion of \tilde{k}_{10} close to the bandgap as explained in Ref. 17, while still valid for what happens in the pore. In the latter, the effective bulk modulus is negative inside the bandgaps as noticed by several authors since the seminal publication.³² The classical homogenization result for $K_{\text{hom}}\phi_{\text{tot}}/P_0$ is also plotted and fits well the result below 750 Hz, i.e., far below the first bandgap.

Effective parameters of configurations involving several pores can be derived in a similar way, i.e., deriving the effective properties for each pore. Noticeable is the fact that the classical homogenization theory is not necessarily suitable; the scale separation between the pores being not always satisfied in the general case. Effectively, let us consider a unit cell composed of N pores loaded by QWRs oriented along the x_1 axis only differing from their length $l_1^{(n)}$ and $l_{-1}^{(n)}$. The homogenized density and bulk modulus are in this case

$$\begin{aligned} \frac{1}{\rho_{\text{hom}}} &= \frac{\phi_{\text{tot}}}{\rho} = \sum_{n=1}^N \frac{N\phi^{(n)}}{\rho^{(n)}} = \frac{N\phi^{(1)}}{\rho^{(1)}}, \\ \frac{1}{K_{\text{hom}}} &= \frac{\phi_{\text{tot}}}{K} = \sum_{n=1}^N \frac{\phi^{(n)}}{K^p} + \frac{\phi^{(n)}(l_1^n + l_{-1}^n)w_2}{K^t d_1 d_2} \\ &= N \frac{\phi^{(1)}}{K^p} \left(1 + \frac{\phi^t K^p}{K^t w_1} \sum_{n=1}^N \frac{(l_1^{(n)} + l_{-1}^{(n)})}{N} \right), \end{aligned} \quad (14)$$

which are the parameters of N identical pores loaded by the mean value of the resonators lengths $\sum_{n=1}^N (l_1^{(n)} + l_{-1}^{(n)})/N = \text{mean}(l_1^{(n)} + l_{-1}^{(n)})$. This can only lead to one absorption peak around the quarter-wavelength resonance of the pores which is different from what is expected, for example, in Sec. VI A. In other words, this representation is suitable only when all $\tan(k_3^{(n)}L^{(n)})$ are of the same order.

Noticeable is also the fact that more refine homogenization procedures such as the multi-scale asymptotic method⁹ or non-local theory³³ can be used to account for the resonant features of the present problem in the effective parameters.

VI. RESULTS AND DISCUSSION

A. One pore per spatial period and critical coupling analysis

We first focus on the absorption at normal incidence and low frequency, using the previously derived effective

parameters ρ_{eff} and K_{eff} , Eq. (12), for configuration 1. We note that these effective parameters derived for configuration 1 are those of half of the unit cell, because these parameters do not depend on the pore location and QWR orientations. The critical coupling analysis is performed by use of these parameters and not for the whole calculation because it avoids any problem related to the choice of the correct Riemann sheet. Effectively, the choice of the higher order mode in complex frequency analysis is usually not detailed in the literature. The acoustic response of the configuration can be analyzed as the coupling of resonators. The reflection coefficient takes the classical form $R_{00} = [iZ_{\text{eff}}\cotan(k_{\text{eff}}L) - Z_0] / [iZ_{\text{eff}}\cotan(k_{\text{eff}}L) + Z_0]$. In Ref. 34, the authors performed an analysis of $|R_{00}|^2$ in the complex frequency plan $\Omega = \omega + i\Omega_i$. Figure 4(a) depicts $\log |R_{00}|^2$ for configuration 1 showing that the viscous and thermal losses exactly compensate the radiation losses. In absence of losses, the first zero and pole of $|R_{00}|^2$ are symmetric with respect to the real frequency axis, zero in the upper half space and pole in the lower half space. The leakage does not exactly correspond to $Q_{\text{leak}} = \text{Im}(\Omega_p)/2\text{Re}(\Omega_p)$ where Ω_p is the complex frequency of the pole in the absence of dissipation, because Q_{leak}^{-1} is not small compared to 1 in this case. The introduction of losses induces a complex frequency map deformation. The first zero and pole become symmetric with respect to $\text{Im}(Z_{\text{eff}}\cotan(k_{\text{eff}}L)) = 0$, and therefore the former can be exactly located on the real frequency axis leading to a perfect absorption, Fig. 4(c). The

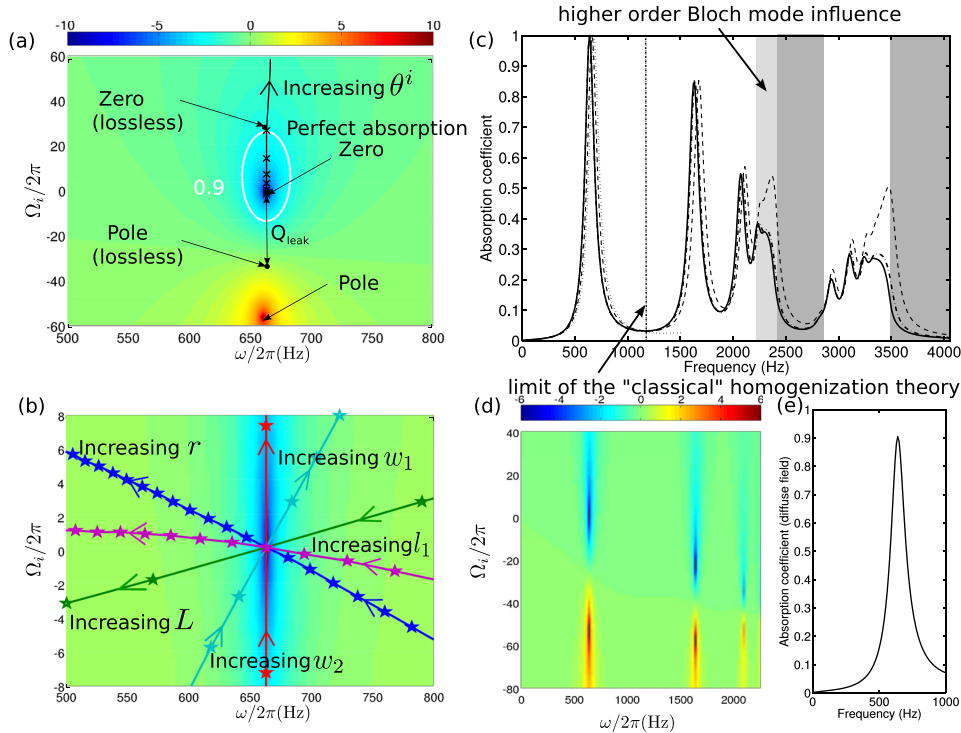


FIG. 4. (Color online) Configuration 1. (a) Map of $\log(|R_0|^2)$ in a function of Ω , the white line depicts the isovalue of an absorption coefficient of 0.9. The evolution of the zero position in function of θ^i is also plotted. (b) Zoom of the $\log(|R_0|^2)$ around the perfect absorption point and evolution of the zero position in function of r , w_1 , w_2 , l_1 , and L : the stars show the exact location in the parametric analysis. (c) Absorption coefficient calculated with the present method (solid line), calculated with the effective parameters derived in Sec. V without (dashed line) and with (dashed-dotted line) length correction, and calculated with the low frequency approximation of the effective parameters derived in Sec. V, i.e., with the classical homogenization theory (dotted line). (d) Map of $\log(|R_0|^2)$ in function of Ω when length correction is accounted for, and (e) diffuse field absorption coefficient calculated with length correction.

reflection coefficient vanishes for $f=663$ Hz. The perfect absorption obtained for this configuration is due to an impedance matching, so to interference phenomena and not to a mode excitation.

The main interest of this representation yields in the parametric analysis. The upper half space is forbidden because it corresponds to exponentially growing terms with increasing t . This is particularly true when the pole is located in this half space. Here we are interested in the effect of the localization of the zero in the complex frequency map on the reflection coefficient along the real axis. Figure 4(b) shows the evolution of the location of zero in the complex frequency map when the different dimensions of the structure vary: r varies in [1.4 mm, 2.35 mm] with a step of 0.05 mm, w_1 varies in [1.3 mm, 1.7 mm] with a step of 0.1 mm, w_2 varies in [1.5 cm, 2.5 cm] with a step of 5 mm, l_1 varies in [2 cm, 7 cm] with a step of 5 mm, and L varies in [2.5 cm, 4 cm] with a step of 5 mm. Some of these steps are constrained by a and obviously a variation of r induces a variation of ϕ^f . This parametric study is quite important despite the fact that some of the results are obvious, because it enables to determine which parameter to tune to locate the zero of $|R_{00}|^2$ on the real frequency axis allowing a perfect absorption condition. Of particular interest is the influence of w_2 which greatly influences the position of zero thanks to a modification of ϕ^p . Similarly, a modification of l_1 (L_{-1} leads to identical results) mainly influences the zero position along the real frequency, but poorly along the imaginary frequency. The zeros corresponding to the higher order resonances of the pore are located below the real frequency axis [Fig. 4(d)], and therefore cannot lead to perfect absorption, but to peaks of large absorption.

Figure 4(c) depicts the absorption coefficient at normal incidence calculated with the effective parameters, Eq. (12), and calculated with the whole procedure, Eq. (8). The absorption is perfect for the effective parameter calculation at 663 Hz and very close to unity for the full calculation at 645 Hz. This is due to the radiation by the pore, which would require a length correction l_{corr} in the effective parameters derivation. This correction length can be evaluated numerically by reconstructing an equivalent impedance \tilde{Z} from the reflection coefficient of the zeroth order Bloch mode (unique propagating mode over the frequency band considered) calculated with the whole model through

$$\tilde{Z} - iZ_{\text{eff}}\cotan(k_{\text{eff}}L) = -i\omega \frac{\rho_0}{\phi^p} l_{\text{corr}}. \quad (15)$$

It is therefore obviously frequency dependent and complex, but we considered the mean value of its real part at low frequency leading to $l_{\text{corr}} = 1.2$ mm. This value corresponds neither to the one of a rectangular orifice in baffle nor to the one of a grid of slits.³⁵ Accounting for this correction length let both calculations matched over the frequency band be considered. The absorption is nearly total for the whole calculation. The classical homogenization theory provides satisfying results below 1200 Hz, which is higher than the one encountered for in Sec. V, but still lower than the first bandgap. Despite the fact that the homogenized parameters

are different from the effective ones as calculated in the present paper, they are still close to them until 1200 Hz. The structure exhibits a full absorption coefficient for wavelength in the air ≈ 17.7 times its thickness. Before the bandgap, the efficiency of the calculation performed with the effective parameters, without correction length, decreases because of the large influence of the higher order Bloch modes enabled by the dispersion of the modes inside the pores. This is usually accounted for through Drude layers,^{36,37} but we show here that a correctly chosen correction length leads to similar results. This implicitly means that in the present case, the Drude layers would only account for an added mass at the entrance of the main pores. The absorption inside the ITB reaches 0.3.

The evolution of the location of the first zero in the complex frequency plan in function of the angle of incidence θ^i is plotted [Fig. 4(a)]. The cross depicts the location of the zero for $\theta^i = [90^\circ, 80^\circ, 70^\circ, 60^\circ, 50^\circ, 40^\circ, 30^\circ, 20^\circ]$. The evolution of the position of the zero is almost vertical. The resonance frequency of the pore, i.e., a QWR, does not depend on the angle of incidence. A small shift at high frequency is noticed for near grazing incidence, which is due to the curvature of the complex frequency plan. The isovalue corresponding to an absorption of 0.9 is an ellipse with the semi-major axis along the imaginary frequency. While this implies that the absorption peak is relatively narrow in frequency, Fig. 4(c), it also implies that the absorption is relatively stable when the position of the zeros is shifted along the imaginary frequency, i.e., when θ^i decreases for example. In practice, the absorption peak is larger than 0.9 for $\theta^i > 30^\circ$, but rapidly decreases for smaller θ^i . This means that this configuration is relatively efficient for diffuse field excitation. The diffuse field absorption as calculated through $\int_0^{\pi/2} (1 - \|R_{00}(\theta)\|^2) \cos \theta \sin \theta d\theta / \int_0^{\pi/2} \cos \theta \sin \theta d\theta$,¹ is depicted in Fig. 4(e), showing an absorption in diffuse field higher than 0.9 at 643 Hz. Note that the first Wood anomaly arises around 2000 Hz at grazing incidence and so does not contribute around the first absorption peak. We will now focus on the normal incidence.

B. Various pores per spatial period and critical coupling analysis

Different coupling between the pores exists: either leading to a single peak whose frequency width is broadened when the resonance frequencies are close enough, or leading to N peaks which can overlap. The first solution enables a perfect absorption from the coupling between pores which does not lead to perfect absorption independently. This particularly enables to consider the coupling of pores of small porosity $\phi^{p(n)}$, due to a very small width enabling low frequency absorption. Nevertheless, the large absorption frequency band is still narrow in this case, but the parameters resulting from the classical homogenization theory, Eq. (14), can be used. The second possibility widens the large absorption frequency band with N perfect absorption peaks. Another design strategy could consist in tuning the different pore contributions for the absorption to be large or perfect at various angles of incidence. Effectively, Eq. (16) clearly

exhibits a dependence on the angle of incidences. While the absorption peak frequency due to the resonance of each pore is not dependent from the angle of incidence, its amplitude is. Designing the pores for one to take over another one at various angles of incidence is doable. We follow the second possibility, focusing on the normal incidence.

Based on the conclusion of Sec. VI A, a unit cell with three pores has been designed using effective parameters in order to broaden the large absorption band by varying the lengths of the loading QWRs. The effective parameters derived for configuration 2 are those of a quarter of the unit cell, see Table I. The reflection coefficient takes the form of Eq. (10). If the resonance frequencies of the pores are close, it suggests to let the numerator of $|R_{00}|^2$ vanish, which will result in the critical coupling condition to be satisfied. In other words it suggests to minimize the following quantity over a specific frequency band:

$$\left| \frac{\sin \theta^i}{Z_0} - \sum_n \frac{i\phi^{(n)} k_3^{(n)} \left(k_3^{(n)} L^{(n)} - \frac{\pi}{2} \right)}{\omega \rho^{(n)}} \right|^2. \quad (16)$$

Doing so at low frequency leads to an optimal configuration exhibiting perfect absorption peaks with identical length resonators loading each pore. Effectively, the main differences of loading a pore with different length resonators happen at a higher frequency, Sec. IV, around the bandgaps and in the ITB, which is absent in the case of identical QWRs. We also adopted a similar technique as for Sec. VI A. The correction length of each pore has been determined independently through the formula used in Sec. VI A. These correction lengths are almost identical, therefore we used $l_{\text{corr}} = 1.9$ mm for each pore.

Figure 5(a) depicts $\log(|R_{00}|^2)$ in the complex frequency plan for configuration C2. The three zeros of $|R_0|^2$ are almost aligned on the real frequency axis, proving critical coupling for different frequencies. This time the deformation of the complex frequency map is performed through the equation $\sum_n \text{Im}(Z_{\text{eff}}^{(n)} \tan(k_{\text{eff}}^{(n)} L)) = 0$. A similar

parametric analysis was performed, showing the interdependence of each parameter, i.e., the coupling between the pores. For clarity of the presentation, this parametric study is not depicted here, the conclusion being more difficult to draw. The absorption coefficient of configuration C2 is depicted in Fig. 5(b). Again the perfect absorption peaks for the whole calculation are encountered for frequencies which are lower than those obtained with calculations run with the equivalent parameters without correction lengths accounted for. Of particular interest is that the absorption coefficient is larger than 0.7 for frequency in [760 Hz; 990 Hz] and perfect for 790, 870, and 960 Hz. The first perfect absorption frequency corresponds to a wavelength in the air 15 times larger than the sample thickness, while the third perfect absorption frequency corresponds to a wavelength in the air 13 times larger than the structure thickness. This time the absorption is larger than 0.9 for angle of incidence $\theta^i > 20^\circ$, but the three peaks collapse into two for $\theta^i < 40^\circ$ because of the coupling which is performed through interferences.

The frequency band over which the absorption is larger than 0.7 for configuration 1 is [609 Hz; 680 Hz]. Defining an indicator as being $q = \Delta f / f_{\text{mean}}$, where Δf is the frequency range and f_{mean} is the central frequency of this frequency range, we find $q = 0.1$ for configuration 1 and $q = 0.2$ for configuration 2, which means that configuration 2 provides, on average, twice more absorption than the first one using this criteria. Another particular interest of this configuration is that no bandgap is noticed anymore at high frequency. This is due to the interference of the higher resonances of the pores and of the waves within in the ITB.

VII. EXPERIMENTAL VALIDATION

Two epoxy resin (Accura 60) samples $4.2 \text{ cm} \times 4.2 \text{ cm} \times 4.2 \text{ cm}$ were produced by stereolithography. The loading resonators were curved in order for them to fit in the unit cell. It is important to note that the total length for configuration 1 for example, $l_1 + w_1 + L_{-1} = 6.05$ cm is larger than the diagonal of the elementary cell $42 \times \sqrt{2} \approx 5.94$ cm. It is even worse for configuration 2 where the maximum length reaches $l_1 + w_1 + L_{-1} = 8.325$ cm.

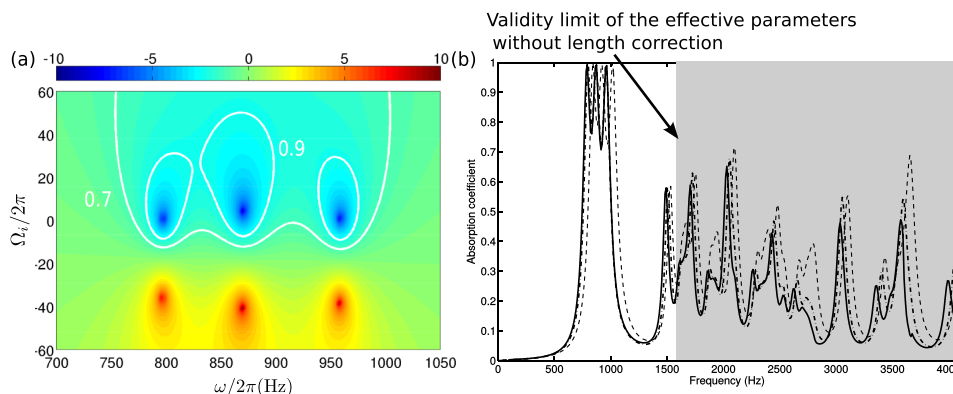


FIG. 5. (Color online) Configuration 2. (a) Map of $\log(|R_{00}|^2)$ in function of Ω (the two white curves depict the absorption contours for, respectively, 0.7 and 0.9) and (b) absorption coefficient calculated with the present method (solid line) and calculated with the effective parameters derived in Sec. V without (dashed line) and with (dashed-dotted line) correction length.

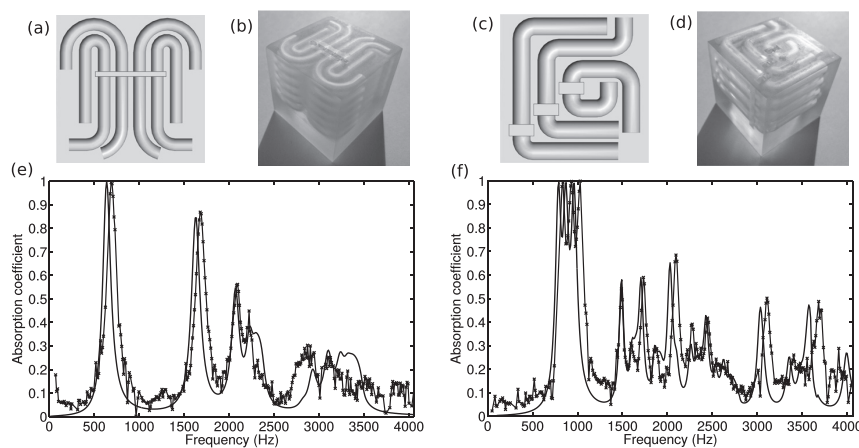


FIG. 6. Frontal section along the resonator diameter cut plane of samples 1 (a) and 2 (c), pictures of samples 1 (b) and 2 (d), and absorption coefficient measured (solid line with crosses) and simulated with the full model (solid line) of samples 1 (e) and 2 (f).

In Ref. 38, simple quarter-wavelength (and Helmholtz) resonators were already produced in a spiral showing correct agreement with the calculations. Figures 6(a) and 6(c) depict a frontal section along the QWR diameter cut plane of sample 1 and 2. This pattern is repeated 6 times for samples 1 and 4 times for sample 2 along the x_3 axis leading to a 3 cm thick pore sample 1 and a 2.8 cm thick pore sample 2. The bottom of the pore is also included in both samples.

The absorption coefficient of the samples is measured in an impedance tube with a square cross section $4.2\text{ cm} \times 4.2\text{ cm}$. The tube cutoff frequency is 4200 Hz. By assuming that plane waves propagate below the cutoff frequency, the infinitely rigid boundary conditions of the tube act like perfect mirrors and create a periodicity pattern in the x_1 and x_2 directions. Samples 1 and 2 are placed in the end of the tube against a copper plug that closes the tube and acts as a rigid boundary, therefore creating a periodicity along the x_1 and x_2 directions of, respectively, 8.4 and 4.2 cm for sample 1 and of, respectively, 8.4 and 8.4 cm for sample 2. This technique was previously used in various articles^{8,17,39} and allows to determine experimentally the absorption coefficient at normal incidence of a quasi-infinite two-dimensional or 3D periodic structure just with half or a quarter of the unit cell.

Figures 6(e) and 6(f) depict the experimental absorption coefficients of samples 1 and 2 and the calculated ones. The discrepancies, in particular, the shift at high frequency of the absorption peaks between the experiments and the calculation, are due to imperfections in manufacturing. Effectively, stereolithography consists in solidifying the liquid resin thanks to a laser. The remaining liquid resin is then removed by use of a solvent. Because of the complicated shape of the samples it was found almost impossible to remove the remaining resin from the bottom loading QWRs resulting in discrepancies in the QWR lengths, which are randomly distributed. In particular, some resonators in the bottom of the sample, where it is the most difficult to remove the resin, are obstructed at half of their lengths. This increases the speed of the waves traveling in the pore leading to a shift of the perfect absorption peak at higher frequencies. Another discrepancy arises from the location of the bandgap and ITB, which are both shifted at low

frequency. This suggests that the longest loading QWRs are longer than they should be. Their lengths were determined by equaling the neutral fiber of the curved resonators with the expected length. This result suggests that the correct way of designing them is not to consider the neutral fiber length but the longest curve of the resonators. Moreover, even if the curved resonators were drawn taking care of the curvatures, some of them exhibit very large ones, almost $\pi/2$. Nevertheless, the experimental curves are in good agreement with the calculations, particularly exhibiting broadband perfect absorption and large absorption in the transparency band for wavelength impinging the structure much larger than 4 times its thickness.

VIII. CONCLUSION

The acoustic properties of a sound absorbing structure consisting in a periodic arrangement of rectangular cross-section pores loaded by detuned QWRs are analyzed. In case of only one pore spatial period, the loading by two sets of QWRs on the opposite lateral faces was found preferable because it enables us (1) to consider smaller section dimension of the pore lowering very efficiently the speed of sound, (2) to shift the first bandgap, in which no absorption can be achieved, to the higher frequency when compared to a configuration with only one set of QWRs, and (3) to reduce the frequency width of the first bandgap by opening an ITB arising from the coupling of the two sets of QWRs. It was shown that the speed of sound possesses a plateau at low frequency whose value is much smaller than the speed of sound in the air. The speed of sound inside the ITB is also much smaller than the speed of sound in the air but is necessarily dispersive. It was shown that these pores are critically coupled to the incoming wave leading to perfect absorption for a wavelength in the air 17 times larger than the structure thickness. The complex frequency analysis, enabling the determination of the critical coupling condition, showed that while the large absorption frequency band is relatively narrow, its amplitude is stable for various angles of incidence, with an absorption peak larger than

0.9 for the angle of incidence in the range of [90°; 30°]. This offers interesting properties to explore in diffuse field perfect absorbers. The case of a unit cell consisting in three pores differing in terms of the lengths of the loading QWRs was then analyzed. The different types of coupling were discussed and the critical coupling condition was found to be more difficult to realize a broadband perfect absorption. Still, the configuration exhibits a broadband large absorption, with 3 perfect absorption peaks, for wavelength in the air 13 to 15 times the thickness of the structure. The pertinence of this structure to maintain a large absorption over the same frequency band was analyzed for various angles of incidence. Absorption at higher frequency can be large due to interferences of higher order quarter-wavelength resonances and waves arising from the ITB. These two configurations were then validated experimentally. The two samples were manufactured by stereolithography. The loading resonators were curved in order to fit in the unit cell. It was shown that the experimental data agreed with the model and exhibited perfect absorption for wavelength 17 times larger than the thickness of the first structure and between 13 to 15 times larger than the thickness of the second structure. Stereolithography was not necessarily

the most adequate rapid manufacturing technique to manufacture such material because (1) it is difficult to remove entirely the photosensitive liquid resin from the bottom loading resonators and (2) the correct length of the corresponding straight resonators is probably larger than the length of the neutral axis. These results offer quite interesting perspectives in terms of the design of perfect, broadband, and incident angular independent more complex sound absorbing structures, involving resonators of different natures.

ACKNOWLEDGMENTS

This work was partly supported by the ANR Project METAUDIBLE No. ANR-13-BS09-0003 co-funded by ANR and FRAE. The authors would like to thank V. Romero-Garcia for useful discussions on this work.

APPENDIX A: MATERIAL PARAMETERS IN STRAIGHT RECTANGULAR AND STRAIGHT CIRCULAR TUBES

When only plane wave propagates in a rectangular tube of section $w_1 \times w_2$, the equivalent complex and frequency dependent bulk modulus and density are⁴⁰

$$K^p = \frac{\gamma P_0}{\gamma + \frac{4i\text{Pr}\rho^a\omega(\gamma-1)}{\eta(w_1/2)^2(w_2/2)^2} \sum_{k \in \mathbb{N}} \sum_{m \in \mathbb{N}} \left(\alpha_k^2 \beta_m^2 (\alpha_k^2 + \beta_m^2) - \frac{i\text{Pr}\omega\rho^a}{\eta} \right)^{-1}}, \quad \rho^p = \frac{-\eta(w_1/2)^2(w_2/2)^2}{4i\omega \sum_{k \in \mathbb{N}} \sum_{m \in \mathbb{N}} \left(\alpha_k^2 \beta_m^2 (\alpha_k^2 + \beta_m^2) - \frac{i\omega\rho^a}{\eta} \right)^{-1}}, \quad (\text{A1})$$

wherein γ is the specific heat ratio, P_0 is the atmospheric pressure, Pr is the Prandtl number, η is the dynamic viscosity, and ρ^a is the air density, and $\alpha_k = 2(k+1/2)\pi/w_1$ and $\beta_m = 2(m+1/2)\pi/w_2$.

When only a plane wave propagates in a circular tube of radius r , the equivalent complex and frequency dependent bulk modulus and density are

$$K^t = \frac{\gamma P_0}{1 + 2(\gamma-1)/\sqrt{i\rho^a\text{Pr}\omega/\eta} J_1(r\sqrt{i\rho^a\text{Pr}\omega/\eta})/r J_0(r\sqrt{i\rho^a\text{Pr}\omega/\eta})}, \quad \rho^t = \frac{\rho^a}{1 - 2/\sqrt{i\rho^a\omega/\eta} J_1(r\sqrt{i\rho^a\omega/\eta})/r J_0(r\sqrt{i\rho^a\omega/\eta})}, \quad (\text{A2})$$

wherein J_n is the Bessel function of n th order.

APPENDIX B: MODAL REPRESENTATION IN A PORE AND DISPERSION RELATIONS

When both opposite surfaces of the pore are rigid, $\Phi_{1m}^{(n)}(x_1) = \cos(k_{1m}^{(n)}x_1)$ and $k_{1m}^{(n)} = m\pi/w_1^{(n)}$. These modes are said orthogonal and the orthogonality relation classically reads as $\int_0^{w_1} \Phi_{1m}^{(n)}(x_1)\Phi_{1M}^{(n)}(x_1)dx_1 = \delta_{Mm}w_1^{(n)}/\epsilon_m$, with $\epsilon_0 = 1$ and $\epsilon_m = 2$ for $m > 1$.

When one surface is rigid and on the other an impedance condition is applied, $\Phi_{1m}^{(n)}(x_1) = \cos(k_{1m}^{(n)}x_1)$ and $k_{1m}^{(n)}$ stratifies the dispersion relation

$$k_{1m}^{(n)} \tan(k_{1m}^{(n)}w_1^{(n)}) = \frac{-i\omega\rho^{p(n)}}{Z_1^{(n)}}. \quad (\text{B1})$$

This last equation is solved by use of a Muller's algorithm initiated with the low frequency approximations, $k_{1m}^{(n)}w_1^{(n)} \ll 1$.¹⁷ These modes are said to be bi-orthogonal and the bi-orthogonality relation reads as²⁷

$$\int_0^{w_1} \Phi_{1m}^{(n)}(x_1)\Phi_{1M}^{(n)}(x_1)dx_1 = \frac{\delta_{Mm}w_1^{(n)}}{2} \left(1 + \text{sinc}(2k_{1m}^{(n)}w_1) \right) = \delta_{Mm}w_1^{(n)}N_{1m}^{(n)}. \quad (\text{B2})$$

Finally, when impedance conditions are applied on both surfaces, $\Phi_{1m}^{(n)}(x_1) = \sin(k_{1m}^{(n)}x_1) + ik_{1m}^{(n)}Z_{-1}^{(n)}\cos(k_{1m}^{(n)}x_1)/\omega\rho^{p(n)}$ and $k_{1m}^{(n)}$ satisfies the dispersion relation

$$\tan\left(k_{1m}^{(n)}w_1^{(n)}\right)\left(\frac{(\omega\rho^{(n)})^2}{Z_{-1}^{(n)}Z_1^{(n)}} + \left(k_{1m}^{(n)}\right)^2\right) + ik_{1m}^{(n)}\left(\frac{1}{Z_1^{(n)}} + \frac{1}{Z_{-1}^{(n)}}\right)\omega\rho^{(n)} = 0. \quad (\text{B3})$$

This last equation is also solved by use of a Muller's algorithm initiated with the low frequency approximations. These modes are again bi-orthogonal and the bi-orthogonality relation reads as²⁸

$$\int_0^{w_1} \Phi_{1m}^{(n)}(x_1)\Phi_{1M}^{(n)}(x_1)dx_1 = \delta_{Mm}w_1^{(n)}\left(\frac{1}{2}\left(1 - \text{sinc}\left(2k_{1m}^{(n)}w_1^{(n)}\right)\right) - \frac{1}{2}\left(\frac{k_{1m}^{(n)}Z_{-1}^{(n)}}{\omega\rho^{(n)}}\right)^2\right) \times \left(1 + \text{sinc}\left(2k_{1m}^{(n)}w_1^{(n)}\right)\right) + \frac{iZ_{-1}^{(n)}}{w_1^{(n)}\omega\rho^{(n)}} \times \left(\text{sinc}\left(k_{1m}^{(n)}w_1^{(n)}\right)\right)^2 = \delta_{Mm}w_1^{(n)}N_{1m}^{(n)}. \quad (\text{B4})$$

APPENDIX C: EXPRESSION OF $I_{mq}^{(n)\pm}$

The terms $I_{mq}^{(n)\pm}$ account for the aperture of the pore and are given by

$$I_{mq}^{(n)\pm} = \frac{e^{\pm ik_{1q}(d^{(n)}+(w/2))}}{2} \left[e^{ik_{1m}(w/2)} \text{sinc}\left((k_{1m} \pm k_{1q})\frac{w}{2}\right) + e^{-ik_{1m}(w/2)} \text{sinc}\left((k_{1m} \mp k_{1q})\frac{w}{2}\right) \right], \quad (\text{C1})$$

when one impedance condition is applied on the right/top surface of the n th pore and

$$I_{mq}^{(n)\pm} = \frac{e^{\pm ik_{1q}(d^{(n)}-(w/2))}}{2} \left[e^{-ik_{1m}(w/2)} \text{sinc}\left((k_{1m} \pm k_{1q})\frac{w}{2}\right) + e^{ik_{1m}(w/2)} \text{sinc}\left((k_{1m} \mp k_{1q})\frac{w}{2}\right) \right], \quad (\text{C2})$$

when one impedance condition is applied on the left/bottom surface of the n th pore and

$$I_{mq}^{(n)\pm} = \frac{e^{\pm ik_{1q}(d^{(n)}+(w/2))}}{2} \left[e^{ik_{1m}(w/2)} \text{sinc}\left((k_{1m} \pm k_{1q})\frac{w}{2}\right) \times \left(\frac{ik_m Z_{-1}^{(n)}}{\omega\rho^{(n)}} - i\right) + e^{-ik_{1m}(w/2)} \times \text{sinc}\left((k_{1m} \mp k_{1q})\frac{w}{2}\right) \left(\frac{ik_m Z_{-1}^{(n)}}{\omega\rho^{(n)}} + i\right) \right], \quad (\text{C3})$$

when an impedance condition is applied on two opposite surfaces.

¹J.-F. Allard and N. Atalla, *Propagation of Sound in Porous Media*, 2nd ed. (John Wiley & Sons, Ltd., Chichester, UK, 2009), pp. 1–351.

²L. De Ryck, Z. Fellah, J.-P. Groby, P. Leclaire, W. Lauriks, A. Wirgin, and C. Depollier, "Acoustic wave propagation and internal fields in macroscopically-inhomogeneous rigid frame porous materials," *J. Appl. Phys.* **102**, 024910 (2007).

³D.-Y. Maa, "Potential of microperforated panel absorber," *J. Acoust. Soc. Am.* **104**, 2861–2866 (1998).

⁴D.-Y. Maa, "Practical single MPP absorber," *Int. J. Acoust. Vib.* **12**, 3–6 (2007).

⁵T. Cox and P. D'Antonio, *Acoustic Absorbers and Diffusers: Theory, Design and Application*, 2nd ed. (Taylor & Francis, Abingdon, UK, 2009), pp. 1–438.

⁶X. Olny and C. Boutin, "Acoustic wave propagation in double porosity media," *J. Acoust. Soc. Am.* **114**, 73–84 (2003).

⁷J. Groby, A. Duclos, O. Dazel, L. Boeackx, and W. Lauriks, "Absorption of a rigid frame porous layer with periodic circular inclusions backed by a periodic grating," *J. Acoust. Soc. Am.* **129**, 3035–3046 (2011).

⁸C. Lagarrigue, J.-P. Groby, V. Tournat, O. Dazel, and O. Umnova, "Absorption of sound by porous layers with embedded periodic array of resonant inclusions," *J. Acoust. Soc. Am.* **134**, 4670–4680 (2013).

⁹C. Boutin, "Acoustics of porous media with inner resonators," *J. Acoust. Soc. Am.* **134**, 4717–4729 (2013).

¹⁰J. Groby, B. Nennig, C. Lagarrigue, B. Brouard, O. Dazel, and V. Tournat, "Enhancing the absorption properties of acoustic porous plates by periodically embedding Helmholtz resonators," *J. Acoust. Soc. Am.* **137**, 273–280 (2015).

¹¹T. Dupont, P. Leclaire, O. Sicot, X. Gong, and R. Panneton, "Acoustic properties of air-saturated porous materials containing dead-end porosity," *J. Appl. Phys.* **110**, 094903 (2011).

¹²P. Leclaire, O. Umnova, T. Dupont, and R. Panneton, "Acoustical properties of air-saturated porous material with periodically distributed dead-end pores," *J. Acoust. Soc. Am.* **137**, 1772–1782 (2015).

¹³Z. Yang, J. Mei, M. Yang, N. Chan, and P. Sheng, "Membrane-type acoustic metamaterial with negative dynamic mass," *Phys. Rev. Lett.* **101**, 204301 (2008).

¹⁴J. Mei, G. Ma, M. Yang, Z. Yang, W. Wen, and P. Sheng, "Dark acoustic metamaterials as super absorbers for low-frequency sound," *Nature Commun.* **3**, 756 (2012).

¹⁵V. Romero-Garcia, G. Theocharis, O. Richoux, A. Merkel, V. Tournat, and V. Pagneux, "Perfect and broadband acoustic absorption by critically coupled sub-wavelength resonators," *Sci. Rep.* **6**, 19519 (2016).

¹⁶A. Merkel, G. Theocharis, O. Richoux, V. Romero-Garcia, and V. Pagneux, "Control of perfect absorption in 1D scattering: An acoustic example," in *Proceedings of Phononics 2015* (2015), pp. 390–391.

¹⁷J. Groby, A. Lardeau, W. Huang, and Y. Aurégan, "The use of slow sound to design simple sound absorbing materials," *J. Appl. Phys.* **117**, 124903 (2015).

¹⁸G. Ma, M. Yang, S. Xiao, Z. Yang, and P. Sheng, "Acoustic metasurface with hybrid resonances," *Nature Mater.* **13**, 873–878 (2014).

¹⁹A. Santillan and S. Bozhevolnyi, "Demonstration of slow sound propagation and acoustic transparency with a series of detuned resonators," *Phys. Rev. B* **89**, 184301 (2014).

²⁰G. Yu and X. Wang, "Acoustical 'transparency' induced by local resonance in Bragg bandgaps," *J. Appl. Phys.* **115**, 044913 (2014).

²¹A. Cicek, O. Kaya, M. Yilmaz, and B. Ulug, "Slow sound propagation in a sonic crystal linear waveguide," *J. Appl. Phys.* **111**, 013522 (2012).

²²Y. Aurégan, L. Xiong, and W. Bi, "Acoustical behavior of purely reacting liners," in *Proceedings of the 19th AIAA/CEAS Aeroacoustics Conference*, American Institute of Aeronautics and Astronautics, Inc., Berlin (2013), pp. 1–8.

²³G. Theocharis, O. Richoux, V. R. García, A. Merkel, and V. Tournat, "Limits of slow sound propagation and transparency in lossy, locally resonant periodic structures," *New J. Phys.* **16**, 093017 (2014).

²⁴W. Robertson, C. Baker, and C. B. Bennet, "Slow group velocity propagation of sound via defect coupling in a one-dimensional acoustic band gap array," *Am. J. Phys.* **72**, 255–257 (2003).

²⁵Y. Xie, A. Konneker, B.-P. Popa, and S. Cummer, "Tapered labyrinthine acoustic metamaterials for broadband impedance matching," *Appl. Phys. Lett.* **103**, 201906 (2013).

²⁶A. Santillan and S. Bozhevolnyi, "Acoustic transparency and slow sound using detuned acoustic resonators," *Phys. Rev. B* **84**, 064304 (2011).

²⁷E. Redon, A.-S. Bonnet-Ben Dhia, J.-F. Mercier, and S. Poernomo Sari, "Non-reflecting boundary conditions for acoustic propagation in ducts with acoustic treatment and mean flow," *Int. J. Numer. Meth. Eng.* **86**, 1360–1378 (2011).

- ²⁸J. B. Lawrie and I. Abrahams, "An orthogonality relation for a class of problems with high-order boundary conditions; applications in sound-structure interaction," *Q. J. Mech. Appl. Math.* **52**, 161–181 (1999).
- ²⁹A. Bensoussan, J. Lions, and G. Papanicolaou, *Asymptotic Analysis for Periodic Structures* (North-Holland, Amsterdam, The Netherlands, 1978), pp. 1–387.
- ³⁰A. Wood, *A Textbook of Sound* (G. Bell and Sons Ltd., London, UK, 1932), pp. 1–593.
- ³¹A. Morel, S. Felix, and J.-F. Mercier, "Enhanced transmission through gratings: Structural and geometrical effects," *Phys. Rev. B* **88**, 115416 (2013).
- ³²N. Fang, D. Xi, J. Xu, M. Ambati, W. Srituravanich, C. Sun, and X. Zhang, "Ultrasonic metamaterials with negative modulus," *Nature Mater.* **5**, 452–456 (2006).
- ³³N. Nemati and D. Lafarge, "Check on a nonlocal Maxwellian theory of sound propagation in fluid-saturated rigid-framed porous media," *Wave Motion* **51**, 716–728 (2014).
- ³⁴T. Luk, S. Campione, I. Kim, S. Feng, Y. Jun, S. Liu, J. Wright, I. Brener, P. Catrysse, S. Fan, and M. Sinclair, "Directional perfect absorption using deep subwavelength low-permittivity films," *Phys. Rev. B* **90**, 085411 (2014).
- ³⁵F.-P. Mechel, *Formulas of Acoustics*, 2nd ed. (Springer-Verlag, Berlin, Heidelberg, 2008), pp. 316–327.
- ³⁶P. Drude, "Transparent isotropic media," *Wied. Ann* **43**, 146 (1891).
- ³⁷C. Simovski, "On electromagnetic characterization and homogenization of nanostructured metamaterials," *J. Opt.* **13**, 013001 (2011).
- ³⁸X. Cai, Q. Guo, G. Hu, and J. Yang, "Ultrathin low-frequency sound absorbing panels based on coplanar spiral tubes or coplanar Helmholtz resonators," *Appl. Phys. Lett.* **105**, 121901 (2014).
- ³⁹J. Groby, W. Lauriks, and T. Vigran, "Total absorption peak by use of a rigid frame porous layer backed with a rigid multi-irregularities grating," *J. Acoust. Soc. Am.* **127**, 2865–2874 (2010).
- ⁴⁰M. Stinson, "The propagation of plane sound waves in narrow and wide circular tubes, and generalization to uniform tubes of arbitrary cross-sectional shape," *J. Acoust. Soc. Am.* **89**, 550–558 (1991).

Ultra-thin metamaterial for perfect and quasi-omnidirectional sound absorption

N. Jiménez,^{a)} W. Huang, V. Romero-García, V. Pagneux, and J.-P. Groby

Laboratoire d'Acoustique de l'Université du Maine (LAUM) - CNRS UMR 6613, Av. Olivier Messiaen, 72085 Le Mans, France

(Received 22 June 2016; accepted 14 August 2016; published online 20 September 2016)

Using the concepts of slow sound and critical coupling, an ultra-thin acoustic metamaterial panel for perfect and quasi-omnidirectional absorption is theoretically and experimentally conceived in this work. The system is made of a rigid panel with a periodic distribution of thin closed slits, the upper wall of which is loaded by Helmholtz Resonators (HRs). The presence of resonators produces a slow sound propagation shifting the resonance frequency of the slit to the deep sub-wavelength regime ($\lambda/88$). By controlling the geometry of the slit and the HRs, the intrinsic visco-thermal losses can be tuned in order to exactly compensate the energy leakage of the system and fulfill the critical coupling condition to create the perfect absorption of sound in a large range of incidence angles due to the deep subwavelength behavior. *Published by AIP Publishing.*

[<http://dx.doi.org/10.1063/1.4962328>]

The ability to perfectly absorb an incoming wave field in a sub-wavelength material is advantageous for several applications in wave physics as energy conversion,¹ time reversal technology,² coherent perfect absorbers,³ or sound-proofing⁴ among others. The solution of this challenge requires to solve a complex problem: reducing the geometric dimensions of the structure while increasing the density of states at low frequencies and finding the good conditions to match the impedance to the background medium.

A successful approach for increasing the density of states at low frequencies with reduced dimensions is the use of metamaterials. Recently, several possibilities based on these systems have been proposed to design sound absorbing structures which can present simultaneously sub-wavelength dimensions and strong acoustic absorption.⁵ One strategy to design these sub-wavelength systems consists of using space-coiling structures.^{6,7} Another way is to use sub-wavelength resonators as membranes^{4,8} or Helmholtz resonators (HRs).^{9,10} Recently, a new type of sub-wavelength metamaterials based on the concept of slow sound propagation has been used for the same purpose. This last type of metamaterials¹¹⁻¹³ makes use of its strong dispersion for generating slow-sound conditions inside the material and, therefore, drastically decreasing frequency of the absorption peaks. Hence, the structure thickness becomes deeply sub-wavelength. All of these structures, however, while they bring potentially solutions to reduce the geometric dimensions, face the challenge of impedance mismatch to the background medium.

The interaction of an incoming wave with a lossy resonant structure, in particular, the impedance matching with the background field, is one of the most studied processes in the field of wave physics.¹⁻³ These open systems, at the resonant frequency, are characterized by both the leakage rate of energy (i.e., the coupling of the resonant elements with the propagating medium) and the intrinsic losses of the resonator. The balance between the leakage and the losses activates

the condition of critical coupling, trapping the energy around the resonant elements and generating a maximum of energy absorption.¹⁴ In the case of transmission systems, degenerate critically coupled resonators with symmetric and antisymmetric resonances should be used to perfectly absorb the incoming energy by trapping the energy in the resonant element, i.e., without reflection or transmission.^{15,16} In the case of purely reflecting system, either symmetric or antisymmetric resonances that are critically coupled can be used to obtain perfect absorption of energy by a perfect trapping of energy around the resonators.^{17,18}

In this work, using the concepts of slow sound and critical coupling, we theoretically and experimentally report a perfect and quasi-omnidirectional absorbing metamaterial panel with deep sub-wavelength thickness. As shown in Fig. 1, the system consists of a thin panel perforated with a periodic arrangement of slits, of thickness h , with periodicity d along the x_1 direction. The upper wall of the slit is loaded by N identical HRs arranged in a square array of side a . The HRs, of square cross-section, are characterized by a neck and a cavity width w_n and w_c , and lengths l_n and l_c , respectively. The presence of the HRs introduces a strong dispersion in the slit producing slow sound propagation, in such a way that the resonance of the slit is down shifted: the slit becomes a deep sub-wavelength resonator. The visco-thermal losses in the system are considered in both the resonators and the slit by using effective complex and frequency dependent parameters.¹⁹ Therefore, by modifying the geometry, the intrinsic losses of the system can be efficiently tuned and the critical coupling condition can be fulfilled to solve the impedance matching to the exterior medium.

We start by analyzing the dispersion properties, along the dimension x_2 , inside the slit in order to inspect the slow sound behavior. Periodic boundary conditions are assumed in the x_1 dimension at boundaries $\Gamma_{x_1=0}$ and $\Gamma_{x_1=d}$, which for normal incidence reduce to symmetry boundary conditions. At this stage, we have to notice that through this work,

^{a)}Electronic mail: noe.jimenez@univ-lemans.fr

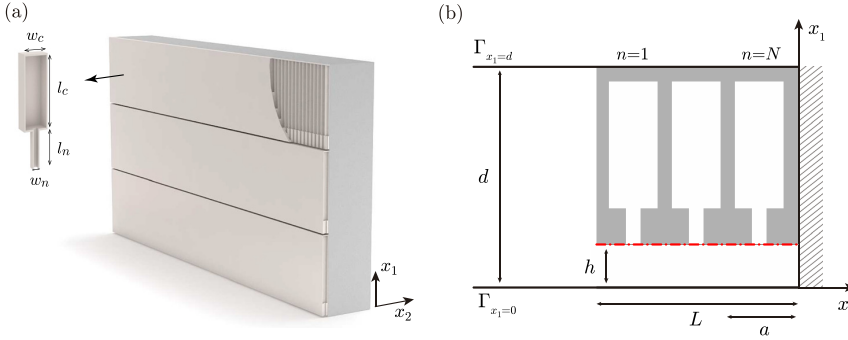


FIG. 1. (a) Conceptual view of the thin panel placed on a rigid wall with one layer of square cross-section Helmholtz resonators, $N=1$. (b) Scheme of the unit cell of the panel composed of a set of N Helmholtz resonators. Symmetry boundary conditions are applied at boundaries $\Gamma_{x_1=d}$ and $\Gamma_{x_1=0}$.

several theoretical models are used to analyze the structure: a full modal expansion model (MEM), its low frequency approximation that gives the effective parameters, an approach based on the transfer matrix method (TMM), and the finite element method (FEM). See [supplementary material](#) for more details of the models. Figure 2(a) shows the real part of the phase velocity in the slit, calculated both in the lossless and in the lossy cases, for a metamaterial with parameters $h=1.2$ mm, $a=1.2$ cm, $w_n=a/6$, $w_c=a/2$, $d=7$ cm, $l_n=d/3$, and $l_c=d-h-l_n$. Figure 2(b) shows the corresponding dispersion relation, where a band gap can be observed above the resonant frequency of the HRs, f_{HR} . Due to the presence of this band gap, slow sound propagation conditions are achieved in the dispersive band below f_{HR} . In the lossless case, zero phase velocity can be observed for frequencies just below f_{HR} . Note also that the maximum wavenumber inside the slit is limited by the discreteness to the value $k_{\text{max}}=\pi N/L$, as shown by the TMM calculations (dashed blue curve in Fig. 2(b)). In the lossy case, the losses limit the minimum value of group velocity,²⁰ but in our system slow sound velocity can be achieved in the dispersive band below f_{HR} . The average sound speed in the low frequency range is much lower (50 m/s) than the speed of sound in air. Therefore, the collective resonances produced by the array of HRs will be in the deep sub-wavelength regime compared with the length, L , of the slit.

The resonant scattering problem analyzed in this work can be characterized by the reflection coefficient. A simple way to obtain this reflection coefficient consists of using the effective bulk modulus, κ_e , and effective density, ρ_e , of the system. The reflection coefficient reads as

$$R_e(\theta) = \frac{iZ'_e \cot(k_e L) - i\omega \Delta l_{\text{slit}} / \phi_t c_0 - 1 / \cos(\theta)}{iZ'_e \cot(k_e L) - i\omega \Delta l_{\text{slit}} / \phi_t c_0 + 1 / \cos(\theta)}, \quad (1)$$

where the normalized effective impedance is $Z'_e = \sqrt{\rho_e \kappa_e} / \rho_0 \kappa_0$ (ρ_0 and κ_0 are the density and bulk modulus of air), the effective wavenumber $k_e = \omega \sqrt{\rho_e / \kappa_e}$, Δl_{slit} is the end correction of the slit accounting for the radiation from the slit to the free space, $\phi_t = h/d$ is the total porosity of the metamaterial, ω is the angular frequency, c_0 is the sound speed of air, and θ is the angle of incidence. The effective parameters can be obtained in the low frequency approximation of the MEM as

$$\kappa_e = \frac{\kappa_s}{\phi_t} \left[1 + \frac{\kappa_s \phi (v_c \kappa_n + v_n \kappa_c)}{\kappa_n h (S_n \kappa_c - v_c \rho_n l_n \omega^2)} \right]^{-1}, \quad (2)$$

$$\rho_e = \frac{\rho_s}{\phi_t}, \quad (3)$$

where ρ_s and ρ_n are the effective densities of the slit and neck; κ_s , κ_n , and κ_c are the effective bulk modulus of the slit, neck, and cavity, respectively; v_n and v_c are the volumes of the neck and cavity of the HRs, respectively.

In the complex frequency plane, the reflection coefficient has pairs of zeros and poles that are complex conjugates one from another in the lossless case. In the $\exp(-i\omega t)$ sign convention, the zeros are located in the positive imaginary plane. The imaginary part of the complex frequency of the poles of the reflection coefficient represents the energy leakage of the system into the free space.¹⁸ Once the intrinsic losses are introduced in the system, the zeros of the reflection coefficient move downwards to the real frequency axis.²¹ For a given frequency, if the intrinsic losses perfectly balance the energy

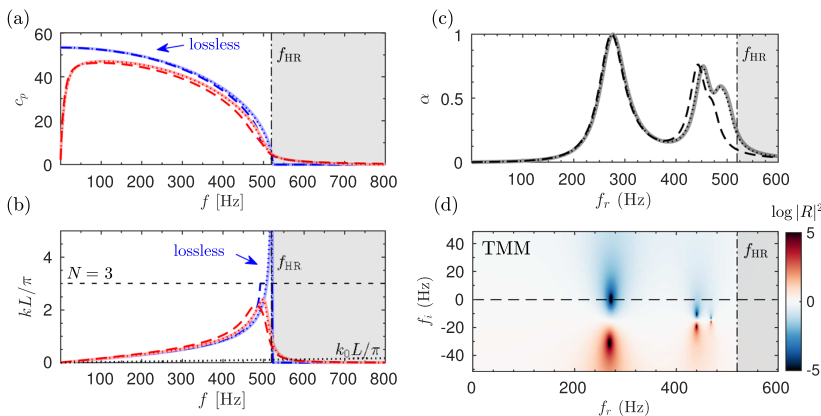


FIG. 2. (a) Phase speed for a panel of $N=3$ resonators calculated by full modal expansion (continuous gray), effective parameters (dotted), and TMM (dashed) for the lossless case (blue) including thermo-viscous losses (red). (b) Corresponding wavenumber, where k_0 is the wavenumber in air. (c) Absorption of the panel. The dashed-dotted line marks the resonant frequency of the HRs and the shaded area corresponds to the band-gap. (d) Complex-frequency planes of the reflection coefficient calculated by TMM, where f_r and f_i are the real and imaginary parts of the complex frequency.

leakage of the system, a zero of the reflection coefficient is exactly located on the real frequency axis and therefore perfect absorption, $\alpha = 1 - |R_c|^2 = 1$, can be obtained. This condition is known as critical coupling.^{14–18,21}

Figure 2(c) shows the absorption predicted by the different models when the geometry of the system has been tuned to introduce the exact amount of intrinsic losses that exactly compensates the energy leakage of the system at 275 Hz for $N=3$. In this situation, as shown in Fig. 2(d), the lower frequency zero is located on the real axis, leading to a peak of perfect absorption. In addition, as we have $N=3$ resonators, other two secondary peaks of absorption are observed at higher frequencies, e.g., 442 Hz and 471 Hz. Their corresponding zeros are located close to the real axis and, although the critical coupling condition is not exactly fulfilled, high absorption values can be observed at these frequencies. The differences between the several model predictions observed in the absorption coefficient are due to the fact that the effect of the discreteness is not captured by neither the MEM nor its effective parameters. MEM leads to an infinite number of zeros and poles close to the resonance, producing the artificial increase of the absorption observed in Fig. 2(c) near f_{HR} . Consequently, the prediction of absorption by MEM is accurate only if these zeros do not interact with the real axis or if the number of resonators is considerably increased. The TMM captures this discreteness effect and shows good results in this range of frequencies (400–500 Hz).

The previous sample provides perfect absorption for a thickness of $L = 3a = \lambda/34.5$. Using an optimization method (sequential quadratic programming (SQP) method²²), the geometry of the system can be tuned in order to minimize the thickness of the material, providing structures with perfect absorption and deep sub-wavelength dimensions. The TMM was employed in the optimization to consider the discreteness

effects on the reflection coefficient. The resulting structure from the optimization procedure is shown in Figure 3(a): a sample with a single layer of resonators, $N=1$ with $h=2.63$ mm, $d=14.9$ cm, $a=L=d/13=1.1$ cm, $w_n=2.25$ mm, $w_c=4.98$ mm, $l_n=2.31$ cm, $l_c=12.33$ cm. The width of the impedance tube used for measurements, d , allows to fit 13 resonators in the transversal dimension as shown in Fig. 3(a). The sample was built using stereolithography techniques using a photosensitive epoxy polymer (Accura 60[®], 3D Systems Corporation, Rock Hill, SC 29730, USA), where the acoustic properties of the solid phase are $\rho_0=1210$ kg/m³, $c_0=[1570, 1690]$ m/s. The structure presents a peak of perfect absorption at $f=338.5$ Hz (different than that of the HR, $f_{HR}=370$ Hz) with a thickness $L=\lambda/88$.

Figure 3(b) shows the absorption coefficient at normal incidence calculated with the different semi-analytical methods, predicted numerically by FEM and measured experimentally. At $f=338.5$ Hz, perfect absorption can be observed. The maximum absorption measured experimentally was $\alpha=0.97$, as shown in the inset of Fig. 3(b). This small discrepancy between the measurements and the models can be caused by experimental reasons including the non perfect fitting of the slit on the impedance tube and the excitation of plate modes of the solid medium that composes the metamaterial.

On the other hand, Fig. 3(c) shows the corresponding reflection coefficient in the complex frequency plane calculated with MEM. The color map corresponds to the case in which the critical coupling condition is fulfilled, i.e., the zero of the reflection coefficient is exactly located on the real frequency axis. As long as the intrinsic losses depend on the geometry of the resonators and the thickness of the slits, we also represent in Fig. 3(c) the trajectory of this zero as the geometry of the system is modified. The crossing of the trajectories with the real frequency axis implies that perfect

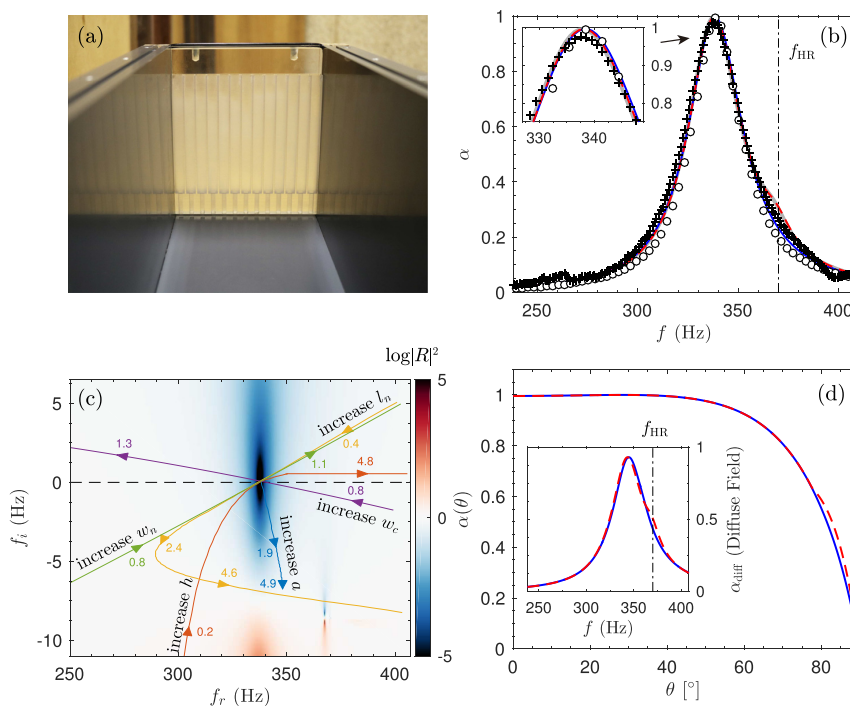


FIG. 3. (a) Photograph of the experimental setup with a vertical unit cell, $N=1$, in the interior of the impedance tube. The translucent resin allows to see the array of HRs. Picture shows the tube open, but it was closed for the experiments. (b) Absorption of the system measured experimentally (crosses), calculated by the full modal expansion (thick continuous gray), effective parameters (dashed red), transfer matrix method (continuous blue), and finite element method (circles). (c) Representation of the reflection coefficient in the complex frequency plane for the optimized sample. Each line shows the trajectory of its zero by changing a geometry parameter. (d) Absorption peak as a function of the angle of incidence calculated by the effective parameters (dashed red), transfer matrix method (continuous blue). The inset in (d) shows the absorption coefficient in diffuse field as a function of frequency.

absorption can be achieved with this system at this particular frequency. It can be seen that the trajectories linked to the resonators geometry, w_n , w_c , l_n have a strong effect in the real part of the complex frequency of the zero, as they modify the HRs resonant frequency. In the case of l_n , due to the geometric constraint $d \geq h + l_n + l_c$, increasing the length of the neck implies also that the reduction of the cavity and the trajectory of the zero is twisted. The trajectory of the slit thickness, h , shows that the intrinsic losses are excessively increased for very narrow slits and critical coupling condition cannot be fulfilled. For very wide slits, the geometrical constraints also imply the reduction of the size of the resonators and therefore the resonant frequency is increased. Finally, the trajectory linked to the lattice size, a , shows how the depth of the slit, $L = Na$, is mainly linked to the intrinsic losses of the system: the peak absorption frequency is almost independent of a ; it mostly depends on the resonator resonant frequency. Moreover, as the slow sound conditions are caused by the local resonance of the HRs, the periodicity of the array of HRs is not a necessary condition for these perfect absorbing panels. However, considering periodicity allows us to design and tune the system using the present analytical methods.

Finally, Fig. 3(d) shows the absorption of the metamaterial panel as a function of the angle of incidence. It can be observed that almost perfect absorption is obtained for a broad range of angles, being $\alpha > 0.90$ for incident waves with $\theta < 60^\circ$. The inset of Fig. 3(d) shows the absorption in diffuse field²³ calculated as $\alpha_{\text{diff}} = 2 \int_0^{\pi/2} \alpha(\theta) \cos(\theta) \sin(\theta) d\theta$, where at the working frequency it reaches a value of $\alpha_{\text{diff}} = 0.93$, showing the quasi-omnidirectional behavior of the absorption in this sub-wavelength structure.

Realistic panels for sound perfect absorption with sub-wavelength sizes are designed in this work with simple structures made of bricks with Helmholtz resonators. Perfect absorption of sound is achieved at 338.5 Hz with a panel thickness of $L = \lambda/88 = 1.1$ cm and without added porous material. It is worth noting here that the total panel size in the vertical dimension is also sub-wavelength $d = \lambda/6.5 = 14.5$ cm. The sub-wavelength feature of the presented structure provides perfect absorption for a wide range of incident angles. This almost omnidirectional sound absorber can be employed in practical applications where the omnidirectional feature is mandatory. In addition, several theoretical approaches have been presented and validated experimentally, where their limits of validity are discussed. In order to provide accurate models, we have

presented the design with standard Helmholtz resonators. However, the thickness of the structure can be even reduced by engineering the geometry using coiled-up channels or embedding the neck into the cavity of the HRs. These promising results open the possibilities to study different configurations based on these metamaterials and to extend the results to broadband and omnidirectional perfect absorption with deep sub-wavelength structures.

See [supplementary material](#) at for more details of the models.

This work has been funded by the Metaudible Project No. ANR-13-BS09-0003, co-funded by ANR and FRAE.

- ¹M. Law, L. E. Greene, J. C. Johnson, R. Saykally, and P. Yang, *Nat. Mater.* **4**, 455 (2005).
- ²A. Derode, P. Roux, and M. Fink, *Phys. Rev. Lett.* **75**, 4206 (1995).
- ³Y. Chong, L. Ge, H. Cao, and A. D. Stone, *Phys. Rev. Lett.* **105**, 053901 (2010).
- ⁴J. Mei, G. Ma, M. Yang, Z. Yang, W. Wen, and P. Sheng, *Nat. Commun.* **3**, 756 (2012).
- ⁵G. Ma and P. Sheng, *Sci. Adv.* **2**, e1501595 (2016).
- ⁶X. Cai, Q. Guo, G. Hu, and J. Yang, *Appl. Phys. Lett.* **105**, 121901 (2014).
- ⁷Y. Li and B. M. Assouar, *Appl. Phys. Lett.* **108**, 063502 (2016).
- ⁸Z. Yang, J. Mei, M. Yang, N. Chan, and P. Sheng, *Phys. Rev. Lett.* **101**, 204301 (2008).
- ⁹A. Merkel, G. Theocharis, O. Richoux, V. Romero-García, and V. Pagneux, *Appl. Phys. Lett.* **107**, 244102 (2015).
- ¹⁰V. Achilleos, O. Richoux, and G. Theocharis, *J. Acoust. Soc. Am.* **140**, EL94 (2016).
- ¹¹P. Leclaire, O. Umnova, T. Dupont, and R. Panneton, *J. Acoust. Soc. Am.* **137**, 1772 (2015).
- ¹²J.-P. Groby, W. Huang, A. Lardeau, and Y. Aurégan, *J. Appl. Phys.* **117**, 124903 (2015).
- ¹³J.-P. Groby, R. Pommier, and Y. Aurégan, *J. Acoust. Soc. Am.* **139**, 1660 (2016).
- ¹⁴K. Y. Bliokh, Y. P. Bliokh, V. Freilikher, S. Savel'ev, and F. Nori, *Rev. Mod. Phys.* **80**, 1201 (2008).
- ¹⁵J. R. Piper, V. Liu, and S. Fan, *Appl. Phys. Lett.* **104**, 251110 (2014).
- ¹⁶M. Yang, C. Meng, C. Fu, Y. Li, Z. Yang, and P. Sheng, *Appl. Phys. Lett.* **107**, 104104 (2015).
- ¹⁷G. Ma, M. Yang, S. Xiao, Z. Yang, and P. Sheng, *Nat. Mater.* **13**, 873 (2014).
- ¹⁸V. Romero-García, G. Theocharis, O. Richoux, A. Merkel, V. Tournat, and V. Pagneux, *Sci. Rep.* **6**, 19519 (2016).
- ¹⁹M. R. Stinson, *J. Acoust. Soc. Am.* **89**, 550 (1991).
- ²⁰G. Theocharis, O. Richoux, V. R. García, A. Merkel, and V. Tournat, *New J. Phys.* **16**, 093017 (2014).
- ²¹V. Romero-García, G. Theocharis, O. Richoux, and V. Pagneux, *J. Acoust. Soc. Am.* **139**, 3395 (2016).
- ²²M. J. Powell, *Numerical Analysis* (Springer, 1978), pp. 144–157.
- ²³T. J. Cox and P. D'antonio, *Acoustic Absorbers and Diffusers: Theory, Design and Application* (CRC Press, 2009).

Rainbow-trapping absorbers: Broadband, perfect and asymmetric sound absorption by subwavelength panels with ventilation

Noé Jiménez*,¹ Vicent Romero-García,¹ Vincent Pagneux,¹ and Jean-Philippe Groby¹
Laboratoire d'Acoustique de l'Université du Maine - CNRS UMR 6613, Le Mans, France

Perfect, broadband and asymmetric sound absorption is theoretically, numerically and experimentally reported by using subwavelength thickness panels in a transmission problem. The panels are composed of a periodic array of varying cross-section waveguides, each of them being loaded by an array of Helmholtz resonators (HRs) with graded dimensions. The low cut-off frequency of the absorption band is fixed by the resonance frequency of the deepest HR, that reduces drastically the transmission. The preceding HR is designed with a slightly higher resonance frequency with a geometry that allows the impedance matching to the surrounding medium. Therefore, reflection vanishes and the structure is critically coupled. This results in perfect sound absorption at a single frequency. We report perfect absorption at 300 Hz for a structure whose thickness is 40 times smaller than the wavelength. Moreover, this process is repeated by adding HRs to the waveguide, each of them with a higher resonance frequency than the preceding one. Using this frequency cascade effect, we report quasi-perfect sound absorption over almost two frequency octaves ranging from 300 to 1000 Hz for a panel composed of 9 resonators with a total thickness of 11 cm, i.e., 10 times smaller than the wavelength at 300 Hz.

Keywords: Metamaterials, perfect absorption, critical coupling, acoustic absorbers

I. INTRODUCTION

Wave manipulation using metamaterials has been extensively studied in electromagnetism¹, elasticity^{2,3} or acoustics^{4,5}, and among the very innovative systems that have been demonstrated are the metamaterial wave absorbers⁶⁻¹¹. In the particular case of sound waves, the selective bandwidth of most studied metamaterials limits their practical applications for audible frequencies: the audible frequency band covers more than ten frequency octaves, while in contrast, visible light spectrum covers less than one octave. Nevertheless, acoustic metamaterials have found practical applications in the design of selective low-frequency sound absorbing materials composed of membrane-type resonators^{4,12-14}, quarter-wavelength resonators (QWRs)¹⁵⁻¹⁹ and Helmholtz resonators (HRs)²⁰⁻²³.

By using the strong dispersion produced by local resonances, slow sound can be generated inside acoustic materials²⁴. Recently, slow sound phenomena have been exploited to design deep-subwavelength thickness absorbing structures^{16-18,21,22}. Of particular interest are perfect absorbing materials, facing the challenge of impedance mismatch to the surrounding medium. To achieve perfect absorption, the intrinsic losses of the system must exactly compensate the energy leakage at one resonance of the structure^{14,20,25,26}. When this condition is fulfilled the system is critically coupled with the exterior medium and perfect absorption is observed.

Perfect acoustic absorption has been reported in rigidly-backed subwavelength structures by using slow sound and QWRs¹⁸ or HRs²¹, or by using membranes and plates^{4,13,14}. Until now, only a few works have presented perfect and broadband absorption in rigid-backed subwavelength metamaterials. One kind of broadband

absorbers are metaporous materials²⁷⁻³⁰, whose low frequency performance is limited by the inertial regime of the porous matrix material. Other configurations include the use of panels composed of a parallel arrangement of different QWRs designed to be impedance matched at selected frequencies, e.g, the used in optimized absorbers based in sound diffusers³¹ or, in the same way, optimally designed panels to the limit imposed by causality³². The use of poroelastic plates that exhibit low quality factor resonances to extend the absorption bandwidth has been also proposed¹⁴. In Ref¹⁵ the authors used a graded set of QWRs in a slightly-subwavelength thickness structure to obtain quasi-perfect and broadband absorption. This last configuration can also fulfil the critical coupling conditions at more than one frequency, then, exhibiting perfect and broadband absorption¹⁸. In Ref.²⁰ a similar approach was presented using detuned HRs in a rigidly-backed waveguide. Finally, an extension of these ideas has been used to produce multiple slow waves inside a rigidly-backed graded structure of porous material to improve the broadband behaviour³³, but critical coupling conditions were not fulfilled at most resonances and perfect absorption was only observed at a single frequency.

However, when the system is not rigidly-backed and transmission is allowed, obtaining perfect absorption becomes challenging because the scattering matrix of the system presents two different eigenvalues. In order to obtain perfect absorption both eigenvalues must vanish at the same frequency³⁴. This implies that symmetric and antisymmetric modes must be simultaneously critically coupled at a given frequency³⁵. When the eigenvalues are both zero but at different frequencies, then the system cannot present perfect absorption, but quasi-perfect absorption can be achieved by approaching the symmetric and antisymmetric modes using strong dispersion²². Perfect acoustic absorption in transmission problems can

be obtained by using degenerate resonators, exciting a monopolar and a dipolar mode at the same frequency³⁶. Using elastic membranes decorated with designed patterns of rigid platelets¹² very selective low-frequency perfect absorption can be observed. Another strategy consists in using asymmetric graded materials, e.g., chirped layered porous structures³⁷, but these structures lack of subwavelength resonances and therefore its thickness is of the order of half of the incoming wavelength. A final configuration to achieve perfect absorption in transmission consists in breaking the symmetry of the structure by making use of double-interacting resonators, then perfect absorption was observed in waveguides at a particular frequency³⁴.

In this work, we address the problem of perfect and broadband acoustic absorption using deep-subwavelength structures, which to our knowledge was never addressed before in non rigidly-backed panels. To do so, we design panels composed of monopolar resonators with graded dimensions, namely *rainbow-trapping absorbers*. The designed panels present broadband, perfect and asymmetric sound absorption, and, due to slow sound, their thickness is reduced to the deep-subwavelength regime. Rainbow trapping phenomenon, i.e., the localization of energy due to a gradual reduction of the group velocity in graded structures, has been observed in optics³⁸, acoustics^{39,40} or elastodynamics⁴¹. However, losses were not accounted for and, therefore, absorption was not studied in these works. In the present configuration, a set of graded HRs is used, allowing to reduce, in addition to the thickness of the panels, the dimension of the unit cell to the deep-subwavelength regime. Using QWRs^{15,33}, rigidly-backed absorbers are about 4 times smaller than the wavelength in the transverse direction of propagation, while in the configuration presented in this paper, and using non-rigidly backed conditions, the size of the structure in the transverse direction is up to 30 times smaller than the absorbed wavelength.

In particular, the structures are composed of a rigid panel, of thickness L , periodically perforated with series of identical waveguides of variable square cross-section loaded by an array of N HRs of different dimensions, as shown in Figs. 1 (a, b). Each waveguide is therefore divided in N segments of length $a^{[n]}$, width $h_1^{[n]}$ and height $h_3^{[n]}$. The HRs are located in the middle of each waveguide section. Two samples were designed. The first one, namely *subwavelength asymmetric panel* (SAP) was composed of $N = 2$ HRs and it is shown in Fig. 1 (a). The second one, namely *rainbow-trapping absorber* (RTA) was composed first, in a design stage, by $N = 8$ and, finally, $N = 9$ HRs for the experimental tests, as shown in Fig. 1 (b). The SAP was designed to produce a single-frequency peak of perfect absorption while the RTAs were designed to exhibit broadband perfect absorption. The geometrical parameters of both structures were tuned using optimization methods (sequential quadratic programming (SQP)⁴²). In the case of the SAP ($N = 2$) the cost

function minimized during the optimization process was $\varepsilon_{\text{SAP}} = |R^-|^2 + |T|^2$, i.e., to maximize the absorption at a given frequency, in this case we selected 300 Hz. The length of the SAP was constrained to $L = 2.64$ cm, i.e., a panel 40 times thinner than the incoming wavelength. In the case of the rainbow trapping absorber ($N = 9$), the cost function was $\varepsilon_{\text{RTA}} = \int_{f_1}^{f_N} |R^-|^2 + |T|^2 df$, i.e., to maximize the absorption in a broad frequency bandwidth, that was chosen from $f_1 = 300$ to $f_N = 1000$ Hz. In the case of the RTA the length of the panel was constrained to $L = 11.3$ cm, i.e. a panel 10 times thinner than the wavelength at 300 Hz. The geometrical parameters obtained by the optimization process are given in Tables I,III for the SAP and RTA, respectively.

II. RESULTS

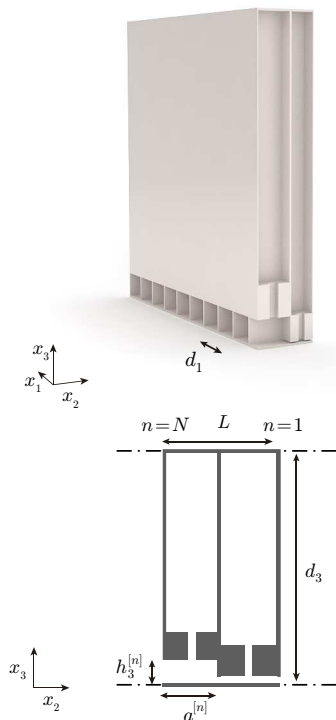
A. Subwavelength asymmetric panel (SAP)

We start analysing the behaviour of the designed SAP with $N = 2$ HRs, considering the two directions of incidence, namely *forward* and *backward*, as depicted in Figs. 2 (a,b). Figures 2 (c-f) show the corresponding absorption, reflection and transmission coefficients for each case. The results is calculated analytically using the transfer matrix method (TMM) in which the thermoviscous losses are accounted for, numerically using finite element method (FEM) and experimentally validated using stereo-lithographic 3D printed structures and impedance tube measurements. See Section Methods for further details. Good agreement is observed between analytical, numerical and experimental results.

First, in the forward configuration, shown in Fig. 2 (a), the resonator $n = 1$ of the waveguide presents a resonance frequency at $f_1 = 285$ Hz. As a consequence, above f_1 , a band gap is introduced and the transmission is strongly reduced, the HR acting effectively as a rigidly-backed wall for the right ingoing waves. Then, the resonator $n = 2$, with a superior resonance frequency at $f_2 = 310$ Hz, is tuned by the optimization process to critically couple the system with the exterior medium, matching the impedance of the waveguide to that of the surrounding medium. This is achieved at 300 Hz. As a consequence, no reflected waves are produced at this particular frequency and therefore, $\alpha = 1 - |R^-|^2 - |T|^2 = 1$ holds. In this situation, perfect absorption is observed in a panel with a thickness 40 times smaller that the wavelength, i.e., a panel of thickness $L = 2.64$ cm. It is worth noting here that the change of section in the main waveguide helps to achieve the impedance matching, specially for very thin SAPs as the one presented here. We will see later on that this steeped change in the cross-section is analogous to the graded profile of the main waveguide for the broadband structure.

Second, in the backward propagation shown in Fig. 2 (b), the wave impinges first the lowest resonance frequency resonator, f_1 . Now at 300 Hz the wave al-

(a) Subwavelength asymmetric panel (SAP)



(b) Rainbow-trapping absorber (RTA)

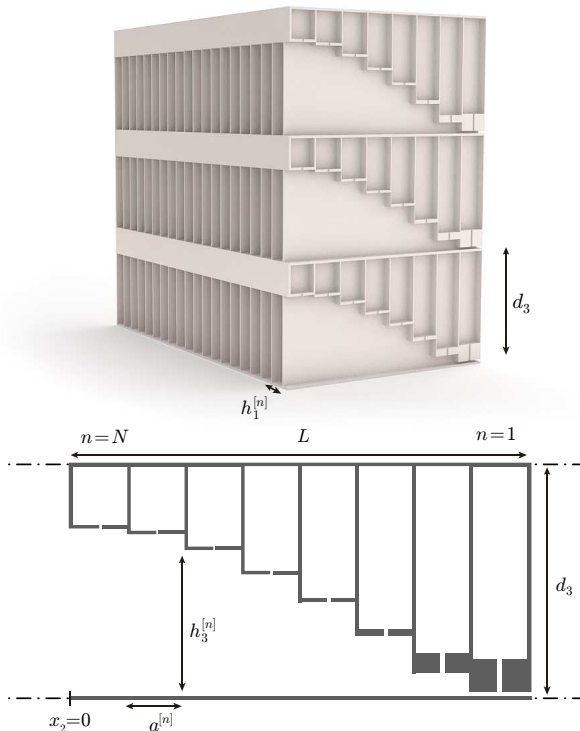


FIG. 1. (a) Conceptual view of a subwavelength asymmetric panel (SAP) ($N = 2$ resonators), where cross-section shows the waveguide and the loading HRs. (b) Conceptual view of a rainbow trapping absorber (RTA) with $N = 8$ HRs. Scheme showing the geometrical variables for (c) the SAP and (d) RTA panels.

most no transmission is allowed in the waveguide. As the waveguide is not impedance matched at 300 Hz in backward direction, reflection is high and absorption is poor ($\alpha^+ = 0.05$). For frequencies below f_2 , propagation is allowed in the main waveguide and the effect of the second HR may be visible inducing a decrease of the reflection coefficient. However, the impedance matching in the backward direction is not fully achieved and only a small amount of absorption is observed near the resonance frequency of the first resonator. Therefore, the absorption in this configuration is highly asymmetric.

In order to go further in the physical understanding of the scattering problem, we analyse the eigenvalues and eigenvectors of the \mathbf{S} -matrix of the SAP in the complex frequency plane. At this stage, it is worth noting that perfect absorption can only be obtained when the two eigenvalues of the \mathbf{S} -matrix are zero at the same purely real frequency. Let us start by considering the lossless propagation, neglecting the thermo-viscous losses by using the air parameters in the calculations. It can be observed that the eigenvalues shown in Fig. 3 (a, b) present pairs of zeros and poles, each pole identified with a resonance of the system. The position of the zeros and poles

in the complex frequency plane characterizes the physical transmission and reflection properties along the real frequency axis. In the lossless case each pole presents a zero that is its complex conjugate, i.e., they are located at the same real frequency but in the opposite half-space²⁰.

Now we turn to the lossy case, accounting for the visco-thermal losses in the resonators and the waveguides. In general, once losses are introduced the zero-pole structure of a given system is translated in the complex plane (also slightly deformed), approaching the zeros to the real frequency axis. Figures 3 (c, d) show the eigenvalues of the \mathbf{S} -matrix once thermo-viscous losses are introduced. At 300 Hz, both eigenvalues, $\lambda_{1,2}$, given by Eq. (9), present a zero exactly located at the real axis. This implies $T = \sqrt{R^+ R^-} = 0$. When this occurs exactly at the real frequency axis and at the same frequency, it implies perfect absorption, as it was observed in the previous section.

However, the information provided by the eigenvalues is not sufficient to determine from which side the perfect absorption is produced. The only information provided when the eigenvalues are zero is that the transmission coefficient and at least one of the two reflection coeffi-

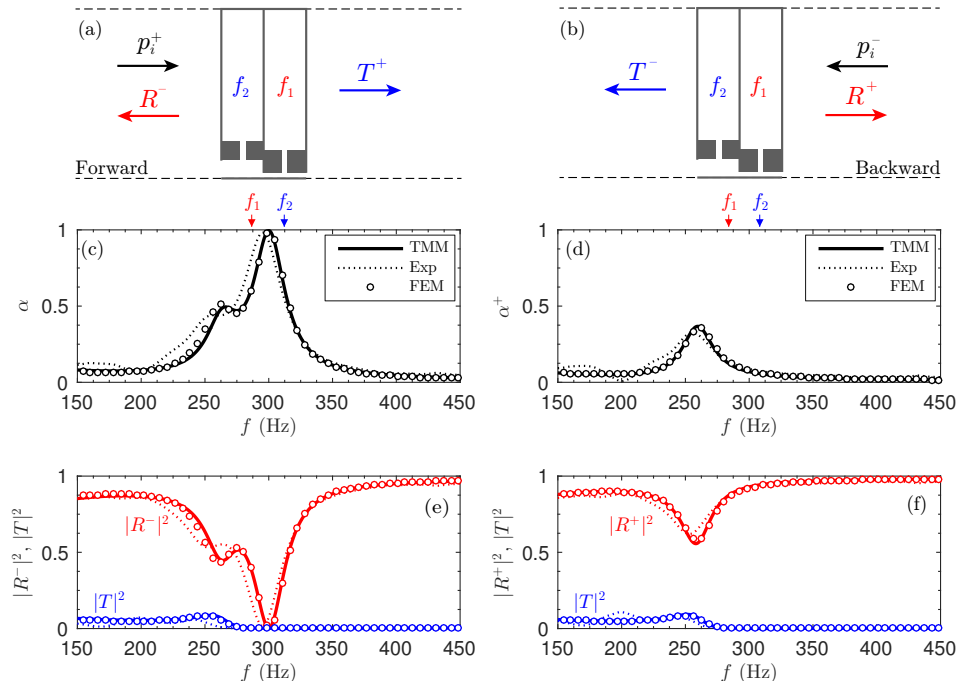


FIG. 2. Scheme of the subwavelength asymmetric panel in (a) forward and (b) reverse configuration. (c) Absorption for the forward configuration obtained using TMM (continuous line), FEM (circles), and experiment (dotted line). Corresponding reflection and transmission coefficients. (d) Absorption for the backward configuration. (f) Corresponding reflection and transmission coefficients. The arrows mark the resonance frequencies of the HRs, f_1 and f_2 .

coefficients vanish at this frequency. Thus, in order to draw the complete picture of the physical process, the corresponding eigenvectors are analysed. Figures 3 (e, f) and Figs. 3 (g, h) show the eigenvectors corresponding to λ_1 and λ_2 , given by Eqs. (10), respectively. From the complex frequency representation of the eigenvectors we can obtain the remaining information, i.e., the reflection coefficients from each side. In this case, we can see that $R^- = 0$ at 300 Hz, while $R^+ \neq 0$. This implies that the structure is only critically coupled with the surrounding medium when the incoming wave impinges the SAP from one side, i.e., in the forward direction the present case. Therefore, asymmetric perfect absorption is observed. In particular, $\alpha = 1$ and $\alpha^+ < 1$ for the designed SAP at the critical coupling frequency ($f = 300$ Hz).

B. Rainbow-trapping absorbers (RTA)

The concept of the SAP can be applied to design broadband perfect absorbers. The idea is to create a frequency-cascade of band-gaps and critically coupled resonators in order to generate a rainbow-trapping effect. The process is as follows. First, we tune the deepest resonator ($n = 1$) in the waveguide to reduce the transmission above a frequency f_1 . Second, in the same way as previously done in the SAP, a second resonator

with slightly higher resonance frequency, f_2 , is placed in the preceding segment of the waveguide. The geometry of this resonator and the section of the waveguide are tuned to impedance match the system at this frequency. Therefore, the reflection vanishes and a peak of perfect absorption is achieved in the same way as in the SAPs. Note this latter HR also reduces the transmission at even higher frequencies. Then, the process can be repeated by extending the waveguide with more segments, each one with a tuned HR being its resonance frequency higher than the preceding one.

Following this process, a rainbow-trapping absorber (RTA) is designed using $N = 8$ resonators. Figure 4 depicts the design process in detail. First, a panel composed of $N = 2$ HRs is optimized. Here, the geometry of the metamaterial is tuned in the same way as in the SAP. Figure 4 (a) shows a peak of perfect absorption and, as shown in Figs. 4 (b-c), both eigenvalues of the scattering matrix present a zero at the same real frequency (as we have already discussed the relevance of the eigenvectors in the previous Section, here we only show the eigenvalues for the sake of simplicity). Then, another HR is added with a slightly higher resonance frequency. The system is again tuned, but this time looking for perfect absorption at two single frequencies, 300 and 320 Hz. Figure 4 (d) shows the obtained absorption coefficients where two peaks of perfect absorption

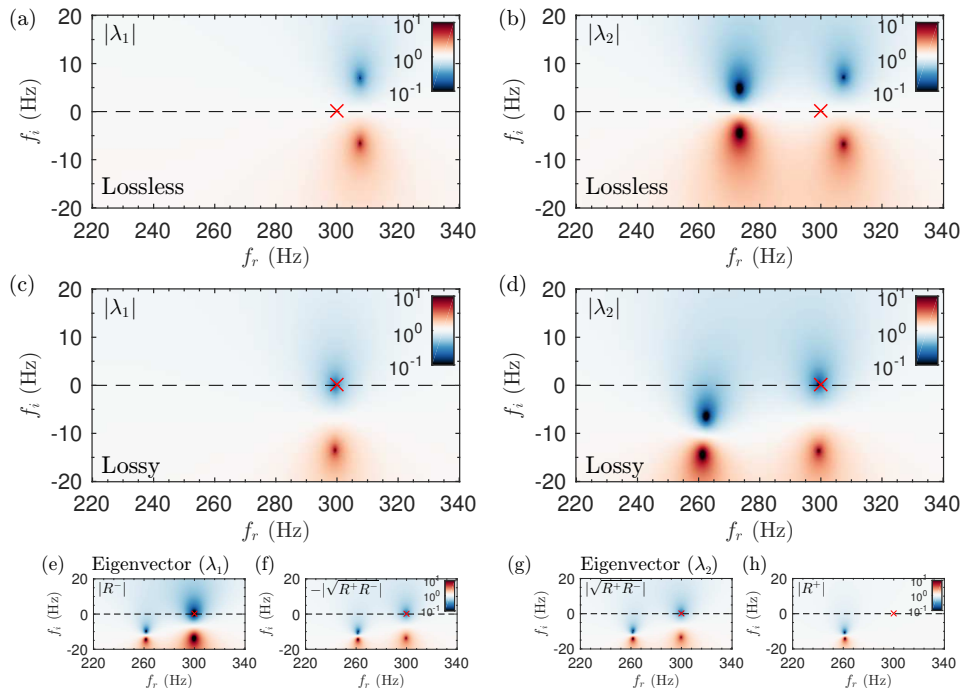


FIG. 3. Complex frequency representation of the two eigenvalues of the scattering matrix, $|\lambda_1|$, $|\lambda_2|$, (a-b) in the lossless case and (c-d) including the thermo-viscous losses in the resonators and the main waveguides. Colormap in $10 \log_{10} |\lambda|^2$ scale.

are observed, as demonstrated also by the location of the zeros of the eigenvalues of the scattering matrix on the real frequency axis, shown in Figs. 4 (e-f). This process is repeated iteratively until $N = 8$ HRs were included. Figures 4 (g-i) show the $N - 1$ peaks of perfect absorption and the corresponding complex frequency plane representation of the eigenvalues of the scattering matrix, respectively. Note that strictly speaking perfect absorption can only be achieved at $N - 1$ singular frequencies due to frequency cascade effect. However, flatter absorption can be generated due to the overlapping of the zeros of $\lambda_{1,2}$ if the quality factor of the resonances is reduced. This can be achieved by tuning again the geometrical parameters of the system, using as the initial condition to the optimization algorithm the previous geometry, and using a cost function covering a broad frequency band as $\varepsilon_{\text{RTA}} = \int_{f_1}^{f_N} |R^-|^2 + |T|^2 df$. The optimized geometrical parameters are listed in Table II. The final flatter, broadband and quasi-perfect absorption is shown in Fig. 4 (j). It is worth noting here that using a wide-bandwidth cost function does not ensure that all the resonances remain critically coupled, as it is shown in the complex frequency plane representation of the eigenvalues of the scattering matrix in Figs. 4 (k-l). However, the ripples in the absorption can be strongly reduced and the total absorption of energy in a frequency band can be maximized.

Due to machine precision of the available 3D printing system (the minimum step was 0.1 mm), the RTA pre-

sented previously cannot be easily manufactured. The main limitation was related to the loss of accuracy of the diameters of the small necks that compose the HRs. Under this technological constraint we redesign the RTA using $N = 9$ HRs and quantizing the dimensions of all the geometrical elements that compose the structure to the machine precision. The manufactured sample is shown in Fig. 5 (a) and the quantized geometrical parameters are listed in Table III. Figures 5 (b-c) show the absorption, reflection and transmission of the device calculated with the TMM, FEM and measured experimentally. The deepest resonator ($n = 1$) presents a resonance frequency of $f_1 = f_{\text{gap}} = 259$ Hz, causing the transmission to drop. A set of 8 resonators were tuned following the process previously described, with increasing resonance frequencies ranging from 330 to 917 Hz. As a result of the frequency-cascade process, the impedance of the structure in the working frequency range is matched with the exterior medium while the transmission vanishes. As a consequence, the RTA presents a flat and quasi-perfect absorption coefficient in this frequency range (see Fig. 5 (b)). Excellent agreement is found between the TMM predictions and FEM simulations, while good agreement is observed between the experimental measurements and both models. It can be observed that at low frequencies there are small differences between the measurements and the models. These disagreements are mainly caused by imperfections in the sample manufacturing, by imperfect

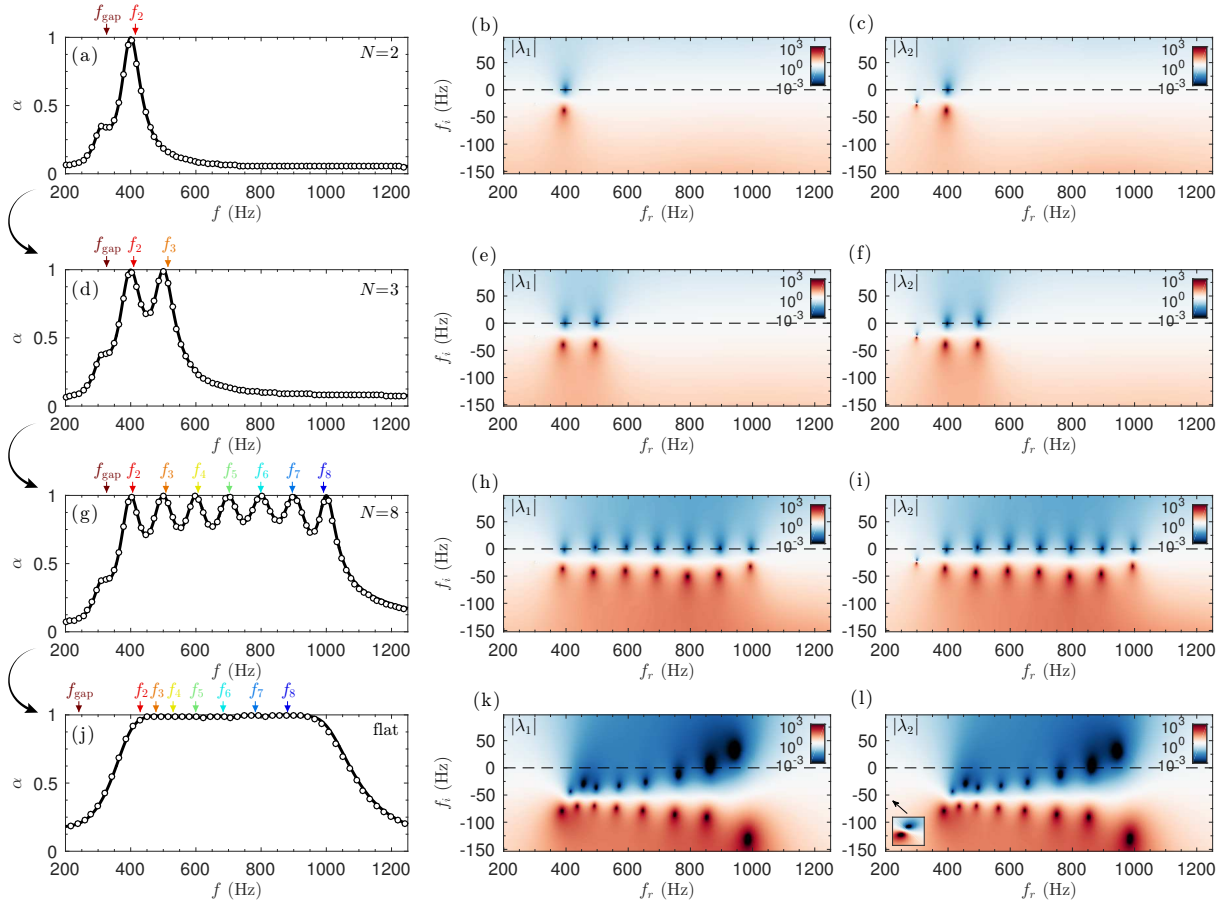


FIG. 4. Process to critically couple the rainbow-trapping absorbers. (a) Absorption using $N = 2$ HRs obtained using TMM (continuous lines) and FEM simulations (markers), (b-c) corresponding complex frequency plane representation of the eigenvalues of the scattering matrix. (d) Absorption using $N = 3$ HRs and (e-f) corresponding complex frequency plane. (g) Absorption using $N = 8$ HRs and (h-i) complex frequency plane. (j) Optimized broadband and flat absorption using $N = 8$ HRs, (k-l) corresponding complex frequency plane.

fitting of the structure to the impedance tube, by the possible evanescent coupling between adjacent waveguides and adjacent HRs, and/or by the limitations of the visco-thermal model used at the joints between waveguide sections.

The corresponding representation of the the two eigenvalues of the \mathbf{S} -matrix in the complex frequency plane is shown in Figs. 5 (d-e). We can see that even under the constraints imposed by the metamaterial construction process, all the $N - 1$ zeros of the eigenvalues that produce the critical coupling of the structure are located very close to the real axis being the zeros of λ_1 at the same frequencies as λ_2 . Note in the manufactured system, not all the zeros are located exactly on the real axis, but the quality factor of the resonances is very low (note the logarithmic colour scale in Fig. 5 (c-d)). Therefore they overlap producing quasi-perfect sound absorption in a frequency band from 300 to 1000 Hz for a panel 10

times thinner than the wavelength at 300 Hz in air.

Finally, the pressure field calculated using FEM simulations is shown in Fig. 6 along the sagittal plane $x_1 = d_1/2$ for frequencies corresponding to the peaks of absorption, i.e., $f = [300, 386, 450, 530, 610, 706, 803, 923]$ Hz. It can be observed that for each frequency the acoustic field is mostly localized in a single resonator, being the field at lower frequencies localized at the deepest resonator, and the higher frequencies at the outer HRs of the metamaterial, thus, creating the rainbow-trapping effect. Note this behaviour is somehow similar to what was observed in sawtooth broadband absorbers^{10,11,15}, but here transmission was considered. It is worth noting here that for low number of resonators, e.g., the previous cases of $N = 2$ and $N = 3$ in Figs. 4 (a,d), the change of section was not mandatory. However, to obtain broadband absorption, the optimization of the geometry produces always a graded profile of the main waveguide. This

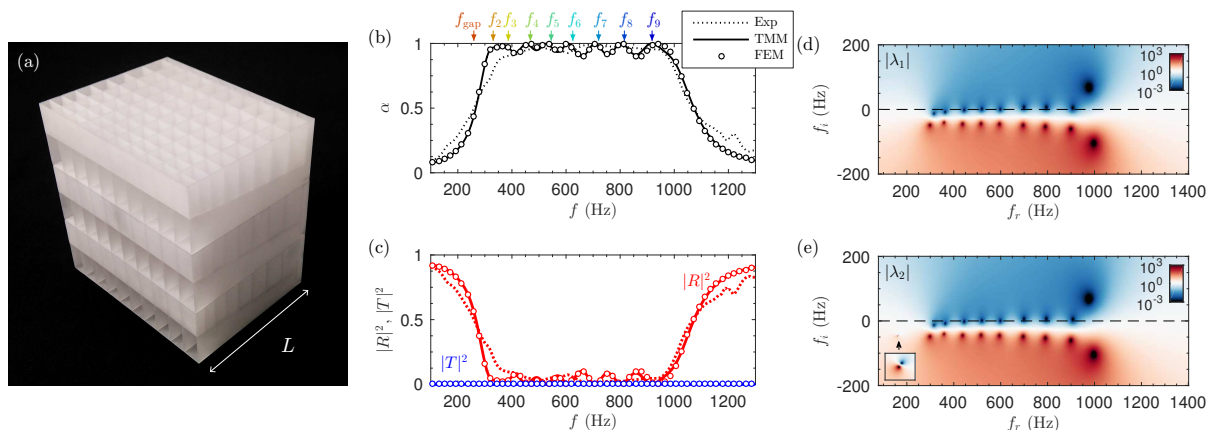


FIG. 5. (a) Photograph of the sample containing 10×3 unit cells. (b) Absorption obtained by using the TMM (continuous line), FEM simulations (circles) and measured experimentally (dotted line). (c) Corresponding reflection (red curves) and transmission (blue curves). (d-e) Complex frequency representation of the eigenvalues of the scattering matrix, $\lambda_{1,2}$. Colormap in $10 \log_{10} |\lambda|^2$ scale.

graded profile helps to obtain the broadband impedance matching by making use of the cavity resonance in the main waveguide. This cavity mode can be observed at around 923 Hz in the main waveguide, see Fig. 6 (h), and is produced by the quarter-wavelength resonance of the waveguide $f \approx c/4 \sum_1^{N-1} a^{[n]}$. We notice that this resonance was also observed at the complex frequency plane in Fig. 5 (d-e), represented by the pairs of zero-poles located at $f \approx 1000 \pm i100$ Hz. Due to the geometrical constraints of the metamaterial, the critical coupling of this quarter-wavelength resonance is not possible. However, this cavity resonance also contributes, in a moderate way to generate broadband and flat absorption. It is worth noting here that a similar cavity resonance was also visible in Figs. 4 (k-l). Therefore, the graded profile of the main waveguides contributes also to generate the flat absorption curve.

III. DISCUSSION

We reported perfect acoustic absorption over a broad frequency band in deep-subwavelength thickness panels including transmission using the rainbow-trapping effect. In particular, we first presented monochromatic perfect absorption for a subwavelength asymmetric panel (SAP) 40 times smaller than the incoming wavelength (2.64 cm at 300 Hz) using two double-interacting Helmholtz resonators. Then, we reported flat and perfect absorption over a frequency range covering from 300 to 1000 Hz, i.e., almost two octaves, using a rainbow-trapping absorber (RTA) composed of nine resonators and ten times smaller than the wavelength at 300 Hz (11.3 cm). We showed that to obtain broadband and perfect absorption in the transmission problem, three conditions must be simultaneously fulfilled: (i) the zeros of the eigenvalues

of the scattering matrix must be located on the real frequency axis, (ii) the zeros of both eigenvalues, $\lambda_{1,2}$, must be at same frequencies, and, (iii) the quality factor of the resonances must be low to overlap in frequency. These three conditions are mandatory to maximize the broadband absorption of the panels and were satisfied by the optimization process.

The limitations to obtain perfect absorption in realistic panels were tested. It is worth noting here that although achieving perfect absorption is theoretically possible, the maximum absorption is, in general, limited in a real situation. Factors as the changes in temperature, the contribution of nonlinearity for finite amplitude waves or manufacturing constraints produce small changes in the resonances and the critical coupling conditions cannot be exactly fulfilled. However, under such considerations we demonstrated that the structures analysed here produce extraordinary values of absorption: for SAP an absorption peak of 0.995 in the analytical model and 0.982 in the measurements was observed, while in the RTA the maximum absorption was 0.999 in the analytical model and 0.989 in the measurements.

The metamaterials presented here paves the way to new investigations by using the rainbow-trapping effect produced by other types of resonators as graded arrangements of membranes or poroelastic plates. The current subwavelength thickness configuration using Helmholtz resonators can also has potential applications managing acoustic waves in civil, automotive or aerospace engineering.

¹Zheludev, N. I. & Kivshar, Y. S. From metamaterials to metadevices. *Nature materials* **11**, 917–924 (2012).

²Ding, Y., Liu, Z., Qiu, C. & Shi, J. Metamaterial with simultaneously negative bulk modulus and mass density. *Physical review letters* **99**, 093904 (2007).

³Christensen, J., Kadic, M., Kraft, O. & Wegener, M. Vibrant

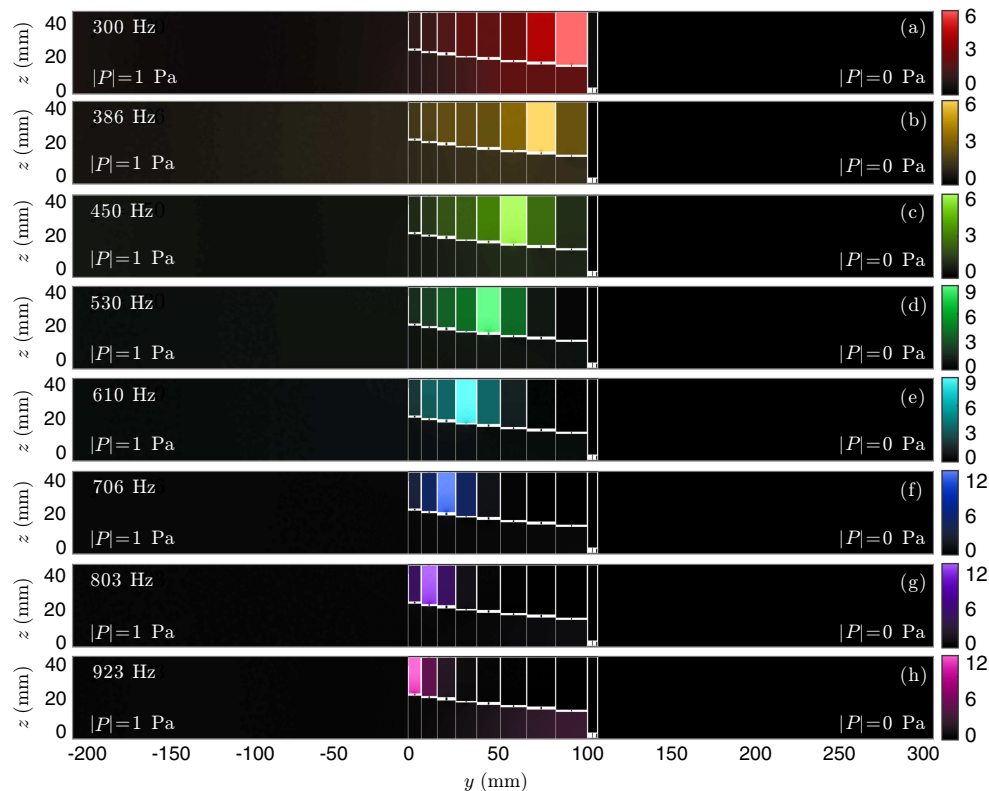


FIG. 6. (a-h) Pressure field inside the structure at $x_1 = d_1/2$ for frequencies corresponding to the peaks of absorption, i.e., $f = [300, 386, 450, 530, 610, 706, 803, 923]$ Hz. Colormap in $|P/P_0|^2$ units, and $P_0 = 1$ Pa.

times for mechanical metamaterials. *Mrs Communications* **5**, 453–462 (2015).

- ⁴Yang, Z., Mei, J., Yang, M., Chan, N. & Sheng, P. Membrane-type acoustic metamaterial with negative dynamic mass. *Phys. Rev. Lett.* **101**, 204301 (2008).
- ⁵Cummer, S. A., Christensen, J. & Alù, A. Controlling sound with acoustic metamaterials. *Nature Reviews Materials* **1**, 16001 (2016).
- ⁶Landy, N. I., Sajuyigbe, S., Mock, J., Smith, D. & Padilla, W. Perfect metamaterial absorber. *Physical review letters* **100**, 207402 (2008).
- ⁷Watts, C. M., Liu, X. & Padilla, W. J. Metamaterial electromagnetic wave absorbers. *Advanced materials* **24** (2012).
- ⁸Cui, Y. *et al.* Plasmonic and metamaterial structures as electromagnetic absorbers. *Laser & Photonics Reviews* **8**, 495–520 (2014).
- ⁹Lee, Y. P., Rhee, J. Y., Yoo, Y. J. & Kim, K. W. Metamaterials for perfect absorption. *Springer series in materials science (ISSN 0933-033X)* **236** (2016).
- ¹⁰Cui, Y. *et al.* Ultrabroadband light absorption by a sawtooth anisotropic metamaterial slab. *Nano letters* **12**, 1443–1447 (2012).
- ¹¹Ding, F., Cui, Y., Ge, X., Jin, Y. & He, S. Ultra-broadband microwave metamaterial absorber. *Applied physics letters* **100**, 103506 (2012).
- ¹²Mei, J. *et al.* Dark acoustic metamaterials as super absorbers for low-frequency sound. *Nat. Commun.* **3**, 756 (2012).
- ¹³Ma, G., Yang, M., Xiao, S., Yang, Z. & Sheng, P. Acoustic metasurface with hybrid resonances. *Nat. Mater.* **13**, 873–878 (2014).
- ¹⁴Romero-García, V. *et al.* Perfect and broadband acoustic absorption by critically coupled sub-wavelength resonators. *Sci. Rep.* **6**, 19519 (2016).
- ¹⁵Jiang, X. *et al.* Ultra-broadband absorption by acoustic metamaterials. *Applied Physics Letters* **105**, 243505 (2014).
- ¹⁶Leclaire, P., Umnova, O., Dupont, T. & Panneton, R. Acoustical properties of air-saturated porous material with periodically distributed dead-end pores. *J. Acoust. Soc. Am.* **137**, 1772–1782 (2015).
- ¹⁷Groby, J.-P., Huang, W., Lardeau, A. & Aurégan, Y. The use of slow waves to design simple sound absorbing materials. *J. Appl. Phys.* **117**, 124903 (2015).
- ¹⁸Groby, J.-P., Pommier, R. & Aurégan, Y. Use of slow sound to design perfect and broadband passive sound absorbing materials. *J. Acoust. Soc. Am.* **139**, 1660–1671 (2016).
- ¹⁹Li, Y. & Assouar, B. M. Acoustic metasurface-based perfect absorber with deep subwavelength thickness. *Appl. Phys. Lett.* **108**, 063502 (2016).
- ²⁰Romero-García, V., Theocharis, G., Richoux, O. & Pagneux, V. Use of complex frequency plane to design broadband and sub-wavelength absorbers. *The Journal of the Acoustical Society of America* **139**, 3395–3403 (2016).
- ²¹Jiménez, N., Huang, W., Romero-García, V., Pagneux, V. & Groby, J.-P. Ultra-thin metamaterial for perfect and quasi-omnidirectional sound absorption. *Applied Physics Letters* **109**, 121902 (2016).
- ²²Jiménez, N., Romero-García, V., Pagneux, V. & Groby, J.-P. Quasiperfect absorption by subwavelength acoustic panels in transmission using accumulation of resonances due to slow sound. *Phys. Rev. B* **95**, 014205 (2017).

- ²³Achilleos, V., Theocharis, G., Richoux, O. & Pagneux, V. Non-hermitian acoustic metamaterials: Role of exceptional points in sound absorption. *Physical Review B* **95**, 144303 (2017).
- ²⁴Santillán, A. & Bozhevolnyi, S. I. Acoustic transparency and slow sound using detuned acoustic resonators. *Phys. Rev. B* **84**, 064304 (2011).
- ²⁵Chong, Y., Ge, L., Cao, H. & Stone, A. D. Coherent perfect absorbers: time-reversed lasers. *Physical review letters* **105**, 053901 (2010).
- ²⁶Wan, W. *et al.* Time-reversed lasing and interferometric control of absorption. *Science* **331**, 889–892 (2011).
- ²⁷Groby, J.-P., Duclos, A., Dazel, O., Boeckx, L. & Lauriks, W. Absorption of a rigid frame porous layer with periodic circular inclusions backed by a periodic grating. *J. Acoust. Soc. Am.* **129**, 3035–3046 (2011).
- ²⁸Lagarrigue, C., Groby, J., Tournat, V., Dazel, O. & Umnova, O. Absorption of sound by porous layers with embedded periodic arrays of resonant inclusions. *J. Acoust. Soc. Am.* **134**, 4670–4680 (2013).
- ²⁹Boutin, C. Acoustics of porous media with inner resonators. *J. Acoust. Soc. Am.* **134**, 4717–4729 (2013).
- ³⁰Groby, J.-P. *et al.* Enhancing the absorption properties of acoustic porous plates by periodically embedding helmholtz resonators. *J. Acoust. Soc. Am.* **137**, 273–280 (2015).
- ³¹Wu, T., Cox, T. & Lam, Y. From a profiled diffuser to an optimized absorber. *The Journal of the Acoustical Society of America* **108**, 643–650 (2000).
- ³²Yang, M., Chen, S., Fu, C. & Sheng, P. Optimal sound-absorbing structures. *Materials Horizons* (2017).
- ³³Yang, J., Lee, J. S. & Kim, Y. Y. Multiple slow waves in metaporous layers for broadband sound absorption. *Journal of Physics D: Applied Physics* **50**, 015301 (2016).
- ³⁴Merkel, A., Theocharis, G., Richoux, O., Romero-García, V. & Pagneux, V. Control of acoustic absorption in one-dimensional scattering by resonant scatterers. *Appl. Phys. Lett.* **107**, 244102 (2015).
- ³⁵Piper, J. R., Liu, V. & Fan, S. Total absorption by degenerate critical coupling. *Appl. Phys. Lett.* **104**, 251110 (2014).
- ³⁶Yang, M. *et al.* Subwavelength total acoustic absorption with degenerate resonators. *Appl. Phys. Lett.* **107**, 104104 (2015).
- ³⁷Jiménez, N. *et al.* Broadband quasi perfect absorption using chirped multi-layer porous materials. *AIP Advances* **6**, 121605 (2016).
- ³⁸Tsakmakidis, K. L., Boardman, A. D. & Hess, O. Trapped rainbow storage of light in metamaterials. *Nature* **450**, 397–401 (2007).
- ³⁹Zhu, J. *et al.* Acoustic rainbow trapping. *Scientific reports* **3** (2013).
- ⁴⁰Romero-García, V., Picó, R., Cebrecos, A., Sanchez-Morcillo, V. & Staliunas, K. Enhancement of sound in chirped sonic crystals. *Applied Physics Letters* **102**, 091906 (2013).
- ⁴¹Colombi, A., Colquitt, D., Roux, P., Guenneau, S. & Craster, R. V. A seismic metamaterial: The resonant metawedge. *Scientific reports* **6** (2016).
- ⁴²Powell, M. J. A fast algorithm for nonlinearly constrained optimization calculations. In *Numerical analysis*, 144–157 (Springer, 1978).
- ⁴³Stinson, M. R. The propagation of plane sound waves in narrow and wide circular tubes, and generalization to uniform tubes of arbitrary cross-sectional shape. *J. Acoust. Soc. Am.* **89**, 550–558 (1991).
- ⁴⁴Theocharis, G., Richoux, O., García, V. R., Merkel, A. & Tournat, V. Limits of slow sound propagation and transparency in lossy, locally resonant periodic structures. *New J. Phys.* **16**, 093017 (2014).
- ⁴⁵Kergomard, J. & Garcia, A. Simple discontinuities in acoustic waveguides at low frequencies: critical analysis and formulae. *J. Sound Vib.* **114**, 465–479 (1987).
- ⁴⁶Dubos, V. *et al.* Theory of sound propagation in a duct with a branched tube using modal decomposition. *Acta Acustica united*

with Acustica **85**, 153–169 (1999).

⁴⁷Mechel, F. P. *Formulas of acoustics, 2nd ed.* (Springer Science & Business Media, 2008).

IV. METHODS

A. Theoretical model

The theoretical modelling is performed by using the transfer matrix method (TMM), which relates the sound pressure, p , and normal acoustic particle velocity, v_x , at the beginning ($x = 0$) and at the end of the panel ($x = L$). Under the assumption that only plane waves propagate in the waveguides, the transfer matrix \mathbf{T} is derived and the reflection and transmission coefficients can be calculated. The system is written as

$$\begin{bmatrix} p \\ v_x \end{bmatrix}_{x=0} = \mathbf{T} \begin{bmatrix} p \\ v_x \end{bmatrix}_{x=L} = \begin{bmatrix} T_{11} & T_{12} \\ T_{21} & T_{22} \end{bmatrix} \begin{bmatrix} p \\ v_x \end{bmatrix}_{x=L}, \quad (1)$$

where \mathbf{T} is given by the product of the transfer matrices of the N different cross-section waveguides loaded by HRs,

$$\mathbf{T} = \mathbf{M}_{\Delta l_{\text{slit}}}^{[1]} \prod_{n=1}^N \mathbf{M}_{\text{s}}^{[n]} \mathbf{M}_{\text{HR}}^{[n]} \mathbf{M}_{\text{s}}^{[n]} \mathbf{M}_{\Delta l_{\text{slit}}}^{[n+1]}. \quad (2)$$

The transmission matrix for the n -th waveguide half-segment, $\mathbf{M}_{\text{s}}^{[n]}$, takes the form

$$\mathbf{M}_{\text{s}}^{[n]} = \begin{bmatrix} \cos\left(k_{\text{s}}^{[n]} \frac{a^{[n]}}{2}\right) & iZ_{\text{s}}^{[n]} \sin\left(k_{\text{s}}^{[n]} \frac{a^{[n]}}{2}\right) \\ \frac{i}{Z_{\text{s}}^{[n]}} \sin\left(k_{\text{s}}^{[n]} \frac{a^{[n]}}{2}\right) & \cos\left(k_{\text{s}}^{[n]} \frac{a^{[n]}}{2}\right) \end{bmatrix}, \quad (3)$$

where $k_{\text{s}}^{[n]}$ and $Z_{\text{s}}^{[n]} = \sqrt{\kappa_{\text{s}}^{[n]} \rho_{\text{s}}^{[n]}} / S_{\text{s}}^{[n]}$ are the effective wavenumber and the characteristic impedance of the n -th waveguide segment, $\kappa_{\text{s}}^{[n]}$ and $\rho_{\text{s}}^{[n]}$ are the effective bulk modulus and the density respectively, provided in the IVD, and $S_{\text{s}}^{[n]} = d_1^{[n]} h_3^{[n]}$ are the cross-sectional areas. The resonators, accounted for as point scatterers in the middle of each waveguide segment by a transmission matrix $\mathbf{M}_{\text{HR}}^{[n]}$, and the radiation correction of the n -th waveguide segment due to cross-section changes, $\mathbf{M}_{\Delta l_{\text{slit}}}^{[n]}$, are respectively

$$\mathbf{M}_{\text{HR}}^{[n]} = \begin{bmatrix} 1 & 0 \\ 1/Z_{\text{HR}}^{[n]} & 1 \end{bmatrix}, \quad \mathbf{M}_{\Delta l_{\text{slit}}}^{[n]} = \begin{bmatrix} 1 & Z_{\Delta l_{\text{slit}}}^{[n]} \\ 0 & 1 \end{bmatrix}, \quad (4)$$

where $Z_{\text{HR}}^{[n]}$ is the impedance of the HR and $Z_{\Delta l_{\text{slit}}}^{[n]}$ is the characteristic radiation impedance of the n -th waveguide, both provided in the IVE. Notice that the length corrections of the HRs are already accounted for in the impedance $Z_{\text{HR}}^{[n]}$.

The reflection coefficients from both sides of the structure, R^+ and R^- , and the transmission coefficient, T , are

given by the elements of the \mathbf{T} -matrix as

$$T = \frac{2e^{ikL}}{T_{11} + T_{12}/Z_0 + Z_0T_{21} + T_{22}}, \quad (5)$$

$$R^- = \frac{T_{11} + T_{12}/Z_0 - Z_0T_{21} - T_{22}}{T_{11} + T_{12}/Z_0 + Z_0T_{21} + T_{22}}, \quad (6)$$

$$R^+ = \frac{-T_{11} + T_{12}/Z_0 - Z_0T_{21} + T_{22}}{T_{11} + T_{12}/Z_0 + Z_0T_{21} + T_{22}}, \quad (7)$$

where $Z_0 = \rho_0 c_0 / S_0$ is the characteristic impedance of the surrounding medium, usually air, with $S_0 = d_1 d_3$, and the superscripts $(+, -)$ denoting the incidence direction, i.e., the positive and negative x_2 -axis respectively. Finally the asymmetric absorption coefficients are calculated as $\alpha = \alpha^- = 1 - |R^-|^2 - |T|^2$ for the positive x_2 -axis ingoing waves, namely here and beyond *forward* propagation, and $\alpha^+ = 1 - |R^+|^2 - |T|^2$ for the negative x_2 -axis ingoing waves, namely *backward* propagation. In symmetric systems $T_{11} = T_{22}$ and, as a consequence, $R^+ = R^-$. This property is not satisfied by rainbow trapping absorbers and, therefore, the absorption depends on the direction of incidence. The reciprocal behaviour of the system implies that the determinant of transfer matrix is one ($T_{11}T_{22} - T_{12}T_{21} = 1$). This property is satisfied by the present linear and time invariant system and the transmission does not depend on the direction of incidence.

On the other hand, the scattering matrix, \mathbf{S} , relates the amplitudes of the incoming waves with those of the outgoing waves. The total pressures at both sides of the structure are given by $p(x_a) = Ae^{-ikx_a} + Be^{ikx_a}$ for $x_a < 0$, and $p(x_b) = Ce^{-ikx_b} + De^{ikx_b}$ for $x_b > L$. Thus, the relation between the amplitudes of both waves is given by the \mathbf{S} -matrix as

$$\begin{bmatrix} A \\ D \end{bmatrix} = \mathbf{S} \begin{bmatrix} C \\ B \end{bmatrix} = \begin{bmatrix} T & R^- \\ R^+ & T \end{bmatrix} \begin{bmatrix} C \\ B \end{bmatrix}. \quad (8)$$

The \mathbf{S} -matrix is widely used in wave physics to characterize and interpret the wave scattering. The scattering matrix possesses two eigenvalues

$$\lambda_{1,2} = T \mp \sqrt{R^+ R^-}, \quad (9)$$

while the eigenvectors corresponding to λ_1 and λ_2 are

$$\vec{v}_1 = [R^-, -\sqrt{R^+ R^-}], \quad \vec{v}_2 = [\sqrt{R^+ R^-}, R^+], \quad (10)$$

respectively. The poles and zeros of the eigenvalues as well as the eigenvectors of the \mathbf{S} -matrix in the complex-frequency plane provide rich information, as we will see later.

B. Numerical model

In order to validate the analytical models we use a numerical approach based on the Finite Element

Method (FEM) using COMSOL Multiphysics 5.2TM. The thermo-viscous losses were accounted for by using the effective parameters of the air in the ducts, i.e., by using the complex and frequency dependent density and bulk modulus, given in the IV D. At the external sides of the panel, rigid boundary conditions were considered and viscous losses were neglected here. This is justified because losses are mainly produced by thermo-viscous processes at the narrow ducts that compose the metamaterial and the contribution of other sources is minor. The unstructured mesh was designed ensuring a maximum element size 20 times smaller than the wavelength.

C. Sample design and experiments

Both samples were 3D printed by means of stereolithography techniques using a photosensitive epoxy polymer (Accura 60[®], 3D Systems Corporation, Rock Hill, SC 29730, USA). The acoustic properties of the solid phase were $\rho_0 = 1210 \text{ kg/m}^3$ and $c_0 = 1630 \pm 60 \text{ m/s}$. Therefore, the characteristic acoustic impedance was almost 5 thousand times greater than the one of air and therefore the structure is considered motionless. The transmission, reflection and absorption were measured in a impedance tube with squared cross-section whose side was 15 cm. During the experiments the amplitude of the acoustic source was low enough to neglect the contribution of the nonlinearity of the HRs.

D. Visco-thermal losses model

The visco-thermal losses in the system are considered both in the HRs and in the waveguide by using its effective complex and frequency dependent parameters. Considering only plane waves propagate inside the metamaterial, the effective density, $\rho_i^{[n]}$, and bulk modulus, $\kappa_i^{[n]}$, of the n -th waveguide segment, $\rho_s^{[n]}$, $\kappa_s^{[n]}$, the neck, $\rho_n^{[n]}$, $\kappa_n^{[n]}$, and the cavity, $\rho_c^{[n]}$, $\kappa_c^{[n]}$, of each resonator are given by⁴³:

$$\rho_i^{[n]} = - \frac{\rho_0 b_1^2 b_2^2}{4G_\rho^2 \sum_{k \in \mathbb{N}} \sum_{m \in \mathbb{N}} [\alpha_k^2 \beta_m^2 (\alpha_k^2 + \beta_m^2 - G_\rho^2)]^{-1}}, \quad (11)$$

$$\kappa_i^{[n]} = \frac{\kappa_0}{\gamma + \frac{4(\gamma-1)G_\rho^2}{b_1^2 b_2^2} \sum_{k \in \mathbb{N}} \sum_{m \in \mathbb{N}} [\alpha_k^2 \beta_m^2 (\alpha_k^2 + \beta_m^2 - G_\rho^2)]^{-1}}, \quad (12)$$

where $G_\rho = \sqrt{i\omega\rho_0/\eta}$ and $G_\kappa = \sqrt{i\omega\text{Pr}\rho_0/\eta}$, γ is the specific heat ratio of air, P_0 is the atmospheric pressure, Pr is the Prandtl number, η the dynamic viscosity, ρ_0 the air density, $\kappa_0 = \gamma P_0$ the air bulk modulus and ω the angular frequency. The constants $\alpha_k = 2(k + 1/2)\pi/b_1$ and $\beta_m = 2(m + 1/2)\pi/b_2$, and b_1 and b_2 are the dimensions of the duct. Thus, in the case of the n -th waveguide

segment $b_1 = h_1^{[n]}$, $b_2 = h_3^{[n]}$; in the case of the neck of the HR $b_1 = b_2 = w_n^{[n]}$; and in the case of the cavity of the HR $b_1 = w_{c,1}^{[n]}$ and $b_2 = w_{c,2}^{[n]}$. Finally, the effective wave number and acoustic impedance are given by $k_i^{[n]} = \omega \sqrt{\rho_i^{[n]}/\kappa_i^{[n]}}$ and $Z_i^{[n]} = \sqrt{\kappa_i^{[n]}\rho_i^{[n]}}/b_1 b_2$ respec-

tively.

E. Resonator impedance and end corrections

Using the effective parameters for the neck and cavity elements given by Eqs. (11-??), the impedance of a Helmholtz resonator, including a length correction due to the radiation can be written as⁴⁴:

$$Z_{\text{HR}}^n = -1 \frac{\cos(k_n^{[n]} l_n^n) \cos(k_c^n l_c^n) - Z_n^n k_n^{[n]} \Delta l^n \cos(k_n^{[n]} l_n^n) \sin(k_c^n l_c^n)/Z_c^n - Z_n^n \sin(k_n^{[n]} l_n^n) \sin(k_c^n l_c^n)/Z_c^n}{\sin(k_n^{[n]} l_n^n) \cos(k_c^n l_c^n)/Z_n^n - k_n^{[n]} \Delta l^n \sin(k_n^{[n]} l_n^n) \sin(k_c^n l_c^n)/Z_c^n + \cos(k_n^{[n]} l_n^n) \sin(k_c^n l_c^n)/Z_c^n}, \quad (13)$$

where l_n^n and l_c^n are the neck and cavity lengths, k_n^n and k_c^n are the effective wavenumbers and Z_n^n and Z_c^n effective characteristic impedance in the neck and cavities respectively, and Δl^n the correction length for the HRs. These correction lengths are deduced from the addition of two correction lengths $\Delta l^n = \Delta l_1^{[n]} + \Delta l_2^{[n]}$ as

$$\begin{aligned} \Delta l_1^{[n]} &= 0.41 \left[1 - 1.35 \frac{w_n^{[n]}}{w_c^{[n]}} + 0.31 \left(\frac{w_n^{[n]}}{w_c^{[n]}} \right)^3 \right] w_n^{[n]}, \quad (14) \\ \Delta l_2^{[n]} &= 0.41 \left[1 - 0.235 \frac{w_n^{[n]}}{w_s} - 1.32 \left(\frac{w_n^{[n]}}{w_s} \right)^2 \right. \\ &\quad \left. + 1.54 \left(\frac{w_n^{[n]}}{w_s} \right)^3 - 0.86 \left(\frac{w_n^{[n]}}{w_s} \right)^4 \right] w_n^{[n]}. \end{aligned}$$

The first length correction, $\Delta l_1^{[n]}$, is due to pressure radiation at the discontinuity from the neck duct to the cavity of the HR⁴⁵, while the second $\Delta l_2^{[n]}$ comes from the radiation at the discontinuity from the neck to the principal waveguide⁴⁶. This correction only depends on the radius of the waveguides, so it becomes important when the duct length is comparable to the radius.

Another important end correction arises due the radiation from the waveguides to the free air, and the radiation correction between waveguides segments due to change of section. On one hand, in the case of radiation to the free air, for the element $n = N$ in Eq.(2), the radiation correction is equivalent to the one of a periodic distribution of slits, that can be expressed as⁴⁷:

$$\Delta l_{\text{slit}}^{[N]} = \sigma h_3^{[N]} \sum_{m=1}^{\infty} \frac{\sin^2(m\pi\sigma)}{(m\pi\sigma)^3}, \quad (15)$$

with $\sigma = h_3^{[N]}/d_3$. Using these values, the radiation impedance of the N waveguide segment is $Z_{\Delta l_{\text{slit}}}^{[N]} = -i\omega \Delta l_{\text{slit}}^{[N]} \rho_0 / \phi_t^{[N]} S_0$ with $\phi_t^{[N]} = d_3/h_3^{[N]}$ and the unit

cell surface $S_0 = d_1 d_3$. On the other hand, for the radiation correction between slits due to change of section, i.e., from $n = 1$ to $n = N - 1$ in Eq.(2), the following end correction has been applied:

$$\Delta l_{\text{slit}}^{[n]} = 0.82 \left[1 - 1.35 \frac{h^{[n]}}{h^{[n-1]}} + 0.31 \left(\frac{h^{[n]}}{h^{[n-1]}} \right)^3 \right] h^{[n]}. \quad (16)$$

Using this value, the radiation impedance reads $Z_{\Delta l_{\text{slit}}}^{[n]} = -i\omega \Delta l_{\text{slit}}^{[n]} \rho_0 / \phi_t^{[n]} S_s^{[n]}$ with $\phi_t^{[n]} = h^{[n-1]}/h^{[n]}$ and $S_s^{[n]} = h_1^{[n]} h_3^{[n]}$.

F. Geometrical parameters

The geometrical parameters for the SAP ($N = 2$), corresponding to Fig. 2, are listed in Table I. The total structure thickness is $L = \sum a^{[n]} = 28.6$ mm, and its height and width of the unit cell are $d_3 = 148.1$ mm and $d_1 = 14.8$ mm respectively.

The geometrical parameters for the RTA ($N = 8$), corresponding to Fig. 4 (j-1), are listed in Table III. The total structure thickness is $L = 120$ mm, and its height and width of the unit cell are $d_3 = 48.7$ mm and $d_1 = 6.3$ mm respectively.

The geometrical parameters for the RTA ($N = 9$), corresponding to Fig. 5, are listed in Table III. The total structure thickness is $L = \sum a^{[n]} = 113$ mm, and its height and width of the unit cell are $d_3 = 48.7$ mm and $d_1 = 14.6$ mm respectively.

ACKNOWLEDGEMENTS

The authors acknowledge financial support from the Metaudible Project No. ANR-13-BS09-0003, cofunded by ANR and FRAE.

n	$a^{[n]}$ (mm)	$h_3^{[n]}$ (mm)	$h_1^{[n]}$ (mm)	$l_n^{[n]}$ (mm)	$l_c^{[n]}$ (mm)	$w_n^{[n]}$ (mm)	$w_{c,1}^{[n]}$ (mm)	$w_{c,2}^{[n]}$ (mm)
2	16.8	12.7	13.8	15.4	119.1	4.5	13.8	15.7
1	11.8	1.0	13.8	12.0	134.1	3.2	13.8	10.8

TABLE I. Geometrical parameters for the SAP ($N = 2$).

n	$a^{[n]}$ (mm)	$h_3^{[n]}$ (mm)	$h_1^{[n]}$ (mm)	$l_n^{[n]}$ (mm)	$l_c^{[n]}$ (mm)	$w_n^{[n]}$ (mm)	$w_{c,1}^{[n]}$ (mm)	$w_{c,2}^{[n]}$ (mm)
8	15.0	28.8	5.3	1.0	17.9	0.8	5.3	13.5
7	15.0	27.4	5.3	1.2	19.2	0.8	5.3	14.0
6	15.0	25.9	5.3	1.5	20.3	0.8	5.3	14.0
5	15.0	24.5	5.3	1.8	21.3	0.8	5.3	14.0
4	15.0	23.1	5.3	2.2	22.4	0.7	5.3	14.0
3	15.0	22.1	5.3	2.6	23.0	0.7	5.3	14.0
2	15.0	21.9	5.3	3.2	22.6	0.7	5.3	14.0
1	15.0	0.8	0.8	5.7	41.2	0.7	5.3	13.5

TABLE II. Geometrical parameters for the RTA ($N = 8$).**AUTHOR CONTRIBUTIONS STATEMENT**

N.J., V.R.G. and J.P.G. conducted the theoretical modelling and numerical experiment; N.J., V.R.G. J.P.G. and

V.P. wrote the manuscript. All authors reviewed the manuscript.

Competing financial interests The authors declare no competing financial interests.

n	$a^{[n]}$ (mm)	$h_3^{[n]}$ (mm)	$h_1^{[n]}$ (mm)	$l_n^{[n]}$ (mm)	$l_c^{[n]}$ (mm)	$w_n^{[n]}$ (mm)	$w_{c,1}^{[n]}$ (mm)	$w_{c,2}^{[n]}$ (mm)
9	7.9	25.6	14.0	1.1	21.4	1.2	14.0	7.2
8	9.5	24.2	14.0	1.0	22.8	1.2	14.0	9.0
7	11.0	22.8	14.0	1.7	23.6	1.4	14.0	10.6
6	12.6	21.6	14.0	0.7	25.9	1.0	14.0	12.0
5	14.1	20.2	14.0	1.5	26.5	1.2	14.0	13.6
4	15.7	18.8	14.0	1.1	28.3	1.0	14.0	15.2
3	17.3	17.4	14.0	1.6	29.2	1.0	14.0	16.8
2	18.8	16.0	14.0	1.1	31.2	0.8	14.0	18.4
1	6.4	1.0	1.0	3.0	44.7	0.6	14.0	5.6

TABLE III. Geometrical parameters for the RTA ($N = 9$).

SCIENTIFIC REPORTS

OPEN

Metadiffusers: Deep-subwavelength sound diffusers

Noé Jiménez¹, Trevor J. Cox², Vicent Romero-García¹ & Jean-Philippe Groby¹

Received: 2 March 2017

Accepted: 7 June 2017

Published online: 14 July 2017

We present deep-subwavelength diffusing surfaces based on acoustic metamaterials, namely *metadiffusers*. These sound diffusers are rigidly backed slotted panels, with each slit being loaded by an array of Helmholtz resonators. Strong dispersion is produced in the slits and slow sound conditions are induced. Thus, the effective thickness of the panel is lengthened introducing its quarter wavelength resonance in the deep-subwavelength regime. By tuning the geometry of the metamaterial, the reflection coefficient of the panel can be tailored to obtain either a custom reflection phase, moderate or even perfect absorption. Using these concepts, we present ultra-thin diffusers where the geometry of the metadiffuser has been tuned to obtain surfaces with spatially dependent reflection coefficients having uniform magnitude Fourier transforms. Various designs are presented where, quadratic residue, primitive root and ternary sequence diffusers are mimicked by metadiffusers whose thickness are 1/46 to 1/20 times the design wavelength, i.e., between about a twentieth and a tenth of the thickness of traditional designs. Finally, a broadband metadiffuser panel of 3 cm thick was designed using optimization methods for frequencies ranging from 250 Hz to 2 kHz.

There are many applications in physics and electrical engineering for objects and surfaces that disperse waves. To take a few examples, such scatterers can be applied to sonar and radar camouflage, electromagnetic reverberation chambers and reducing unwanted ultrasound reflections from surgical equipment. To study how metamaterials might create scattering, this study has focussed on sound diffusers applied in room acoustics. This allows the work to build on a large body of knowledge concerning how such surfaces are measured, predicted and designed. Common wall treatments are made of flat panels, leading to specular sound reflections. In critical environments such as auditoria, professional broadcast and recording control rooms, recording studios or conference rooms, such reflections can decrease sound quality due to echoes or cause sound coloration¹. Even when these specular reflections are damped by absorption, the sound field inside a room may be non-diffuse, affecting the quality of the listening. In these situations, diffusers can often help by evenly spreading the acoustic energy in both space and time. Specialist diffusers are panels whose scattering function is uniform, so the reflected waves are dispersed in many different directions.

The far-field polar pressure distribution can characterize the performance of a diffuser. For a finite panel of side $2b$, the far-field polar pressure distribution, $p_s(\theta)$, of a locally-reacting reflecting surface with a spatially dependent reflection coefficient, $R(x)$, can be calculated using the Fraunhofer integral as ref. 2

$$p_s(\theta) = \int_{-b}^b R(x) e^{jk_0 x \sin \theta} dx, \quad (1)$$

where θ is the polar angle and k_0 is the wavenumber in air. Note the scattered pressure in the far-field is essentially a Fourier transform of the reflected field along the surface. Therefore, structures whose reflection coefficient distributions present a uniform magnitude Fourier transform present good sound diffusion properties³.

The generation of spatially dependent reflective surfaces have been achieved in the past by using phase grating diffusers, also known as Schroeder's diffusers after its first proposal³ using maximum length sequences. The most used configurations are rigid-backed slotted panels where each well acts as a quarter wavelength resonator^{4,5}, as shown in Fig. 1(a). Due to the different resonance frequency of each well, the phase of the reflection coefficient locally depends on the wavenumber and depth of each well. Thus, one approach is to set the spatially-dependent reflection coefficient according to a number sequence that presents a uniform magnitude Fourier spectrum at the design frequency. In this case, a periodic array of the panel presents grating lobes with the same pressure magnitude in the far field at the design frequency.

¹Laboratoire d'Acoustique de l'Université du Maine - CNRS UMR 6613, Le Mans, 72000, France. ²Acoustics Research Centre, University of Salford, Salford, M5 4WT, United Kingdom. Correspondence and requests for materials should be addressed to N.J. (email: noe.jimenez@univ-lemans.fr)

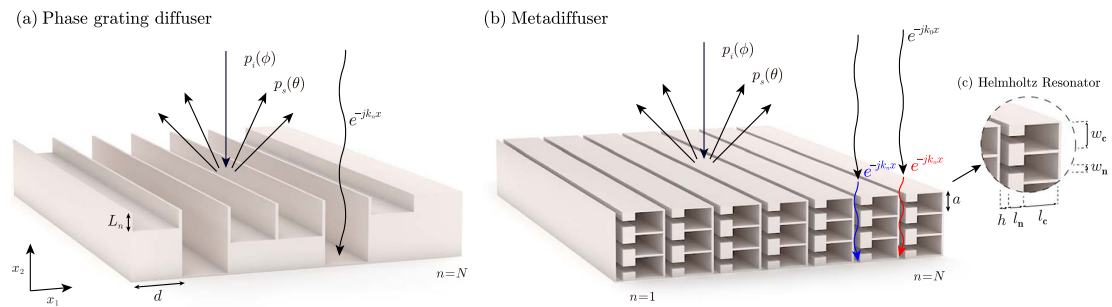


Figure 1. (a) Scheme of a QRD Schroeder diffuser composed by $N=7$ wells or quarter wavelength resonators. (b) Metadiffuser composed of $N=7$ sub-wavelength slits, each of them loaded by $M=3$ Helmholtz resonators, with slightly different geometry. (c) Detail of a slit of the metadiffuser showing the geometrical parameters of the cavity of a HR (w_c and l_c) and its neck (w_n and l_n).

The maximum phase shift of the reflection coefficient achieved by a single well in a phase grating diffuser occurs at its quarter wavelength resonance, i.e., $L = c_0/4f$ where f is the frequency, L is the depth of the well and c_0 is the speed of sound in air. Therefore, a limitation of Schroeder diffusers is that the depth becomes large for low design frequencies. This results in thick and heavy panels, limiting the use of phase grating diffusers for low-frequencies where the wavelength of sound in air is of the order of several meters. In the context of smart building design and sustainable building, leading-edge technologies can be applied to optimize space and design lightweight materials, improving the performance of the acoustic solutions using less resources.

Various approaches have been carried in the past to reduce the total thickness of the panels. As the wells of Schroeder diffusers present different lengths, well folding strategies have been proposed^{6–8} to minimize the unused space. At high frequencies the sound does not bend through the folded wells and so care in design is needed. Using well-folding the total thickness of a diffuser can only be reduced to about half the depth of a standard Schroeder diffuser. Other approaches include the use of single Helmholtz resonators instead of quarter wavelength resonators to construct the phase grating diffuser. This strategy was first reported by placing perforated sheets at the front of a Schroeder diffuser⁹. The added-mass effect reduces the resonance frequency of the well and consequently the thickness can be reduced. In this system losses are inevitably introduced and therefore, some of these devices were proposed as sound absorbers¹⁰. Using “T” shaped wells, 2 dimensional resonators can be designed and the full structure can be optimized to extend its low frequency response¹. Flat panels have been also proposed using hybrid surfaces that combine patches of absorption and reflection¹¹, but their performance is limited because of weak edge diffraction. Other approaches include the use of active surfaces¹², but their use is limited due to cost. Recently, sonic crystals (SC) were used to construct acoustic diffusers¹³. A SC is a periodic arrangement of acoustic scatters, typically rigid bars embedded in air. The periodicity leads to a modification of the dispersion relations and propagation through these structures becomes strongly dispersive and anisotropic. The diffusion was achieved at low frequencies of a bi-periodic SC mainly caused by the internal Fabry-Pérot resonances of the structure. The main drawback of this promising approach is the lack of simple and/or analytical methods to design these complex structures. Therefore, optimization of these structures have been proposed¹⁴, but the lack of fast analytical models make the design tedious and, until now, the inherent thermo-viscous losses have not been accounted for in these designs.

Local resonances have also been exploited to introduce strong dispersion in acoustic metamaterials¹⁵. In these structures the phase speed can be strongly modified and materials with exotic properties as either negative effective bulk modulus or negative mass density^{16,17} can be designed. Metamaterials have been widely used to design acoustic absorbers as metaporous materials^{18–21}, dead-end porosity materials^{22,23} or absorbing resonant metamaterials composed by membrane-type resonators^{17,24–26}, quarter-wavelength resonators (QWRs)^{23,27–29} and Helmholtz resonators (HRs)^{26,30–32}. These last types of metamaterials^{23,27,28,31,32} make use of strong dispersion giving rise to slow-sound propagation inside the material. Using slow sound results in a decrease of the cavity resonance frequency and, hence, the structure thickness can be drastically reduced to the deep-subwavelength regime³¹. Moreover, these structures can fulfil the critical coupling conditions²⁶, having their impedance matched with the exterior medium and resulting in perfect absorption (PA), as recently demonstrated for panels using slow sound and QWRs²⁸ or HRs³¹.

In this paper, we present deep-subwavelength diffusers based on acoustic metamaterials to reduce the thickness of Schroeder diffusers. The system works as follows: first, we consider a rigid panel of finite length with a set of N slits. Second, we modify the dispersion relations inside each slit by loading one of their walls with a set of HRs, as shown in Fig. 1(b). The sound propagation in each slit becomes strongly dispersive and the sound speed inside it, c_p , can be drastically reduced. Each slit behaves effectively as a deep-subwavelength resonator and, therefore, the effective depth of the slits can be strongly reduced as $L = c_p/4f$ holds. By tuning the geometry of the HRs and the thickness of the slits, the dispersion relations inside each slit can be modified. As a result the phase of the reflection coefficient can be tailored, e.g., to those of an Schroeder phase grating diffuser. Furthermore, by tuning the thermo-viscous losses, which are inherent in the HRs and in the narrow slits, the leakage of the structure can

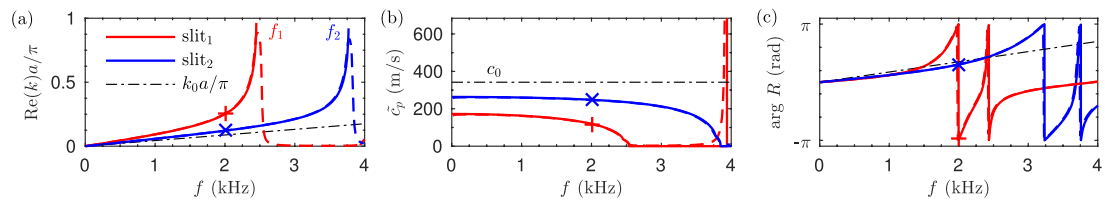


Figure 2. (a) Dispersion relation inside the (blue) first and (red) second slits of a metadiffuser for the lossless case (continuous lines) and accounting for the thermo-viscous losses (dashed lines), and wavenumber in air (dashed-dotted). The resonance frequencies of the HR are shown as f_1 and f_2 . (b) Corresponding phase speed. (c) Phase of the reflection coefficient for each individual slit.

n	s_n	h (mm)	l_n (mm)	l_c (mm)	w_n (mm)	w_c (mm)
1	1.0	14.7	13.0	16.4	6.2	9.0
2	4.0	30.9	9.1	4.3	3.5	9.0
3	4.0	30.9	9.1	4.3	3.5	9.0
4	1.0	15.7	13.3	17.0	6.3	9.0
5	0.0	20.3	18.0	20.7	3.2	9.0

Table 1. Geometrical parameters of the QR-metadiffuser.

be compensated by the intrinsic losses of the system and PA can be obtained. Thus, the magnitude of the reflection coefficient can be also tuned, and the behaviour of the slits ranges from perfect reflectors to perfect absorbers. Perfect absorbing slits allows the construct of ternary sequence diffusers³³ for low frequencies.

Results

Slow sound and dispersion relations in the slits. We consider a 2D flat panel composed of a periodic distribution of unit cells. As shown in Fig. 1(b,c), the unit cell is composed by N slits of width h separated a distance d and distributed in the x_1 direction. Each slit is loaded by M HRs separated a distance a , each one composed of a squared cross-section neck and a cavity with length and width dimensions l_n and w_n , l_c and w_c respectively. The propagation inside each slit was calculated using the transfer matrix method (TMM) and the finite element method (FEM) including the thermoviscous losses by means of its effective parameters (see methods section). The methods and unit cell used in this work are the same as in refs 31 and 32. In those works, the TMM and FEM using the effective parameters were accurately validated experimentally to model the thermoviscous losses of metamaterials using a set of $N=13$ by $M=1$ HRs³¹ and $N=3$ by $M=10$ HRs³².

Figure 2(a) shows the dispersion relations inside two different slits, $n=1$ and $n=2$, obtained by using $M=2$ HR with the geometrical parameters listed in Table 1. First, above the resonance frequency of the HRs, f_m , a band gap is generated. Below the resonance frequency of the HRs a dispersive band is observed and the wavenumber is increased with respect to the wavenumber in air. In this regime, slow sound conditions are produced, as shown in Fig. 2(b), i.e., the phase speed inside the slits is strongly reduced. The phase of the reflection coefficient produced by each slit is shown in Fig. 2(c). We can see that for some frequencies the phase of the reflection coefficient of both slits (blue and red lines) is strongly modified when compared to the reflection phase of a slit without HRs (dashed line). At 2 kHz, the 1st slit (red curve) reacts inverting the phase of the incoming wave, while for the 2nd slit (blue curve) this occurs at 3.2 kHz. In this way, by tuning the geometry a specific phase profile can be tailored, while the total thickness of the panel can be greatly reduced when compared with a quarter wavelength resonator of length L . By using these features, we show in this article that the phase profile of Schroeder and ternary sequence diffusers can be mimicked by a sub-wavelength metadiffuser in a given frequency band. Therefore by tuning the geometry of a metadiffuser we can maximize sound diffusion in a broad frequency band for room acoustics applications using a deep sub-wavelength panel.

Quadratic residue metadiffusers. The first numerical sequence mimicked is the one used in quadratic residue diffusers (QRD). The sequence is given by $s_n = n^2 \bmod N$, where mod is the least non-negative remainder of the prime number N . If the phase grating diffuser is based on quarter wavelength resonators (wells), the depth of the wells is given by $L_n = s_n \lambda_0 / 2N$, where λ_0 is the design wavelength. Here, we use optimization methods, e.g., sequential quadratic programming³⁴, to tune the geometry of the metamaterial so the spatially-dependent reflection coefficient matched between the QR-metadiffuser and the QRD only at 2000 Hz. A QRD with $N=5$ QRD, a total thickness of $L=27.4$ cm and side $Nd=35$ cm was designed for a frequency of 500 Hz. Due to the small lateral size of the panel, the response was evaluated at 2000 Hz considering 6 repetitions of the unit cell in order to clearly generate the characteristic N diffraction grating lobes of the QRD in the far-field. Figure 3(a,b) shows the phase and magnitude of the reflection coefficient along the surface the ideal QRD and a QR-metadiffuser of $L=2$ cm thickness and $M=2$ HRs of same lateral dimensions. The geometrical parameters for the metadiffuser are listed in Table 1 and a scheme of the panel is shown in Fig. 3(c). Perfect agreement is found between the reflection coefficients of the QR-metadiffuser and the target phase grating QRD. Figure 3(g) shows the far-field calculation at

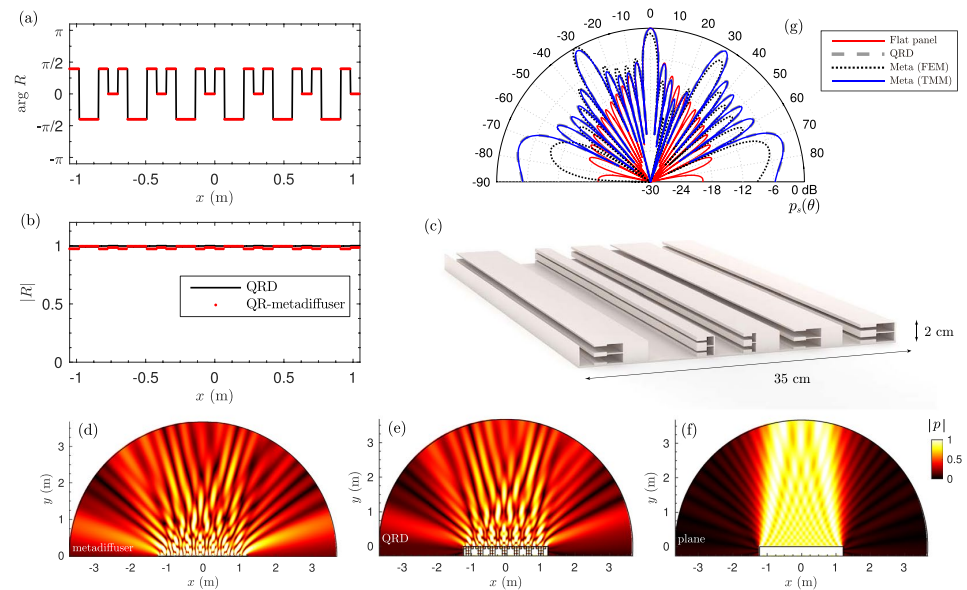


Figure 3. (a) Phase and (b) magnitude of the spatially-dependent reflection coefficient of a QRD (black line) and the QR-metadiffuser (red dotted). (c) Scaled scheme of the QR-metadiffuser with $N=5$ and $M=2$. (d) Near field pressure distribution at 2 kHz of QR-metadiffuser with thickness $L=2$ cm (e) phase grating QRD of thickness $L=27.4$ cm and (f) flat plane reflector. (g) Far-field polar distribution of the QR-metadiffuser obtained by TMM (continuous blue) and FEM (dotted black), the reference QRD (dashed-grey), and a plane reflector with same width of the diffusers (continuous red).

2000 Hz using Eq. (1) for both structures. Excellent agreement is obtained between the polar responses using the TMM. To validate the design a full-wave numerical solution using the finite element method (FEM) and accounting for the thermo-viscous losses is also provided. The FEM numerical solution agrees with the theoretical prediction, although small discrepancies can be observed. They are caused first because the radiation corrections used in the TMM are only approximate, and, second, because the evanescent coupling between near slits in the TMM is not considered while it is implicitly included in the FEM simulations. The near field pressure distributions are shown in Fig. 3(d–f) for the QR-metadiffuser, the QRD and a reference flat surface of the same width, respectively. Excellent agreement is observed between both diffusers, where it is clear how the field is scattered in other directions rather than specular. The presented QR-metadiffuser is 17.1 times thinner than the QRD (34 times smaller than the QRD design wavelength (500 Hz) and 8.5 times smaller than the evaluation wavelength (2000 Hz).

Primitive root metadiffusers. The second numerical sequence presented here is the primitive root sequence, given by $s_n = r^n \bmod P$, where P is a prime number and r is the primitive root of P . The primitive root sequence have $N = P - 1$ different values. A primitive root diffuser (PRD) is constructed using a set of N wells with depths $L_n = s_n \lambda_0 / 2N$. The scattered field by these diffusers presents a notch at specular directions at multiples of the design frequency⁴. Figure 4(a,b) show both the phase and magnitude of the spatially-dependent reflection coefficient of a $P=7$ phase grating PRD of thickness $L=17.1$ cm with $d=7$ cm, and for a PR-metadiffuser of $L=3.5$ cm and $M=1$ HR with the same lateral dimensions. Excellent agreement is found between both responses. The corresponding geometrical parameters of the PR-metadiffuser are listed in Table 2, while a scaled scheme is drawn in Fig. 4(c). Figure 4(d–f) show the near field corresponding to the PR-metadiffuser, the PRD, and the reference plane surface. The characteristic notch is observed at normal reflection angle, i.e., $\theta=0$. Note, because the structures are not symmetric, neither is the field. The far-field is presented in Fig. 4(g), where good agreement is found between the theory and the full-wave numerical solutions. Both panels produce the same scattering, but the thickness of the PR-metadiffuser is around 10 times thinner than the phase grating PRD (20 times smaller than the design wavelength).

Absorption in QR- and PR-metadiffusers. These metamaterials show high flexibility to tailor their reflection response to a specific spatial function. However, the presented QR- and PR-metadiffusers are tuned to fit the desired phase response only at a single frequency. In order to quantify the frequency dependent performance of a diffusing panel, the normalized diffusion coefficient, δ_n , can be evaluated from the far-field polar responses (see methods section). This parameter measures the uniformity of the scattering pattern, i.e., a high value indicates that there is no privileged reflection direction, zero indicates that the energy is reflected only in one direction. The frequency dependent diffusion coefficient is shown in Fig. 5(a,b) for the QR- and PR- metadiffusers respectively. Although the phase of the reflection coefficient of the metadiffusers does not follow the QRD and PRD

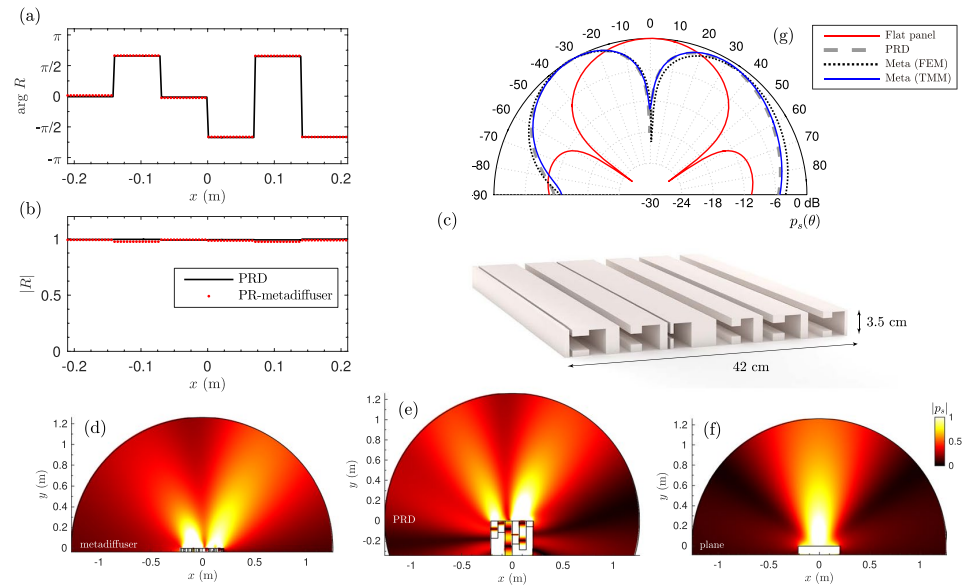


Figure 4. (a) Phase and (b) magnitude of the spatially-dependent reflection coefficient of a PRD (black line) and the PR-metadiffuser (red dotted). (c) Scaled scheme of the metadiffuser using $N=6$ and $M=1$. (d) Near field pressure distribution at 1 kHz of a PR-metadiffuser with prime number $P=7$ and thickness $L=3.5$ cm (e) phase grating QRD of thickness $L=17.1$ cm and (f) reference flat plane reflector. (g) Far-field polar distribution of the PR-metadiffuser obtained by TMM (continuous blue) and FEM (dotted black), the reference PRD (dashed-grey) and a plane reflector with same width of the diffusers (continuous red).

n	s_n	h (mm)	l_n (mm)	l_c (mm)	w_n (mm)	w_c (mm)
1	1.5	0.5	26.1	23.4	19.4	34.0
2	1.0	14.4	16.7	26.0	14.7	34.0
3	3.0	1.1	5.7	26.2	7.3	34.0
4	2.0	22.0	14.3	19.1	13.9	34.0
5	2.5	14.6	18.6	24.7	14.7	34.0
6	0.5	22.4	14.9	19.9	18.3	34.0

Table 2. Geometrical parameters of the PR-metadiffuser.

design for all frequencies, the surface impedance still varies spatially and creates dispersion. Note, the magnitude of the reflection coefficient is strongly spatially dependent. Compared with the corresponding Schroeder’s diffusers, the magnitude of the diffusion coefficient is of the same order at the design frequency. In the case of the QR-metadiffuser a broadband diffusion is observed when compared with the PR-metadiffuser. This broadband diffusion is mainly achieved by the multiple collective modes of the HRs³² produced by a higher M value.

In all the previous results, thermo-viscous losses were accounted for in the ducts that comprise the meta-material. The acoustic absorption due to these thermo-viscous losses is shown in Fig. 5(c,d) for the QR- and PR-metadiffusers respectively. It can be observed that for some frequencies, peaks of absorption are generated (blue curves in Fig. 5(c,d)). Moreover, if the absorption of each individual slit is calculated, very sharp peaks of absorption appear at selected frequencies, as those marked by the arrows (grey curves in Fig. 5(c,d)). For the case of the QR-metadiffuser, at $f=2270$ Hz the reflection coefficient vanishes at the $n=1$ slit because it is impedance matched with the exterior air and the critical coupling condition fulfils. The complex frequency plane representation of the eigenvalues of the scattering matrix, i.e., the reflection coefficient, is shown in the insets for the slits $n=5$ and $n=1$. The different resonances can be identified with zero-pole pairs in the complex frequency plane. In the case of $n=5$, the zeros of the eigenvalue of the scattering matrix are close to the real frequency axis and, therefore, it produces a peak of absorption. In the case of $n=1$ slit, we can observe that the eigenvalues of the scattering matrix present a zero which is exactly located on the real frequency axis. Therefore, at this particular frequency perfect absorption is achieved. It is worth noting here that these structures were first proposed as perfect acoustic absorbers³¹. A similar behaviour is observed for the case of the PRD diffuser at $f=1510$ Hz, but in this case, imperfect absorption is achieved as also shown in the inset of Fig. 5(d) where the zero of the eigenvalues of the scattering matrix is not exactly on the real frequency axis. Thus, in this case, the critical coupling conditions are not fulfilled.

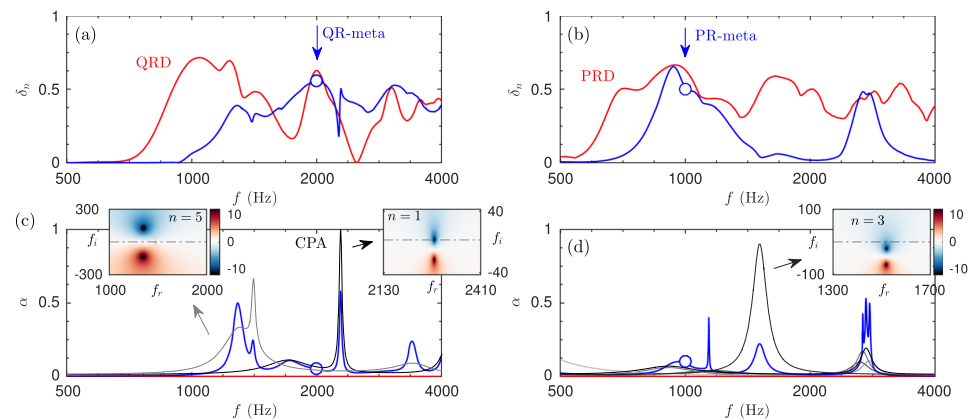


Figure 5. (a) Diffusion coefficient of the QR-metadiffuser (blue) optimized at 2000 Hz (marker) and a reference QRD (red). (b) Diffusion coefficient of the PR-metadiffuser (blue) optimized at 2000 Hz (marker) and a reference PRD (red). (c) Corresponding absorption for the QRD case, where the grey lines shows the absorption of individual slits $n = 1$ and $n = 5$. For these slits, the insets show the complex frequency representation²⁶ of the reflection coefficient ($\log|R(f_r, f_i)|^2$), where $f_r = \text{Re}(f)$ and $f_i = \text{Im}(f)$. (e) Corresponding absorption for the PRD where the complex frequency representation of the reflection coefficient is shown for the individual slit $n = 1$ in the inset.

s_n	h (mm)	l_n (mm)	l_c (mm)	w_n (mm)	w_c (mm)
1	0	—	—	—	—
-1	8.5	1.8	88.7	8.4	29.0
0	10.0	69.4	10.2	2.4	29.0

Table 3. Geometrical parameters of the PA-metadiffuser.

Hybrid metadiffusers. The induced absorption can be used to obtain diffusion. Perfect absorption is mandatory to design diffusers based on index³⁵, ternary or quadriphase³³ sequences. The family of ternary sequence diffusers³³ are based on numerical sequences composed by 3 possible states, $[-1, 0, 1]$, organized in such a way that the magnitude of its Fourier spectrum is uniform. Schroeder's diffusers based on these sequences use phase gratings (quarter wavelength resonators) to obtain the inverted phase reflection, $[-1]$ state, flat surfaces for the in-phase reflection, $[1]$ state, and high absorptive materials for the zeros of the sequence, $[0]$ state. This can be achieved by filling a well with porous absorbent such as mineral wool. Even when these devices are constructed with long wells, the main limitation is that the reflection does not vanish at low and medium frequencies, due to the poor impedance matching of the rigidly-backed porous material with the air: the porous material enters in the viscous frequency regime and inside it a diffusion-dominated wave equation is satisfied.

The use of metadiffusers offers the possibility of accurately creating both the inverted phase and the zeros of ternary sequences: the geometry of the system can be tuned to obtain sub-wavelength wells with inverted phase and perfect absorbers (PA)³¹. In addition, the optimization process is simplified because only 2 different sub-wavelength wells are required with independence of the length of the sequence. A PA-metadiffuser was designed using $N = 8$ and $M = 1$. The phase inverted and perfect absorbers have been obtained by tuning the geometry of the metamaterial using optimization methods with the constraint of $L < 3$ cm, i.e., a panel thickness 23 times smaller than the wavelength at $f = 500$ Hz. The retrieved parameters are listed in Table 3 and a scaled scheme of the metadiffuser is shown in Fig. 6(c). Figure 6(a,b) show the sequence, s_n , used to design a ternary sequence diffusers and the corresponding phase and magnitude of the reflection coefficient. Small discrepancies can be observed between the ideal and the calculated spatially dependent reflection coefficient, mainly caused by the inherent absorption of the phase-inverter slits. When the metadiffuser becomes deep-subwavelength, the small ducts that compose the metamaterial lead to unavoidable thermoviscous losses, mainly localized at the neck of the HRs. In contrast, the perfect absorbing slits are accurately obtained. Figure 6(d) shows the frequency dependent absorption of each slit and the total absorption produced by the metadiffuser. The eigenvalues of the scattering matrix in the complex frequency plane are shown in the inset for the PA slit. It can be observed that the eigenvalues of the scattering matrix present a zero that is located exactly on the real frequency axis. Under these conditions the material is critically coupled to the exterior medium and at this particular frequency sound is perfectly absorbed. Figure 6(f) shows the far-field pressure distribution of an ideal ternary sequence diffuser, a PA-metadiffuser using TMM and its corresponding FEM simulation accounting for the thermo-viscous losses. The characteristic notch in the polar response at the specular direction is obtained because the magnitude of the first component of the Fourier spectrum of the used ternary sequence is zero. Only small discrepancies are observed caused by the non-perfect phase inverting slits due to the thermo-viscous losses that appear in this

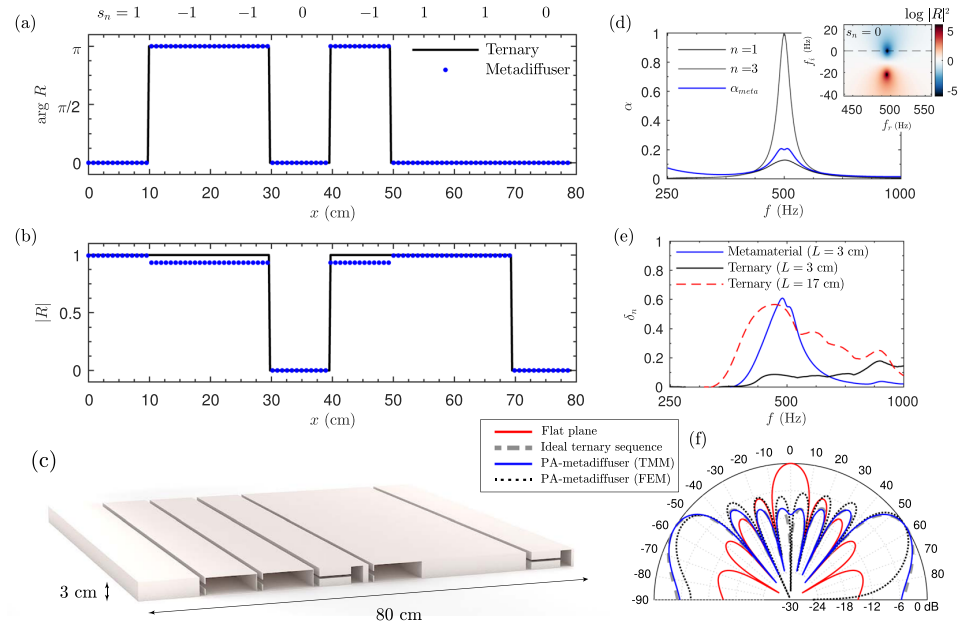


Figure 6. (a) Phase and (b) magnitude of the spatially dependent reflection coefficient for an ideal ternary sequence diffuser (black) and a PA-metadiffuser (blue dots). The ternary sequence used, s_n , is shown on top. (c) Scaled scheme of the geometry of the hybrid PA-metadiffuser. (d) Frequency dependent absorption for the total structure (blue curve) and individual slits (black curves). The inset shows the complex frequency plane representation of the reflection coefficient for the perfect absorber slits, $s_n = 0$. (e) Frequency dependent diffusion for the PA-metadiffuser of $L = 3$ cm (blue), a ternary sequence diffuser using phase gratings of $L = 17$ cm (dashed red) and ternary sequence diffuser using phase gratings of $L = 3$ cm (black). (f) Far field polar response at 500 Hz of a ternary sequence with $N = 8$ wells (dashed-grey), the PA-metadiffuser obtained by TMM (continuous black) and FEM (dotted black), and a plane reflector of the same width as the diffusers (red line).

n	1	2	3	4	5	6	7	8	9	10	11
h (mm)	5.7	4.9	7.7	82.9	48.4	74.9	20.0	6.6	76.2	29.5	7.6
l_n (mm)	16.3	7.3	37.1	0.0	35.3	22.1	14.7	0.1	0.0	0.1	4.8
l_c (mm)	97.1	106.8	74.2	36.0	35.3	22.1	84.3	112.2	42.7	89.4	106.5
w_n (mm)	6.7	6.5	10.0	29.0	29.0	29.0	14.0	9.5	29.0	27.6	6.2
w_c (mm)	29.0	29.0	29.0	29.0	29.0	29.0	29.0	29.0	29.0	29.0	29.0

Table 4. Geometrical parameters used for the broadband metadiffuser using N different slits.

deep-subwavelength thickness structure. The frequency dependent diffusion coefficient is shown in Fig. 6(e). Due to the fact that the metamaterial only present PA at the design frequency, the diffusion coefficient presents a high value only in a narrow frequency band. Note the corresponding correlation scattering coefficient¹ is almost one, reaching a value of $\sigma_c = 0.996$, indicating that specular reflection almost vanishes. Using PA other sequences with flat Fourier spectrum can also be mimicked, including binary maximum length sequences³ or complex Legendre sequences based on the index function³⁵.

Broadband optimal metadiffusers. To design a metadiffuser useful for room acoustics, its diffusion must be broad in frequency. Thus, we extended the bandwidth of the optimization procedure, where the cost function to minimize was $\varepsilon = 1 - \int_{f_{low}}^{f_{high}} \delta_n df$. In particular, we look for deep-subwavelength thickness metadiffusers that present maximum normalized diffusion coefficient in the frequency range from $f_{low} = 250$ Hz to $f_{high} = 2000$ Hz. Here, we used a set of $N = 11$ slits separated by $d = 12$ cm, and constrained the thickness of the panel to $L = 3$ cm. The obtained geometrical parameters are listed in Table 4. Here we used square cross-section HRs. Figure 7(a) shows the scheme of the metadiffuser with the retrieved geometry. First, the polar responses at two frequencies, 300 and 2000 Hz are shown in Fig. 7(b,c). The maximization of the diffusion coefficient implies that the polar responses are uniform. In addition, we show the angular dependence of the near field at shorter distances, e.g., at 1 and 5 m. Due to the lateral dimension of the structure is 1.32 m, Eq. (1) is not accurate at distances much shorter than the Rayleigh distance. However, although the near field does not exactly follow the polar distribution given by Eq. (1), the structure scatters the waves uniformly in broad range of angles when compared with a flat plane of

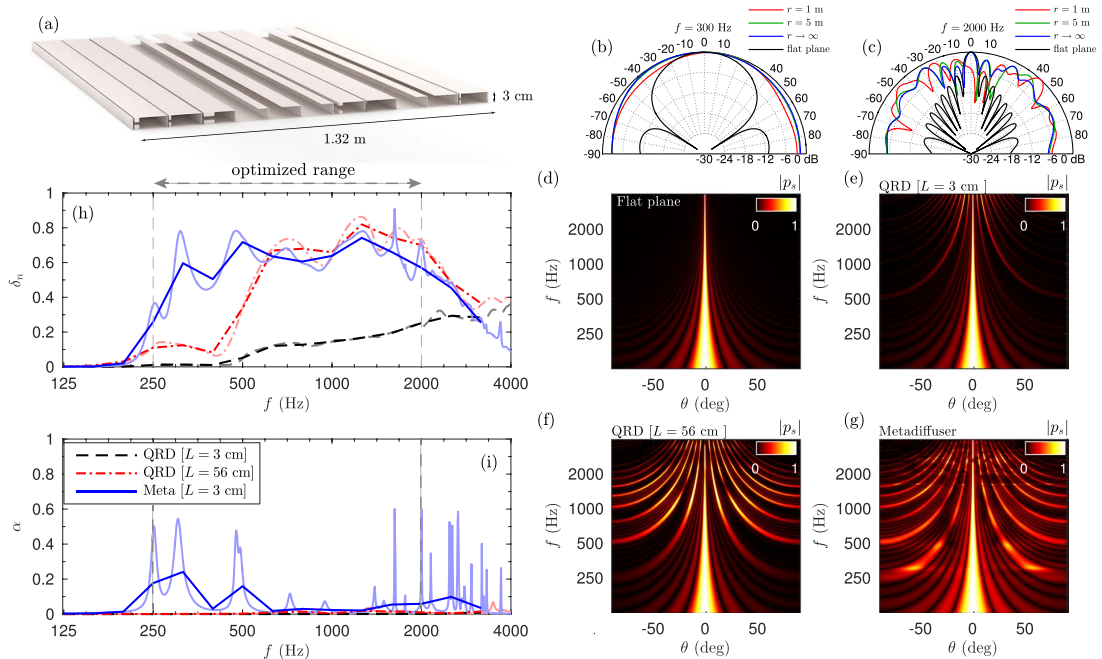


Figure 7. Far field polar response as a function of the frequency for (a) reference flat plane, (b) $N = 11$ QRD panel with a total thickness of 3 cm, (c) QRD panel with total thickness of 56 cm and (d) optimized metadiffuser thickness of 3 cm. (e) Normalized diffusion coefficient of the 3 cm QRD (dashed black), 32 cm QRD (dashed-dotted red) and optimized metadiffuser using TMM (blue) integrated in third of octaves. The third octave integration is shown in thick lines according to ISO 17497-2:2012⁴³. (f) Corresponding absorption.

same dimensions. See Supplementary material for details about the near field produced by this structure. Figure 7(d–g) show the frequency dependent polar responses in the far field for a reference flat plane with the same width than the metadiffuser, a thick QRD with a design frequency of 250 Hz ($L_{\text{QRD}} = 56$ cm), a thin QRD with the same thickness of the metadiffuser $L_{\text{QRD,thin}} = 3$ cm, and the optimized metadiffuser, respectively. Here, we calculated the polar responses using 6 repetitions of the panel to clearly observe the diffraction grating lobes. First, the scattering of the thin QRD, Fig. 7(e), is almost the same as a flat plane, Fig. 7(d). It only starts to scatter waves at different angles above 2 kHz. Second, the deep wells that compose the thick QRD, Fig. 7(f), resonate near their quarter-wavelength resonances at lower frequencies and, therefore, the reflection coefficient follows the QR sequence and the panel scatters sound waves into oblique angles. Finally, the optimized metadiffuser, Fig. 7(g), also shows strong grating lobes, but, in addition, at medium and high frequencies energy is spread in other directions at low frequencies, e.g., between 250 and 500 Hz.

The normalized diffusion coefficient shown in Fig. 7(h) quantifies this behaviour. It is observed that over the optimized range the diffusion coefficient of the metadiffuser takes values with a mean value of about $\delta_n = 0.65$, with peaks of $\delta_n = 0.9$. When compared to the thick QRD, its frequency band is extended to one octave below. The corresponding absorption is shown in Fig. 7(f). Here, the wide slits that form the QRD produce almost no losses, while the thermo-viscous losses produced in the narrow ducts that comprise the ultra-flat metamaterial lead to some peaks of absorption at the resonance of the cavities. These losses can be reduced if the thickness of the panel is increased, but here we presented a structure whose thickness is 46 times smaller than the wavelength. It is worth noting here that the size of some of the neck of the resonators is almost the same as their cavities, as can be observed in Fig. 7(a). In these cases the resonator acts as a coiled QWR and the losses in these wide ducts are decreased. The resonance frequency of these QWR is higher than the corresponding HRs, contributing to the high frequency diffusion, while, in contrast, the HRs introduce spatial changes on the reflection coefficient at low frequencies. Moreover, the position of the low frequency absorption peaks can be engineered to solve other typical problems in room acoustics, as placing them at the resonant modes of small control rooms to produce a flatter spectral response, or reduce sound coloration in the reverberation. This can be achieved using multi-objective optimization techniques.

Discussion

Metadiffusers, a novel design of locally reacting surfaces with tailored acoustic scattering was presented. These new structures are based on metamaterials comprising a slotted panel, with the slits loaded by a set of Helmholtz resonators. The propagation inside the metamaterial presents strong dispersion and the sound speed can be significantly reduced so that each slit effectively behaves as a deep-subwavelength resonator. Thus, by tuning the material geometry, the dispersion of acoustic waves in the slits is modified and the spatially-dependent reflection

coefficient can be tailored to specific functions with uniform magnitude Fourier transform. In these conditions, the grating lobes produced by a periodic arrangement of the panel all have the same energy. The acoustic energy can be scattered in other directions than specular. Different designs were presented based on number-theoretical sequences as quadratic residue and primary root sequences (QR and PR-metadiffusers). Moreover, using the concept of critical coupling, sub-wavelength perfect absorbers were introduced to accurately model ternary sequence metadiffusers (PA-metadiffusers). Finally, it was shown that the structures can be optimized to work in a broad frequency range covering 3 octaves. In particular, we presented a diffuser of 3 cm thickness working from 250 to 2000 Hz, demonstrating the potential of the metadiffusers to be used in critical listening environments due to their deep-subwavelength nature: the thickness of the panels was 1/46 to 1/20 times the design wavelength, i.e., between about a twentieth and a tenth of the thickness of traditional designs. In the context of smart building design and sustainability, metadiffusers can be used to save space and to produce lightweight materials, improving the performance of the acoustic solutions using less resources. Moreover, the proposed designs have the potential to meet the aesthetic requirements that are mandatory for modern auditoria design.

While the focus of the study has been sound diffusers for rooms, dispersed, broadband reflections are of interest beyond architectural acoustics. Example of structures creating diffuse reflections are found in nature, for example *Cyphochilus* and *Lepidoptera stigma* beetles have chitin networks that achieve an exceptionally bright white colour from all observation angles³⁶. A second example would be the use of acoustic camouflage by insects to avoid predation by bats. The latest research suggests that insects look for rough surfaces, ones that create dispersion, to reduce the chances of being detected via echolocation³⁷. We would anticipate applications for deliberately designed dispersive surfaces: in underwater acoustics; in airborne acoustics and for other wave types (e.g. light, seismic waves). As in nature, applications might involve signalling, reducing interference from unwanted reflections and acoustic camouflage.

Methods

Transfer matrix method. The system described before has been theoretically modelled by using the transfer matrix method. Under the assumption of plane waves travelling inside the metamaterial, either the transfer matrix or the scattering matrix can be obtained, providing directly the reflection of the metamaterial, as well as its effective parameters.

The transfer matrix is used to relate the sound pressures and normal acoustic particle velocities at the beginning and at the end of each slit. The transfer matrix of the n -th slit, \mathbf{T}^n , of length L , extending from $y=0$ to $y=L$ is written as

$$\begin{bmatrix} P^n \\ V^n \end{bmatrix}_{y=0} = \mathbf{T}^n \begin{bmatrix} P^n \\ V^n \end{bmatrix}_{y=L} = \begin{bmatrix} T_{11}^n & T_{12}^n \\ T_{21}^n & T_{22}^n \end{bmatrix} \begin{bmatrix} P^n \\ V^n \end{bmatrix}_{y=L}. \quad (2)$$

For an identical set of M resonators, the transmission matrix \mathbf{T}^n is written as

$$\mathbf{T}^n = \begin{bmatrix} T_{11}^n & T_{12}^n \\ T_{21}^n & T_{22}^n \end{bmatrix} = \mathbf{M}_{\Delta_{\text{slit}}}^n (\mathbf{M}_s^n \mathbf{M}_{\text{HR}}^n \mathbf{M}_s^n)^M.$$

Here, the transmission matrix for each lattice step in the n -th slit, \mathbf{M}_s^n , is written as

$$\mathbf{M}_s^n = \begin{bmatrix} \cos(k_s^n a/2) & iZ_s^n \sin(k_s^n a/2) \\ \frac{i}{Z_s^n} \sin(k_s^n a/2) & \cos(k_s^n a/2) \end{bmatrix}, \quad (3)$$

where the slit characteristic impedance is written as $Z_s^n = \sqrt{\kappa_s^n \rho_s^n / S_s^n}$ and $S_s^n = h^n a$. The resonators are introduced as punctual scatters by a transmission matrix \mathbf{M}_{HR}^n as

$$\mathbf{M}_{\text{HR}}^n = \begin{bmatrix} 1 & 0 \\ 1/Z_{\text{HR}}^n & 1 \end{bmatrix}, \quad (4)$$

and the radiation correction of the n -th slit to the free space as

$$\mathbf{M}_{\Delta_{\text{slit}}}^n = \begin{bmatrix} 1 & Z_{\Delta_{\text{slit}}}^n \\ 0 & 1 \end{bmatrix}, \quad (5)$$

with the characteristic radiation impedance of the n -th slit $Z_{\Delta_{\text{slit}}}^n = -i\omega \Delta l_{\text{slit}}^n \rho_0 / \phi_i^n S_0$, where $S_0 = da$, ρ_0 the air density and Δl_{slit}^n the proper end correction that will be described later.

Finally, the reflection coefficient of the rigidly backed slit can be directly calculated from the elements of the matrix \mathbf{T}^n as

$$R^n = \frac{T_{11}^n - Z_0 T_{21}^n}{T_{11}^n + Z_0 T_{21}^n}. \quad (6)$$

with $Z_0 = \rho_0 c_0 / S_0$, and finally the absorption as $\alpha^n = 1 - |R^n|^2$. The effective parameters of each slit can be obtained from the transfer matrix elements as follows

$$k_{\text{eff}}^n = \frac{1}{L} \cos^{-1} \left(\frac{T_{11}^n + T_{22}^n}{2} \right), \quad Z_{\text{eff}}^n = \sqrt{\frac{T_{12}^n}{T_{21}^n}}. \quad (7)$$

In the case of different HRs, the total transfer matrix of the whole system can be obtained by the product of the transfer matrices of each layer of the material. Thus, the total transfer matrix method of the system is given by

$$\mathbf{T}^n = \begin{bmatrix} T_{11}^n & T_{12}^n \\ T_{21}^n & T_{22}^n \end{bmatrix} = \mathbf{M}_{\Delta l_{\text{slit}}} \prod_{m=1}^M (\mathbf{M}_s^n \mathbf{M}_{\text{HR}}^{n,m} \mathbf{M}_s^n).$$

where the matrix $\mathbf{M}_{\text{HR}}^{n,m}$ is calculated for each m resonator in each n slit.

Visco-thermal losses model. The visco-thermal losses in the system are considered both in the HRs and in the slits by using its effective complex and frequency dependent parameters. Considering only plane waves propagate inside the metamaterial, the effective parameters of the ducts that conform 2D resonators and the slits of width $2r$ are given by ref. 38:

$$\rho_{\text{eff}} = \rho_0 \left[1 - \frac{\tanh(rG_\rho)}{rG_\rho} \right]^{-1}, \quad (8)$$

$$\kappa_{\text{eff}} = \kappa_0 \left[1 + (\gamma - 1) \frac{\tanh(rG_\kappa)}{rG_\kappa} \right]^{-1}, \quad (9)$$

with $G_\rho = \sqrt{i\omega\rho_0/\eta}$ and $G_\kappa = \sqrt{i\omega\text{Pr}\rho_0/\eta}$, and where γ is the specific heat ratio of air, P_0 is the atmospheric pressure, Pr is the Prandtl number, η the dynamic viscosity, ρ_0 the air density and $\kappa_0 = \gamma P_0$ the air bulk modulus. The effective parameters of the n -th main slit, ρ_s^n and κ_s^n , are obtained by setting $r = h^n/2$ in Eqs (8 and 9). The visco-thermal losses inside the 2-dimensional resonator's neck and cavity are modelled in the same way by these effective parameters, $\rho_n^{n,m}$, $\kappa_n^{n,m}$ and $\rho_c^{n,m}$, $\kappa_c^{n,m}$ respectively, by setting $r = w_n^{n,m}/2$ and $r = w_c^{n,m}/2$ for the m -th resonator located at the n -th slit.

Resonator impedance and end corrections. Using the effective parameters for the neck and cavity elements given by Eqs (8 and 9), the impedance of a Helmholtz resonator, including a length correction due to the radiation can be written as ref. 39:

$$Z_{\text{HR}}^{n,m} = -i \frac{\cos(k_n l_n) \cos(k_c l_c) - Z_n k_n \Delta l \cos(k_n l_n) \sin(k_c l_c) / Z_c - Z_n \sin(k_n l_n) \sin(k_c l_c) / Z_c}{\sin(k_n l_n) \cos(k_c l_c) / Z_n - k_n \Delta l \sin(k_n l_n) \sin(k_c l_c) / Z_c + \cos(k_n l_n) \sin(k_c l_c) / Z_c}, \quad (10)$$

where (note superscripts were omitted for the sake of simplicity) $l_n^{n,m}$ and $l_c^{n,m}$ are the neck and cavity lengths, $k_n^{n,m}$ and $k_c^{n,m}$ are the effective wavenumbers and $Z_n^{n,m}$ and $Z_c^{n,m}$ effective characteristic impedance in the neck and cavities respectively, and $\Delta l^{n,m}$ the correction length for the HRs. These correction lengths are deduced from the addition of two correction lengths $\Delta l^{n,m} = \Delta l_1^{n,m} + \Delta l_2^{n,m}$ as

$$\Delta l_1^{n,m} = 0.41 \left[1 - 1.35 \frac{w_n^{n,m}}{w_c^{n,m}} + 0.31 \left(\frac{w_n^{n,m}}{w_c^{n,m}} \right)^3 \right] w_n^{n,m}, \quad (11)$$

$$\Delta l_2^{n,m} = 0.41 \left[1 - 0.235 \frac{w_n^{n,m}}{w_s^n} - 1.32 \left(\frac{w_n^{n,m}}{w_s^n} \right)^2 + 1.54 \left(\frac{w_n^{n,m}}{w_s^n} \right)^3 - 0.86 \left(\frac{w_n^{n,m}}{w_s^n} \right)^4 \right] w_n^{n,m}. \quad (12)$$

The first length correction, $\Delta l_1^{n,m}$, is due to pressure radiation at the discontinuity from the neck duct to the cavity of the Helmholtz resonator⁴⁰, while the second $\Delta l_2^{n,m}$ comes from the radiation at the discontinuity from the neck to the principal waveguide⁴¹. This correction only depends on the radius of the waveguides, so it becomes important when the duct length is comparable to the radius, i.e., for small neck lengths and for frequencies where $k_n^{n,m} w_n^{n,m} \ll 1$.

Another important end correction comes from the radiation from the slits to the free air. The radiation correction for a periodic distribution of slits can be expressed as ref. 42:

$$\Delta l_{\text{slit}}^n = h^n \sigma^n \sum_{n=1}^{\infty} \frac{\sin^2(n\pi\sigma^n)}{(n\pi\sigma^n)^3}. \quad (13)$$

with $\sigma^n = h^n/d$. Note for $0.1 \leq \sigma^n \leq 0.7$ this expression reduces to $\Delta l_{\text{slit}}^n \approx -\sqrt{2} \ln |\sin(\pi\sigma^n/2)|/\pi$.

Diffusion coefficient. The diffusion coefficient⁴³, d_ϕ , is estimated from a polar response as

$$\delta_\phi = \frac{\left(\int_{-\pi}^{\pi} I_s(\theta) d\theta\right)^2 - \int_{-\pi}^{\pi} I_s(\theta)^2 d\theta}{\int_{-\pi}^{\pi} I_s(\theta)^2 d\theta}, \quad (14)$$

where $I_s(\theta)$ is the polar scattering intensity for a wave with incident angle ϕ . This coefficient is normalized to that of a plane reflector, δ_{flat} , to eliminate the effect of the finite size of the structure as $\delta_n = (\delta_\phi - \delta_{\text{flat}})/(1 - \delta_{\text{flat}})$.

Finite element simulations. In order to validate the results we use a numerical approach based on the Finite Element Method (FEM) using COMSOL Multiphysics 5.2™. The thermo-viscous losses were accounted for using the effective parameters (complex phase speed and complex density) given by Eqs (8 and 9) for each domain. Rigid boundary conditions were considered at the external sides of the panel and viscous losses were neglected here. This is justified because the losses are mainly produced at the narrow slits that conform the metamaterial and the contribution of other sources is minor. Absorbing boundary conditions (a perfectly matched layer) with a thickness of λ_0 , were placed at the boundaries of the numerical domain. The unstructured grid was designed ensuring a maximum element size of $\lambda_0/20$. As usual, to obtain the scattering of the panel a background pressure field was set as initial condition in the main domain and the scattered field was computed. By measuring the scattered field over a closed contour the far-field can be obtained¹.

References

- Cox, T. J. & D'Antonio, P. *Acoustic absorbers and diffusers: theory, design and application*, 3rd edn. (CRC Press, 2016).
- Cox, T. J. & Lam, Y. Prediction and evaluation of the scattering from quadratic residue diffusers. *The Journal of the Acoustical Society of America* **95**, 297–305 (1994).
- Schröder, M. R. Diffuse sound reflection by maximum-length sequences. *The Journal of the Acoustical Society of America* **57**, 149–150 (1975).
- Cox, T. J. & D'Antonio, P. Acoustic phase gratings for reduced specular reflection. *Applied Acoustics* **60**, 167–186 (2000).
- Cox, T. & D'Antonio, P. Schroeder diffusers: A review. *Building Acoustics* **10**, 1–32 (2003).
- Mechel, F. The wide-angle diffuser—a wide-angle absorber? *Acta Acustica united with Acustica* **81**, 379–401 (1995).
- Jrvinen, A., Savioja, L. & Melkas, K. Numerical simulations of the modified schroeder diffuser structure. *J. Acoust. Soc. Am* **103**, 3065 (1998).
- Hargreaves, J. & Cox, T. Improving the bass response of Schroeder diffusers. *Proceedings of the Institute of Acoustics* **25**, 199–208 (2003).
- Hunecke, J. *Schallstreuung und Schallabsorption von Oberfl: ahen aus mikroperforierten Streifen*. Ph.D. thesis, University of Stuttgart (1997).
- Wu, T., Cox, T. J. & Lam, Y. A profiled structure with improved low frequency absorption. *The Journal of the Acoustical Society of America* **110**, 3064–3070 (2001).
- D'Antonio, P. Inventor. RPG Diffusor Systems, Inc., assignee. Planar binary amplitude diffusor. United States patent US 5,817,992. Jun 5 (1998).
- Xiao, L., Cox, T. J. & Avis, M. R. Active diffusers: some prototypes and 2D measurements. *Journal of sound and vibration* **285**, 321–339 (2005).
- Redondo, J., Picó, R., Sánchez-Morcillo, V. J. & Woszczyk, W. Sound diffusers based on sonic crystals. *The Journal of the Acoustical Society of America* **134**, 4412–4417 (2013).
- Redondo, J., Sánchez-Pérez, J., Blasco, X., Herrero, J. & Vorländer, M. Optimized sound diffusers based on sonic crystals using a multiobjective evolutionary algorithm. *The Journal of the Acoustical Society of America* **139**, 2807–2814 (2016).
- Santillán, A. & Bozhevolnyi, S. I. Acoustic transparency and slow sound using detuned acoustic resonators. *Phys. Rev. B* **84**, 064304 (2011).
- Ding, Y., Liu, Z., Qiu, C. & Shi, J. Metamaterial with simultaneously negative bulk modulus and mass density. *Physical review letters* **99**, 093904 (2007).
- Yang, Z., Mei, J., Yang, M., Chan, N. & Sheng, P. Membrane-type acoustic metamaterial with negative dynamic mass. *Phys. Rev. Lett.* **101**, 204301 (2008).
- Groby, J.-P., Duclos, A., Dazel, O., Boeckx, L. & Lauriks, W. Absorption of a rigid frame porous layer with periodic circular inclusions backed by a periodic grating. *J. Acoust. Soc. Am.* **129**, 3035–3046 (2011).
- Lagarrigue, C., Groby, J., Tournat, V., Dazel, O. & Umnova, O. Absorption of sound by porous layers with embedded periodic arrays of resonant inclusions. *J. Acoust. Soc. Am.* **134**, 4670–4680 (2013).
- Boutin, C. Acoustics of porous media with inner resonators. *J. Acoust. Soc. Am.* **134**, 4717–4729 (2013).
- Groby, J.-P. *et al.* Enhancing the absorption properties of acoustic porous plates by periodically embedding Helmholtz resonators. *J. Acoust. Soc. Am.* **137**, 273–280 (2015).
- Dupont, T., Leclaire, P., Sicot, O., Gong, X. L. & Panneton, R. Acoustic properties of air-saturated porous materials containing dead-end porosity. *J Appl Phys* **110**, 094903 (2011).
- Leclaire, P., Umnova, O., Dupont, T. & Panneton, R. Acoustical properties of air-saturated porous material with periodically distributed dead-end pores. *J. Acoust. Soc. Am.* **137**, 1772–1782 (2015).
- Mei, J. *et al.* Dark acoustic metamaterials as super absorbers for low-frequency sound. *Nat. Commun.* **3**, 756 (2012).
- Ma, G., Yang, M., Xiao, S., Yang, Z. & Sheng, P. Acoustic metasurface with hybrid resonances. *Nat. Mater.* **13**, 873–878 (2014).
- Romero-García, V. *et al.* Perfect and broadband acoustic absorption by critically coupled sub-wavelength resonators. *Sci. Rep.* **6**, 19519 (2016).
- Groby, J.-P., Huang, W., Lardeau, A. & Aurégan, Y. The use of slow waves to design simple sound absorbing materials. *J. Appl. Phys.* **117**, 124903 (2015).
- Groby, J.-P., Pommier, R. & Aurégan, Y. Use of slow sound to design perfect and broadband passive sound absorbing materials. *J. Acoust. Soc. Am.* **139**, 1660–1671 (2016).
- Li, Y. & Assouar, B. M. Acoustic metasurface-based perfect absorber with deep subwavelength thickness. *Appl. Phys. Lett.* **108**, 063502 (2016).
- Romero-García, V., Theocharis, G., Richoux, O. & Pagneux, V. Use of complex frequency plane to design broadband and sub-wavelength absorbers. *The Journal of the Acoustical Society of America* **139**, 3395–3403 (2016).
- Jiménez, N., Huang, W., Romero-García, V., Pagneux, V. & Groby, J.-P. Ultra-thin metamaterial for perfect and quasi-omnidirectional sound absorption. *Applied Physics Letters* **109**, 121902 (2016).
- Jiménez, N., Romero-García, V., Pagneux, V. & Groby, J.-P. Quasiperfect absorption by subwavelength acoustic panels in transmission using accumulation of resonances due to slow sound. *Phys. Rev. B* **95**, 014205 (2017).

33. Cox, T. J., Angus, J. A. & D'Antonio, P. Ternary and quadriphase sequence diffusers. *The Journal of the Acoustical Society of America* **119**, 310–319 (2006).
34. Powell, M. J. A fast algorithm for nonlinearly constrained optimization calculations. In *Numerical analysis*, 144–157 (Springer, 1978).
35. Schroeder, M. Phase gratings with suppressed specular reflection. *Acta Acustica united with Acustica* **81**, 364–369 (1995).
36. Burrelli, M. *et al.* Bright-white beetle scales optimise multiple scattering of light. *Scientific reports* **4**, 6075 (2014).
37. Clare, E. L. & Holderied, M. W. Acoustic shadows help gleaning bats find prey, but may be defeated by prey acoustic camouflage on rough surfaces. *eLife* **4**, e07404 (2015).
38. Stinson, M. R. The propagation of plane sound waves in narrow and wide circular tubes, and generalization to uniform tubes of arbitrary cross-sectional shape. *J. Acoust. Soc. Am.* **89**, 550–558 (1991).
39. Theocharis, G., Richoux, O., García, V. R., Merkel, A. & Tournat, V. Limits of slow sound propagation and transparency in lossy, locally resonant periodic structures. *New J. Phys.* **16**, 093017 (2014).
40. Kergomard, J. & Garcia, A. Simple discontinuities in acoustic waveguides at low frequencies: critical analysis and formulae. *J. Sound Vib.* **114**, 465–479 (1987).
41. Dubos, V. *et al.* Theory of sound propagation in a duct with a branched tube using modal decomposition. *Acta Acustica united with Acustica* **85**, 153–169 (1999).
42. Mechel, F. P. *Formulas of acoustics*, 2nd ed. (Springer Science & Business Media, 2008).
43. ISO Standard: ISO 17497-2:2012. Acoustics/Sound-scattering properties of surfaces/Part 2: Measurement of the directional diffusion coefficient in a free field. International Organization for Standardization, Geneva, Switzerland, <https://www.iso.org/standard/55293.html> (2012).

Acknowledgements

This article is based upon work from COST Action DENORMS - CA15125, supported by COST (European Cooperation in Science and Technology). The authors acknowledge financial support from the Metaudible Project No. ANR-13-BS09-0003, cofunded by ANR and FRAE.

Author Contributions

N.J., V.R.G. and J.P.G. conducted the theoretical modelling and numerical experiment; N.J., V.R.G., J.P.G. and T.C. wrote the manuscript. All authors reviewed the manuscript.

Additional Information

Supplementary information accompanies this paper at doi:10.1038/s41598-017-05710-5

Competing Interests: The authors declare that they have no competing interests.

Publisher's note: Springer Nature remains neutral with regard to jurisdictional claims in published maps and institutional affiliations.



Open Access This article is licensed under a Creative Commons Attribution 4.0 International License, which permits use, sharing, adaptation, distribution and reproduction in any medium or format, as long as you give appropriate credit to the original author(s) and the source, provide a link to the Creative Commons license, and indicate if changes were made. The images or other third party material in this article are included in the article's Creative Commons license, unless indicated otherwise in a credit line to the material. If material is not included in the article's Creative Commons license and your intended use is not permitted by statutory regulation or exceeds the permitted use, you will need to obtain permission directly from the copyright holder. To view a copy of this license, visit <http://creativecommons.org/licenses/by/4.0/>.

© The Author(s) 2017

Chapter **8**

Articles related to Chapter 3: Acoustic
characterization of materials and structures

Contents

J. Acoust. Soc. Am., 127:764-772, 2010	195
J. Appl. Phys., 120:135107, 2016	203
Appl. Phys. Lett., 110:051902, 2017	211

Analytical method for the ultrasonic characterization of homogeneous rigid porous materials from transmitted and reflected coefficients

J.-P. Groby^{a)}

Département de Recherche en Électromagnétisme-Laboratoire de Signaux et Systèmes, UMR8506
CNRS/Supélec/Univ. Paris-Sud, F-91192 Gif-sur-Yvette, France

E. Ogam

Laboratoire de Mécanique et d'Acoustique, UPR7051 CNRS, F-13402 Marseille Cedex 20, France

L. De Ryck,^{b)} N. Sebaa, and W. Lauriks

Laboratory of Acoustics and Thermal Physics, K.U.Leuven, B-3001 Heverlee, Belgium

(Received 8 December 2008; revised 9 December 2009; accepted 11 December 2009)

A frequency domain method dedicated to the analytic recovery of the four relevant parameters of macroscopically homogeneous rigid frame porous materials, e.g., plastic foams, at the high frequency range of the Johnson–Champoux–Allard model is developed and presented. The reconstructions appeal to experimental data concerning time domain measurements of the ultrasonic fields reflected and transmitted by a plate of the material at normal incidence. The effective density and bulk modulus of the material are first reconstructed from the frequency domain reflection and transmission coefficients. From the latter, the porosity, tortuosity, and thermal and viscous characteristic lengths are recovered. In a sense, the method presented herein is quite similar in the ultrasonic range, but also quite complementary, to the method developed by Panneton and Olny [J. Acoust. Soc. Am. **119**, 2027–2040 (2006); **123**, 814–824 (2008)] at low frequency, which appeal to experimental data measured in an impedance tube.

© 2010 Acoustical Society of America. [DOI: 10.1121/1.3283043]

PACS number(s): 43.35.Zc, 43.20.Jr, 43.20.Ye, 43.40.Sk [KVH]

Pages: 764–772

I. INTRODUCTION

A rigid frame porous material is a porous material whose frame is immobile. This assumption is not only conditioned by the saturating fluid usually a light fluid such as air, but also by the frequency of the acoustic solicitation. The frequency band suitable for the rigid frame approximation is bounded at high frequency by the diffusion limit, when the wavelength is of the order of, or smaller than the pore size, and at low frequency by the fluid-solid decoupling frequency below which the skeleton may vibrate. These bounds depend on the material properties, and so on its characteristics.

The equations of motion in a rigid frame porous material, derived from Biot's theory^{1,2} and in later publications,^{3–8} reduce to those of an equivalent fluid, with complex frequency-dependent effective density and bulk modulus. These later publications present semiphenomenological models that describe the viscous and thermal dissipations over specific frequency ranges, assuming known the characteristics of the saturating fluid, i.e., the viscosity η , the saturating pressure P_0 , the specific heat ratio γ , and density ρ_f . Concerning the viscous dissipation, the Johnson *et al.* model³ was made to fit the exact high- and low- (imaginary) frequency limits of the effective density, while the Wilson⁷

model was contrived to match the mid frequency range of the latter. Concerning the thermal dissipation, the Champoux–Allard model⁴ was developed to fit the exact high frequency limits of the effective bulk modulus, while the Wilson⁷ model was contrived to match the mid frequency range of the latter. Inspired by the fact that the low frequency development of the Champoux–Allard model is not exact, Lafarge *et al.*⁶ proposed an alternative expression of the effective bulk modulus and introduce the static thermal permeability. However, this parameter seems to be difficult to determine, even at low frequency.^{6,9,10}

Herein, the Johnson–Champoux–Allard model^{3,4} (JCAM) is considered, because high frequency measurements are performed. The parameters involved in this model are the porosity ϕ , which is the ratio of the fluid volume to the total sample volume; the tortuosity α_∞ , which describes the change in magnitude and direction of the fluid microvelocity due to curliness of the pores; the characteristic viscous and thermal lengths Λ and Λ' , which relate to the geometry of the pores through the viscous and thermal losses; and the flow resistivity σ , which is the ratio of the fluid viscosity η to the fluid permeability κ_f . The inverse problem consists in recovering some or all of these five parameters from measurements of the scattered fields, i.e., the reflected and transmitted fields in the case of a rigid frame porous plate.

Subsequent to the experimental apparatus of Beranek¹¹ to determine the porosity (porosimeter), or the flowmeter of Brown and Bolt¹² to determine the flow resistivity, several methods have been developed to characterize macroscopi-

^{a)} Author to whom correspondence should be addressed. Electronic mail: jean-philippe.groby@univ-lemans.fr. Present address: Laboratoire d'Acoustique de l'Université du Maine, UMR6613 CNRS/Univ. du Maine, F-72085 Le Mans Cedex 9, France.

^{b)} Present address: LMS international NV, B-3001 Leuven, Belgium.

cally homogeneous porous samples, or layered porous samples. From ultrasonic measurements, methods developed either in the frequency or in the time domain allow the determination of the porosity,¹³ the tortuosity,¹⁴ the porosity and tortuosity simultaneously,¹⁵ the viscous and thermal characteristic lengths¹⁶ (using the $Q\delta$ method), or the porosity, tortuosity, and viscous characteristic length (the thermal characteristic length being set to three times the viscous one) simultaneously.^{17,18} Specific methods have been developed for the characterization of highly absorbent porous materials, based on the variation of the static pressure of the saturating fluid,¹⁹ mainly for the determination of the viscous characteristic length and the tortuosity. Recently, the simultaneous reconstruction of the three profiles of porosity, tortuosity, and viscous characteristic length of a macroscopically inhomogeneous rigid frame porous plate from simulated reflection coefficients for various angles of incidence was carried out²⁰ through an optimization process.

A characteristic of these many studies and methods, particularly in the frequency domain, is the difference in sensitivity of each parameter on the physical quantities. For example, both the density and bulk modulus do not depend on σ in the asymptotic high frequency range. Moreover, most of the methods for the simultaneous reconstruction of the parameters appeal to minimization techniques.^{18,19} On the other hand, two analytic methods were developed^{9,10} appealing to measurements in an impedance tube.²¹ The idea is first to reconstruct the equivalent density and bulk modulus for various frequencies from the measurement of the impedance and the acoustic index of refraction and then to recover the parameters involved in several dissipation models mainly through analytic inversion, but also after extrapolation if needed. This leads to four equations at each frequency formed by the real and imaginary parts of the effective density and bulk modulus. Concerning the JCAM, these methods enable the recovery of the tortuosity, viscous and thermal characteristic lengths, and flow resistivity assuming the porosity to be known. This assumption seems to be due to the necessary use of the complex form of the complete JCAM, which involves five parameters, for the correct modeling of the phenomena in the frequency range considered therein. For the number of to-be-reconstructed parameters to be lower than or equal to the number of equations, a simplified model should be used, for example, the asymptotic high frequency one. In this ultrasonic frequency range, only four parameters are relevant. Complete analytical recovery of the latter is also enabled from the knowledge of the *complex* density and bulk modulus. The low frequency bound of this asymptotic regime is not clear and depends on the material, but it can be assumed that for frequencies higher than 100 kHz, this regime is reached for most of the porous foams. The high frequency bound is the diffusion limit, which is related to some of the parameters to be reconstructed, particularly the characteristic length.²²

The aim of this article is to present a simple, efficient, and analytic frequency domain method for the simultaneous recovery of the four parameters appealing to the high frequency approximation of the JCAM, i.e., ϕ , α_∞ , Λ , and Λ' , for a macroscopically homogeneous rigid frame porous plate

saturated by air, i.e., $\eta=1.839 \times 10^{-5} \text{ m}^2 \text{ s}^{-1}$, $P_0=1.01325 \times 10^5 \text{ Pa}$, $\rho_f=1.213 \text{ kg m}^{-3}$, and $\gamma=1.4$, by means of ultrasonic measurements at normal incidence. This method can be considered as complementary to those proposed in Refs. 9 and 10 for a complete analytical characterization of macroscopically homogeneous porous materials.

II. ANALYTICAL CHARACTERIZATION OF A MACROSCOPICALLY HOMOGENEOUS RIGID FRAME POROUS PLATE

In what follows, the pressure $p(x,t)$ is related to its Fourier transform $P(x,\omega)$ through

$$p(x,t) = \int_{-\infty}^{\infty} P(x,\omega) e^{-i\omega t} d\omega. \quad (1)$$

A. Basic theoretical retrieval equations

When solicited by a normally incident plane wave, the reflection $\mathcal{R}(\omega)$ and transmission $\mathcal{T}(\omega)$ coefficients of a homogeneous plate of thickness L occupied by the equivalent fluid medium $M^{[1]}$ and surrounded by the same fluid, denoted as medium $M^{[0]}$, take the following forms:²³

$$\begin{aligned} \mathcal{R} &= \frac{R(1 - e^{2ik^{[1]}L})}{1 - R^2 e^{2ik^{[1]}L}}, \\ \mathcal{T} &= \frac{(1 - R^2)e^{i(k^{[1]} - k^{[0]})L}}{1 - R^2 e^{2ik^{[1]}L}}, \end{aligned} \quad (2)$$

wherein $R = (Z^{[1]} - Z^{[0]}) / (Z^{[1]} + Z^{[0]})$ is the reflection coefficient at the interface between two semi-infinite media $M^{[1]}$ and $M^{[0]}$, with $Z^{[j]} = \rho^{[j]} c^{[j]} = \sqrt{K^{[j]} \rho^{[j]}}$ the impedance of $M^{[j]}$, and $\rho^{[j]}$, $c^{[j]}$, and $K^{[j]}$ being the density, sound speed, and bulk modulus, respectively, $j=0,1$. Let us now introduce $S_{11}(\omega)$ and $S_{21}(\omega)$, the coefficients of the scattering matrix \mathbf{S} , related to \mathcal{R} and \mathcal{T} through

$$\begin{aligned} S_{11} &= \mathcal{R} = \frac{R(1 - e^{2ik^{[0]}L})}{1 - R^2 e^{2ik^{[0]}L}}, \\ S_{21} &= \mathcal{T} e^{ik^{[0]}L} = \frac{(1 - R^2)e^{ik^{[0]}L}}{1 - R^2 e^{2ik^{[0]}L}}, \end{aligned} \quad (3)$$

wherein $\zeta(\omega) = k^{[1]} / k^{[0]} = c^{[0]} / c^{[1]} = \sqrt{K^{[0]} \rho^{[1]} / K^{[1]} \rho^{[0]}}$ is the acoustic index of refraction, i.e., the ratio between the wavenumbers of media $M^{[1]}$ and $M^{[0]}$. The acoustic index of refraction and the impedance ratio $z(\omega) = Z^{[1]} / Z^{[0]} = \sqrt{K^{[1]} \rho^{[1]} / K^{[0]} \rho^{[0]}}$ can be obtained analytically by inverting Eq. (3), yielding²⁴⁻²⁶

$$z = \pm \sqrt{\frac{(1 + S_{11})^2 - S_{21}^2}{(1 - S_{11})^2 - S_{21}^2}}, \quad (4a)$$

$$\zeta = \frac{-i}{k^{[0]}L} (\ln(X \pm i\sqrt{1 - X^2})) + \frac{2m\pi}{k^{[0]}L}, \quad (4b)$$

wherein $X = (1 - S_{11}^2 + S_{21}^2) / 2S_{21}$ and m is an integer.

For a rigid frame porous plate, the signs in Eqs. (4a) and (4b) can be determined by the requirements $\text{Re}(z) \geq 0$ and

$\text{Im}(z) \geq 0$ for Eq. (4a), and $\text{Im}(\zeta) \geq 0$ for Eq. (4b). Both requirements result from the outgoing wave condition together with the Fourier transform convention. In fact, z and ζ are related and their relationship can be used to determine the sign in Eqs. (4a) and (4b) as reported in Ref. 24. Effectively, a small perturbation of S_{11} and S_{21} easily produced in experimental measurements may change the sign of $\text{Re}(z)$ and $\text{Im}(\zeta)$, making it impossible to satisfy the previous requirements, as discussed in Ref. 27. The derived method is particularly adapted when $\text{Re}(z)$ and $\text{Im}(\zeta)$ are close to zero and is also of impractical interest for rigid frame porous materials because $\text{Re}(z)$ is always greater than unity. Nevertheless, once the value of z is obtained, ζ can be determined without sign ambiguity through

$$\zeta = \frac{-i}{k^{[0]}L} \left(\ln \left(\frac{S_{21}(z+1)}{z+1 - S_{11}(z-1)} \right) \right) + \frac{2m\pi}{k^{[0]}L}. \quad (5)$$

The integer m related to the branch index of $\text{Re}(\zeta)$ can be determined by the requirement $\text{Re}(\zeta) \geq \sqrt{\alpha_\infty}$ [because $\text{Re}(c^{[1]}(\omega)) \leq c^{[0]}/\sqrt{\alpha_\infty}$]. Its determination is not straightforward, because the requirement depends on one of the parameters to reconstruct.

The condition $\text{Re}(\zeta) \geq 1$ should normally be sufficient for its correct determination, but problems occur for large α_∞ and/or for high frequency solicitation because of large $k^{[0]}L$. This usually leads authors to use small thickness sample. This problem can be solved by use of an iterative scheme. The latter is initialized with m as determined through the condition $\text{Re}(\zeta) \geq 1$ and consists in adding 1 to the previously calculated m as long as the slope of $\text{Re}(\zeta(\omega))$ is not negative. This condition is a mathematical translation of the fact that the phase velocity $c^{[1]}(\omega)$ associated with a rigid frame porous material is an increasing function of the frequency toward its high frequency limit $c^{[0]}/\sqrt{\alpha_\infty}$; i.e., $\text{Re}(\zeta) = \text{Re}(c^{[0]}/c^{[1]}(\omega))$ is a decreasing function of ω . The latter iterative scheme is chosen because the condition $\text{Re}(\zeta) \geq 1$ can lead to an undervaluated m for large $k^{[0]}L$ and so an undervaluated ζ . The reconstructed value of α_∞ is then undervaluated and can reach a nonphysical value less than unity. An iterative scheme based on the reconstructed value of α_∞ is also of impractical interest.

Another condition for the correct determination of the integer m is connected to the fact that both effective density and bulk modulus should be continuous functions of frequency. This problem was not encountered during the experiments presented here, but is also related to large values of $k^{[0]}L$. The reader can also refer to Ref. 24, keeping in mind that the high frequency limit clearly defines the initialization of the continuity condition that must be applied.

B. Reconstruction of ϕ , α_∞ , Λ , and Λ' from the high frequency approximation of the JCAM

Let us assume in what follows that z and ζ can be evaluated for frequencies ν ($\omega=2\pi\nu$) in the interval $[\nu_1, \nu_2]$ over which the high frequency approximation of the JCAM is valid. The equivalent density and bulk modulus ratios reduce to

$$\begin{aligned} \tilde{\rho} &= \frac{\rho^{[1]}}{\rho^{[0]}} = \frac{\alpha_\infty}{\phi} \left(1 + \frac{2}{\Lambda} \sqrt{\frac{i\eta}{\omega\rho_f}} \right), \\ \tilde{K} &= \frac{K^{[1]}}{K^{[0]}} = \frac{1}{\phi} \left(1 + \frac{2(1-\gamma)}{\Lambda'} \sqrt{\frac{i\eta}{\omega \text{Pr} \rho_f}} \right), \end{aligned} \quad (6)$$

wherein $\text{Pr}=0.71$ is the Prandtl number.

Noting that $\tilde{K}(\omega)=z/\zeta$ and $\tilde{\rho}(\omega)=z\zeta$, several reconstruction algorithms can be developed for the recovery of the four parameters appealing to the high frequency approximation of the JCAM. The algorithm that was found to give the most accurate results is based on a phase and amplitude analysis of both the equivalent density and bulk modulus. At each frequency, a value $\bar{x}(\omega)$ of the parameter x is recovered analytically, $x=\phi$, α_∞ , Λ , or Λ' . The final value of x is taken to be the average value of $\bar{x}(\omega)$ over $[\omega_1, \omega_2]$; i.e., $x=\text{mean}[\bar{x}(\omega)]$. The latter operation regularizes the inverse problem.

From $\text{Im}(\tilde{K})/\text{Re}(\tilde{K})$ and $\text{Im}(\tilde{\rho})/\text{Re}(\tilde{\rho})$, which are both independent of α_∞ and ϕ , the two characteristic lengths are first recovered from

$$\begin{aligned} \bar{\Lambda} &= \sqrt{\frac{2\eta}{\omega\rho_f}} \left(\frac{\text{Re}(\tilde{\rho}) - \text{Im}(\tilde{\rho})}{\text{Im}(\tilde{\rho})} \right), \\ \bar{\Lambda}' &= (1-\gamma) \sqrt{\frac{2\eta}{\omega \text{Pr} \rho_f}} \left(\frac{\text{Re}(\tilde{K}) - \text{Im}(\tilde{K})}{\text{Im}(\tilde{K})} \right). \end{aligned} \quad (7)$$

Then, ϕ is recovered from $\|\tilde{K}\|$ via

$$\bar{\phi} = \frac{1}{\|\tilde{K}\|} \left(1 + \frac{2(1-\gamma)}{\Lambda'} \sqrt{\frac{2\eta}{\omega \text{Pr} \rho_f}} + \frac{4(1-\gamma)^2\eta}{\Lambda'^2\omega \text{Pr} \rho_f} \right)^{1/2}, \quad (8)$$

and finally α_∞ is recovered from $\|\tilde{\rho}\|$ by means of

$$\bar{\alpha}_\infty = \phi \|\tilde{\rho}\| \left(1 + \frac{2}{\Lambda} \sqrt{\frac{2\eta}{\omega\rho_f}} + \frac{4\eta}{\Lambda^2\omega\rho_f} \right)^{-1/2}. \quad (9)$$

III. EXAMPLE OF A RECONSTRUCTION FROM EXPERIMENTAL DATA

The method has been applied to efficiently characterize several homogeneous rigid frame porous samples (polyurethane foam, melamine foam, etc.) with low and medium flow resistivities.

In what follows, a $L=27.5$ mm thick medium resistivity rigid frame porous material sample is considered. This material has already been characterized at various frequencies (100 and 200 kHz) in the ultrasonic range by some of the authors of the present paper,¹⁸ wherein a smaller sample of 7 mm thick was employed. Its characteristic parameters were also previously determined by use of different methods^{15,16} and are recalled in Table I. Its flow resistivity is $\sigma=38\,000$ N m s⁻⁴ (measured with a flowmeter).

A. Experimental setup and procedure

The experimental setup is shown in Fig. 1. Two air-coupled piezoelectric Ultrason NCG100-D25 transducers de-

TABLE I. Properties of the studied homogeneous material as recovered in Refs. 15 and 16, as recovered in Ref. 18, and as recovered with our analytic method.

	ϕ	α_z	Λ (μm)	Λ' (μm)
Use of Refs. 15 and 16	0.7 ± 0.05	1.25 ± 0.05	50 ± 10	$3 \times \Lambda = 150 \pm 30$
Ref. 18	0.72–0.74	1.21–1.26	42–66	$3 \times \Lambda = 126\text{--}198$
Present method	0.752	1.246	55.4	178.4

noted T_a and T_b , whose central frequencies are 100 kHz, are placed at x_a and x_b . The airborne wave is generated by T_a and detected by T_a in the pulse-echo mode in the reflection experiments or by T_b in the transmission experiments. All recorded signals are averaged over 512 waveforms.

The method is very sensitive to small variations of the sample alignment during the recording of the reflected $p^r(x_a, t)$ and the transmitted $p^t(x_b, t)$ fields. The sample remains in place for the measurement of both of these fields, its first interface being placed at the origin of the Cartesian coordinate system such that $p^r(x_a, t)$ and $p^t(x_b, t)$ can be recorded over the same time window of the oscilloscope; i.e., the first interface of the sample is placed approximately at equal distance from the two transducers; i.e., $x_a \approx |x_b|$. This procedure avoids problems caused by temporal shift between the windows used to measure reflected or transmitted waves with and without the sample, which is a source of error as discussed in Ref. 28 for the reconstruction of ζ and z .

The main difficulty with ultrasonic measurements is the evaluation from the time domain responses of the frequency domain reflection and transmission coefficients \mathcal{R} and \mathcal{T} , with sufficient accuracy for the inversion to be carried out, and over a sufficiently large interval of frequency for the inverse problem to be regularized. This operation requires particular care, because it is often considered to be highly uncertain and/or ill-posed. This has led some authors to prefer a time domain inversion algorithm based on fractional derivatives^{17,18} or to use time domain deconvolution.

The Fourier transforms of $p^r(x_a, t)$ and $p^t(x_b, t)$ are related to \mathcal{R} and \mathcal{T} through

$$P^r(x_a) = \mathcal{R}A^i e^{ik^{[0]}x_a} = \mathcal{T}P^{ri}(x_a),$$

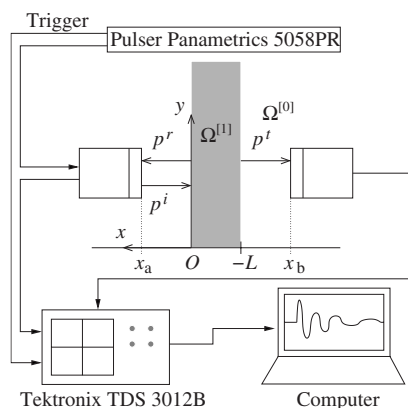


FIG. 1. Experimental setup and description of the configuration. The transducers are Ultrasonics NCG100-D25 air-coupled piezoelectric transducers.

$$P^t(x_b) = \mathcal{T}A^i e^{-ik^{[0]}x_b} = \mathcal{T}P^i(x_b), \quad (10)$$

wherein $A^i(\omega)$ is the spectrum of the incident field, $P^i(x_b)$ is the incident field as recorded with T_b in absence of the sample, and $P^{ri}(x_a)$ corresponds to time delay of the reflected field between the first interface of the sample and the location of T_a . The latter field, abusively called here “incident field,” can be recorded in time domain with T_a in pulse-echo mode when a perfectly reflecting plate is placed such that its first interface is located at the origin. Any time delay between $p^{ri}(x_a, t)$ and $p^r(x_a, t)$ is expected if the first interface of the sample and the perfectly reflecting plate are located at the same position. Nevertheless, to avoid such source of error, $p^r(x_a, t)$ is translated in time in such a way that its maximum of amplitude occurs at the same time as the one of $p^{ri}(x_a, t)$. The frequency domain reflection and transmission coefficients are then evaluated by means of $\mathcal{R} = P^r(x_a, \omega) / P^{ri}(x_a, \omega)$ and $\mathcal{T} = P^t(x_b, \omega) / P^i(x_b, \omega)$ over the intersection of the two -3 dB bandwidths as calculated for $P^{ri}(x_a, \omega)$ and $P^i(x_b, \omega)$. These bandwidths are effectively different because the latter incorporate, to some extent, transfer functions of the transducers T_a and T_b , which are close but not identical.

In addition, the amplitude of $p^r(x_a, t)$ is often very small with a very poor signal to noise ratio (SNR) for relatively low and medium flow resistivity porous materials. The noise in a signal is usually assumed to be a stationary random process; i.e., its mean value is independent of the time origin. In the experiments, the acquisitions are done using a triggering process, which ensures the time origin of the signals. Recorded signals are averaged. The averaging operation induces a large decrease in the noise that is incoherent with respect to the trigger signal. Therefore, the main part of the remaining noise is coherent²⁹ with the trigger signal, which is the same for all the experiments. The remaining noise is mainly electronic from the measurement devices. In the reflection experiments only one transducer is used. To get rid of this remaining noise component, which is coherent, reproducible, and somewhat synchronized with the trigger, the latter, called $p^n(x_a, t)$, is recorded without the sample and perfectly reflecting plate, the emission being still on (the experimental setup is identical). The incident and reflected fields used for the inversion are $\tilde{p}^r(x_a, t) = p^r(x_a, t) - p^n(x_a, t)$ and $\tilde{p}^t(x_b, t) = p^t(x_b, t) - p^n(x_b, t)$, as shown Fig. 2 for $\tilde{p}^r(x_a, t)$.

For highly absorbent foam and/or large flow resistivity porous material, a similar procedure can be employed to determine $\tilde{p}^t(x_b, t)$ and $\tilde{p}^i(x_b, t)$, by a prior recording of $p^n(x_b, t)$ with T_b , without the sample and by turning off the excitation delivered by T_a . This procedure is certainly less efficient than the one described for the experiment in reflection because two transducers are needed in transmission experiments, this imposing the excitation to be switched off.

In summary, the incident fields are recorded, without the sample, as follows: (1) Record $p^i(x_b, t)$ using T_b , (2) record the noise $p^n(x_a, t)$ using T_a in pulse-echo mode, (3) place an infinitely rigid plate (here an aluminum plate is used) whose first interface is located at the origin, and (4) record $p^{ri}(x_a, t)$

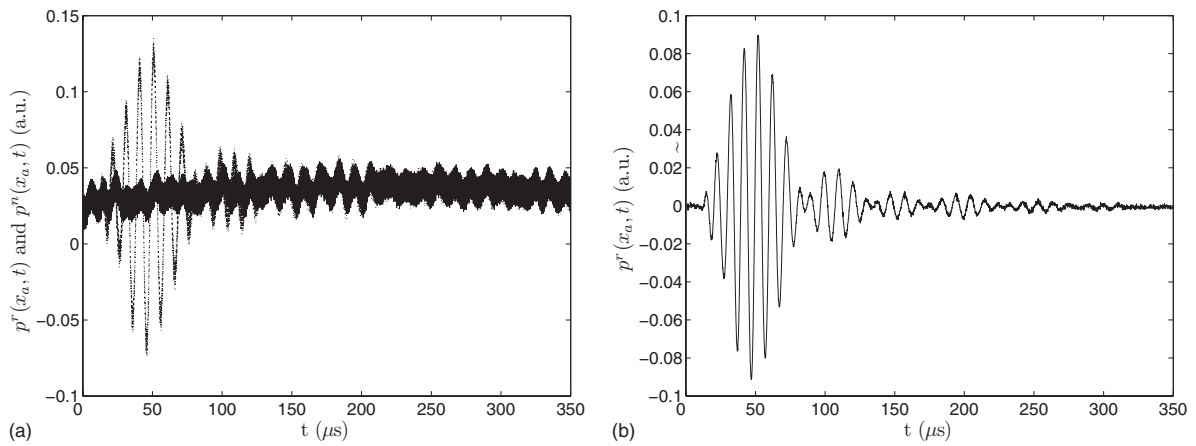


FIG. 2. (a) $p^r(x_a, t)$ (dotted curve) and $p^n(x_a, t)$ (solid curve) as recorded on the oscilloscope and (b) $\tilde{p}^r(x_a, t)$ as used for the inversion.

using Ta in pulse-echo mode. The infinitely rigid plate is then replaced with the sample, carefully placed at the origin, and $p^r(x_a, t)$ is recorded in the pulse-echo mode using Ta while $p^l(x_b, t)$ is recorded employing Tb.

B. Numerical reconstruction from experimental data

Once m is correctly determined, the following parameters are recovered from $\bar{\phi}(\nu)$, $\bar{\alpha}_\infty(\nu)$, $\bar{\Lambda}(\nu)$, and $\bar{\Lambda}'(\nu)$,

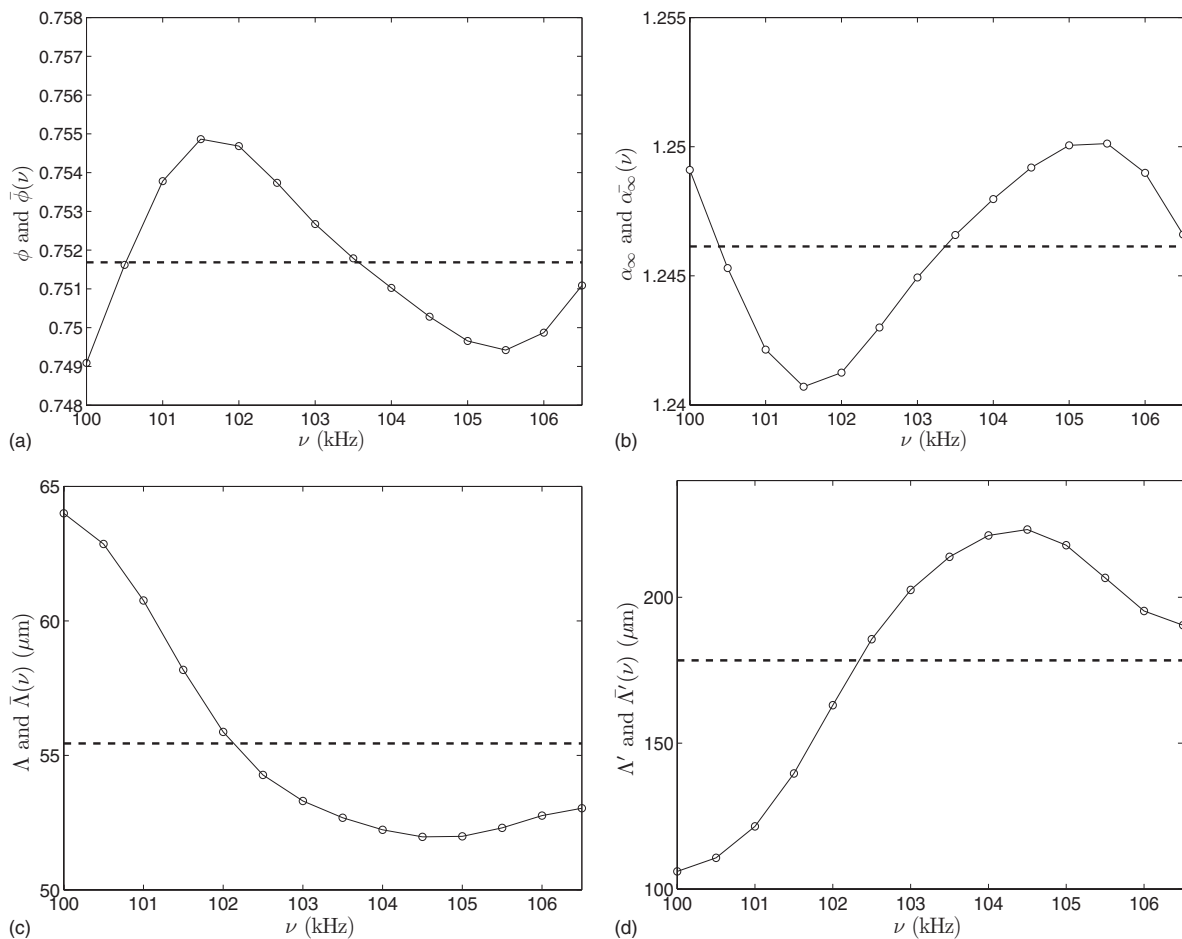


FIG. 3. (a) $\bar{\phi}(\nu)$ (solid curve) and its average value ϕ (dashed line), (b) $\bar{\alpha}_\infty(\nu)$ (solid curve) and its average value α_∞ (dashed line), (c) $\bar{\Lambda}(\nu)$ (solid curve) and its average value Λ (dashed line), and (d) $\bar{\Lambda}'(\nu)$ (solid curve) and its average value Λ' (dashed line). The frequency range corresponds to the intersection of the two -3 dB bandwidths as calculated for $P^r(x_a, \omega)$ and $P^l(x_b, \omega)$.

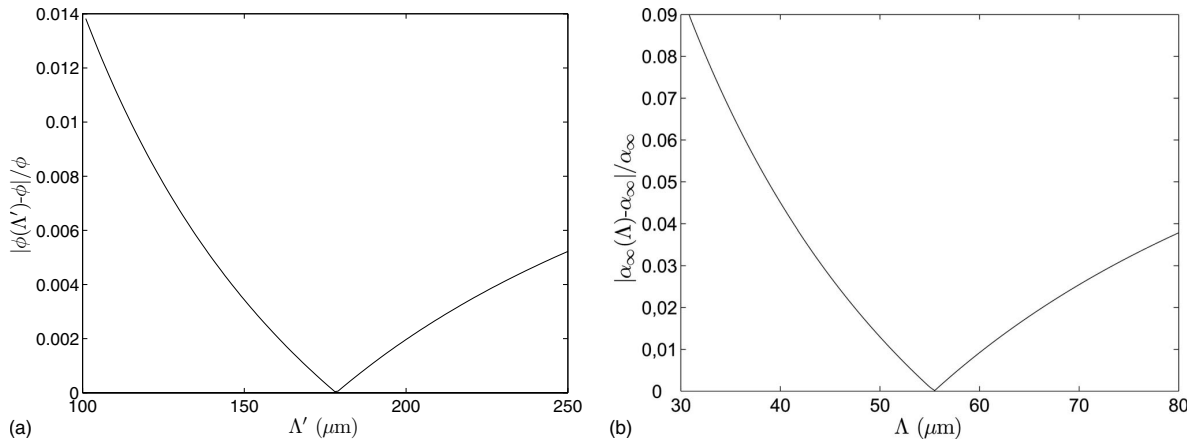


FIG. 4. Absolute value of the relative error of the recovered parameter ϕ as a function of Λ' (a) and α_∞ as a function of Λ (b), over the frequency bandwidth used for the reconstruction.

which are plotted in Fig. 3: $\phi=0.752$, $\alpha_\infty=1.246$, $\Lambda=55.4 \mu\text{m}$, and $\Lambda'=178.4 \mu\text{m}$. These parameters agree with those found in Ref. 18 via a time domain method and other ultrasonic methods^{15,16} (see Table I). The unbiased estimators of the standard deviation, as calculated for the vector x as $s(x)=\sqrt{1/(n-1)\sum_{i=1}^n(x_i-\text{mean}(x))^2}$, are $s(\phi)=2 \times 10^{-3}$, $s(\alpha_\infty)=3.3 \times 10^{-3}$, $s(\Lambda)=4.25 \mu\text{m}$, and $s(\Lambda')=42.3 \mu\text{m}$. The latter estimator for Λ' seems large at first glance, but the constraint $\Lambda'=3\Lambda$ used in Ref. 18 leads to a value $\Lambda'=150 \pm 30 \mu\text{m}$, whose error is also of the same order as $s(\Lambda')$. The latter constraint, i.e., $\Lambda'=3\Lambda$, is debatable because the value of Λ' is usually between 2Λ and 3Λ for most of the porous foams.²²

A specific feature of the reconstruction of the parameters appealing to the high frequency approximation of the JCAM is the fact that for given S_{11} and S_{21} , the reconstruction of ϕ through Eq. (8) is, as expected, rather insensitive to a variation of Λ' , Fig. 4. Likewise, the influence of $s(\Lambda')$ is not significant on the reconstruction of the other parameters. The reconstruction of α_∞ is strongly sensitive on Λ , Fig. 4.

The reconstructed normalized density and bulk modulus, as calculated by introducing the reconstructed parameters in Eq. (6), over the frequency range used for the reconstruction

are in good agreement with the measured ones, Fig. 5. It is clear that the developed analytic method for the recovery of the characteristic parameters realizes some kind of least squares fitting of both density and bulk modulus. This fit is much more efficient than a direct fitting of the curve. For example, use of an algorithm based on a basic fit of $\text{Im}(\rho^{[1]}/\rho^{[0]})$, which is theoretically equal to $1/\Lambda\sqrt{2\eta/\omega\rho_f}$, leads to a negative value of Λ because the experimental slope is clearly positive. Use of such an algorithm would require reconstructions over a larger frequency range.

The time domain reconstructed reflected and transmitted fields, as calculated from the reconstructed parameters introduced in Eqs. (6) and (2) via inverse Fourier transform of Eq. (10), $P^{ri}(x_a)$ and $P^i(x_b)$ being the measured incident signals, agree quite well with the experimentally recorded fields, Fig. 6. The Bravais-Pearson linear correlation coefficients between the latter fields are 0.9811 in reflection and 0.9819 in transmission.

The method was applied to characterize various samples with other piezoelectric Ultrasonic transducers, whose central frequency is 200 kHz. Table II presents the values of the parameters as recovered with the present method and as recovered with other ultrasonic methods.¹⁵⁻¹⁷ The flow

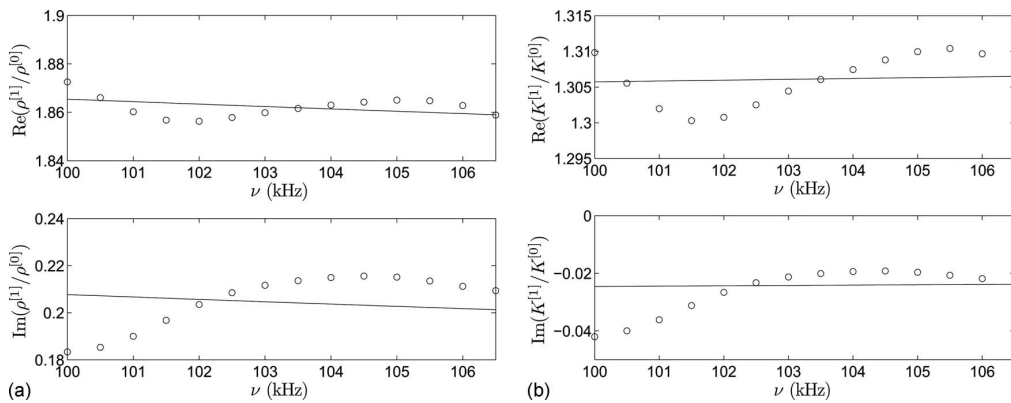


FIG. 5. Comparison between experimental (o) and reconstructed (—) real and imaginary parts of (a) the normalized density $\tilde{\rho}$ and (b) the bulk modulus \tilde{K} .

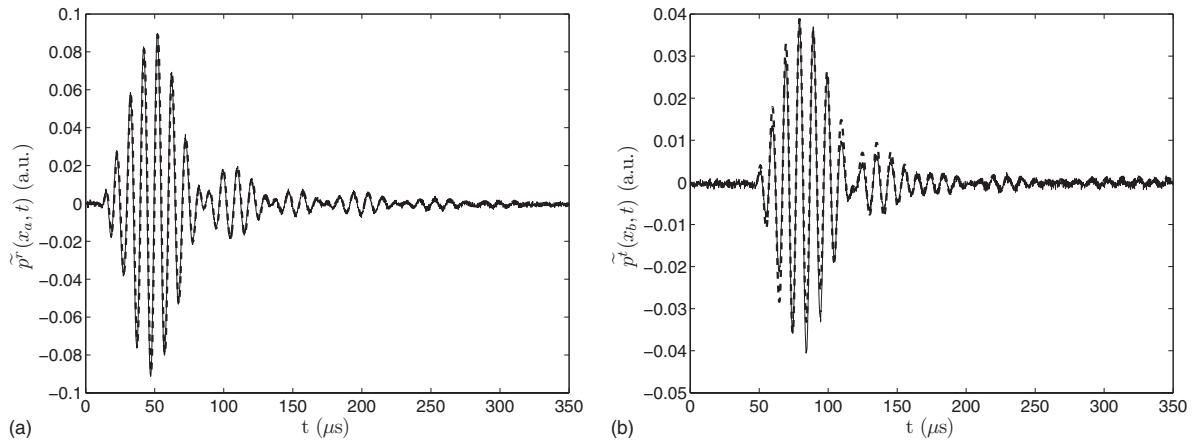


FIG. 6. Comparison between experimental (—) and simulated (---) signals, with recovered $\phi=0.752$, $\alpha_\infty=1.246$, $\Lambda=55.4 \mu\text{m}$, and $\Lambda'=178.4 \mu\text{m}$: (a) reflected signal and (b) transmitted signal.

resistivity of the polyurethane foam is low, i.e., $\sigma = 2830 \text{ N m s}^{-4}$, while the one of the melamine is $\sigma = 12\,000 \text{ N m s}^{-4}$.

C. Discussion

The method is sensitive to the approximation of the continuous Fourier transform by a discrete one and to the temporal shift, especially for the evaluation of S_{11} , as was pointed out in Ref. 28. Nevertheless, assuming that the Fourier transformed is correctly performed, and that the proposed process does not lead to temporal shift, other sources of error arise.

From

$$\frac{\partial z^2}{\partial S_{21}^2} = \frac{8S_{21}S_{11}}{((1-S_{11})^2 - S_{21}^2)^2},$$

$$\frac{\partial z^2}{\partial S_{11}^2} = \frac{4(1-S_{11}^2 - S_{21}^2)}{((1-S_{11})^2 - S_{21}^2)^2}, \quad (11)$$

it is obvious that a weak transmission, i.e., large flow resistivity materials, has little influence on the retrieval of z . For the low and medium flow resistivity foams tested, S_{11} is

TABLE II. Properties of other homogeneous materials as recovered with Refs. 15–17 and as recovered by our analytic method.

	L (mm)	ϕ	α_∞	Λ (μm)	Λ' (μm)
Melamine foam					
Use of Refs. 15–17	10	0.99	1.001	150	250
Present method		0.99	1.011	159.2	259.2
Polyurethane foam					
Use of Refs. 15–17	27	0.97	1.07	270	670
Present method		0.975	1.057	319.4	621

close to zero. The reconstruction is also highly sensitive when S_{21} is close to one, which is in contradiction with the use of thin layer sample, for which reconstruction is much more efficient. On the other hand, from

$$\frac{\partial \zeta}{\partial S_{11}} = \frac{-1}{ik^{[0]}L} \frac{z-1}{z+1-S_{11}(z-1)},$$

$$\frac{\partial \zeta}{\partial S_{21}} = \frac{-1}{S_{21}ik^{[0]}L}, \quad (12)$$

it is obvious that ζ , for S_{11} close to zero, is rather insensitive to S_{11} , while it is very sensitive to S_{21} when the latter is close to zero. This also imposes conditions not only on the absorption of the sample to characterize, but also on its thickness: both should be small. This method seems particularly adapted to low and medium resistive materials, but less to highly resistive ones, for which S_{21} vanishes.

On the other hand, it is obvious from Eq. (7) that Λ and Λ' are, respectively, highly sensitive to $\text{Im}(\tilde{\rho})$ and $\text{Im}(\tilde{K})$, when the latter is small. Particularly, the reconstructed characteristic lengths are singular when the imaginary part of the density or of the bulk modulus vanishes. Both of these quantities are close to zero in the asymptotic high frequency regime of the JCAM. The regularization process partly avoids such problems, but decreasing the frequency of the solicitation is the best way to increase the value of both imaginary parts. From Eqs. (8) and (9), it is clear that reconstructed porosity is highly sensitive to $\|\tilde{K}\|$ when the latter is small, while the reconstructed tortuosity is less sensitive to variation of $\|\tilde{\rho}\|$.

One of the biggest limitations of the present method is closely linked to experiments, and particularly to the SNR for the evaluation of the reflection coefficient. The flow resistivity of the sample should not be very small. Effectively, very low resistivity foams exhibit quasi-null reflected fields. Their characterization by the present method is also impossible. A similar remark arises for highly resistive porous material, such as rock wool, which exhibits quasi-null transmitted fields.

Another limitation is strongly linked to ultrasonic measurements, for which $k^{[0]}L$ is high. This induces possible difficulties in the evaluation of the correct branch of $\text{Re}(\zeta)$. The frequency band used to perform the inversion, chosen to be the intersection of the -3 dB bandwidth of both Fourier transform of the recorded fields by T_a and T_b without sample, is thin. Use of larger band transducers should help in the regularization of the inverse problem and in its resolution. In this case, particular care should be paid to the frequency range used for the reconstruction, in a sense the model should be valid. Check of the constancy and to some extent to the continuity of the recovered parameters over the frequency range, as proposed in Refs. 9 and 10, should avoid this possible problem.

One of the main advantages of the present method is that the reconstructed parameters are not constrained, as it is usually the case when minimization techniques are applied. On the other hand, this is also a disadvantage because nonphysical values, such as negative characteristic lengths, porosity larger than 1, or tortuosity smaller than 1, can be reconstructed if experiments are not performed with sufficient care. Moreover, among all the experiments performed, it was found that whatever the reconstructed parameters are, even nonphysical ones, the reconstructed time domain signals are always in agreement with the experimental ones. An a priori correct ratio between the reconstructed Λ' and Λ seems to be indicative of the quality of the experiments, and leads to the accurate reconstructions of the other parameters. This a priori is connected to the type of material tested. For most of the industrial foams, a ratio Λ'/Λ that lies between 2 and 3 seems to be a good indicator of the reconstruction. For other industrial porous materials, other ratios can be used, for example, a ratio close to 2 for fibrous materials.

It is then important to check the consistency of the recovered parameters with regard to the frequency of solicitation in order to validate the use of the asymptotic high frequency JCAM. This can be simply achieved at high frequency (diffusion limit) by checking if the wavelength of the central frequency of the incident field is larger than the thermal characteristic length. Effectively, the latter characteristic length represents a measure of the average pore size (although the "pore" is not always straightforwardly defined) while the viscous characteristic length corresponds to the average size of the "constrictions" in the porous medium,²² i.e., the average distance between pore walls in the narrower areas of the pore volume. For example, the ratio of the wavelength in air at 100 kHz over the recovered value of Λ' for the first medium resistivity porous sample studied in this article is around 19. As stated in the Introduction, the low frequency bound of the asymptotic high frequency JCAM being not clear, it is then quite difficult to validate the use of the dissipation model with regard to the latter, particularly because the flow resistivity is not recovered through our method and despite the fact that a frequency higher than 100 kHz usually ensures this validation. Nevertheless, this problem can be partly solved by performing ultrasonic experiments for various central frequencies of the transducers, for example, at 100 and 200 kHz, keeping in mind that the dissipation model should be valid, that additional problems re-

lated to large $k^{[0]}L$ could occur, and that a correct SNR is required. If the reconstructed parameters are quite similar, the constancy of the dissipation model and so of the reconstructed parameters is achieved. This operation is similar to use of larger band transducers, in the sense it would help the regularization of the problem, when the dissipation model is valid.

IV. CONCLUSION

A frequency domain method has been developed, which allows the analytic reconstruction of the four parameters appealing to the high frequency approximation of the JCAM (porosity, tortuosity, and thermal and viscous characteristic lengths) for macroscopically homogeneous rigid frame porous materials. The reconstruction is achieved by first retrieving the complex and frequency-dependent acoustic index of refraction and impedance ratio, from which the four latter parameters are reconstructed. The method and algorithm were tested on relatively low and medium flow resistivity porous samples, which mainly cover the range of resistivity values of plastic foams, and its accuracy has been demonstrated in the ultrasonic domain on three materials. The experiments must be very precise even if the reconstructed time traces are very close to the experimental ones. This is to avoid reconstructed parameters that are meaningless. This situation is often avoided when minimization techniques are used to solve inverse problems. It was found empirically that when the ratio of the recovered thermal and viscous characteristic lengths lies between 2 and 3, as it is the case for most industrial foams, the experiments are performed with sufficient efficiency and the recovered parameters turn out to be accurate.

For the reconstruction to be performed, time domain reflected and transmitted signals should be recorded with a high SNR. Some methods have been employed here to increase the SNR, especially for the reflected field, but it also imposes some constraints on the materials that can be tested with the present method. The flow resistivity should not be very small for the record of the reflected field, while it should not be very large for the record of the transmitted field.

This algorithm being based on analytic developments, further investigations should lead to the development of a more complex algorithm for the complete analytic characterization of homogeneous foam samples, i.e., the recovery of additional parameters such as the flow resistivity from additional lower frequency measurements or parameters of other models relevant for mid frequency range, for example. This method can be viewed as a complementary to the low frequency method developed in Refs. 9 and 10 in the sense that it allows the recovery of the porosity, which should be known in Refs. 9 and 10. The other recovered parameters in the two frequency ranges may then be compared.

ACKNOWLEDGMENT

The authors would like to thank A. Wirgin for his useful help during the experiments and the writing of this paper.



Spatial Laplace transform for complex wavenumber recovery and its application to the analysis of attenuation in acoustic systems

A. Geslain,¹ S. Raetz,² M. Hiraiwa,³ M. Abi Ghanem,³ S. P. Wallen,³ A. Khanolkar,³ N. Boechler,³ J. Laurent,⁴ C. Prada,⁴ A. Duclos,² P. Leclaire,¹ and J.-P. Groby^{2,a)}

¹DRIVE EA1859, Univ. Bourgogne Franche Comté, 58000 Nevers, France

²Laboratoire d'Acoustique de l'Université du Maine, UMR-6613 CNRS/Université du Maine, Avenue Olivier Messiaen, 72085 Le Mans, France

³Department of Mechanical Engineering, University of Washington, Seattle, Washington 98195, USA

⁴Institut Langevin, CNRS, ESPCI Paris, PSL Research University, 1 rue Jussieu, 75005 Paris, France

(Received 18 April 2016; accepted 18 September 2016; published online 7 October 2016)

We present a method for the recovery of complex wavenumber information via spatial Laplace transforms of spatiotemporal wave propagation measurements. The method aids in the analysis of acoustic attenuation phenomena and is applied in three different scenarios: (i) Lamb-like modes in air-saturated porous materials in the low kHz regime, where the method enables the recovery of viscoelastic parameters; (ii) Lamb modes in a Duralumin plate in the MHz regime, where the method demonstrates the effect of leakage on the splitting of the forward S_1 and backward S_2 modes around the Zero-Group Velocity point; and (iii) surface acoustic waves in a two-dimensional microscale granular crystal adhered to a substrate near 100 MHz, where the method reveals the complex wavenumbers for an out-of-plane translational and two in-plane translational-rotational resonances. This method provides physical insight into each system and serves as a unique tool for analyzing spatiotemporal measurements of propagating waves. *Published by AIP Publishing.*

[<http://dx.doi.org/10.1063/1.4963827>]

I. INTRODUCTION

Understanding the dispersive and dissipative properties of materials is critical to the study of wave phenomena. Extracting complex wavenumber information is important, particularly in the context of understanding wave attenuation. In addition to dispersive effects, such as the existence of band gaps, wave attenuation can be caused by factors such as geometric attenuation or intrinsic material loss (e.g., heat dissipation). In any of these cases, the wave attenuation can be interpreted in terms of complex wavenumbers. The recovery of complex wavenumbers is of particular interest for the characterization of the viscoelastic properties of materials, in systems such as thin-films,^{1,2} or coated plates,³ the study of mode interactions, i.e., hybridization or repulsion,⁴⁻⁶ or the recovery of complex band structures arising from structural periodicity or resonant elements.^{4,7,8} The dispersion of waves propagating through materials is typically interpreted in the context of frequency and wavenumber domain information and obtained from discrete spatiotemporal data via discrete Fourier transforms and related methods.⁹⁻¹⁴ However, such techniques typically only supply real wavenumber information (or their magnitudes) from two-dimensional, discrete, spatiotemporal wave propagation information, such as may be obtained from scanned receiver measurements. Several methods have been proposed to characterize wave attenuation and extract complex wavenumber information,¹⁵⁻²² however, each has restrictions, as: (i) they are usually based on measurements of wave amplitude decrease

with respect to time,¹⁵⁻¹⁸ (ii) they are iterative methods applied in space, like the modified Prony method,¹⁹ (iii) the number of modes has to be known in advance or a unique mode has to be isolated,^{15-17,20,21,23} (iv) the modes contributing significantly to the signal are presumed to not interact or overlap with one another, or (v) they must include a third dimension of information, such as would be the case in an experiment with a scanned emitter and a receiver.^{21,22}

In this work, a method presenting none of these restrictions is proposed and applied to the analysis of complex attenuation phenomena in the scanned spatiotemporal measurements of three acoustic systems. After presenting the implementation of the method making use of a spatial Laplace transform in Sec. II, we discuss its application in the following three diverse scenarios. In Sec. III, the method is applied to the study of low frequency (200 Hz–4095 Hz) guided elastic waves in porous materials, which are highly dissipative systems such that the wavenumbers associated with each mode are complex. The method is utilized to characterize skeleton (matrix) viscoelastic parameters. In Sec. IV, the method is applied to the analysis of Zero-Group Velocity (ZGV) Lamb modes at MHz frequencies (1.85 MHz–2 MHz) in a Duralumin plate. The ZGV modes are composed of two interfering counter-propagating Lamb modes, and the method reveals mode separation due to leakage and their associated complex wavenumbers, along with motivating the need for more complex multilayer models. Finally, in Sec. V, the method is applied to characterize the resonant attenuation of high frequency (10 MHz–400 MHz) surface acoustic waves (SAWs) propagating through a two-dimensional (2D) microscale granular crystal adhered to a substrate with three contact-based resonances. While

^{a)}Author to whom correspondence should be addressed. Electronic mail: jean-philippe.groby@univ-lemans.fr

hybridization due to the out-of-plane mode can be seen using a usual spatial Fourier transform,²⁴ the two combined rotational and in-plane translational resonances are only noticeable by studying the attenuation of the modes, which is further highlighted by this method.

II. THE RECOVERY OF COMPLEX WAVENUMBERS: THE SLaTCoW METHOD

The acronym of the proposed method is SLaTCoW for Spatial Laplace Transform for COMplex Wavenumber recovery. In what follows, we focus on the extraction of complex wavenumber information from guided elastic wave measurements. However, we note that the SLaTCoW method is sufficiently general that it may be applied to wave fields of any type. Assume that a wave field ξ has been recorded discretely along a line of length L and has a time dependence of $e^{-i\omega t}$, where $\omega = 2\pi f$ is the angular frequency. This field (after neglecting the branch integrals arising from the application of the residue theorem) can be written in the frequency domain as the sum of the contributions of each of the modes (ω is dropped for clarity)

$$\xi(x) = \sum_{m \in \mathcal{M}} \tilde{\xi}^m \exp(iK^m x) \Pi(x, L), \quad (1)$$

where x is the spatial coordinate, $\tilde{\xi}^m$ is the complex amplitude of the m -th mode, K^m is the complex wavenumber of the m -th mode, \mathcal{M} is the set of modes, and $\Pi(x, L)$ is the gate function equal to 1 when $x \in [0, L]$ and equal to 0 elsewhere. The complex wavenumber is defined as $K^m = k_r^m + ik_i^m$, with $k_r^m > 0$ and $k_i^m > 0$, such that Eq. (1) only involves forward propagating modes. Applying the usual spatial Fourier transform only enables the recovery of k_r^m . In order to recover both real and imaginary parts of K^m , a spatial Laplace transform is applied to $\xi(x)$ denoted $\Xi(s) = \int_{-\infty}^{\infty} \xi(x) \exp(-sx) dx$, where s is a complex number wavenumber parameter $s = s_i + is_r$, with real numbers s_i and s_r . This spatial Laplace transform takes the form

$$\begin{aligned} \Xi(s) &= \sum_{m \in \mathcal{M}} \tilde{\xi}^m \int_0^L \exp[(iK^m - s)x] dx \\ &= L \sum_{m \in \mathcal{M}} \tilde{\xi}^m \exp[(iK^m - s)L/2] \frac{\sinh[(iK^m - s)L/2]}{(iK^m - s)L/2}. \end{aligned} \quad (2)$$

The meaning of the spatial Laplace transform of the m -th mode is ensured only if $s_i \geq -k_i^m$ because this ensures the energy decay of each mode. Thus, the upper half space, the lower bound of which is the maximum value of $-k_i^m$ with $m \in \mathcal{M}$, is the only admissible half space in the complex s -plane and defines the region of absolute convergence of the Laplace transform. We note that the slice of $\Xi(s)$ in the complex s plane at $s_i = 0$ exactly corresponds to the spatial Fourier transform $\text{TF}(s_r)$ of a finite window. Along this line, Eq. (2) reduces to $\text{TF}(s_r) = L \sum_{m \in \mathcal{M}} \tilde{\xi}^m \exp[i(k_r^m - s_r + ik_i^m)L/2] \text{sinc}[(k_r^m - s_r + ik_i^m)L/2]$, where $\text{sinc}(x) = \sin(x)/x$, as can be seen in Fig. 1.

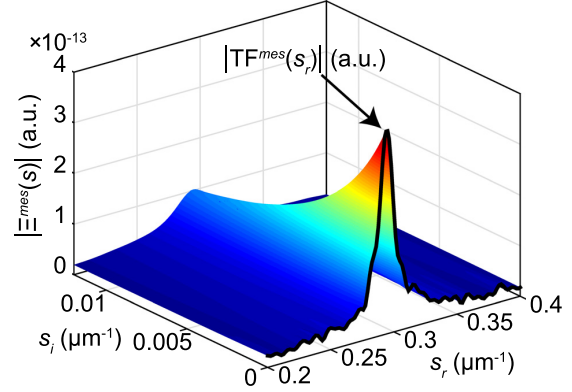


FIG. 1. Laplace transform $\Xi^{mes}(s)$ corresponding to $f = 149$ MHz, for the scanned measurements discussed in Section V. The solid black line shows the corresponding amplitude of the spatial Fourier transform $\text{TF}^{mes}(s_r)$.

The problem when trying to recover K^m is twofold: the amplitude and phase of the mode are unknown and the position of $-k_i^m$ in the complex s -plane is by definition unknown. Therefore, we will focus the analysis on the upper half space $s_i \geq 0$ where no mode K^m is included, thus making the method stable by preventing the divergence of the transform due to the poles. Inspired by previous works on the recovery of the reflection coefficients of higher order modes propagating in a square cross-section impedance tube,²⁵ the recovery of K^m is performed for each frequency by minimizing the following cost function:

$$\begin{aligned} F(|\tilde{\xi}^m|, \phi^m, k_r^m, k_i^m, \mathcal{M}) &= \sum_{s_r} \sum_{s_i} \left| \Xi^{mes}(s) - L \sum_{m \in \mathcal{M}} |\tilde{\xi}^m| \right. \\ &\quad \times \exp(i\phi^m) \times \exp((i(k_r^m + ik_i^m) - s_i - is_r)L/2) \\ &\quad \times \left. \frac{\sinh((i(k_r^m + ik_i^m) - s_i - is_r)L/2)}{(i(k_r^m + ik_i^m) - s_i - is_r)L/2} \right|, \end{aligned} \quad (3)$$

where $\Xi^{mes}(s)$ is the spatial Laplace transform of the measured field $\xi(x)$, and $|\tilde{\xi}^m|$ and ϕ^m are, respectively, the theoretical amplitude and phase of the m -th mode. Note that the \mathcal{L}_1 -norm is used in Eq. (3) because it leads to quite similar results as the usual \mathcal{L}_2 -norm. The latter may be preferable when analyzing signals with a low signal-to-noise ratio. The minimization is performed under constraints with the Nelder-Mead simplex algorithm ([®]Matlab function *fminsearchbnd*). In Eq. (3), it can be seen that there are $4|\mathcal{M}|$ number of unknowns, corresponding to the wave amplitude, phase, and real and imaginary parts of the complex wavenumber K^m of each mode. To solve for these unknowns, we first determine the number of modes to be recovered, along with their real wavenumbers, amplitudes, and phases, by looking at the spatial Fourier transform for each frequency. As an example, the solid black line in Figure 1 shows the amplitude of the spatial Fourier transform $\text{TF}(s_r)$, corresponding to $f = 149$ MHz, for the scanned measurements discussed in Section V. It can be seen from the Fourier spectrum that there is one clear

peak (mode) at this frequency, with real wavenumber $k_r^1 \approx 0.29 \mu\text{m}^{-1}$. The spatial Laplace transform $\Xi^{mes}(s)$ is shown by the complex s -plane surface plot of Fig. 1. We then calculate a similar surface for varied values of $(|\xi^1|, \phi^1, k_r^1, k_i^1)$ and minimize the difference between the calculated and measured s -plane surface in Eq. (3) to end with $K^1 = 0.294 + i3.71 \times 10^{-3} \mu\text{m}^{-1}$, where the superscript denotes that this is the first identified mode (in this case only one mode is identified).

When $|\mathcal{M}| \neq 1$, each mode may, in practice, interact in the complex s -plane, which emphasizes the necessity of using a model involving all possible modes at a given frequency and the minimization of the previous cost function to efficiently determine all the possible K^m . This approach may offer advantages over related approaches in that highly attenuating and closely spaced modes may be distinguished from each other and from peaks associated with the finite measurement domain.

III. APPLICATION TO GUIDED ELASTIC WAVES IN POROUS MATERIALS

We first apply the SLaTCoW method to the case of guided elastic waves in porous materials. Porous materials are known to be highly dissipative due to viscothermal

losses, interaction between the solid and fluid phases, and viscoelasticity of the skeleton. Seminal works by Boeckx *et al.*¹⁸ have paved the way for the characterization of the skeleton, porous material mechanical parameters by means of guided waves. These works mainly focus on the experimental recovery of the phase velocity $v_\phi^m = \omega/k_r^m$, in part, because of a lack of experimental data and analysis tools for the efficient determination of k_i^m . The present method is applied to experimentally determine both real and imaginary parts of the wavenumbers, thereby filling the existing gap in attenuation characterization capabilities, and enabling future works concerning the experimental measurement and modeling of viscoelastic parameters of porous materials.

The experimental setup, which is similar to the one used in Ref. 18, is depicted in Fig. 2(a). A high porosity ($\phi > 0.95$) melamine foam sample 85 cm long, 45 cm wide, and 5.5 cm thick is glued on a rigid backing. The excitation is provided by a shaker (Bruel and Kjaer type 4810), which is rigidly attached to the sample with a threaded steel rod (20 mm in length and 5 mm diameter) fixed to the shaker on one side and glued on a 1 mm thick aluminum plate of width 10 cm and height 1.5 cm. This plate is cut at the edge opposite to the threaded steel rod and glued to the porous sample, creating a line source 15 cm from the edge of the sample.

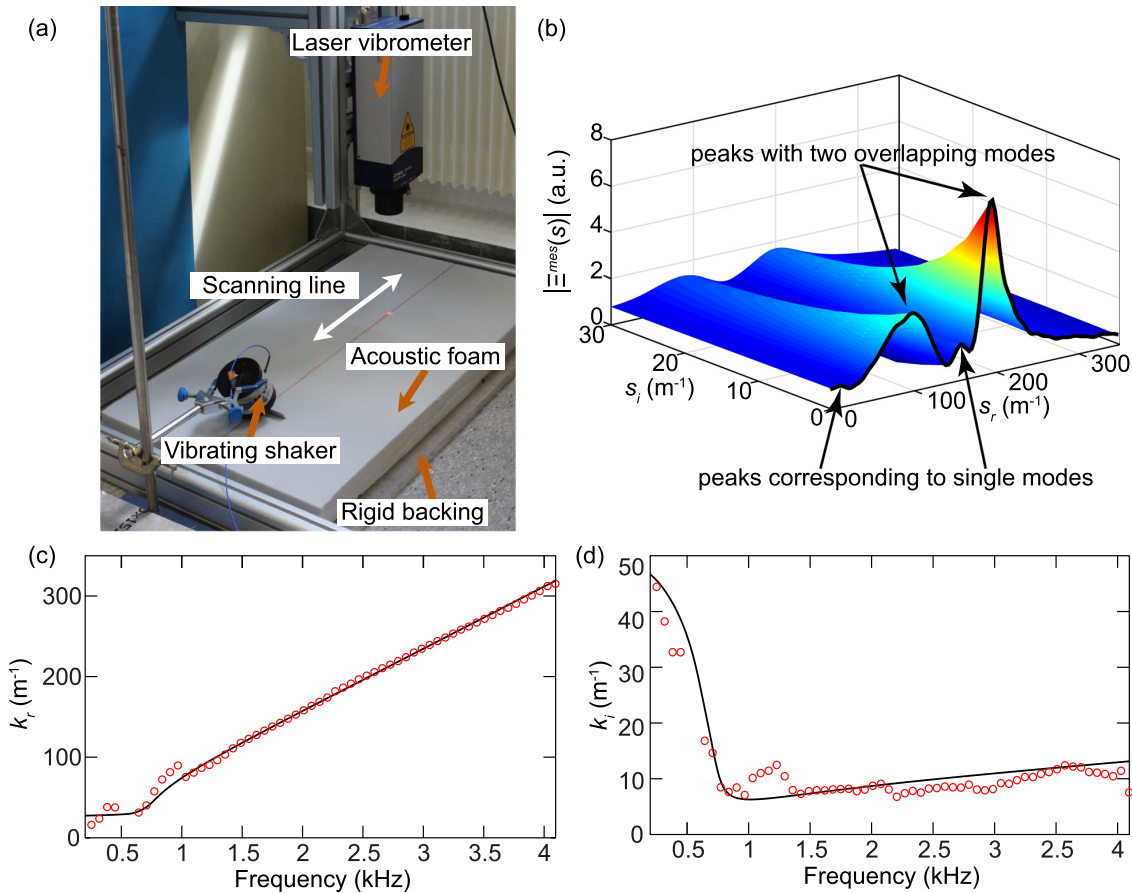


FIG. 2. (a) Photograph of the experimental setup. (b) Laplace transform $\Xi^{mes}(s)$ corresponding to $f = 2453$ Hz. Arrows point out peaks, whose main component is a single mode, and peaks, whose main component are two modes overlapping. (c) k_r and (d) attenuation (k_i) of the first guided mode. Red circles depict the results obtained with the SLaTCoW method and solid lines depict the theoretical predictions.

The resonance of this part was measured to be 4500 Hz. While the measurement could be made at higher frequencies (up to 8000 Hz with a relatively good signal to noise ratio), the results are only shown for frequencies below this limit. The excitations are 300 sine functions equally spaced between 200 Hz and 4095 Hz. The normal displacement $u_n(x)$ is acquired at 801 positions along a length of $L = 40$ cm with a laser vibrometer (Polytec OFV-503) mounted on a one-dimensional moving stage, which moves the laser along the x -axis after each frequency measurement is accomplished. The vibrometer is connected to a spectral analyzer (Stanford Research Systems SR785), which allows us to directly measure $u_n(x)$ in the frequency domain. Each measurement is averaged 100 times.

The 1962 Biot model²⁶ parameters of the porous material, density ρ , porosity ϕ , flow resistivity σ , viscous and thermal characteristic length Λ and Λ' (respectively), real part of the shear modulus N_r , and Poisson ratio ν were determined independently using standard methods²⁷ and are given in Table I. Viscous and thermal losses are accounted for by use of the Johnson-Champoux-Allard model,^{28,29} leading to complex and frequency dependent effective density and bulk modulus of the fluid phase. The imaginary part of the shear modulus N_i , which is usually considered constant in frequency, has been determined using the SLaTCoW method.

This type of measurement is known to be difficult due to large dissipation. More than 8 modes can be theoretically recovered over this frequency range, the velocities of which asymptotically tend towards the Rayleigh or shear velocities at high frequencies. Fig. 2(b) depicts the Laplace transform $\Xi^{mes}(s)$ at $f = 2453$ Hz, where 6 modes can be seen. We choose to focus on the first guided mode, which was the one that was excited most efficiently. Extracting the complex wavenumber for this mode is typically difficult, as several modes are present in its vicinity. The procedure was applied to recover three modes around the first guided mode in order to remove the remaining components of the others. The real and the imaginary wavenumber, k_r^1 and k_i^1 , respectively, versus frequency are found via the SLaTCoW method and plotted in Figs. 2(c) and 2(d), respectively. Theoretical predictions obtained using Stroh formalism^{30,31} and a Müller algorithm agree well with the wavenumbers extracted using the SLaTCoW method when the complex shear modulus $N = N_r - iN_i$ is fixed such that $N = 38 - i1.52$ kPa (damping factor $N_i/N_r = 0.04$). This value is in accordance with the literature.³² This demonstrates the efficiency of the present method to discriminate modes when several are overlapping, and its effectiveness for extracting attenuation parameters. This paves the way for the extraction of new experimental information that enables the development of improved models of viscoelastic porous materials.

TABLE I. Material parameters for the melamine foam.

ϕ	ρ (kg m ⁻³)	α_∞	σ (N s m ⁻⁴)	Λ (μ m)	Λ' (μ m)	N (kPa)	ν
0.989	6.1	1	8060	215	215	38 - i1.52	0.3

IV. APPLICATION TO ZGV LAMB MODE IN A DURALUMIN PLATE

We now apply the SLaTCoW method to obtain the complex dispersion curves of Lamb waves propagating in a 1.515 mm thick Duralumin plate. Particular attention is paid to the first symmetric S_1S_2 ZGV Lamb mode. This mode is composed of two counter-propagating modes: the forward propagating S_1 Lamb mode and the backward propagating S_{2b} Lamb mode.³³ In the ideal case of a non-absorbing material and free-standing plate, there are a unique wavenumber and frequency ($K^{S_1S_2}, f^{S_1S_2}$) where these two modes coexist. At this point, the interference of S_1 and S_{2b} leads to the so-called S_1S_2 -ZGV resonance.³⁴ When the material absorption is significant or when there is leakage to the surrounding medium, the Lamb modes are inhomogeneous, their dispersion curves are no longer real valued, and their wavenumbers are complex.³⁵⁻³⁷ As previously noted for measurements made in a 50 μ m-thick tungsten plate, attenuation leads to a separation of the S_1 and S_{2b} mode branches.³⁸

Here, we illustrate a similar effect due to leakage. Using the SLaTCoW method, we estimate the complex dispersion branches in the vicinity of the ZGV point. The experimental setup is shown Fig. 3(a). A linear array ultrasound transducer probe (Imasonic SAS, 0.417 mm element pitch) made of 128 elements centered at 3.5 MHz, with a large frequency bandwidth, was used to generate Lamb waves in a Duralumin plate of thickness 1.515 mm, width, and length 100 mm. The probe was operated with the OPEN System of Lecoer Electronique. The probe was coupled to the Duralumin plate using a thin layer of echographic gel approximately 0.150 mm thick. The first element of the array was used to generate an acoustic wave and then the 128 elements were used in receiver mode to record the normal displacement of the plate. The contact of the transducer array with the plate modifies the boundary conditions, induces leakage of the Lamb modes, and breaks the symmetry of the problem, such that the Lamb modes can no longer be separated in symmetric and antisymmetric families.

The results of the application of the SLaTCoW method to these experimental data concerning the two modes (M^3 and M^{4b}) within the ranges $k_r \in [0; 1.8]$ mm⁻¹, $k_i \in [-0.5; 0.5]$ mm⁻¹, and $f \in [1.85; 2.03]$ MHz are shown in Figs. 3(b) and 3(c). We denote the Lamb modes with a capital letter M , where the associated index indicates the mode number. The measured M^3 and M^{4b} Lamb modes have opposite phase velocities. While the real part of K^{4b} is negative, both wavenumbers K^3 and K^{4b} (where the superscripts of K^3 and K^{4b} correspond to modes M^3 and M^{4b}) have positive imaginary parts as their amplitudes decay from the source to the receiver. However, for convenience, the backward mode wavenumber is represented with a positive real part and a negative imaginary part. Theoretical complex dispersion curves, using the classic Müller algorithm, are superimposed for comparison. Two cases have been considered: a free-standing Duralumin plate and a more realistic model. In both cases, the velocities of compressional and shear waves in Duralumin are set to $V_L = 6380$ m s⁻¹ and $V_T = 3080$ m s⁻¹, respectively, and the density is $\rho = 2790$ kg m⁻³. The

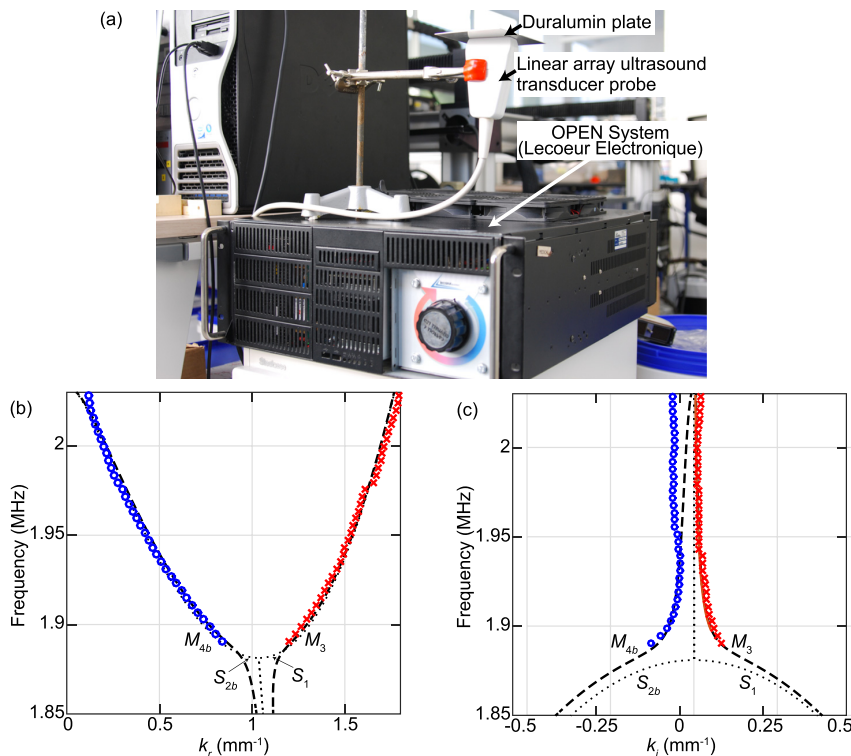


FIG. 3. (a) Photograph of the experimental setup. (b) and (c) Dispersion of Lamb waves in a 1.525 mm thick Duralumin plate: (b) real part and (c) imaginary part of the wavenumber. Markers denote the points identified using the SLaTCoW method. The chosen ranges, $k_r \in [0; 1.8] \text{ mm}^{-1}$, $k_i \in [-0.5; 0.5] \text{ mm}^{-1}$, and $f \in [1.85; 2.03] \text{ MHz}$, include two Lamb modes: M^3 (cross) and M^{4b} (circle). Theoretical complex dispersion curves using two different models are displayed for comparison: a model considering a free-standing Duralumin plate (dotted lines) and a more complex model (dashed lines).

attenuation coefficient of Duralumin is taken from the literature as 0.9 dB m^{-1} at 5.86 MHz .¹⁵ Considering the dotted lines in Figs. 3(b) and 3(c), which represent the calculated dispersion curves accounting for intrinsic loss in a free-standing Duralumin plate, the differences between these curves and the SLaTCoW results are clear. This emphasizes the effects of the leakage of acoustic energy due to the contact of the transducer array, and the necessity to use a model that accounts for this. A more realistic model is composed of three perfectly bonded media: a layer of Duralumin in contact with a fluid layer (modeling the echographic gel), which is in contact with a half-space solid media representing the probe array. This model is used to calculate the theoretical dispersion curves shown as dashed lines in Figs. 3(b) and 3(c), using the previously stated properties for Duralumin. The 0.15 mm thick fluid layer is modeled as water, and it is assumed that no shear waves can propagate in it. The properties of the half-space have been chosen to be $V_L = 3000 \text{ m s}^{-1}$, $V_T = 1300 \text{ m s}^{-1}$, and $\rho = 1100 \text{ kg m}^{-3}$. No attenuation is assumed for both the fluid layer and the half-space. A good agreement between the theoretical curves and the points obtained using the SLaTCoW method can be seen. In Fig. 3(b), a separation of M^3 (cross) and M^{4b} (circle) branches is observed. These modes are typically not observed because of attenuation when approaching the position of the ZGV point. As shown in Fig. 3(b), as the position of the ZGV point of a free plate is approached, the imaginary part of the wavenumber and thus the attenuation become larger.

Although the chosen model may be considered overly simple, it is sufficient to reach good qualitative agreement with the results obtained using the SLaTCoW method. Note

that the discrepancy in Fig. 3(c) between experiments and theory on the M^{4b} mode is due to the fact that this experimental branch is attenuated in the vicinity of $k_r = 0$, making the SLaTCoW recovery harder to perform due to the very low signal-to-noise ratio. However, for the M^3 mode, where the signal-to-noise ratio is high, the agreement between the SLaTCoW results and the theoretical dispersion curves is excellent. The good qualitative agreement between the SLaTCoW results and the theoretical dispersion curves paves the way for new insights regarding the ZGV modes in free-standing plates and related multilayer systems.

V. APPLICATION TO SURFACE ACOUSTIC WAVES IN A TWO-DIMENSIONAL MICROSCALE GRANULAR CRYSTAL ADHERED TO A SUBSTRATE

We apply the SLaTCoW method to obtain the complex dispersion curves of SAWs propagating in a 2D microscale granular crystal adhered to a substrate. Ordered and reduced-dimensional granular structures, often referred to as granular crystals,^{39–41} have proven to be systems of interest, as they represent an avenue for gaining a broader understanding of granular media dynamics, and have been suggested for use in stress wave manipulation and acoustic signal processing applications.⁴⁰ While granular crystals have typically been constructed from macroscale particles,⁴¹ the acoustics of microscale granular crystals is an emerging field.^{24,42,43}

In a recently published work,²⁴ the resonant attenuation of SAWs propagating through a 2D microscale granular crystal adhered to a substrate was studied using a laser ultrasonic technique. A schematic of the sample and the laser ultrasonic setup used in the study of Ref. 24 is shown in Fig. 4.

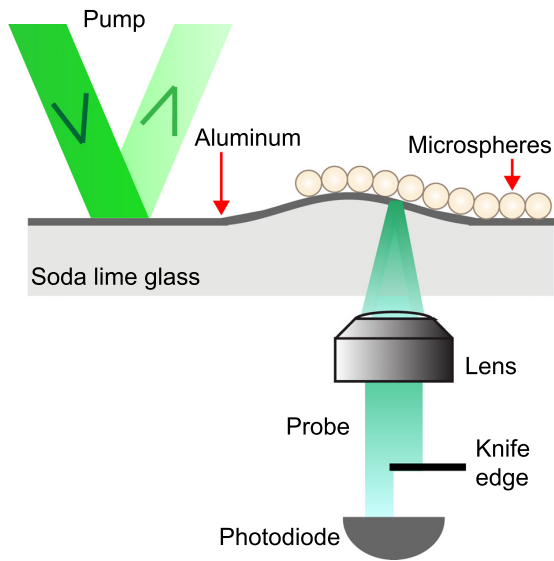


FIG. 4. Schematic of sample and laser ultrasonic experimental setup used in Ref. 24.

In summary, the microscale granular crystal is a monolayer of $2\ \mu\text{m}$ diameter silica spheres, which were assembled via a convective self-assembly process.⁴⁴ An interface between regions with and without the monolayer was created using a microcontact printing technique.⁴⁵ Surface acoustic waves were generated by focusing a pulsed laser into the sample surface (430 ps pulse duration, 532 nm optical wavelength, and $1.2\ \text{mm} \times 20\ \mu\text{m}$ spot size), such that they traversed the interface, whereafter they were measured using a photo-deflection technique (continuous wave laser, 514 nm optical wavelength, $6\ \mu\text{m}$ spot size) at 185 positions along a scan length of $740\ \mu\text{m}$. Additional experimental details can be found in Ref. 24. By calculating the 2D Fourier transform magnitudes of the spatiotemporal data corresponding to the

SAWs propagating in the region with the monolayer, the dispersion of SAWs propagating in the granular crystal was visualized. While this method did not separate the real and imaginary wavenumber components of the SAW dispersion, the calculated dispersion curves revealed the interaction between three contact-based resonances of the monolayer,^{24,46} including one with out-of-plane motion of the spheres and two with combined rotational and in-plane translational motion.

We apply the SLaTCoW method to the spatiotemporal measurement data obtained and presented in Ref. 24 (corresponding to the sample without any additional aluminum coating on top of the spheres). The resulting complex dispersion curves are shown in Fig. 5(a) (k_r^1) and in Fig. 5(b) (k_i^1). As can be seen in Fig. 5(a), an avoided crossing with the out-of-plane contact resonance (f_N) of the monolayer is present and is the only visible feature disturbing the straight line corresponding to Rayleigh waves propagating in the substrate. We compare the dispersion curves calculated from experimentally obtained data with those calculated in Ref. 24 using a lossless theoretical model,⁴⁶ and find a reasonable agreement in the neighborhood of the out-of-plane contact resonance. As in Ref. 24, avoided crossings due to the two rotational-translational modes (including the rotation dominated resonance f_{RH} and the translation dominated resonance f_{HR}) are both absent. In contrast, the two rotational-translational resonances are both clearly visible in the dispersion curves corresponding to the imaginary part of the wavenumber shown in Fig. 5(b) as smaller peaks surrounding the large out-of-plane resonance.

This work and the SLaTCoW method pave the way for the development of new models of microscale granular dynamics, which may find use in discerning the contributions of various sources of loss observed in experiments.^{24,42} For example, there is currently no model for the imaginary part of K^m for the 2D microscale granular crystal adhered to a

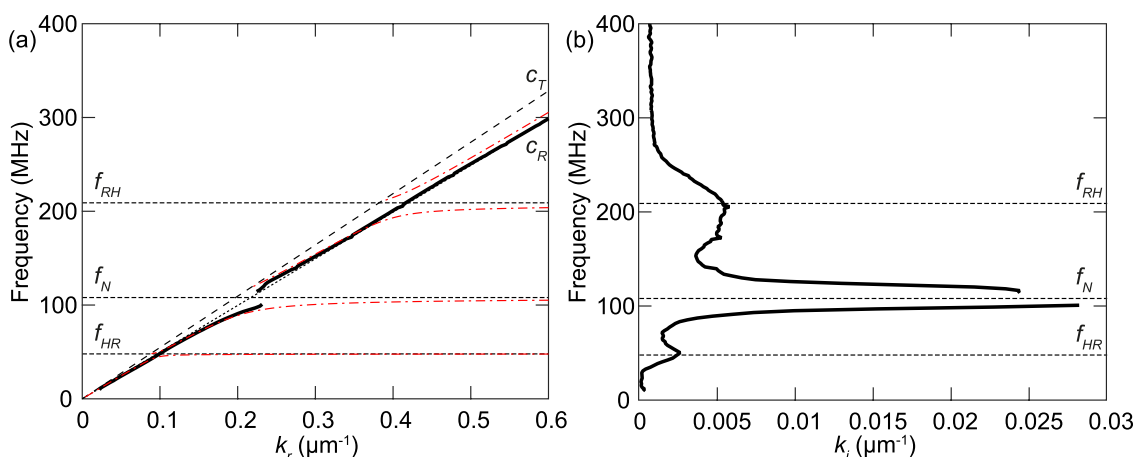


FIG. 5. (a) Dispersion curves of SAWs propagating in a substrate with an adhered microsphere monolayer, corresponding to the real part of the wavenumber, k_r^1 . Solid lines are dispersion curves calculated using the SLaTCoW method. Red dash-dotted lines are the dispersion curves calculated using a lossless model and the fitted contact resonance frequencies (denoted by the horizontal dotted lines). Rayleigh (c_R) and transverse (c_T) wave speeds are the straight dotted and dashed lines, respectively. (b) Dispersion curves of SAWs propagating in a substrate with an adhered microsphere monolayer calculated using the SLaTCoW method, corresponding to the imaginary part of the wavenumber, k_i^1 . Horizontal dotted lines denote the fitted contact resonance frequencies. Solid lines in both panels are computed using experimental data originally obtained and presented in Ref. 24.

substrate. This demonstrates the efficacy of the method to advance relevant modeling efforts.

VI. CONCLUSION

A method for the recovery of complex spatial frequency domain information from spatiotemporal data is presented. This method, named SLATCoW (Spatial Laplace Transform for COMplex Wavenumber recovery), is based on a spatial Laplace transform of the measured wave field in the frequency domain, instead of the usual spatial Fourier transform. The Laplace transform, providing information on both the real and imaginary parts of the poles, is analyzed by the minimization of a correctly chosen cost function. This allows the reconstruction of complex wavenumbers (as well as the complex amplitude) of the modes, even when they are interacting with other modes. The SLATCoW method was applied to three completely different dispersive and attenuating systems, involving three different set-ups in three different frequency ranges, and showed use in the analysis of attenuation phenomena occurring in each system. This method provides information that cannot be obtained from 2D Fourier transforms, including the separation of modes that are almost overlapping, as well as amplitude independent information. The SLATCoW method paves the way for new theoretical developments in various fields of physical acoustics such as attenuating and locally resonant materials.

ACKNOWLEDGMENTS

J.-P. Groby gratefully acknowledges the support from the ANR Project METAUDIBLE No. ANR-13-BS09-0003 co-founded by ANR and FRAE. J.-P. Groby and A. Duclos are grateful for the support of the LMAc projects DECIMAP and PAVNat. N. Boechler, A. Khanolkar, S.P. Wallen, and M. Abi Ghanem acknowledge the support by the U.S. National Science Foundation (Grant No. CMMI-1333858), the U.S. Army Research Office (Grant No. W911NF-15-1-0030), and the University of Washington Royalty Research Foundation. M. Hiraiwa acknowledges the support from the National Science Foundation Graduate Research Fellowship Program under Grant No. DGE-1256082. The contribution by J. Laurent and C. Prada was supported by LABEX WIFI (Laboratory of Excellence ANR-10-LABX-24) within the French Program Investments for the Future under Reference No. ANR-10-IDEX-0001-02 PSL*.

¹R. D. S. Yadava, R. Kshetrimayum, and M. Khaneja, "Multifrequency characterization of viscoelastic polymers and vapor sensing based on saw oscillators," *Ultrasonics* **49**, 638–645 (2009).

²C. Ruppert, J. Neumann, J. B. Kinzel, H. J. Krenner, A. Wixforth, and M. Betz, "Surface acoustic wave mediated coupling of free-space radiation into surface plasmon polaritons on plain metal films," *Phys. Rev. B* **82**, 081416 (2010).

³H.-X. Sun, S.-Y. Zhang, and B.-Q. Xu, "Influence of viscoelastic property on laser-generated surface acoustic waves in coating-substrate systems," *J. Appl. Phys.* **109**, 073107 (2011).

⁴J. H. Page, P. Sheng, H. P. Schriemer, I. Jones, X. Jing, and D. A. Weitz, "Group velocity in strongly scattering media," *Science* **271**, 634–637 (1996).

⁵Z. Liu, C. T. Chan, P. Sheng, A. L. Goertzen, and J. H. Page, "Elastic wave scattering by periodic structures of spherical objects: Theory and experiment," *Phys. Rev. B* **62**, 2446–2457 (2000).

⁶H. Pichard, A. Duclos, J.-P. Groby, V. Tournat, and V. E. Gusev, "Two-dimensional discrete granular phononic crystal for shear wave control," *Phys. Rev. B* **86**, 134307 (2012).

⁷R. J. P. Engelen, D. Mori, T. Baba, and L. Kuipers, "Subwavelength structure of the evanescent field of an optical Bloch wave," *Phys. Rev. Lett.* **102**, 023902 (2009).

⁸V. Romero-García, J. V. Sánchez-Pérez, S. Castañeira-Ibáñez, and L. M. García-Raffi, "Evidences of evanescent Bloch waves in phononic crystals," *Appl. Phys. Lett.* **96**, 124102 (2010).

⁹R. Schmidt, "Multiple emitter location and signal parameter estimation," *IEEE Trans. Antenna Propag.* **34**, 276–280 (1986).

¹⁰E. C. Shang, H. P. Wang, and Z. Y. Huang, "Waveguide characterization and source localization in shallow water waveguides using the prony method," *J. Acoust. Soc. Am.* **83**, 103–108 (1988).

¹¹R. Roy, A. Paulraj, and T. Kailath, "Esprit—a subspace rotation approach to estimation of parameters of cisoids in noise," *IEEE Trans. Acoust. Speech* **34**, 1340–1342 (1986).

¹²R. Roy and T. Kailath, "Esprit-estimation of signal parameters via rotational invariance techniques," *IEEE Trans. Acoust. Speech* **37**, 984–995 (1989).

¹³F. Schöpfer, F. Binder, A. Wöstehoff, T. Schuster, S. Ende, S. Föll, and R. Lammering, "Accurate determination of dispersion curves of guided waves in plates by applying the matrix pencil method to laser vibrometer measurement data," *CEAS Aeronaut. J.* **4**, 61–68 (2013).

¹⁴F. Philippe, P. Roux, and D. Cassereau, "Iterative high-resolution wavenumber inversion applied to broadband acoustic data," *IEEE Trans. Ultrason. Ferroelectr. Freq. Control* **55**, 2306–2311 (2008).

¹⁵C. Prada, D. Clorennec, and D. Royer, "Power law decay of zero group velocity Lamb modes," *Wave Motion* **45**, 723–728 (2008).

¹⁶G. Rix, C. Lai, and A. Spang, Jr., "In situ measurement of damping ratio using surface waves," *J. Geotech. Geoenviron. Eng.* **126**, 472–480 (2000).

¹⁷J. F. Allard, O. Dazel, J. Descheemaeker, N. Geebelen, L. Boeckx, and W. Lauriks, "Rayleigh waves in air saturated axisymmetrical soft porous media," *J. Appl. Phys.* **106**, 014906 (2009).

¹⁸L. Boeckx, P. Leclaire, P. Khurana, C. Glorieux, W. Lauriks, and J. F. Allard, "Guided elastic waves in porous materials saturated by air under Lamb conditions," *J. Appl. Phys.* **97**, 094911 (2005).

¹⁹K. J. Ellefsen, C. H. Cheng, and K. M. Tubman, "Estimating phase velocity and attenuation of guided waves in acoustic logging data," *Geophysics* **54**, 1054–1059 (1989).

²⁰S. Foti, "Small-strain stiffness and damping ratio of pisa clay from surface wave tests," *Geotechnique* **53**, 455–461 (2003).

²¹A. S. Misbah and C. L. Strobbia, "Joint estimation of modal attenuation and velocity from multichannel surface wave data," *Geophysics* **79**, EN25–EN38 (2014).

²²J.-G. Minonzio, J. Foiret, M. Talmant, and P. Laugier, "Impact of attenuation on guided mode wavenumber measurement in axial transmission on bone mimicking plates," *J. Acoust. Soc. Am.* **130**, 3574–3582 (2011).

²³G. Rix, C. Lai, and S. Foti, "Simultaneous measurement of surface wave dispersion and attenuation curves," *Geotech. Test. J.* **24**, 350–358 (2001).

²⁴M. Hiraiwa, M. Abi Ghanem, S. P. Wallen, A. Khanolkar, A. A. Maznev, and N. Boechler, "Complex contact-based dynamics of microsphere monolayers revealed by resonant attenuation of surface acoustic waves," *Phys. Rev. Lett.* **116**, 198001 (2016).

²⁵J. Prisutova, K. Horoshenkov, J.-P. Groby, and B. Brouard, "A method to determine the acoustic reflection and absorption coefficients of porous media by using modal dispersion in a waveguide," *J. Acoust. Soc. Am.* **136**, 2947–2958 (2014).

²⁶M. Biot, "Mechanics of deformation and acoustic propagation in porous media," *J. Appl. Phys.* **33**, 1482–1498 (1962).

²⁷J. F. Allard and N. Atalla, *Propagation of Sound in Porous Media: Modelling Sound Absorbing Materials 2e* (Wiley, Chichester, 2009), Chap. 5.

²⁸D. L. Johnson, J. Koplik, and R. Dashen, "Theory of dynamic permeability and tortuosity in fluid-saturated porous media," *J. Fluid Mech.* **176**, 379–402 (1987).

²⁹Y. Champoux and J. Allard, "Dynamic tortuosity and bulk modulus in air-saturated porous media," *J. Appl. Phys.* **70**, 1975–1979 (1991).

³⁰G. Gautier, L. Kelders, J. P. Groby, O. Dazel, L. De Ryck, and P. Leclaire, "Propagation of acoustic waves in a one-dimensional macroscopically inhomogeneous poroelastic material," *J. Acoust. Soc. Am.* **130**, 1390–1398 (2011).

- ³¹O. Dazel, J.-P. Groby, B. Brouard, and C. Potel, "A stable method to model the acoustic response of multilayered structures," *J. Appl. Phys.* **113**, 083506 (2013).
- ³²L. Jaouen, A. Renault, and M. Deverge, "Elastic and damping characterizations of acoustical porous materials: Available experimental methods and applications to a melamine foam," *Appl. Acoust.* **69**, 1129–1140 (2008).
- ³³D. Clorennec, C. Prada, D. Royer, and T. W. Murray, "Laser impulse generation and interferometer detection of zero group velocity lamb mode resonance," *Appl. Phys. Lett.* **89**, 024101 (2006).
- ³⁴C. Prada, D. Clorennec, and D. Royer, "Local vibration of an elastic plate and zero-group velocity lamb modes," *J. Acoust. Soc. Am.* **124**, 203–212 (2008).
- ³⁵R. D. Mindlin and M. A. Medick, "Extensional vibrations of elastic plates," *J. Appl. Mech.* **26**, 561–569 (1959).
- ³⁶R. D. Mindlin and J. Yang, "Solutions of the three-dimensional equations," in *An Introduction to the Mathematical Theory of Vibrations of Elastic Plates* (World Scientific, 2012), Chap. 2, pp. 23–78.
- ³⁷B. Auld, *Acoustic Fields and Waves in Solids* (R. E. Krieger Publishing Company, Malabar, FL, 1990), Chap. 10, pp. 73–94.
- ³⁸C. Prada, O. Balogun, and T. W. Murray, "Laser-based ultrasonic generation and detection of zero-group velocity lamb waves in thin plates," *Appl. Phys. Lett.* **87**, 194109 (2005).
- ³⁹V. Nesterenko, *Dynamics of Heterogeneous Materials* (Springer-Verlag New York, 2001).
- ⁴⁰G. Theocharis, N. Boechler, and C. Daraio, "Nonlinear periodic phononic structures and granular crystals," in *Acoustic Metamaterials and Phononic Crystals* (Springer, Berlin, 2013), pp. 217–251.
- ⁴¹M. Porter, P. Kevrekidis, and C. Daraio, "Granular crystals: Nonlinear dynamics meets materials engineering," *Phys. Today* **68**(11), 44–50 (2015).
- ⁴²N. Boechler, J. K. Eliason, A. Kumar, A. A. Maznev, K. A. Nelson, and N. Fang, "Interaction of a contact resonance of microspheres with surface acoustic waves," *Phys. Rev. Lett.* **111**, 036103 (2013).
- ⁴³P. Ruello, A. Ayouch, G. Vaudel, T. Pezeril, N. Delorme, S. Sato, K. Kimura, and V. E. Gusev, "Ultrafast acousto-plasmonics in gold nanoparticle superlattices," *Phys. Rev. B* **92**, 174304 (2015).
- ⁴⁴J. Sun, C.-J. Tang, P. Zhan, Z.-I. Han, Z.-S. Cao, and Z.-L. Wang, "Fabrication of centimeter-sized single-domain two-dimensional colloidal crystals in a wedge-shaped cell under capillary forces," *Langmuir* **26**, 7859–7864 (2010).
- ⁴⁵B. H. Lee, H. Shin, and M. M. Sung, "Patterning a two-dimensional colloidal crystal by water-mediated particle transfer printing," *Chem. Mater.* **19**, 5553–5556 (2007).
- ⁴⁶S. P. Wallen, A. A. Maznev, and N. Boechler, "Dynamics of a monolayer of microspheres on an elastic substrate," *Phys. Rev. B* **92**, 174303 (2015).

Complex dispersion relation of surface acoustic waves at a lossy metasurface

Logan Schwan,^{1,a)} Alan Geslain,² Vicente Romero-García,¹ and Jean-Philippe Groby¹

¹LAUM, Université du Maine, UMR CNRS 6613, Le Mans, France

²ISAT, DRIVE EA1859, Université Bourgogne Franche Comté, Nevers, France

(Received 17 November 2016; accepted 17 January 2017; published online 31 January 2017)

The complex dispersion relation of surface acoustic waves (SAWs) at a lossy resonant metasurface is theoretically and experimentally reported. The metasurface consists of the periodic arrangement of borehole resonators in a rigid substrate. The theoretical model relies on a boundary layer approach that provides the effective metasurface admittance governing the complex dispersion relation in the presence of viscous and thermal losses. The model is experimentally validated by measurements in the semi-anechoic chamber. The complex SAW dispersion relation is experimentally retrieved from the analysis of the spatial Laplace transform of the pressure scanned along a line at the metasurface. The geometrical spreading of the energy from the speaker is accounted for, and both the real and imaginary parts of the SAW wavenumber are obtained. The results show that the strong reduction of the SAW group velocity occurs jointly with a drastic attenuation of the wave, leading to the confinement of the field close to the source and preventing the efficient propagation of such slow-sound surface modes. The method opens perspectives to theoretically predict and experimentally characterize both the dispersion and the attenuation of surface waves at structured surfaces. *Published by AIP Publishing.* [<http://dx.doi.org/10.1063/1.4975120>]

While surface waves propagating at the interfaces between two propagative media or at impedance surfaces have been studied theoretically^{1–4} and investigated experimentally,⁵ they have also been shown to emerge at the surface of impervious media when structured with resonant grooves⁶ or boreholes.⁷ The parallel between such surface waves and surface plasmons⁷ has paved the way to novel applications in imaging,^{8,9} focusing,¹⁰ or lensing,¹¹ for which the dispersion relation of the surface waves can be tuned by designing the micro-structure properties. However, while the dispersion relation of such “spoon surface plasmon” is usually presented for real wavenumbers¹² without accounting for losses, the surface wavenumber is actually a complex quantity, the imaginary part of which accounts for the attenuation of the waves induced by the losses. These latter are unavoidable in practice and govern the magnitude of resonances that can be responsible for bandgaps. If methods to predict theoretically^{6,7} the real part of the surface wavenumber and retrieve it experimentally, e.g., from spatial Fourier transform,¹³ are now sufficiently robust, retrieving the imaginary part of it can be challenging,¹⁴ notably because it requires to distinguish the attenuation of the wave induced by the losses from that induced by the geometrical spreading of energy in space.

Here, the propagation of surface acoustic waves (SAWs) at a metasurface is investigated both theoretically and experimentally to predict and retrieve in a systematic method both the real and imaginary parts of the complex SAW wavenumber in the presence of the viscous and thermal losses. The theoretical model is based on a Boundary Layer (BL) approach using plane wave expansion, and its predictions are used to validate the complex dispersion relation retrieved experimentally. The

metasurface Γ under study consists of the two-dimensional Σ -periodic repetition of circular borehole resonators with the radius a and the depth h , at the otherwise rigid plane surface (see Fig. 1). The resonators are arranged in a square lattice, with the lattice constant ℓ , and the unit lattice vectors (\mathbf{e}_1 , \mathbf{e}_2). Denoting $\mathbf{e}_3 = \mathbf{e}_1 \times \mathbf{e}_2$ the out-of-plane unit vector directed at air, the position vector reads $\mathbf{x} = \mathbf{x}_\Gamma + x_3\mathbf{e}_3$, where $\mathbf{x}_\Gamma = x_1\mathbf{e}_1 + x_2\mathbf{e}_2$ is the projection of \mathbf{x} on Γ . The SAW propagation at the surface Γ is studied in the linear harmonic regime at the circular frequency ω (time convention $e^{-i\omega t}$), and under the ambient conditions, with the air density ρ_e , the atmospheric pressure P_e , the adiabatic constant γ , the viscosity η , the Prandtl number Pr , the sound speed $c = \sqrt{\gamma P_e / \rho_e}$, and the air wavenumber $k_0 = \omega/c$. The BL analysis is performed for the SAW with the pressure $p = P e^{i\mathbf{k}\cdot\mathbf{x}_\Gamma - b x_3}$, where P is the complex amplitude, $\mathbf{k} = k\mathbf{e}_z$ is the in-plane wave-vector with the complex wave-number k and the in-plane unit vector \mathbf{e}_z , which makes the angle α counted from \mathbf{e}_1 , and where $b = \sqrt{k^2 - k_0^2}$ is the complex attenuation parameter in the direction \mathbf{e}_3 . For actual

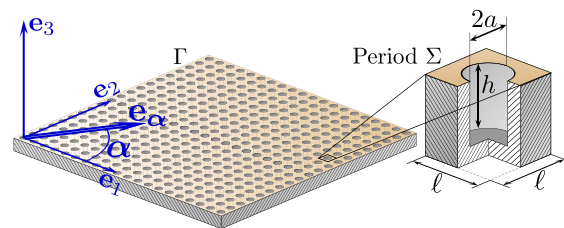


FIG. 1. Schematic of the Σ -periodic metasurface and details of the unit cell (lattice size ℓ) bearing a $2a$ -diameter and h -deep borehole resonator. \mathbf{e}_1 and \mathbf{e}_2 are the unit lattice vectors; \mathbf{e}_3 is the normal vector; and \mathbf{e}_z gives the direction of the SAW propagation.

^{a)}Electronic mail: logan.schwan@gmail.com

propagation along \mathbf{e}_x and wave attenuation, the following conditions hold: $\text{Re}(k) \geq 0$, $\text{Im}(k) \geq 0$ and $\text{Re}(b) \geq 0$.

When excited by p , the resonators act as mutually interacting secondary sources that prescribe the distribution of normal velocity $v_\Gamma \mathbf{e}_3$ at the surface Γ . Emitted by the periodic lattice while forced by the SAW, the velocity v_Γ is locally Σ -periodic, while modulated by the factor $e^{i\mathbf{k}\cdot\mathbf{x}_\Gamma}$. Since the SAW cannot resolve the array periodicity on its own, locally Σ -periodic perturbations localized in the vicinity of Γ are induced, which can be described in the low frequency range (typically $k_0\ell < 2\pi$) by a BL^{15,16} with the pressure p^* in the form

$$p^* = \sum_{(n,q) \neq (0,0)} P_{nq}^* e^{i(\mathbf{k} + \mathbf{G}_{nq}) \cdot \mathbf{x}_\Gamma - b_{nq}^* x_3}, \quad (1)$$

where n and q are integers, P_{nq}^* are complex scattering coefficients, $\mathbf{G}_{nq} = 2\pi(n\mathbf{e}_1 + q\mathbf{e}_2)/\ell$ are the reciprocal lattice vectors, and $b_{nq}^* = \sqrt{(\mathbf{k} + \mathbf{G}_{nq})^2 - k_0^2}$ are the complex out-of-plane attenuation parameters with $\text{Re}(b_{nq}^*) \geq 0$. The dispersion relation is found from the following boundary conditions that have to be satisfied by the superposition of the surface wave p and the BL pressure p^* . At the reference cell Σ , the surface is rigid, except for the borehole aperture S at its center, where a uniform particle velocity $v_o \mathbf{e}_3$ is assumed in the long-wavelength approximation.¹⁷ The velocity v_o is then related to the mean value $\langle p + p^* \rangle = |S|^{-1} \int_S (p + p^*) dS$ of the pressure $p + p^*$ acting at the aperture S through the frequency-dependent admittance Y of the resonator, that is, $v_o = Y \langle p + p^* \rangle$. For the quarter-wavelength resonator, the admittance Y takes the form (see [supplementary material](#) for details)

$$Y = i \tan(\omega h / \sqrt{B^*/\rho^*}) / \sqrt{\rho^* B^*}, \quad (2)$$

where ρ^* and B^* are the complex effective density and bulk modulus in the resonator. They account for the viscous and thermal losses in the circular borehole and are classically given by^{18,19}

$$\rho^* = \frac{\rho_e}{1 - F\left(\sqrt{2i} \frac{a}{\delta_v}\right)}; \quad B^* = \frac{\gamma P_e}{1 + (\gamma - 1)F\left(\sqrt{2i} \frac{a}{\delta_t}\right)}, \quad (3)$$

where $\delta_v = \sqrt{\eta/(\rho_e \omega)}$ and $\delta_t = \delta_v / \sqrt{\text{Pr}}$ are viscous and thermal skin-depths, and $F(y) = 2J_1(y)/[yJ_0(y)]$ is a form function^{18,19} with J_n the Bessel function of order n . The admittance Y is thus complex for the lossy resonators. Now, denoting Π_S the gate function equal to 1 over S and 0 elsewhere at Σ , the boundary conditions at the reference cell can be summarized as

$$\frac{\partial(p + p^*)}{\partial x_3} = ik_0 \rho_e c Y \langle p + p^* \rangle \Pi_S \quad \text{at } \Sigma. \quad (4)$$

First, the mean pressure over the aperture S reads

$$\langle p + p^* \rangle = P \mathcal{H}_{00} + \sum_{(n,q) \neq (0,0)} P_{nq}^* \mathcal{H}_{nq}, \quad (5)$$

where the structure factors \mathcal{H}_{nq} are given by

$$\mathcal{H}_{nq} = \frac{1}{|S|} \int_S e^{i(\mathbf{k} + \mathbf{G}_{nq}) \cdot \mathbf{x}_\Gamma} dS = \frac{J_1(K_{nq}a)}{K_{nq}a/2}, \quad (6)$$

with $K_{nq} = \sqrt{(\mathbf{k} + \mathbf{G}_{nq})^2}$. Next, multiplying Eq. (4) by $e^{-i(\mathbf{k} + \mathbf{G}_{ms}) \cdot \mathbf{x}_\Gamma}$, where (m, s) are integers, and taking the mean value over the period Σ yield Equations (7a) and (7b) for $(m, s) = (0, 0)$ and $(m, s) \neq (0, 0)$, respectively

$$-bP = ik_0 \frac{\rho_e c Y |S|}{|\Sigma|} \langle p + p^* \rangle \mathcal{F}_{00}, \quad (7a)$$

$$-b_{ms}^* P_{ms}^* = ik_0 \frac{\rho_e c Y |S|}{|\Sigma|} \langle p + p^* \rangle \mathcal{F}_{ms}, \quad (7b)$$

where the structure factors \mathcal{F}_{ms} read

$$\mathcal{F}_{ms} = \frac{1}{|S|} \int_S e^{-i(\mathbf{k} + \mathbf{G}_{ms}) \cdot \mathbf{x}_\Gamma} dS = \frac{J_1(K_{ms}a)}{K_{ms}a/2}. \quad (8)$$

Combining Eqs. (5) and (7b) provides the equation satisfied by the BL scattering coefficients. Re-arranging the double-indexation $(n, q) \neq (0, 0)$ into a single indexation, the following vectors are defined, $\{P^*\} = \text{vect}(P_{nq}^*)$, $\{\mathcal{H}\} = \text{vect}(\mathcal{H}_{nq})$, and $\{\mathcal{F}\} = \text{vect}(\mathcal{F}_{nq})$, and the diagonal matrix $[b^*] = \text{diag}(b_{nq}^*)$. With those notations, the BL scattering coefficients are given by

$$\{P^*\} = -ik_0 \frac{\rho_e c Y |S|}{|\Sigma|} \mathcal{H}_{00} P [B^*]^{-1} \{\mathcal{F}\}, \quad (9)$$

where the matrix $[B^*]$ reads, with \otimes the tensor product

$$[B^*] = [b^*] + ik_0 \frac{\rho_e c Y |S|}{|\Sigma|} \{\mathcal{F}\} \otimes \{\mathcal{H}\}. \quad (10)$$

Combining Eqs. (5), (7a) and (9), the boundary condition for the SAW takes the form $\partial p / \partial x_3 = -i\omega \rho_e Y p$ at Γ , where the effective normalized admittance is

$$\rho_e c Y = -\frac{\rho_e c Y |S|}{|\Sigma|} \left(1 - ik_0 d^* \frac{\rho_e c Y S}{|\Sigma|} \right) \mathcal{F}_{00} \mathcal{H}_{00}, \quad (11)$$

with the scalar $d^* = \{\mathcal{H}\} \cdot \{[B^*]^{-1} \{\mathcal{F}\}\}$ having the dimension of a length. More details about the derivation of Eqs. (9)–(11) are provided in the [supplementary material](#). Eq. (11) provides the micro/macro relation between the resonator properties and the effective admittance actually resolved by the SAW. The SAW dispersion relation is found by solving for k in the equation $b = ik_0 \rho_e c Y$, which shows that b and hence the wavenumber k are complex quantities when the admittance Y is not purely imaginary, which is the case for lossy resonators.

In the experiments, the resonators consist of circular boreholes with the radius $a = 18 \pm 0.5$ mm and the depth $h = 40.5 \pm 0.5$ mm drilled with the lattice size ℓ in a rigid wooden substrate. Such quarter-wavelength resonator, with the undamped eigenfrequency $\omega_o/(2\pi) = c/(4h) \approx 2117$ Hz, has been characterized in the impedance tube with the square cross-section $\Sigma = 42$ mm \times 42 mm that enables to emulate plane wave reflection at normal incidence on

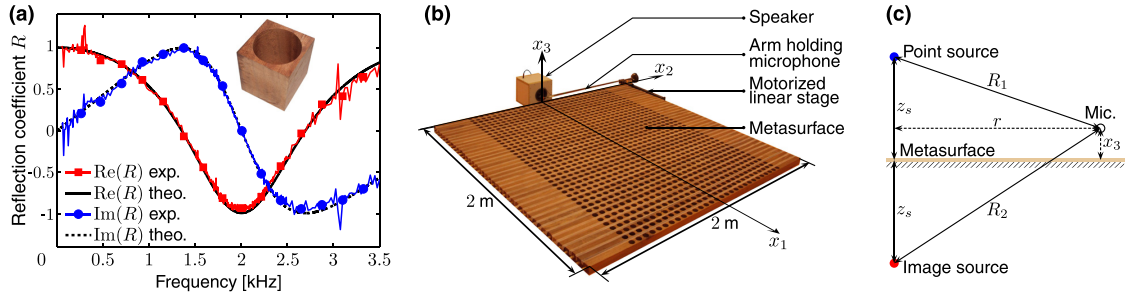


FIG. 2. (a) Comparison of the real and imaginary parts of the reflection coefficient provided by the impedance tube measurements—exp.—on a $42\text{ mm} \times 42\text{ mm}$ unit cell (see inset) and those provided by the theoretical effective admittance—theo.—(b) Experimental set-up for characterisation of SAW propagation at the metasurface prototype. (c) Model of the experimental set-up by a point source and a microphone—Mic.—above the metasurface admittance.

the metasurface with an infinite extent. Noting that the effective admittance $\rho_e c \Upsilon$ is also valid for plane wave reflection, the reflection coefficient measured experimentally is compared with the theoretical one $R = [1 - \rho_e c \Upsilon] / [1 + \rho_e c \Upsilon]$ in Fig. 2(a). The results confirm the accuracy of Eqs. (2) and (11) to describe the lossy resonators and the effective metasurface admittance.

To investigate the SAW propagation at the metasurface, semi-anechoic chamber measurements have been performed. The metasurface consists of 1160 resonators (40 along $\mathbf{e}_1 \times 29$ along \mathbf{e}_2) drilled periodically with the lattice size $\ell = 50 \pm 1\text{ mm}$ in a $2\text{ m} \times 2\text{ m}$ rigid wooden board (see Fig. 2(b)). The speaker has been positioned at the center of the smaller edge ($x_1 = 0 = x_2$) with the center of its membrane at $z_s \approx 7.5\text{ cm}$ above the metasurface. The system has been excited with a sine-sweep signal over the frequency range $[0.1; 1.6]\text{ kHz}$, in order to focus on the frequency range, wherein the SAW mode theoretically exists according to the

BL model (see Fig. 3). The pressure field has been measured with the microphone secured to a motorized linear stage. The experimental spectra have been recorded with the Dynamic Signal Analyzer (Stanford Research Systems type SR785) every 0.5 cm along the line $x_2 = 0$ at the distance $x_1 \in [x_0; L] = [5; 180]\text{ cm}$ from the speaker and at $x_3 \approx 1\text{ cm}$ above the surface.

Due to the geometrical spreading of the field from the speaker, the experimental set-up is modelled as a point-source above the metasurface admittance. Hence, the sound field consists of the pressure $p_s(\mathbf{x}) = A_0 \mathcal{G}_0(\mathbf{x}) + A_s \mathcal{G}_s(\mathbf{x})$, where A_0 and A_s are complex amplitudes, \mathcal{G}_0 is the Green function for the point source above the rigid surface, and \mathcal{G}_s is the perturbation produced by the metasurface admittance, including the SAW³

$$\mathcal{G}_0 = e^{ik_0 R_1} / (4\pi R_1) + e^{ik_0 R_2} / (4\pi R_2), \quad (12a)$$

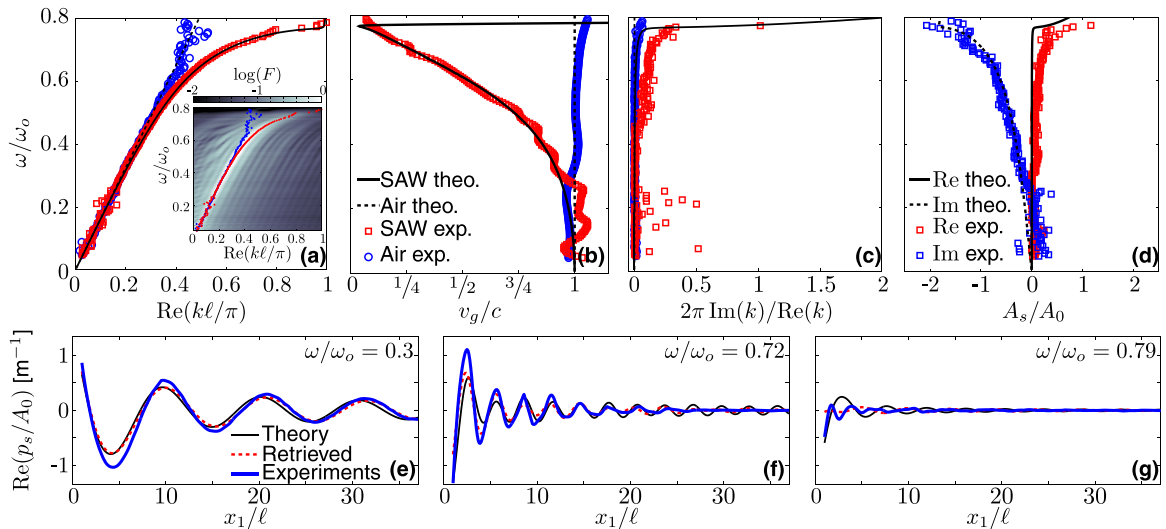


FIG. 3. Comparison between theoretical (theo.) and experimental (exp.) results. Plotted against the normalized frequency ω/ω_o are: (a) the real part and (c) the imaginary part of the air and SAW wavenumbers; (b) the normalized group velocity; (d) the amplitude ratio between the SAW and the air modes. Plotted against the normalized distance x_1/ℓ from the speaker are: (e)–(g) the pressure profile along the scan-line at three frequencies. (a) and (c) have the same legend as (b). (f) and (g) have the same legend as (e). The inset in (a) shows the spatial Fourier transform of the experimental pressure against the frequency and the dispersion relations retrieved from the SLATCoW method.

$$\mathcal{G}_s = -k_0 \operatorname{erfc}(-iw) H_0^{(1)}(kr) e^{-b(x_3+z_s)}/4. \quad (12b)$$

Here, the geometrical parameters R_1 , R_2 , and r are defined in Fig. 2(c); erfc is the complementary error function; $H_0^{(1)}$ is the Hankel function of the first kind and order 0; and $w = \sqrt{ik_0 R_2 - ikr + b(x_3 + z_s)}$ is the numerical distance. Eq. (12) shows that the field $p_s(\mathbf{x})$ vanishes as the distance from the speaker increases: the field \mathcal{G}_0 decreases typically as $1/R_1$, while the term $H_0^{(1)}(kr) e^{-b(x_3+z_s)}$ in the expression of \mathcal{G}_s decreases as $1/\sqrt{r}$. Using the pressure $p_s(\mathbf{x})$ as the ansatz field, and hence accounting for the geometrical spreading from the source, the real and imaginary parts of the wavenumbers k_0 and k , and the complex amplitudes A_0 and A_s are retrieved from the experimental data by means of the *Spatial Laplace Transform for Complex Wavenumbers—SLaTCoW—method*¹⁴ (see [supplementary material](#) for more details about the SLaTCoW procedure). The experimental results are compared with those from the BL model in Figs. 3(a)–3(d), where the complex wavenumbers, the group velocity $v_g = d\omega/d\operatorname{Re}(k)$ and the amplitude ratio A_s/A_0 (theoretically equal to³ $\rho_e c \Upsilon$) have been plotted against the frequency.

While the air line $\operatorname{Re}(k_0) = \omega/c$ with the sound speed $c \approx 342$ m/s, and negligible attenuation, $2\pi\operatorname{Im}(k_0)/\operatorname{Re}(k_0) \sim 5 \times 10^{-3}$, are recovered, three regimes can be identified in the SAW dispersion relation: at low frequency $\omega \ll \omega_o$, around the resonance $\omega \rightarrow \omega_o$, with $\operatorname{Re}(k) < \pi/\ell$, and around the Bragg limit $\operatorname{Re}(k) \rightarrow \pi/\ell$.

In the low-frequency regime, the low admittance contrast $|\rho_e c \Upsilon| \ll 1$ leads the complex SAW dispersion relation $k(\omega)$ to be asymptotic to that of air $k_0(\omega)$. Although it allows an actual propagation of the SAW with negligible attenuation, its contribution in the field remains limited due to its low amplitude $|A_s/A_0| \ll 1$. Besides, this low value of the SAW amplitude makes it difficult to retrieve the mode experimentally, which can explain the scattered experimental data below $\omega/\omega_o = 0.2$. In contrast, around the resonance at $\omega/\omega_o \sim 0.7$, the significant admittance contrast $|\rho_e c \Upsilon| \sim 1$ results in the deviation of the SAW dispersion relation from the air-line. The SAW group velocity decreases down to $v_{g,c} \sim 1/5$, while the SAW wavelength becomes $\approx 1/8$ of the characteristic attenuation length $1/\operatorname{Im}(k)$. That enables the actual propagation of the “slow sound” SAW that could be used for sub-wavelength imaging, for instance. Note that the resonant behavior of the surface microstructures is essential for this phenomenon to occur, since it is responsible for the significant admittance contrast $|\rho_e c \Upsilon| \sim 1$ at the origin of the SAW excitation. However, the capacity to guide waves along the surface with such a “slow sound” is rapidly hindered by the SAW attenuation, as the dispersion curve approaches the Bragg limit $\operatorname{Re}(k) \rightarrow \pi/\ell$. As the group velocity approaches zero, the SAW attenuation increases drastically with a characteristic attenuation length $1/\operatorname{Im}(k)$ of the order of the SAW wavelength, which prevents the effective propagation of the wave at the surface. Note that the interaction of the resonance-induced dispersion relation with the Bragg limit $\operatorname{Re}(k) = \pi/\ell$ makes the “bandgap” occur at $\omega/\omega_o \approx 0.8$. Lowering the resonance frequency would certainly make the dispersion relation cross the Bragg limit at the resonance frequency $\omega/\omega_o \approx 1$.

The retrieved dispersion relation is in good agreement with the maxima of the experimental spatial Fourier transform $F(k_r) = \int_{x_0}^L p_s/A_0 e^{-ik_r x_1} dx_1$ plotted in the inset of Fig. 3(a). This latter also exhibits clearly the regime of highly attenuated waves around $\omega/\omega_o \approx 0.8$, wherein $|F(k_r)| \rightarrow 0$. The experimental results are also in well agreement with the theoretical model derived for plane waves. It highlights the accuracy of the effective admittance $\rho_e c \Upsilon$ and underlines that the complex dispersion relation is related more to the metasurface admittance and less to the nature of the excitation.

Finally, Figs. 3(e)–3(g) show the pressure profile $\operatorname{Re}(p_s/A_0)$ for frequencies in each SAW propagation regime. It is compared with the profile computed using either the effective admittance $\rho_e c \Upsilon$ or the parameters retrieved from the SLaTCoW method. A good agreement is reached between them. Discrepancies between the theoretical and experimental results in Fig. 3(g) can be due to the conjugate effect of near-fields produced by the speaker in its close-vicinity (where the field is actually confined), and the low level of the signal near the bandgap. Nevertheless, the results show the strong confinement of the field close to the speaker as the frequency increases. That suggests that tracking pulses on distances sufficiently long to perform imaging could be more challenging than in optics.²⁰

In conclusion, a boundary layer model that enables to find the effective surface condition satisfied by plane waves at the metasurface has been proposed, which takes full account of multiple interactions, surface periodicity, and viscothermal losses in the resonators. The complex dispersion relation theoretically derived has served to validate that experimentally retrieved using the SLaTCoW method, adapted for point-source excitation. The results have exhibited the mode conversion that occurs between bulk and surface waves in the presence of the metasurface, and they have shown that SAW propagation, while strongly slowed around the resonance, can become drastically attenuated even with weakly damped resonators, hence preventing actual propagation. This underlines the importance of considering the imaginary part of wavenumbers when designing spoof surface plasmon acoustic devices.

See [supplementary material](#) for more details about the boundary layer model and the adaptation of the SLaTCoW procedure to the problem of the point source above the metasurface admittance.

The authors are grateful to the French ANR project Metaudible (ANR-13-BS09-0003) and the COST Action DENORMS-CA15125, supported by COST (European Cooperation in Science and Technology).

¹K. A. Norton, *Proc. IRE* **24**, 1367 (1936).

²A. R. Wenzel, *J. Acoust. Soc. Am.* **55**, 956 (1974).

³C. F. Chien and W. W. Soroka, *J. Sound Vib.* **43**, 9 (1975).

⁴K. Attenborough, S. I. Hayek, and J. M. Lawther, *J. Acoust. Soc. Am.* **68**, 1493 (1980).

⁵D. G. Albert, *J. Acoust. Soc. Am.* **113**, 2495 (2003).

⁶L. Kelders, J. F. Allard, and W. Lauriks, *J. Acoust. Soc. Am.* **103**, 2730 (1998).

⁷J. B. Pendry, L. Martín-Moreno, and F. J. Garcia-Vidal, *Science* **305**, 847 (2004).

⁸H. Jia, M. Lu, Q. Wang, M. Bao, and X. Li, *Appl. Phys. Lett.* **103**, 103505 (2013).

⁹H. Jia, M. Lu, X. Ni, M. Bao, and X. Li, *J. Appl. Phys.* **116**, 124504 (2014).

- ¹⁰Y. Ye, M. Ke, Y. Li, T. Wang, and Z. Liu, *J. Appl. Phys.* **114**, 154504 (2013).
- ¹¹M. Addouche, M. A. Al-Lethawe, A. Choujaa, and A. Khelif, *Appl. Phys. Lett.* **105**, 023501 (2014).
- ¹²D. Torrent and J. Sánchez-Dehesa, *Phys. Rev. Lett.* **108**, 174301 (2012).
- ¹³Z. He, H. Jia, C. Qiu, Y. Ye, R. Hao, M. Ke, and Z. Liu, *Phys. Rev. B* **83**, 132101 (2011).
- ¹⁴A. Geslain, S. Raetz, M. Hiraiwa, M. A. Ghanem, S. P. Wallen, A. Khanolkar, N. Boechler, J. Laurent, C. Prada, A. Duclos, P. Leclaire, and J.-P. Groby, *J. Appl. Phys.* **120**, 135107 (2016).
- ¹⁵C. Boutin and P. Roussillon, *Int. J. Eng. Sci.* **44**, 180 (2006).
- ¹⁶C. L. Holloway and E. F. Kuester, *Radio Sci.* **35**, 661, doi:10.1029/1999RS002162 (2000).
- ¹⁷C. Lagarrigue, J.-P. Groby, V. Tourmat, O. Dazel, and O. Umnova, *J. Acoust. Soc. Am.* **134**, 4670 (2013).
- ¹⁸C. Zwikker and C. W. Kosten, *Sound Absorbing Materials* (Elsevier Publishing Company, Inc., 1949).
- ¹⁹M. R. Stinson, *J. Acoust. Soc. Am.* **89**, 550 (1991).
- ²⁰H. Gersen, T. J. Karle, R. J. P. Engelen, W. Bogaerts, J. P. Korterik, N. F. van Hulst, T. F. Krauss, and L. Kuipers, *Phys. Rev. Lett.* **94**, 073903 (2005).

